ENCAPSULATION MATERIALS FOR FLEXIBLE ELECTRONICS



JUSTIN SY LIMKAICHONG

ST. PETERS COLLEGE

UNIVERSITY OF OXFORD

DPhil in MATERIALS

July 2025

SUPERVISOR: PROF. HAZEL ASSENDER

© 2025 by Justin Sy Limkaichong
All rights reserved.

Abstract

Advancements in the encapsulation of flexible electronics have been significantly impeded by the limitations of water vapor barrier properties in protective layers. This study employs a novel defect imaging calcium test (Ca test) with a copper backing layer to explore and characterize defects that serve as permeation pathways leading to device failure. A foundational methodology was established by comparing estimated water vapor transmission rate (WVTR) values from the Ca test with those obtained using the conventional Mocon Aquatran 2 permeation tester on standard polyethylene terephthalate (PET) substrates. By validating the Ca test on bare PET samples and addressing the relationships due to temperature and relative humidity, permeability coefficients and apparent activation energies were derived. These thermodynamic parameters served as a baseline for distinguishing between solubility dominated transport mechanisms (characteristic of the bare substrate) and diffusion dominated transport (characteristic of effective barrier layers), elucidating the nature of defect mediated permeation.

The research subsequently explored aluminium oxide (AlO_x) barrier layers made by atomic layer deposition (ALD), a deposition technique selected for its potential to deposit with making uniform and conformal coatings, on PET substrates. Application of the coating resulted in significant improvements in water vapor barrier properties, though still above the ultra-barrier targets typically reported for flexible OLED/OPV encapsulation (WVTR ~10^{-6} g/m^2·day at 25 °C at 40% RH, and ~ 10^{-4} - 10^{-6} g/m^2·day for > 10,000 – hour device lifetimes). Analysis was made of the nature and spatial density of defects in the coated PET substrates across various coating thicknesses. Findings

indicate that despite a very low contribution to permeation of nano defects of ALD coatings in comparison to radio frequency (RF) magnetron sputtered films, microdefects such as contaminations, inclusions, or coating damage limit further reduction in WVTR.

The thesis also investigates ALD-coated polyvinyl alcohol (PVAl) substrates as an example of an ALD coating to enhance water vapor barrier properties of a hydrophilic biodegradable substrate with a rough surface. The addition of an ALD coating not only improved barrier properties but also provided insights into defect characteristics and potential improvements for PVAl substrates. Thin AlO_x coatings on PVAl exhibited more linear defects, which were less evident in thicker coatings, contrasting with the spot-like defects observed in ALD-coated PET substrates.

Extensive coding and spot identification work was performed, demonstrating a correlation between the total defect area and the permeability of both types of coated substrates; showing how the total defect area can be used to potentially model future barrier layers for the studied coating thicknesses.

Overall, this work advances the field of thin film encapsulant layers, for example for application in flexible electronics, by enhancing the understanding of permeation mechanisms using the Ca test, improving its reliability, and employing statistical analysis and coding to obtain spatial density information in coated PET and PVAl samples. It provides a solid foundation for future research on barrier layers, coating methods, substrates, and multi-structure systems requiring ultra-low water vapor permeation rates.

Dedicated:

To Prof. Hazel Assender and Lawrence Limkaichong Jr.

For giving me strength and being the bravest people,

I know and aspire to be, and for F!@#ing (“Fighting”) Cancer up.

I began this journey almost a decade ago (11 years – 2014 – 2025),

Filled with the hope of changing the world.

But along the way, I discovered it was

I who needed to change.

As Seneca once said, “*What need is there to weep over parts of life?”*

“The whole of it calls for tears.”

And in their unique ways, art such as this work you are going to read and philosophy, as Alain de Botton reminds us, help us transform those tears into wisdom, and echoing Schopenhauer's insight that our struggles that can lead to understanding.

Was it all worth it?

I cannot say for certain.

But the seeds we sow today will, in time,

Bear fruit and grow.

To everyone who took a chance on this lovable idiot—thank you.

This journey has been as much yours as it has been mine.

Acknowledgements:

Playing Buds: Dr. Shiling Dong*, Dr. Kai Ling and Dr. Tongshan Liu
Grandma's: Petra Limkaichong and Anesia Sy.
My Moms: Jocelyn Limkaichong, Linda Ybarsabal, Feling Tambiga, and Nina Patawaran, - for reminding to always take a bath, brush my teeth and go to Church.
Big Boy Man / **Best Xue Zhang:** Dr. Botao Hao – let's go buddy, lightweight!, **Best Technicians:** Richard Turner and Greg Cook, **My favourite Wizard (Most important Australian):** Dr. Harry Potter., **Kindest Brother and Life Adviser:** Wu Zheng, **XC!:** Xiaohang Cai, **Kindest Sister and Life Adviser:** Nayantara Srinivasan, **The dude with the best Rizz:** George Tebbutt, **Love of my Life and my King:** Dr. John Ballentine, **Bester Mathematiker, Brother from another mother:** Finn Wiersig,, **deutscher Bruder:** Michael Metzler, **Midnight Shower Thoughts:** Katherina Majer, **Taiwan Captain:** Ping Yuan Mr. Allen Lee, **Begbroke and Life mom**: Dr. Yun Deng
Mola, Jinja, Chemi-opso – Molang: Dr. Insung Han, **Ni Zai Na Li? Ni Zai wo Xin li**: Dr. Zhonghua Ren, **I'm unranked my lord:** Cameron Favell Gallifant, **Xie Xie:** Runing Jin, **Still owe Ryan since 1st year!:** Ryan Schofield, **Future Doctor:** Alana Chandler
Avocado Bud: Dr. Barbara Macijiewska, **London Penthouse:** Dr. Jieming Zhang
Kindest Post Doc Award: Dr. Yige Sun, **Live life to the fullest:** Dr. Dillon McGurty, **Toughest but most mellow guy I know:** Dr. Eoin Sullivan, **We got this:** Dr. Qianfang Zheng, **We survived the Synchrotron!:** Dr. Sean Telford, **Future Economic Leader**: Dr. Wentao Li, **The man who will save us from AI:** Dr. Andrew Campbell, **UK Government:** Molly Lewis, **French Emperor:** Dr. Oscar Clivio, **Multi-linguist Educator**: Phil Mahoney, Blood Brother: Amaury Jousset-Drouhin
OPS society – Tita's and Tito's (Atty. Patricia Geraldez, Dr. Liezel Tamon, Dr. Ivan Lazarte, Dr. Danica Salazar, Tito Jose Medriano, Dr. Zython Lachica, Dr. Jesus Acapulco, Atty. Julia Pineda.), Dr. Shania Ibarra, Dr. Danilo Dela Cruz, Dr. Greco Malijan, Dr. Paolo Cerrado, Dr. Leo Tyrpak.
St. Peter's Rugby: (Capt. Jonah Veakins, Chris Gilmore, Rueben Harris, Brian Kwizera, Will Vanhinsbergh, Hector Wilton, George Robson, Gus Sandham, Capt. Freddy Wood, Michael Donlon) Ben Aldridge
Begbroke Prisoners: Nathan Brown, Yixin Xu, Elysia Zdolyny, and Quinxan Yang
Oxford Chinese Basketball and Basketball: Dr. Chen Chen, Dr. Xin Liu, and Dr. Yuxing Zhou, Dr. Romain Guyon.
Materials: Prof. Sebastian Bonilla Xinya Niu for ALD, Dr. Kai Zhang and Dr. Xudong Tao, Lorraine Laird, Sharmaine Iljada, Dr. Adrian Taylor,
Begbroke Science Park: Nicola Mason (née Flanagan), Dr. Colin Johnston, Lucy Penny, Chris Salter, Begbroke Reception and drivers Sean and Dave.
Important Corporate / Industry Thank you: Aquapak Polymers (Lucia Blaco Loarte)
Disability Adviser: Jane Clark
Brothers: Lawrence (Lance) Limkaichong III, Luke Limkaichong, Leonard Limkaichong worst brothers one can ask for, but the best one's Justin has.
Sisters: Ebony Ariane Lautner and Stephanie Uymatiao
Aunts and Uncles: Julieth Sy De Alwis, Jeanne Krebs, Julio Sy Jr, Pia Sy, Jonathan Sy and Lily Sy, Anil De Alwis, Ellen Limkaichong, Dolly Litam,, Ann Limkaichong, Sha

Sha Sy Chua, Jun Chua, Jame and Thien Sylora, Karen Chu, Vernon Chu, Roxanne Tracy – Sylora, Margie Vivit, Ed Vivit, Mei-Ai Kho, Valentina Sy, Edelina Go, Rosalinda Sy, Len Chua, Patrick Chua, John Sylora, Shirley Uy, Katherine Chua, Linda Kho, Marvin Kho, Sarah Tan, Misael Tan, George Bustamante, Dean Sy, Joy Kho, Marlyn Lee, David Meija, Amy Khalili, Ann Beth Sy, Danford Sy, Nadine Bustamente, Raena Sy, Kristine / Ris Ris Sy, Marianne Mae Sy-Ang, Neil Ang, Raena Sy, Laura Sy, Lea Bersamin, Beulah Cabillo, Louis Deval
Cousins: Annika Sy, Sebastian (Sage) Sy, Jay Sy, Louie Sy, Karina Krebs, Kyle Krebs, Jermaine Sy, Maia Sy, Jade Sy, Aldric Chua, Jai Jeun, , Catherine Lee, Stefan Jeun, Riley Chua, Ashley Chua, Aira Chua, Derrick Chu, Brandon Chu, Andrew Sylora, Rachel Sylora, Christina Vivit, Jeremy Vivit, Rendell Uy, Ronan Uy, Emmanuel Iway, Patrick James Iway, Lourdes Iway, Benedcit Lim, Don Lim, Mandy Iway, Darryl Juan, Charles Juan, Darlene Litam, Danessa Litam, Jojo Litam, Joseph Alcalde, Ariane Marchis Mouren, Nicolas Mouren
Examiners: Prof. Robert Hoye and Dr. Glen West.
Work Colleagues at Unilever: Dr. Alexandra Collet, Pratik Kanade, Dr. Mohammad Marvi-Mashhadi, Dr. Brian Jones, Dr. Georgia Duffy, Dr. Joshua Booth, Dr. Maria Jimenez-Solomon, Dr. Emile Engel, Dr. Mark Newman, Dr. Christopher Ellingford, Dr. Myles Blurton, Dr. James Boden, Dr. Marta Chiapasco, Jill Cowell, Dr. Devon Crouch, Rachel Ganzon, Dr. Rebecca Gibson, Dr. Kane Heard, Daniel Hall, Dr. Natalia Herrera-Vargas, Ezgi Kuru, Dion Moran, Elena Pensa, Anna Colley, Amy Wetton, Jessica Peake, Oliver Evenden, Liam Breen, Morgan Adams, Pearl Onyeneke and Matthew Daniels.

For Elliot, Sabine, and Franco best screen savers of my DPhil Life
Some Awesome Friends –
to the three people who shouldn't meet in the Asakusa Shrine:

Washington – Igbo and Shayo, maybe in another life my ayo; Xiao Ben Dan

Lavender – Thank you for everything; I know I wasn't good enough, but I hope you find the 6'5" Taylor Swift–singing, Harry Potter–loving, Michelin-star–cooking finance bro you deserve.

To the last one who I have yet to meet (have now met).*

My other friends (One's I atleast remember),
Avocado, Philippines, Fencing, Tennis, Basketball, SPC, Touch Rugby, Netball

Blue – Thank you for always being there for me. We laugh about it now!
Piao Liang Peng You

White Yellow Lion – Marmite and Twiglets! You're the most compassionate and kindest person on the Milky Way. Here's to the friendship, and I'd love to fund that Polar trip someday.
:)
Avocados are growing well.

Table of Contents

Abstract 3

Dedicated: 5

Acknowledgements: 6

Table of Contents 8

List of Illustrations 22

List of Abbreviations 71

1 Introduction 73

1.1 Improving the field of Flexible Electronics (FE) 73

1.2 What are Flexible Barriers? 76

1.3 Permeation Barrier 79

1.4 Background on Permeation Theory 82

1.5 Pinhole Defects (Nano and Macro) 88

1.5.1 Macro and Nano Defects 89

1.5.2 Contaminants 91

1.5.3 Sideways Permeation 92

1.5.4 Bulk Permeation 93

1.6 Characterization of Films 93

1.6.1 Calcium Test 93

1.6.2 MOCON Aquatran (Water Vapour Permeation Analyser)..... 97

1.7 Creation of Barrier Layers (Thin film Deposition)..... 99

1.7.1 Physical Vapour Deposition (PVD)..... 100

1.7.1.a Thermal Evaporation..... 100

1.7.1.b Sputter Deposition 102

1.7.2 Chemical Vapour Deposition (CVD)..... 103

1.7.2.a Atomic Layer Deposition (ALD)..... 104

1.8 Conclusion 108

1.9 Summary and Outlook..... 109

2 Methodology..... 110

2.1 Overview of Testing Methodology..... 110

2.2 Testing Standards..... 110

2.3 MOCON Aquatran 2..... 111

2.4 Calcium Test..... 112

2.4.1 Calcium Test Overview (Standard) 113

2.4.1 Calcium Test Structure 117

2.4.2 Copper Thickness..... 122

2.4.3 Calcium Test Set-up..... 126

2.4.4 Calcium Deposition Caveats and Contamination 130

2.4.5 Measuring WVTR, Permeability and Activation Energy..... 131

2.4.5.a WVTR Calcium Test Estimation 131

2.4.6 Fluence Calculation Example 140

2.4.6.a Mean Intensity Measurement 141

2.4.6.b Edge Effects / Non-Uniformity Calcium Depletion 145

2.4.7 Permeability and Activation Energy 147

2.4.8 Normalizing the Images 149

2.4.8.a Image to Image Variations 149

2.5 ALD Parameters 150

2.6 Surface Characterization Tools 155

3 Uncoated Polyethylene Terephthalate (PET) Substrates 157

3.1 Introduction to Uncoated PET Substrates 157

3.2 Properties and Performance of PET Films 158

3.3 WVTR Measurements for Uncoated PET Films (MOCON) 163

3.3.1 Preparation of PET Film Samples for MOCON Testing 163

3.3.2 MOCON Temperature and Relative Humidity on Uncoated PET . 164

3.3.3 Determination of the Ea of Uncoated PET Substrate (MOCON) ... 168

3.4 Calcium Test: Uncoated PET film Substrate 170

3.4.1 Transition Time and WVTR Determination for Uncoated PET 170

3.4.1.a Transition Region, and Fluence at Saturation 170

3.4.2 Example Calculation and Environmental Influence 171

3.4.3 Factors that affect Onset Time 172

3.4.3.a Influence of Temperature and RH on Onset Time 173

3.4.3.b Other Factors that Influence Onset Time (Ca and Cu layer) 175

3.4.4 Effect of Temperature and RH on WVTR Using the Ca Test 177

3.4.5 Activation Energy of Uncoated PET (Calcium Test) 179

3.5 Comparison of Activation Energy in Literature 181

3.5.1 Calculating Activation Energy of Literature 181

3.5.2 Summary of Activation Energies 182

3.6 Permeation Analysis of Uncoated PET Films 183

3.6.1 Intrinsic Permeation of PET Films 184

3.6.1.a Permeation of PET at Different Thicknesses (Literature) 184

3.6.1.b Permeation Variations Due to Testing Methods 186

3.6.1.c Permeation Across Temperature and Humidity Ranges 187

3.6.2 Permeation Analysis: Role of Water Vapour Partial Pressure and Comparative Methodologies 189

3.6.3 Permeability of PET 193

3.6.3.a Effect of Temperature on Permeability of PET 195

3.6.4 Estimating Activation Energy (Permeability Coefficients) 198

3.6.4.a Calcium Test Ea (Permeability) 198

3.6.4.b MOCON Test Ea (Permeability) 200

3.6.4.c Literature Values Ea (Permeability) 202

3.6.4.d Summary Activation Energy (Permeability) 203

3.7 Summary 208

4 Aluminium Oxide - AlO_x (ALD) Coated PET 210

4.1 Encapsulation with ALD 210

4.2 AlO_x on PET – MOCON Aquatran 212

4.2.1 Key Factors in Measuring WVTR of AlO_x Using MOCON Aquatran 212

4.2.1.a Temperature Effects on WVTR of ALD AlO_x 212

4.2.1.b Influence of ALD Thickness of WVTR of ALD AlO_x 214

4.2.2 Permeability of AlO_x-Coated PET (MOCON Aquatran) 217

4.2.3 Ea of AlO_x-Coated PET (MOCON Aquatran) using WVTR 219

4.2.4 Ea of AlO_x-Coated (MOCON Aquatran) using Permeability 222

4.3 AlO_x on PET (ALD) – Ca Test 226

4.3.1 Permeability Estimations of AlO_x on PET 226

4.3.2 ALD – AlO_x and RF Sputtered - Al_2O_3 or (AlOx) 228

4.4 Edge Permeation in the Calcium Test 234

4.4.1 Estimating WVTR using Constant Region of Interest and Accounting for Edge Effects (Calcium Region Isolation) 236

4.5 Activation Energy of AlO_x on PET Substrate 238

4.5.1 Ea of AlO_x Coatings (Ca test) using WVTR 238

4.5.1 Ea of AlO_x Coated PET (Ca test) using Permeability 240

4.6 Analysis of Defects (Spots) in ALD AlO_x coating 242

4.6.1 Pre-Analysis (Thresholding) of Spots – Using Fiji/ImageJ 243

4.6.2 Differentiating Isolated and Coalescing Spots (Python) 250

4.6.2.a Methodology for Enhanced Spot Detection (Python Based) 250

4.6.2.b Limitations and Challenges of Current Python Workflow 253

4.6.2.c Spot Density Example (14.0 nm AlO_x – PET) 256

4.6.3 Spot Density Estimation Results (Python Code) 259

4.6.3.a Summary of Spot Density – Python Estimations 259

4.7 Calcium Test Defect Size Calculations 264

4.7.1 Defect Size Definition 268

4.7.1.a Summary of Defect Sizes 269

4.8 Influence of Spots and Defect Sizes to AlO_x Barrier Properties 272

4.8.1 Total Defect Area Index 272

4.8.1.a Total Defect Area over Coating Thickness 273

4.8.1.b Impact of Total Defect Area on WVTR 275

4.9 Surface Analysis of AlO_x Barrier Layers on PET 280

4.9.1 Film Characterization of Uncoated PET 280

4.9.2 Film Characterization of Coated AlO_x ALD PET 284

4.9.2.a Microscopy Defect Probability Analysis 285

4.9.2.b Surface Morphology and Defects 287

4.10 Conclusions 290

5 Aluminium Oxide (ALD) Coated PVAl 292

5.1 Biodegradable Substrates for Flexible Electronics 292

5.2 Comparison of Uncoated PVAl MOCON Aquatran Results 295

5.3 Activation Energy of PVAl Mocon Aquatran 296

5.4 Evaluating WVTR of PVAl Using Ca Test 299

5.4.1 Presence of Nano defects in Coated PVAl Layers 300

5.4.2 Overall Barrier Measurements of Coated PVAl (Ca Test) 304

5.4.2.a WVTR of AlO_x Thin PVAl (Betol) 304

5.4.2.b WVTR of AlO_x Thick PVAl (Alpine) 306

5.4.2.c Permeability of AlO_x Thin PVAl (Betol) 308

5.4.2.d Permeability of AlO_x Thick PVAl (Alpine) 310

5.5 Surface Analysis of Uncoated and AlO_x-Coated PVAl Films 311

5.5.1 Uncoated / Bare Thin PVAl and Thick PVAl 313

5.5.2 Coated AlO_x Thin and Thick PVAl 315

5.5.2.a Coated AlO_x Thin PVAl 319

5.5.2.b Coated AlO_x Thick PVAl 322

5.5.3 Relationship to Calcium Test and Estimated WVTR 324

5.5.4 Impact of Humidity on Surface Morphology and Defect Formation in PVAl 326

5.6 Defect Analysis of Coated PVAl Films 331

5.6.1 Defect Characterization Using Python for Isolation and Coalescing Features 332

5.6.2 Defect Distribution of AlO_x Thin PVAl 333

5.6.2.a 26 nm Defect Distribution of AlO_x Thin PVAl 333

5.6.2.b 96 nm Defect Distribution of AlO_x Thin PVAl 338

5.6.3 Statistics of Defect Populations in AlO_x on Thin PVAl and Thick PVAl 342

5.6.3.a Summary of Spot Densities of Coated PVAl Substrates 350

5.7 Defect Size / Area Estimation in Coated PVAl Films 352

5.7.1 Assumptions of Defect Size / Area 353

5.7.2 Example of Defect Size Calculation (26 nm Thin PVAl Substrate Defects) 353

5.7.3 Summary of Defect Size and Area 360

5.8 Total Defect Area Calculation of PVAl 362

5.9 Conclusions and Insights AlO_x (ALD) Coated PVAl 366

6 Methodological Uncertainty and Limitations 369

6.1 Introduction 369

6.2 Critical Evaluation of Material Synthesis and Deposition Fidelity 369

6.2.1 Stoichiometry and Structural Limitations of Low Temperature Alumina 370

6.2.2 Nucleation Delay and Substrate Dependent Growth 372

6.2.3 Extrinsic Defect Sources and Process Control Variability 373

6.2.4 Clarification on Negative Activation Energy 376

6.3 Calcium Test Methodology Analysis 378

6.3.1 Calcium Film Purity and Deposition Artefacts..... 378

6.3.2 UV Induced Substrate Degradation during Epoxy Encapsulation.. 380

6.3.3 Assumptions in WVTR Estimation (Stoichiometry and Chemical Specificity) 384

6.3.4 Effect Ex-Situ Observation (Intermittent Measurement) in Ca Test 385

6.4 Future Strategies for Defect Characterization 387

7 Conclusion 390

7.1 Future work and Recommendations 391

8 Bibliography 394

9 Appendix..... 427

9.1 Methodology Supporting Material..... 427

9.1.1 Sample Masks 427

9.1.2 Calcium Test Negative and Positive Control 430

9.1.3 Miscellaneous Improvements 431

9.1.3.a Temperature Profile and Issue of Fogging 432

9.1.3.b Solutions to Fogging 432

9.1.3.c Calibration Bar 433

9.1.3.d Cleanliness Protocol and Epoxy Curing Time 436

9.2 Uncoated PET Substrate Supporting Materials 438

9.2.1 Linear Dependence of Permeation on WVPP: Influence of Temperature and Experimental Variability 438

9.3 Aluminium Oxide (ALD) Coated PET Supporting Materials 443

9.3.1 Relevant Literature Summary on ALD AlO_x Barrier Coatings 443

9.3.2 Sample Preparation 449

9.3.3 ALD AlO_x Thickness (Ellipsometer) 450

9.3.4 ALD Processing Temperature and Sample Masking Considerations 455

9.3.4.a Influence of ALD Processing Temperature 455

9.3.4.b Masking and Sample Defects in ALD AlO_x WVTR 457

9.3.4.c Summary of Processing Temperature and Masking in ALD 459

9.3.5 Statistically Verifying Influence of Temperature and Relative Humidity Towards Permeability of AlO_x films on PET Substrate. 460

9.3.6 Methodology for Addressing Edge Permeation and Barrier Assessment 462

9.3.7 Impact of Edge Permeation on ALD AlO_x-Coated PET: Whole-Region and Localized Error Analysis 466

9.3.7.a Whole Region: Impact of Sideways Permeation and Potential Errors on WVTR and Particle Analysis 466

9.3.7.b Particle Analysis and Regional Variability in Permeation Dynamics 468

9.3.7.c Percent Error of Not Accounting for Edge Permeation 471

9.3.8 Particle Analysis on RF Sputtered Films 472

9.3.9 Influence of Thickness and Environmental Conditions on Spot Formation 476

9.3.9.a Low Relative Humidity (39.5% $MgCl_2$ at 25°C) 477

9.3.9.b High Relative Humidity (78.5% $MgCl_2$ at 25°C) 480

9.3.9.c Influence of Temperature on Spot Density 483

9.3.9.d Spot Density (Low RH – 39.5%) 487

9.3.9.e Spot Density (High RH – 78.5%) 490

9.3.10 Example: Defect Size Estimation Calculations 492

9.3.10.a Defect Calculations for Various Thicknesses 494

9.4 Aluminium Oxide (ALD) Coated PVAl Supporting Materials 499

9.4.1 Biodegradable Substrates for Flexible Applications 499

9.4.2 Polyvinyl Alcohol (PVAl) Substrate 500

9.4.3 Synthesis of PVAl..... 501

9.4.4 Properties of PVAl..... 502

9.4.4.a Mechanical Properties Dependent on Water Content:..... 503

9.4.4.b Degradation:..... 504

9.4.4.c Crosslinking: 505

9.4.4.d Applications:..... 506

9.4.5 WVTR Measurement for uncoated PVAl MOCON Aquatran..... 507

9.4.5.a Challenges in Measuring PVAl WVTR with Mocon Aquatran 507

9.4.5.b Discussion on Mocon Aquatran WVTR Results 508

9.4.5.c Thin PVAl (Betol) Mocon Aquatran 509

9.4.5.d Thick PVAl (Alpine) Mocon Aquatran 511

9.4.5.e Estimations of coated PVAl Samples at Diff. Humidities. 513

9.4.6 Supplementary Ca Test Results for Uncoated and Coated PVAl Films 514

9.4.6.a Measuring Uncoated Thin and Thick PVAl Ca Test 514

9.4.6.b Measuring ALD AlO_x Coated Thin and Thick PVAl Calcium Test 520

9.4.6.c Thin PVAl (Betol) Representative Plots Over Thickness..... 520

9.4.6.d Thick PVAl (Alpine) Representative Plots Over Thickness 524

9.4.6.e Representative Features in Coated PVAl Layers 529

9.4.7 Supplementary Defect Analysis of ALD-Coated PVAl Films 530

9.4.7.a Initial Methodology Estimations (Image J) - Imprecisions 530

9.4.7.b Defect Density Estimations – Initial Methodology (Image J) ... 531

9.4.7.c Average Defect Spot Size of Coated PVAl Films Initial Methodology (Image J) 532

9.4.7.d Initial Methodology (Image J) – Main Points 533

9.4.8 Spot Density and Identification of Defects (Python Code) 533

9.4.8.a 50 nm Defect Distribution of AlO_x Thin PVAl 534

9.4.8.b Defect Distribution of AlO_x Thick PVAl 539

9.4.8.c 26 nm Defect Distribution of AlO_x Thick PVAl 539

9.4.8.d 50 nm Defect Distribution of AlO_x Thick PVAl 542

9.4.8.e 96 nm Defect Distribution of AlO_x Thick PVAl 545

9.4.9 Supporting information - Statistics of Defect Populations in ALD – AlO_x PVAl 547

9.4.9.a AlO_x PVAl Thin PVAl Statistics 547

9.4.9.b AlO_x PVAl Thick PVAl Statistics 552

9.4.10 Supporting information - Statistics of Defect Sizes in ALD – AlO_x PVA 557

9.4.10.a 50 nm Thin PVAl Substrate Defects 557

9.4.10.b 96 nm Thin PVAl Substrate Defects 561

9.4.10.c 26 nm Thick PVAl Substrate Defects 567

9.4.10.d 50 nm Thick PVAl Substrate Defects 571

9.4.10.e 96 nm Thick PVAl Substrate Defects 576

9.5 MOCON Aquatran Data Set for Uncoated PET 580

9.6 Calcium Test Data Set for Uncoated PET 582

9.7 Python - Code for Isolated (Labelled Unique Here) and Coalescing Spots (Condensed) 584

9.8 Defect Analysis Largest Particle Assumption 590

10 Appendix Bibliography 595

List of Illustrations

Figure 1-1.: (a) General Parts of a Flexible Electronic device, (b) Parts of an Encapsulated OLED and Common types of Encapsulations (c) Inorganic or Rigid Encapsulation, (d) Thin Glass or Flexible Metal Foil and (e) Thin Film Organic Polymers, collated from sources: [10, 12, 45, 48, 62-65]. 79

Figure 1-2: WVTRs: Number line of current existing materials (top), requirements for common applications (bottom) and WVTR limits of common test methods [14, 26, 28, 45, 46, 59, 61, 62, 64, 68-71, 87]. 82

Figure 1-3: Process of Solution and Diffusion of Permeants through a Polymer Film of Thickness (l). The left side represents high concentration or partial pressure, while the right side shows low concentration and partial pressure (Redrawn from: [51, 60, 70, 90, 91]). 84

Figure 1-4: Modes of Permeation – (1) Pinhole Defects (nano and macro), (2) Contaminants (dust particles and inclusions), (3) Sideways Permeation (between encapsulant layer and substrate) and (4) Bulk Permeation (through oxide layer or encapsulant layer). 89

Figure 1-5: Schematic representation of different gas/vapor permeation pathways through barrier materials: (a) Macro-defect (unhindered) – permeants pass freely through large openings, with Ea determined by the substrate; (b) Nano-defect (hindered) – permeants interact with defect walls, increasing Ea relative to substrate; (c) Lattice permeation – permeants traverse the bulk polymer matrix, requiring tight passage through sub-nanometre gaps, resulting in a sharp rise in Ea. Adapted from [11, 92, 102]. 90

Figure 1-6: Representative relationship of Transmission Rates to Encapsulant (Coating) Thickness describing a critical thickness and limit or optimal encapsulant thicknesses. 92

Figure 1-7: Variations of Calcium Tests for WVTR Measurement – (a) Total Rate Test, (b) Electrical Calcium Test – type of Total Rate Test, (c) Optical Imaging Test, (d) Defect Imaging Test with Copper – type of Optical Imaging Test..... 95

Figure 1-8: Diagram of the MOCON Water Vapor Transmission Rate (WVTR) test system, consisting of two chambers: (a) Chamber I, which contains a cell with controlled water vapour levels, regulated by (f) generated relative humidity and monitored by (g) probe, and circulated through the (h) outlet; and (c) Chamber II, a dry cell with (e) carrier gas. Water vapour permeates through the (b) test sample and is detected by a (d) phosphorous pentoxide (P_2O_5) sensor..... 98

Figure 1-9: Schematic of ALD process: (a) initial substrate prepared for functionalization through repeated cycles, (b) mass adsorbed per cycle to achieve desired layer thickness, (c) the four key steps are (c.1) Introduction of Precursor A, which reacts with the substrate, producing by-products, (c.2) Purging of Precursor A and by-products using an inert carrier gas, (c.3) Addition of Precursor B, which reacts with the surface to form a monolayer, and (c.4) Final purge to remove unreacted by-products, completing the cycle [171, 175, 176, 178]. 106

Figure 1-10: Comparison of Main Thin Film Coating Process layer formation (1) PVD, (2) CVD – General, (3) ALD [124, 175]. 108

Figure 2-1: The thermal evaporation process is illustrated, where (1) the material source is (2) evaporated into the (3) gas phase, then (4) travels and deposits onto the (5)

substrate as a solid layer. The accompanying image shows the Edwards 306 with arm configurations, where calcium is evaporated first, followed by copper, ensuring an even and uniform coating on the substrate. 118

Figure 2-2: The coated substrate is placed onto a small amount of UV-curing epoxy, ensuring full coverage on the copper side to prevent sideways permeation. Any bubbles or unevenness is addressed before curing the sample under a UV lamp for at least 5 minutes. Once fully cured, the sample is labelled with the relevant conditions and information before being placed into the appropriate test box for further analysis..... 119

Figure 2-3: (a) Calcium test sandwich, consisting of an inorganic coating applied to the top of the polymer substrate, followed by deposited calcium and copper layers, and fully encapsulated onto a glass substrate using UV-cured epoxy for sealing. (b) Vapour ingress pathway diagram that illustrates vapor ingression in a dual barrier system. (1) The top barrier contains random, unknown defects that allow vapor to pass through. (2) As vapor travels through these defects, it diffuses laterally within the substrate. (3) The bottom barrier layer's defects are then pathways for the vapor to the Ca layer, which reveals the spatial density information of the barrier layer (defect sizes and counts). ... 121

Figure 2-4: (a) Uncoated polymer film with calcium open to a room environment, demonstrating rapid calcium depletion within 3 minutes due to exposure to moisture; (b) Calcium Test Regions: (1) Onset/Initial period – water uptake and adsorption onto the barrier layer (Henry's Law) and establishment of the permeation, (2) Transition region – water vapor diffusion through the coating and substrate (Fick's Law), with pinhole defects indicated by calcium depletion, (3) Saturation – complete calcium depletion, revealing the bare copper layer; (c) Images of test samples with copper layers of various

thickness: (1) 5 nm, (2) 15 nm, and (3) 35 nm, showing how too a thin copper layer allows premature calcium reaction, while too thick a copper layer blocks visual observation of calcium depletion. 126

Figure 2-5: Schematic of a Calcium Test Box setup for both poor and good barriers. (a) Poor Barriers: This setup enables unattended monitoring of calcium tests, capturing images over minutes to days. (b) Good Barriers: Designed for longer tests that can span weeks to years, allowing multiple samples to be conditioned and tested over extended periods. (c) Calcium test sample: Depicts the location of the calibration bar and the region of interest where images are captured using a backlit light source. Below the schematic are the current setups, showing the camera positions (with adjustable arms) for the poor barrier test boxes, alongside a top view of the test box interior. The setup for good barriers is displayed next to it, featuring two ovens with different saturated salts to control humidity, and the backlit light arrangement for imaging the coated barrier samples..... 130

Figure 2-6: Calcium is deposited onto a 'smiley' indicator, with its thickness monitored by a Quartz Crystal Monitor (QCM) to gauge when the indicator becomes invisible, or the sample turns opaque. A potential issue arises from the glass barrier or seal in the Edwards 306 Thermal Evaporator, which may impact the perceived opacity. The calcium layer is estimated to reach full opacity, blocking all light, at approximately 145 nm. 139

Figure 2-7: (a) Six representative images from an uncoated PET Calcium Test conducted at 14.5 ± 2.5°C in LiCl (RH ≈ 65%), illustrating the gradual depletion of calcium over time. (b) Corresponding mean intensity surface plots, calculated from the

images, depict the progressive change in calcium, quantified through the mean light intensity values..... 142

Figure 2-8: Intensity calibration using an 11-step neutral density Calibration bar glass strip. (a) Mean grey value of each glass square is plotted versus image number for an uncoated PET Ca test at 14.5 ± 2.5°C in LiCl (RH ≈ 65%). The legend shows the notional normalized % transmittance values, assigned by equally dividing the 11-step glass strip into 10% increments from 0% to 100% T. These serve as fixed reference points for intensity normalisation in each frame. (b) Normalised mean light intensity values plotted over time (days), alongside individual calibration plots with corresponding normalised values for representative images – (mean intensity value, normalized value) – (c) Image No. 1 (5.51, 67.1), (d) Image No. 40 (9.55, 73.3), (e) Image No. 45 (19, 89.6), (f) Image No. 50 (40.5, 128), (g) Image No. 53 (52.6, 148), and (h) Image No. 90 (62.8, 165). 144

Figure 2-9: Lag-time model of an uncoated PET Calcium Test conducted at 14.5 ± 2.5°C in LiCl (RH ≈ 65%), highlighting three distinct regions: (1) **Initial Region**, where the calcium layer is fully opaque, blocking light transmission, despite initial water uptake and adsorption; (2) **Transition Region**, beginning at the onset time, marked by a significant increase in fluence as the calcium reacts with water, causing the layer to thin; and (3) **Saturation Region**, where full calcium depletion results in a plateau in intensity and fluence, leaving only the bare copper layer visible. The plot includes representative image locations on the fluence graph and an example calculation for Image 53, estimating the fluence and determining a WVTR of 1.25 ± 0.031 g/cm²·day for this sample..... 145

Figure 2-10: Fluence-over-time plot for an uncoated PET substrate at 14.5 ± 2.5°C in LiCl (RH ≈ 65%) with varying ROI to account for potential edge permeation. Transition region images illustrate the compensations of possible edge effects made, showing decreasing ROI area but increasing normalised mean grey values. A slight decrease in WVTR is observed, with an estimated value of 1.13 ± 0.0914 g/cm²·day. . 147

Figure 2-11: Effect of room lights (top-left), the camera settings (top-right) and the camera itself or position of it (bottom) towards the overall image captured. 150

Figure 2-12: (a) Veeco Savannah S200 ALD setup, showing the TMA bottles and PET sheets inside the ALD chamber placed on the valve manifold; below are the processing parameters for PET deposition. (b) Recipe: water is pulsed for 0.15s, followed by a 30s chamber evacuation before pulsing TMA for 0.15s, allowing the reaction and purging before the next cycle. (c) PVA samples processed at 150°C exhibit significant degradation, while those processed at 80°C retain film clarity with no visible damage. 155

Figure 3-1: Chemical of the Two common ways to produce Polyethylene Terephthalate: (1) Polycondensation using: Terephthalic Acid and (2) Poly esterification using: Dimethyl Terephthalate, respectively with Ethylene Glycol. 158

Figure 3-2: WVTR as a function of film thickness for uncoated PET substrates from various literature sources. The figure highlights the influence of increasing thickness on WVTR, with variations in relative humidity and temperature depicted as bubble colour and size, respectively [14, 25, 93, 230, 246-252, 254-257, 259-262, 264-270]. 163

Figure 3-3: WVTR measurements of two uncoated PET samples (masked to 1 cm² area) using a MOCON Aquatran 2 system. (a) WVTR as a function of RH at three

distinct temperatures (14°C, 25°C, and 38°C), showing WVTR increases with RH and temperature. (b) WVTR as a function of temperature across RH levels (35–100%), illustrating heightened sensitivity of WVTR to temperature at higher RH. These results underscore the significant and interconnected effects of temperature and RH on PET permeability within its glassy state. 165

Figure 3-4: Arrhenius plot of ln(WVTR) [$g \cdot m^{-2} \cdot day^{-1}$] vs. 1000/T [$K^{-1}$] for uncoated PET substrates at RH levels from 35% to 100% and temperatures of 14°C, 25°C, and 38°C. Each series exhibits a negative slope, as expected, reflecting the Arrhenius-type dependence of WVTR on temperature. Multiplying this slope by R (8.314 $J \cdot K^{-1} \cdot mol^{-1}$) yields the activation energy (Ea) in KJ/mol. Although Ea appears largely independent of RH within this range, it is important to note that increasing temperature at a given RH raises the absolute partial pressure of water vapour, influencing the permeation driving force. Below the graph, a table presents the average activation energy for both tested samples at each RH. 169

Figure 3-5: A fluence (g/m^2) vs. time (days) graph of an uncoated PET sample tested at 31.5°C and 54% RH (LiCl solution) estimates the transition region time, assuming full saturation at 0.2 g/m^2 fluence. The estimated transition time is 0.051 days or 73.47 minutes..... 172

Figure 3-6: Representative fluence plots from calcium tests show (a) four temperatures and (b) three humidities, using saturated salt solutions to maintain equilibrium with the samples. The legend indicates the Ca thickness for each sample. The figure highlights the impact of temperature and relative humidity on WVTR (gradient in the transition region) and onset time..... 173

Figure 3-7:(a) Onset time versus Ca thickness for uncoated PET samples, categorised by RH and temperature. This plot shows the combined influence of RH, temperature and Ca thickness on onset time. Higher temperatures and RH generally lead to shorter onset times, while thicker Ca layers result in longer onset times due to the greater amount of material needing to degrade before light transmission begins. (b) Main effects plot showing the average onset time and WVTR with respect to Ca thickness, aggregated across RH and temperature. In this plot, the grey line represents the average onset time for each Ca thickness, while the red line shows the corresponding average WVTR values. The trend confirms that onset time increases with Ca thickness, but calculated WVTR remains relatively stable, with only a slight upward trend. This reinforces that Ca thickness affects the degradation behaviour (onset time), not the WVTR calculation, which is based only on the slope of the transition region and is independent of when the transition begins..... 177

Figure 3-8: Ca Test of uncoated PET substrate: (a) WVTR plotted against relative humidity grouped by temperature, and (b) WVTR plotted against temperature grouped by relative humidity. Both plots show a direct proportionality—higher temperature or humidity significantly increases WVTR. The accompanying table provides a detailed comparison of average WVTR values obtained from the Ca test and MOCON Aquatran measurements under corresponding temperature and relative humidity conditions. The data reveal differences such that the MOCON Aquatran reporting higher WVTR values, while the Ca test aligns closely with literature (~6 $g/m^2 \cdot day$) [288], indicating greater accuracy. The larger deviations in MOCON data at higher temperature and humidity

suggest potential calibration issues or methodological differences, underscoring the reliability of the Ca test and the need for caution with MOCON results..... 179

Figure 3-9: The Activation Energy of uncoated PET, tested under three relative humidities using the Ca test, shows WVTR variability but remains within the range of MOCON Aquatran and literature values. These results help in understanding the permeation mechanisms of barrier layers and estimating potential pinhole or defect sizes. The Activation Energy plot also enables estimating WVTR at higher temperatures for the same humidity..... 180

Figure 3-10: Plot of ln[WVTR ($g/m^2 \cdot day$)] vs. 1000/T (K^{-1}) for literature values, showing variations in slopes used to calculate the activation energy of uncoated PET substrates. The figure also includes ln(WVTR) values from the Ca test and MOCON Aquatran measurements at similar relative humidities (~95%–100%), highlighting alignment and differences with literature sources [25, 93, 249, 250, 252, 254]..... 182

Figure 3-11: (a) Activation Energy (Ea) vs. Water Vapor Transmission Rates (WVTR) over relative humidity shows the variability and overall consistency of Ea. The values range from 36.0 to 49.14 KJ/mol, with an average of 41.73 ± 3.22 KJ/mol, excluding Deng as an outlier..... 183

Figure 3-12: Literature data for uncoated Mylar PET films (DuPont Teijin Films data sheet {Films, 2011 #404;Films, 2021 #360 tested at 38 °C and 90% RH by ASTM F1249. Black squares: measured WVTR vs film thickness, red circles: the same data converted to thickness normalised permeation (WVTR × thickness). The plot illustrates two key points (1) thickness matters for WVTR, a longer diffusion path lowers the measured rate (inverse trend), (2) Intrinsic permeability is thickness-independence, once

WVTR is normalised for thickness, the values collapse onto a nearly constant line, confirming that residual scatter is due to minor sample or test method variations not substrate gauge. These Mylar datasheet values are used because these have been one of the few publicly available data sets that reports the same PET grade at several thicknesses under identical T/RH conditions, most other studies as cited in Figure 3-10 do not satisfy that same material same conditions requirement are therefore not included in this thickness normalisation example. 185

Figure 3-13: Calculated Permeation values - PET tested at difference test methods (HTO, e-Ca and MOCON), at two thicknesses, two temperatures and four relative humidities, showing that even with similar testing conditions the test methodology may change the WVTR and in turn the calculated permeation [30, 230]. 187

Figure 3-14: Verification of Fickian diffusion in bare PET, showing that thickness normalised water vapour permeation is independent of film thickness. The plot shows permeation (mol/m·s) as a function of substrate thickness (μm) under varying temperature and relative humidity (RH) conditions. Data include measurements from MOCON Aquatran 2 (●), Calcium Tests (✶), and values extracted from the literature (■) [25, 93, 246-252, 254-260, 262, 264, 266-270, 289-292]. For each temperature band (indicated by colour), the data form a horizontal cluster, confirming the expected flat response once the diffusion path length is normalised. The plot also reveals a clear temperature dependence with intrinsic permeation increasing by approximately one decade between 10°C and 80°C. Systematic deviations are noted include the experimental MOCON results attributed to instrumental artefact and two elevated

literature points near 80°C, which may reflect genuine increases in polymer chain mobility above the glass transition temperature of PET. 188

Figure 3-15: Permeation vs. Water Vapour Partial Pressure (saturated vapour pressure at the sample temperature multiplied by relative humidity), accounting for thickness differences and comparing WVTR across various testing conditions and methods. While the plot confirms the linear relationship predicted by Henry's law, the data are not explicitly grouped by temperature to allow any influence of temperature to emerge within in the observed trends. Deviations and subtle groupings within the same experimental conditions suggest that temperature affects permeation behaviour, with MOCON Aquatran data showing a consistent trend and minimal scatter, while the Ca Test data exhibits more variability. Broader distributions in the literature data further emphasise the role of temperature effects and variations in testing conditions. 192

Figure 3-16: Permeability [mol/(m·s·Pa)] vs. Water Vapor Partial Pressure (KPa), showing distinct temperature groupings in the Mocon data, while the calcium test closely aligns with literature values. Overall, data from individual studies fall within a consistent permeability range and are close in absolute permeability coefficient values. 195

Figure 3-17: Permeability [mol/(m·s·Pa)] vs. Temperature (°C) shows a downward trend in the experimental data, supported by some literature. However, not all studies agree, with some showing an opposite, upward trend, where films become more permeable at higher temperatures. This highlights disagreement on how temperature directly affects permeability. 198

Figure 3-18: The natural log of permeability coefficients ($mol \cdot m^{-1} \cdot s^{-1} \cdot Pa^{-1}$) versus reciprocal temperature (K^{-1}) for Ca tests, shows that multiplying the slope by the

universal gas constant ($R = 8.314\ J \cdot K^{-1} \cdot mol^{-1}$) yields a negative apparent activation energy (E_{app}) in terms of permeability. The negative value reflects the exothermic sorption mechanism of water vapor in PET. The scatter in the data and the low coefficient of determination suggest that the temperature dependence is complex and potentially non-Arrhenius, likely induced by humidity-induced plasticization of the matrix which varies with temperature. 200

Figure 3-19: The natural log of permeability coefficients for MOCON Aquatran 2 plotted against reciprocal temperature (K^{-1}) estimates Ea. The data shows a slight influence of relative humidity, but its effect is minimal and not significantly impactful on the Ea. 201

Figure 3-20: The natural log of permeability coefficients from literature, plotted against reciprocal temperature, generally follows a constant trend, except for Deng (upward slope) and BM Henry (downward slope), which produces interestingly a negative and positive Ea respectively. 202

Figure 3-21: Summary of Activation energy (Ea) based on permeability coefficients across relative humidity ranges, comparing experimental data (MOCON and Ca Test) with literature. Negative values indicate solubility-dominated behaviour, where PET absorbs fewer water molecules at higher temperature, reducing overall permeability. Positive Ea values from other studies point to diffusion-drive increases in permeability with temperature, underscoring how polymer structure, additives, and test conditions can shift the balance between solubility and diffusion. 208

Figure 4-1: Proposed Mechanism for a Thermal ALD Al_2O_3 from TMA/H_2O. Gaseous trimethylaluminum reacts with surface hydroxyl groups to form a methyl-

terminated aluminium species and methane, – OH $_{(surface)}$ + $Al(CH_3)_{3\ (g)}$ → – O – $Al(CH_3)_{2\ (surface)}$ + $CH_{4\ (g)}$. An N_2 purge remove excess TMA and CH_4. Subsequent exposure to water vapour hydrolyses the surface methyl groups, regenerating – OH $_{(surface)}$ and evolving methane, – O – $Al(CH_3)_{2\ (surface)}$ + $2H_2O$ → – O – $Al(OH)_{(surface)}$ + 2 $CH_{4\ (g)}$. A second N_2 purge clears residual H_2O and CH_4, leaving the surface re-hydroxylated for the next cycle. Net per cycle is then: 2 $Al(CH_3)_3$ (g) + 3 $H_2O_{(g)}$ → $Al_2O_{3\ (surface)}$ + 6 $CH_{4\ (g)}$/ Gas phase species are denotated (g) and chemisorbed species as (surface); the deposited Al_2O_3 is also thought to be an amorphous solid (s) on PET under a typical temperature window. Importantly, the final step in this diagram also illustrates the potential for incomplete hydrolysis (residual – CH_3 units) often observed at lower temperatures, such as what is observed in this work. These type of deviations from the ideal cycle contribute to higher – OH content and the formation of non-stoichiometric AlO_x rather than pure Al_2O_3 [33, 178, 322, 328-333]. 211

Figure 4-2 WVTR of uncoated and ALD AlO_x PET tested using MOCON Aquatran of varying thicknesses tested across a range of temperatures, highlighting the expected temperature dependence of WVTR. Thinner coatings exhibit a stronger sensitivity to temperature, while thicker coatings (> 26 nm) demonstrate a notable reduction in this effect. 214

Figure 4-3: WVTR of AlO_x coatings on PET substrates as a function of coating thickness, measured tested at three different temperatures (14°C, 25°C, and 38°C), under 100% RH using Mocon Aquatran 2. The linear scale highlights the overall decrease in WVTR with increasing coating thickness, showing a noticeable plateau at larger thicknesses. The logarithmic scale reveals more detailed trends, indicating that the lowest

WVTR values are predominantly achieved at a thickness of ~50 nm, suggest the optimal thickness to be around this point..... 217

Figure 4-4: Permeability [mol/(m·s·Pa)] of AlO_x-coated PET as a function of coating thickness (oxide thickness), based on measured WVTR values using Mocon Aquatran at different temperatures at a constant RH of 100%. Permeability was calculated using Equation **2-3**, where the total film thickness (oxide and PET substrate) was used as the diffusion path length. Although the oxide thickness is used on the x-axis, the calculated permeability accounts for the full sample thickness. Using a logarithmic scale shows that permeability decreases with increasing oxide thickness, reaching an optimal level around 50 nm, after which further thickness provides minimal additional improvement or an increase in permeability..... 218

Figure 4-5: Natural log plot of WVTR vs. inverse temperature (Arrhenius plot), grouped by AlO_x thickness. The slope can be used to estimate an Ea of the barrier film for each thickness of coating..... 220

Figure 4-6: Activation Energy (Ea) of AlO_x-coated PET substrates across thicknesses, showing an initial increase followed by a plateau and decrease in coatings beyond 300 nm. The figure highlights variability in Ea, with some thin coatings sometimes falling below the Ea of bare PET, indicating potential film damage..... 222

Figure 4-7: Natural log plot of Permeability coefficients over inverse temperature, grouped by AlO_x thickness, shows varied trends and slopes, indicating that permeability does not consistently increase with temperature. This behaviour reflects a complex interplay between diffusion and solubility coefficients. Thicker coatings may influence water vapor interaction due to surface properties or defects, potentially trapping or

repelling water molecules, combine with temperature dependent changes in solubility, may explain the non-monotonic trends observed. 223

Figure 4-8: Ea for water vapor permeability in PET samples with various thickness of AlO_x via ALD. Positive Ea values (top rows) suggest a diffusion-dominated regime where permeability rises with temperature, while negative Ea values (bottom rows),m indicate solubility controlled behaviour – coating and substrate combination admits fewer water molecules as temperature increases. The large variability and standard deviations may reflect differences in microstructure, pinholes and possible measurement uncertainties. 225

Figure 4-9: Permeability [mol/(m·s·Pa)] versus AlO_x thickness on PET, shown on both linear and logarithmic scales, reveals a consistent decline in permeability with increasing thickness, as observed through the Ca test. This trend holds across varying water vapor pressures, relative humidity, and temperatures. The data spread is like MOCON Aquatran results, with the trend clearly visible despite variations in test conditions and system controls. Note: temperature coverage limitation: some sets only include two temperatures and any Ea inferred from these points would be treated as apparent Ea's and cannot be extrapolated beyond the measured (T, RH), hence in subsequent Ea estimations required at least three temperatures. 228

Figure 4-10: Ca test images with marked and pre-labelled points that lie between bright pin-hole-type bright spots used to measure mean grey values at these labelled points, showing the progression of background calcium degradation over time: A.1 and B.1 are RF Sputtered AlO_x on Biaxially Oriented Polypropylene and Polyethylene Naphthalate respectively, 2 cm diameter disc. 145 nm on BOPP and 148 nm on PEN at

38°C and 85% RH, as shown by Tobin *et al.* with seven randomly selected points around the sample and region of interest. For comparison this studies ALD AlO_x films on PET with varying thicknesses - 14 nm at 25°C, 39.5% RH (Saturated Salt: $MgCl_2$); 50 nm at 50.5°C, 27% RH (Saturated Salt: LiCl); 50 nm at 48°C, 50% RH (Saturated Salt: $MgCl_2$); and 100 nm at 25°C, 78.5% RH (Saturated Salt: $MgCl_2$) – also selected random points to measure mean grey values. These mean grey values at the selected points are plotted against time to allow localized tracking of permeation between macro defects. The results demonstrate significant greying in RF-sputtered films, indicative of nano-defects, while ALD films maintain stable grey values, highlighting better uniformity and barrier properties..... 233

Figure 4-11: WVTR ($g/m^2 \cdot day$) as a function of AlO_x thickness (nm) under two relative humidities (39.5% and 78.5% at a constant temperature of 25°C). Data points are differentiated by shape to represent individual samples (*i.e.*, Sample 1 is square, Sample 2 is circle, Sample 3 is triangle), while they are also colour differentiated by edge correction status (red/orange = uncorrected, blue = corrected). Edge-corrected data consistently show lower WVTR values, highlight the significance of excluding perimeter artefacts like edge permeation in accurately assessing the true barrier performance for certain samples..... 238

Figure 4-12: Arrhenius plot of ln (WVTR) versus inverse temperature (1/T) for ALD AlO_x films of varying thicknesses, based on edge-corrected WVTR data from the Ca test. The plot accounts for sideways permeation effects and the calculated apparent activation energies E_{app} from slopes are 112.03 ± 17.77 kJ/mol for 63 cycles, 61.70 ± 74.91 kJ/mol for 125 cycles, and 45.13 ± 4.64 kJ/mol for 250 cycles; and 83.62 ± 49.45

for 500 cycles. While linear best-fit lines are applied, the visible scatter (likely due to variations in sample geometry or measurement sensitivity) affects the confidence in assuming a strictly Arrhenius relationship. Wherein, a true non-Arrhenius behaviour may be present if the underlying trend is non-linear, potentially caused by temperature dependent changes in defect geometry (crack opening / closing) or competing transport mechanisms. These values consequently represent the effective temperature sensitivity of the permeation flux over this specific temperature range rather than a single static energy barrier. 240

Figure 4-13 Natural logarithm of permeability of Ca tests over the reciprocal of its temperature, considering edge effects. The data illustrates the relationship between diffusion and solubility mechanisms as a function of AlO_x coating thickness. Thinner coatings exhibit diffusion dominated behaviour, where permeability increases with temperature, thicker coatings transition to solubility dominated behaviour, showing reduced permeability with increasing temperature. Showing how increasing thickness influences the balance between diffusion and solubility, impacting overall permeability behaviour..... 242

Figure 4-14: Pre-processing of an image from a Ca Test of a Barrier Layer (14.0 nm AlO_x on PET at 25°C, 39.5% RH) starts by converting raw RGB images into an 8-bit grayscale stack for easier identification of calcium, copper, and background regions using Trainable Weka Segmentation. The Otsu method binarizes the image, and background subtraction isolates the spots. The lookup table is inverted to analyse particles, focusing on size and circularity. Caution is to be taken as artifacts from the raw image may affect

the grayscale, requiring careful thresholding to avoid overestimating defects or miscounting spots..... 246

Figure 4-15: Bright area boundaries and particle analysis of a 14.0 nm AlO_x PET substrate (25°C, 39.5% RH), tracking calcium depletion over time using stacked Ca test images. (a) Pink contour lines show the recession of the calcium front and emergence of localized bright spots (water vapour ingress sites). (b) Particle analysis highlights individually detected spots, colour-labelled by appearance time; edge regions have been excluded. (c) Cumulative map showing the isolated internal spots used for defect quantification across the test duration. (d) Perimeter tracking of the active Ca region illustrating degradation and reduction of testable area over time. Spots are classified as isolated, saved as repeated in the memory, or coalesced (joined together), based on their formation and interaction, with spot density (spots per unit area) used to account for changing Ca coverage as the test progresses. 249

Figure 4-16: Idealized representation of spot classification logic across four timepoints. At time 0, four isolated green spots are identified. At t, two of these merge to form a single coalescing spot (magenta), while the other two isolated spots persist (white). By 2t, previously merged spots remain coalesced, and a newly emerged isolated spot appears near this cluster. At 3t, continued merging results in a single large coalescing cluster, collapsing distinct initiation events into one region. This schematic illustrates the centroid-proximity logic in the Python-based classification and highlights how coalescence and merging can obscure the true number and evolution of defect origins. 256

Figure 4-17: Spot detection and classification results for a 14.0 nm AlO_x layer on a coated PET substrate at 25°C and 39.5% RH ($MgCl_2$ salt solution). (a) Raw grayscale images showing the progressive degradation of the Ca indicator layer. (b) Corresponding edge detected images produced via the Canny method. (c) Final spot classification results based on centroid proximity and temporal memory, distinguishing between isolated (green – blue contours represent estimated size of spot) and coalescing (magenta) spots. The updated Python-based pipeline enables more reliable defect classification by reducing the likelihood of double-counting and tracking spot evolution across frames. This demonstrates the method's ability to account for spatial continuity over time and supports a more accurate assessment of defect development and identification. 258

Figure 4-18: The estimated spot density (spots/cm²) is plotted against coating thickness (nm) for multiple calcium test samples, identifying isolated spots as potential defects in the coated film. The average defect density is **13 ± 3 spots/cm²**, with a maximum of **18 spots/cm²** and a minimum of **5 spots/cm²**. The data suggests that spot density (*i.e.*, the number of defects) remains relatively independent of variations in relative humidity and temperature. However, while thin films can exhibit low defect densities, the probability of creating good films increases with higher coating thicknesses as suggested with previous WVTR and permeability results. Additionally, this analysis provides a more accurate defect estimation, as it focuses exclusively on isolated spots, avoiding potential overestimation caused by coalescence, which was a limitation in previous ImageJ methodologies. 264

Figure 4-19: (a) Schematic illustrating that the calcium depletion spot (not the defect itself) expands radially over time. For the purpose of the model, the physical defect

is idealised as constant in size to calculate an effective hydraulic diameter, though the actual geometry may evolve due to degradative mechanisms. Aside from this the illustration also shows the maximum spot area measured just before the coalescence of the adjacent or neighbouring spot. (b) Cross-section view of water vapour ingress and lateral diffusion within a multilayer barrier structure. Vapour enters through random, unaligned defects in the top barrier, diffuses laterally in the polymer substrate and only reaches the Ca layer where it encounters a defect in the bottom barrier. The Ca test therefore detects only those bottom side defects that allow vapour transmission. After critical time (T) larger defect areas enable greater vapour flux (proportional to WVTR × defect area), leading to faster radial spot growth and more rapid localised Ca degradation. 267

Figure 4-20: Defect Radius (µm) over Coating Thickness (nm), under varying temperature and RH conditions. The plot illustrates the variability in defect sizes across different measurement spots, highlighting the range of defects observed under different environmental conditions. While no clear trend is evident, the data suggests a consistent range of expected defect sizes within AlO_x barrier films. The accompanying table provides an overview of sample distribution across thickness levels, indicating that although multiple defect points were analysed, the limited number of samples may affect the statistic robustness off the findings. Note: The driving force for water-vapour transport may differ from that of an uncoated film because the opposite side of the PET is also covered by an AlO_x barrier. 271

Figure 4-21: The total defect area (Spots·µm²/cm²) plotted against coating thickness for samples tested at 25°C under 39.5% and 78.5% relative humidity shows

significant variability with no clear correlation. Outliers at 26 nm, 50 nm, and 73 nm, along with large standard deviations, suggest inconsistencies likely due to sample preparation, measurement errors, or environmental factors. 275

Figure 4-22: WVTR as a function of total defect area for ALD barrier layers at 25°C 39.5%. The data confirms a strong correlation between WVTR and total defect area, with slight deviations likely due to measurement limitations in the Ca test, edge permeation effects or inaccuracies in defect size estimation. The results align with literature predictions from Blunt et. al. and Klumbies et. al. describes how barrier performance is dictated by total defect area, particularly large defects, rather than coating thickness alone. Highlight the critical role on defect minimization strategies in ALD fabrication for moisture barrier performance. As acknowledged, while there is noticeable scatter and most points do not fall within the estimated error bounds of the linear fit, the overall trend and its quantification remain well supported. The deviations may reflect sample-to-sample variability, limitations in the Ca test measurement of WVTR, or defect area estimation uncertainty. 276

Figure 4-23: WVTR as a function of total defect area for ALD barrier layers at 25°C 78.5%, shows the same predicted relationship – demonstrating the fidelity of the predictive model to experimental data, particularly at higher defects beyond those observed at lower humidity levels. However, the slight deviation in the 73.0 nm sample may be attributed to either an underestimation of defect size (indicating a lower actual total defect area) or an overestimation of edge effects in WVTR estimation. These findings further emphasize the importance of ALD AlO_x quality over thickness alone in achieving superior barrier performance. 279

Figure 4-24: Permeability as a function of total defect area, demonstrating a clear increasing trend. This highlight the dependence of ALD AlO_x permeability on the quality of the barrier layer, reinforcing the notion that defect density is the primary determinant of overall permeability–rather than external environmental factors such as RH..... 280

Figure 4-25: (a) Optical microscope image of the peeled side of uncoated PET on a glass slide (Yenway CX40 Upright Microscope), (b) Zoomed 5x image highlighting scratches, discontinuities, or possible contaminants, (c) Scanning Electron Microscope (Jeol 6500F SEM) image of uncoated PET showing no significant surface defects at higher resolution, indicating the film is generally defect-free, (d) Optical microscope image of damaged PET substrate, revealing sever defects, fractures and possible contaminants. These irregularities can compromise the uniformity and effectiveness of a barrier layer coating. 282

Figure 4-26: (a) Optical Profilometer (3D Optical Profiler by Filmetrics) of an uncoated PET substrate (1,522 μm × 1,323 μm) shows a mean height of 0.18 μm and a maximum height of 0.36 μm, using a non-contact method to analyse surface features over a wide area. (b) Atomic Force Microscope (AFM - Agilent 5400) image of a smaller region (55 μm × 55 μm) confirms surface features within the 0.10 to 0.30 μm range, supporting the profilometer findings. 284

Figure 4-27: Probability of detecting a defect (%) as a function of AlO_x coating thickness (nm) on PET, illustrating the influence of coating thickness on the occurrence of defects within a $1\ mm \times 1\ mm$ region of interest in coated samples..... 285

Figure 4-28: (a) Optical Microscopy ($5\times$ Magnification, 2,417 μm by 1,810 μm) shows ~42.72% defect detection probability, with blemishes and possible defects. (b)

SEM (220 µm by 165 µm) has a low ~0.46% detection probability, but any defect present would be large and easily recognizable (49.67 ± 12.51), also revealing surface damage, contaminants and edge degradation. Note: As a visualization samples with a smaller area will often appear cleaner or defect free because of the lower chance of a defect entering the field of view is low. However, when a defect as noted is present it should appear with a high contrast and without any possible glass slide artifacts – further explaining possible differences on images between SEM and Optical micrographs even with the same conditions. 287

Figure 4-29: Surface analysis images (Optical and SEM) and profilometry data of 26 nm, 50 nm, and 96 nm coatings reveal distinct features, possible defect spots, and surface roughness. The profilometer data highlights the overall uniformity of AlO_x coating on the PET substrate, with thicker coatings showing better coverage and consistency. As noted: optical images were acquired with the sample on a glass microscope slide. Any straight or branched lines seen in transmission that reproduce on the blank slide are slide scratches or fractures and not cracks in the PET/AlO_x film, while SEM (no glass slide) and profilometry do not show any through film fracture features. Note: A possible interpretation of the straight lines seen in 26 nm as suggested would be PET processing lines or substrate marks that are increasingly masked upon coating of AlO_x, and are not interpreted as coating cracks on PET, and possibly progressively masked with increasing AlO_x thickness as it is no longer visible in thicker coatings at 50 nm and 96 nm..... 289

Figure 4-30: Surface analysis images of 250 nm and 375 nm ALD AlO_x under optical, SEM and profilometer data, that shows the coverage of macro scale irregularities

of PET that are no longer visible but further coatings show internal stresses and collapse that indicate new defects within the film. 290

Figure 5-1: Activation Energy Comparison for Defect Analysis in PVAl Films. Arrhenius Plot of ln [WVTR ($g/m^2 \cdot day$)] vs. 1000/T (K^{-1}), for uncoated and coated PVAl films. The linear fits provide estimates of the apparent activation energy of the water vapor transmission rate. However, the hydrogel like nature of PVAl implies that transport is governed by couple diffusion-swelling mechanisms, making these values effective temperature coefficients for this hydration state rather than static energy barriers. 299

Figure 5-2: Representative samples of Thin PVAl substrates at (a) 26 nm (13 points), (b) 50 nm (12 points), and (c) 96 nm (12 points) show areas with remaining calcium, suggesting no nano defects are present, as indicated by the consistent average mean grey values..... 301

Figure 5-3: Representative sample points in Thick PVAl (a) 26 nm: 12 points, (b) 50 nm: 11 points, (c) 96 nm: 12 points, showing slow greying, indicating potential nano defects. This suggests that nano defects, in addition to microdefects, may be present in AlO_x 303

Figure 5-4: Scatter group plot of ALD AlO_x-coated PVAl (Betol) showing the effects of coating thickness, temperature, and relative humidity on estimated WVTR. The plot demonstrates that different coating thicknesses have similar WVTRs, indicating a reduced influence of environmental factors. The broad scatter at fixed T/RH and coating thickness gives the suggestion of defect dominated permeation such that it is the quality of the coating that may be the main determinant of WVTR; as argued local defect size and density along with potential interfacial pathways can overwhelm environmental

trends in coated substrates, where thicker coatings can lower the overall median WVTR but residual scatter remains due to defect statistics. 306

Figure 5-5: Scatter group plot of ALD AlO_x - coated thick PVAl (Alpine) showing the effects of coating thickness, temperature, and relative humidity on estimated WVTR. Like the thin PVAl substrates, environmental factors do not significantly influence WVTR and increasing coating thickness does not greatly improve performance. It is peculiar that elevated temperatures and higher humidity like 25 °C shows a decrease in WVTR where an increase should be expected instead, likely due to scatter rather than systematic effect. Where the observed variation arise more from sample inconsistencies, measurement sensitivity, or localized defect distributions within the coatings. The broad scatter may also confirm that permeation in this system may be governed by randomized defect density (extrinsic factors) rather than intrinsic material properties. 308

Figure 5-6: Scatter group plot of ALD AlO_x-coated thin PVAl (Betol), grouped by coating thickness and temperature, showing the range of permeability. While some variations and outliers exist, possibly due to sample damage or inconsistencies, the coated thin PVAl generally achieves low permeability regardless of temperature and coating thickness. Interestingly, permeability appears lower at higher temperatures and elevated conditions, following a trend like WVTR. While the exact cause remains unclear, this behaviour may have been influenced by factors such as changes in film morphology, reduced microdefect impact or temporary effects like moisture interaction. Further studies would be needed to determine whether the mechanisms such as defect reduction or structural rearrangement contribute to this trend..... 310

Figure 5-7: Scatter group plot of ALD AlO_x-coated thick PVAl (Alpine), grouped by coating thickness and temperature, showing consistent permeability estimates in the range of ~10^{-15} to 10^{-17} [mol/(m·s·Pa)], slightly lower than thin PVAl but still within a similar range..... 311

Figure 5-8: Optical, SEM, and optical profilometer images of uncoated thin and thick PVA films reveal a clear film with blob- or spot-like features that could affect coated film characteristics. The surface is rougher compared to bare PET and shows potential dust-like artifacts, which may also be present in the ALD-coated barrier layers. The optical images span a field of approximately 2500 µm × 2000 µm, which is roughly comparable to the 1600 µm × 1600 µm area analysed by profilometry; though not identical, both views are sufficient to capture representative surface features..... 315

Figure 5-9: Ca-test images (a) of a 26 nm AlO_x coated thin PVAl film, highlighting four 1 cm × 1 cm regions that show perturbations or bright area that are localized increases in grey level relative to the surrounding background between potential macro defects that indicate moisture ingression. These manifest as linear features and irregularities rather than the spot-like defects seen on coated PET substrates. The estimated defect density from these Ca-test images is ~13 defects/cm^2 (Figure 5-16), which translates to a ~12.2% probability of observing at least one defect in a 1 mm by 1mm field of view based on a Poisson analysis. Subsequently, Optical microscope images (b) show possible defect sizes ranging from ~1,600 μm^2 (edge length ~40 µm) to ~36,100 μm^2 (edge length ~190 µm – average defect size of this 26 nm AlO_x thin PVAl sample), where the largest visible defect detected in all the various tested samples in 5.7 Defect Size / Area Estimation in Coated PVAl Films was around ~409,600 μm^2 (edge length

~640 μm). SEM images (c) at two magnifications (c.1 at 100× and c.2 at 1k×) reveal additional straight lines and finer features, some of which may be film processing related or true defects, indicating a higher density of small, possibly interconnected features. These results suggest that Ca test may undercount defects by merging finer structures into larger more prominent features, illustrating the challenge in distinguishing true defects from possible surface irregularities in PVAl films. Moreover, this multi-modal analysis also provides the justification for assigning these perturbations to defects: the bright linear perturbations seen in the Ca-test images in (a) are assigned to defects due to these sites of moisture ingress directly correlate with the physical straight lines and finer features observed in corresponding SEM images (c) these kinds of defects are therefore interpreted as possible micro cracks or linear separations in the AlO_x (potentially associated with stress or substrate shrinkage of the hydrophilic PVAl substrate)..... 319

Figure 5-10: Coated Thin PVAl films with AlO_x thicknesses of 26 nm, 50 nm, and 96 nm was analysed using optical, SEM, and profilometer images. The results explain the calcium test observations: linear defects at 26 nm, a mix of spot- and linear-like features at 50 nm, and island or ravine-like mixed with linear features at 96 nm, likely due to coating collapse at higher thicknesses. 321

Figure 5-11: Coated thick PVAl films with AlO_x thicknesses of 26 nm, 50 nm, and 96 nm show similar optical, SEM, and profilometer results to the coated thin PVAl samples. These observations suggest that the coating plays a key role in the defects seen in the calcium test, providing insight into the permeation pathways of water vapor through the barrier layer..... 324

Figure 5-12: (a) Optical microscopy images of uncoated thin PVAl (Betol) films under different storage conditions. (a.1) Undried PVAl sample exposed to ambient humidity shows a dense network of linear features, suggesting shrinkage-induced stress patterns and possible crack nucleation sites. (a.2) A comparable sample after oven drying (~50 °C overnight) and desiccator storage shows a smoother surface with minor linear and dot-like features, consistent with dried samples described in Section 0. These images highlight the impact of environmental humidity on PVAl's surface morphology. (b.1) 50 nm AlO_x – coated PVAl film after ambient humidity exposure, displaying prominent crack-like or linear network features, like those seen in thicker (96 nm) coated samples. These features suggest that moisture ingress, followed by drying-induced shrinkage, can promote crack formation even in coated samples. (c) Schematic representations of proposed permeation pathways for these linear features. (c.1) Outward (width wise) expansion stabilizes, the crack width over time, while (c.2) lengthwise propagation along cracks acts as low-resistance channel for moisture diffusion. This behaviour aligns with Ca test observations, where elongated cracks expand significantly in length rather than width, indicating anisotropic permeation driven by stress localization and drying shrinkage. 331

Figure 5-13: Defect evolution and spatial distribution for a 26 nm AlO_x barrier on thin PVAl (5.26 × 4.88 cm – cell size ≈ 1.05 × 0.98 mm). (a.1) Raw Ca-test frames at six representative times, illustrating the progressive dark-to-bright conversion that accompanies calcium depletion. (b.1) Same frames with automated classifications super-imposed: isolated spots are first-appearance features of 15–30 px^2 whose centroids lie > 20 px (~2.1 mm) from any earlier isolated centroid are marked by green dots with

blue contours; coalescing spots, new features whose centroids fall within that 20 px radius are marked by magenta dots and contours. Panel titles give the cumulative counts of isolated and coalescing spots detected in each frame. (b.1.1) Two zoom-in examples highlight algorithm behaviour: a dust-/lighting artefact in the yellow dashed box is present in Frame 1 but absent in Frame 2, and the algorithm responds accordingly, whereas a genuine defect (red circle) emerges in Frame 2 and is correctly detected. (c.1) Fixed 50 × 50 grid maps showing the cumulative number of detections per cell over the whole sequence, left, isolated-spot counts (green scale 0–2); right, coalescing-spot counts (purple scale 0 to >120), allowing direct spatial comparison across samples. Counts represent totals accumulated over time (not temporal frequency), and "total detected spots" is therefore omitted from the legend. Brightening at specimen borders caused by lateral water ingress is excluded through the calcium-layer mask, so the maps reflect only intrinsic barrier defects. 338

Figure 5-14:Ca-test results for the 96 nm AlO_x coating on thin PVAl (4.91 × 5.13 cm - cell size ≈ 0.98 × 1.03 mm). (a.3) Raw images reveal island-like calcium-depleted zones surrounded by irregular bright microdefects. This morphology contrasts with the finer, linear fissures in thinner coatings (26 nm and 50 nm), and differs from the pinhole-type defects in PET. Instead, the rounded, widely spaced features suggest a stress-induced fragmentation regime. As the PVAl swells under moisture uptake, in-plane tensile stress develops in the oxide. This behaviour aligns with prior work by Leterrier *et al.* (2004, 2010) [219, 220] and Howells *et al.* (2008) [351], which showed that thicker brittle films fragment into fewer, broader segments, with saturation crack density scaling inversely with coating thickness ($CD_{sat} \propto 1/hc$; see Equation 5-2)

(b.3) Overlays of detected spots show strong agreement with raw frames. Isolated defects appear early and are later replaced by coalescing features as cracks merge and grow. Minor detection errors arise where features nucleate or merge between frames. (c.3) Spatial maps show isolated spots distributed uniformly, suggesting widespread initial permeation. In contrast, coalescing spots cluster in localized areas, indicating heterogeneous defect growth, possibly influenced by local stress concentrations or coating variability. These patterns support a fragmentation-driven mechanism with spatially variable evolution. 342

Figure 5-15: Schematic showing the progression and classification challenges of linear defect features over time. At time 0, isolated features are visible as separate entities (green). As time progresses to t, spatial overlap and merging begin, triggering classification as coalesced based on centroid proximity. By 2t, pink dashed lines highlight apparent connections between defects—interpreted here as possible crack growth or joining paths. These are not considered a new class but remain coalesced under the algorithm's distance rule. At 3t, the dashed red box marks an example of a potential misclassification: a newly emerging defect located near a larger network may be wrongly grouped as coalesced. This schematic illustrates how evolving linear geometries especially those that extend or form networks can complicate accurate identification. Because the algorithm relies on a fixed spatial threshold, such features may be joined prematurely, particularly in cases of asymmetric growth or swelling. The result is increased ambiguity when distinguishing isolated defects from extensions, highlighting the need to interpret connectivity and growth behaviour alongside spatial proximity. .. 349

Figure 5-16: Scatter group plot of total isolated spot density versus substrate thickness and AlO_x coating thickness shows the spread and effect of substrate and coating thickness. For thin substrate, no clear trend is observed; 50 nm coatings show higher isolated spot counts, while 26 nm and 96 nm coatings show significantly fewer spots. In contrast, thicker PVAl exhibits a clear trend of decreasing isolated spots with increased thickness. 351

Figure 5-17: Six selected regions of interest from a 26 nm AlO_x ALD-coated thin PVAl substrate, with surrounding outlines and binary image montages, highlighting the dominant defect in each region. These largest defects were chosen to minimize errors from coalescing or interfering features and provide consistent water uptake rate estimations. The water uptake rate (slope of the grey value change over time) is calculated for each defect, and the corresponding defect area is determined, revealing typical sizes ranging from approximately $4.70 \times 103\ \mu m2\ \pm\ 1.09\ \times 105\ \mu m2$. Despite variation in region sizes, the defect area depends more strongly on growth rate than absolute region size. Variability in fit (R^2 values from 0.10 to 0.79) reflects differences in defect growth behaviour and image fidelity. 359

Figure 5-18: Grouped scatter plot comparing estimated defect areas (μm^2) for thin and thick PVAl substrates with varying AlO_x coating thicknesses (26 nm, 50 nm and 96 nm). Defect areas span nearly six orders of magnitude, from the smallest isolated spot (~1.6×10^3 μm^2 in thin 96 nm PVAl) to the largest dendritic feature (~4.2×10^5 μm^2 in thin 50 nm PVAl). Data points are coloured by substrate and coating thickness, with error bars reflecting the standard deviation of area estimates. 362

Figure 5-19: The WVTR plotted against total defect area for coated PVAl films, illustrating the general trend that larger defect areas lead to increased permeation rates. Despite some deviations (notably in the 96 nm thin and thick PVAl, and 50 nm thin PVAl samples), the data supports a defect driven permeation mechanism consistent with findings in coated PET substrates. 364

Figure 5-20: Permeability plotted against total defect area for coated PVAl films of two varying substrate thicknesses and AlO_x coating thicknesses. The trend underscores a defect drive permeation mechanism where larger defect areas yield higher permeability, while lower defect areas result in reduced permeation. Although some discrepancies exist (notably in thick PVAl samples), the overall pattern remains clear across the data range. 365

Figure 9-1: (a) Punched aluminium foil masks with adhesive backing, (b) standard mask sizes used in the MOCON Aquatran, and images depicting (c-1) the interior of a MOCON Aquatran cell, (c-2) a full-size BOPP film, and (c-3) masked 1 cm^2 samples 429

Figure 9-2: Control calcium tests to establish baseline settings and verify sample preparation. (a) Top view of the negative control (glass slides) and positive control (DuPont PET film), (b) front view of the specimens (positive control unhinged), and (c.1 and c.2) schematics of the negative and positive controls. The epoxy layer is illustrated extending around the edges to reduce sideways permeation. Samples were stored at room temperature (~23–25 °C) and 40% relative humidity for approximately one year..... 431

Figure 9-3: The Calcium Test Box Temperature Profile shows the air temperature inside the test box (measured by a data logger with a thermocouple) plotted against the hotplate's-controlled set temperature. While slight variations occur due to uneven heating

on the hotplate, the ambient temperature typically remains within a degree or two of the target range. Another challenge is condensation or fogging on the glass window, caused by the warm air inside the test box meeting the cooler surface of the window. This fogging can obstruct visibility and affect image clarity..... 432

Figure 9-4: The issue of glass fogging at higher ambient temperatures, which caused condensation on the window walls, was resolved using two methods: (1) applying a hydrophobic coating to increase the contact angle and reduce condensation, and (2) heating the window walls to prevent warm air inside the calcium test box from condensing on the cooler surface. 433

Figure 9-5: (a) Influence of Calibration Strip on fluence calculations, showing regions of interest and changes in mean grey values (reference max for calibration strip mean intensity of 202.0 = 100 normalized, darkest shade mean intensity at 19.0 = 0 normalized; measured initial frame opaque at Frame #1: 19.42, the mean or final mean intensity value when all of the calcium has been depleted at Frame #75: 69.24). (b) Uncalibrated vs. calibrated calculated fluence over time, highlighting how shifts in mean grey values impact fluence calculations, corrected by normalizing with the calibration strip. (c) Calibration strips mean intensity values, illustrating the downshift between images 23 and 24 and constant grey values across the eleven regions of interest. (d) Average normalized mean grey values of the calibration strip, grouped into "lighter" (pre-shift) and "darker" (post-shift) portions, used to correct fluence plots for each calcium test sample. 436

Figure 9-6: A cleanliness protocol was developed to prevent contamination and reduce dust artifacts during calcium testing, particularly during the deposition of calcium

and copper. A dedicated container was introduced for transporting samples between the thermal evaporator and the calcium test box to limit contamination, it was also observed that varying epoxy curing times had no significant effect after five minutes of curing reducing the time of cure would reduce the amount of possible exposure to any possible impurities within the surrounding environment. 437

Figure 9-7: Permeation plots over water vapor pressure highlight factors affecting the applicability of Henry's law and its linear relationship. (a) MOCON Aquatran 2 data shows permeation rates clustering by temperature, displaying a clear linear trend. (b) Calcium test data aligns with the general trend observed in the MOCON data and literature. (c) Piergiovanni's data reports numerous WVTRs under varying conditions, showing a strong linear trend originating from the origin [249]. (d) A compilation of literature data on uncoated PET substrates at various temperatures shows consistent linear trends, though variations increase with different methods, parameters, and film types [25, 93, 110, 246, 250, 254, 258]. 443

Figure 9-8: (a) A half-coated Si chip (10 x 10 mm) with 1000 cycles of AlO_x shows a clear visual contrast between the coated side (left) and the uncoated Si surface (right). (b) Four Si chips were placed at equidistant corners inside the ALD chamber to assess thickness variation. Ellipsometer measurements from both front (F) and back (B) sides after 750 cycles showed an average AlO_x thickness of ~73.51 ± 4.45 nm across the chips. 451

Figure 9-9: Ellipsometer measurements of AlO_x-coated Si chips (front and back) over various ALD cycles show significant deviations at lower cycles (63 and 125) and underestimations at higher cycles (750 and 1000), while 250 and 500 cycles yielded

optimal growth. Interestingly, at 750 cycles, the back side (75.23 ± 0.37 nm) was more consistent with the predicted 75.0 nm than the front (68.89 ± 3.38 nm), despite appearing less coated. This suggests visual inspection of the Si chip alone may be misleading in assessing coating quality or deposition for barrier films. 453

Figure 9-10: WVTR values (log scale) of 96 nm AlO_x barriers (1000 cycles) on PET, processed at 80°C and 150°C, tested with the Mocon Aquatran. The results show low WVTRs overall, with minimal variation except for one outlier at 80°C processed sample, likely due to damage on the exposed side during testing. **Note:** 50 cm² full-size samples were tested without an Al mask. 456

Figure 9-11: Natural log of WVTR vs. reciprocal temperature, using the Arrhenius Equation to estimate activation energy in barrier samples, illustrating slight variations due to different film production temperatures and their effect on defects and overall barrier properties..... 457

Figure 9-12: Effect of masking on WVTR values for 73 nm (750 cycles) and 96 nm (1000 cycles) with both masked (1.0 cm^2) and unmasked (50 cm^2) AlO_x, showing the slight variation of adding a mask which may increase the overall measured WVTR respective to the same thickness and condition. 459

Figure 9-13: Summary of ALD AlO_x coating thickness, temperature, and relative humidity on permeability, highlighting coating thickness as the primary factor in barrier performance. Indicating that environmental conditions, such as humidity and temperature, influence WVTR but become less significant after a critical thickness (*e.g.*, above 14.0 nm), where defects or holes in the substrate are sufficiently covered..... 462

Figure 9-14: Analysis of the remaining Ca region for the 14.0 nm AlO_x on PET sample at 25°C with 39.5% RH ($MgCl_2$ solution) illustrates the impact of accounting for edge permeation (sideways ingress) on both spot count and average spot size. Edge effects are likely caused by epoxy ingress or layer delamination, can artificially inflate WVTR values and introduce errors in the detected number of spots. When edge affect regions are not excluded and the whole sample is considered as shown in Appendix: Figure 9-15 the measured WVTR increases significantly (*e.g.* $0.026 \pm (2.45 \times 10^{-4})$ $g/m^2 \cdot day$) compared to the corrected value obtained by excluding edge regions $0.0023 \pm (5.66 \times 10^{-4})$ $g/m^2 \cdot day$. Focusing solely on the central calcium region, as done here in this figure, also reduces the estimated spot count showing 27 spots on Day 1 and a maximum of 226 by Day 27, compared to the inflated counts when edge effects are included. Although the absolute values differ, the overall degradation trends remain consistent. The relationship between exposure time, decreasing central masked area (used here as a proxy for remaining calcium – however this also includes spots or areas within this region), and spot size remains evident across both data sets. 466

Figure 9-15: Spot growth analysis for a 14.0 nm AlO_x layer on PET substrate at 25°C and 39.5% RH ($MgCl_2$ solution). The chart illustrates the progression of fluence, which increases approximately linearly (WVTR: $0.0026 \pm 2.45E^{-4}$ $g/m^2 \cdot day$, Permeability: $1.33\ E^{-16} \pm 1.26\ E^{-17}$ [mol/(m·s·Pa)]). Spot growth is tracked at specific intervals (Days 1, 7, 19, 28, 36, and 65, showing an increase of average spot size from 0.002 cm^2 to 0.011 cm^2. 468

Figure 9-16: Six Regions of Interest (ROIs) were identified on a 14.0 nm AlO_x PET substrate at 25°C with an $MgCl_2$ solution at 39.5% RH. ROIs 1-4, divided into equal

rectangular areas, were analysed for permeation behaviour. Fluence plots, combined with defect counts and average sizes, showed a clear correlation between defect size/quantity and fluence. ROI 5, which reached full saturation in a week, and ROI 6, which took two months, highlight contrasting WVTRs. These regions suggest that defect size plays a significant role in barrier performance, with the timing of maximum spot count indicating the onset of increased fluence. 470

Figure 9-17: Absolute Percent Difference (%) WVTR calculations between non-edge accounted and edge accounted estimations for various thicknesses, based on the data presented in Figure 4-11. The figure reveals substantial discrepancies in WVTR values resulting from water permeation through edge defects, with differences ranging from significant to critical, affirming the necessity of accounting for edge effects. 472

Figure 9-18: Defect analysis of images from Tobin, Suttle, and Assender [194]; comparing Ca tests of RF sputtered AlOx films on BOPP (145 nm) and PEN (148 nm), tested at 38°C and 85% RH. Raw images, identified defect spots, and coloured overlays are shown alongside the grayscale Ca images. Limited data and image quality introduce uncertainties in WVTR measurements. Thresholding challenges due to low contrast and noise make it difficult to differentiate true defects from artifacts and background noise, leading to variations in defect identification (*e.g.*, undetected or misidentified spots on PEN). (a) Fluence-over-time graph for BOPP and PEN, with WVTR estimates: 0.01265 ± 0.00176 g/m²·day for BOPP and 0.01112 ± 0.00129 g/m²·day for PEN. These values are lower than the MOCON-reported literature values at 38°C and 100% RH (BOPP: 0.38 g/m²·day, PEN: 0.054-0.076 g/m²·day), Data points were selected from the first detected permeation until saturation or the final recorded image. (b) Defect spot density

analysis, showing that rougher BOPP exhibited a maximum of 112 spots/cm², while smoother PEN had a maximum of 11 spots/cm². (c) Average detected spot area over time, including both individual or isolated and coalesced spots; coalescence of spots was difficult to fully differentiate in the analysis, potentially leading to a slight overestimation of the average spot size. 475

Figure 9-19: Representative raw, grayscale, and analysed images of 26 nm, 50 nm, 73 nm 96 nm ALD AlO_x coatings on PET, tested at 25°C and 39.5% RH ($MgCl_2$ solution). Images show the progression of permeation-induced defects over time with coloured regions marking identified spots. Such that spots are defined as areas of local Ca depletion located within the intact Ca region, excluding areas near the sample edges or classified as background. White regions in the thresholded images represent depleted Ca and/or background or possible edge effects, as known there may occur some errors where Ca intact may not have been classified as spot. Most initial defects appear circular in shape, though this becomes less apparent in coalesced regions where adjacent spots merge and form irregular structures. Below, spot density is plotted over time across samples, revealing similar growth and saturation behaviours. Axes cross at zero to show that spot densities approach near-zero values at long durations. These observations align with the WVTR, and permeability values presented, with edge permeation effects excluded. 479

Figure 9-20: Spot Density Analysis of AlO_x Coatings at 25°C and 78.5% RH. This figure presents representative images and spot density measurements for coatings of varying thicknesses (14.0 nm, 26 nm, 50 nm, 73 nm, and 96 nm) subjected to a high humidity environment (controlled by Saturated NaCl solution). The corresponding

WVTR and permeability values are provided in the table. While higher WVTR and permeability suggest a greater number of defects, the observed spot density (spots/cm^2) estimations, do not fully correlate with this trend. This discrepancy is attributed to the increased water vapor permeation rate at high humidity, which leads to spot coalescence and blurring, hindering accurate spot detection and potentially underestimating the actual defect density. The challenges in accurately characterizing spot density under these conditions highlight the complex interplay between humidity, permeation, and defect visualization. 482

Figure 9-21: The influence of temperature on spot density of 50 nm AlO_x ALD coating at constant humidity (~70.25%-71%) was studied across four batches (A: -25°C, B: 25°C, C: 35.5°C, D: 50.5°C). Raw images, grayscale, and particle analysis were used to track spot growth and count predictions. Spot density was plotted according to temperature over time, highlighting how temperatures affect spot formation where at cold temperatures spot formation takes a substantial amount of time versus a faster spot formation at higher temperatures. Moreover, a table summarizing WVTR, coefficient of determination, and permeability was also included; showing that all the 50 nm samples showed very similar WVTR's and permeabilities; asserting that the number of defects should be the same, and the change in spot detection and growth is due to temperature, underscoring the need for precise environmental control for accurate spot detection. .. 486

Figure 9-22: (a) **Isolated Spots** and (b) **Coalescence Spots** (where spots merge) over time for various samples with different coating thicknesses at lower relative humidity (39.5%). The number of spots per frame has been normalized by the imaged area (spots · cm^{-2} · frame^{-1}) to account for differences in Ca test image sizes, enabling

valid comparisons across samples. The data shows that most isolated spots are detected within the first few days, emphasizing the importance of distinguishing between isolated and coalesced spots. Failure to account for coalescence can significantly impact the estimated number of spots, as merging continues throughout the entire calcium test timeline. 490

Figure 9-23: (a) **Isolated Spots** and (b) **Coalescence Spots** are tracked over time for various samples with different coating thicknesses at higher relative humidity (78.5%); where number of spots per frame has been normalized by the imaged area (spots $\cdot$ cm^{-2} $\cdot$ $frame^{-1}$). The results reveal trends like those observed at lower humidity, where most isolated spots are detected within the first few days. Despite the faster permeation rate, the method demonstrates improved confidence in accurately characterizing and counting spots across the dataset. Additionally, the findings indicate that coalescence begins relatively early and continues throughout the entire test duration, reinforcing the need for careful differentiation between isolated and merged spots..... 492

Figure 9-24: (a) Representative images of a coated PET film at Day 1, Day 22, and Day 50 showing the progression of water ingress at selected defect sites (highlighted in magenta). The bottom panel shows a binarized defect map from Day 50 with ten selected spot locations labelled for tracking. (b) Cumulative water mass uptake over time for the ten selected defects. The pale data points indicate the equilibration period before the onset of noticeable water ingress, highlighting the transition point at which each defect begins to grow significantly. By analysing uptake trends and dividing by the experimentally measured bare PET WVTR (~2.11 ± 1.40 g/m²·day at 29 ± 3.5°C and 48.2 ± 19.6% RH), the original defect areas were estimated. Assuming most defects are

approximately circular ($r = \sqrt{(A/\pi)}$, defect sizes were inferred to lie in the micrometre range..... 494

Figure 9-25: Representative samples of spots for varying thicknesses (a) 26.0 nm, (b) 50.0 nm, (c) 73.0 nm, and (d) 96.0 nm, tested at 25°C and 39.5% RH ($MgCl_2$). The graphs display water uptake (fluence) over time, with corresponding images of sample spots for each thickness, showing different defect sizes..... 499

Figure 9-26: Polyvinyl Alcohol prepared by base catalysed trans-esterification reaction of polyvinyl acetate where it is hydrolysed in a strong base (NaOH) in a alcohol solution (methanol) [457, 458]. 502

Figure 9-27: The WVTR vs. A/D Turns model demonstrates a linear relationship, allowing estimation of PVA's WVTR using A/D turns from the Mocon Aquatran raw data..... 508

Figure 9-28: WVTR (on logarithmic scale) for thin PVAl (21 μm), with AlO_x coatings pf varying thicknesses at different temperatures. Error bars represent the standard deviation of measurements, reflecting variability across replicates, likely due to PVAl's high permeability, errors in A/D estimation, and averaging inconsistencies. No consistent trend was observed with coating thickness beyond an initial reduction in WVTR, but notably, at higher temperatures, PVAl sometimes recorded lower average WVTR values than at lower temperatures. For instance, uncoated PVAl at 38°C showed an average WVTR of 4.76 ± 2.88 g/m²·day, which is lower than the 6.78 ± 4.24 g/m²·day at 14°C. Similarly, for 96 nm AlO_x-coated PVAl, the average WVTR at 38°C was 8.0 ± 5.96 g/m²·day, compared to 6.19 ± 2.65 g/m²·day at 14°C. The relatively high standard

deviations indicate substantial variability across measurements, suggesting possible inconsistencies in barrier performance or experimental conditions. 510

Figure 9-29: WVTR (on logarithmic scale) for thick PVAl (42 μm), with AlO_x coatings pf varying thicknesses at different temperatures. Compared to thinner samples, the thicker PVAl exhibited lower standard deviation, suggesting greater uniformity and improved measurement reliability. This may be due to thicker PVAl having better barrier properties (less permeable) and it being thicker was easier to test and handle, especially for cases like PVAl or highly permeable films where detection limits were over exceeded in the MOCON Aquatran. As with thinner samples, a directly proportional relationship between temperature and WVTR is not consistently observed, like trends seen in PET substrates. For example, for 96 nm AlO_x - coated thick PVAl, WVTR at 38°C was 8.51 ± 1.71 g/m²·day, compared to 23.77 ± 4.95 g/m²·day at 25°C. This suggests that factors beyond temperature alone have influenced WVTR estimations in these systems..... 513

Figure 9-30: (a) Calcium depletion in thin PVAl tested at 23 °C and 40% RH. Red arrows indicate uneven permeation from right to left, likely due to variations in film thickness or substrate imperfections. (b) Calcium depletion in thin PVAl tested at 45 °C and 65% RH, showing accelerated depletion compared to (a), highlighting the influence of elevated temperature on WVTR. The difference in WVTR is approximately ~23 g/m²·day between these conditions. Notably, this estimate is considerably also higher than those obtained from MOCON Aquatran System, which may be due to systematic overestimation in the Ca test (particularly for coated ALD samples). However, at lower conditions, the MOCON Aquatran values align more closely with the results from (a). (c) Thicker PVAl film (42 μm) tested at 45 °C under 65% RH (LiCl) and 71% RH ($MgCl_2$)

further highlights discrepancies between measurement techniques. The Ca test estimates for the WVTR of uncoated PVAl are significantly higher compared to MOCON values. While increased thickness results in a slight reduction in WVTR (20.3 ± 1.62 g/m²·day at 65% RH, and 21.1 ± 2.11 g/m²·day at 71% RH), localized permeation effects remain evident. The primary film layer depletes, yet isolated calcium spots persist, suggesting a more complex WVTR transport mechanism than what is typically observed in PET or other conventional barrier substrates. 519

Figure 9-31: Representative Thin PVAl (Betol) coated samples with three varying thicknesses of AlO_x (a) 26 nm - (4.58 ± 0.857) $\times 10^{-4}$ g/m^2·day, (b) 50 nm - (2.22 ± 0.14) $\times 10^{-3}$ g/m²·day, (c) 96 nm - (9.93 ± 0.44) $\times 10^{-4}$ g/m²·day, showing that a decrease in WVTR is not always observed in increasing thickness (defect controlled permeation); accompanying images of the calcium depletion and sample during the analysis – showing the defect like features that indicate permeation and the degradation or possible presence of hydrolysis upon reaction with water as suggested by the change and disappearance of copper backing layer. 524

Figure 9-32: Representative thick PVAl samples coated with AlO_x at varying thicknesses: (a) 26 nm - (6.18 ± 0.27) × 10^{-5} g/m²·day, (b) 50 nm - (1.24 ± 0.04) × 10^{-3} g/m²·day, (c) 96 nm - (1.05 ± 0.06) × 10^{-3} g/m²·day. (d) The fifth frame of each sequence (highlighted) shows the development of broad, ravine-like bright features, especially prominent in thicker coatings. These features suggest progressive permeation along macro defect pathways, while dark island-like areas reflect regions of effective barrier protection. It also shows that thin coatings can achieve low WVTR's and possibly fewer

defects. While degradation of the copper layer upon hydrolysis is still observed in all cases. 528

Figure 9-33: Thin and Thick PVAl samples coated with AlO_x (50 nm and 96 nm) show characteristic permeation morphologies captured at progressive timepoints. Though taken from individual samples, the spot-like, island-like, and river-like features are representative of those seen across different conditions. These images illustrate the typical defect patterns that emerge depending on coating thickness and substrate type. 530

Figure 9-34: ImageJ-estimated number of defect features ("spots") over time for thin and thick PVAL samples with varying AlO_x thicknesses (26, 50, and 96 nm). Trends show an initial increase followed by a decrease in spot count, likely due to coalescence. Thick PVAL tends to show fewer spots than thin PVAL over time, but no consistent trend is observed with coating thickness. 531

Figure 9-35: Spot size trends over time for thin and thick PVAl samples with varying AlO_x thicknesses (26, 50, and 96 nm). Spot size is defined as the major axis length of each detected feature. While referred to as "spots," features are often elongated or irregular, especially in PVAl. Occasional outliers above 100 µm, likely due to merging or image artifacts, illustrate the limitations of early thresholding methods..... 533

Figure 9-36: Ca test results for 50 nm AlO_x on thin PVAl (5.21 x 5.00 cm), divided into two sections to exclude regions obscured by Kapton tape. (a.2.1) Section 1 (4.60 x 2.56 cm): Raw image showing gradual crack growth. (b.2.1) Detected features include large, coalescing spots identified by the algorithm. (c.2.1) Spatial distribution indicates a relatively uniform spread of isolated spots across the section and a slight bias on top right for coalescing spots. (a.2.2) Section 2: Raw image reveals defects resembling a "turtle

shell" pattern. (b.2.2) Algorithm relatively successfully identifying the defects and features, with (c.2.2) showing a consistent and uniform spatial distribution of the features across the region of interest for both isolated and coalescing. These results also highlight the Ca test's ability to resolved localized defect populations and maintain reliable detection across varying sample regions..... 538

Figure 9-37: (a.4) Raw Ca test images of 26 nm AlO_x on thick PVAl (5.00 x 4.64 cm), showing prominent linear or crack-like features similar to those observed in coated thin PVAl samples. (b.4) The defect detection overlays reveal a staggered appearance of spots, indicating that defects do not emerge simultaneously across the sample. (c.4) Despite this temporal variation, the spatial distribution of isolated spots is uniformly present the film, but the coalescent spots do suggest a slight bias towards the right-hand side of the barrier layer. 541

Figure 9-38: (a.5) Raw Ca test images of 50 nm AlO_x on thick PVAl (5.03 x 5.00 cm) show a shift from linear to more spot-like defects compared to thinner 26 nm coatings, suggesting coating thickness influences defect types. (b.5) Overlaid detection results reveal that isolated defects persist up to day 48 with full coalescence by day 72. However, calcium remains in some regions, indicating partial or delayed permeation. (c.5) Spatial distribution maps show for both isolated and coalescing spots are uniformly spread across the sample, rather than concentrated in specific regions. 544

Figure 9-39: Ca-test results for 96 nm AlO_x (5.78 x 4.84 cm), (a.6) Raw images reveal prominent, wave-like features spanning millimetres, distinct from the finer-scale surface roughness of uncoated PVAl, suggesting macro-scale deformation (*e.g.* swelling or delamination) rather than imprinting from initial topography. (b.6) Spot detection

overlays show strong visual correspondence to raw images, despite challenges posed by overlapping patterns in later frames. The Python-based algorithm effectively distinguishes isolated and coalescing features. (c.6) Spatial maps confirm a relatively uniform distribution of isolated spots, while coalescing spots exhibit a bias toward the upper region possibly indicating preferential permeation pathways or uneven stress response..... 547

Figure 9-40: (a) Isolated and (b) Coalescing Spot Densities over time for ALD AlO_x -coated thin PVAl films with coating thicknesses of 26 nm, 50 nm, and 96 nm. Isolated spot counts initially rise but gradually plateau after ~50 days, suggesting that no new, distinguishable defects form beyond this point. In contrast, coalescing spot density increases significantly after ~20 days as existing isolated features merge, ultimately stabilizing as saturation is reached. The accompanying table summarizes geometric characteristics of these defects. Isolated spots typically measure ~ 0.53 – 0.81 cm in length and exhibit high aspect ratios (3.4 – 4.2), indicating the elongated, slit-like geometry in early stages. Upon coalescence, defect widths increase markedly from ~ 1.5 – 2.5 μm to ~22 μm, supporting the hypothesis of lateral swelling or active permeation during prolonged exposure. These evolving morphologies highlight the importance of early-stage spot detection in assessing barrier integrity. 551

Figure 9-41: Spot densities in thick PVAl films coated with AlO_x at different thicknesses (26 nm, 50 nm, and 96 nm). Panel (a) shows the evolution of isolated spot densities over time, while panel (b) shows coalescing spots. As observed in thin PVAl films, isolated spot counts initially increase and then decline as defects begin to merge. Coalescing spot densities continue to rise until reaching a plateau. Although the total

number of isolated spots appears lower in thicker films, the final number of coalescing spots remains comparable to those in thinner PVAl. Defect size trends seem to be also slightly influenced by coating thickness. Average spot lengths increase with coating thickness from 0.31 ± 0.18 cm at 25 nm to 1.30 ± 0.72 cm at 50 nm, while aspect ratios remain high (3.3–4.2), consistent with elongated morphologies. Notably, the average width of isolated defects is much smaller than that of coalescing ones (*e.g.*, 1.4 ± 7.0 μm vs. 17–24 μm), which is expected as the network continues to grow. 556

Figure 9-42: Six selected regions of interest from a 50 nm AlO_x ALD-coated thin PVAl substrate, with the largest defects in each region highlighted by the red outlines and binary segmentation images. These defect areas range from approximately $2.42 \times 104\ \mu m2$ to over $4.16\ \times 105\ \mu m2$, consistent with higher water uptake rates and slopes in this sample compared to the 26 nm coatings. Despite the smaller ROI sizes in the 50 nm samples, these larger defect areas along with more numerous visible features, correlate with higher WVTR values and suggest that thicker coatings can still develop more and larger isolated defects. This emphasizes the challenges in achieving a uniform barrier performance in thin film encapsulation applications. 561

Figure 9-43: Five linear defects and two distinct circular or spot-like defects in the 96 nm AlO_x ALD-coated thin PVAl substrate, each outlined in red and shown as isolated binary images. These features differ from the finer dendritic structures seen in thinner coatings and instead resemble island-like or “spot” structures with surrounding Ca depletion. While defects areas in these thicker samples are generally smaller – range from $1.6 \times 103\ \mu m2$ to $4.8 \times 104\ \mu m2$ for linear defects, the two circular spot-like features have significant total areas of $2.26 \times 104\ \mu m2$ and $2.45 \times 104\ \mu m2$, respectively. This

supports a possibility that even thicker coatings, large isolated macro-defects can form and compromise barrier performance, explaining the relatively high WVTR observed in these PVAl substrates. 566

Figure 9-44: Six regions of interest from a 26 nm AlO_x ALD-coated thick PVAl substrate show dendritic, or blob-like defect features similar to those observed in thinner PVAl films. The calculated defect total areas range from $1.39 \times 104\ \mu m2$ to $9.92 \times 104\ \mu m2$, comparable to the 26 nm thin PVAl data. This suggests that while the substrate thickness does not strongly influence the overall defect size, the defect morphology in thick PVAl substrates tends to appear more blob-like and with larger defect areas compared to the thinner samples..... 570

Figure 9-45: Fiver regions of interest from a 50 nm AlO_x ALD-coated thick PVAl substrate reveal a transition from a linear or dendritic defects to larger, more spot-like formations, with some resembling features seen in ALD-coated PET substrates. The largest defect areas such as Defect #1 $2.16 \times 105\ \mu m2\ \pm 3.00\ \times 104\ \mu m2$, indicate a trend towards fewer but larger defects in the thicker PVAl, compared to the thinner 26 nm samples. Three additional spots, Spots #1 – 3, show variable sizes, with Spot #1 and Spot #2 having notably larger areas ($8.62 \times 103\ \mu m2\ and\ 1.39 \times 104\ \mu m2$) respectively, compared to Spot #3's smaller $4.86 \times 102\ \mu m2$ area. These defect area measurements highlight the complex and evolving defect morphology in thicker coatings, demonstrating thicker PVAl samples can still develop significant isolated defects that contribute to water vapour permeation. 576

Figure 9-46: Six regions of interest from a 96 nm AlO_x ALD-coated thick PVAl substrate highlight the evolution of defect structures across a range of sizes and shapes.

Binary and outline images show wave- and rive- like defect structures, deviating from the typical circular features seen in thinner coatings or PET substrates. Defect areas range from mid-10^4 μm^2 to as large as 1.85×10^5 μm^2 for Defect #5, illustrating that thicker coatings can still exhibit significant isolated defect areas. Spot #1, measured at 1.18×10^5 μm^2 ($\pm 4.56 \times 10^3$ μm^2), further emphasizes the presence of these large, isolated defects in the thickest coated thick PVAl films. These large defect areas align with observed water uptake rates and highlight once more the complexity between AlO_x coating thickness, defect morphology and WVTR. 580

List of Abbreviations

AFM	Atomic Force Microscope	**PEDOT**	Poly(3,4-ethylenedioxythiophene)
E_a	Activation energy	**PA**	Polyamide
ASTM	American Society for Testing and Materials	**PBAT**	Polybutylene Adipate Terephthalate
ANOVA	Analysis of Variance	**PC**	Polycarbonate
A	Area	**PDMS**	Polydimethylsiloxane
ALD	Atomic Layer Deposition	**PEEK**	Polyether ether ketone
ALE	Atomic Layer Epitaxy	**PES**	Polyether sulfone
S_d	Average defect size	**PEN**	Polyethylene Naphthalate
BOPP	Biaxially Oriented Polypropylene	**PET**	Polyethylene Terephthalate
BSI	British Standards Institution	**PI**	Polyimide
Ca	Calcium	**PLA**	Polylactic acid
Δn	Change in mass or quantity of permeant	**PVA / PVOH / PVAl**	Polyvinyl Alcohol
Δt	Change in time	**PVDF**	Polyvinylidene Fluoride
L	Current light intensity at region of interest	**P_o**	Pre-exponential factor (in Arrhenius equation)
D	Diffusion coefficient	***A***	Proportionality constant for calcium layer thickness and light transmission
J	Diffusive flux	**QCM**	Quartz Crystal Monitor
EVOH	Ethylene vinyl alcohol	**RF**	Radio Frequency
L	Film thickness	**RFID**	Radio Frequency Identification
L_f	Final and initial mean light intensity	***dn/dt***	Rate of substance passing over time
FE	Flexible Electronics	**RH**	Relative Humidity
F	Fluence (mass of water vapor over area of calcium)	**h_{rem}**	Remaining thickness of calcium layer
G(x,y)	Gaussian function (gradients in x and y directions)	**V_{rem}**	Remaining volume of calcium
Θ	Gradient direction (in Canny Edge Detection)	**RMS**	Root Mean Square
H	Henry's constant or solubility within the film	**SEM**	Scanning Electron Microscope

L_i	Initial mean light intensity	**Si**	Silicon
h_o	Initial thickness of calcium	***S***	Solubility coefficient
ISO	International Organization for Standardization	***Ds***	Spot density (Spots/cm²)
$M_{(H_2O)}$	Mass of water vapor permeating through film	F_{ss}	Steady-state flux
M_r	Molar weight	**TFE**	Thin Film Encapsulation
OFET	Organic field-effect transistor	**TGA**	Thermogravimetric Analysis
OLED	Organic light emitting diode	**TPU**	Thermoplastic Polyurethane
OPV	Organic Photovoltaics	A_{PVAl}	Total defect area for coated PVAl layers
V_o	Original volume of calcium	A_{dspots}	Total spot defective area
OTR	Oxygen Transmission Rate	σ_w^2 **(t)**	Total variance between dark calcium and light background at time t
P	Partial pressure	**TR**	Transmission rate
ΔP_{gas}	Partial pressure difference	**TMA**	Trimethyl Aluminium
PH_2O **(T)**	Partial pressure of water at temperature T	**UV**	Ultraviolet
P	Permeability	σ^2	Variance (standard deviation squared)
C	Permeant concentration	V_{Ca}	Volume of reacted calcium
PVD	Physical Vapor Deposition	**WVPP**	Water Vapor Permeation Pressure
PECVD	Plasma Enhanced Chemical Vapor Deposition	**WVTR**	Water Vapor Transmission Rate
PE-ALD	Plasma-Enhanced Atomic Layer Deposition		

1 Introduction

1.1 Improving the field of Flexible Electronics (FE)

Advancing the boundaries of modern flexible technology requires significant progress in protective barrier layers for Flexible Electronics (FE)—bendable and conformable electronic circuits [1]. Once an obscure field, FE has now emerged as a dynamic area of study with promising growth prospects [2-5].

These electronics are vital for diverse applications, including large-area displays (*e.g.*, smartphones and TVs), electronic inks, "electronic paper", medical prosthetics (*e.g.*, flexible sensors and electronic skin for artificial limbs), military equipment, solar cells, and aerobic sensors [6-8]. In addition to their flexibility, these devices offer benefits such as reduced weight and space (through the transition from bulky ceramic or metal casings to lightweight plastic packaging) and lower manufacturing costs via roll-to-roll production methods [7, 9, 10].

One critical challenge is the rapid degradation of these devices when exposed to different environmental factors. For instance, Organic Light Emitting Diodes (OLEDs) and chemical electrodes are highly sensitive to moisture, making them unstable in ambient conditions. Similarly, Organic Photovoltaics (OPVs) have a lifespan of only a few hours without proper encapsulation, despite solar cells requiring industrial lifetimes of 3 to 5 years [11-16].

The critical need for robust Thin Film Encapsulation (TFE) is reflected in the technology's transition from pilot demonstrations to mass production, particularly for flexible OLEDs. Recent peer-reviewed literature, written from a mass production

engineering perspective, documents the industry's consolidation around multilayer inorganic or organic stacks and identifies future growth vectors toward thin and ultra flexible encapsulants that meet the ultra-low water vapour requirements for flexible electronics [17-20].

Analysts estimate that flexible electronic market sizing was reported £18.6 B (2022) to around £40.3 B (2030), with a compound annual growth rate of 10.5% (Source USD Figures: $24.94 B to $54.07 B) [21], other sources showed similar estimates and predictions with £19.5 B (2022) to £42.8 B (2032), CAGR 8.2%. Source (USD figures: $26.2 B to $57.3 B) [22], or £23.6 B (2022) to £66.5 B (2030), CAGR 19.1% Source (USD figures: $31.7 B to $89.2 B) [23]. The reliability of these devices is critically dependent on high performance encapsulation, which in turn propels a corresponding demand for the advanced materials required to protect them. Such that the global market for electronic potting and encapsulating materials was valued at approximately £2.42 billion ($3.1 Billion) in 2019 and is on a steady growth with forecasts of it reaching to £3.32 billion ($4.1 billion) in 2027 [24].

However, these encapsulants or substrates must meet several key criteria to ensure the viability of FE. These include suitable mechanical properties, chemical resistance, cost-effectiveness, UV stability, and controlled permeability. For specific applications, such as in medical devices, biocompatibility is also essential [25-28]. Unlike conventional electronics, which rely on rigid enclosures, FE need to maintain conformability while ensuring complete hermeticity [10].

Balancing flexibility, the ability to bend without functional loss, and reliability, including device lifespan and robustness, remains a key challenge. Thicker encapsulation

layers enhance and performance by increasing diffusion path length, lowering the concentration gradient across the layer, and delaying the establishment of dynamic equilibrium conditions for permeation. However, they often compromise flexibility and, in the case of vapor-deposited layers, require longer processing times and higher costs [29]. Careful material design is essential to minimize this trade off and achieve both flexibility and durability.

Another critical hurdle is the development of accurate and sensitive methods to measure permeation of the species of interest, such as the Oxygen Transmission Rate (OTR) and Water Vapor Transmission Rate (WVTR) - the rates at which oxygen or water permeate through a sample [30]. Accurate characterization of these parameters is essential for determining the performance of barrier layers.

There is considerable potential in multi-layer structures (organic – inorganic multilayers) to achieve ultra-low WVTR on flexible substrates [13, 31]. For example, on P*ET AL*D TiO_2/SAM (self-assembled monolayer) dyads have reached WVTR equal to 7.0×10^{-4} g/m^2/day at 60 °C / 85% RH during a 155 hour lag time using 5 dyads [31], with each dyad around 80 nm SAM plus a 9.6 nm TiO_2 and single layer TiO_2 experiments at various thicknesses (1.2, 2.4 and 4.8 nm) confirm that lag time scales with TiO_2 thickness [31]. On the other hand sputtered-oxide system like in the work by Graff and Burrows employ a 37 nm AlOx per dyad and ~0.20 to 0.34 μm acrylic interlayer reporting to have WVTR's equal to 10^{-6} to 10^{-5} g/m^2/day in such stacks lag time dominates rather than true steady state [13]. As a single layer reference, 10 nm of cyclic chemical vapour deposition aluminium oxide demonstrated ≈ 1.5×10^{-5} g/m^2/day at 85°C / 85% RH with stability for around 15,000 hours before humidity driven hydrate

reconstruction increases permeation [32]. In reporting the made film, it is an important distinction that the general formula AlOx is used for materials from energetic deposition methods, where incomplete reactions yield a film with uncertain stoichiometry, incorporated hydroxyl impurities, and structural defects. Conversely specific formulas like Al_2O_3 and TiO_2 are reserved for high fidelity films produced by precision chemical synthesis, whose self-limiting reactions ensure the formation of a pure and perfectly stoichiometric compound [33, 34].

In line with this, a widely used commercial embodiment is the Vitex Systems Barix^{TM} multilayers, which are alternating sputtered AlOx and UV-cure acrylate layers (~ 10 nm – hundreds of nm for AlOx; and ~0.25 – several μm for the organic), where the organic strata planarize and decouple defects to force a tortuous path for water vapour, 5 – 6 dyads have yielded ~10^{-4} g/m^2/day barriers and > 5,000 hour OPV lifetimes [35].

Moreover, as shown above and known: Atomic Layer Deposition (ALD) the main coating method has garnered interest due to its ability to produce high-quality barrier layers with excellent performance in FE even with thin, single layer coatings [36, 37]. This technique shows promise in providing a robust solution to encapsulation challenges while retaining the flexibility needed for next-generation devices.

1.2 What are Flexible Barriers?

These protective layers are typically composed of (1) inorganic materials: thin glass or metal foil, (2) hard organic materials: thin-film polymers (coated and uncoated), or (3) soft organic materials: elastomers [26, 38]. Rigid and flexible hermetically sealed packages made from metals and ceramics offer excellent moisture and gas

impermeability due to their tightly packed atomic structures, unlike more permeable polymeric materials with higher free volumes [10].

For instance, aluminium foil is nearly impermeable to water (*e.g.*, ≤ 0.01 g/m^2/day at 12 μm, and effectively zero for ≥ 15 μm gauges [39]; such that even 9 μm gives ~ 0.3 g/m^2/day at 38°C / 90% RH [40]), also resistant to corrosion by fats and mild organics, easily sterilized, and recyclable [8, 40-43]. However, it has limitations such as opacity or is opaque, rolled - surface roughness that affects over coatings, and is susceptible to tearing and pinholes or flex cracking at thin gauges, it can also often necessitate the use of adhesives or epoxy for complete encapsulation of FE [10, 14, 40, 44, 45]**.**

Ceramics, such as ultrathin glass, provide a promising solution for encapsulating FE, offering high optical transparency (exceeding 90% in the visible spectrum) and a WVTR of less than 1×10^{-6} g/m²/day [46-48]. Despite these advantages, ultrathin glass has poor mechanical properties, including low strain tolerance and brittleness, making it prone to edge damage during processing. These drawbacks make it less suitable for large sheets, even though it can be flexible at a thickness of 30–200 μm [14, 45, 49].

In response to these challenges, polymer materials may be preferred. The chemical structure and morphology of these polymers significantly affect their permeability [50-52]. The permeability of plastic materials is influenced by their crystallinity (the ratio of crystalline to amorphous phases), polarity (solubility of the permeating species), and glass transition temperature (related to free volume).

Organic materials or plastic packages coated with ceramics (*e.g.*, Al_2O_3, AlO_x, Si_3N_4, SiO_xN_γ, SiO_2, TiO_x, ZnO_x, or combinations thereof) [10, 11, 14, 26, 53-58] have gained popularity. These materials are lighter, more versatile, and less costly to design

and manufacture [10]. Their compatibility with roll-to-roll manufacturing also makes them attractive [59]. When structured as high-barrier multilayers, these oxide-coated materials reduce gas and vapor permeability by extending the diffusion path and mitigating defects [13, 25, 45].

Additionally, as Klopffer *et al.* note, permeation is also influenced by the size and nature of the permeants, as well as environmental factors such as temperature and pressure [60].

Figure 1-1 (a) illustrates the basic components of an electronic device, consisting of a substrate, interconnects, and a functional component, like a silicon chip. Devices are typically sandwiched or fully encapsulated on both sides to ensure longevity [47]. Figure 1-1 (b) depicts an encapsulated OLED, a typical example of FE. It includes an anode, conductive layer, emissive layer, and cathode, all on a flexible substrate. The OLED is encapsulated in an inert atmosphere (argon or nitrogen gas) with inorganic materials (metal or glass) sealed using adhesives or epoxy, and a getter or desiccator (such as calcium oxide or barium oxide) to absorb residual moisture [47, 61, 62].

Various encapsulation methods include: (c) Inorganic or rigid lid encapsulation, which offers environmental protection but lacks flexibility [12]; (d) Thin glass or flexible metal foil, providing barrier properties while maintaining flexibility, though adhesives may be required for full encapsulation [12]; and (e) Thin-film organic polymers or organic films coated with oxides, which fully conform to FE by sandwiching them between two films or forming encapsulant layers on the substrate. Some organic flexible barriers also use pressure-sensitive adhesives, but these can become failure points due to potential leaks at the adhesive sites [10, 45, 48, 62-65].

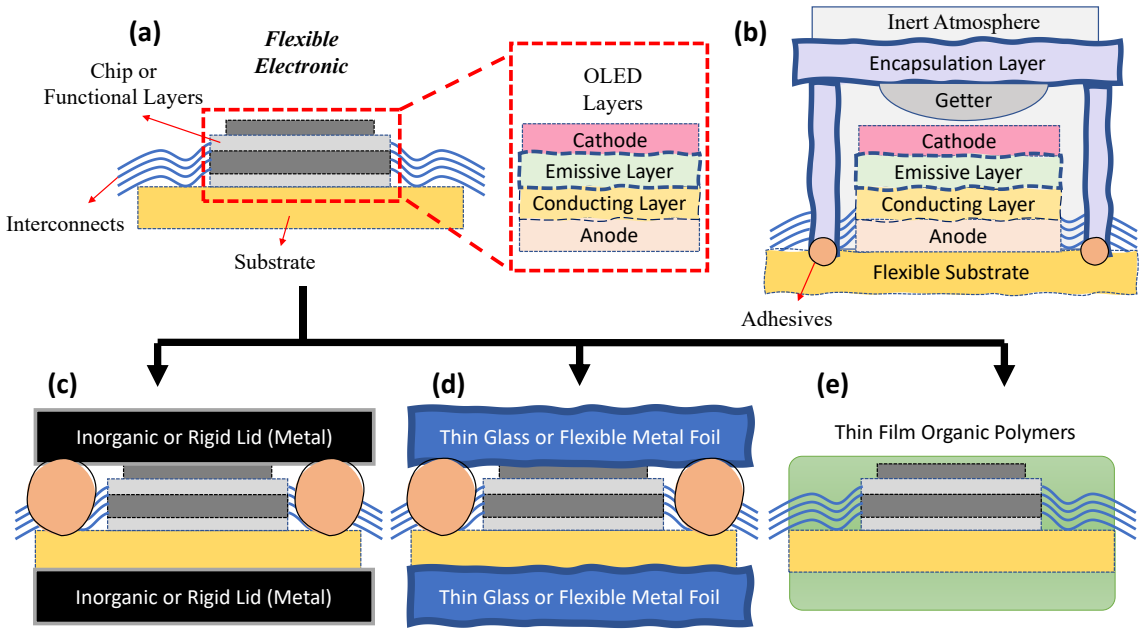


Figure 1-1.: (a) General Parts of a Flexible Electronic device, (b) Parts of an Encapsulated OLED and Common types of Encapsulations (c) Inorganic or Rigid Encapsulation, (d) Thin Glass or Flexible Metal Foil and (e) Thin Film Organic Polymers, collated from sources: [10, 12, 45, 48, 62-65].

1.3 Permeation Barrier

The WVTR directly impacts the degradation time of encapsulated devices. For example, reducing water vapor permeation from 10^{1} g/m²/day to 10^{-3} g/m²/day significantly extends the lifetime of water-sensitive devices[46]. Hauch *et al*, demonstrated that flexible polymer solar cells, encapsulated with barrier films exhibiting a WVTR of 0.2 g/m²/day reached operational lifetimes exceeding 1,250 hours under accelerated conditions (65°C, 85% RH) [66]. Meanwhile, Lungenschmied *et al*, reported that ultra-high barrier encapsulation (PECVD on PEN substrate) showed lifetime of organic solar cells over 6,000 hours [67]. This highlights the importance of controlling water vapor to ensure the longevity of organic electronics such as OLEDs, OPVs, and OTFTs. Achieving lifetimes beyond 10,000 hours requires WVTR values between 10^{-4}

and 10^{-6} g/m²/day, and OTR values between 10^{-3} and 10^{-5} cm³/m²/day/atm [14, 26, 45, 46, 59, 61, 62, 64, 68-71].

OLEDs degrade much faster due to water vapor than oxygen, by three orders of magnitude at room temperature, making water vapor permeation the critical factor to control [72, 73].

Figure 1-2 illustrates the available encapsulant materials and their alignment with device requirements. It highlights the stringent WVTR demands for organic electronics and the materials that may meet them. Currently, only a few options, such as Barix multilayers and experimental multilayer combinations of organic and inorganic layers, come close to the requirements for the most sensitive organic electronics.

Alternating thin layers like Al_2O_3 / SiO_x multilayers supress through-thickness defect percolation and enhance mechanical robustness. In single-layer architectures, intrinsic pinholes or microcracks provide direct pathways for moisture ingress. Interleaving these materials statistically decuples these defects, forcing water vapor to migrate laterally to reach subsequent pathways. This establishes a tortuous diffusion path and a longer, shallower concentration gradient, which significantly extends the barrier lag time [74].

Mechanically, this architecture exploits a significant elastic mismatch for internal stress management. ALD-grown Al_2O_3 films exhibit a high Young's modulus of approximately 160-182 GPa [75], and intrinsic tensile stresses that influence cracking behaviour [76]. In contrast, vapor-deposited amorphous SiO_x layers are notably more compliant, with a modulus of ~72 GPa [77]. The introduction of these more compliant layers alters the stress distribution within the stack, enabling the deflection or blunting of

crack tips at the interfaces during substrate bending, thereby preventing catastrophic brittle failure [78, 79].

Chemically, Al_2O_3 deposited via low temperature ALD is susceptible to hydrolytic degradation due to residual hydroxide (-OH) groups. Exposure to humidity triggers a transformation into boehmite, leading to film swelling and structural breakdown [80]. The integration of SiO_x layers which are thermodynamically stable and chemically robust, provides a capping effect that suppresses this degradation [13, 81-83]. This synergistic approach improves the environmental reliability of the stack for FE, where polymer substrates alone fail to meet barrier requirements (WVTR's ~ 10^{-1} to 10^2 $g/m^2/day$) [35, 71, 74].

The schematic also points out the limitations of common test methods. Gravimetric methods work only for high WVTRs, while low WVTR measurements require more precise techniques such as the isostatic method (MOCON or coulometric detectors) or the calcium test [27, 84-86].

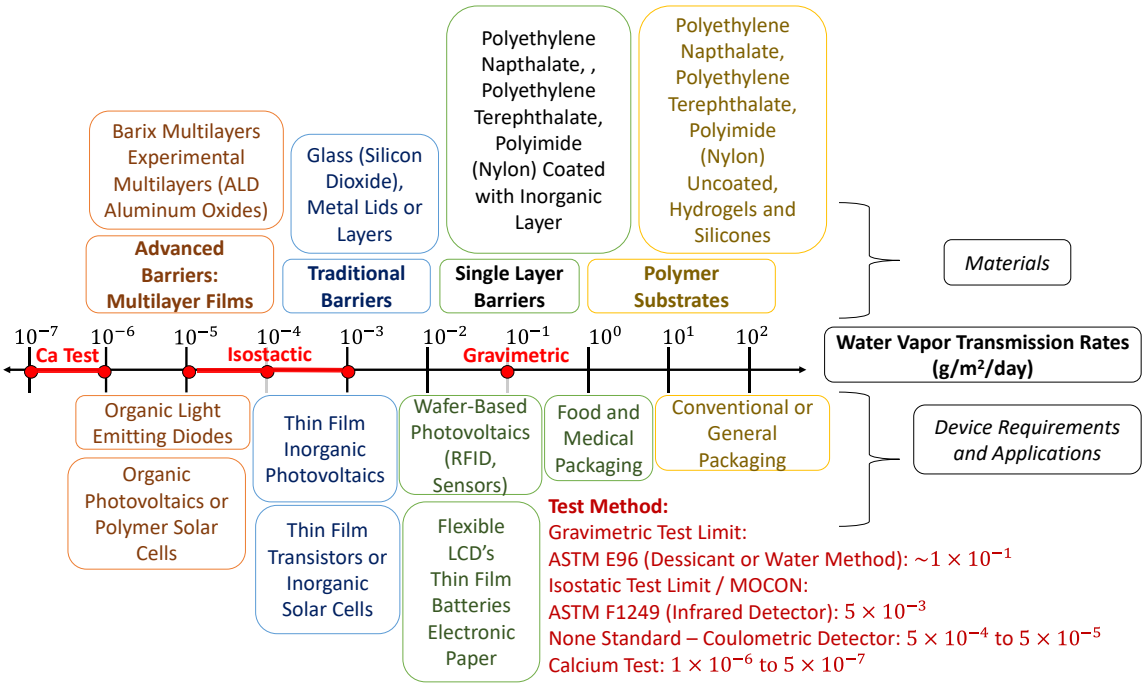


Figure 1-2: WVTRs: Number line of current existing materials (top), requirements for common applications (bottom) and WVTR limits of common test methods [14, 26, 28, 45, 46, 59, 61, 62, 64, 68-71, 87].

1.4 Background on Permeation Theory

Permeation refers to the transport of a permeant (*e.g.*, gas—water vapor—or liquid—water) passing through a resistant material, and is influenced by film thickness, surface area exposed to the permeation, duration of exposure, and the driving force across the layer. For gases, the driving force is typically partial pressure difference; for liquids it is a concentration gradient or chemical potential difference [8, 51].

Fick's 1st law [88] (Equation 1-1) describes how the diffusion rate of permeants at equilibrium depends on three factors: (1) the concentration gradient across the layer, (2) the effective cross-sectional area for diffusion and (3) the diffusion coefficient (D), which characterizes the material's resistance to permeation. The diffusive flux (*J*), which is the

amount of substance per unit time ($\frac{dn}{dt}$) passing through a unit area (A) is given by the product of the diffusion coefficient and the concentration gradient across the layer ($\frac{dC}{dx}$).

$$J = -D\frac{dC}{dx} = \frac{1}{A}\frac{dn}{dt} \qquad \textit{Equation 1-1}$$

For vapor permeation one can apply Henry's law [89], which states that at equilibrium or in steady-state diffusion (at a given temperature), permeant concentration (C) is directly proportional the partial pressure (p) via Henry's constant (H) or the solubility within the film (Standard Units: $\frac{mol}{m^3 \cdot Pa}$) (Equation 1-2). This relationship allows us to express the flux in terms of the partial pressure.

$$C = H \cdot p \qquad \textit{Equation 1-2}$$

Note: In this context, Henry's constant *H,* is equivalent to the solubility coefficient *S* used in later expression for flux (*e.g.* Equation 1-3),

The permeation process can be broken down into three key steps, as shown in Figure 1-3, assuming the absence of defects such as pinholes.

Step I: Adsorption and dissolution occur at the interface on the side with the higher concentration or partial pressure, which may be governed by Henry's Law.

Step II: Permeants diffuse through the film, where Fick's First Law may govern the movement due to the concentration gradient across the film.

Step III: Desorption occurs as the permeants pass through to the side with lower concentration and partial pressure.

This breakdown simplifies understanding of how permeants interact with encapsulant layers, emphasizing the critical roles of thickness, concentration gradients,

and surface area in the diffusion process. While Henry's law and Fick's first law are commonly used to describe gas or vapor permeation in polymers, they are idealized models and may not fully capture the behaviour in all systems, especially in the presence of non-linear sorption, multiphase materials or defects [70, 90, 91].

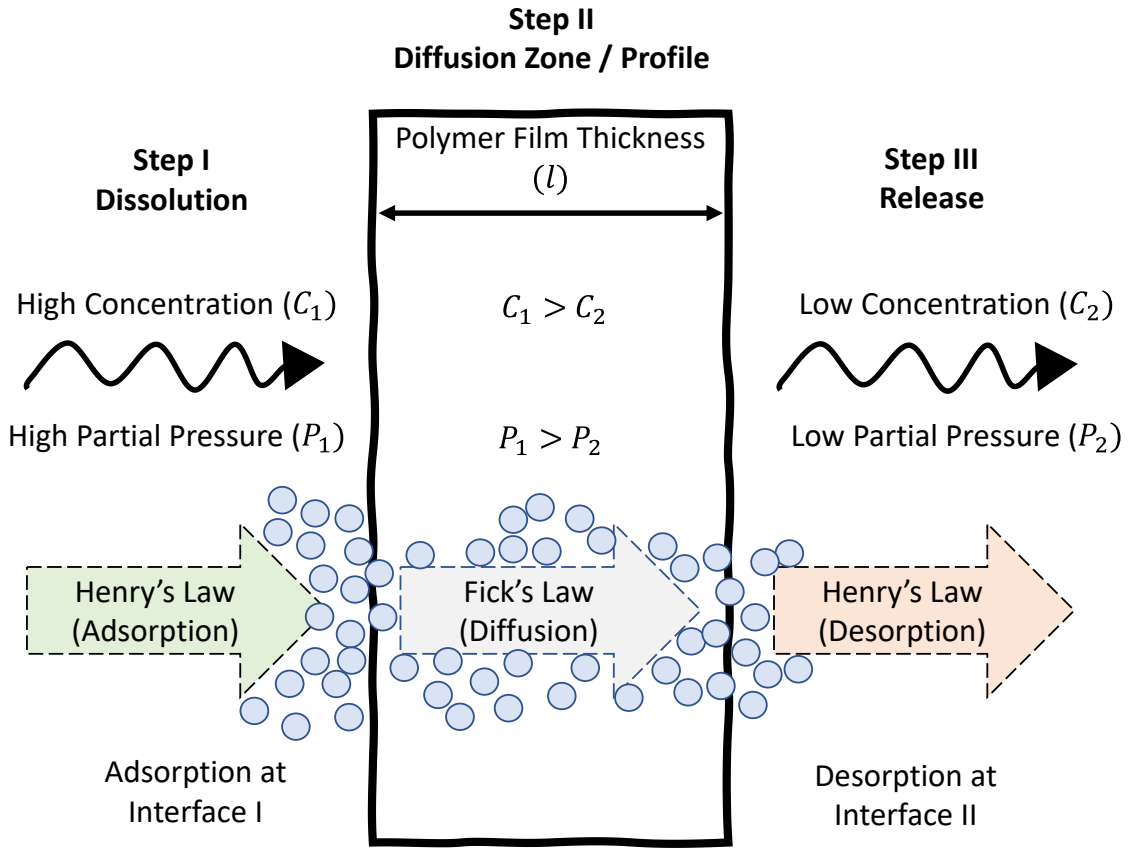


Figure 1-3: Process of Solution and Diffusion of Permeants through a Polymer Film of Thickness (l). The left side represents high concentration or partial pressure, while the right side shows low concentration and partial pressure (Redrawn from: [51, 60, 70, 90, 91]).

Using the concepts for the steady-state diffusion mechanism as expressed in Equation 1-1, one can obtain the flux in terms of the change in partial pressure ($P_2 - P_1$ or ΔP_{gas}, *Pa)* of the permeants, diffusion coefficient (*D:* $\frac{m^2}{s}$), solubility coefficient (*S,* $\frac{mol}{m^3 \cdot Pa}$) and the film thickness (*l, cm)* as seen in Equation 1-3.

$$J = D \cdot S \cdot \frac{(P_2 - P_1)}{l} \qquad \textit{Equation 1-3}$$

The flux can also be represented as *WVTR* or *OTR*. It is often reported as ($g/m^2 \cdot day$) or ($kg/m^2 \cdot s$). *WVTR* is expressed in Equation 1-4 in terms of the solubility of water in membrane ($S^m_{H_2O}$); the partial pressure of water at a specified temperature, $P_{H_2O}(T)$, and the change in relative humidity between the barrier Δrh [51, 70].

$$WVTR = \frac{\Delta n}{A \cdot \Delta t} = \frac{D \cdot S^m_{H_2O}}{l} \cdot P_{H_2O}(T) \cdot \Delta rh \qquad \textit{Equation 1-4}$$

On the other hand, the *OTR* is detailed Equation 1-5 and has units of ($cm^3/m^2 \cdot day \cdot atm$) or ($m/s \cdot Pa$), representing the volume of oxygen transmitted per unit area per day at standard atmospheric conditions. The term $\Delta V^0_{O_2}$ represents the volume of oxygen under standard temperature and pressure (STP), while ΔP_{O_2} is the partial pressure difference of oxygen across the membrane. One can also equate or account this in terms of the solubility of oxygen in the membrane as $S^V_{O_2}$ [70].

$$OTR = \frac{\Delta V^0_{O_2}}{A \cdot \Delta t} = \frac{D \cdot S^V_{O_2}}{l} \cdot \Delta P_{O_2} \qquad \textit{Equation 1-5}$$

Permeability (P, $\frac{mol}{s \cdot m \cdot Pa}$), is an intrinsic material property that does not depend on material thickness and driving force (*e.g.*, pressure difference). It represents the material's ability to allow permeant (such as water vapour) to pass through it. Permeability can be expressed in terms of two fundamental properties: the diffusion coefficient (how easily the permeant molecules diffuse through the material) and the solubility coefficient (how much of the permeant can dissolve into the material) as shown in Equation 1-6 [90, 92, 93].

$$P = D \cdot S \qquad \textit{Equation 1-6}$$

Hence by rearranging equation 1.5 the permeability can be found in terms of the WVTR: Equation 1-7. For WVTR of multilayers (systems composed of multiple stacked layers with distinct properties) each with a known permeability, Graf, Williford and Burrows suggested that the overall WVTR can be calculated by Equation 1-7, where, number of layers in the multilayer system (n) pressure difference (ΔP), and the total resistance is the sum of individual layer calculated as $\frac{l_i}{P_i}$, l_i: thickness of the i^{th} layer, P_i: permeability of the i^{th} layer [13].

$$WVTR = \frac{\Delta P}{\sum_{i=1}^{n} \frac{l_i}{P_i}} \qquad \textit{Equation 1-7}$$

The temperature dependence of WVTR and the permeability coefficient (P) can be described by the Arrhenius equation expressed in terms of permeability (Equation 1-8). The value of the activation energy indicates the permeation mechanism and can be used to reveal the presence and nature of defects in a barrier coating, as further discussed in section 1.5.

$$P = P_o e^{-\frac{E_{app}}{RT}} \qquad \textit{Equation 1-8}$$

The Arrhenius equation suggests that with increasing temperature one observes increasing transmission rates (WVTR and OTR), for polymers or inorganic coated films, [70] – observed in studies measuring Biaxially-oriented Polypropylene (BOPP) [94], Polyvinyl Alcohol (PVAl) [94], Ethyl Vinyl Alcohol (EVOH) [95], Polylactic acid (PLA)

with nano-cellulose fibre [96], PET, Polyimides (PI) and Polyethylene naphthalate (PEN) [97], acrylic coatings [98] and inorganic coated thin films [11].

The quantity E_{app} is best defined as the apparent activation energy of permeation. It represents the total energy required for the permanent to dissolve into and diffuse through the barrier material. Unlike a simple kinetic energy barrier, E_{app} is the sum of two distinct terms: the activation energy of diffusion (E_d) and the enthalpy of sorption ($\triangle H_s$) equivalent to $E_{app} = E_d + \triangle H_s$.

While E_d represents the thermal energy required for permeants to execute a diffusive jump, $\triangle H_s$ reflects the thermodynamic interaction between the permeant and the matrix. For non-condensable permeant gases like (O_2), E_{app} is typically positive leading to the standard observation of transmission rates increasing with temperature. However for condensable vapours like water interacting with polar substrates the sorption process is often exothermic ($\triangle H_s < 0$). If this exothermic term is large enough to dominate the kinetic diffusion barrier ($\triangle H_s > E_d$), the apparent activation energy becomes negative. In such cases the permeability decreases with rising temperature because the solubility of the permeant drops faster than its diffusivity increases. Making E_{app} serve as a diagnostic parameter characterizing the balance between kinetic diffusion and thermodynamic sorption, rather than solely measuring a physical barrier height [8, 11, 52, 70, 90].

Additionally, the importance of the Arrhenius equation is evident in permeation testing, where small temperature fluctuations, even by 1% can result in as much as a 10% change in permeability [99]. Humidity plays an equally important role as it dictates the

pressure gradient driving vapour transport. Both temperature and humidity influence permeation rates, making controlled conditions essential for accurate results.

1.5 Pinhole Defects (Nano and Macro)

Despite the advantages of oxide-coated barrier layers on polymer substrates, achieving low WVTRs remains challenging due to "pinhole defects" and nano- and macro-defects in the oxide coating that allow water to penetrate the barrier layer [10, 11, 14, 58]. In OLEDs, these defects trigger "dark spots," caused by cathode failure rather than issues with the organic layer [63].

So and Kondakov argue that degradation mechanisms in organic electronics, such as OLEDs, are complex and depend on the device's materials and architecture. Their study of two systems — (1) polyfluorene polymer and (2) small-molecule heterostructure OLED—demonstrates that degradation is driven by charge transport/injection issues and chemical transformations, respectively. They also link dark spots to "pre-existing particle defects on the substrate," where contaminants like moisture breach the encapsulation, delaminate the cathode, and create non-emissive areas [15].

Schaer *et al.* further identify three external causes of dark spots: (1) water vapour, (2) oxygen, and (3) dust particles introduced during fabrication [65, 73].

Researchers from Princeton University and others have mapped out four typical modes of permeation, illustrated in Figure 1-4 [63, 85, 100, 101].

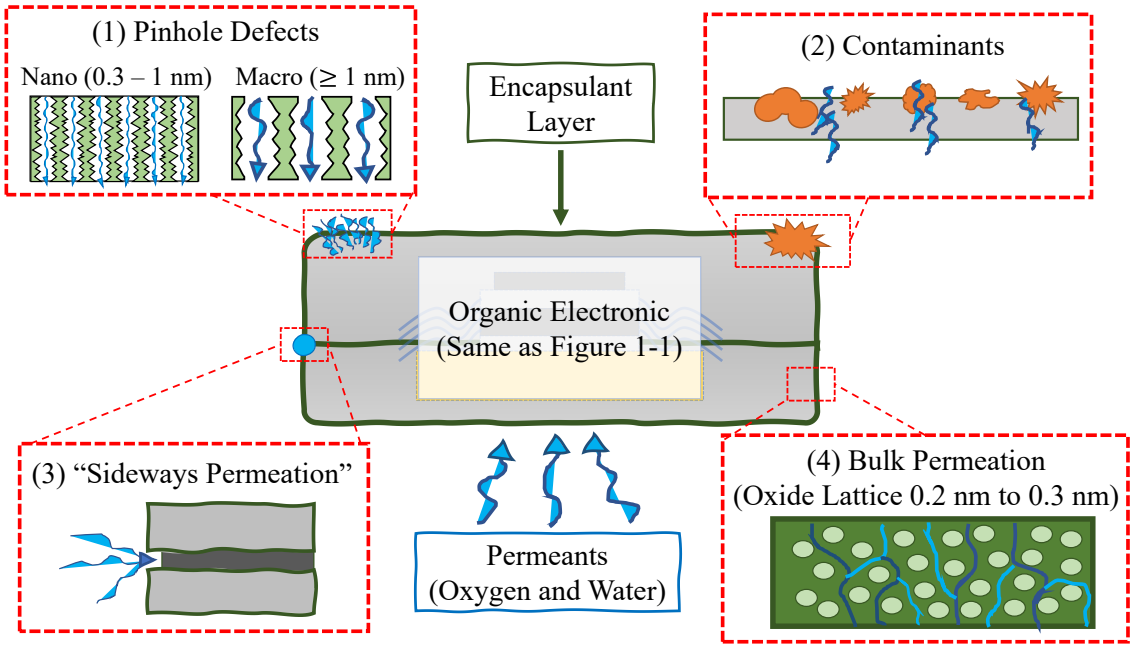


Figure 1-4: Modes of Permeation – (1) Pinhole Defects (nano and macro), (2) Contaminants (dust particles and inclusions), (3) Sideways Permeation (between encapsulant layer and substrate) and (4) Bulk Permeation (through oxide layer or encapsulant layer).

1.5.1 Macro and Nano Defects

The first type of defect, **(1) pinhole defects** (both macro- and nano-defects), occurs on the encapsulant film or layer. These defects are defined in various ways. Roberts *et al.* classify macro-defects as those equal to or larger than 1 nanometre (nm) and nano-defects as breaks between 0.3 to 1.0 nm in size [102]. However, Erlat *et al.* dispute this, defining nano-defects as anything smaller than 1 micrometre (μm) and introducing "macro and micro channels" for defects larger than 5 μm and between 1 to 5 μm, respectively [14].

Another way to categorize defects is through the Arrhenius equation, which shows the temperature dependence of permeability. Tobin, as noted in Fahlteich *et al.*, defines

that a nano-defect in a coating increases the activation energy with respect to that of the underlying substrate, while a macro-defect does not [11, 25]. As illustrated in Figure 1-5, defect types influence permeation pathways and Ea in distinct ways. In (a) macro-defects, the permeant travels through large, unobstructed openings in the barrier layer, with minimal interaction with the material, leading to an Ea governed primarily by the underlying substrate. In contrast, (b) nano-defects are narrow enough that permeant molecules interact significantly with the defect walls as they pass through, resulting in an increased Ea relative to the substrate alone. Finally, (c) bulk or lattice permeation occurs when the permeant molecule ($Radius_{molecule}$) is smaller than the intrinsic gaps ($Radius_{gap}$) in the polymer matrix. This pathway, involving close interaction with the polymer lattice, typically results in a sharp increase in Ea due to higher resistance. While all three pathways may be present, macro-defects dominate permeation behaviour if present in sufficient number, making their control essential in effective barrier design.

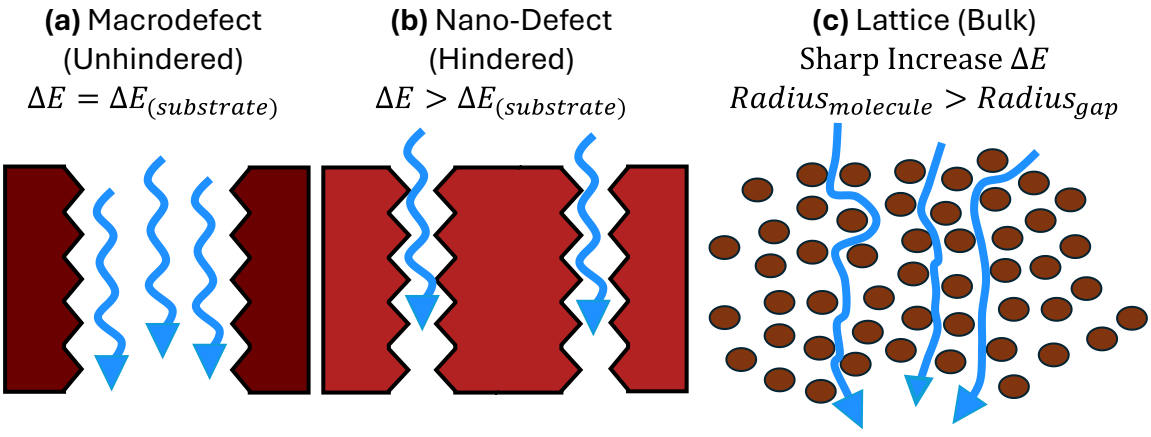


Figure 1-5: Schematic representation of different gas/vapor permeation pathways through barrier materials: (a) Macro-defect (unhindered) – permeants pass freely through large openings, with Ea determined by the substrate; (b) Nano-defect (hindered) – permeants interact with defect walls, increasing Ea relative to substrate; (c) Lattice permeation – permeants traverse the bulk polymer matrix, requiring tight passage through sub-nanometre gaps, resulting in a sharp rise in Ea. Adapted from [11, 92, 102].

1.5.2 Contaminants

The second type of defect: **(2) contaminants** or particles are a major cause of gas or water permeation, creating pathways for permeants through the substrate or encapsulant. These defects may arise from improper handling during processing or deposition, or from deliberately included particles in the substrate such as anti-block agents [11, 14, 92, 100, 101].

Fundamentally, such defects can be classified as pinhole defects due to discontinuity in the barrier, but a distinction is made contaminate-related pinhole defects involve the physical presence of particles, while pinhole defects may arise from other causes – coating damage, cracking or stressed induce delamination where no external particles are involved.

A potential solution is increasing the thickness of the oxide or encapsulant to cover the defects. However, as described in Figure 1-6, there is often a "critical thickness (Ct)" and "critical limit (Cl)" for coating thickness. Research indicates that the relationship between permeation rates and encapsulant thickness can be divided into three regions [11, 14, 25, 100, 103, 104]:

- **Region I:** Permeation rates are high due to limited coverage by a thin coating. Increasing the coating thickness first improves barrier performance mainly by sealing pinholes and shrinking the effective defect area; once a continuous, defect-free film is established, any further gain is then governed by the classical increase in diffusion path length through the layer.
- **Region II:** After reaching the critical thickness, further increases yield diminishing returns, and permeation rates plateau.

- **Region III:** Beyond the critical limit, transmission rates begin to rise again. Fahlteich *et al.* attribute this increase to stress-induced cracking [25].

Additionally, increasing encapsulant thickness can reduce flexibility, making the film more rigid, and increase processing time and costs due to additional layers [14, 25, 100]. The optimal thickness varies for each oxide or polymer and low permeation rates must be balanced with the need for flexibility [14].

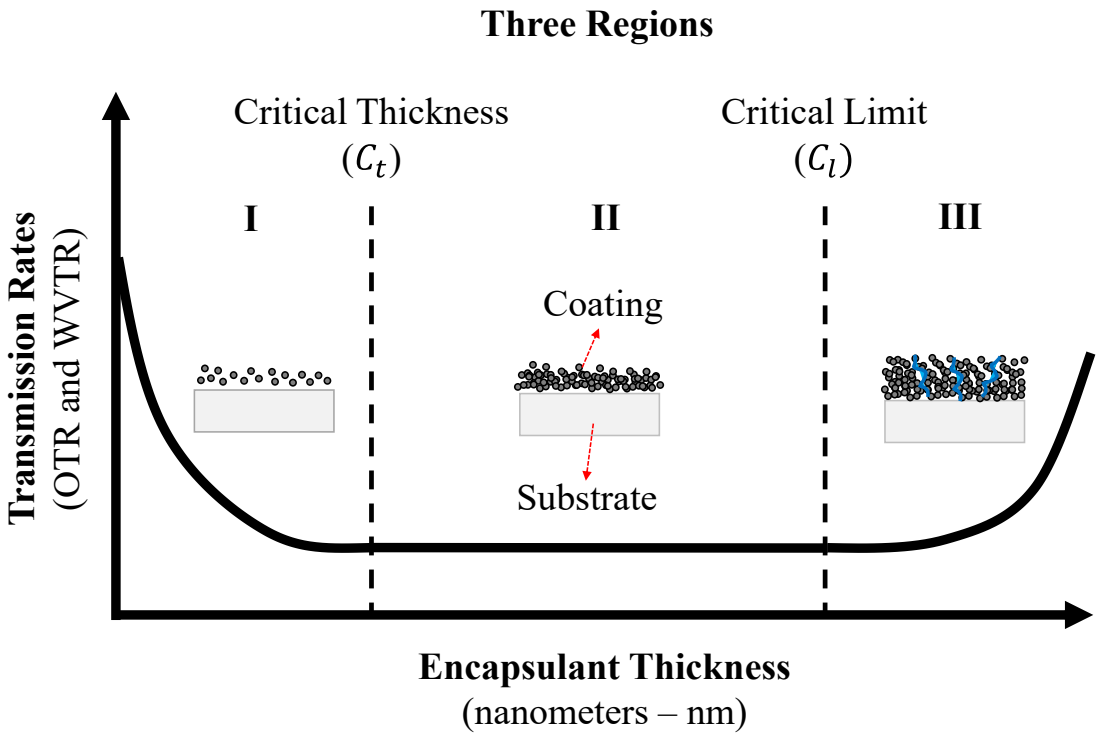


Figure 1-6: Representative relationship of Transmission Rates to Encapsulant (Coating) Thickness describing a critical thickness and limit or optimal encapsulant thicknesses.

1.5.3 Sideways Permeation

(3) **Sideways permeation** refers in this context to the diffusion that occurs laterally along the interface between the encapsulant layer and the adjacent barrier or substrate, particularly when this interface is compromised or poorly adhered. This failure allows

permeants to travel parallel to the layers, bypassing the normal through-thickness barrier [100]. Such lateral permeation can occur along features like delaminated regions, grain boundaries, or interfacial voids, and is often associated with long-term, slow degradation of device performance [101].

1.5.4 Bulk Permeation

(4) **Bulk permeation** occurs when permeants pass through the film itself, independent of cracks or defects, leading to slow degradation. This is more common in organic polymers, which have higher transmission rates than inorganic materials [100, 101].

1.6 Characterization of Films

Accurately assessing the permeation and barrier properties of different oxides or films requires precise characterization. Two widely used methods for testing barrier performance in terms of water vapour permeation are: (1) the Calcium Test, and (2) MOCON Aquatran. These tests offer crucial insights into the effectiveness of barrier layers in blocking water vapour permeation.

1.6.1 Calcium Test

The calcium test is a widely used method for measuring WVTR by utilizing the reaction between pure metallic calcium and water. It measures the amount of reacted calcium over time as water permeates through the barrier film [59]. Common variations as presented in Figure 1-7 include the (a) "Total Rate Test" and the (c) "Optical Imaging Test", with various enhancements of each [11, 14, 30, 59].

In Figure 1-7 (a) Total Rate Test, calcium is evaporated onto an impermeable substrate (typically glass) and sealed with the barrier film using adhesive *e.g.* epoxy around its edges. As water permeates the film, it reacts with the calcium (solid) to form calcium hydroxide (Reaction 1-1, solid - transparent), enabling measurement of water permeation through the film [14, 59, 105, 106].

$$Ca\ (s) + 2H_2O\ (g)\ \rightarrow Ca(OH)_2(s) + H_2(g) \qquad \textit{Reaction 1-1}$$

Most water permeation should occur through the barrier film, leading to uniform corrosion. However, minor ingress can sometimes happen through the adhesive, depending on the adhesive type and preparation method [11, 14, 30, 90]. Research shows that oxygen at room temperature does not react with metallic calcium, meaning the primary reactant is water, not oxygen [11, 14, 85, 107]. This ensures an accurate WVTR measurement by contrasting the opaque metallic calcium with the transparent calcium hydroxide. The (a) Total Rate Test uses a photodetector and light source to measure calcium's light transmittance. WVTR is estimated through the change in optical density, relative to film thickness and geometry [11, 14].

Another variation, is the Electrical Calcium Test, Figure 1-7 (b), which measures WVTR by tracking the electrical resistance of calcium in a specific test area over time, revealing water permeation through the barrier film [11, 59]. Paetzold *et al.*'s version assumes uniform calcium corrosion on the substrate and shows that resistance is proportional to calcium’s resistivity and length, and inversely proportional to its width and remaining height [108]. However, some debate exists regarding this assumption, as localized defects can cause uneven corrosion. Later work by Paetzold confirmed this

assumption holds even at micron-scale levels [30, 86, 109]. Similar to the (a) Total Rate Test, the (b) Electrical Calcium Test typically does not provide any spatial data [92].

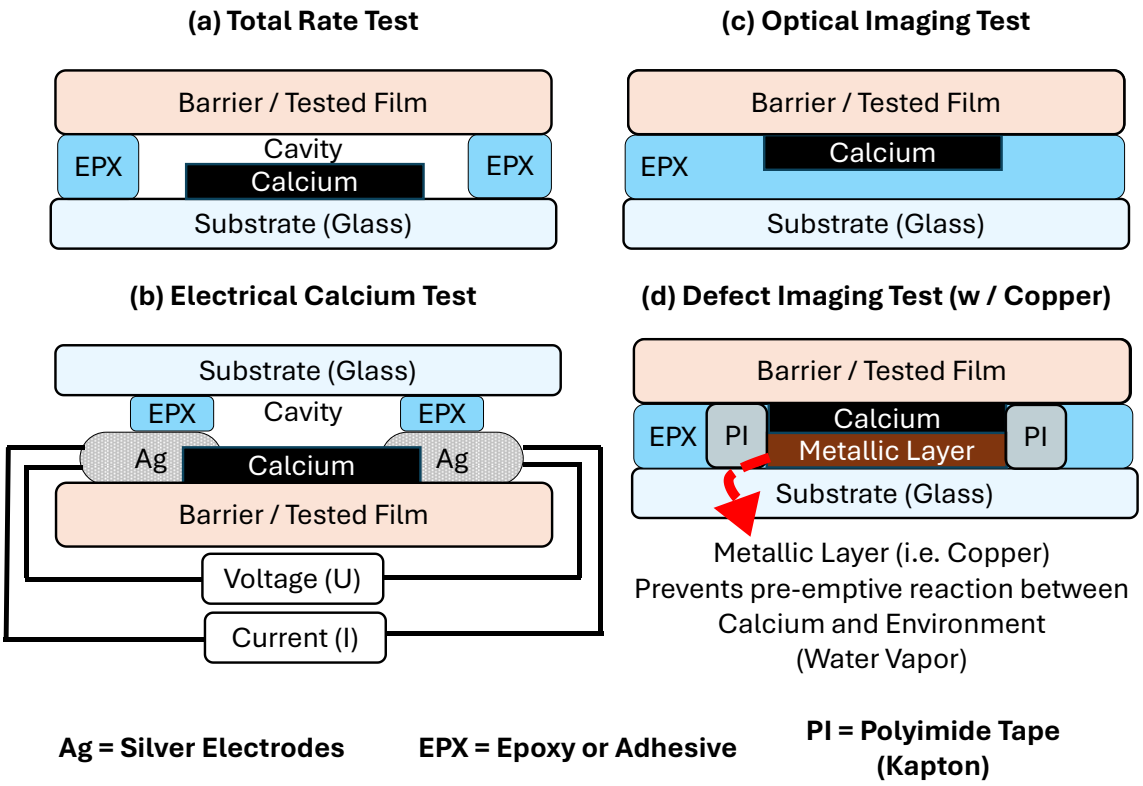


Figure 1-7: Variations of Calcium Tests for WVTR Measurement – (a) Total Rate Test, (b) Electrical Calcium Test – type of Total Rate Test, (c) Optical Imaging Test, (d) Defect Imaging Test with Copper – type of Optical Imaging Test.

The next main variation is the Figure 1-7 (c) Optical Imaging Test, introduced by Nisato *et al.* at Philips Research in 2001 [30]. This test involves evaporating metallic calcium, sandwiched between a perfect barrier (glass) and the tested film (polymer), inside a glove box or test box [11, 14, 30, 59, 92].

The calcium (c) optical imaging test enables the detection of localised defects and formations within the tested film, addressing the limitations of earlier calcium tests. Unlike the (a) total rate test, which lacks calcium directly on the barrier layer, and the (b) electrical calcium test, which does not capture images, by directly evaporating calcium

onto the barrier substrate and using time-lapse imaging, this method reveals reaction spots or defects and weak points in the barrier layer [11, 110].

Despite the advancements in the calcium optical imaging test, challenges remain. A primary issue has been the premature reaction of metallic calcium with the environment when the sample is not prepared in a glove box. To address this, Sim and Assender *et al.*, introduced a thin protective metallic layer over the calcium that acts as a transparent but impermeable layer on top of the applied Ca before it is encapsulated with epoxy and impermeable glass substrate, as shown in Figure 1-7 (d) Optical Imaging Test with copper. This innovation allows sufficient time to encapsulate the test specimen behind glass before the Ca is eroded [92, 112]. A detailed description of the setup of the calcium test used in this study is provided in the methodology section (2.4 Calcium Test).

In brief, the water vapour transmission rate for Optical Imaging Test is measured by capturing images at intervals and evaluating the area of reacted calcium and its growth rate, by assuming homogeneous oxidation. Additionally, the optical calcium test presented remains the most robust method for measuring intrinsic WVTR (material properties / defect free), due to its high spatial resolution, allowing exclusion of defects [30]. Other calcium-based methods, like electrical calcium test typically only measure effective WVTR (contribution of individual layers and defects); as it averages the results over the entire area and assumes uniform degradation. It is possible for electrical test and other methods to approximate intrinsic WVTR with careful calibration and defect exclusion, but the lack of spatial resolution makes it less precise than optical methods, for isolating intrinsic material properties.

However, the calcium test has drawbacks, including issues with reproducibility, environmental consistency, and sample preparation (such as sealing). Additionally, variations in testing methods and non-standardized procedures can make results difficult to compare with one another [11, 14, 30].

Recent publications have introduced variations of the calcium test, such as infrared imaging with copper backing layers [113], and broadened its application, using optical Ca tests to assess the effectiveness of barrier layers designed to encapsulate perovskite cells [114, 115].

1.6.2 MOCON Aquatran (Water Vapour Permeation Analyser)

Common equipment for measuring WVTR includes the PERMATRAN or AQUATRAN from MOCON (Ametek Corporation) [11, 14, 93]. These devices operate by placing a barrier or test film between two chambers: one with a controlled concentration of water vapour (WVTR), and the other with a dry, moisture-free carrier gas (nitrogen with a small amount of hydrogen), as detailed in Figure 1-8. Over time, moisture permeates through the test film and is carried by the gas to a sensor or detector [116-119].

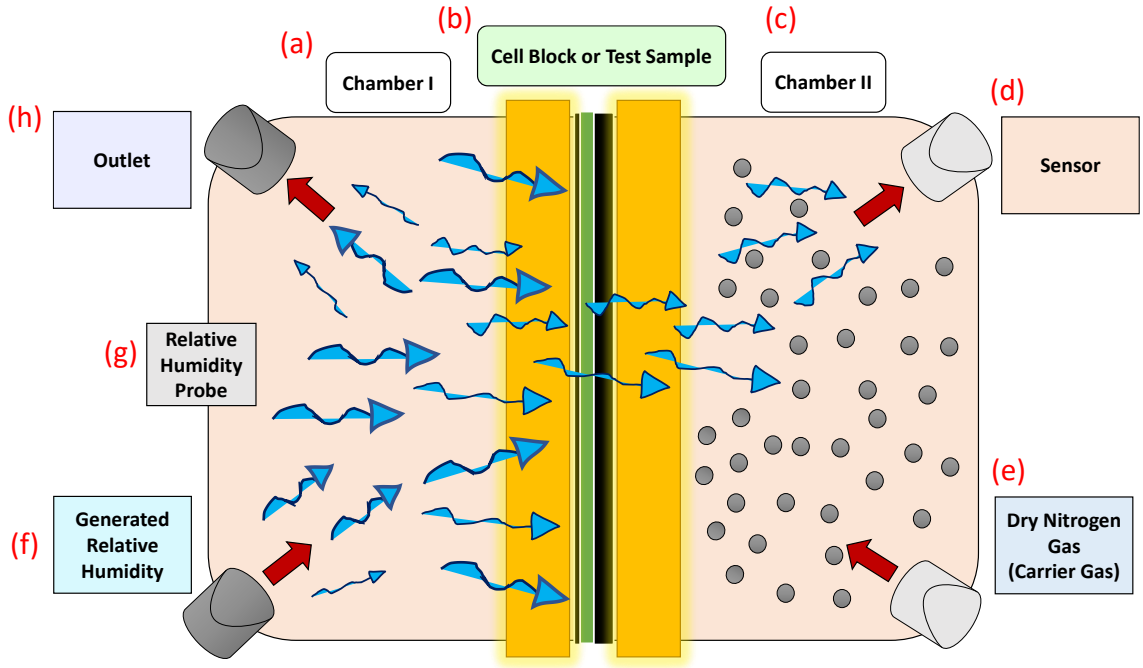


Figure 1-8: Diagram of the MOCON Water Vapor Transmission Rate (WVTR) test system, consisting of two chambers: (a) Chamber I, which contains a cell with controlled water vapour levels, regulated by (f) generated relative humidity and monitored by (g) probe, and circulated through the (h) outlet; and (c) Chamber II, a dry cell with (e) carrier gas. Water vapour permeates through the (b) test sample and is detected by a (d) phosphorous pentoxide (P_2O_5) sensor.

Before testing, the sample is conditioned, which involves placing the sample in the temperature- and relative humidity-controlled chamber to stabilise the conditions and to allow the necessary diffusion into the sample. The conditioning continues until consistent WVTR readings are measured, *i.e.* once steady state concentration gradient is set up across the layers.

At steady state, the MOCON device begins recording transmission rate data at that temperature and relative humidity [11, 14, 99]. MOCON provides an accurate (industry-accepted) WVTR but lacks the ability to detect local variations in permeation (due to defects) as can be seen in calcium tests.

Other methods for measuring barrier transmission rates include mass spectrometry (sensitivity: 5×10^{-5} to 1.2×10^{-6} g/m²·day) [120, 121], the radioactive tracer or "tritium diffusion test" (ASTM F1249, hazardous, sensitivity: $<10^{-6}$ g/m²·day), though the latter involves hazardous material handling [99, 122]. X-ray or neutron reflectivity techniques offer even higher sensitivity but are currently limited in practical barrier applications by long equilibrium times and the need for specialized research into the interfacial structural changes of thin film coatings [14, 123].

For context, the MOCON Aquatran 2 equipment (2.4 Calcium Test) used in this work has a specified lower detection limit of around ~ 1×10^{-4} g/m²·day, set by the Phosphorous Pentoxide (P_2O_5) sensor baseline and possible electronic noise. Meanwhile the optical Ca test, in principle can reach to ~ 1×10^{-6} g/m²·day, but in practice as discussed in 4.4.1 Estimating WVTR using Constant Region of Interest and Accounting for Edge Effects (Calcium Region Isolation), that possible leaks through the epoxy and environmental drift over very long timescales can limit the test. These comparative limits as illustrated in Figure 1-2, which shows the performance range of the main barrier measurement techniques relative to current and target WVTR values for flexible electronics.

1.7 Creation of Barrier Layers (Thin film Deposition)

Barrier layers can be created and categorized based on how they are applied—whether coated or embedded within the substrate, influenced by the manufacturing process, or determined by the materials used. One prominent category is vacuum-

processed barriers, which utilize atomistic deposition to form thin films with low WVTRs [70, 124, 125].

Thin-film deposition for flexible barriers involves condensing metallic or inorganic materials onto a polymer substrate, where nucleation and film growth occur until the desired thickness is achieved. A critical challenge is forming uniform, defect-free layers, as imperfections such as voids, grain boundaries, microdefects, and lattice mismatches significantly impact barrier performance. Grain boundaries and microdefects serve as permeation pathways, reducing the barrier's effectiveness. These defects often originate from thermal stresses, deposition inconsistencies, or the inherent behaviour of adatoms. For example, adatoms with high-energy configurations may fail to bond completely or diffuse uniformly, leaving gaps that compromise the coating's integrity [124, 125].

Two main classes of thin film deposition techniques exist: (1) Physical Vapor Deposition (PVD) and (2) Chemical Vapor Deposition (CVD). The following sections provide a brief overview of these methods, with a detailed discussion on the method used in this research: (1.7.2.a) Atomic Layer Deposition (ALD).

1.7.1 Physical Vapour Deposition (PVD)

PVD is deposition of either a liquid or solid source through evaporation or sublimation onto the substrate under various environments (*e.g.*, plasma) [126]. The two common methods of PVD are Thermal Evaporation, and Sputtering.

1.7.1.a Thermal Evaporation

Thermal Evaporation, a PVD technique involves heating a source material in a vacuum chamber (~10^{-9} MPa to ~10^{-13} MPa) to produce vapour that condenses into a thin

film. The vacuum ensures a long mean free path for the vapourised material, reducing particle collisions – an inverse relationship exists between pressure and mean free path [127-129].

The process varies depending on the material's phase change behaviour. Metals such as Magnesium and Chromium, which are solid at room temperature, are heated beyond their boiling points to vaporise directly. Other metals like Aluminium and Tungsten typically melt before evaporation. Sublimation, where a solid transitions directly into vapour without melting is less common but can occur under specific conditions. For example, Titanium may either melt or sublimate depending on deposition parameters such as temperature and pressure [128]. Additionally, non-metals such as oxides and nitrides are often deposited using reactive thermal evaporation, where a base metal is evaporated in the presence of a reactive gas (*e.g.*, O_2 or N_2), forming the compound film on the substrate during deposition [130].

Vapour formation in thermal evaporation can arise from resistive heating (*e.g.* in tungsten boats), as well as advanced methods like an electron-beam, ion-beam, or laser ablation. The primary method in this research employs resistive heating, a fast and cost-effective approach offering high deposition rates (µm/s) and scalability. However, thermal evaporation has limitations: it struggles with uniform microstructure growth, restricts substrate heating to below 1500°C, offers fewer inorganic material options, and introduces higher impurity levels compared to other vapour deposition techniques such as sputtering or ALD. These drawbacks make it less suitable for applications requiring ultra-low water vapour permeation barriers or highly complex multicomponent films. Nonetheless, it remains widely employed for coating flexible polymer substrates (web-

coating), thin-film devices, wafer bonding, and calcium deposition for optical imaging tests, as utilised in this project [129, 131].

1.7.1.b Sputter Deposition

Sputter deposition, once known as cathode disintegration, is a PVD process conducted in a plasma environment [132, 133]. It works by bombarding a target material (solid or liquid) with energetic particles, typically ions, from a plasma, often using an inert gas such as argon. This ion bombardment ejects atoms from the target, creating a vapour that condenses onto the substrate. Initially, sputtering relied on high-voltage pulses, but modern techniques like magnetron sputtering provide improved control over plasma density, enhancing the process's precision and efficiency [124, 132, 134-140].

Moreover, sputter deposition is known for producing exceptional oxide films, offering good control over film functionality. It can create homogeneous films, with similar stoichiometry as the target material (depends on sputtering yield variations, gas phase interactions, and control of deposition conditions) [141, 142]. Sputtering also has good step coverage compared with evaporation – forming uniform thin films over substrates with complex topographies, including trenches, steps, and irregularities, while promoting strong adhesion to substrate. Sputtering surpasses thermal evaporation in step coverage but does not achieve the same level of conformality as ALD. Sputtering is a cost-effective technique capable of covering large areas. It can accommodate a wide range of materials, operate at low source temperatures (without requiring target heating), and deposit materials with extremely high melting points [135, 136, 143-146].

However, sputtering suffers from low deposition rates (< 1 nm/s), complex equipment, low directionality (which can lead to contamination), radiation issues, and

unwanted substrate heating [129, 144, 147, 148]. Despite these drawbacks, it remains widely used in the production of thin-film transistors, microfluidic devices, superconductors, ferroelectrics, and emissive coatings [144, 149].

1.7.2 Chemical Vapour Deposition (CVD)

The next key group of thin-film vapour transfer processes is CVD, which technique involves a chemically active environment, thermally activated by resistance heat, light/laser, or plasma. The substrate, heated in a vacuum reactor (though some CVD variants, such as Pyrosol, Electrostatic spray-assisted, Flame-assisted, and Combustion CVD, do not require high vacuum), is exposed to volatile gaseous or vapour-phase precursors like organometallics, metal hydrides, and halides [124, 150-161].

In CVD, precursors react and decompose on the substrate surface, forming non-volatile thin films, such as metals, semiconductors, alloys, or refractory compounds, including polycrystalline and monocrystalline materials like diamond films at pressures below 1 atm [124, 150-161]. CVD involves the condensation of a gas-phase compound onto the substrate, where a film is generated through thermal decomposition or chemical reduction [162].

A key difference between PVD and CVD is that PVD requires a direct line of sight for deposition, while CVD is multi-directional, allowing more flexibility in substrate placement within the chamber [150].

This capability enables coatings on complex 3D shapes and high aspect ratio holes [155, 163]. Additionally, CVD's chemically driven process allows for highly tuneable deposition rates, maintaining conformity, fine structure regularity, and purity [154, 161] .

Many systems, such as plasma-enhanced CVD and activated sputtering, are hybrids of PVD and CVD [163]. CVD offers a wide range of processing flexibility with various methods. Some employ hot or cold wall reactors at different pressures, from sub-torr to ultra-high vacuum. Other variations include plasma-enhanced, laser-assisted, hot filament, aerosol-assisted, or photo-initiated CVD, such as Chemical Beam Epitaxy or Spray Pyrolysis. CVD operates across a broad temperature range (200–1600°C) and can scale up to produce large-area, uniform films that are defect-free, conformal, dense, and highly pure at atomic or nanometre scales [150, 152, 153, 164, 165].

However, CVD can be limited by factors such as substrate compatibility, high costs (due to complex reactor or vacuum systems), and chemical hazards (*e.g.*, toxic Nickel Tetracarbonyl [$Ni(CO)_4$], explosive Diborane [B_2H_6], and corrosive Silicon Tetrachloride [$SiCl_4$]). Other challenges include handling multicomponent materials, high temperature requirements (which can limit substrates and cause thermal stress), and the need for volatile precursors at room temperature and pressure. Despite these limitations, CVD has been used to create 2D nanosheets (*e.g.*, graphene, metal carbides) and thin films (including amorphous and polycrystalline polymers, semiconductors, dielectrics, metallic films, and refractory ceramic fibres) [150, 154, 155, 158, 161, 163, 166-169].

1.7.2.a Atomic Layer Deposition (ALD)

ALD, or sometimes Atomic Layer Epitaxy (ALE) when a highly crystalline flat substrate is used, was first cited as Molecular Layering and originated in the Soviet Union in 1960's, while a decade later Tuomo Suntola and colleagues independently developed Atomic Layer Epitaxy Method now known as Atomic Layer Deposition – ALD [170-172] – as a variant of CVD.

ALD operates through a self-limiting, sequential surface chemical reaction, distinct from most CVD processes. It separates the chemical reactions into two steps, pulsing precursors alternately through inert gas purging (nitrogen or argon, ~1 mbar), creating a film growth cycle [124, 173-176]. ALD requires two or more precursors, introduced cyclically to the substrate, to build thin films with atomic precision [175, 177].

ALD typically follows a cyclical, four-step process (Figure 1-9), involving the sequential exposure of a substrate to two precursors: (1) **Metal Precursor**: Typically inorganic or organometallic compounds such as halides, chlorides, alkoxides, or alkyl compounds (*e.g.*, Aluminium Chloride - $AlCl_3$ or Trimethylaluminium - $Al_2(CH_3)_6$ to produce Al_2O_3 – verification of whether correct stoichiometry is produced is required, possible AlO_x production). (2) **Non-Metal Precursor**: Compounds such as hydrides, water (H_2O), hydrogen sulfide (H_2S), or hydrogen peroxide (H_2O_2 [171, 175, 176, 178]:

It then follows a step-by-step process:

1. **Metal Precursor Pulse -** Figure 1-9 (c.1)**:** The metal precursor enters the chamber via carrier gas, reacting with the substrate. This self-limiting reaction continues until all reactive sites are saturated.
2. **Purge/Evacuation -** Figure 1-9 (c.2): Any unreacted metal precursor and gaseous by-products are removed, clearing the chamber.
3. **Non-Metal Precursor Pulse -** Figure 1-9 (c.3): The non-metal precursor reacts with the newly formed monolayer on the substrate, contributing to thin film formation.
4. **Final Purge/Evacuation -** Figure 1-9 (c.4): Remaining non-metal precursor and by-products are evacuated, completing one ALD cycle.

The reaction cycle in ALD is typically on the order of seconds, with about 1 – 20 seconds per complete cycle (with individual pulses and purges around ~0.1 – 5 seconds each), this is repeated to build up the film's thickness. As shown in Figure 1-9 (b), in step 1, mass adsorption increases significantly, then stabilizes after purging in step 2. In step 3, the non-metal precursor may cause an increase or decrease in mass adsorption, depending on ligands or surface species, but it stabilizes again after the final purge in step 4 [171, 175, 176, 178].

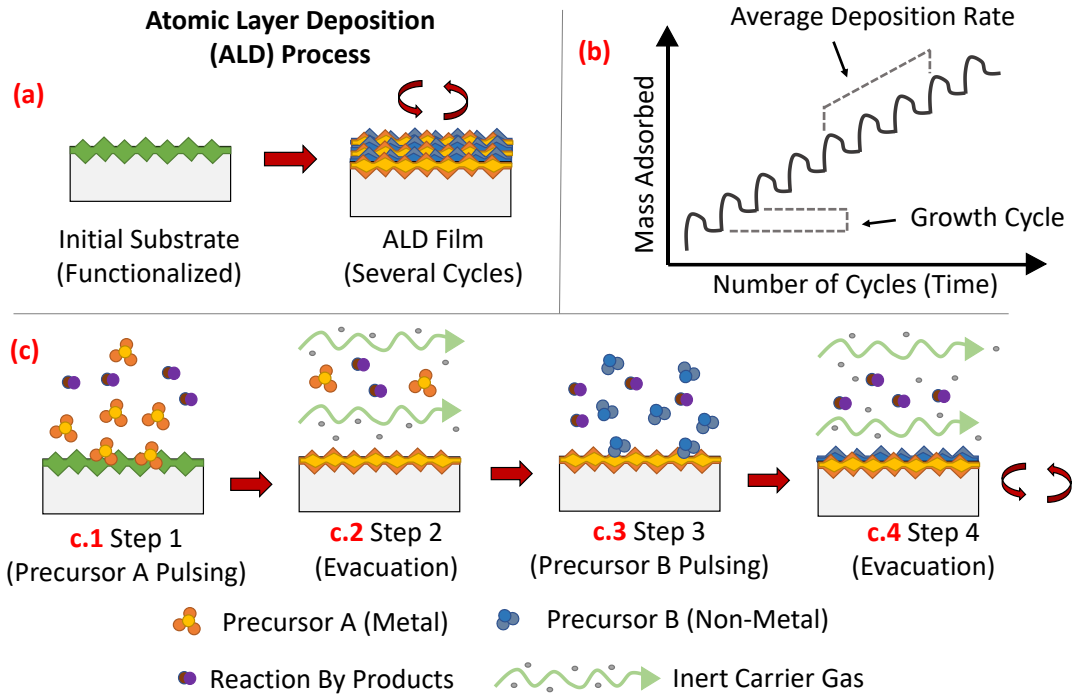


Figure 1-9: Schematic of ALD process: (a) initial substrate prepared for functionalization through repeated cycles, (b) mass adsorbed per cycle to achieve desired layer thickness, (c) the four key steps are (c.1) Introduction of Precursor A, which reacts with the substrate, producing by-products, (c.2) Purging of Precursor A and by-products using an inert carrier gas, (c.3) Addition of Precursor B, which reacts with the surface to form a monolayer, and (c.4) Final purge to remove unreacted by-products, completing the cycle [171, 175, 176, 178].

This self-limiting chemical reaction process prevents unwanted gas-phase reactions, producing a perfectly conformal, pinhole-free, and chemically bonded uniform

film at nanoscale precision (0.1 to 3 Å per monolayer). Final thicknesses typically range from 1 to 500 nm, controlled by the number of cycles and molecule size. ALD can be applied to a variety of shapes and structures, including porous media, powders, cavities, trenches, large-area surfaces, and high aspect ratio features such as nanotubes, nanowires, diffractive optics, and semiconductors [124, 173-175, 177-179].

ALD primarily depends on the precursors, substrate, and process temperature. Its surface-controlled nature prevents reactant condensation, which ensures precise stoichiometric control for high-density films, achieving full, uniform coatings outperforming most PVD and CVD methods [124, 172, 175].

However, due to ALD's sequential nature, the growth rates are typically below 0.5–1 nm/min (up to 10 nm/min or 100–300 nm/h in some cases), making thick layers is time-consuming. Advanced techniques, such as batch reactors or spatial ALD, can reach growth rates of 3600 nm/h. Additionally, achieving the desired film requires an ultraclean environment, and limitations related to surface chemistry and precursor materials must be considered [171, 175-179]. ALD has been used to successfully deposit various inorganic films, including oxides (HfO_2, Al_2O_3, TiO_2), nitrides, carbides, fluorides, metals, organic materials, and II-VI and III-V compounds [171, 175].

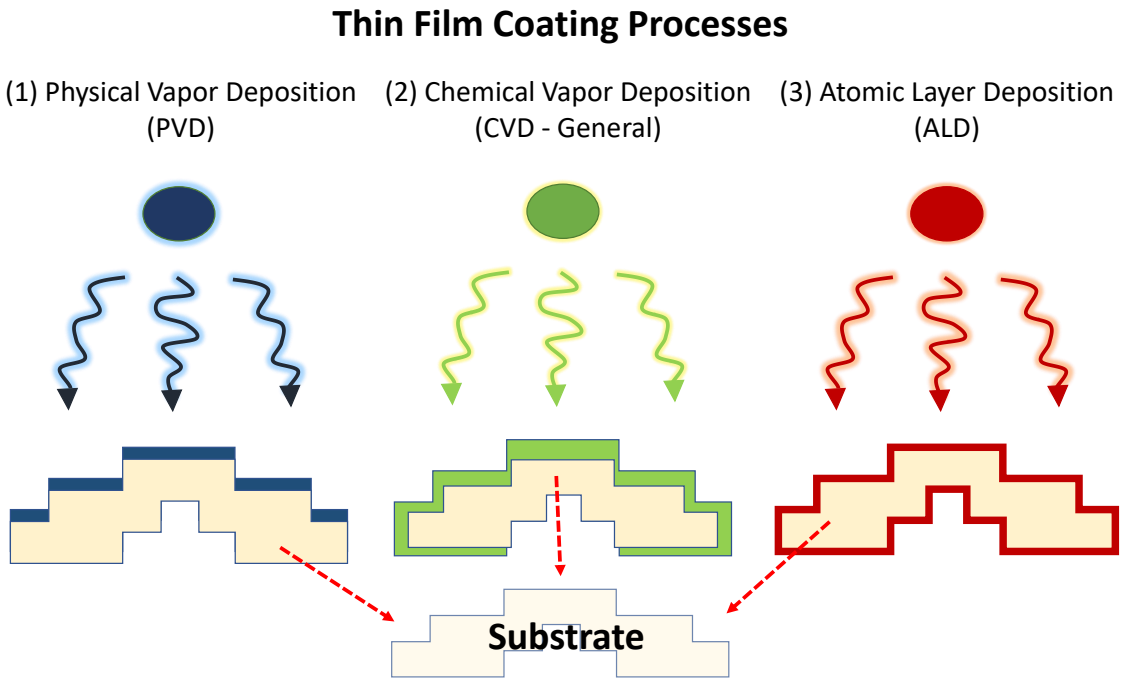


Figure 1-10: Comparison of Main Thin Film Coating Process layer formation (1) PVD, (2) CVD – General, (3) ALD [124, 175].

1.8 Conclusion

A direct comparison shows that no thin film deposition method is universally superior, the right choice depends on device requirement and the material system [160, 180]. CVD generally requires elevated substrate temperatures (≈ 300 to 900 °C) for standard processes and up to ≈1,500 for refractory epitaxy such as SiC, whereas the baseline PVD runs with substrate near room temperature and seldomly above anything beyond 250 °C (even when deliberately heated, industrial tools typically stay ≤ 600 °C). ALD typically occupies the lower edge of the CVD window with most chemistries proceeding between 20 °C and ≈ 350 °C [160, 181-185]. The cool substrate nature of the PVD means it cannot support deposition routes that require high temperature surface reactions or crystal growth, yet this same feature makes it the method of choice for

coating heat sensitive substrate that would distort or degrade under CVD conditions. Importantly, the low substrate temperature in PVD does not preclude deposition of high melting point materials, where the energy needed to vaporise, the target is supplied in the source, allowing refractory metals and ceramics to be routinely sputtered or evaporated.

CVD processes are often considered environmentally friendly due to their efficient material utilization, potentially leading to reduced waste compared to some PVD methods, as the chemical precursors in CVD react at the substrate surface to form the desired film, minimizing excess material. However, CVD has specialized requirements and potential hazards, due to reactive or toxic precursors and need for high temperature substrate heating. In contrast, PVD, such as sputtering, avoids toxic chemical precursors, and excels in film adhesion [160, 186]. Ultimately, the selection of a thin-film coating technique must consider factors such as application objectives, film thickness, material properties (substrate and precursors), and can be further informed by kinetic or displacement energy models to ensure the most appropriate method is chosen [160].

1.9 Summary and Outlook

The field of encapsulating flexible electronics has made significant progress toward achieving ultra-low water vapour permeation barriers. However, further studies are required, including this project, which will explore the diffusion mechanisms of these encapsulants. This work will delve into ALD (CVD) films of PET and PVAl substrates to assess their water barrier effectiveness using reliable characterization methods—namely, the Calcium Defect Imaging Test and MOCON Aquatran. The following sections will provide a detailed background, methodology, and comprehensive analysis of the data.

2 Methodology

2.1 Overview of Testing Methodology

The primary methods used in this thesis to measure water vapour transmission rates (WVTR) are the MOCON Aquatran 2 and the calcium test (defect imaging method), both discussed in Chapter 1. While the MOCON is an industry standard for testing barrier layers, the specific Aquatran 2 unit available for this study could not measure WVTR values below ~10^{-3} g/m^2·day which is necessary for ultra-low water vapour barriers in FE. It is noted that more recent Models offer a wider range of detection limits (*i.e.* MOCON AQUATRAN 3 – can measure as low as 5×10^{-5} g/m^2·day). In contrast, the calcium test, also covered in this thesis, can detect WVTR values as low as 10^{-6} g/m²·day [14, 26, 28, 45, 46, 59, 61, 62, 64, 68-71, 87]. Beyond the testing limits, the primary motivation for using these methods is to understand the permeation mechanisms, particularly through the imaging of local permeation through defects such as pinholes.

2.2 Testing Standards

Table 2-1 lists the various testing standards related to WVTR measurement. Most standards specify testing at temperatures of either 25°C or 38°C, with varying humidity levels. These general conditions were applied in the MOCON tests and considered, for comparison, when conducting the calcium tests. For this study, the temperature guidelines from BS ISO 15106 (Electrolytic Detection Sensor Method) [187] and BS ISO 15106-7 (Calcium Corrosion Method) [188] were followed to align with established literature values.

Table 2-1 Testing Standards (ASTM and BSI) [189]

Test	Temperature (℃)	Humidity (%)
ASTM F1249-20 - Water Vapor Transmission Rate Through Plastic Film and Sheeting Using an Electrolytic Detection Sensor (Coulometric P2O5 Sensor)	37.8 ± 0.5	90 ± 3
British Standard Methods of Testing Plastics – Method 513 (Temperate Conditions)	25 ± 0.5	75 ± 2
British Standard Methods of Testing Plastics – Method 513 (Tropical Conditions)	38 ± 0.5	90 ± 2
EN ISO 15106-2:2005 – Plastics Film and Sheeting Determination of Water Vapour Transmission Rate – Part 2: Infrared Detection Sensor Method.	23 ± 2	50 ± 10
BS ISO 15106−3:2005 – Plastics Film and sheeting Determination of water Vapor transmission rate — Part 3: Electrolytic detection sensor method. Notes the use of phosphorous pentoxide or P2O5 Sensor	25 ± 0.5	90 ± 2
	38 ± 0.5	90 ± 2
	40 ± 0.5	90 ± 2
	23 ± 0.5	85 ± 2
	25 ± 0.5	75 ± 2
BS ISO 15106-7: 2015 - Plastics Film and Sheeting Determination of Water Vapor Transmission Rate – Part 7: Calcium corrosion method. (Currently no equivalent ASTM Standard for “Calcium Test”)	25 ± 0.5	90 ± 3
	40 ± 0.5	90 ± 3
	60 ± 0.5	90 ± 3
	85 ± 0.5	85 ± 3

2.3 MOCON Aquatran 2

The MOCON Aquatran (Serial No. 0413FF007) as previously illustrated in Figure 1-8 provides a quantitative measurement of WVTR by detecting the amount of water vapour permeating through a film over time [116-119]. Before testing, the sample is conditioned at a set temperature until equilibrium is reached. According to ASTM data,

uncoated PET films take approximately 1.06 to 1.33 days to reach equilibrium, depending on thickness (25.4 to 127 μm) [190]. This relationship illustrates that while thinner films exhibit faster permeation rates, equilibrium times do not scale linearly with WVTR due to the interplay of permeation, diffusion dynamics, and environmental factors. The MOCON records transmission rate data at the specified temperature (10°C to 40°C, ± 0.5°C) and relative humidity (35% to 90% RH, ± 3 RH, or 100% RH with HPLC-grade water), using precise heating and cooling for accurate, stable measurements [11, 14, 99].

The MOCON, is compliant with ASTM E96 and ISO 15106-3 has a detection range of: 5×10^{-5} g/m²·day to 5 g/m²·day) [118, 191], ensures precise and consistent water vapour permeation measurements, but does not capture information on the nature or distribution of local defects in the film. However, it serves as an excellent confirmatory test alongside the Calcium test for the overall amount of water transmission at a given temperature and partial pressure. Moreover, as some of the samples go beyond the MOCON's sensor range masking and its effects are discussed in 9.1.1 Sample Masks.

2.4 Calcium Test

As discussed in Chapter 1, this study focuses on the defect imaging method of the calcium test with copper backing layer, which tracks the depletion of calcium over time using sequential imaging as the sample is held in a controlled environment (the "Calcium Test Box" or oven). The following sections detail the experimental setup, methodology of the calcium test, and the testing process for both uncoated ("poor barriers") and coated ("good barriers") samples.

2.4.1 Calcium Test Overview (Standard)

Table 2-2, provides a comparison between the standard optical imaging calcium test (Calcium Corrosion Test by the British Standards Institution, BSI – ISO 15106-7) [192] and the "Defect Imaging Test" used in this study, based on the methodology developed within the Assender research group and described in European Patent EP3669168A1 [193]. While both methods utilize the stoichiometric reaction of metallic Ca with water vapour as an indicator for permeation, they differ significantly in setup, structure and data resolution.

Comparing the methodologies, the primary distinction between the two methods lies in the placement of the Ca (acts as the sensor). In the ISO 15106-7 standard, Ca is deposited onto a separate sensor plate (typically a glass slide), which is then sealed against the barrier sheet but integrates the total flux over the entire area resulting in a single bulk value [30].

On the other hand, the method used in this study deposits the Ca layer directly onto the barrier coating of the polymer substrate. By eliminating the head-space, the degradation of the Ca layer correlates spatially with the defects in the barrier layer immediately beneath it. This enables imaging of localized permeation pathways (pinholes) and the calculation of spatial defect density (spots / cm^2), rather than just a total global transmission rate [194].

In terms of data processing and resolution both methods use light transmission to estimate WVTR but differ in data processing and assumptions. The BSI standard method measures the uniform reduction in transmitted light intensity through the Ca layer, assuming a direct correlation with Ca depletion caused by water vapour permeation.

While it provides a bulk WVTR measurement across the sample, it lacks spatial resolution.

The study's optical Ca meanwhile enhances the analysis by using sequential imaging to track localised Ca depletion over time. Instead of relying on a single overall intensity value, it evaluates changes in localised mean grey values (the average pixel intensity within a defined image region, which reflects the amount of Ca present). This approach allows for spatially resolved tracking of Ca degradation across the sample, offering higher resolution to detect non-uniform permeation and enabling temporal resolution to monitor dynamic depletion processes (Verified in 9.1.2 Calcium Test Negative and Positive Control).

In depositing the sample and mitigating errors like pre-calcium depletion (environmental handling with the addition of the copper layer), the standard Ca testing detailed by BSI protocols, involves the vapour deposition of the Ca layer onto a sensor plate. This is said to be done within a controlled atmosphere glove box to prevent premature reaction of the Ca with ambient moisture or oxygen before the test cell is sealed [108]. Notably the BSI standard does not explicitly require a glove box, its use is standard practice to mitigate Ca's high reactivity to the surrounding environment.

The Assender method used in this thesis eliminates the need for a glove box through a modified deposition protocol. As detailed in the fabrication parameters described in 2.4 Calcium Test, this involved a sequential thermal evaporation process within a vacuum chamber (base pressure $\approx 1.0 \times 10^{-4}$ mbar). The first step is evaporating a Ca layer directly onto the barrier. Crucially this is immediately followed by the deposition of a thin copper capping layer ($\approx 15 – 30$ nm) without breaking the vacuum.

The copper layer acts as a temporary sacrificial barrier, retarding the oxidation of the underlying Ca sensor for a sufficient window (typically seconds to minutes) to allow the sample to be removed from the vacuum chamber and encapsulated with UV-curing epoxy and a glass cover slip under ambient laboratory conditions.

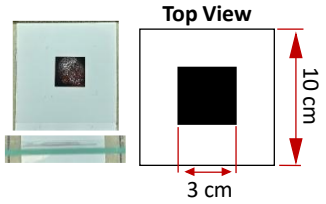
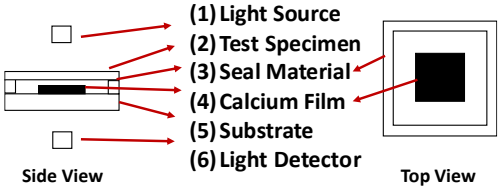
However there are various considerations and limitations of using the Ca test; while direct deposition method like the Assender method provides spatial resolution it can introduce some issues compared to the BSI standard method:

(1) Thermal Load: Thermal evaporation of Ca requires high source temperatures (~ 450 to 500 °C at the Tungsten boat), subjecting the polymeric substrate or barrier layer to radiant heat which could theoretically induce micro-cracks in a brittle coating like ALD deposited layer [195].

(2) Interface Stress: Direct contact between the corroding Ca (which swells upon oxidation), and the barrier coating may also induce localized stress at the interface, potentially altering defect propagation compared to a non-contact method (further adding potential errors) – can be mitigated by adding more repeats and ensuring that Ca depletion is even and uniform.

(3) Copper Oxidation: The copper layer is also not entirely inert; for certain coatings this may affect it such that the copper layer eventually oxidizes. While it protects the Ca during handling, it may also introduce a slight opacity and lag time that needs to calibrated out during image analysis.

Table 2-2: Comparison - "Assender, Sim and Tobin Ca-Test" [196] vs BSI Standard – Calcium Test

Parameter	Defect Imaging Test ("Assender, Sim and Tobin Ca-Test")	Standard Ca Test (BS ISO 15106-7) BSI Standard
Sensor Configuration	Ca deposited directly onto the barrier / substrate	Ca deposited on a separate glass plate (Test Cell).
Primary Output	Spatial Defect Density and Localized WVTR	Global Effective WVTR (Average Flux)
Thickness of Calcium	~220 nm of Calcium with ~30 nm copper layer on top.	10 nm to 500 nm.
Test Cell Size	Glass: 10 mm by 10 mm, Mask / Test Cell Size: 3 mm by 3 mm (Flexible can be small scale also between ~ 1 to 3 cm^2)	Test Cell Size: 20 mm to 100 mm. (Considered large – typically should be ~50 to 100 cm^2 required for standard cells).
Diagram	 (Sideview: "Sandwich Structure Figure 2-3")	 BSI Standard – Structure
Sensor Configuration	Substrate / Barrier / Calcium / Copper / Glass – sealed with Adhesive	Glass with Calcium (No Copper) below the barrier layer adhesive.
Number of Samples Per Temperature	Varied	Minimum of 3 Specimens
Detection Limit	~ 10^{-6} g/m^2/day (limited by edge seal).	~ 10^{-5} to 10^{-6} g/m^2/day
Environmental Handling /	Ambient Air: Permissible for short durations due to Cu protective layer. The	Inert Gas (Glovebox): usually Mandatory during preparation to prevent instant oxidation. (Strict Inert

Specimen Conditioning	copper capping layer acts as a sacrificial barrier, allowing sample transfer and encapsulation in air without degradation.	Atmosphere – sample preparation and transfer must occur in a glove box (< 40 ppm H_2O / O_2) or vacuum to prevent instant Ca oxidation.
Main Difference	Place Calcium Directly on Film to image permeation through film defects)	Calcium deposited on a substrate – separated from the test specimens (Measures Average amount of WVTR coming through the film).
Limitation	Direct contact stress and copper oxidation over time or copper opaqueness prevents Ca detection. (Also possible edge leak and pre-Ca depletion if copper not deposited properly).	No information on defect location or spatial density; possible edge leaks in headspace.

2.4.1 Calcium Test Structure

The calcium test stack (Figure 2-3) is prepared via thermal evaporation described in Figure 2-1. The process begins within a vacuum chamber (b), with the sample attached fastened to the substrate holder (c) using a combination of Kapton or polyimide tape, aluminium foil, and magnets. After initially pumping down the chamber with a rotary pump to achieve a rough vacuum, the pressure is further reduced using a diffusion pump to reach a base pressure of approximately 1.0×10^{-4} mBar, aided by liquid nitrogen cooling of the oil vapor trap to enhance pumping efficiency and minimize contamination. Once this pressure is reached a tungsten (f) boat loaded with calcium pieces (f.1) (1) is heated to evaporate the calcium, depositing it onto the sample (covering the whole area – inverted cone) (d) through a 3 by 3 cm^2 mask. The deposited calcium thickness (typically $\geq$ 145 nm, within a 100 – 800 nm range) is monitored by a QCM and controlled by an (e) shutter.

Subsequently, (2) the (f.2) copper filings are then heated in a second tungsten boat and the thin protective copper layer (10–25 nm, discussed in 2.4.2 Copper Thickness) is then deposited on top of the calcium layer. Both layers are thermally evaporated in the Edwards 306 bell-jar coater, which is evacuated to the mentioned base pressure (~ 1.0×10^{-4} mBar) by the (h) diffusion pump. A (g) metal separator is also placed between the copper and calcium boats, to prevent cross-contamination between the boats during deposition.

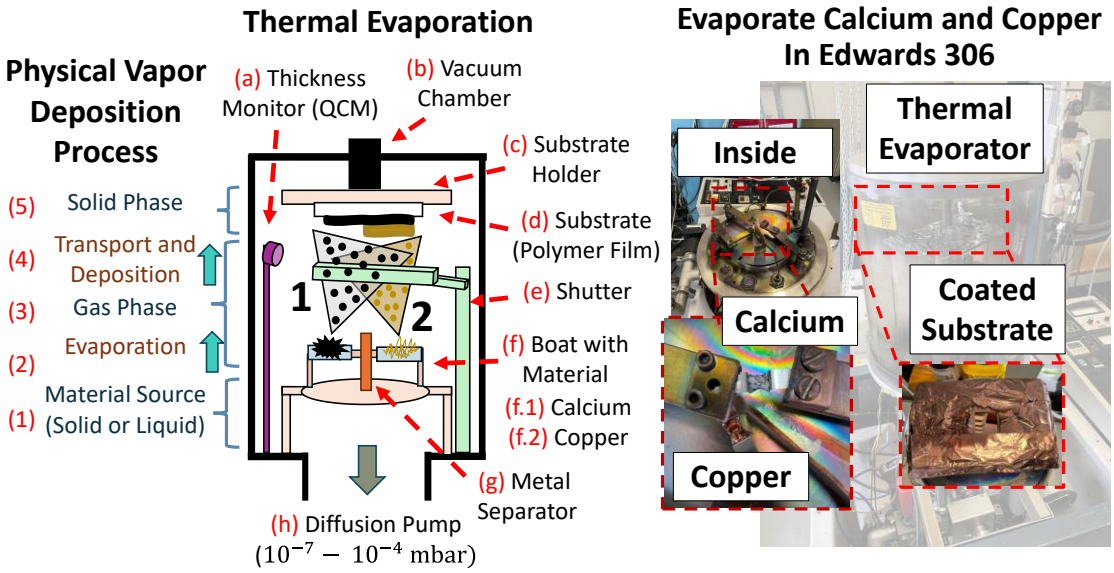


Figure 2-1: The thermal evaporation process is illustrated, where (1) the material source is (2) evaporated into the (3) gas phase, then (4) travels and deposits onto the (5) substrate as a solid layer. The accompanying image shows the Edwards 306 with arm configurations, where calcium is evaporated first, followed by copper, ensuring an even and uniform coating on the substrate.

As shown in Figure 2-2, the coated substrate is then removed from the vacuum chamber and attached to a 100 mm x 100 mm, 3 mm thick glass slide, with the Ca/Cu side facing towards the glass, by sealing the film with UV-curing epoxy (ELC-2500 UV Encapsulating Material). The assembled specimen, described in Figure 2-3, is then exposed to UV light (Intersonic IUV 250 Handlamp, 230V, 50Hz, 250W) for at least 5

minutes until the epoxy is fully cured. Once cured, the specimen is placed in the designated test setup, as described in Figure 2-5.

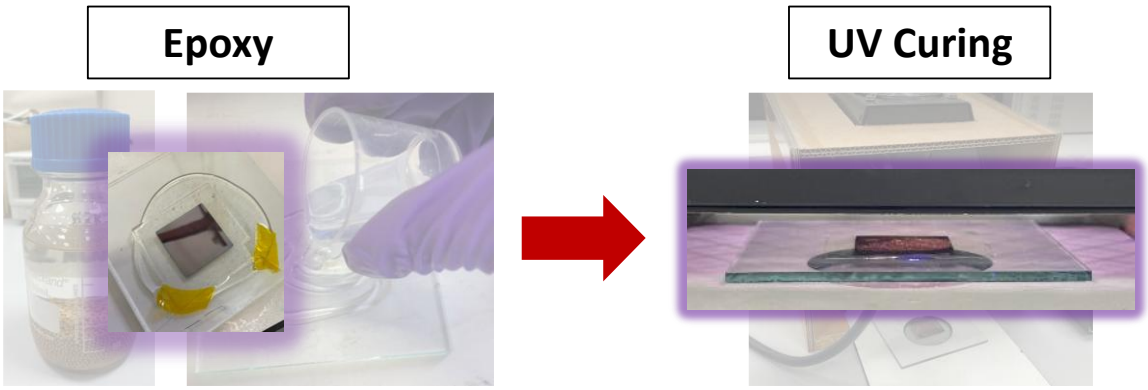


Figure 2-2: The coated substrate is placed onto a small amount of UV-curing epoxy, ensuring full coverage on the copper side to prevent sideways permeation. Any bubbles or unevenness is addressed before curing the sample under a UV lamp for at least 5 minutes. Once fully cured, the sample is labelled with the relevant conditions and information before being placed into the appropriate test box for further analysis.

As detailed in Figure 2-3, the (a) "Calcium Test Sandwich" or structure for a coated film (polymer with ALD layer), consists of seven layers (five layers without the ALD coating on both sides: uncoated film). The thickness and placement of the epoxy are critical, as they determine the water vapor permeation path and prevent sideways permeation, which could also promote premature calcium depletion.

Care must be taken to ensure the epoxy does not cover the side of the sample away from the glass as this would create an extra layer in the structure through which the water vapour would need to permeate. This can lead to inaccurate measurements by testing the combined performance of the epoxy, barrier layer and substrate, instead of isolating and accurately evaluating the barrier layer's performance on the substrate alone.

The encapsulation step involves exposing the sample to high intensity UV light to cure the epoxy. This introduces a potential source of error regarding the degree of cure of the sealant. Marsh *et al.* established that moisture solubility and diffusion in epoxy resins

are dependent on the specific chemistry and degree of cure. If the UV exposure is uneven due to shadowing by the sample holder, the epoxy may remain under-cured. An under-cured epoxy seal can have altered diffusion properties, potentially increasing the risk of edge permeation where water bypasses the barrier layer [197]. This possibility underscores the necessity of the edge exclusion methodology detailed in 4.4 Edge Permeation in the Calcium Test to ensure calculated WVTR values represent the barrier film rather than seal integrity.

(b) As introduced here (further discussed in 4.7 Calcium Test Defect Size Calculations), vapour ingresses through defects on the top barrier coating (unknown – number of defects or sizes), however after it goes through these defects it travels laterally through the substrate where the spatial information about the top defects is lost. The defects in the bottom barrier act as pathways for the permeant to leave the sample and can be seen, as vapour locally interacts with the Ca. This interaction of the vapor and the Ca layer in the bottom barrier visualizes the spatial density permeation through defects in the bottom coating. It is important to note that while the vapor ingress is driven by the defects in the top barrier, the visualization is primarily observed through the bottom barrier. This means that the effect of the top barrier on the ingress is indirect and not directly observable in the Ca test, which only detects the vapor's interaction with the bottom barrier. Because defects in the top barrier set the water concentration at the polymer surface, an unusually low defect density can also lower the driving gradient and therefore suppress the estimated WVTR, without altering the Ca test's visualisation of pathways in the bottom barrier.

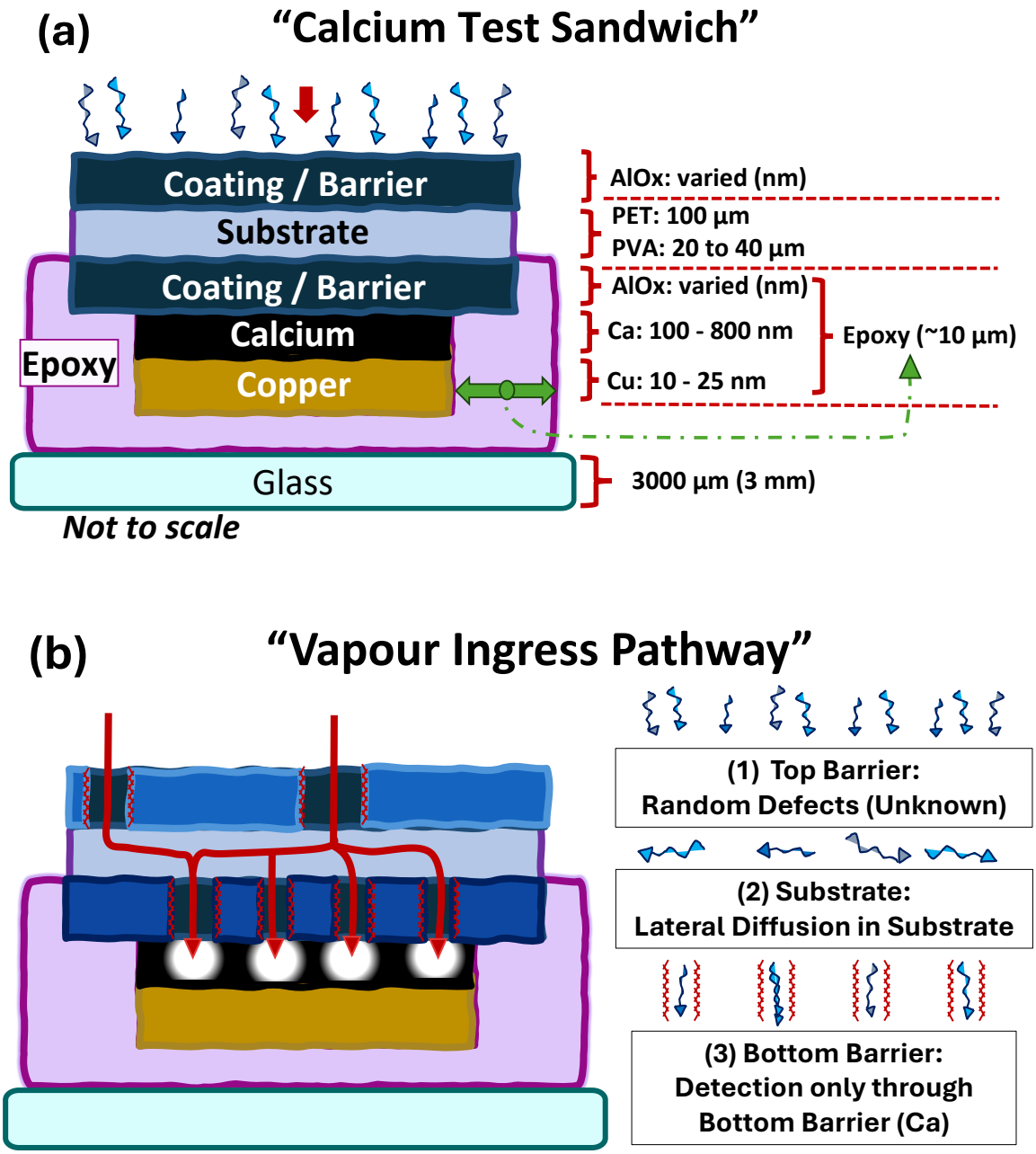


Figure 2-3: (a) Calcium test sandwich, consisting of an inorganic coating applied to the top of the polymer substrate, followed by deposited calcium and copper layers, and fully encapsulated onto a glass substrate using UV-cured epoxy for sealing. (b) Vapour ingress pathway diagram that illustrates vapor ingression in a dual barrier system. (1) The top barrier contains random, unknown defects that allow vapor to pass through. (2) As vapor travels through these defects, it diffuses laterally within the substrate. (3) The bottom barrier layer's defects are then pathways for the vapor to the Ca layer, which reveals the spatial density information of the barrier layer (defect sizes and counts).

Another consideration is the Ca microstructure and how this can also vary the reaction rate. It is critical to recognize that the evaporated Ca sensor is not a dense uniform slab, but more of a porous microstructure that directly dictates its own reaction rate. In Ca is thermally evaporated onto a cold polymer substrate (low homologous temperature $T/T_m < 0.3$), forming a Zone 1 microstructure characterized by tapered vertical columns separated by open physical voids as defined in the Structure Zone Models by Kell and Arnell [198].

Consequently these inter-columnar voids act as high speed diffusion pathways for moisture, effectively increasing the reactive surface area of the sensor, Because water does not corrode the Ca evenly from the surface down; instead, it penetrates these voids to initiate localized, internal degradation. Klumbies *et al.*, verified this mechanism using *in-situ* AFM, showing that Ca degradation is laterally inhomogeneous, initiating at specific nucleation sites, likely the grain boundaries or voids identified in the Zone 1 model, and spreading sideways. Therefore any slight variation in deposition pressure or rate that alters the grain size, and the density of these voids will also change the sensors reaction speed introducing an intrinsic variable to the measurement independent of the barrier itself [109].

2.4.2 Copper Thickness

An essential addition to the calcium test in this work is the copper layer, which prevents pre-calcium depletion (refers to the partial reaction of the calcium layer caused by exposure to the ambient moisture and oxygen before testing, unrelated to water vapour permeation through the barrier or polymer film) and eliminates the need for a glovebox. Without this layer, calcium would deplete too quickly, even before the test starts, making

it impossible to observe the transition phase or slow decay critical for measuring WVTR and understanding permeation mechanisms of barrier layer [196].

As summarized Table 2-3, alternative layers such as (1) Oxides (SiO_2 or SiO_x and Al_2O_3 or AlO_x), and (2) Precious Metals (Ag, Noble Metals: Au and Pt) can also provide excellent moisture protection. However, these materials are typically more expensive and impractical for only addressing pre-calcium depletion, as they require additional deposition steps, unlike the more economical and direct thermal evaporation of copper directly onto the calcium layer [30, 196, 199, 200].

Table 2-3: Pre-Calcium Depletion Backing Layer Materials

Material	Properties	Pros	Cons	Deposition
Oxides (SiO_2 or SiO_x, Al_2O_3 or AlO_x)	Dense, amorphous or tetrahedral structures block moisture. Chemically stable, thermally robust. Hydrophilic surfaces adsorb water but prevent bulk diffusion.	Excellent moisture barriers. Durable and stable. Transparent in thin layers.	Brittle and prone to cracking. Requires precise deposition.	PECVD and ALD for thin, defect-free films. Sputtering for thicker films. May need surface pre-treatment on polymers.
Precious Metals (Silver, Noble Metals: Gold and Platinum)	Dense FCC lattice effectively blocks moisture and oxygen. Chemically inert (Au, Pt) or moderately reactive (Ag). High durability and stability under extreme conditions.	Superior moisture barriers. Long-lasting and highly reliable. Effective for harsh environments.	High cost (Au, Pt). Silver tarnishes in reactive environments (*e.g.*, sulphur). Reduced flexibility in thick layers.	Sputtering or evaporation. Precision required for uniform coatings. Silver may require protective overcoats.
Base Metals (Copper)	Dense FCC metallic structure limits moisture	Cost-effective. Flexible and durable.	Susceptible to oxidation and corrosion.	Sputtering or evaporation.

	permeation. Good adhesion to substrates. Moderate reactivity; forms a porous oxide layer without protection.	Suitable for many applications.	Protective coatings may be necessary.	Optimization needed for thickness and coating durability.

Figure 2-4 (a) shows time-lapse images of an uncoated PET substrate with only calcium deposited, without a copper layer or glass cover, exposed to ambient moisture, shortly after thermal evaporation (the polymer film is between the 3×3 cm mask and a sheet of aluminium foil). Initially, the calcium appears shiny metallic black, but begins to disappear within seconds, moving from right to left, indicating the high reactivity of calcium to the environment or typical lab conditions (~25°C, 30% RH). As the calcium reacts to form transparent calcium hydroxide, the aluminium foil behind the sample becomes visible.

The calcium also displays apparent brightness variations, shiny in the centre, brown at the edges and different brightness, due to differences in background lighting or reflections rather than intrinsic inhomogeneity. This highlights the importance of using a calibration strip to normalize measured grey values and minimize the impact of external lighting difference between images when estimating fluence (Discussed: 2.4.8 Normalizing the Images).

The rapid depletion of calcium is a critical issue, as the sample preparation process—requiring a total of at least 10 minutes on average to apply and UV cure epoxy for encapsulating the sample onto the glass substrate—must be completed before the Ca is sealed by the glass from direct depletion by the ambient atmosphere. This highlights

the essential role of the copper layer in protecting the calcium during preparation outside an inert environment. Figure 2-4 (b) illustrates the three key regions of time in a calcium test with a copper layer:

1. **Onset/initial period**: Water vapor accumulates on the outer surface and gradually diffuses through the barrier and substrate, eventually reaching the calcium layer. The Ca can start to deplete but has not yet become sufficiently thin that light starts to be transmitted. During this time the concentration gradient of water vapour through the thickness of the sample can be established.
2. **Transition region**: As water vapor permeates, it slowly reacts with the calcium layer and depletes it, increasing the amount of light the layer can transmit. For coated films bright spots or patterns can be observed where the calcium is locally depleted, indicating permeation pathways or defects in the barrier film. These defects are critical in determining the barrier's effectiveness against water vapor.
3. **Saturation region**: Once the calcium is fully consumed, the copper layer beneath is exposed, showing a red-orange hue, and the amount of transmitted light can no longer increase, signalling the test's completion.

These stages provide spatial data on defect density, which helps evaluate the barrier's water vapor resistance and its overall encapsulation performance.

Moreover, the thickness of the copper layer is critical, Figure 2-4 (c), shows that an optimal copper thickness of around 15 nm (within a 10–25 nm range) providing sufficient protection for the calcium while allowing clear observation of its depletion during the test, also shown in previous work by colleagues Sim [111], Vouilloz [90] and Matsui [92].

As seen in Figure 2-4 (c) a copper layer that is too thin (~5 nm) may not adequately protect the calcium from reacting with moisture before encapsulation, meaning that the film is already transparent when the test starts, while a thicker layer (>35 nm) can block visible light, even once all the Ca has been depleted, making the transition region unobservable.

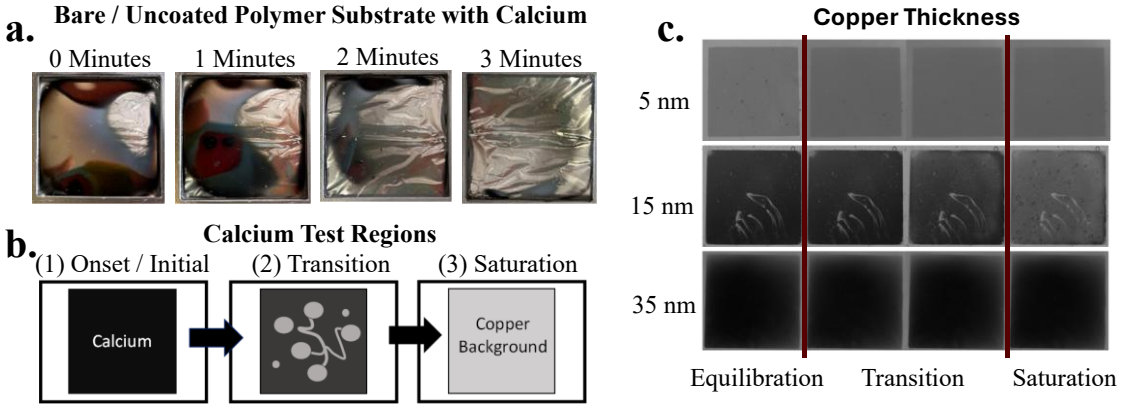


Figure 2-4: (a) Uncoated polymer film with calcium open to a room environment, demonstrating rapid calcium depletion within 3 minutes due to exposure to moisture; (b) Calcium Test Regions: (1) Onset/Initial period – water uptake and adsorption onto the barrier layer (Henry's Law) and establishment of the permeation, (2) Transition region – water vapor diffusion through the coating and substrate (Fick's Law), with pinhole defects indicated by calcium depletion, (3) Saturation – complete calcium depletion, revealing the bare copper layer; (c) Images of test samples with copper layers of various thickness: (1) 5 nm, (2) 15 nm, and (3) 35 nm, showing how too a thin copper layer allows premature calcium reaction, while too thick a copper layer blocks visual observation of calcium depletion.

2.4.3 Calcium Test Set-up

The prepared Calcium test sandwich is then placed in the designated calcium test box, as outlined in Figure 2-5. There are two distinct barrier setups depending on the quality of the barrier being tested. Poor barriers ($\geq 10^{-1}$ g/m^2·day) allow for rapid calcium depletion, transitioning from opaque to transparent within minutes to days. Good barriers

(ranging from 10^{-1} to 10^{-7} g/m^2·day) maintain their integrity for much longer, lasting anywhere from days to several years.

The setup illustrated in Figure 2-5 (a) for testing poor barriers utilizes a camera (either an Olympus SP-320/SP-350 or a Logitech C922 webcam) to capture periodic images of the sample at short intervals while the sample is held continuously under controlled conditions.

Temperature is adjusted with the hot plate; to cool the chamber to ≈ 14°C the plate is switched off and pre-chilled gel packs are placed beneath it. Relative humidity is fixed by a saturated salt: Lithium Chloride (LiCl), Magnesium Chloride ($MgCl_2$), and Sodium Chloride (NaCl) and together with temperature, is logged every minute by an onboard data logger or sensor (*e.g.*, Lascar EL-USB-2-LCD High Accuracy Data Logger - ±2% RH, ±0.5 °C). An adjacent K-type thermocouple provides an independent temperature check. A diffuse LED panel placed behind the chamber supplies a uniform backlighting, ensuring high contrast between the Ca film and the background and eliminating shadows.

In contrast, the setup for testing good barriers (Figure 2-5 (b)) uses a hermetically sealed oven (Genlab, Models: MINO/18/SS/DIG and MINO/6/SS/DIG), which provides more stable temperature and humidity control. For sub-zero testing conditions, some samples were placed in a Bosch Series 2 GTV15NWEAG freezer, achieving temperatures of approximately -25 °C, to simulate cold storage environments. While saturated salts are still used for humidity regulation, the better sealing minimizes environmental variation and enhances consistency during testing. Samples are periodically removed from the oven, placed on a light source, and photographed using a

camera connected to a computer, before being returned to the oven. This arrangement also allows multiple samples to undergo testing in parallel in comparison to the (a) Poor Barrier set-up where it is not large enough to accommodate more than one sample. The amount of time that the sample is out of the controlled environment in for photographing is minimal compared to the lifetime of the test.

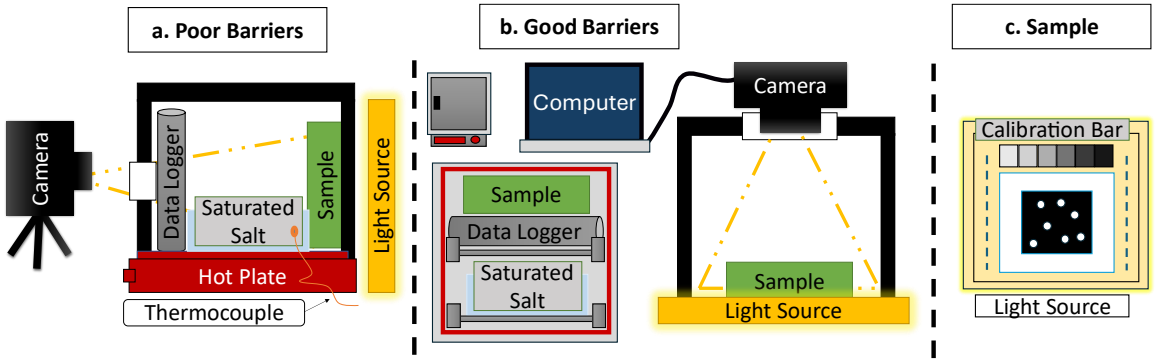
As the intensity of light transmitted is the key measurement to establish WVTR it is important to have this well calibrated. Use of a planar, constant light source and a rig to hold all elements in a constant position reduces variations during the test. Variations in ambient lighting may, however, affect the measurement, so a calibration bar, a strip of film with 11 blocks of graded transmissivity is mounted in the imaging rig to and is recorded along with every image of the sample. Figure 2-5 (c) illustrates a schematic plan view of a sample within a calcium testing arrangement, featuring the addition of a calibration bar and a planar light source. This calibration bar allows the normalization of the transmissivity measurement against these known standards and reduces the effect of any light or brightness variations between the images.

Doubling down on the light source stability, the system does not rely on periodic hardware calibration of the LED panel, which can be prone to drift over long test durations. Instead this study employs an in frame normalization strategy that is further expounded in 2.4.8 Normalizing the Images.

This approach aligns with methodology in literature (Klumbies *et al.*), who defined lower and upper bounds for Ca calculations based on 0% (initial opaque Ca) and 100% (fully corroded) transmission reference points to ensure consistency and precision. By capturing a neutral density reference standard within every single image frame, the

analysis normalizes the Ca intensity against a known constant at the exact moment of capture. This acts as an internal standard, simultaneously compensating for light source dimming, camera auto-exposure shifts, and ambient lighting changes, ensuring that measured changes in grey value are attributable solely to the Ca oxidation.

The schematic in Figure 2-5**,** below, shows the set-up for both variations (1) the poor barrier calcium test, the photograph showing two cell boxes for *in-situ* observations with each test cell box equipped with adjustable camera arms for precise positioning for the viewing angle of the sample. Meanwhile for the (2) good barrier setup, two ovens containing different saturated salts and data loggers are used. The camera, connected to a computer, captures ex-situ images of the sample on a backlit planar platform.



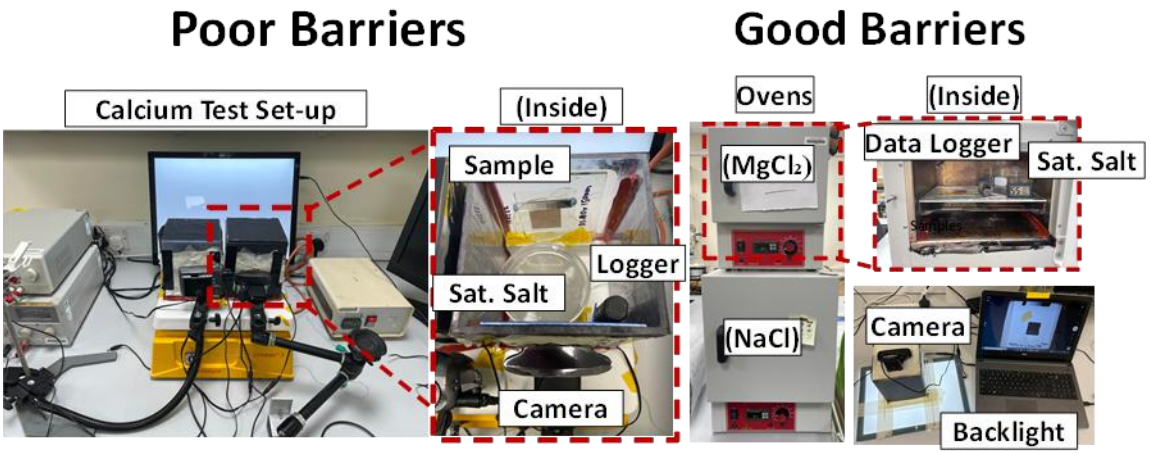


Figure 2-5: Schematic of a Calcium Test Box setup for both poor and good barriers. (a) Poor Barriers: This setup enables unattended monitoring of calcium tests, capturing images over minutes to days. (b) Good Barriers: Designed for longer tests that can span weeks to years, allowing multiple samples to be conditioned and tested over extended periods. (c) Calcium test sample: Depicts the location of the calibration bar and the region of interest where images are captured using a backlit light source. Below the schematic are the current setups, showing the camera positions (with adjustable arms) for the poor barrier test boxes, alongside a top view of the test box interior. The setup for good barriers is displayed next to it, featuring two ovens with different saturated salts to control humidity, and the backlit light arrangement for imaging the coated barrier samples.

2.4.4 Calcium Deposition Caveats and Contamination

The Ca test is a relatively robust process and was kept consistent, the presence of errors and some issues arising with individual samples are inevitable. For example, while the copper capping layer is designed to mitigate oxidation during sample transfer, several sources of contamination inherent to the deposition environment must be acknowledge as potential contributors to measurement variability.

Both the Edwards 306 thermal evaporator, used for Ca deposition, and the ALD coating facility are multi-user systems and hence are prone to cross contamination. Defects in the barrier film occur from dust particles and surface imperfections that may become the dominant limiting factors of film performance. In the context of the Ca-sensor, particulates on the substrate prior to Ca deposition can be causes or reasons for pinholes in the sensor layer itself, leading to localized false-positive signals and errors [201].

Moreover, the base pressure of the system can also contain residual water vapor further introducing contaminants and uncertainties. Higgs *et al.* demonstrated that Ca films exhibit complex oxidation kinetics, including a lag time that is sensitive to surface conditions. Unlike an Ultra-high vacuum system, the vacuum environment in the

Edwards 306 may not have been sufficient (especially with constant usage despite maintenance) to avoid the incorporation of oxygen and hydrogen during deposition which in turn can alter the initial passivation layer and resulting onset time of the test [202].

Finally, the transport of the samples between labs and chambers involves exposure to the ambient laboratory environment (can be varying). Cros *et al.*, showed with ion beam analysis that even thin Ca electrodes degrade rapidly upon exposure to moist atmospheric conditions. Although a copper layer provides a temporary shield, any micro-scratches or incomplete coverage still exposes the underlying Ca to immediate hydration before the epoxy seal is applied, necessitating the strict cleanliness protocol as described in Section 9.1.3.d Cleanliness Protocol and Epoxy Curing Time [107].

2.4.5 Measuring WVTR, Permeability and Activation Energy

2.4.5.a WVTR Calcium Test Estimation

The overall WVTR or permeation is determined by estimating the fluence, *i.e.* the cumulative total mass of water vapor (M_{H_2O}) that has permeated through the barrier film or material per unit area over time (area of water vapor exposure A_{H_2O}, which is equal to the area of the calcium layer, A_{Ca}). The assumption is that it is directly related to the total intensity of transmitted light, which corresponds to the amount of calcium remaining (defined in Table 2-4) and follows a lag time model (Figure 2-9). Despite slight variations in assumptions or methods in estimating the WVTR, all calcium tests share the common principles to be presented for estimating the fluence over time [6, 32, 46, 196, 203-211].

WVTR in the Ca Defect Imaging Optical test is estimated by measuring changes in the mean grey value of the calcium layer over time. The mean grey value refers to the average pixel intensity within a defined region of interest; in this study it was done from a grayscale or grayscale-converted image. As the calcium reacts with water vapor, the layer becomes more transparent, allowing more light to pass through, which increases the mean grey value. This increase is approximately proportional to the extent of calcium consumption, and therefore, serves as a quantitative indicator of water vapor transmission. While related to how much the light is observed, mean grey value is a direct numerical output from image analysis, unlike brightness, which is a perceptual quality affected by external imaging conditions such as lighting and camera settings.

This is captured in sequential images of the specimen at various time intervals. As shown in Figure 2-9, there are three key regions in the "lag time model", which represent the initial rate of permeation across the film as previously outlined in Figure 2-4 (b).

The (1) first region, Onset/Initial, is the start of the test when the sample is still fully opaque with no measurable calcium depletion—referred to as "lag time" [110, 202, 203]. During this phase, they may be initial calcium reacting with water vapor, however the thickness of the calcium layer remains high enough for that no transmitted light can be detected. Two key processes mainly occur during this stage:

1. Establish Steady State Diffusion: A constant gradient of water vapor concentration forms across the sample, creating a stable driving force of diffusion (or constant within each layer of the sample).

2. Calcium Reaction without Measurable Depletion: Any calcium reacting with water vapour does not deplete the calcium sufficiently to allow measurable light transmission, with the sample remaining opaque.

Once steady-state diffusion has been established, typically indicated by a linear increase in fluence over time, a marked increase in transmitted intensity can also be observed, signifying the end of the "onset time". This increase occurs when the calcium layer has become sufficiently thin, due to conversion to calcium hydroxide, to allow some light to pass through. This point is independent of whether steady state diffusion has been reached, although in practice the typically linear increase in intensity in the transition regions suggests that the steady state has been established.

In the (2) transition region, for bare (substrate-only) samples, calcium depletion is generally uniform across the surface, with minimal observed sideways ingress of water from the epoxy. For coated samples, defects or pinholes may appear, revealing the permeation mechanisms through the barrier layer. However, as calcium tests typically run for longer durations now, sideways permeation through the sealing epoxy can also be observed in some cases.

The final stage, (3) Saturation, occurs when all the calcium in the test layer has been fully consumed or reacted with water vapor, as indicated by a plateau in the calculated fluence (detailed in Table 2-4). This plateau signifies that the optical imaging test, which tracks calcium depletion through changes in transmitted light intensity can no longer record permeation due to the absence of reactive calcium.

The plateau reflects the end of measurable chemical interactions (calcium forming calcium hydroxide), not the cessation of water vapour permeation. At this stage, the

barriers' ability to block water vapor can no longer be quantified through the calcium layer, as the optical signal of calcium becomes insensitive to further permeation. WVTR represents the steady-state rate of water vapor transmission through the barrier material, measured during the transition phase, providing a measure of the barrier's performance while reactive calcium remains.

Table 2-4: Derivation of Fluence Lag time model

Step	Concept / Explanation	Key Equation
Definition of Fluence (F)	Fluence is the total mass of water vapor (M_{H_2O}) that has permeated through the barrier material per unit area, where area of water vapor exposure A_{H_2O} is equal to the calcium layer area (A_{Ca}). It is also related to the intensity of transmitted light and the amount of calcium consumed.	$F = \frac{M_{H_2O}}{A_{H_2O}} = \frac{M_{H_2O}}{A_{Ca}}$
Behaviour in Regimes	The permeation behaviour is divided into three regimes: 1) Lag time: Water vapor begins adsorbing onto the surface but hasn't diffused through yet. 2) Steady state diffusion (transition region): Water vapor diffuses at a constant rate. 3) Full reaction or saturation region.	Fluence graph: *F* vs. *t* (time). Since transition region represents the steady-state diffusion, the WVTR is calculated using the slope of the fluence vs. time graph during this regime. This gives the steady permeation rate of water vapor through the material.
Calculating WVTR from Regime 2	WVTR is calculated from the slope of the fluence vs. time curve during the stead-state transition regime, representing the constant water vapor permeation rate.	Fluence is related to WVTR, as WVTR measures the rate of permeation over time.

Calculating the fluence as defined in Equation 2-2 as the amount of reacted calcium requires a few assumptions and derivations. Based on the reaction between calcium and water (Reaction 1-1) the fluence can be estimated by taking account the stoichiometric ratio "n" equal to 2 ($n_{Ca}: n_{H_2O} = 1:2, \text{or } n_{H_2O} = 2n_{Ca}$), Mr_{H_2O} is the

molar weight of water 18.01 g/mol, Mr_{Ca} molar weight of Calcium 40.08 g/mol, $\rho_{(Ca)}$ is the density of Calcium 1.55 g/cc, where the volume can be estimated by using:, $A_{(Ca)}$ is the area of calcium deposited, $A_{(Barrier)}$ the area of the barrier (if the calcium is deposited directly on the barrier its areas are equal and cancel out) – detailed in Table 2-5

Table 2-5: Mass of Water Permeating through Film

Step	Concept / Explanation	Key Equation
Reaction Stoichiometry	The reaction between calcium and water vapor: for every mole of calcium, 2 moles of water vapor react, establishing the ratio $\mathrm{n}_{Ca}:\mathrm{n}_{H_2O} = 1:2$	$Ca + 2H_2O \rightarrow Ca(OH)_2 + H_2$ Where: $\mathrm{n}_{H_2O} = 2\mathrm{n}_{Ca}$
Moles and Mass Conversion	The moles of water vapor can be converted into mass using the molar mass of water vapor $M_r(H_2O) = 18g/mol$	$M_{H_2O} = 36\mathrm{n}_{Ca}$
Molar Mass of Calcium	The molar mass of calcium $M_r(Ca) = 40g/mol$ The moles of calcium are calculated by dividing the mass of calcium M_{Ca} by its molar mass.	$n_{Ca} = \frac{M_{Ca}}{M_{r\,(Ca)}} = \frac{M_{Ca}}{40}$
Mass of Water Vapor	Using the molar mass of calcium and the stoichiometric ratio, the mass of water vapor M_{H_2O} is related to the mass of calcium M_{Ca}	$M_{H_2O} = 36 \times \frac{M_{Ca}}{40}$ $= 0.9\, M_{Ca}$
Density and Volume Relationship	The mass of calcium is also related to its volume and density. The volume of reacted calcium V_{Ca} is given by the area A_{Ca} and thickness h_{Ca}.	$M_{Ca} = \rho_{Ca} \times V_{Ca}$ $= \left(1.55 \times 10^6 \frac{g}{m^3}\right)$ $\times A_{Ca} \times h_{Ca}$
Final Mass of Water Vapor	Substituting the mass of calcium into the mass of water vapor, the final equation for M_{H_2O} becomes:	$M_{H_2O} =$ $0.9 \times \left(1.55 \times 10^6 \frac{g}{m^3}\right)$ $\times V_{Ca}$

The next critical step involves estimating the volume of the calcium (V_{Ca}) by determining the difference between the initial volume of calcium (V_o) —when the layer is

fully opaque— and the remaining volume of calcium (V_{rem}). This is calculated based on the area (A_{Ca}) and the thickness of the calcium (h_{Ca}). Given the setup, where the calcium layer is deposited on the barrier, and the assumption of uniform water vapor exposure across the barrier film, the areas of reacted calcium and water vapor exposure are equivalent, effectively cancelling out in the fluence calculation as shown in Equation 2-2. Highlighting calcium thickness as the key factor in determining the mass of water permeated. The volume of reacted calcium is then expressed using Equation 2-1, where h_i represents the initial calcium thickness at opacity and h_{rem} is the remaining calcium thickness.

$$V_{Ca} = V_o - V_{(rem)} = A_{Ca} \cdot h_{Ca} = A_{Ca} \cdot (h_i - h_{rem}) \qquad \textit{Equation 2-1}$$

Subsequently to measure the h_{Ca} it is assumed that the light transmitted is linearly proportional to the thickness of the Ca (with a negative coefficient *i.e.* the light transmitted increases as the Ca becomes thinner) Table 2-6.

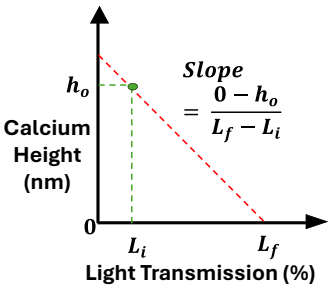
This assumption introduces a proportionality constant that relates Ca thickness to transmitted light intensity, modelled as linear approximation with a negative slope, not an inverse proportionality. The slope is defined using the initial Ca thickness (h_i), and the change in measured light intensity between the initial (L_i) and final (L_f) states. Here, L_i refers to the light intensity at the beginning of the test (time zero), when the calcium layer is thick and fully opaque, and transmission is effectively zero. L_f corresponds to the light intensity once the calcium is fully depleted.

While h_i refers to the actual deposited or starting thickness of the Ca layer, h_o can be interpreted as the minimum thickness at which the Ca layer becomes fully opaque, *i.e.*, the point at which light transmission becomes negligible. In this model, h_i and h_o are

treated equivalently for estimating the slope, since the focus is on the relationship between transmitted intensity and optical response, rather than precise physical thickness at submicron resolution.

While the transmission-thickness curve for Ca is formally exponential, a straight-line fit is used only while the fading film still transmits ≥ 90% of the probe light (absorbance A ≤ 0.05, extinction coefficient k < 0.1). Optical spectroscopy studies label this weak absorption window and show that first order linearization of Beer-Lambert departs from the exact solution by around ≤ 6% which is smaller than the experimental noise in the Ca test [212, 213].

Table 2-6: Thickness of Calcium

Step	Concept / Explanation	Key Equation
Relationship of Calcium Thickness and Light	The thickness of the remaining calcium layer, h_{rem}, decreases approximately linearly (with a negative slope) as the percentage of light transmitted through the sample increases. Thinner calcium layers allow more light to pass through.	
Proportionality Constant (Slope)	The proportionality constant is defined as the ratio of initial calcium thickness h_o to the change in light transmission over time or the slope.	$\text{Slope} = \frac{-h_o}{L_f - L_i}$
Equation for Initial Ca Thickness	The initial thickness (h_i) is equal to the proportionality constant multiplied by the initial light transmission (L_i) at time zero. Here, h_i is the estimated starting Ca thickness, while h_o represents the minimum thickness required to block light.	$h_i = \frac{-h_o \cdot L_i}{L_f - L_i}$
Equation for Remaining Ca Thickness	The remaining thickness (h_{rem}) on the other hand is equal to the proportionality constant multiplied by mean light intensity measured at the	$h_{rem} = \frac{-h_o \cdot L}{L_f - L_i}$

	current region of interest of the analysed image (L)	
Calcium Thickness	The estimated calcium thickness is equal to the difference between initial thickness and estimated remaining calcium thickness.	$h_{Ca} = \frac{-h_o \cdot L_i}{L_f - L_i} - \frac{-h_o \cdot L}{L_f - L_i}$ $h_{Ca} = h_o[\frac{L - L_i}{L_f - L_i}]$

As noted, experimentally determining h_o – the exact minimum thickness at which the Ca layer becomes opaque (*i.e.*, fully blocks light transmission) – is challenging due to inherent measurement limitations. Accurate determination of Ca thickness during deposition is complicated by several factors, including the deposition rate, which can influence growth uniformity and layer density, especially for reactive materials like calcium. Fast or fluctuating deposition rates may also introduce inconsistencies in the actual thickness deposited compared to the target value.

In particular, the thickness values obtained from the quartz crystal monitor (QCM's) require calibration specific to the system configuration and material. For Ca, this presents a challenge, to calibrate the QCM accurately, one must independently verify the thickness of the deposited Ca layer – typically through a secondary, non-optical method. However, this is difficult in practice due to Ca's high reactivity, which hinders precise post-deposition characterization. These combined uncertainties make it difficult to precisely determine the opacity threshold thickness (h_o) through direct measurement.

As shown in Figure 2-6, are images that depict the point where the calcium layer fully covers the "smiley" behind the polymer film (PET), turning the sample opaque, where it was estimated to be on average around the 145 nm (h_o) mark using the values from the QCM monitor. This thickness may vary slightly, but it provides a reliable estimate of when the calcium layer begins to turn grey or show possible defects. Other

researchers have reported different calcium thickness assumptions: electrical calcium tests, for example, use an initial height of 270 nm [203], while some studies report that even a 40 nm calcium layer shows an opaque film [214]. Despite these variations, the 145 nm assumption, corroborated by former colleagues [111], is used here to estimate the WVTR in this study's calcium tests.

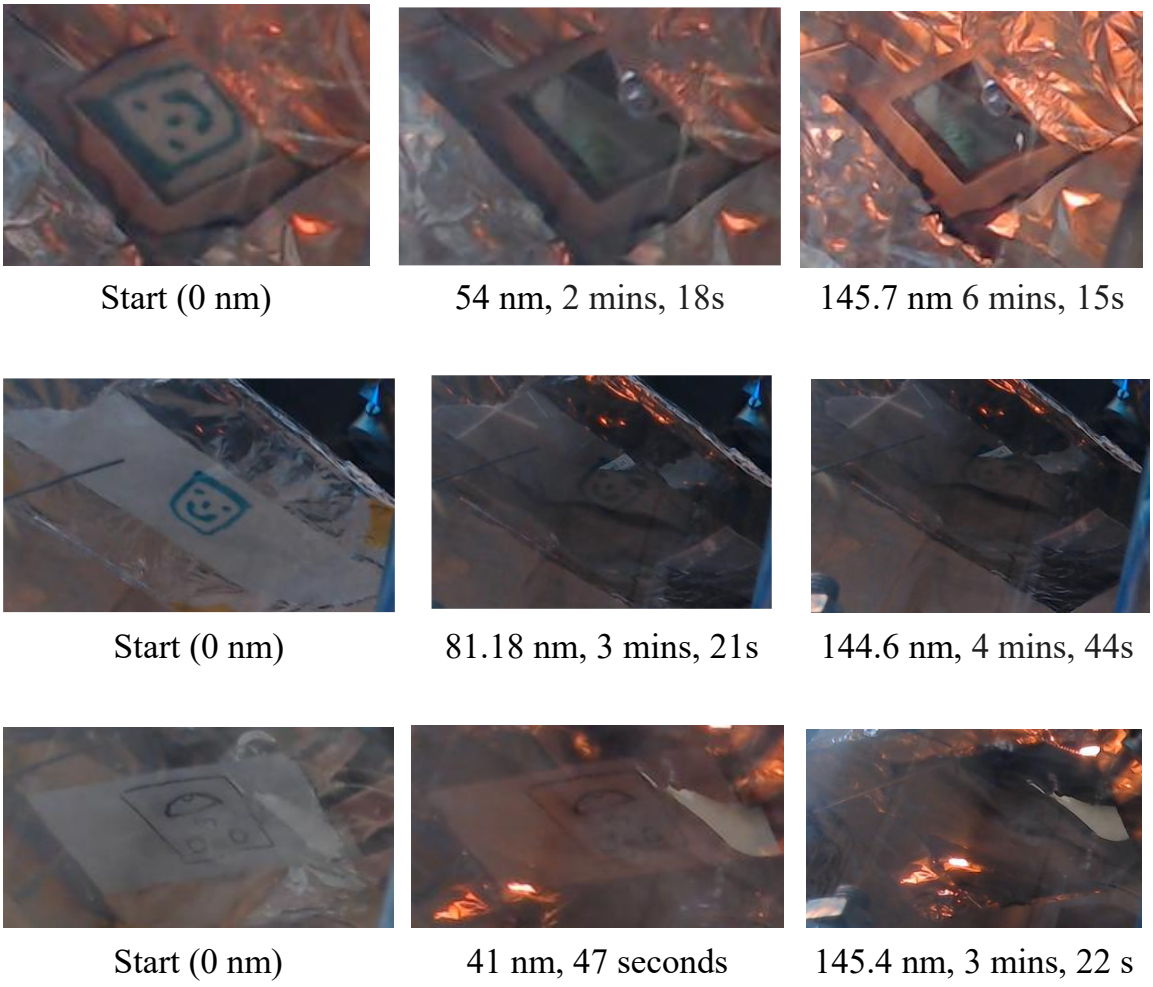


Figure 2-6: Calcium is deposited onto a 'smiley' indicator, with its thickness monitored by a Quartz Crystal Monitor (QCM) to gauge when the indicator becomes invisible, or the sample turns opaque. A potential issue arises from the glass barrier or seal in the Edwards 306 Thermal Evaporator, which may impact the perceived opacity. The calcium layer is estimated to reach full opacity, blocking all light, at approximately 145 nm.

Substituting the different equations into the fluence equation, it can now be fully expressed in Equation 2-2, then simplified and estimated as detailed in Table 2-7.

$$Fluence = n\frac{Mr_{H_2O}}{Mr_{Ca}} \times \frac{\rho_{(Ca)} \cdot A_{(Ca)}}{A_{(Ca)}} \times h_o \cdot \left[\frac{L - L_i}{L_f - L_i}\right] \qquad \textit{Equation 2-2}$$

Table 2-7: WVTR from the Fluence (Simplified)

Step	Concept / Explanation	Key Equation
Substitute into Equation for M_{H_2O}	Substitute The Final Equation for thickness into the equation for Final Mass Vapor: we can express the mass of water vapor permeating through the film in terms of transmittance L and initial calcium thickness h_o .	$M_{H_2O} = 0.9 \times \left(1.55 \times 10^6 \frac{g}{m^3}\right) \times A_{Ca} \times h_o \times \left[\frac{L - L_i}{L_f - L_i}\right]$
Substitute this into the Fluence Equation	Substituting M_{H_2O} into the fluence equation gives the final expression for fluence, *F*, in terms of transmittance L and initial and final light values.	$F = 0.9 \times \left(1.55 \times 10^6 \frac{g}{m^3}\right) \times (145 \times 10^{-9}\, m) \times \left[\frac{L - L_i}{L_f - L_i}\right]$
Calculation of WVTR	The steady state Water Vapor Transmission Rate (WVTR) is simply the slope of the linear section of the graph of F vs. t (fluence vs. time).	$WVTR = m_{F\ vs.t}$

2.4.6 Fluence Calculation Example

An example of fluence calculation and eventual estimation of WVTR is seen below, using an uncoated PET Calcium Test at 14.5 ± 2.5°C, in LiCl, RH ≈65%, as a representative sample.

2.4.6.a Mean Intensity Measurement

The intensity measurements are obtained using image analysis software (*e.g.*, ImageJ/Fiji, MATLAB, or Python), which converts images into a matrix of pixel values. Each pixel is assigned a grey value ranging from 0 (pure black) to 255 (pure white), with intermediate values representing shades of grey. The software calculates the mean grey value by averaging the intensities of all pixels within a defined region of interest (ROI). This provides a quantitative measure of brightness or light intensity, which, in this case, is used to track calcium depletion over time.

Figure 2-7 (a), shows six (6) representative images, illustrating the gradual depletion of calcium over time. By Image 40 (585 minutes), near the onset time, calcium begins to show visible erosion. An hour later, at Image 45 (660 minutes), the erosion becomes more pronounced, marking the transition region, which is further evident in Images 50 and 53 (735 and 780 minutes, respectively). By Image 90 (1335 minutes), the process is complete, leaving only the copper layer visible. This progression is further explained in the time-lag model (Figure 2-9).

Figure 2-7 (b) presents the mean intensity measurements as surface plots alongside the calibration strip, which is unique to each image (example calibration bar for Image No. 1). For these specific examples, the calibration strip is identical but becomes more relevant for samples discussed later such as in Figure 9-5. The surface plots illustrate the increasing intensity over time, inverted here for visual clarity. Notably, the data also highlights the slight non-uniformity in calcium depletion, potentially attributed to edge effects and permeation through the epoxy. This slight non-uniformity is critical for low-

WVTR samples: when only isolated defects admit vapour, Ca corrodes locally first, and a simple average-intensity method can mis-represent the true permeation rate.

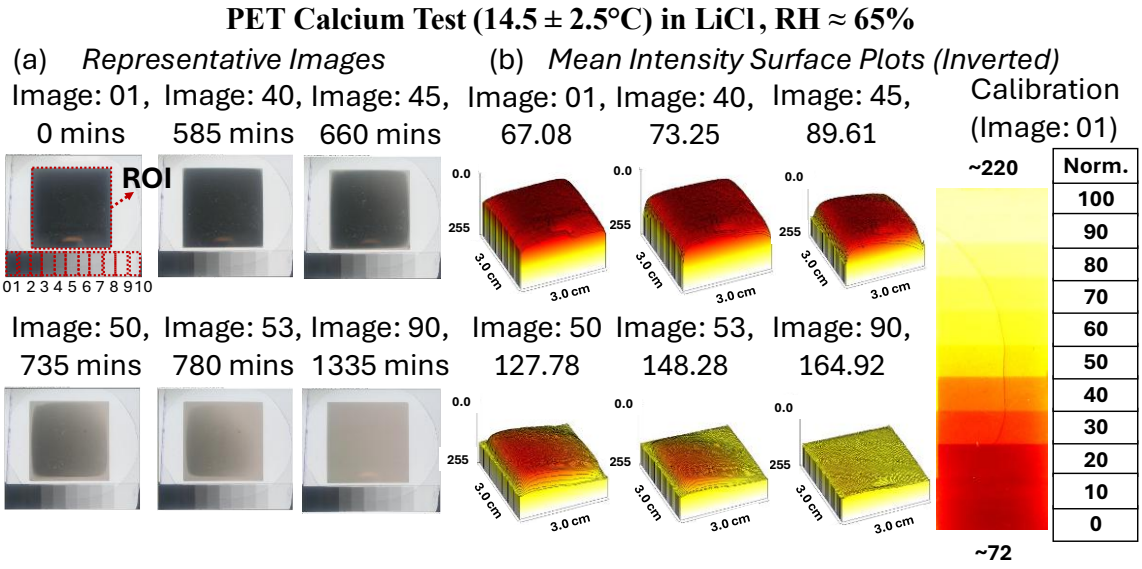


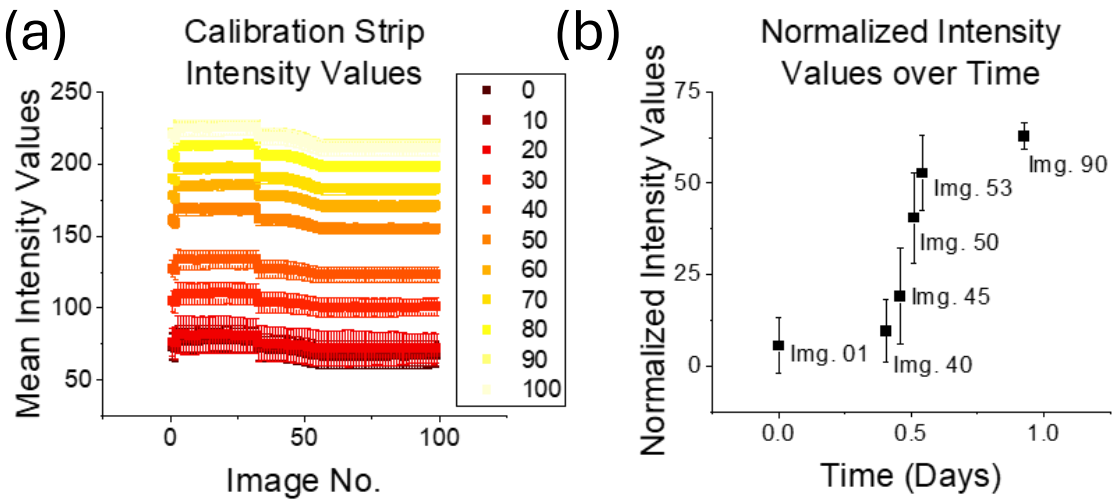
Figure 2-7: (a) Six representative images from an uncoated PET Calcium Test conducted at 14.5 ± 2.5°C in LiCl (RH ≈ 65%), illustrating the gradual depletion of calcium over time. (b) Corresponding mean intensity surface plots, calculated from the images, depict the progressive change in calcium, quantified through the mean light intensity values.

As discussed, raw mean intensity values can be utilised; however, as demonstrated later (*e.g.*, in Figure 2-9 and explored further in Section 2.4.8 Normalizing the Images), relying solely on raw values can introduce inaccuracies in fluence estimations due to external variations, such as light intensity fluctuations and other environmental factors. To address this, calibration strip values are used, providing a unique reference for each image. These calibration strip values are plotted for this example, as illustrated in Figure 2-8 (a).

Figure 2-8, also shows panels (c-h) are calibration plots (not the direct photographs) that each represent a single frame in the image sequence. In Figure 2-8 (c), the plot corresponding to Image 1 shows a sample-ROI mean intensity or mean grey level

of 67.1 pixel value (0 – 255, 8 bit scale); where this horizontal line intersects the linear calibration fit gives a normalized transmittance of 5.51%. Figure 2-8 (d) (Image 40) still contains appreciable Ca, yielding 73.1-pixel value that equates to 9.55%. As the transition progresses, the normalised value rises sharply: Figure 2-8 (e), (Image 45) 89.6 pixel value to 19.0%, Figure 2-8 (f) (Image 50) 128 pixel value to 40.5%, and Figure 2-8 (g) (Image 53) 148 pixel value corresponds to 52.6%. When only the copper backing remains, the response saturates at ≈165-pixel value, corresponding to a final normalised transmittance of 62.8% in Figure 2-8 (h).

These values are collated and plotted in Figure 2-8 (b), showing the normalised intensity values over time (days). These values are used to represent the light intensity for ROI in fluence calculations to be used in the equation $[\frac{L-L_i}{L_f-L_i}]$.



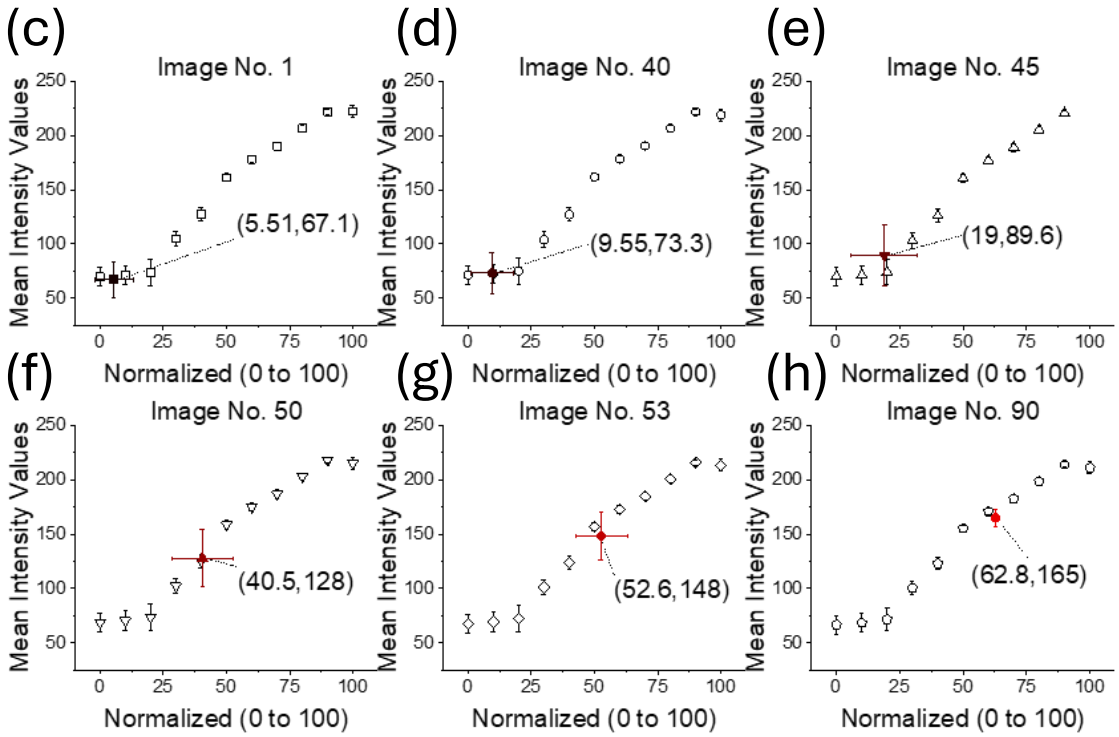


Figure 2-8: Intensity calibration using an 11-step neutral density Calibration bar glass strip. (a) Mean grey value of each glass square is plotted versus image number for an uncoated PET Ca test at 14.5 ± 2.5°C in LiCl (RH ≈ 65%). The legend shows the notional normalized % transmittance values, assigned by equally dividing the 11-step glass strip into 10% increments from 0% to 100% T. These serve as fixed reference points for intensity normalisation in each frame. (b) Normalised mean light intensity values plotted over time (days), alongside individual calibration plots with corresponding normalised values for representative images – (mean intensity value, normalized value) – (c) Image No. 1 (5.51, 67.1), (d) Image No. 40 (9.55, 73.3), (e) Image No. 45 (19, 89.6), (f) Image No. 50 (40.5, 128), (g) Image No. 53 (52.6, 148), and (h) Image No. 90 (62.8, 165).

Using Equation 2-2, the fluence is calculated from the normalised light intensity values, as illustrated in the lag-time model (Figure 2-9). For example, in Image 53, the average initial normalised light value at equilibration (onset stage) is approximately 4.53, while the final normalised value at saturation is 62.76. Applying the fluence equation, the fluence at 780 minutes is estimated to be 0.17. This calculation is repeated for all data points to produce the fluence vs. time plot. The slope of the linear region is determined to

be 1.25 ± 0.031 g/cm²·day, indicating that the transition begins around Image 40 and ends near Image 56.

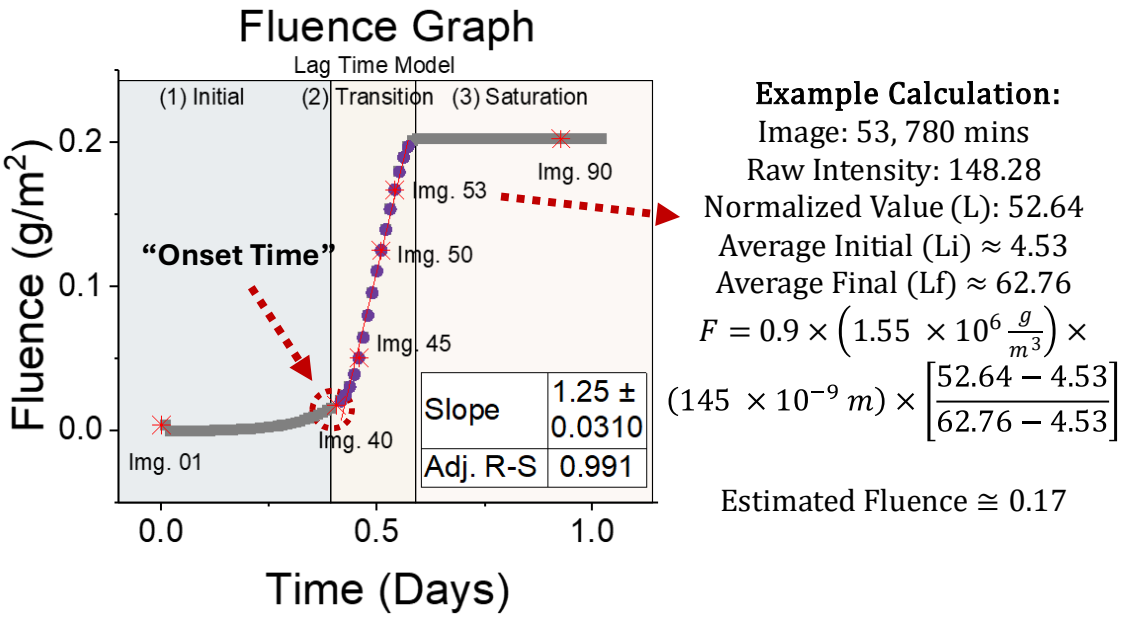


*Figure 2-9: Lag-time model of an uncoated PET Calcium Test conducted at 14.5 ± 2.5°C in LiCl (RH ≈ 65%), highlighting three distinct regions: (1) **Initial Region**, where the calcium layer is fully opaque, blocking light transmission, despite initial water uptake and adsorption; (2) **Transition Region**, beginning at the onset time, marked by a significant increase in fluence as the calcium reacts with water, causing the layer to thin; and (3) **Saturation Region**, where full calcium depletion results in a plateau in intensity and fluence, leaving only the bare copper layer visible. The plot includes representative image locations on the fluence graph and an example calculation for Image 53, estimating the fluence and determining a WVTR of 1.25 ± 0.031 g/cm²·day for this sample.*

2.4.6.b Edge Effects / Non-Uniformity Calcium Depletion

As previously discussed and evident in the images and surface plots (Figure 2-7), calcium depletion is uneven, with the edges showing premature depletion compared to the central region. To address this, a varying ROI is applied to account for potential permeation through the epoxy or other unaccounted factors contributing to edge depletion. A slight caveat, the observed non-uniform calcium depletion may not solely

result from edge permeation but could also be influenced by factors such as substrate irregularities, including micro-scale thickness variations.

Nonetheless, to address the potential contribution of edge permeation, the ROI is adjusted to focus on regions with visible calcium, as illustrated in Figure 2-10. Fluence values are then calculated for these adjusted ROIs, compensating for possible edge effects. The transition region images highlight this approach, showing outlined ROIs with progressively decreasing areas, yet increasing normalised intensity values, emphasising the continued reaction dynamics despite the reduced ROI size resulting in a WVTR of 1.13 ± 0.0914 g/cm^2·day.

Accounting for this adjustment slightly decreases the estimated WVTR value; however, the change is not significant enough to justify meticulous ROI selection for all samples. Using a constant area or the entire region still provides a reasonable and reliable WVTR estimate while minor differences are observed, they do not substantially impact the results, as the majority of water vapor permeation still occurs through the polymer layer or substrate, rather than edge effects. For uncoated substrates this small difference and overestimation in WVTR values are not as significant but for coated barrier layers as shown which do account for the edge permeation it is more relevant and important.

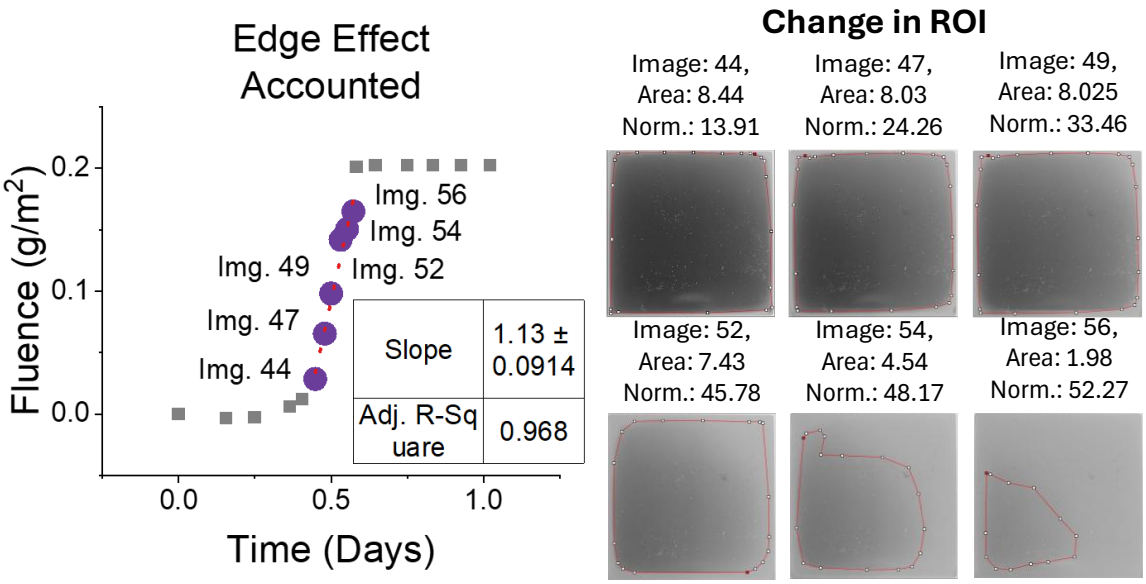


Figure 2-10: Fluence-over-time plot for an uncoated PET substrate at 14.5 ± 2.5°C in LiCl (RH ≈ 65%) with varying ROI to account for potential edge permeation. Transition region images illustrate the compensations of possible edge effects made, showing decreasing ROI area but increasing normalised mean grey values. A slight decrease in WVTR is observed, with an estimated value of 1.13 ± 0.0914 g/cm²·day.

2.4.7 Permeability and Activation Energy

The calculation of permeability, introduced in Equation 1-6, is given by the product of WVTR and film thickness, divided by the water vapor partial pressure difference. In the calcium test, it is assumed that the partial pressure of water vapor on the P1 side (calcium and copper) is negligible, as the sample is fully encapsulated in glass and epoxy. This encapsulation prevents any significant water vapor presence on the P_1 side, as water vapor permeating through the barrier reacts with the calcium. Consequently, the driving force for diffusion is the water vapor partial pressure difference across the film, not a difference in overall pressure, as both sides are maintained at the same atmospheric pressure during the test. The pressure difference is thus determined by P_2, the water vapor saturation pressure at the specified temperature,

adjusted for the relative humidity. For the calcium test, permeability (Equation 2-3) can be expressed as WVTR multiplied by thickness (l) divided by the vapor saturation pressure (P_{*H_2O}) and relatively humidity ($\emptyset$)

$$P_{Ca\ Test} = \frac{WVTR\ \cdot\ l}{(P_2 - P_1)} = \frac{WVTR\ \cdot\ l}{\emptyset \cdot P_{*H_2O}} \qquad \textit{Equation 2-3}$$

To calculate activation energy, a temperature profile is developed using Equation 1-8, based on the Arrhenius equation. This is achieved by measuring the WVTR of a barrier layer at different temperatures while maintaining constant relative humidity. The relationship is expected to follow Arrhenius behaviour, with a linear trend when plotting the natural log of WVTR against the inverse of the absolute temperature (Kelvin).

Table 2-8: Activation Energy of Permeation

Step	Concept / Explanation	Key Equation
Arrhenius Relationship	The diffusion coefficient D follows an Arrhenius relationship with temperature. This relationship describes how the diffusivity changes with temperature, with E_a as the activation energy, R as the gas constant, and T as temperature.	$D = D_o \cdot \exp\left(-\frac{Ea}{RT}\right)$
WVTR Arrhenius Equation	The WVTR is generally modelled with the Arrhenius equation form, where A is a pre-exponential factor incorporating constants such as the solubility coefficient (S), film thickness and pressure difference, all assumed to be temperature independent over the range studied.	$WVTR = A \cdot \exp\left(-\frac{Ea}{RT}\right)$
Logarithmic Form	Taking the natural log of both sides of the equation simplifies the expression and allows linearization for plotting. This helps determine the activation energy from experimental data.	$\ln(WVTR) = -\frac{Ea}{RT} \cdot \frac{1}{T} + constant$
Linear Regression	By plotting ln(WVTR) against $\frac{1}{T}$, the slope (m) of the line provides a way to calculate the Ea.	$m = -\frac{Ea}{1000\ \cdot T}$

Activation Energy Calculation	The activation energy Ea can be determined by multiplying the slope of the line by the gas constant (8.314 KJ/mol)	$Ea = -m \cdot R(\frac{KJ}{mol})$

2.4.8 Normalizing the Images

2.4.8.a Image to Image Variations

Image-to-image variations in the calcium test are significantly influenced by external factors such as lighting, camera settings (aperture, shutter speed, ISO), and the position, location, or angle of the camera as shown in Figure 2-11. These factors can affect image brightness and overall contrast, leading to inconsistencies. To minimize these effects and reduce error, this section outlines the optimized camera settings used throughout the study. In addition, a calibration strip was included in each image to provide a reference point for post-processing normalization, helping to further correct for any remaining variations between images.

The optimal settings found were ISO 100 (light sensitivity), shutter speed 1/125 (exposure time), and aperture F3.5 (light entry), which provided the best contrast and brightness for consistent image quality (further additions are discussed in 9.1.3 Miscellaneous Improvements).

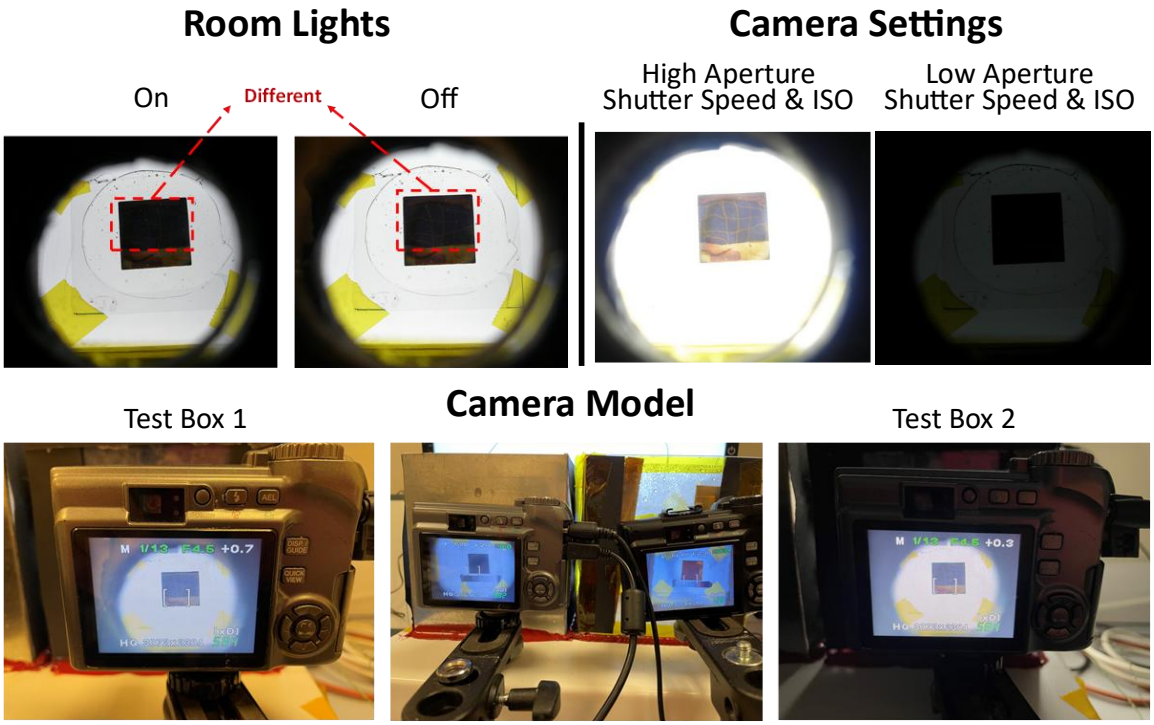


Figure 2-11: Effect of room lights (top-left), the camera settings (top-right) and the camera itself or position of it (bottom) towards the overall image captured.

2.5 ALD Parameters

The primary coating method in this study was Atomic Layer Deposition (using a Veeco Savannah S200 ALD at the Denys Wilkinson Building Clean Room – Physics Department of the University of Oxford) depositing Aluminium Oxide (AlO_x).

The AlOx was grown using Triethylaluminium (TMA) and water (H_2O) precursor to grow various thickness ranging from 6.3 nm to around 100 nm (some samples were consequentially grown / or left inside the ALD machine after one specific run accumulating thicker layers reaching up to 450 nm).

The recipe, as shown in Figure 2-12 (a) with images of the ALD set-up, TMA Bottle and Valve Manifold (with uncoated PET films and Silicon chips), that was chosen was previously optimized to grow at around 0.91 Å/cycle at 150°C with a valve manifold

temperature, and outer / inner ring at 80°C, exhaust line and trap line at 150°C, TMA bottle heated at 60°C, The system operated under a constant pressure nitrogen gas flow of 20 sccm and an overall operating chamber pressure of around ~300 mTorr (~40.0 Pa), with no substrate bias applied. The pulse and purge times remained fixed across all runs to maintain consistency rather than being dynamically adjusted for specific substrate loadings. As known these factors are important such that the growth rate for an ALD process is temperature and pressure dependent and changes in these settings will affect the total amount AlO_x deposited per cycle [175, 176].

It is also important to distinguish the stoichiometry of these films from those typically produced by PVD / typical sputtered alumina coatings (AlO_x) from the ALD coatings produced in this work. As in reactive PVD, the oxygen flow and the state of the sputter target can drift during deposition, so aluminium oxide films often end up sub or over stoichiometric AlO_x rather than the exact Al_2O_3 and related oxides [198]. In contrast the self-limiting surface chemistry of ALD inherently drives the film toward a stoichiometric Al_2O_3 ratio (Al:O ≈ 0.66 or O:Al ≈ 1.5) [33]. However, given the low-temperature regime used in this study, the films are expected to deviate from pure crystalline alumina by retaining structural amorphicity and chemical hydration; thus it cannot be reasonably assumed that without verification that AlO_x was deposited and not necessarily Al_2O_3.

To conclusively verify the stoichiometry and differentiate the film from non-stoichiometric AlO_x, a characterization workflow involving X-ray Photoelectron Spectroscopy (XPS) and Rutherford Backscattering Spectrometry (RBS) would be required. In an XPS analysis, the primary indicator of phase purity is the O:Al atomic

ratio, for hydrated low temperature ALD, this ratio should exceed the ideal 1.5 (often ~1.6 to 1.8), signalling the presence of excess oxygen associated with incorporated hydroxyl groups [215]. This can be also structurally identified by the deconvolution of the O – 1s spectrum, where the primary lattice oxide peak (Al – O – Al, ~531.1 eV) is distinguishable from a secondary shoulder at a higher binding energy (~532.4 eV) corresponding to the Al-OH species [216]. Furthermore, complementary analysis via RBS would measure the absolute elemental areal density (atoms/cm^2) [215, 217]. Finally, Elastic Recoil Detection Analysis (ERDA) would be necessary to directly quantify the hydrogen content (at. %), which is invisible to standard XPS and RBS, providing a definitive profile of the films hydration level [215].

Going back to what influences the growth rate, the processing temperature and reactor pressure also fundamentally dictate the microstructural quality and defect landscape of the AlO_x barrier.

Deposition temperature governs the completeness of surface half-reactions and controls the overall coating quality. As established by Groner *et al*, lower deposition (*e.g.*, 80°) results in incomplete removal of methyl ligands and hydroxyl groups. This also leads to films with lower mass density (approximately 2.5 g/cm^3 versus 3.0 g/cm^3 at 177°C), and higher concentrations of residual impurities (H, C, OH) [217]. In line with this Carcia et.al shows that these chemical defects increase the intrinsic free volume of the bulk oxide which in turn makes it more water permeable [218]. On the other hand higher temperatures generally yield denser, stoichiometrically purer films, the increased temperature can introduce thermal stress upon cooling; this mismatch in thermal expansion coefficients between the ceramic coating and polymer substrate as noted by

Leterrier *et al*, can induce substantial stress can potentially lead to mechanical instability or delamination [219, 220]. This all again leads to uncertainty on the possible of Al_2O_3 coating.

The reactor pressure and purge dynamics of the system are equally crucial for macroscopic defect control. Literature shows that insufficient purging or excessive pressure can lead to the overlap of precursor pulses in the gas phase. This triggers a parasitic like CVD reaction, generating gas phase particulates that deposit onto the substrate as dust which then creates pinholes and macro defects [33].

In this specific study, a batch process was employed using a standard recipe (shown in Figure 2-12 (b)) provided for the shared reactor configuration, rather than a process individually optimized for each substrate. Although the 30 second purge aimed to remove excess precursors, non-optimal purging in this configuration can inadvertently trigger such gas phase CVD-like parasitic reactions. Furthermore as the equipment was a shared resource, the condition of the reactor walls and chamber history varied between runs. This introduced uncertainty regarding reproducibility; despite using silicon witness samples to verify film thickness for every batch, uncontrolled variables like wall conditioning or environmental contamination remain potential factors in the observed scatter of barrier performance. To mitigate this variability, at least three independent deposition batches were prepared for each condition, with representative samples selected for WVTR testing.

Moreover, other work by Parsons *et al.* highlights how on certain polymer substrates insufficient precursor partial pressure during the pulse step can lead to delayed nucleation and island growth, resulting in incomplete coverage rather than the expected

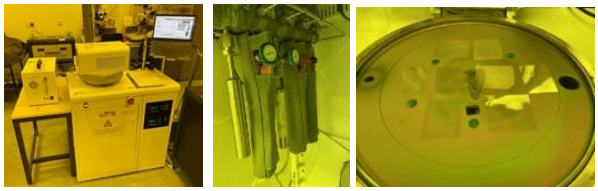
conformal and continuous coating on the film; making the overall process window for ALD a need to balance kinetic energy for densification against thermal stress limits, and precursor saturation against potential gas phase reaction risks [221].

As seen below in Figure 2-12 (b) the recipe used shows that water (H_2O) is first pulsed for 0.15 seconds and then allowed to settle until TMA is then pulsed also for 0.15 seconds and allowed to reset for another cycle. The appropriate number of cycles were then done to achieve the desired thickness.

An important observation as done later, was that in growing the PVAl films, further explained in Chapter 5: Aluminium Oxide (ALD) Coated PVAl. Setting the valve manifold temperature at 150 °C degrades the PVAl such that its “yellows” and shrinks as shown in the Figure 2-12 (c). If valve manifold temperature is lowered to 80 °C (lowest practical temperature to grow TMA with the previous parameters), which is just around the glass transition range of PVAl at 75 to 85°C [177], ALD AlO_x could be grown onto the PVAl films without any visible damage.

(a) Veeco Savannah S200

ALD Set-up | TMA Bottle | Valve Manifold (w/ PET)



Part	Parameter
Valve Manifold	Temp: 150°C - PET / 80°C - PVA
Outer / Inner Ring	Temp: 80°C
Exhaust / Trap Line	Temp: 150°C
TMA Bottle	Temp: 60°C
Nitrogen	Flow: 20 sccm
Chamber Pressure	300 mTorr / 40.0 Pa

(b) Recipe

Instruction	Time(s)
Pulse H2O	0.15
Wait	30
Pulse TMA	0.15
Wait	30

(c) PVA Samples

Manifold 150°C | Manifold 80°C

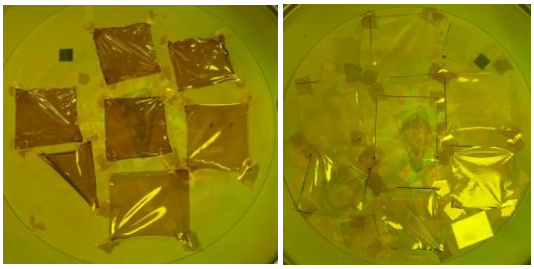


Figure 2-12: (a) Veeco Savannah S200 ALD setup, showing the TMA bottles and PET sheets inside the ALD chamber placed on the valve manifold; below are the processing parameters for PET deposition. (b) Recipe: water is pulsed for 0.15s, followed by a 30s chamber evacuation before pulsing TMA for 0.15s, allowing the reaction and purging before the next cycle. (c) PVA samples processed at 150°C exhibit significant degradation, while those processed at 80°C retain film clarity with no visible damage.

2.6 Surface Characterization Tools

The surface roughness and morphology were examined to relate the surface of the substrate to the coating quality of the ALD layers, and its corresponding effect on the water vapour barrier properties.

The primary surface characterization tools used in this study included a combination of microscopy and profilometry techniques. Light microscopy was conducted using a Yenway ISH500 (Nano Materials by Design Group). For Scanning Electron Microscopy (SEM), two systems were employed: (1) the JEOL 6500 F (Oxford Materials Characterisation Service, imaged by Dr. Zhonghua Ren) and (2) the Zeiss

Merlin (David Cockayne Centre for Electron Microscopy, imaged by Tongshan Liu and Dr. Shiling Dong), where polymer film samples were coated with a 6 nm platinum (Pt) layer using either a Cressington Sputter Coater 208HR or Leica ACE 600 Coater.

Meanwhile, surface profilometry involved Atomic Force Microscopy (AFM) with an Agilent 5400 AFM (assisted by Nicola Flanagan and Dr. Kai Ling Ng), and 3D Optical Profiling using a Filmetrics system (assisted by Dr. Chris Salter, Yixin Xu, and Xiaohang Cai). As presented, to correct for substrate buckling and bending artefacts in large field-of-view images, particularly in ALD-coated PET samples, a band-pass FFT filter was applied. This filter removed low-frequency distortions related to large scale background variations while preserving mid-to-high-frequency structural details relevant to defect analysis. The filter had a low cutoff of ~28 μm, and a high cutoff of ~14 μm, effectively eliminating spatial frequencies associated with global warping. Additionally, a gaussian filter was applied to prevent sharp frequency cutoffs, minimizing potential artefacts.

3 Uncoated Polyethylene Terephthalate (PET) Substrates

3.1 Introduction to Uncoated PET Substrates

Understanding the permeation properties of Polyethylene Terephthalate (PET) is critical, as the substrate forms the structural foundation for barrier coatings. The effectiveness of these coatings, and the overall functionality of the barrier layer, is strongly influenced by the substrate's surface properties, composition, and uniformity, which determine its suitability for flexible electronics and encapsulated systems.

Measuring the water vapor permeation of uncoated PET is essential for understanding the substrate's intrinsic properties, independent of barrier layers, establishes a baseline to examine the effects of permeation mechanisms, such as water molecule diffusion through the polymer matrix and surface adsorption and desorption, influenced by temperature, humidity, and material structure. Determining the activation energy for permeation provides deeper insight into the processes governing PET's permeability and its behaviour under varying conditions; (further supported by MOCON Aquatran 2 results).

The Ca test is crucial in this context, providing sensitive and precise real-time measurements of WVTR. Applying this method to uncoated PET not only validates the reliability of the test but also identifies potential limitations, such as edge effects or substrate non-uniformity, that may impact measurement accuracy. This evaluation ensures methodological validity and strengthens the robustness of future testing protocols.

In summary, measuring the permeation of uncoated PET is not only crucial for understanding its intrinsic properties but also for validating methodologies, determining activation energy, and improving the reliability of coated barrier layer systems

3.2 Properties and Performance of PET Films

PET, a common substrate for thin film applications, is primarily synthesized through the polycondensation of purified terephthalic acid (PTA) or esterification of dimethyl terephthalate (DMT) with ethylene glycol [222-224], as shown in Figure 3-1. PET can be extruded and drawn into biaxially oriented semi-crystalline films, offering ideal properties for flexible electronics and barrier layers. These include high tensile strength (PET: 2-2.7 GPa; Biaxial PET: 5.3 GPa), ease of manufacturing, low density, chemical and thermal stability (stable up to 150-180°C, CTE: 20-80 ppm/K, Tg: 60-70°C), cost-effectiveness, optical clarity, dielectric performance, and recyclability [225-232]. As a non-crosslinked polymer, PET exhibits creep under stress, affecting its appearance and longevity [233, 234].

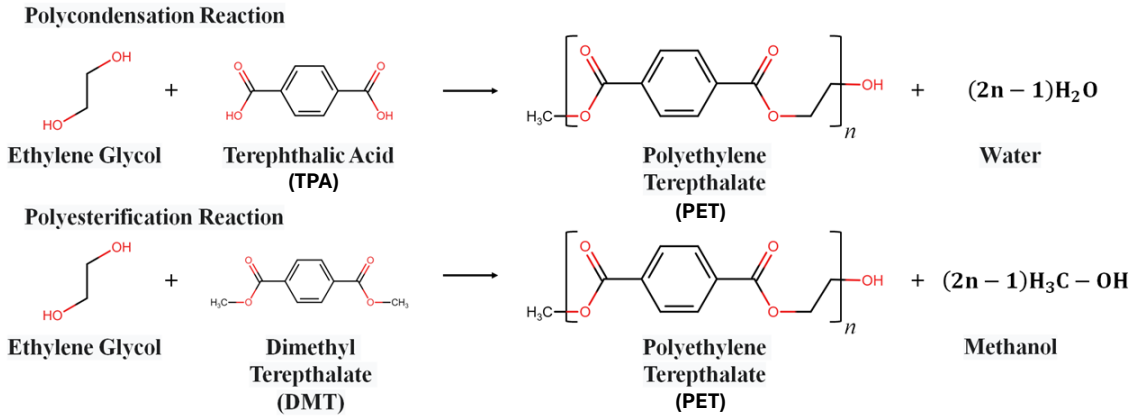


Figure 3-1: Chemical of the Two common ways to produce Polyethylene Terephthalate: (1) Polycondensation using: Terephthalic Acid and (2) Poly esterification using: Dimethyl Terephthalate, respectively with Ethylene Glycol.

Uncoated PET is hydrophobic, with a water contact angle of 60-80° and low water absorption (0.5% at saturation) [225, 235-237]. It absorbs moisture slowly, requiring about 12 hours at 20°C and 40% humidity to reach 1000 ppm [225, 226, 232]. The inherent surface roughness of biaxially oriented semicrystalline PET films is <1 nm [226]. This surface roughness is primarily attributed to thermally induced capillary waves, (well-documented for polymer surfaces) but are influenced by substrate interactions and film thickness limitations [238], biaxial strength and heat setting also enhances crystallinity and smoothness, though the degree of improvement depends on precise control of processing conditions, including temperature and strain [239]. Moreover, interfacial irregularities are sensitive to environmental factors such as humidity and processing treatments like plasma [240].

Commercial PET films, affected by internal cleanliness, additives, and processing-related imperfections (*e.g.*, contamination, inclusions or structural irregularities), can often exhibit practical roughness between 10-100 μm.

Peaks in the surface can reduce the performance of multilayer structures, though intentional roughening can enhance adhesion for coatings and prevent film-to-film adhesion during rolling.

The PET substrate used in this study, provided by DuPont Teijin Films, was a 100 μm thick biaxially oriented polyethylene terephthalate (BOPET) film (specifically Melinex® PCS) – featuring a 25 μm protective peel layer removed immediately before coating to ensure a clean surface for oxide and barrier layer deposition [226, 231, 241]. This substrate is identified as a thermoplastic semi-crystalline polymer, where the biaxial orientation process locks polymer chains into specific lattice structure to enhance thermal

and mechanical performance. In terms of surface quality, the protective peel layer is a co-extruded sacrificial skin designed to minimize surface contamination without the use of adhesives that might otherwise leave residue upon removal. Experimental characterization of the surface topography via AFM and optical profilometry was performed in this work (4.9.1 Film Characterization of Uncoated PET) confirming a low surface roughness consistent with high grade substrates. Similarly technical literature provides further insight into the film's engineered structure. The standard industrial grade of PET films typically exhibit high surface defect densities due to protruding anti-block agents (> 10 peaks > 100 nm per 2.5 nm^2). In contrast, the optical grade or surface tailored films used here are engineered to sequester and reduce these particles, resulting in a substantial reduction of surface peaks to negligible levels (<5 peaks > 50 nm per 2.5 mm^2). Consequently, the substrate was used in its as-received condition immediately following the removal of the protective peel layer with no additional chemical pre-treatment or planarization applied [242-244].

An important caveat, is that despite the use of an optical grade film, substrate-induced variability remains a critical factor in barrier performance. Surface characterization of the PET substrates (Type Mylar, DuPont Teijin Films) used in this study confirmed the presence of these topographical features, including residual anti-block particles (silica or zeolite additives used to prevent film sticking) and microscopic scratches generated during the removal of the protective peel layer. While these features are stochastically distributed and maintain a relatively low overall surface density making precise statistical quantification challenging, but qualitatively evident across the sampled areas [245]. As established by Hanika *et al.* and Yan *et al.*, these micron scale

topographical features can cause geometric shadowing effects during deposition, leading to local discontinuities or non-conformal growth in the barrier layer. Consequently, the random probability of such a defect occurring within the active test area introduces intrinsic sample to sample variability in the measured WVTR, contribute to further experimental scatter in the observed study as seen in 4.8 Influence of Spots and Defect Sizes to AlO_x Barrier Properties [28, 201]

However, due to its low surface free energy, PET faces challenges with wettability, adhesion, and printability, often requiring surface modifications like plasma or heat treatment for better material deposition [233].

Table 3-1 highlights the significant variability in WVTR values for uncoated PET substrates reported in the literature. These variations are influenced by testing methods, temperature, relative humidity, and, most notably, film thickness.

Thickness was identified as the primary factor affecting WVTR, with grouping based on thickness providing clearer insights. For reference, ASTM F1249 reports WVTR values of 4.81 ± 0.212 g/m²·day for 127 µm PET and 26.05 g/m²·day for 25 µm PET at 23°C and 50% RH [190].

As illustrated in Figure 3-2, WVTR decreases significantly with increasing film thickness across all uncoated PET substrates. Temperature and relative humidity also play important roles but have a less pronounced effect compared to thickness. This trend can be normalized and analysed further, as shown in the subsequent sections (3.6 Permeation Analysis of Uncoated PET Films) and permeation calculations in Figure 3-14.

Castro-Hermosa *et al.* report a WVTR of 2.9 g/m^2·day for uncoated PET, measured using the British Standard BS3177 method at 38°C/90% RH. In contrast, using an optical calcium test at 25°C/35% RH for heat-stabilized PET (175 µm thickness), a much higher WVTR of 75 ± 25 g/m²·day was observed. Notably, the electrical calcium test for the same material under similar conditions yielded a significantly lower WVTR of (4.4 ± 0.2) × 10^{-1} g/m²·day, highlighting substantial discrepancies between the testing methods [46].

Table 3-1: WVTR of Uncoated PET Films / Substrates

Film Thickness Category	Specific Thicknesses (µm)	Temperature Range (°C)	Relative Humidity Range (%)	WVTR Range (g/m²·day)	Source(s)
Ultrathin PET Films (≤20 µm)	12, 13, 19	9.5–85	47–100	0.55–90.7	Esguerra [246], Murray[247], Deng[93], Burst [248], Piergiovanni [249], Sobrinho [250]
Thin PET Films (20–50 µm)	24–125, 30, 50	25–45	36–100	0.63–11.54	Schubert[110], Ascione [251], BM Henry [252, 253], Erlat [14, 254], Mahmood [255], Hanada [256], Saitoh [257]
Medium PET Films (75–130 µm)	75, 100, 127, 130	15–68	47.5–100	0.5–10.5	Nehm [258], Fahlteich [25], Abbas[259], Jarvis [230, 260], Barber (NREL) [261], Chen [94, 262, 263]

Thick PET Films (150–200 µm)	175, 179, 188, 190	23–40	85–100	2.9–16	Kiese [264], Qin [265], Wuu [266], Low [267], Mariello[268]
Variable Thickness PET Films	52, 193, 252	23–80	100	0.03–90.0	Hulsmann [269]

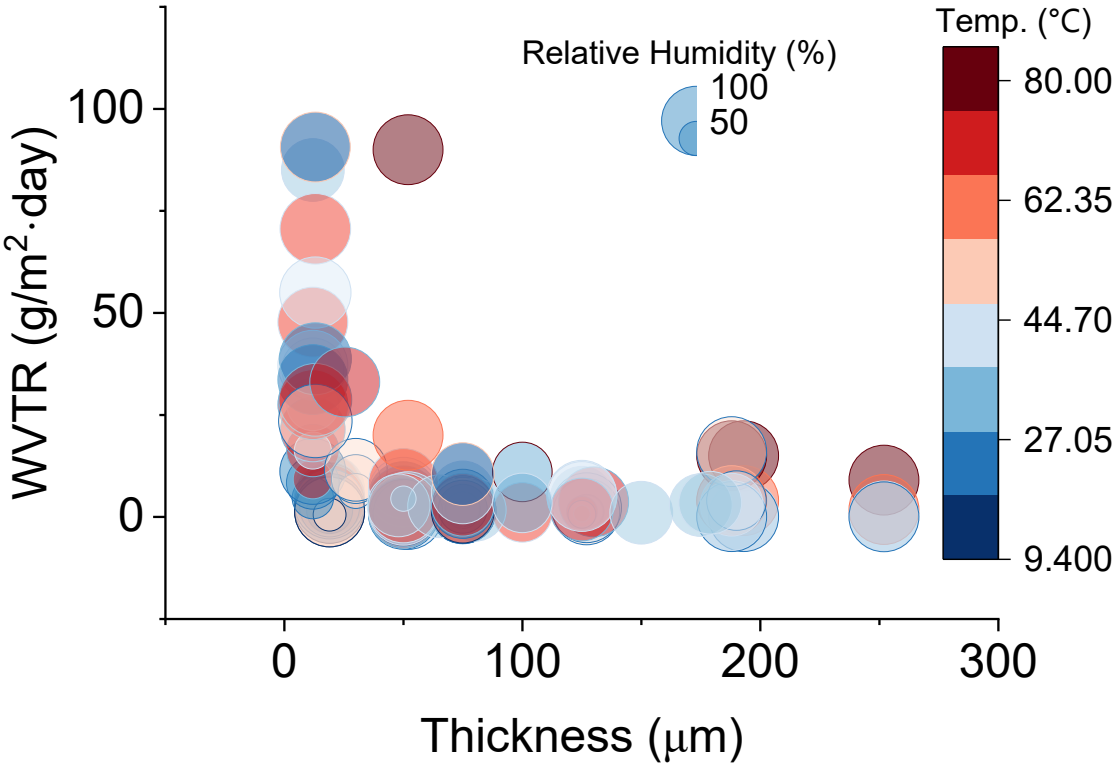


Figure 3-2: WVTR as a function of film thickness for uncoated PET substrates from various literature sources. The figure highlights the influence of increasing thickness on WVTR, with variations in relative humidity and temperature depicted as bubble colour and size, respectively [14, 25, 93, 230, 246-252, 254-257, 259-262, 264-270].

3.3 WVTR Measurements for Uncoated PET Films (MOCON)

3.3.1 Preparation of PET Film Samples for MOCON Testing

Uncoated PET films were tested using a MOCON Aquatran 2 to determine the WVTR of the base substrates, helping to clarify the permeation mechanisms in coated

samples. Tests were conducted at three temperatures (14°C, 25°C, and 38°C) with relative humidities from 35% to 100% in 5% increments, controlled by nitrogen pressure and monitored by sensors. WVTR values ranged from 2.18 ± 0.02 g/m²·day (14°C, 35% RH) to 26.66 ± 1.03 g/m²·day (38°C, 100% RH), which is relatively high for the Aquatran 2, optimized for high-barrier films. A 1 cm² mask was used to adjust for the test area, allowing for more accurate WVTR calculation, as the smaller permeable area reduces the overall measured value. Aluminium foil masks protect the phosphorus pentoxide (P_2O_5) sensors used in the Aquatran system, to not overload the detection and lead to overall equipment damage or failure.

3.3.2 MOCON Temperature and Relative Humidity on Uncoated PET

Figure 3-3 illustrates the effect of temperature (Figure 3-3, a) and relative humidity (RH) (Figure 3-3, b) on the WVTR of single-layer PET. WVTR increases with both temperature and humidity, a phenomenon observed since William Henry's work on gases and water [89]. However, the material itself largely determines WVTR, with factors like molecular structure or coatings playing a key role [271]. The rise in WVTR with temperature is attributed to increased polymer chain mobility and the higher energy of water vapor molecules [272, 273].

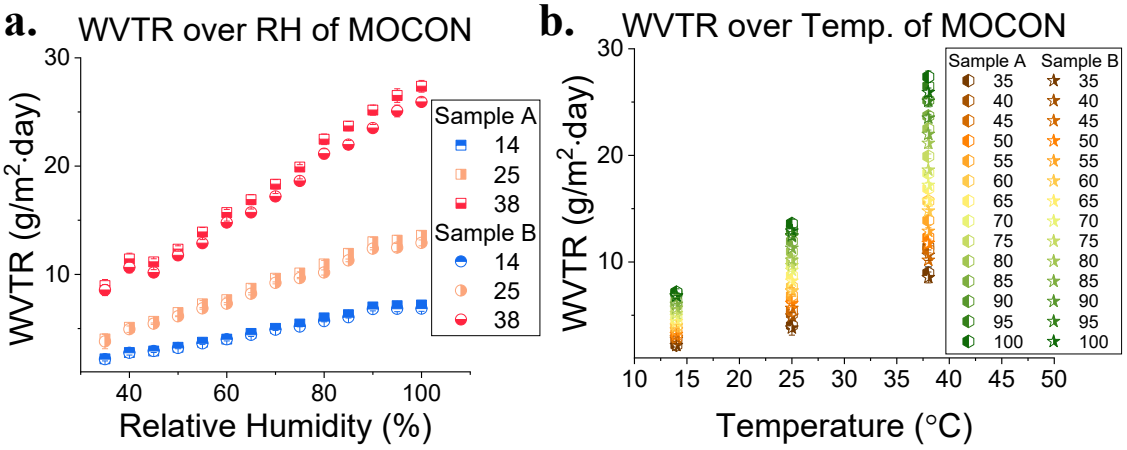


Figure 3-3: WVTR measurements of two uncoated PET samples (masked to 1 cm² area) using a MOCON Aquatran 2 system. (a) WVTR as a function of RH at three distinct temperatures (14°C, 25°C, and 38°C), showing WVTR increases with RH and temperature. (b) WVTR as a function of temperature across RH levels (35–100%), illustrating heightened sensitivity of WVTR to temperature at higher RH. These results underscore the significant and interconnected effects of temperature and RH on PET permeability within its glassy state.

The relationship between WVTR, temperature, and RH is complex and material specific. While WVTR generally increases with temperature due to enhanced molecular mobility and diffusivity of water vapor, the nature of this increase varies across polymers. Hydrophobic polymers such as polypropylene (PP) and polyethylene (PE) exhibit stable WVTR due to their low water affinity. In contrast, hydrophilic polymers like polyvinyl alcohol (PVAl), nylon, and ethylene-vinyl alcohol (EVOH) experience sharp WVTR increases at high RH. These increases result from water-induced plasticisation and swelling, which disrupt the polymer matrix and increase molecular free volume. PVAl can exhibit up to a five to ten-fold WVTR rise under high RH, while nylon and EVOH display nonlinear responses due to water sorption and crystallinity loss, respectively. The magnitude of these effects depends on polymer polarity, crystallinity, and molecular structure [94, 271, 274, 275].

Water vapor diffusion through PET follows Fickian behaviour, with the diffusion coefficient rising with temperature, as noted by Launay *et al.* [234], PET's activation energy shifts depending on whether it is in its glassy (42 KJ/mol) or rubbery (36 KJ/mol) state. Interactions between water and the polymer can also create micro-voids, affecting material properties [276].

To rigorously evaluate the influence of environmental conditions on the WVTR of PET films, a two-way Analysis of Variance (ANOVA) was performed on the 9.5 MOCON Aquatran Data Set for Uncoated PET. This statistical method tests whether temperature, RH or their interactions significantly affect WVTR. It does so by comparing the variability between groups to the variability within groups. A p-value below 0.05 indicates a statistically significant effect, meaning the observed differences in WVTR are unlikely due to random variation. In this context, small p-values confirm that both temperature and RH have meaningful and independent effects on WVTR.

As explained, the resulting P-values quantify the likelihood of observing the measured differences, or larger ones, under the null hypothesis that no true effect exists.

The analysis of the Uncoated PET MOCON Aquatran data set indicates that temperature ($P = 2.41\times10^{-11}$), RH ($P = 2.06\times10^{-12}$), and their interaction ($P = 2.41\times10^{-11}$) all significantly affect WVTR. These extremely low p-values (well below 0.05) indicate the very likelihood that these factors, are not random chance, and are driving the changes in WVTR. This underscores the importance of controlling and reporting environmental conditions during testing to ensure reliable and comparable results.

In Figure 3-3 within the experimental range (14–38°C and 35–100% RH), WVTR increases with both temperature and RH. Although a visual trend of increasing WVTR with temperature can be observed in Figure 3-3b.

To more rigorously assess the temperature dependence, Figure 3-4 presents the Arrhenius plots of ln (WVTR) versus 1000/T, which demonstrate a clear linear relationship consistent with Arrhenius type behaviour. From these slopes Ea was calculated and found to be relatively stable across RH levels, indicating that the temperature dependence of WVTR in PET follows thermally activated diffusion processes, even below glass transition temperature (Tg).

These measurements are taken below PET's Tg which typically ranges from 69–85°C (depending on crystallinity) and well below its melting temperature (Tm) of 250–260°C [277-280]. At these temperatures molecular mobility is restricted in the glassy state, suppressing large-scale segmental motion, however, water diffusion in this regime remains a thermally activated process. As shown in Figure 3-4, the relationship between ln(WVTR) and 1000/T follows an Arrhenius-type behaviour. This indicates that water molecules overcome localized energy barriers by "pushing past" polymer chains, consistent with Ea models. The observed linearity in the Arrhenius plot validates this mechanism.

While PET is generally hydrophobic, its ester groups exhibit mild hygroscopicity, enabling limited water absorption at higher RH. This absorbed water can act as a plasticizer, increasing chain flexibility and creating transient diffusion pathways, reflected in the higher absolute WVTR measured at elevated RH (Figure 3-3b). The larger baseline amplifies the absolute change with temperature, the Ea (and intrinsic

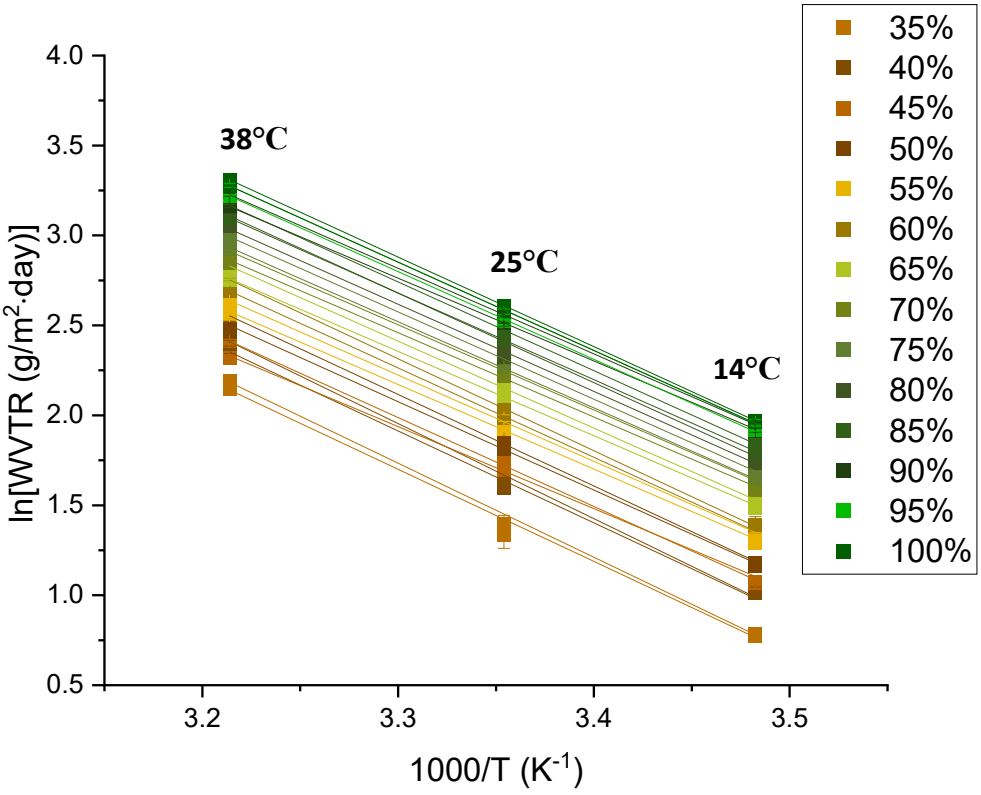
temperature sensitivity) should remain unchanged. However, the primary driver of WVTR at higher RH is the increased concentration gradient of water vapor across the film. The interplay between plasticization (affecting polymer dynamics) and the thermodynamic driving force (concentration gradient) underscores the need to consider both RH and temperature in permeability analysis.

3.3.3 Determination of the Ea of Uncoated PET Substrate (MOCON)

As discussed in the previous section (2.4.7 Permeability and Activation Energy); the activation energy, calculated from the product of the slope of the Arrhenius plot (ln(WVTR) vs. 1000/T) and the gas constant ($R = 8.314\ J \cdot K^{-1} \cdot mol^{-1}$), provides a baseline for analysing permeation mechanisms in uncoated and coated PET films.

Figure 3-4 presents the MOCON Aquatran data (Figure 3-3) as log WVTR vs. 1000/T across different relative humidities, showing a negative slope and decreasing WVTR with lower humidity. Notably, activation energy remains consistent across relative humidities, ranging from 36.55 to 46.78 KJ/mol, with an average of 41.19 KJ/mol.

This range aligns with reported values for PET below its glass transition temperature: 42 KJ/mol (250 µm thickness, Rhône-Poulenc) [234], 36.1 KJ/mol (Mitsubishi Plastics) [281], 43.51 KJ/mol (DuPont Mylar A) [282], and 36 to 40.4 KJ/mol (various thicknesses) [269, 283] or 41.5 ± 5 (12 µm) [253]. Slight variations in activation energy are attributed to factors like polymer grade, crystallinity, and test methods.



RH (%)	35	40	45	50	55	60	65	70	75	80	85	90	95	100
ΔE (KJ/mol)	43.5 ± 1.37	42.6 ± 1.48	44.0 ± 2.78	42.4 ± 2.19	41.1 ± 0.69	37.9 ± 1.35	42.2 ± 1.85	40.9 ± 1.53	39.9 ± 1.38	39.2 ± 1.62	42.4 ± 0.21	41.3 ± 0.84	39.0 ± 0.60	40.2 ± 0.79

Figure 3-4: Arrhenius plot of ln(WVTR) [g·m⁻²·day⁻¹] vs. 1000/T [K⁻¹] for uncoated PET substrates at RH levels from 35% to 100% and temperatures of 14°C, 25°C, and 38°C. Each series exhibits a negative slope, as expected, reflecting the Arrhenius-type dependence of WVTR on temperature. Multiplying this slope by R (8.314 J·K⁻¹·mol⁻¹) yields the activation energy (Ea) in KJ/mol. Although Ea appears largely independent of RH within this range, it is important to note that increasing temperature at a given RH raises the absolute partial pressure of water vapour, influencing the permeation driving force. Below the graph, a table presents the average activation energy for both tested samples at each RH.

In short, WVTR, in polymers like PET increase with temperature as shown in the Arrhenius type relationship, attributed to enhanced molecular mobility and reduced

polymer density [284, 285]. Higher RH elevates the partial pressure of water vapour, increasing the driving force for diffusion [286] and, in some cases can result in polymer swelling, creating additional free volume for permeation [287]. However, the Ea, an intrinsic property of the polymer, remains relatively constant across RH levels, as shown in Figure 3-4, suggesting that RH primarily influences WVTR by enhancing the thermodynamic driving force for permeation rather than significantly altering the diffusion energy barrier or path. While some literature suggests that polymer hydration may affect chain flexiblilty or free volume, such effects are not clearly reflected in the Ea trends observed in this study.

3.4 Calcium Test: Uncoated PET film Substrate

3.4.1 Transition Time and WVTR Determination for Uncoated PET

Using the same PET material, several calcium (Ca) tests were conducted under different temperatures and humidity levels. Due to the high permeability of the uncoated PET, the "Poor Barrier" setup was applied.

3.4.1.a Transition Region, and Fluence at Saturation

As explained in section 2.4.5.a, WVTR Calcium Test Estimation involves assessing the transition region, which refers to the interval between the onset of detectable permeation and full saturation (complete calcium depletion). Calculating the transition time allows for the optimisation of imaging intervals, ensuring proper observation of calcium depletion to obtain the WVTR. By understanding how quickly the calcium layer transitions from black to white (or depletes), one can set up appropriate

image capture intervals, avoiding unnecessarily high-frequency imaging or missing the critical period of change.

The saturation point, where the fluence (the cumulative mass of permeant per unit area) reaches 0.2 g/m², indicates that all the calcium has been depleted. This point serves as a practical stopping point for the estimation. Permeation continues beyond this point, it provides a standardised reference for measurement times, ensuring consistency when comparing samples.

While it neglects the initial time lag for establishing the concentration gradient, dividing the saturation point fluence (0.2 g/m²) by the WVTR (g/m² per day) offers a straightforward estimate of the subsequent time required for the system to reach a near saturated permeation state. This approach allows an appropriate number of images to be taken and analysed for a good measure of WVTR.

3.4.2 Example Calculation and Environmental Influence

As an example, (Figure 3-5) consider an uncoated PET sample tested at 31.5°C and 54% RH, with a WVTR of approximately 3.92 g/m²·day, the transition time to reach a fluence of 0.2 g/m² is about 0.05 days (~73 minutes). Based on uncoated PET WVTR values (Min: 2.18 ± 0.02 g/m²·day at 14°C, 35% RH; Max: 26.66 ± 1.03 g/m²·day at 38°C, 100% RH), the transition time can range from range from 10.8 to 132.1 minutes.

Using the MOCON-measured WVTR values directly, one can also tailor this calculation. At lower temperatures and RH (*e.g.*, 14°C, 35% RH with a WVTR of ~2.18 g/m²·day), the transition time extends to over two hours, whereas at higher temperatures and RH (*e.g.*, 38°C, 100% RH with a WVTR of ~26.66 g/m²·day), it can be under 11

minutes. Minor changes in environmental conditions can also dramatically influence how frequently one should capture images to monitor the transition effectively.

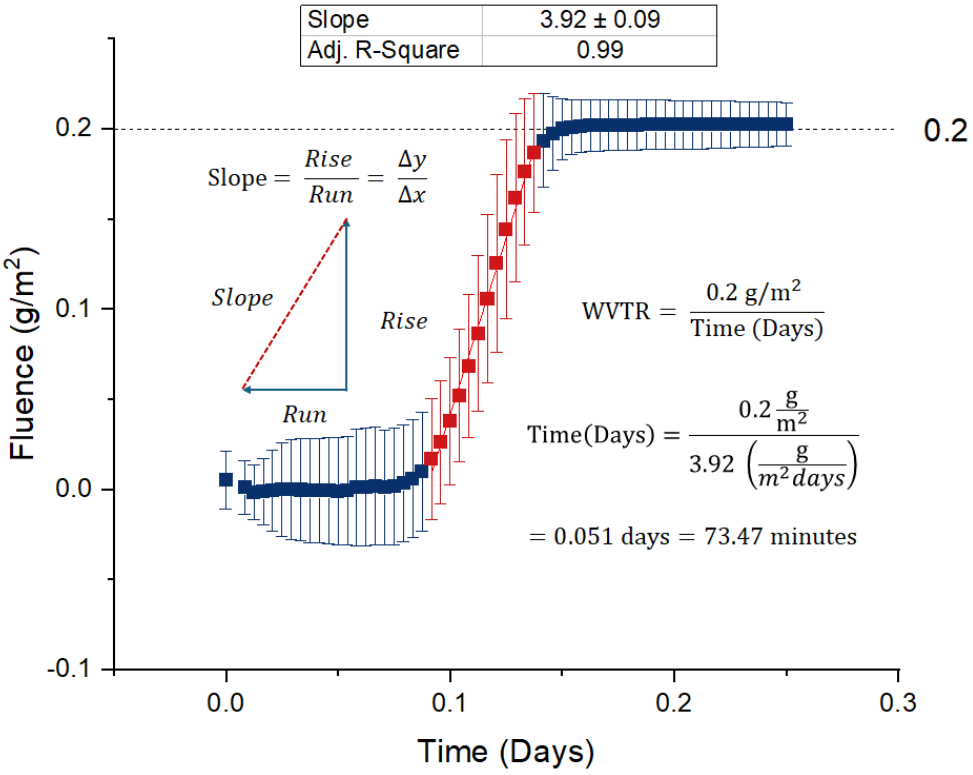


Figure 3-5: A fluence (g/m²) vs. time (days) graph of an uncoated PET sample tested at 31.5°C and 54% RH (LiCl solution) estimates the transition region time, assuming full saturation at 0.2 g/m² fluence. The estimated transition time is 0.051 days or 73.47 minutes.

3.4.3 Factors that affect Onset Time

Similarly, as introduced in sectioned 2.4.5.a WVTR Calcium Test Estimation, the onset time is defined as the time it takes before the first observable change in light intensity or Ca thickness; it is caused by gradual depletion of calcium and is reflected in the fluence calculation; like the WVTR, and supported by Fick's law, this can be influenced by temperature and RH.

3.4.3.a Influence of Temperature and RH on Onset Time

Figure 3-6 presents calcium test results for a bare PET substrate, showing fluence at (a) four temperatures (14.5 ± 2.5°C, 25.0 ± 3.0°C, 35.5 ± 2.5°C, and 50.5 ± 4.5°C) at the same humidity (LiCl ≈ 65% RH), and (b) three relative humidities (LiCl ≈ 65% RH, $MgCl_2$ ≈ 71% RH, NaCl ≈ 95% RH) at the same temperature (25 ± 3°C). This illustrates how environmental factors, like temperature and humidity, can affect and shift the onset time, and the WVTR.

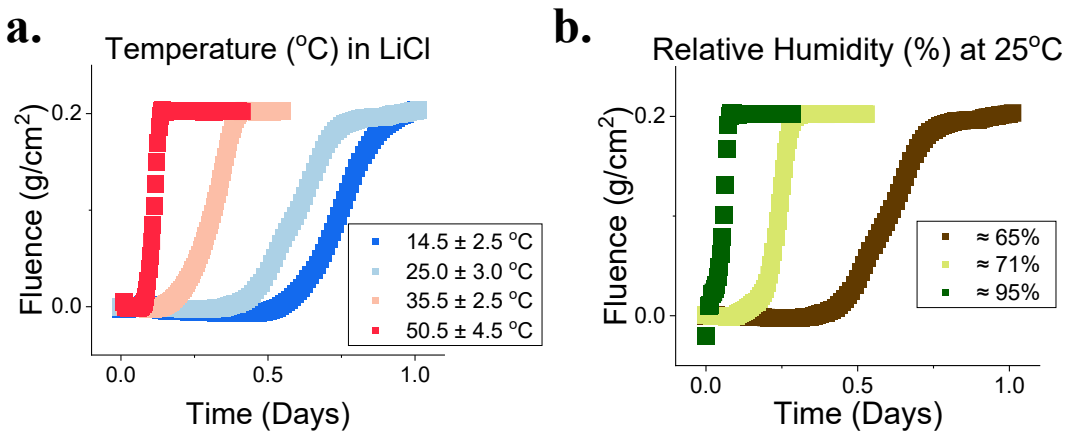


Figure 3-6: Representative fluence plots from calcium tests show (a) four temperatures and (b) three humidities, using saturated salt solutions to maintain equilibrium with the samples. The legend indicates the Ca thickness for each sample. The figure highlights the impact of temperature and relative humidity on WVTR (gradient in the transition region) and onset time.

The onset time is the delay between placing the specimen under humid conditions and the first visible degradation of the Ca layer; once this point is reached, the transition region can be tracked and the WVTR estimated. Both temperature and RH shorten this delay though through distinct physical mechanisms.

The primary role of RH is to raise the external water vapour partial pressure, which establishes a steeper concentration gradient across the barrier and provides a greater

driving force for diffusion. While RH does not significantly alter the diffusion coefficient, at very high levels it can cause the film to swell or plasticise, which may further ease transport.

In contrast, temperature directly raises the diffusion coefficient, as described by the Arrhenius relation. This increase reflects two complementary effects (1) greater polymer chain mobility and free volume within the barrier lowers the intrinsic Ea for permeation motion, (2) the higher kinetic energy of the water molecules themselves enables them to surmount that energy barrier more readily. By acting on these factors, temperature on the diffusion kinetics and RH on the driving force, these conditions together accelerate the moisture flux through the film, leading to faster Ca consumption and shorter onset time.

Statistical evaluation of the aggregated Calcium test data for uncoated bare PET (details of which are given in the supplementary information, Section 9.6) reveals that temperature ($P = 2.62\times10^{-6}$) and RH ($P = 3.29\times10^{-6}$) are statistically significant factors influencing onset time. These low P-values indicate a high level of confidence in the effect of these environmental conditions. The conclusion from this that, as expected, the onset time depends on water vapor permeating into the layer and initiating the depletion of calcium, progressing until the calcium becomes sufficiently thin to allow light transmission. Accordingly, onset time depends on temperature and RH the same way WVTR does. These findings are consistent with established diffusion principles: elevated temperatures increase molecular kinetic energy, allowing water molecules to overcome Ea barriers, while higher RH increases with concentration gradient, enhancing the rate of permeation. Importantly temperature and RH influence permeation dynamics without altering the intrinsic interaction between permeating specific and the substrate.

3.4.3.b Other Factors that Influence Onset Time (Ca and Cu layer)

The preparation of the Ca and Cu layer during the Ca test introduces additional factors that may influence the onset time. Although the onset time does not directly factor into the calculation of WVTR, it is still physically meaningful, where a longer onset time generally indicates a delay in calcium degradation, which suggests slower permeation and potentially better barrier performance.

It is to be expected that the initial Ca layer thickness will significantly affect the onset time, as the onset time includes the period required for the Ca to be eroded to a thickness that allows light transmission. Statistical analysis supports this, with a p-value of 0.00323 indicating that Ca layer thickness is a statistically significant factor in determining the onset time.

As shown in Figure 3-7 (a), at any fixed temperature and RH, the onset time increases with Ca-layer thickness. This occurs simply because more Ca must be consumed before the underlying copper becomes optically visible, not because of a change in the permeation rate itself (discussed further in Section 3.4.3.b). The actual rate of this consumption is governed by how quickly water vapour permeates the barrier to reach the Ca layer. Therefore, temperature and RH primarily influence the onset time by accelerating this water permeation; the subsequent Ca and water reaction is sufficiently fast that it is not considered rate-limiting in this analysis.

To better understand the influence of calcium thickness, Figure 3-7 (b) presents main effects plots that average onset time and WVTR for each calcium thickness, regardless of temperature and RH.

These plots show that while a thicker Ca layer increases the onset time, this does not affect the final calculated WVTR. The onset is delayed simply because a greater amount of Ca must be consumed by permeating water vapour before a change in optical transmission is detectable. The WVTR value itself, however, is derived solely from the slope of the subsequent transition region. This slope is fixed by the steady state flux of water arriving at the reaction front and is therefore independent of the initial Ca thickness.

This distinction is critical when measuring low permeability coated barrier layers that are the focus of this work. For these high-performance films, the permeation rate is very low, and using a Ca layer that is too thin can cause the transition region to be truncated before a stable gradient can be measured, compromising the accuracy of the fit. Therefore, while the initial Ca thickness is not a parameter in the final performance calculation, it is a crucial experimental variable that ensures the reliability of the measurement itself. In contrast, temperature and RH remain the dominant factors influencing both onset time and WVTR, overshadowing any small variations introduced by change in Ca thickness.

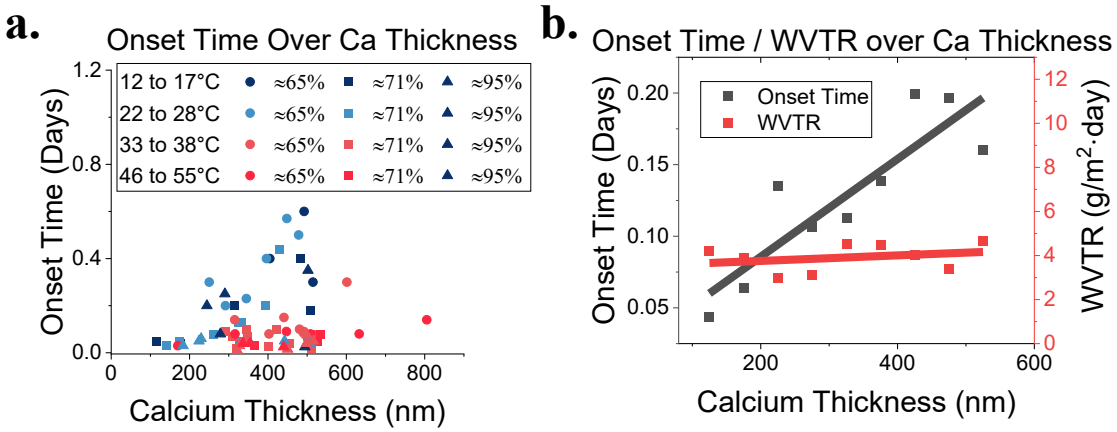


Figure 3-7:(a) Onset time versus Ca thickness for uncoated PET samples, categorised by RH and temperature. This plot shows the combined influence of RH, temperature and Ca thickness on onset time. Higher temperatures and RH generally lead to shorter onset times, while thicker Ca layers result in longer onset times due to the greater amount of material needing to degrade before light transmission begins. (b) Main effects plot showing the average onset time and WVTR with respect to Ca thickness, aggregated across RH and temperature. In this plot, the grey line represents the average onset time for each Ca thickness, while the red line shows the corresponding average WVTR values. The trend confirms that onset time increases with Ca thickness, but calculated WVTR remains relatively stable, with only a slight upward trend. This reinforces that Ca thickness affects the degradation behaviour (onset time), not the WVTR calculation, which is based only on the slope of the transition region and is independent of when the transition begins.

Copper-layer thickness, statistical analysis of the data (Appendix 9.6) shows that varying the thermally evaporated copper capping layer between 13.0 nm and 34.5 nm has no statistically significant effect on either onset time ($P = 0.088$) or calculated WVTR ($P = 0.473$). This confirms that the copper layer's role is purely sacrificial, it prevents premature Ca oxidation before water vapour reaches the layer but once the transition region begins, the WVTR is governed solely by steady state water vapour flux and reaction stoichiometry, not by residual Cu thickness. These findings reinforce that Cu thickness does not influence long term diffusion behaviour and thus need not be considered a variable in WVTR interpretation within the tested range.

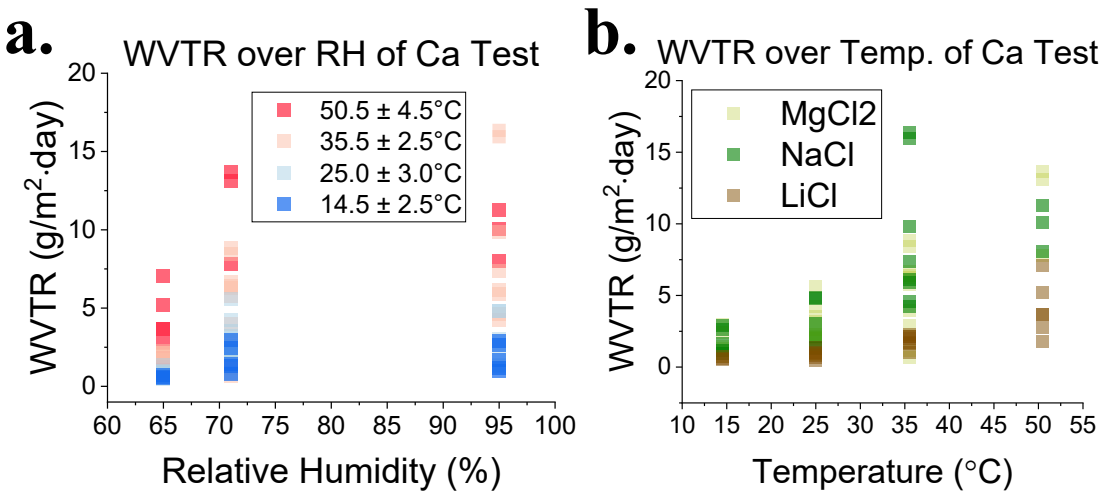
3.4.4 Effect of Temperature and RH on WVTR Using the Ca Test

This section further supports and explores the accuracy and validity of the Ca test, and seeks to determine whether the underlying trends in terms of temperature and relative humidity are the same as those observed in 3.3.2 MOCON Temperature and Relative Humidity on Uncoated PET. ANOVA analysis shows the Ca test data (2.4.6: Fluence Calculation Example) of uncoated PET data (raw data given in Section 9.6), show that

the temperature ($P = 1.47\times10^{-9}$) and relative humidity ($P = 4.07\times10^{-7}$) are statistically significant and affects the WVTR as expected.

Figure 3-8, (a) shows WVTR plotted against RH, grouped by temperature, while Figure 3-8 (b) shows WVTR plotted against temperature, grouped by RH. These plots highlight the expected influence of temperature and RH on WVTR, with the Ca test data showing consistent trends. This alignment with anticipated trends provides additional confidence in the Ca test's ability to estimate WVTR. The results are further supported by literature, which reports a similar WVTR value for uncoated PET (6 g/m²·day, PET Melinex PCS, 38°C, RH: 90-95% at 100 µm w/ 25 µm peel layer) using the ISO 15106-03 electrolytic detection method [288]; as also shown in the Table 3-1.

Notably, the MOCON Aquatran data consistently shows WVTR values of around 3 to 5 times higher than those from the Ca test. While the precise cause for this discrepancy id undetermined, it may stem from methodological biases. It is possible the MOCON's electrolytic sensor overestimates the WVTR of highly permeable films due to its sensitivity to minor edge leaks. Conversely, the reaction-based Ca-test could potentially underestimate high flux rates.

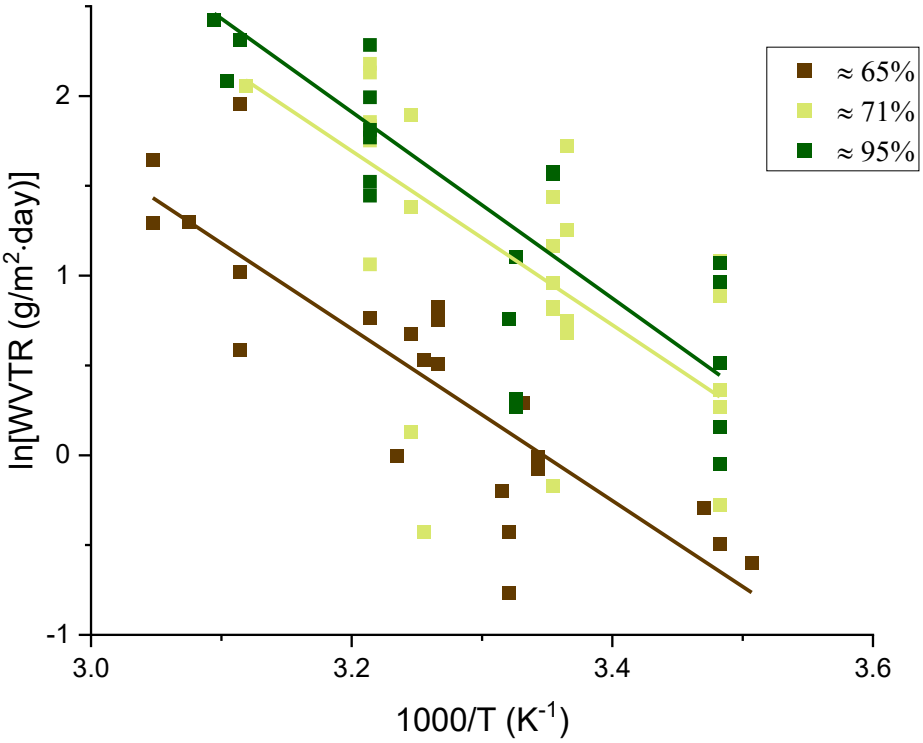


Temperature (°C)	Relative Humidity (%)	WVTR (g/m²·day)	
		Ca Test	MOCON
14	65	0.64 ± 0.10	4.48 ± 0.09
	95	1.87 ± 0.87	6.96 ± 0.20
25	65	0.87 ± 0.30	8.47 ± 0.36
	95	2.91 ± 1.60	12.82 ± 0.48
36	65	1.84 ± 0.44	16.31 ± 0.84
	95	8.79 ± 4.86	25.80 ± 1.01

Figure 3-8: Ca Test of uncoated PET substrate: (a) WVTR plotted against relative humidity grouped by temperature, and (b) WVTR plotted against temperature grouped by relative humidity. Both plots show a direct proportionality—higher temperature or humidity significantly increases WVTR. The accompanying table provides a detailed comparison of average WVTR values obtained from the Ca test and MOCON Aquatran measurements under corresponding temperature and relative humidity conditions. The data reveal differences such that the MOCON Aquatran reporting higher WVTR values, while the Ca test aligns closely with literature (~6 g/m²·day) [288], indicating greater accuracy. The larger deviations in MOCON data at higher temperature and humidity suggest potential calibration issues or methodological differences, underscoring the reliability of the Ca test and the need for caution with MOCON results.

3.4.5 Activation Energy of Uncoated PET (Calcium Test)

By testing uncoated PET in the Calcium test under various temperatures and specific relative humidity, we can now estimate the activation energy (Ea), similarly to Section 3.3.3 Determination of the Ea of Uncoated PET Substrate (MOCON). Despite higher sample deviation of WVTR's values in the Ca test data set (raw data given in Section 9.6) compared to MOCON Aquatran (raw data given in Section 9.5) and literature, the estimated Ea (~42 KJ/mol for all humidities, Figure 3-9 aligns with expectations. This confirms the Ca test's ability to reveal factors controlling WVTR measurements.



Salt Solution	LiCl (~65%)	$MgCl_2$ (~71%)	NaCl (~95%)
ΔEa (KJ/mol)	39.76 ± 5.41	40.30 ± 8.91	43.17 ± 7.68
Adj. R Squared	0.72	0.41	0.60

Figure 3-9: The Activation Energy of uncoated PET, tested under three relative humidities using the Ca test, shows WVTR variability but remains within the range of MOCON Aquatran and literature values. These results help in understanding the permeation mechanisms of barrier layers and estimating potential pinhole or defect sizes. The Activation Energy plot also enables estimating WVTR at higher temperatures for the same humidity.

3.5 Comparison of Activation Energy in Literature

3.5.1 Calculating Activation Energy of Literature

To understand the permeation mechanisms of uncoated PET, literature values for activation energy were collected from Sobrinho [250], Deng [93], Piergiovanni [249], Erlat [254], Fahlteich [25], and BM Henry *et al.*, [252] and plotted in Figure 3-10. This figure shows the ln (WVTR) versus 1000/T plots for these studies.

The gradient of the downward trend in all plot's points to a common activation energy across the literature. Directly comparing published WVTR values and figures, however, is tricky: temperature, RH, film thickness and even small protocol tweaks in measurement methods can all shift the value. To reduce the errors and make values from literature and studies comparable, the WVTR's are aggregated to a common, thickness- and condition adjusted basis, as further discussed in Section 3.6 Permeation Analysis of Uncoated PET Films.

Comparing data at similar relative humidity levels (~95%–100%) from the Ca test and MOCON Aquatran measurements with literature reveals interesting trends. The Ca test data (Figure 3-9), with a narrower ln (WVTR) range of 0.5 to 2, closely aligns with values reported by Piergiovanni, Erlat, Fahlteich, and BM Henry. In contrast, the MOCON Aquatran data (Figure 3-4), with ln(WVTR) values ranging from 1.0 to 3.3, aligns well with results from Sobrinho and Deng. As noted in Section 0, the activation energies are similar across these studies. These slight differences can be attributed to possible thickness of the uncoated PET substrates which directly relate to the WVTR.

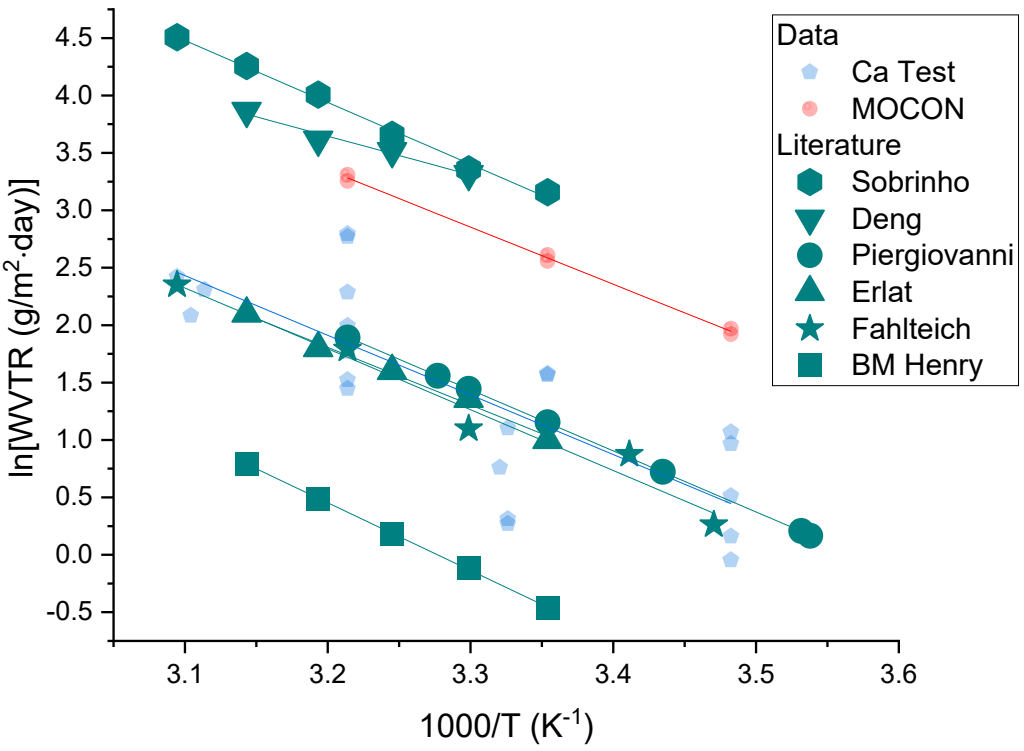


Figure 3-10: Plot of ln[WVTR (g/m²·day)] vs. 1000/T (K⁻¹) for literature values, showing variations in slopes used to calculate the activation energy of uncoated PET substrates. The figure also includes ln(WVTR) values from the Ca test and MOCON Aquatran measurements at similar relative humidities (~95%–100%), highlighting alignment and differences with literature sources [25, 93, 249, 250, 252, 254].

3.5.2 Summary of Activation Energies

Now is an appropriate time to compare activation energies (KJ/mol) over relative humidity, as shown in Figure 3-11. The activation energy of uncoated PET is around 41.73 ± 3.22 KJ/mol (excluding Deng's outlier). The figure confirms that the activation energies from the Ca Test and MOCON Aquatran closely align with published literature, increasing confidence in the experimental data.

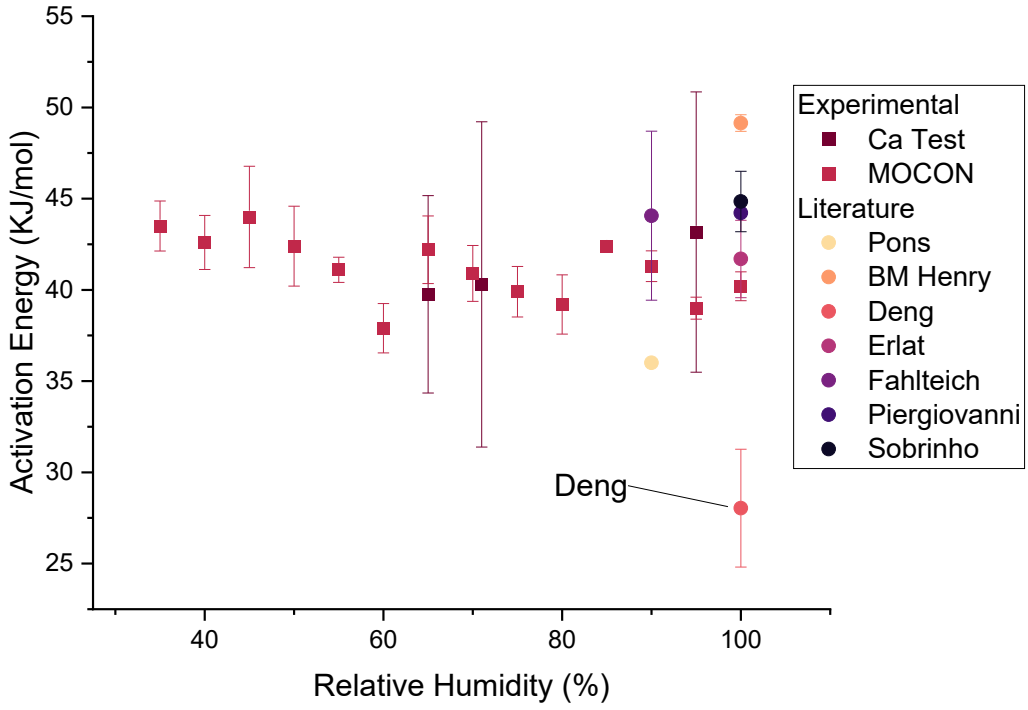


Figure 3-11: (a) Activation Energy (Ea) vs. Water Vapor Transmission Rates (WVTR) over relative humidity shows the variability and overall consistency of Ea. The values range from 36.0 to 49.14 KJ/mol, with an average of 41.73 ± 3.22 KJ/mol, excluding Deng as an outlier.

3.6 Permeation Analysis of Uncoated PET Films

Water vapor permeation through polymer substrates is significantly influenced by film thickness. A thicker film increases the diffusion path length, which reduces the flux of water vapor across the film, as described by Fick's First law of diffusion (Equation 1-1). While the diffusion coefficient (D) remains constant for a given material, the flux is inversely proportional to the film thickness due to the extended transport path. Therefore, thicker films exhibit lower WVTR values, not because of a change in intrinsic permeability, but due to this geometric factor.

3.6.1 Intrinsic Permeation of PET Films

As said above, comparing the raw WVTR value is not the best way to compare the barrier properties of different films, Permeation, defined as the rate of water vapor transport per unit area and normalized by film thickness (l), provides a more intrinsic measure of the material's barrier properties. This approach ensures that differences in WVTR are not solely attributed to variations in substrate dimensions. Alternatively, it can be expressed in terms of (mol/m²·s), where M_{H_2O} $(18.015\,\frac{g}{mol})$ - Equation 3-1.

$$Permeation = \frac{WVTR \cdot l}{M_{H_2O}} \qquad \textit{Equation 3-1}$$

Accounting for thickness variations in the permeation data, environmental parameters such as temperature and RH still exert a pronounced influence on water vapor transport. As mentioned beforehand, elevated temperatures increase molecular mobility, thus enhancing permeation rates [285], while higher RH augments the thermodynamic driving force for diffusion [286].

3.6.1.a Permeation of PET at Different Thicknesses (Literature)

When permeation rates are calculated, it becomes easier to compare the barrier properties across different film thicknesses. In this section, data from DuPont Teijin Films' Mylar PET are examined under standardized conditions (38 °C and 90% RH). As shown in Figure 3-12, thicker films exhibit lower WVTR, an expected outcome because the longer diffusion path length for water molecules leads to reduced permeation flux. However, once permeation is calculated, the results are normalized for thickness; any remaining variations are more likely related to sample or inherent material properties than

substrate thickness. In theory, permeation values for the same material should be comparable, yet slight deviations do occur—likely due to test methodology, sample preparation, or subtle inconsistencies in the film [289].

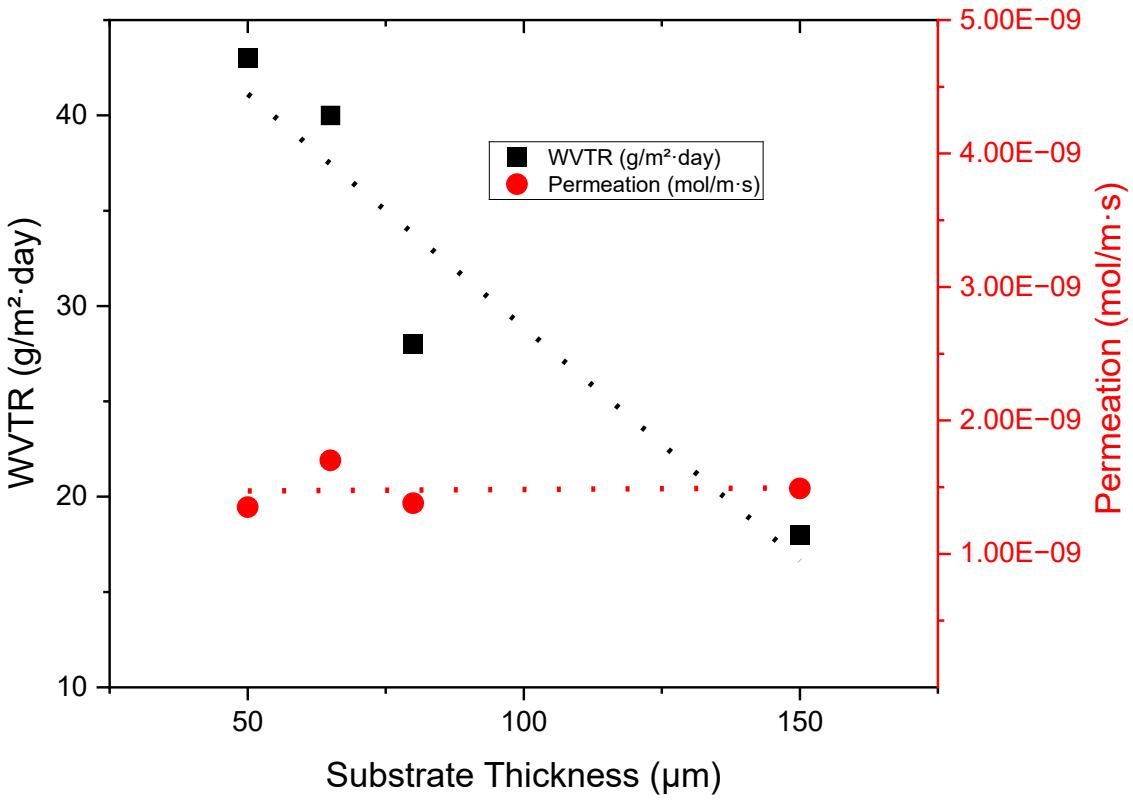


Figure 3-12: Literature data for uncoated Mylar PET films (DuPont Teijin Films data sheet {Films, 2011 #404;Films, 2021 #360 tested at 38 °C and 90% RH by ASTM F1249. Black squares: measured WVTR vs film thickness, red circles: the same data converted to thickness normalised permeation (WVTR × thickness). The plot illustrates two key points (1) thickness matters for WVTR, a longer diffusion path lowers the measured rate (inverse trend), (2) Intrinsic permeability is thickness-independence, once WVTR is normalised for thickness, the values collapse onto a nearly constant line, confirming that residual scatter is due to minor sample or test method variations not substrate gauge. These Mylar datasheet values are used because these have been one of the few publicly available data sets that reports the same PET grade at several thicknesses under identical T/RH conditions, most other studies as cited in Figure 3-10 do not satisfy that same material same conditions requirement are therefore not included in this thickness normalisation example.

3.6.1.b Permeation Variations Due to Testing Methods

This sub-section examines how different testing methodologies can lead to variations in calculated permeation rates. While thickness and environmental conditions (*e.g.* RH and temperature) are known to influence permeation. Figure 3-13 shows that even under similar testing conditions, the choice of methodology, whether Tritiated Water Permeation (HTO), Electrical Calcium Test (e-Ca), or MOCON Permatran—on 127 μm and 75 μm PET films, can result in different calculated permeation values [30, 230]. This highlights the importance of method selection when comparing values across literature.

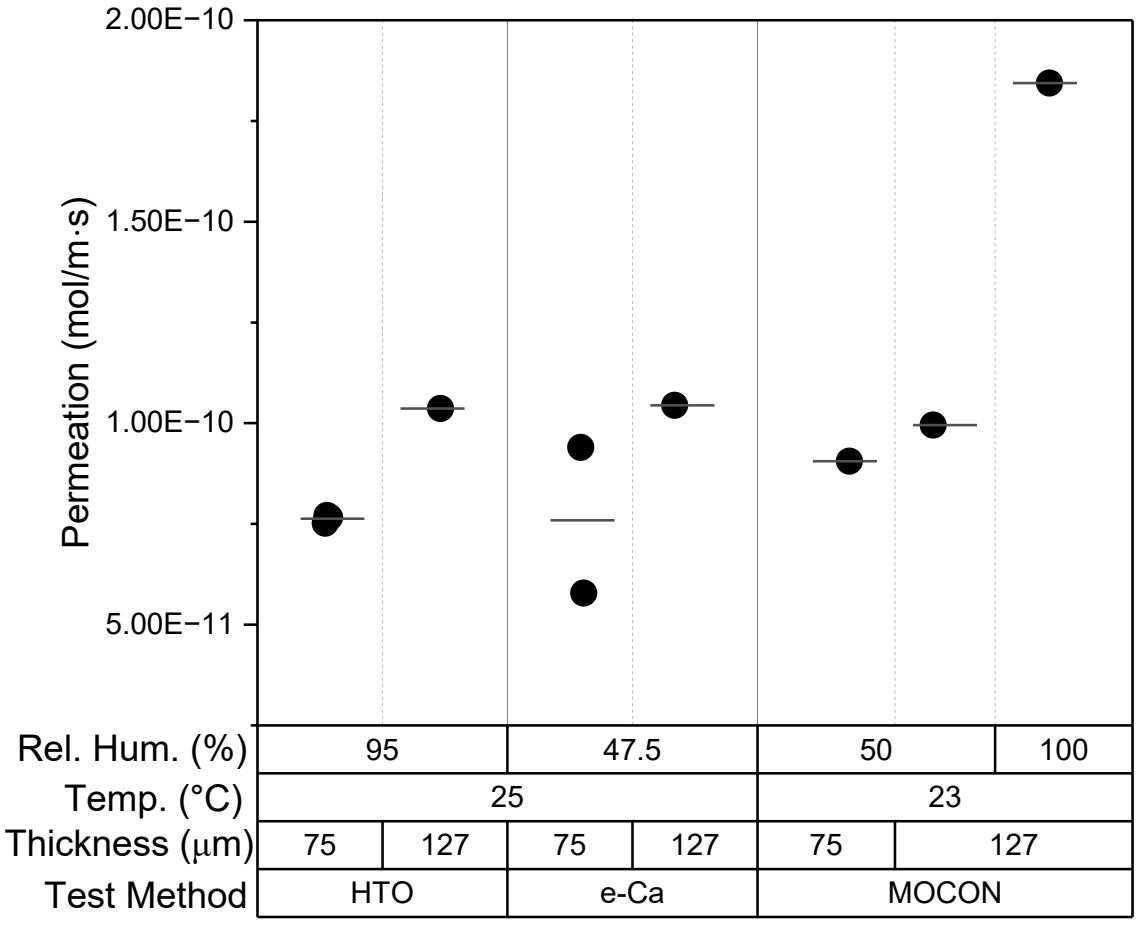


Figure 3-13: Calculated Permeation values - PET tested at difference test methods (HTO, e-Ca and MOCON), at two thicknesses, two temperatures and four relative humidities, showing that even with similar testing conditions the test methodology may change the WVTR and in turn the calculated permeation [30, 230].

3.6.1.c Permeation Across Temperature and Humidity Ranges

Figure 3-14 collates thickness-normalised permeation values ($mol \cdot m^{-1} \cdot s^{-1}$) for uncoated PET films measured at 90 to 100% RH in seven temperature bands: (≈10-15°C, ~20-25°C, ~30-35°C, ~38-40°C, ~45-50°C, ~60°C, and ~80°C). Symbols show data origin: experimental Calcium Test (⋆ - star), experimental Mocon Aquatran 2 (∘ - circle), and literature sources (□ - square) taken mainly from reports that follow ASTM F1249 or utilized isostatic method like MOCON equipment [25, 93, 246-252, 254-260, 262, 264, 266-270, 289-292].

Dividing WVTR by film thickness removes the extrinsic length term in Fick's law, A homogenous polymer should therefore give a flat line with thickness [293, 294]. In Figure 3-14 each colour (temperature band) does just that: the points form a horizontal band whose level rises roughly a factor of ten between 10°C to 80°C, expected with temperature dependence. Similarly, a higher RH increases the driving force and in the MOCON cell can also promote edge condensation. At 38 °C / 100% RH the MOCON values lie around 3 to 5 above both Ca test and literature results. Repeat runs and fresh calibrations produced similar overshoot, thus these are logged as possible method-specific artefact at full and use the internally consistent Ca-test values for modelling. All other MOCON data do sit inside the literature or Ca envelope.

Two literature points near 80°C (above T_g) also plot high, reflecting the increased chain mobility but this should be unrelated to the 38°C MOCON offset [269]. Apart from those isolated cases, thickness normalised permeation from all methods collapses onto a

common, temperature or RH governed trend, confirming that intrinsic PET permeability is gauge independent and validating the use of normalised data for cross study comparison.

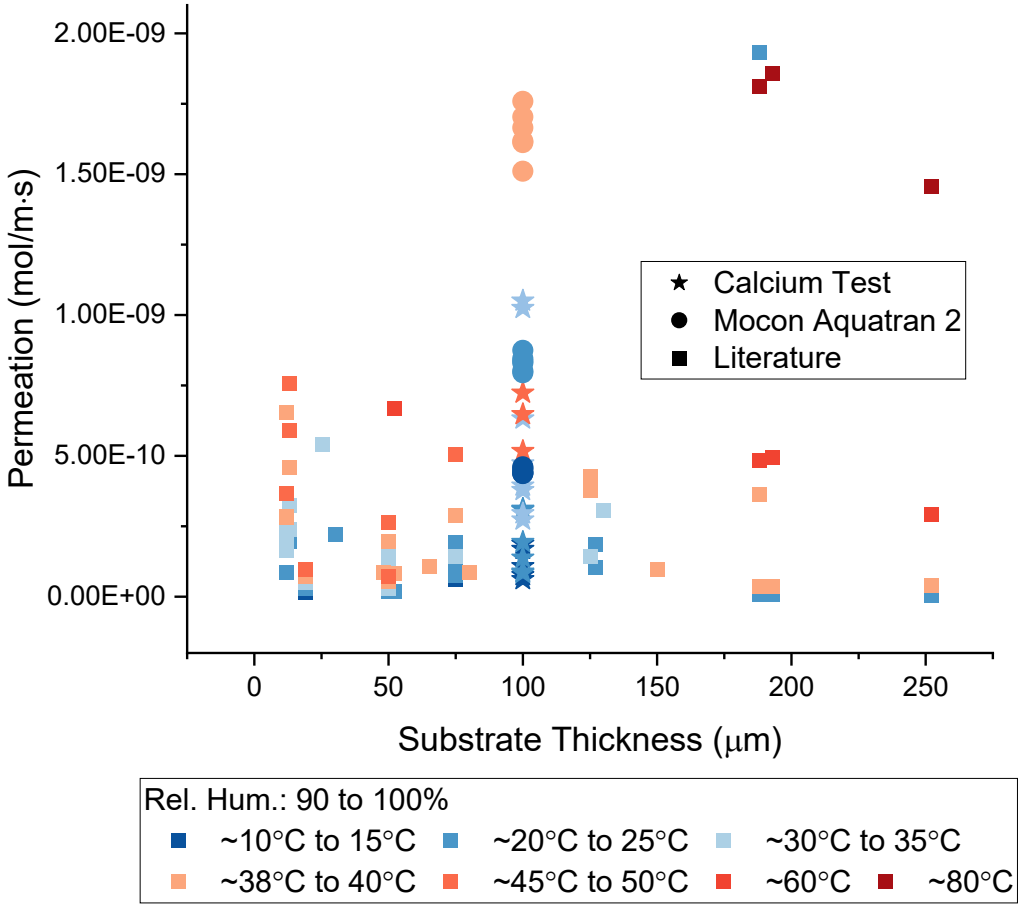


Figure 3-14: Verification of Fickian diffusion in bare PET, showing that thickness normalised water vapour permeation is independent of film thickness. The plot shows permeation (mol/m·s) as a function of substrate thickness (μm) under varying temperature and relative humidity (RH) conditions. Data include measurements from MOCON Aquatran 2 (●), Calcium Tests (✶), and values extracted from the literature (■) [25, 93, 246-252, 254-260, 262, 264, 266-270, 289-292]. For each temperature band (indicated by colour), the data form a horizontal cluster, confirming the expected flat response once the diffusion path length is normalised. The plot also reveals a clear temperature dependence with intrinsic permeation increasing by approximately one decade between 10°C and 80°C. Systematic deviations are noted include the experimental MOCON results attributed to instrumental artefact and two elevated

literature points near 80°C, which may reflect genuine increases in polymer chain mobility above the glass transition temperature of PET.

3.6.2 Permeation Analysis: Role of Water Vapour Partial Pressure and Comparative Methodologies

This section transitions from the initial focus on permeation analysis and expands to incorporate the role of Water Vapour Partial Pressure (WVPP) in explaining water vapour transport behaviour. Following the earlier brief report of WVTR measurements, the standard calculation of activation energy (Ea) was introduced to evaluate the temperature dependence of diffusion processes. Ea, derived from the Arrhenius relationship, provided a baseline comparison between the two experimental techniques (MOCON Aquatran 2 and Calcium Test) and with literature values.

Subsequently, the analysis addressed the influence of film thickness on permeation, introducing corrections to ensure meaningful comparisons across varying sample dimensions. All subsequent results are presented as thickness-corrected permeation values, enabling direct comparison with literature data under identical relative humidity (RH) conditions. These steps established a robust methodological framework for evaluating water vapour transport.

Building on this foundation, the focus now shifts to WVPP. Rather than combining RH and temperature into a single parameter, WVPP expresses the driving force for water vapor permeation in terms of the partial pressure of water vapor, which varies with both ambient temperature and RH. While this reflects how water activity changes with conditions, temperature also independently influences permeation through its effect on molecular diffusivity and the ability of permeating species to overcome energy barriers (as described by Henry's Law). WVPP (P_{WVVP}) represents the actual driving force for

water vapour transport and is calculated as delineated in Equation 3-2 as the product of the saturation vapour pressure of water at the ambient temperature (P_{*H_2O}) and the relative humidity ($\emptyset$) [295].

$$P_{WVVP} = P_{*H_2O} \times \emptyset \qquad \textit{Equation 3-2}$$

Moreover, contextually it is important to discuss the Clausius-Clapeyron equation (Equation 3-3) [296], which describes how the saturation vapour pressure increases exponentially with temperature. This relationship directly influences the WVPP, as temperature rises, more energy is available for water molecules to escape the liquid phase, thereby increasing saturation vapour pressure, and consequently, the driving force for WVPP also increases. Understanding this thermally driven equilibrium is therefore essential for accurately interpreting WVPP-based comparison of permeation behaviour, where $\Delta_{vap}H$ is the enthalpy of vaporisation (energy required of the phase transition), T is the absolute temperature and R is the universal gas constant (8.314 KJ/mol)

$$\frac{d\ (ln\ P_{*H_2O})}{dT} = \frac{\Delta_{vap}H}{RT^2} \qquad \textit{Equation 3-3}$$

The relationship between permeation and WVPP is systematically examined to determine whether WVPP alone governs the transport process or if temperature remains a significant factor. This is evaluated by assessing whether all permeation vs WVPP data from the two methods, as well as from literature as plotted in Figure 3-15 collapses onto a single line with a consistent gradient across the data set. Any deviations from this behaviour are further explored to understand the relative contributions of WVPP and temperature to the transport process.

Figure 3-15 demonstrates a broadly linear relationship between permeation and WVPP [89], implying that WVPP strongly governs water vapour transport. However, the data taken at different temperatures can show slightly different gradients, suggesting that temperature can also have some independent influence.

Figure 3-15 sets out the data from MOCON Aquatran 2 measurements, Calcium test data, and literature values. Notably, while the plot provides a useful visualisation that within each study there is a broadly linear relationship with WVPP, the gradients are quite different for different measurement sets.

The MOCON Aquatran 2 data demonstrates minimal sample to sample variation and a higher slope, as expected from the higher measured permeation rates. When this data is examined more closely (Figure 9-7 (a)) the points form a distinct cluster based on temperature with each temperature having a slightly different linear trend. This suggests that while WVPP is the primary driving force, temperature exerts an independent influence on the permeation process not captured by WVPP alone. In contrast, the Ca test data exhibits more scatter, but the absolute permeation values align more closely with those reported in the literature.

A review of the literature values further supports this analysis. Some studies like Piergiovanni's work on 19 μm PET, shows a strong linear trend that passes directly through the origin, which is a clear illustration of Henry's law (Figure 9-7 (c)) [249]. However, data from other sources (Figure 9-7(d)), such as Nehm, Esguerra, Erlat, Schubert, Deng, Sobrinho, Fahlteich and BM Henry show that while the relationship is broadly linear, there are clear variations in the slope depending on the material and testing method used [25, 93, 110, 246, 250, 254, 258].

These observations confirm that plotting permeation solely against WVPP is insufficient to create a single master curve. The distinct temperature groupings and variations between methods indicate that temperature affects the permeability coefficient itself. This effect is explored in Section 3.6.3.

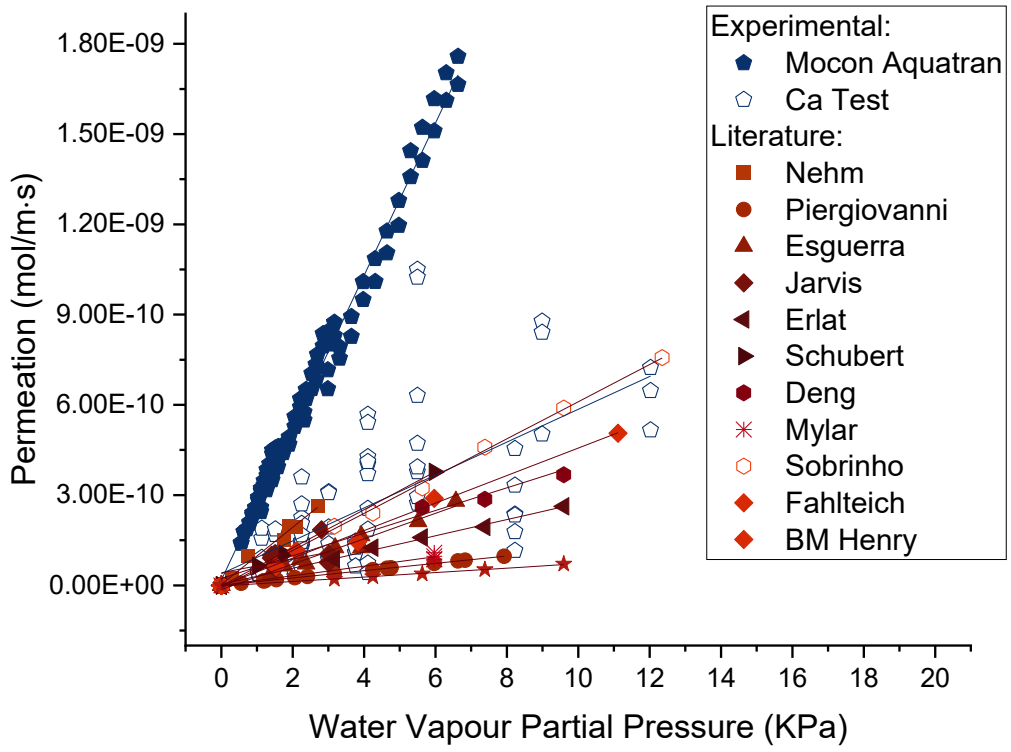


Figure 3-15: Permeation vs. Water Vapour Partial Pressure (saturated vapour pressure at the sample temperature multiplied by relative humidity), accounting for thickness differences and comparing WVTR across various testing conditions and methods. While the plot confirms the linear relationship predicted by Henry's law, the data are not explicitly grouped by temperature to allow any influence of temperature to emerge within in the observed trends. Deviations and subtle groupings within the same experimental conditions suggest that temperature affects permeation behaviour, with MOCON Aquatran data showing a consistent trend and minimal scatter, while the Ca Test data exhibits more variability. Broader distributions in the literature data further emphasise the role of temperature effects and variations in testing conditions.

3.6.3 Permeability of PET

Permeability (P, sometimes referred to as the permeability coefficient in polymer barrier literature) can also be explained as the permeance or permeation divided by the pressure gradient across the film. Assuming negligible pressure on one side, the pressure difference equals the product of the saturated water vapor pressure at a given temperature and the relative humidity. Permeability (Equation 1-6) as noted is the product of the diffusion and solubility coefficients.

The diffusion coefficient (D) is governed by the Arrhenius temperature dependence. Above the glass transition temperature (Tg), the polymer enters a rubbery regime where greater segmental mobility and free volume give much larger D values, whereas below Tg, the glassy matrix immobilizes the chains and D drops by several orders of magnitude. In this glassy state physical ageing can introduce a slow time dependence, for amorphous PET the first detectable change appears after around ≈ 2–3 days at room temperature, with appreciable shifts taking more than around a week to be realized [297-299]. Noting that physical ageing might be negligible in uncoated PET, but relevant in coated barriers. Barrier researchers therefore need to be aware that a Ca test or other ultra-low barrier measurement that extends to multi day window needs a routine examination of the trace for any downward drift, and if necessary, pre-anneal or re-measure to confirm that the fall is genuine permeation behaviour rather than ageing.

Under Henry's law, permeability (P) remains constant if both diffusion coefficient (D) and solubility coefficient (S) are both independent of water vapor partial pressure (WVPP) at a given temperature. Experimentally, however, deviations can arise from external sources (*e.g.*, calibration errors, temperature fluctuations) or intrinsic factors

such as WVPP-dependent changes in polymer dynamics. Notably, near the Tg, the sudden increase in segmental mobility causes a sharp rise in the diffusion coefficient (D) and makes it and to a lesser extent the solubility coefficient (S) highly sensitive to moisture uptake. Consequently, once Tg is exceeded, the plasticised polymer departs from Henry's law behaviour and it's permeability (P) is no longer WVPP independent [300-302].

This implies that permeability coefficients for PET under identical conditions should be the same. However, Figure 3-16 shows discrepancies when plotting calculated permeability against WVPP. The Mocon Aquatran 2 data shows significantly higher permeability coefficients than most literature values, this discrepancy is an expected consequence of the elvated WVTR previously observed from the initial measurements that stem from possible calibration or sample specific issues. It also shows temperature dependent groupings further explored in the following subsection (3.6.3.a)

Conversely, the calcium test data generally gives similar values as literature, with most values falling within the range of 1.25×10^{-13} to 2.50×10^{-14} mol/(m·s·Pa). When considering individual studies and publications, the data tends to be closer in absolute value than the MOCON Values.

In summary, while there is variability in absolute permeability across different measurement methods or studies, but with the same material and data set permeability remains relatively constant with respect to WVPP.

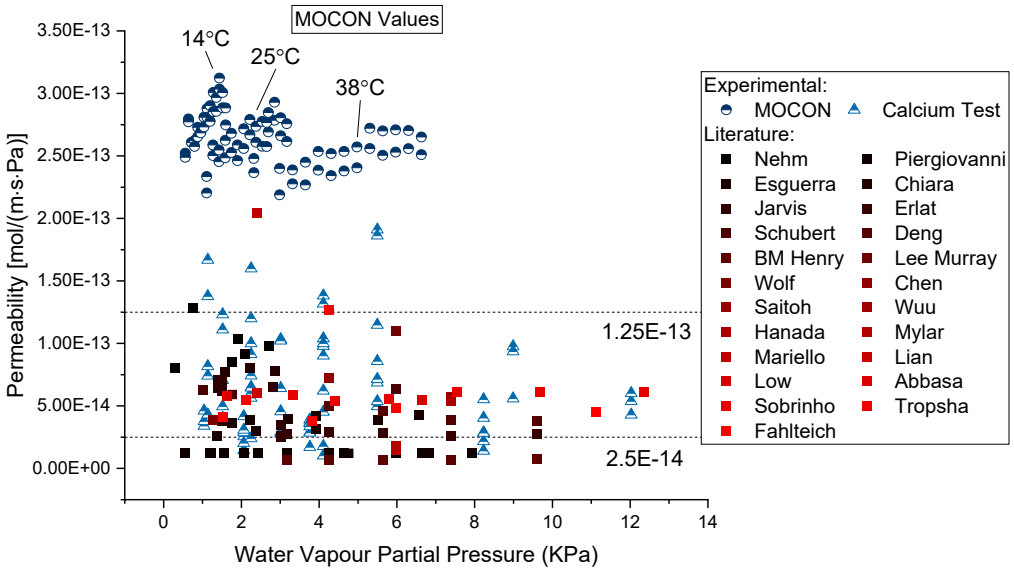


Figure 3-16: Permeability [mol/(m·s·Pa)] vs. Water Vapor Partial Pressure (KPa), showing distinct temperature groupings in the Mocon data, while the calcium test closely aligns with literature values. Overall, data from individual studies fall within a consistent permeability range and are close in absolute permeability coefficient values.

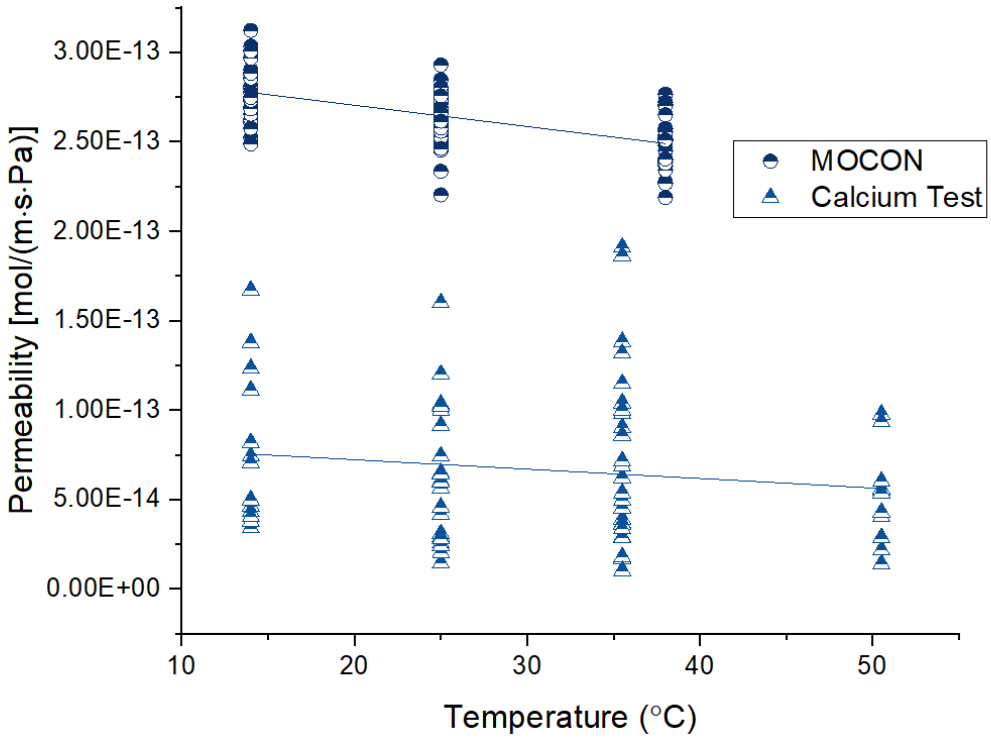
3.6.3.a Effect of Temperature on Permeability of PET

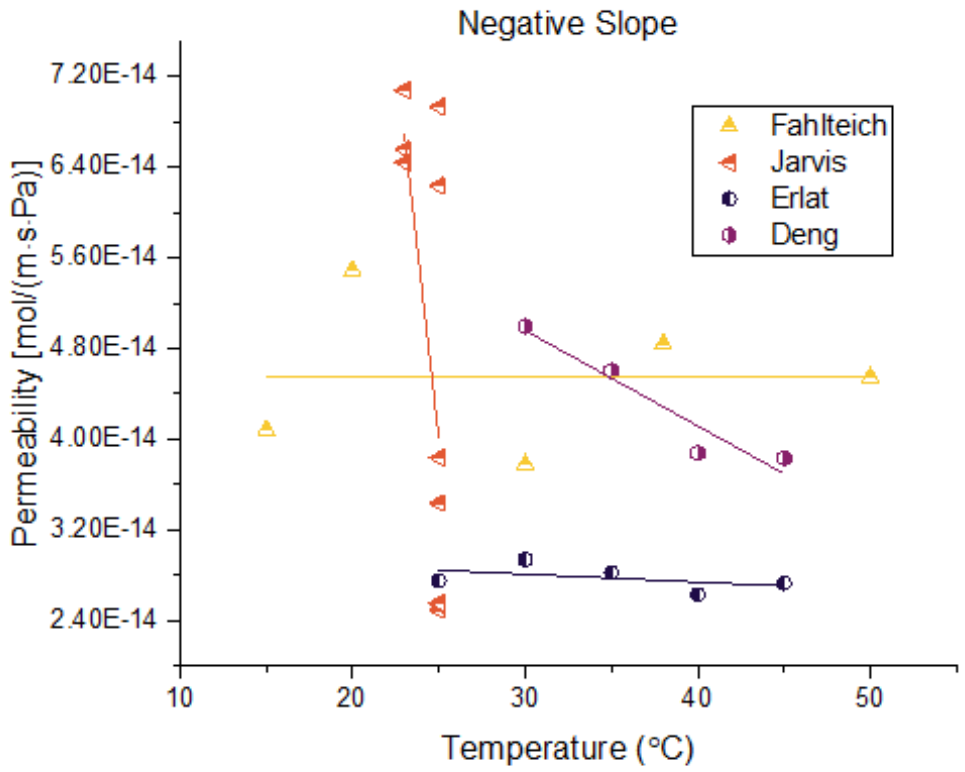
Figure 3-17 explores how temperature affects permeability. The Mocon and Calcium test data suggest a general downward trend, indicating that the film may become less permeable with higher temperatures. This downward trend is also supported by literature, such as Fahlteich [25], Jarvis [230], Erlat [254] and Deng [93]. However, other studies, including Nehm, [258], Piergiovanni [249], Esguerra [246], Hulsmann [269], Schubert [110], BM Henry [252], Burst [248] and Sobrinho [250] show a positive slope, suggesting increased permeability with rising temperature.

The permeability coefficient of polymers is the intrinsic material property, as outlined by Crack's diffusion theory ([285]). Higher temperatures may enhance polymer chain mobility, increasing diffusivity and thereby elevating the permeability coefficient, a phenomenon widely documented by Barrer [303], Yampolskii [304] and Bernardo *et al.*

[305]. However, this relationship can reverse in some polymer-permeant systems, especially those involving water vapor. When the permeant's solubility within the polymer decreases at elevated temperatures (due to exothermic mixing, or negative enthalpy of solution), it can overshadow the increases in diffusivity, leading to an overall reduction in the permeability coefficient—a downward trend observed.

This seemingly contradictory behaviour can be evident in glassy polymers, where physical aging and chain packing can further alter free volume, yielding unexpected temperature-dependent trends. Consequently, the literature presents both upward and downward slopes in the permeability coefficient with temperature. This apparent contradiction possibly arises from the complex interplay of different factors that influence permeability, and the specific behaviour of a system depends on the relative importance of these factors.




Negative Slope
Permeability [mol/(m·s·Pa)]
7.20E-14
6.40E-14
5.60E-14
4.80E-14
4.00E-14
3.20E-14
2.40E-14
10
20
30
40
50
Temperature (°C)
Fahlteich
Jarvis
Erlat
Deng

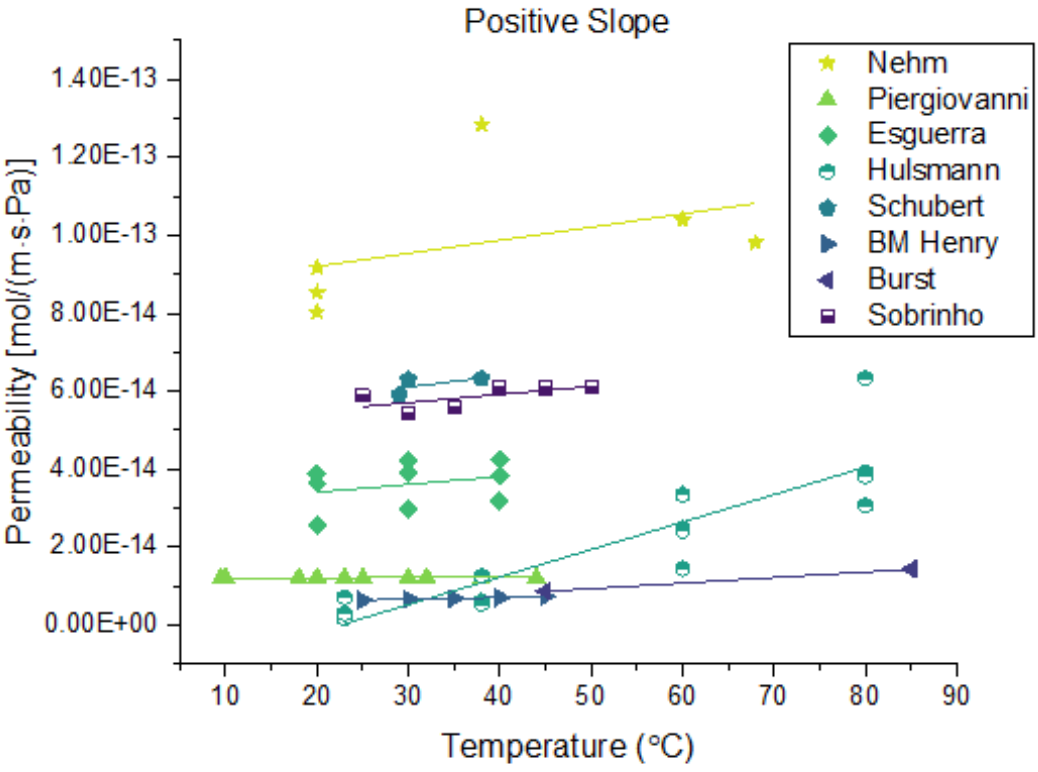

Positive Slope
Permeability [mol/(m·s·Pa)]
1.40E-13
1.20E-13
1.00E-13
8.00E-14
6.00E-14
4.00E-14
2.00E-14
0.00E+00
10
20
30
40
50
60
70
80
90
Temperature (°C)
Nehm
Piergiovanni
Esguerra
Hulsmann
Schubert
BM Henry
Burst
Sobrinho

Figure 3-17: Permeability [mol/(m·s·Pa)] vs. Temperature (°C) shows a downward trend in the experimental data, supported by some literature. However, not all studies agree, with some showing an opposite, upward trend, where films become more permeable at higher temperatures. This highlights disagreement on how temperature directly affects permeability.

3.6.4 Estimating Activation Energy (Permeability Coefficients)

3.6.4.a Calcium Test Ea (Permeability)

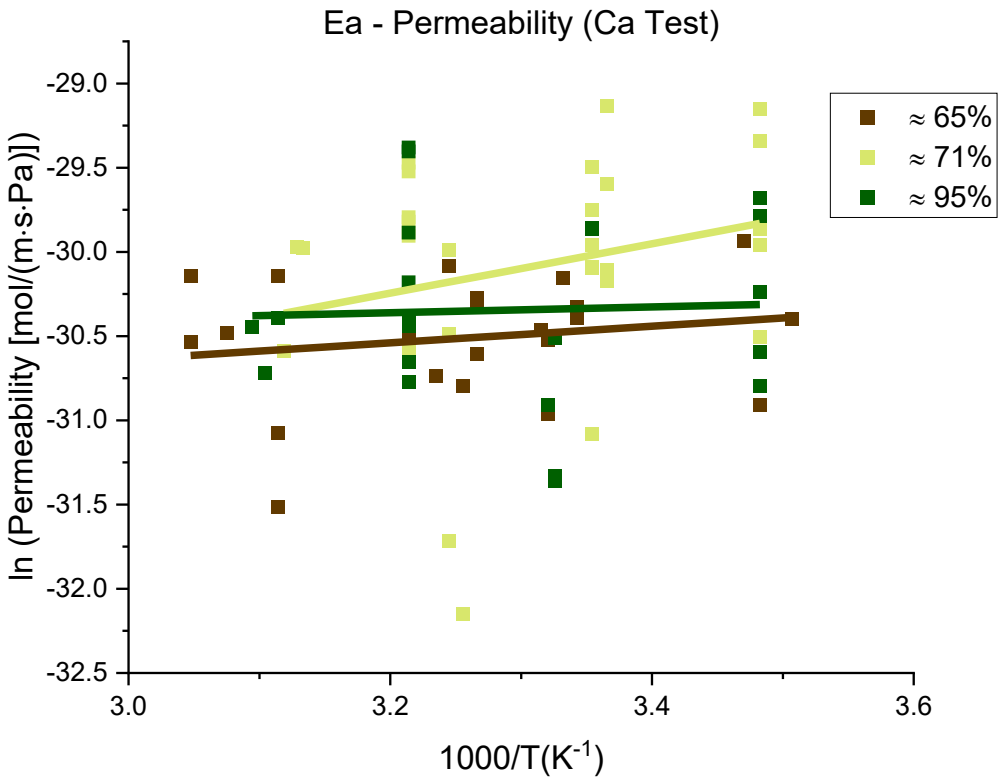
Now considering the temperature dependence of the intrinsic permeability coefficient (P). Unlike WVTR, which is a flux, and is heavily influenced by the exponential rise in saturation vapor pressure with temperature; the permeability coefficient normalizes for these external driving forces.

Figure 3-18, plots the natural log of permeability coefficients from the Ca test data against reciprocal temperature to estimate the Arrhenius relationship. The data exhibits a positive slope, which according to the relationship $\ln(P) \propto -E_{app} / RT$, indicates a negative apparent activation energy (E_{app})

This negative value signifies a solubility controlled permeation regime rather than a vanishing physical barrier. As temperature increases, the solubility coefficient (S) of water in the semi-crystalline PET matrix decreases sharply due to the exothermic nature of hydrogen boding between water and the polar ester linkages. This is supported by Launay *et al.*, that reported apparent enthalpies of dissolution around -28 kJ/mol below 80°C and -45 kJ/mol above 80°C. In contrast the activation energy of diffusion is positive (36 – 42 kJ/mol). This indicates that the decrease in permeability with temperature arises from reduce solubility rather than the disappearance of the said physical diffusion barrier [234, 282]. This thermodynamic reduction in the concentration of mobile permeant molecules outweigh the kinetic increase in the diffusivity (D).

Consequentially, the overall permeability decreases with rising temperature. It is inaccurate to label this as a negative energy barrier; but rather it is a negative temperature coefficient of permeability arising from the dominance of the enthalpy of sorption - (implications further discussed in: 3.6.4.d Summary Activation Energy (Permeability).

The absolute values of E_{app} are small compared with the scatter in the data. The data sets were segregated by relative humidity, and the apparent activation energy is shown in the table below. While the linear fit suggests some consistency, the activation energy values have high uncertainty due to the variability in the Ca test measurements. These values are numerically lower than the WVTR Ea, due to permeability accounting for additional factors like partial pressure gradients, and film thickness. There is no clear trend of higher activation energy with increasing humidity, possibly due to complex interdependencies in permeability measurements. Despite this, the results also reflect the variability observed in permeability coefficients, as discussed in the previous section.



Salt Solution	LiCl (~65%)	$MgCl_2$ (~71%)	NaCl (~95%)
ΔEa (KJ/mol) (Permeability Coefficients)	-4.09 ± 5.08	-12.19 ± 9.43	-1.43 ± 7.92
Adj. R Squared	-0.017	0.023	-0.048

Figure 3-18: The natural log of permeability coefficients ($mol \cdot m^{-1} \cdot s^{-1} \cdot Pa^{-1}$) versus reciprocal temperature (K^{-1}) for Ca tests, shows that multiplying the slope by the universal gas constant ($R = 8.314\ J \cdot K^{-1} \cdot mol^{-1}$) yields a negative apparent activation energy (E_{app}) in terms of permeability. The negative value reflects the exothermic sorption mechanism of water vapor in PET. The scatter in the data and the low coefficient of determination suggest that the temperature dependence is complex and potentially non-Arrhenius, likely induced by humidity-induced plasticization of the matrix which varies with temperature.

3.6.4.b MOCON Test Ea (Permeability)

A similar analysis was performed using the MOCON Aquatran 2 data as shown Figure 3-19, where the natural logarithm of permeability coefficients was plotted against reciprocal temperature. The results indicate a minor influence of temperature and relative

humidity, with only small changes observed in permeability coefficients. Compared to the more scattered Ca test data, the MOCON measurements are more precise, with smaller standard deviations.

While a couple of the gradients appear to slope downward, suggesting the potential for positive Ea values, these may fall wtihin the bounds of experimental uncertainty. The observed values of Ea are small and the variation in the data is comprable to the magnitude of the slopes, suggesting that the true Ea is too low to be measured reliably. The measured Ea's range between: [-1 to -5 KJ/mol].

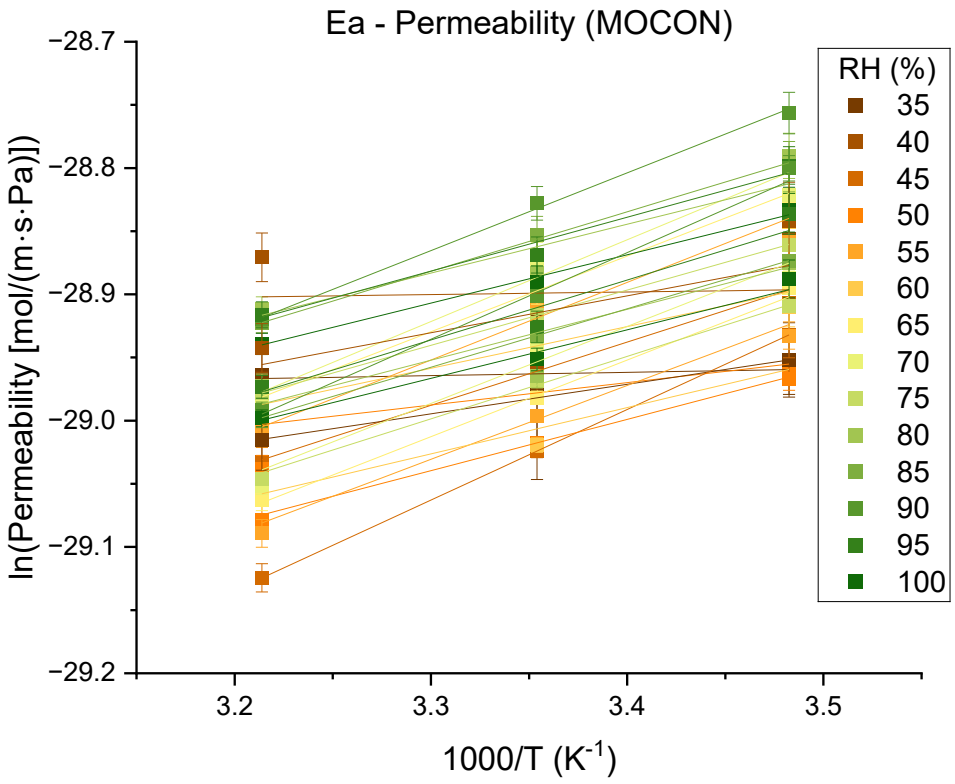


Figure 3-19: The natural log of permeability coefficients for MOCON Aquatran 2 plotted against reciprocal temperature (K^{-1}) estimates Ea. The data shows a slight influence of relative humidity, but its effect is minimal and not significantly impactful on the Ea.

3.6.4.c Literature Values Ea (Permeability)

The same methodology was applied to literature values tested at the same relative humidity but different temperatures. Figure 3-20 shows the natural log of the permeability coefficient versus reciprocal temperature, demonstrating relative consistency, except for Deng [93] and BM Henry [252], which show a slight increase and decrease, respectively, as temperature changes. These graphs allow for comparison between experimental trends and findings from published studies.

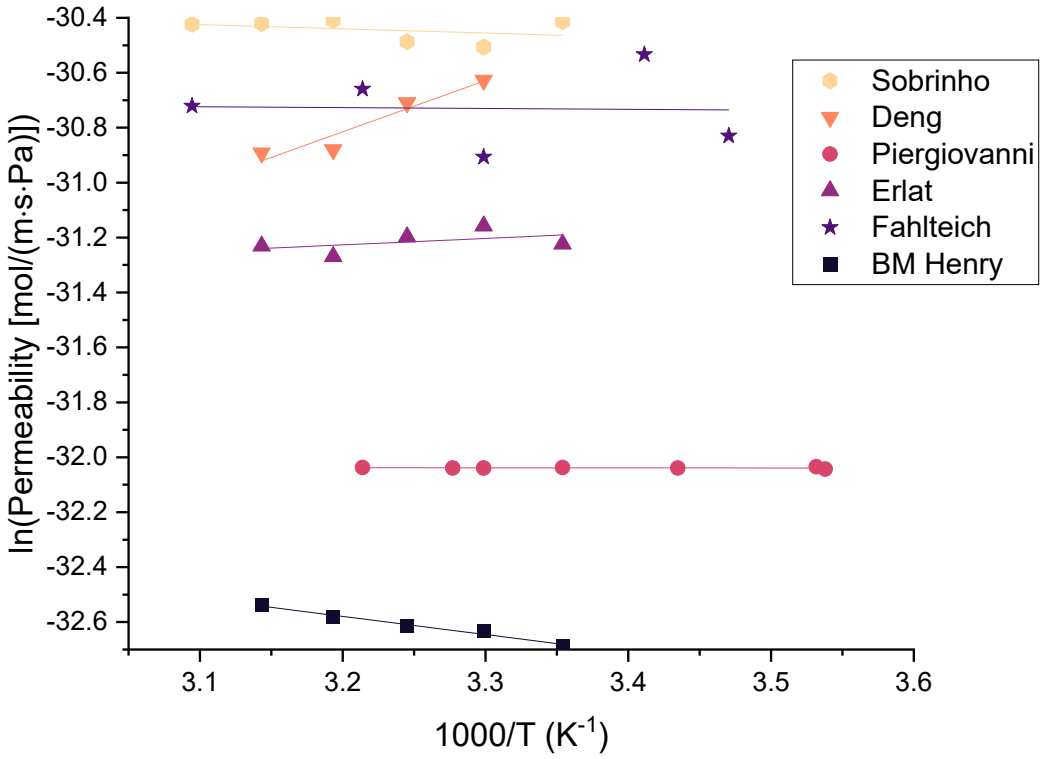


Figure 3-20: The natural log of permeability coefficients from literature, plotted against reciprocal temperature, generally follows a constant trend, except for Deng (upward slope) and BM Henry (downward slope), which produces interestingly a negative and positive Ea respectively.

3.6.4.d Summary Activation Energy (Permeability)

A key distinction in this context is the Ea derived from WVTR measurements versus the Ea derived from permeability coefficients. The WVTR-based Ea (Section 0) as used extensively in previous studies primarily reflected the concept of an apparent energy barrier for water vapor movement through the sample that would be better overcome at higher temperatures, but the WVTR value did not account for the layer thickness, and partial pressure of water. This approach does not fully account for changes in the water vapor partial pressure at different temperatures and RH. At varying RH and temperature, the WVPP changes, which in turn alters the concentration of water vapor in the polymer according to Henry's law.

In contrast, the Ea derived from permeability coefficients addresses both the diffusion coefficient (D) and the solubility coefficient (S), since permeability is the product of D and S. The diffusion coefficient is expected to follow an Arrhenius type temperature dependence as molecular motion through the polymer matrix requires overcoming energy barriers [285], however the solubility coefficient often deviates from this simple behaviour especially in semi-crystalline polymers like PET, where sorption may involve specific site interactions, clustering or phase heterogeneity [303, 306].

The permeability coefficient is typically derived under assumptions of Fick's first law and Henry's law, which together imply that diffusion is driven solely by concentration gradients, and that solubility is linear. However, many polymers, solvent systems deviate from these assumptions due to additional mechanisms such as polymer swelling, viscoelastic relaxation, and concentration-dependent diffusivity.

For example, Peppas and Merrill (1977) show that swelling behaviour of crosslinked PVAl hydrogels is governed by variable polymer to solvent interaction parameters, indicating that the uptake process cannot be fully described by classical diffusion theory [307]. On the other hand, Thomas and Windle (1982), developed a mechanistic model where solvent transport in glass polymers is coupled to stress induced deformation, resulting in sharp diffusion fronts and constant rate uptake, characteristic of non-Fickian behaviour driven by polymer relaxation rather than simple diffusion [308]. Vrentas and Duda (1977) further expanded on this by introducing a free-volume theory in which the diffusion coefficient varies with temperature, molecular weight and concentration, capturing the deviations from idealized Fickian transport [309]. More recently, El Aissaoui and El Afif (2017) modelled mass transfer in swelling, viscoelastic membranes using a fully coupled diffusion stress framework, highlighting how internal stresses reshape solvent flux in time and space [310].

This type of behaviour is not limited to hydrogels or glassy polymers. As seen in literature, semicrystalline materials like PET can exhibit non-Fickian transport, especially when penetrants induce significant swelling or interact with amorphous regions. For instance, Billovits and Durning (1988) reported that diffusion of acetone and DMF in semicrystalline PET films deviated strongly from Fickian kinetics, with behaviour depending on both the solvent type and the crystalline fine structure [311]. These findings illustrate that the standard assumptions behind permeability calculations may not always valid, particularly in systems where the polymer morphology or solvent-polymer interactions introduce complex transport dynamics.

Moreover, while Henry's law is often used to describe gas sorption into polymers, it does not adequately describe water sorption in PET, particularly because Henry's law in its simplest form does not explicitly incorporate temperature effects. As shown in (Figure 3-16), experimental data indicate that the solubility of water in PET decreases with increasing temperature in contrast to temperature invariant solubility predicted by Henry's law.

In terms of literature, Sammon *et al*, showed that water diffusion in PET follows Fickian kinetics with minimal swelling, but they do not examine temperature effects or test Henry's law assumptions [312]. Burgess *et al.* showed that diffusion remains Fickian only up to a water activity of ~0.6 (*i.e.* 60% RH), beyond which non-Fickian relaxations and concentration-dependent transport emerge. While neither study directly addresses Henry's law, these findings imply deviations from its assumptions at elevated humidity [313].

In line with this, consequently, as temperature increases, two opposing effects arise: (1) the diffusion coefficient tends to increase (making water permeate faster), but (2) the solubility of water may decrease (reducing the driving force for water uptake in the polymer). These competing factors can explain why permeability might not increase monotonically with temperature.

This discussed, Figure 3-21 presents Ea for water vapour permeability in uncoated PET, tested under various RH conditions using two different experimental methods:

1. **MOCON Aquatran**, yielding a relatively narrow range of negative Ea values (-3.67 ± -0.73 KJ/mol), with a range of -5.96 to -0.17 KJ/mol, some

low Ea estimations at low RH (35 to 40%), while Ea's above 45% RH all field a similar range.

2. **Ca test**, which shows a wider scatter (likely due to less precise environmental control) also yields a negative Ea, values consistent with MOCON Results except for the 71% RH, with a significantly lower estimation.

Comparing the activation energies derived from WVTR and permeability coefficients reveals the critical role of partial pressure gradients. The positive activation energy observed for WVTR is driven largely by the exponential increase in saturation water vapor pressure with temperature. However, the intrinsic permeability of the PET substrate exhibits a negative apparent activation energy, confirming that transport mechanism is thermodynamically limited by solubility [285, 304].

Moreover, it is pertinent to mention that the linear Arrhenius fits applied here provide an average value over the temperature range (14 to around 50°C). The interactions between water and PET, including clustering and plasticization, are concentration dependent. Since water concentration in the polymer changes with both humidity and temperature, the activation energy of diffusion is likely not constant but varies with the state of plasticization. Therefore, the observed behaviour may not be purely Arrhenius, and the reported apparent activation energy values should be interpreted as effective temperature coefficients for this specific environmental window rather than fundamental material constants representing a static energy barrier.

Several literature data sets (*e.g.*, Deng and Erlat) also reported a negative Ea, corroborating that in some formulations or testing conditions solubility can be the

governing factor. Conversely, Fahlteich, Piergiovanni, Sobrinho, and B.M. Henry present positive Ea results, indicating that the PET samples these groups used became more permeable with increasing temperature (diffusion dominated). Such differences can arise from polymer additives, manufacturing processes, variations in crystallinity or moisture interactions. If the substrate is sufficiently "open" or plasticized at higher temperatures, diffusion can dominate and lead to a net positive Ea.

Overall, the data underscore the complex interplay between diffusion and solubility in dictating permeability. When solubility drops quickly as temperature climbs, the Ea for permeability can become negative. When chain mobility and free volume increase more significantly and solubility does not decline as much, permeability may rise with temperature giving a positive Ea.

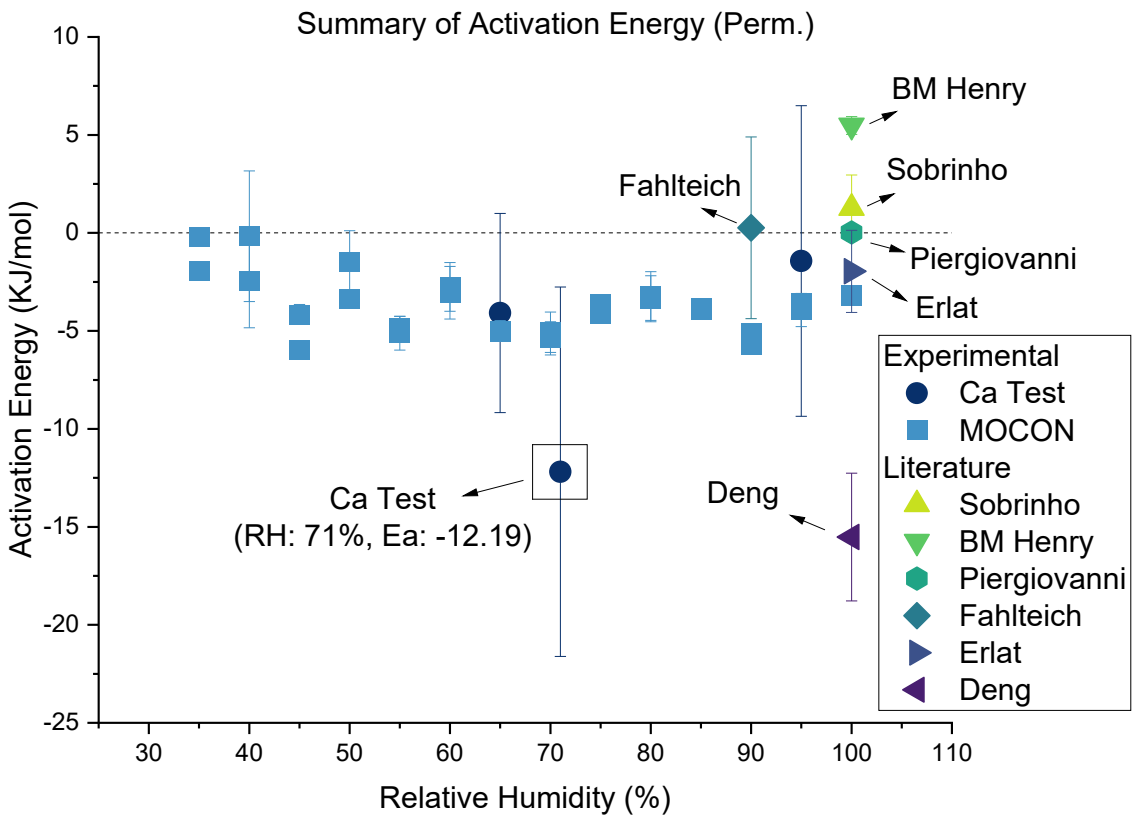


Figure 3-21: Summary of Activation energy (Ea) based on permeability coefficients across relative humidity ranges, comparing experimental data (MOCON and Ca Test) with literature. Negative values indicate solubility-dominated behaviour, where PET absorbs fewer water molecules at higher temperature, reducing overall permeability. Positive Ea values from other studies point to diffusion-drive increases in permeability with temperature, underscoring how polymer structure, additives, and test conditions can shift the balance between solubility and diffusion.

3.7 Summary

This chapter focuses on the application of two test methods—MOCON Aquatran 2 and the calcium (Ca) test—to evaluate uncoated PET substrates. It highlights how elevated temperature and relative humidity (RH) conditions affect the water vapor transmission rate (WVTR), consistent with literature findings that higher temperatures and RH generally increase WVTR. Notably, while trends agree between methods, the absolute WVTR values obtained from MOCON Aquatran 2 are substantially higher than those measured using the Ca test and referenced literature values, raising concerns about the MOCON testing conditions and/or sample handling protocols. These differences underscore the importance of proper calibration and standardized measurement procedures when characterizing barrier properties.

In addition to reporting WVTR data, the chapter delves into permeation calculations for PET. Henry's law was also tested to examine the relationship between water vapour pressure and permeation, with results indicating a generally linear dependence—particularly for the MOCON Aquatran measurements and certain literature. Furthermore, calculated permeability coefficients were used to normalize for thickness and the prevailing pressure gradient across the PET layer, providing a more comprehensive comparison of barrier performance under different testing conditions.

This approach emphasizes the necessity of considering both material geometry and partial pressure differences when interpreting permeation data.

Furthermore, a key discussion in this chapter centres on the activation energy (Ea) derived from both WVTR and permeability measurements. The WVTR-based Ea reflects the apparent energy barrier for water vapor transport through the polymer film, capturing how temperature influences the rate of molecular diffusion. By contrast, the Ea based on permeability provides insight into the intrinsic properties of the polymer itself, separating the contributions of diffusion and solubility. These findings serve as a baseline for subsequent chapter, where it will help explain the nature of defects or permeation mechanisms in coated PET barrier layers.

4 Aluminium Oxide - AlO_x (ALD) Coated PET

4.1 Encapsulation with ALD

As discussed in the literature review (Section 1.7.2.a), atomic layer deposition (ALD) is a form of chemical vapor deposition (CVD) known for producing uniform, dense, featureless barriers, regardless of surface roughness (*i.e.* there is excellent step coverage), and consistent films with precise thickness control down to the angstrom level. Such coatings provide a promising route to prevent water and oxygen degradation for moisture sensitive electronics [73, 177, 217, 314-320].

The ALD method also enables multilayer deposition, doping, and operates at relatively low temperatures, with reports as low as 33°C—ideal for direct integration in OLED manufacturing processes[217, 321, 322]). ALD coatings are highly conformal, covering high aspect ratio structures and various surface morphologies, including 3D substrates [323].

However, ALD is slow (increasing costs), has limited material options, and large-scale production methods like spatial and roll-to-roll ALD are still under development [324] Ultraclean surfaces (*e.g.* cleanroom [325]) and some inherent deposition process issues (self-limiting or elimination of precursor before switching to next precursor, deposition under high vacuum) are required [177, 179, 314, 315, 326, 327].

ALD has gained interest as an encapsulant and barrier layer for gas and water vapor due to its ability to coat over inclusions and roughness in polymer substrates. The following studies explore ALD's effectiveness as a barrier through WVTR characterization and defect detection.

For example, for widely used thermal ALD process uses Aluminium oxide using trimethyl aluminium (Al $(CH_3)_3$ (g) and water vapour (H_2O) (g). In each cycle, Al $(CH_3)_3$ reacts with surface hydroxyls (OH) to form a methyl-terminated Al species and evolve methane. The subsequent H_2O pulse hydrolyses the methyl groups, regenerating – OH (surface). This prepares the surface for the next TMA pulse to create Al – O – Al linkages, growing a solid AlO_x or possible Al_2O_3 (s) film grows in a self-limiting manner (Figure 4-1). The conventional ALD window (~150 to 200°C) has a growth per cycle on the order of ~1.0 Å per cycle; at lower temperatures (sometimes those used in this work), the effective growth rate can deviate due to incomplete reactions and higher -OH content [33, 178, 322, 328-333].

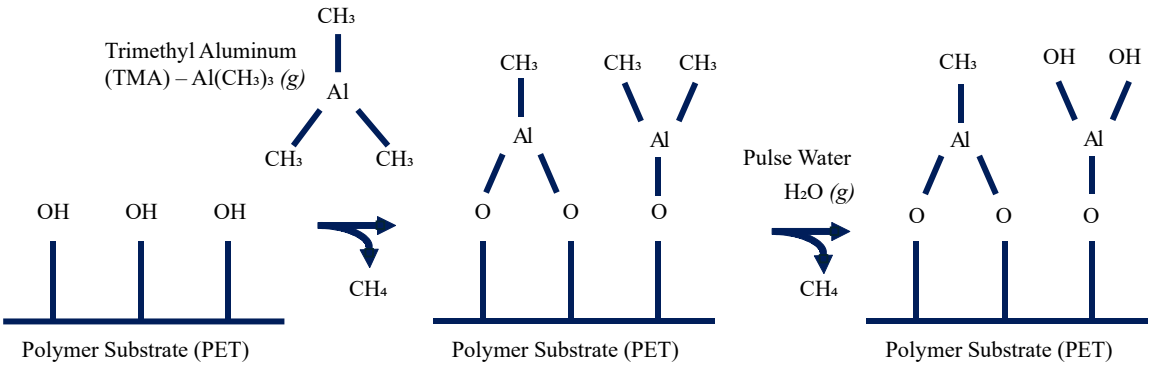


Figure 4-1: Proposed Mechanism for a Thermal ALD Al_2O_3 from TMA/H_2O. Gaseous trimethylaluminum reacts with surface hydroxyl groups to form a methyl-terminated aluminium species and methane, – OH $_{(surface)}$ + $Al(CH_3)_{3\ (g)}$ → – O – $Al(CH_3)_{2\ (surface)}$ + $CH_{4\ (g)}$. An N_2 purge remove excess TMA and CH_4. Subsequent exposure to water vapour hydrolyses the surface methyl groups, regenerating – OH $_{(surface)}$ and evolving methane, – O – $Al(CH_3)_{2\ (surface)}$ + $2H_2O$ → – O – $Al(OH)_{(surface)}$ + 2 $CH_{4\ (g)}$. A second N_2 purge clears residual H_2O and CH_4, leaving the surface re-hydroxylated for the next cycle. Net per cycle is then: 2 $Al(CH_3)_3$ (g) + 3 $H_2O_{\ (g)}$ → $Al_2O_{3\ (surface)}$ + 6 $CH_{4\ (g)}$/ Gas phase species are denotated (g) and chemisorbed species as (surface); the deposited Al_2O_3 is also thought to be an amorphous solid (s) on PET under a typical temperature window. Importantly, the final step in this diagram also illustrates the potential for incomplete hydrolysis (residual – CH_3 units) often observed at lower temperatures, such as what is observed in this work. These type of deviations from the ideal cycle contribute to higher – OH content and the formation of non-stoichiometric AlO_x rather than pure Al_2O_3 [33, 178, 322, 328-333].

Numerous studies have validated the performance of ALD AlO_x or Al_2O_3 coatings as effective moisture and oxygen barriers across a range of polymer substrates. Barrier performance has been shown to depend strongly on factors such as processing temperature, film density, thickness and substrate preparation. Higher processing temperatures generally lead to denser films with lower WVTR values, while plasma enhanced ALD (PE-ALD) and multilayer configurations (*e.g.* Al_2O_3/SiO_2 stacks) have been employed to improve hydrolytic stability. Reported WVTR's span several orders of magnitude with values as low as 10^{-5} g/m^2·day under specific conditions.

Given the breadth and technical details of these studies, a structured comparative summary, including deposition conditions, film thickness, substrate type and observed WVTR's is provided in the supplementary information: 9.3.1 Relevant Literature Summary on ALD AlOx Barrier Coatings.

These findings were used to inform the encapsulation strategies used in this work and served as a benchmark for evaluating the performance of ALD-coated PET and also PVAl substrates in subsequent sections (5 Aluminium Oxide (ALD) Coated PVAl)

4.2 AlO_x on PET – MOCON Aquatran

4.2.1 Key Factors in Measuring WVTR of AlO_x Using MOCON Aquatran

4.2.1.a Temperature Effects on WVTR of ALD AlO_x

An important consideration is the environmental influence on coated barrier layers, particularly the impact of testing temperature on measured WVTR. While RH was not varied for this data set, analysing the temperature dependence of WVTR under constant RH is crucial. This analysis allows for the calculation of an apparent Ea, for permeation a

valuable tool for understanding the origins of water vapor permeation and the nature of defects in the barrier coatings. Although the discussion in Chapter 3.6.2 Permeation Analysis: Role of Water Vapour Partial Pressure and Comparative Methodologies shows that temperature was not a major factor for uncoated PET once WVPP was taken into account, this section focuses on how temperature dependence can reveal the permeation mechanisms in coated films (other supporting and relevant discussion is also found in 9.3 Aluminium Oxide (ALD) Coated PET Supporting Materials).

Figure 4-2, demonstrates a clear temperature dependence of WVTR for both the uncoated (bare) and coated ALD AlO_x substrates. As expected from thermally activated diffusion processes, WVTR increases with temperature across all samples. However the magnitude of this temperature dependence varies significantly, which is key to understanding the permeation mechanism.

Bare substrates exhibit the highest WVTR values and the strongest sensitivity to temperature changes. This temperature dependence is used to distinguish between different permeation pathways. If permeation is dominated by macro defects (*e.g.* pinholes or scratches), where there is little interaction between water vapour and the barrier coating, the permeation Ea is expected to be like that of the uncoated PET substrate (~42 kJ/mol). Conversely, if permeation occurs through nano-defects or the oxide lattice itself, where interaction with the coating is significant, an increase in the permeation Ea would be expected.

The presence of ALD AlO_x coatings significantly alters this behaviour. As shown in Figure 4-2, thinner coatings exhibit a stronger sensitivity to temperature, while thicker coatings (>26 nm) show a notable reduction in this effect. This suggests a change in the

dominant permeation mechanism with increasing coating thickness, moving from substrate-controlled transport through macro defects towards barrier-controlled transport.

Further analysis, discussed in following section (4.2.1.b Influence of ALD Thickness of WVTR of ALD AlO_x), explores the degree of this resistance influenced by the AlO_x coating thickness.

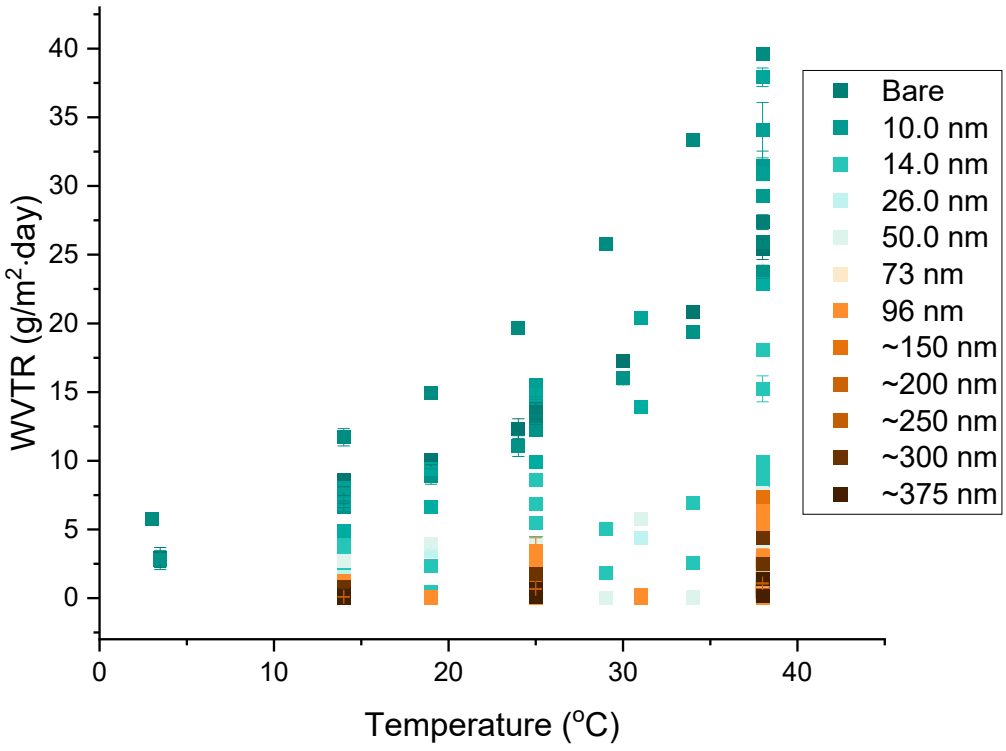


Figure 4-2 WVTR of uncoated and ALD AlO_x PET tested using MOCON Aquatran of varying thicknesses tested across a range of temperatures, highlighting the expected temperature dependence of WVTR. Thinner coatings exhibit a stronger sensitivity to temperature, while thicker coatings (> 26 nm) demonstrate a notable reduction in this effect.

4.2.1.b Influence of ALD Thickness of WVTR of ALD AlO_x

The process temperature and structural properties of ALD AlO_x coatings influence their water vapor barrier performance (for data, see the supplementary information: 9.3.4.a Influence of ALD Processing Temperature). While a rigorous evaluation of

barrier function requires accounting for both thickness and the partial pressure gradient (WVPP), the present section begins with WVTR-based analysis for comparison with previously published studies.

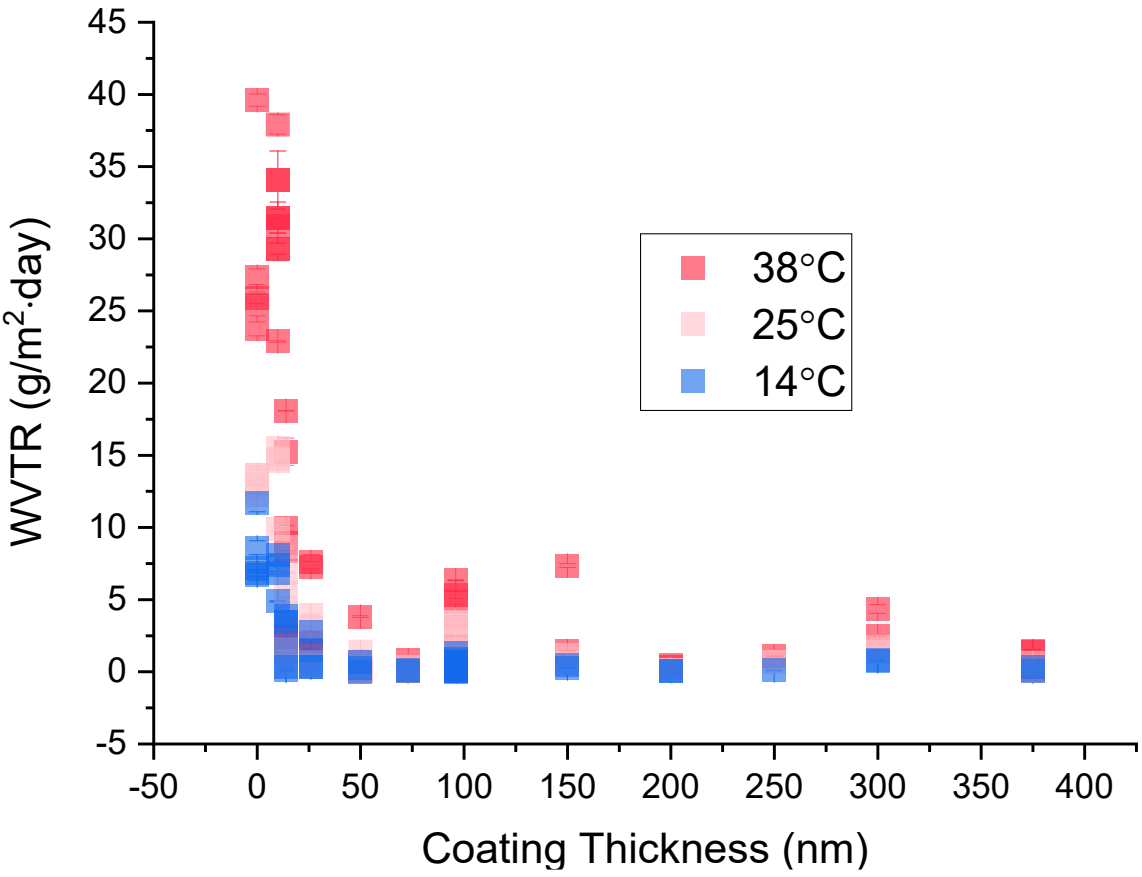
Moreover, identifying the optimal ALD thickness for achieving the lowest WVTR is informative. Literature shows that layers between 25 to 43 nm thick typically offer best barrier performance, coatings below this range (undercoating) leads to inadequate coverage, while thicker films beyond this range yield diminishing returns, offering minimal additional improvement in WVTR while incurring higher material and processing costs [255, 334]. This balance is particularly important for ALD, as its deposition rate is significantly lower than other deposition techniques.

Honing this point further**,** Figure 4-3 highlights the relationship between AlO_x coating thickness and WVTR, segmented by temperatures (14°C, 25°C, and 38°C, all at 100% RH). The WVTR decreases significantly with thickness, particularly below ~14 nm, where the coating coverage remains insufficient. However, differences between thicker coatings are harder to distinguish visually. To address this, a logarithmic scale reveals the nuanced relationship: WVTR values reach their lowest levels around 50 nm, plateauing beyond 100 nm. While significant improvements are observed even at ~26 nm, the best barriers occur up to ~50 nm, where the WVTR can be as low as 0.00525 ± 0.004 $g/m^2 \cdot day$ at 14°C and 100% RH.

Notably, this optimal thickness is slightly higher than ranges reported in some literature. However, the study by Klumbies *et al.* supports a sub-exponential decrease in WVTR with thickness beyond ~25 nm, attributed to reductions in defect density which

continues to improve exponentially up to ~100 nm [334]. This connection is further explored in Section 4.8 Influence of Spots and Defect Sizes to AlO_x Barrier Properties

In summary, the data suggest that an optimal thickness for ALD AlO_x coatings on PET barriers may lie around 50 nm.



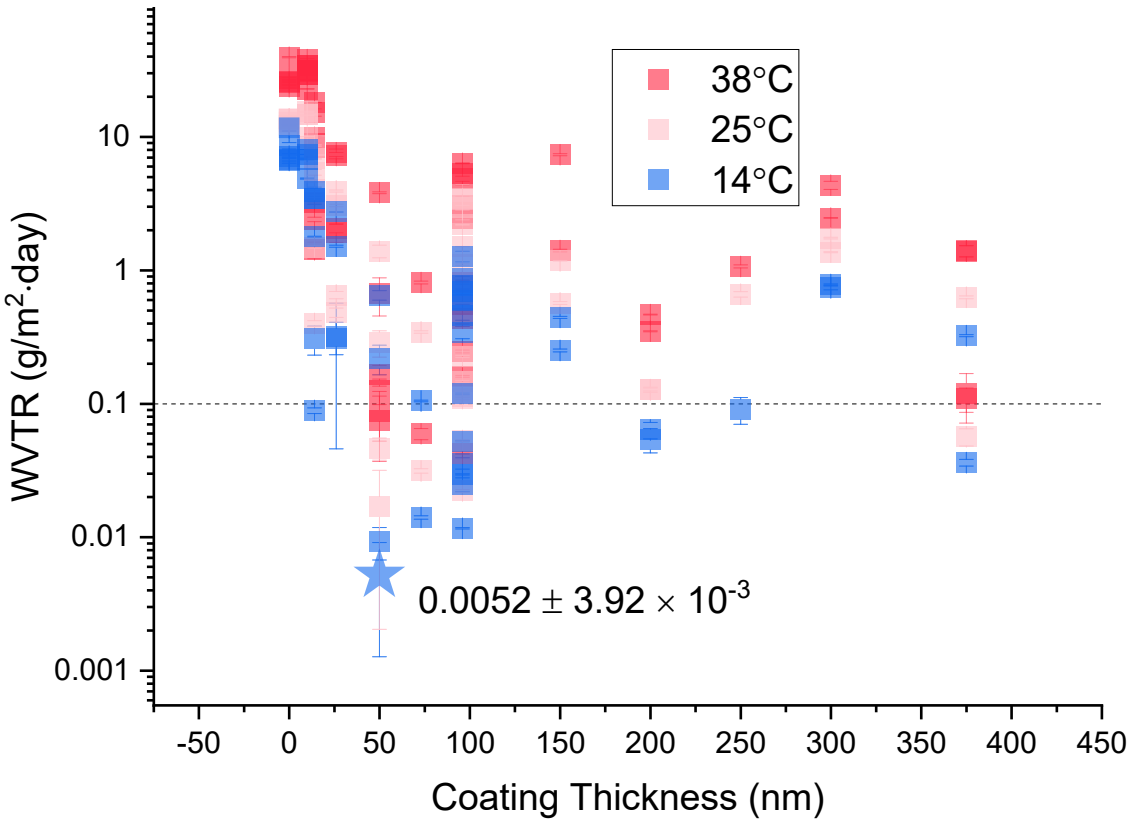


Figure 4-3: WVTR of AlO_x coatings on PET substrates as a function of coating thickness, measured tested at three different temperatures (14°C, 25°C, and 38°C), under 100% RH using Mocon Aquatran 2. The linear scale highlights the overall decrease in WVTR with increasing coating thickness, showing a noticeable plateau at larger thicknesses. The logarithmic scale reveals more detailed trends, indicating that the lowest WVTR values are predominantly achieved at a thickness of ~50 nm, suggest the optimal thickness to be around this point.

4.2.2 Permeability of AlO_x-Coated PET (MOCON Aquatran)

The permeability of AlO_x-coated PET was calculated using the MOCON Aquatran results for all tested conditions and samples. To reiterate, permeability is an intrinsic material-specific property that normalizes WVTR by the film thickness and the water vapour partial pressure difference, enabling direct comparison across different samples and conditions.

As shown in Equation 2-3, for this case, the assumed total thickness comprises both the ALD AlO_x coating, and the PET substrate was used. This approach aligns with the physical configuration of the samples as tested in the MOCON Aquatran system and considers that both layers contribute to the total diffusion path length. The oxide thickness (~10 to 375 nm) is orders of magnitude smaller than the substrate thickness (~ 100 µm), its inclusion does slightly influence the calculated permeability.

Figure 4-4**,** illustrates permeability as a function of coating thickness, the trend observed aligns with the WVTR results shown in Figure 4-3, confirming that the optimal coating thickness is approximately 50 nm. Beyond this thickness, additional improvements in permeability are minimal, indicating a point of diminishing returns.

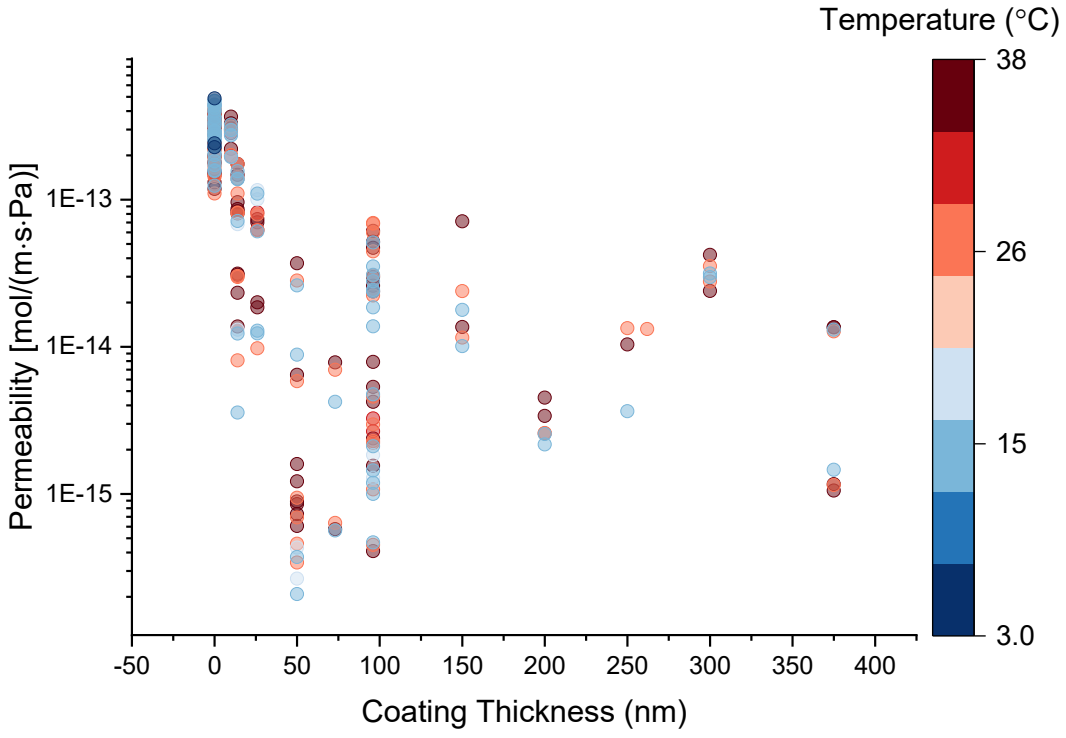


Figure 4-4: Permeability [mol/(m·s·Pa)] of AlO_x-coated PET as a function of coating thickness (oxide thickness), based on measured WVTR values using Mocon Aquatran at different temperatures at a constant RH of 100%. Permeability was calculated using

*Equation **2-3**, where the total film thickness (oxide and PET substrate) was used as the diffusion path length. Although the oxide thickness is used on the x-axis, the calculated permeability accounts for the full sample thickness. Using a logarithmic scale shows that permeability decreases with increasing oxide thickness, reaching an optimal level around 50 nm, after which further thickness provides minimal additional improvement or an increase in permeability.*

4.2.3 Ea of AlO_x-Coated PET (MOCON Aquatran) using WVTR

The issues discussed prompt a deeper examination of permeation mechanisms in AlO_x - coated barrier layers. Figure 4-5 shows the natural log of WVTR over inverse temperature, with slopes used to estimate a WVTR Activation Energy (Ea) for samples with various AlO_x thickness, where these slopes are used for Ea calculations in Figure 4-6.

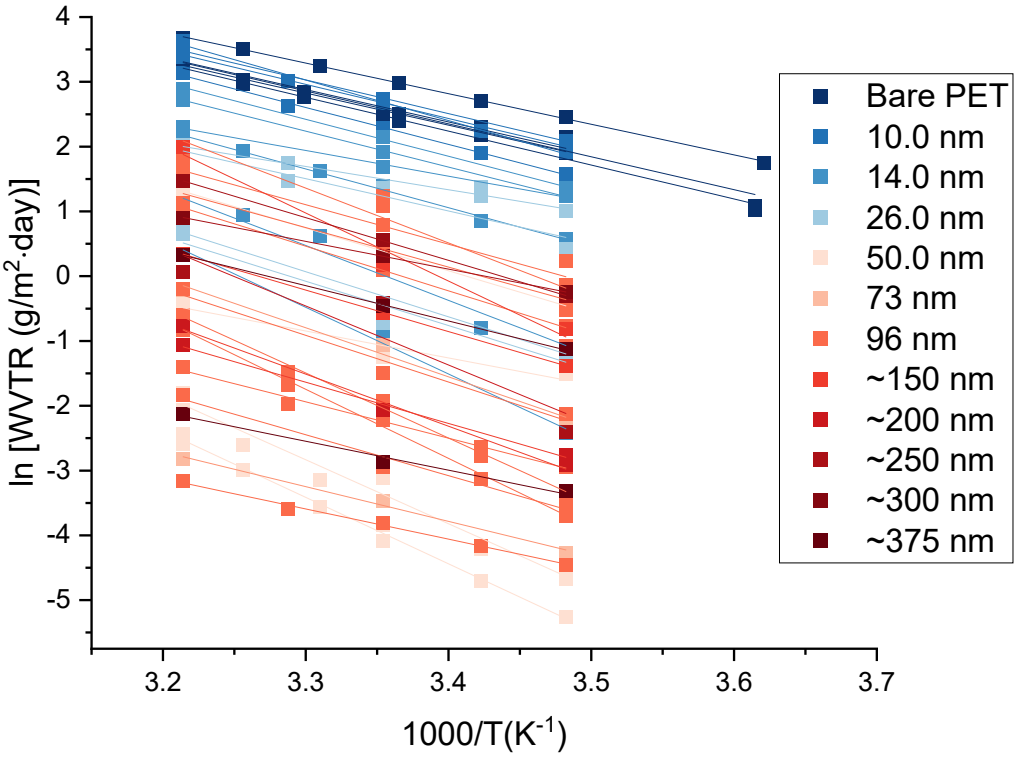


Figure 4-5: Natural log plot of WVTR vs. inverse temperature (Arrhenius plot), grouped by AlO_x thickness. The slope can be used to estimate an Ea of the barrier film for each thickness of coating.

Ea or apparent activation energy of permeation (in this case for WVTR) has been used to gain insight into the permeation mechanisms of a barrier film. For AlO_x-coated PET, a baseline Ea of ~42 kJ/mol (the PET substrate) indicates whether permeation occurs through macro defects (Ea near or below 42 kJ/mol – shown in 3.5.2 Summary of Activation Energies) or nano defects (Ea significantly above 42 kJ/mol) explained in 1.5.1 Macro and Nano Defects.

Deviations from this baseline can indicate interaction with coating material, a significant shift toward a positive Ea value suggests a transition to diffusion dominated transport through nano defects or grain boundaries within the oxide lattice. In this regime a high kinetic energy barrier is required for water molecules to pass through dense ceramic structures that dominate the thermodynamics that result in the positive temperature coefficient. Conversely intermediate values may also suggest a mixed regime where surface diffusion along pore walls contribute to the total flux.

Figure 4-6, plots Ea against AlO_x thickness, revealing variability in Ea as the coating thickness increases. While a notable increase in Ea is observed after ~14 nm (125 cycles, indicated by the dashed vertical line) for some samples, there is not a consistently higher Ea across all samples. Instead, the variability suggests that the formation of a good coating with minimal defects is critical, and the coating thickness alone does not guarantee this, with a spread of results within conditions, perhaps due to the different defect populations within the small testing area. The highest Ea recorded, at 88.73 ± 3.77 kJ/mol for a 96 nm sample, indicates that at this thickness, macro defects are sufficiently

reduced, and a significant proportion of the permeation is through nano defects or intrinsic diffusion mechanisms through the coating.

For thinner samples (~10 nm, 63 cycles), no significant increase in Ea is observed, with macro defects as the primary permeation pathway. Interestingly at around ~14 nm, while the Ea remains comparable to that of the substrate, there is potential for producing good-quality films, as indicated by two samples with significantly higher Ea values. For thicker films, there is some indication of higher Ea values, suggesting a reduction in macro defects but still with a lot of variability. Notably, very thick coatings do not consistently result in higher Ea, with tested samples often exhibiting relatively low values. Some samples even showed lower-than-expected Ea, falling outside the PET substrate's standard deviation range (36.55–46.78 kJ/mol). These findings suggest that these samples may contain significant macro-type defects or imperfections within the small area tested (masked samples), which dominate the permeation process. Further work is needed to clarify these effects and better understand the variability in Ea across different coating thicknesses.

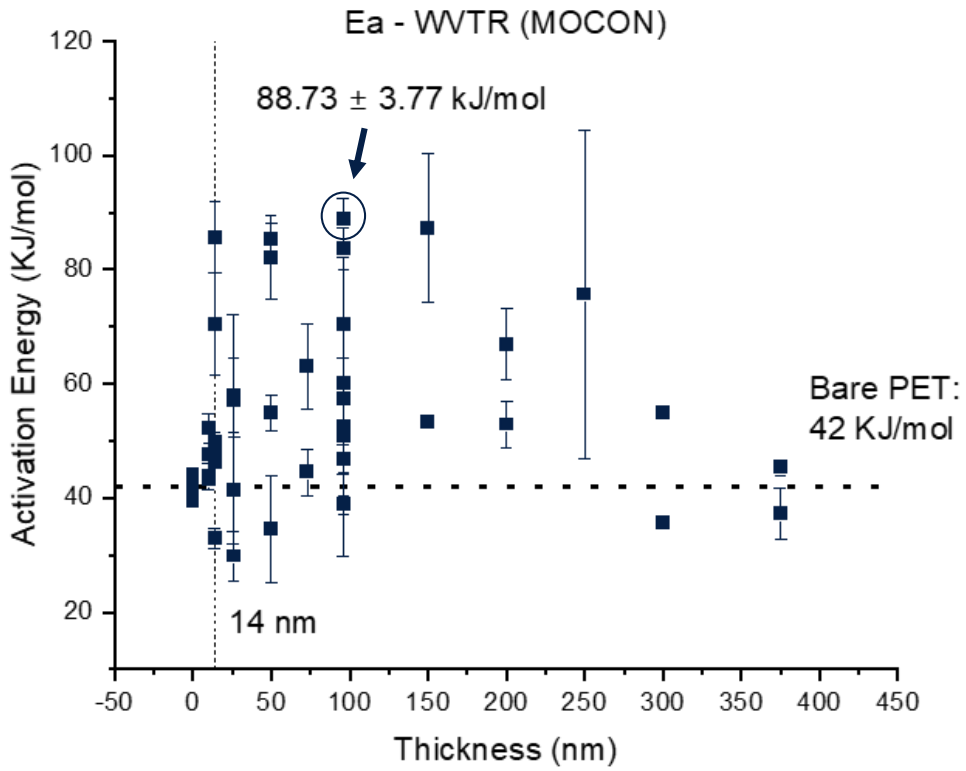


Figure 4-6: Activation Energy (Ea) of AlO_x-coated PET substrates across thicknesses, showing an initial increase followed by a plateau and decrease in coatings beyond 300 nm. The figure highlights variability in Ea, with some thin coatings sometimes falling below the Ea of bare PET, indicating potential film damage.

4.2.4 Ea of AlO_x-Coated (MOCON Aquatran) using Permeability

As discussed, calculating Ea using permeability considers the dependence of the product of the diffusion and solubility coefficients with temperature. For the uncoated PET films (see Figure 3-19) the gradients were small and often slightly positive suggesting there is a low influence of temperature on D.S *e.g.* the effect of the activation energy required for a water molecule to diffuse through the polymer (D) may be comparable to the effects (in the opposite direction) of temperature on S. For these coated layers, the same observation can be made for many of the samples. However, in

some cases, and this is particularly the case where there a lower value of permeability with coatings of moderate thickness, there is a significant negative gradient in the plots of Figure 4-7. This may reflect examples in which the polymer is no longer controlling the mechanism of permeation (such as would be expected through micro-defects), but that now there is some element of interaction between the water and the coating playing a part in the observed permeation.

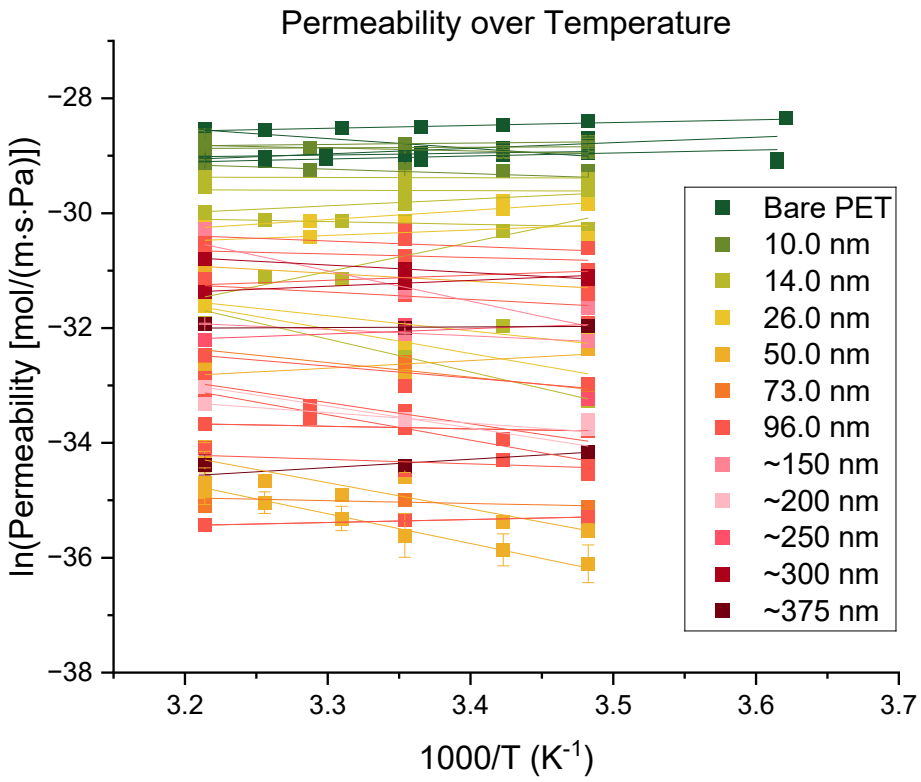


Figure 4-7: Natural log plot of Permeability coefficients over inverse temperature, grouped by AlO_x thickness, shows varied trends and slopes, indicating that permeability does not consistently increase with temperature. This behaviour reflects a complex interplay between diffusion and solubility coefficients. Thicker coatings may influence water vapor interaction due to surface properties or defects, potentially trapping or repelling water molecules, combine with temperature dependent changes in solubility, may explain the non-monotonic trends observed.

Figure 4-8, illustrates the apparent activation energy for water vapor permeability as a function of AlO_x coating thickness on PET. A fundamental thermodynamic transition is observed: uncoated PET (0 nm), and very thin coatings exhibit negative E_{app} values, indicating solubility-dominated behaviour characteristic of a hydrophilic polymer substrate like PET (where exothermic enthalpy of sorption dominates the kinetics).

In contrast, as coating thickness increases (>10 nm), the system shifts to positive E_{app} values. This polarity reversal indicates a transition to diffusion dominated regime. The rate limiting step is no longer the thermodynamic equilibrium of sorption into the polymer but the kinetically hindered diffusion of water molecules through the AlO_x structure or restricted nano defects within it. The positive activation energy of diffusion associated with the rigid oxide lattice outweighs the solubility term. This transition confirms that the AlO_x layer has achieved sufficient continuity to define the transport kinetics, acting as a true kinetic barrier rather than the system being limited by the substrate solubility.

For very thin coatings (< 10 nm), the coverage may be incomplete with pinholes or large penetration pathways dominating permeability. Intermediate thicknesses often achieve better coverage giving rise to significant, positive values of Ea, but the samples still exhibit variability due to microdefects or localized imperfections. At higher thicknesses (>100 nm), accumulated film stress may lead to a population of microdefects that again reduce the Ea.

Overall while positive Ea values dominate for thicker coatings, indicating some element to activated diffusion not observed for uncoated films, the data show that understanding defect populations is valuable to distinguish the origin of the WVTR value

in terms of defect nature (*e.g.* size such that coating interaction may become important) and population. The same value of WVTR can be achieved with many nano defects of higher Ea as a few microdefects with the low Ea associated with the substrate polymer. The Ca test imaging can thus be a useful tool for better understanding these populations.

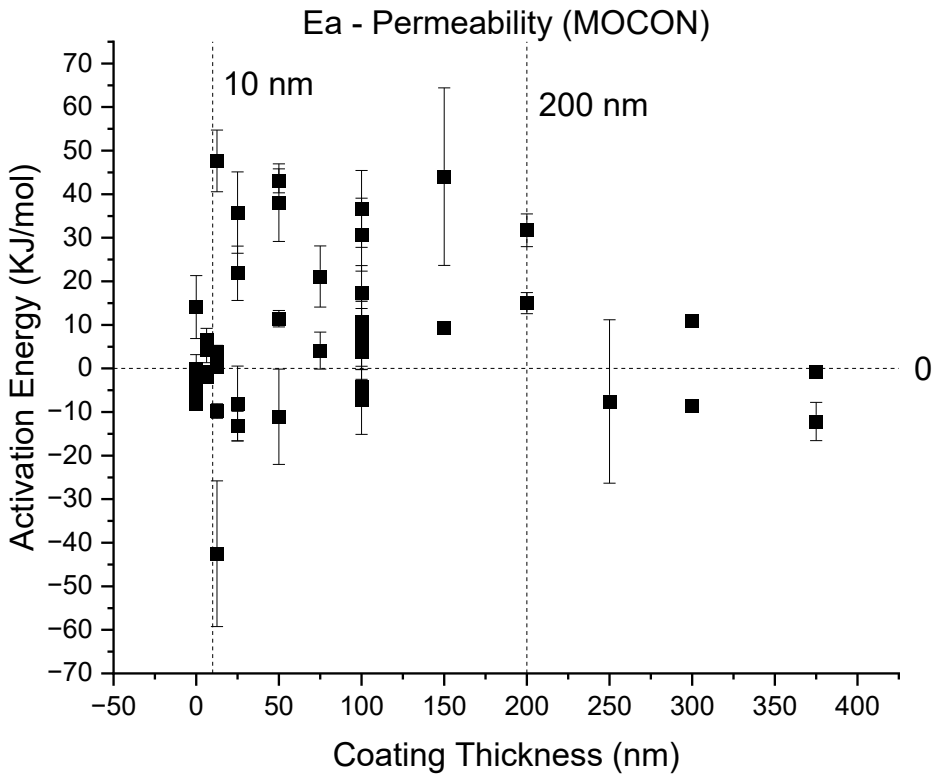


Figure 4-8: Ea for water vapor permeability in PET samples with various thickness of AlO_x via ALD. Positive Ea values (top rows) suggest a diffusion-dominated regime where permeability rises with temperature, while negative Ea values (bottom rows),m indicate solubility controlled behaviour – coating and substrate combination admits fewer water molecules as temperature increases. The large variability and standard deviations may reflect differences in microstructure, pinholes and possible measurement uncertainties.

4.3 AlO_x on PET (ALD) – Ca Test

4.3.1 Permeability Estimations of AlO_x on PET

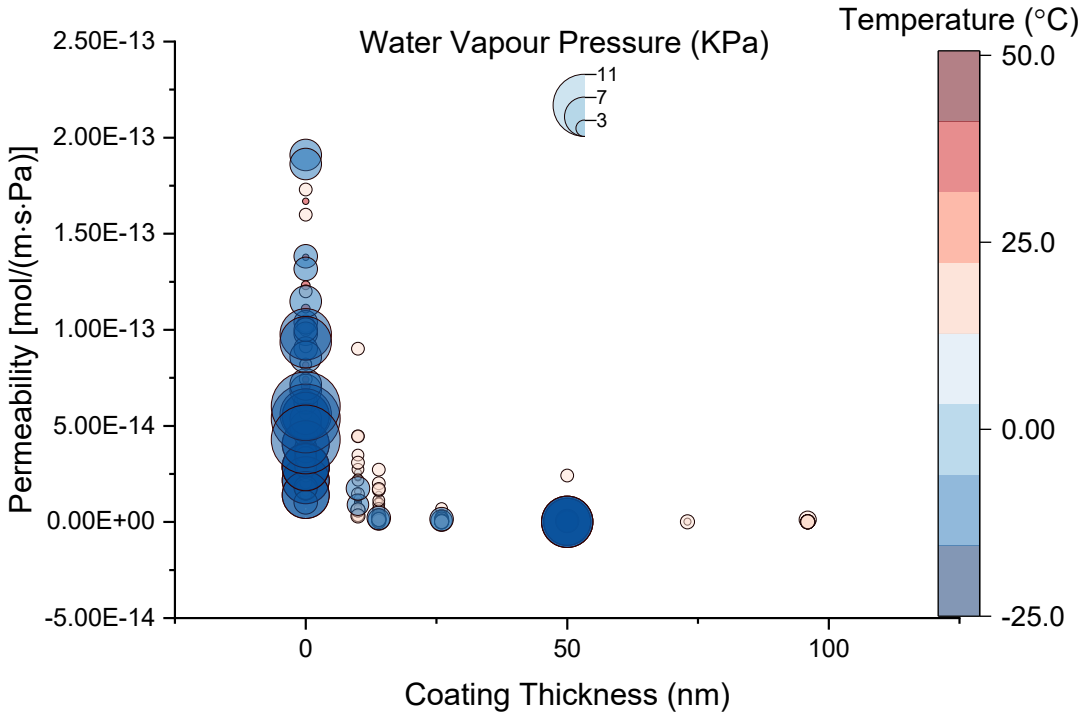
Calcium tests were conducted on AlO_x - coated PET samples at varying thicknesses and under different environmental conditions, as humidity and temperature directly impact WVTR. These tests aimed to rapidly estimate the coating's barrier performance across a wide range of scenarios.

It is also relevant to clarify which Ca test up was used (Reference: 2.4.3 Calcium Test Set-up). For coatings above 14.0 nm, the "good barrier" setup was consistently used to allow for multiple samples to be tested simultaneously over the long test times involved. Below this threshold, particularly in the thinnest coatings ~10 nm or below and bare or uncoated substrates, rapid calcium degradation occurs and the "bad barrier" or *in-situ* setup was used to capture the Ca degradation.

A general "total" WVTR measurement was initially conducted from the images, considering the entire calcium-covered area (constant area), to quickly assess the influence of coating thickness on permeability. While this method does not account for edge defects or sideways permeation, potentially inflating WVTR, it still demonstrates the trend effectively as shown in Figure 4-9. The data set includes 236 measurements across samples with coating thicknesses from 10 nm (63 cycles) to 96 nm (1000 cycles), tested under different conditions: freezer at -25°C (69% RH), low temperatures around 18°C (43% RH), moderate at 29°C (48% RH), and high at 40°C (68% RH). Additional tests were conducted at 25°C with two relative humidities: 39.5% and 78.5%. As noted not all thickness / conditions sets were measured across the full temperature span – with

fewer than three temperatures this affects the Arrhenius fits of ln(WVTR) vs 1/T to yield an apparent activation energy (Ea) with a higher uncertainty. Limited temperature coverage also weakens the usual mechanism check to determine if it is a macro (defect or polymer limited – Ea) versus a nano (oxide or coating limited Ea).

Permeability decreases sharply with increasing coating thickness, plateauing around 50 nm, beyond which further thickness increases yield minimal improvement. This trend, consistent with MOCON Aquatran data, confirms that thickness is the key factor in determining permeability, with little benefit from exceeding 50 nm (statistically verified in 9.3.5 Statistically Verifying Influence of Temperature and Relative Humidity Towards Permeability of AlO_x films on PET Substrate.).



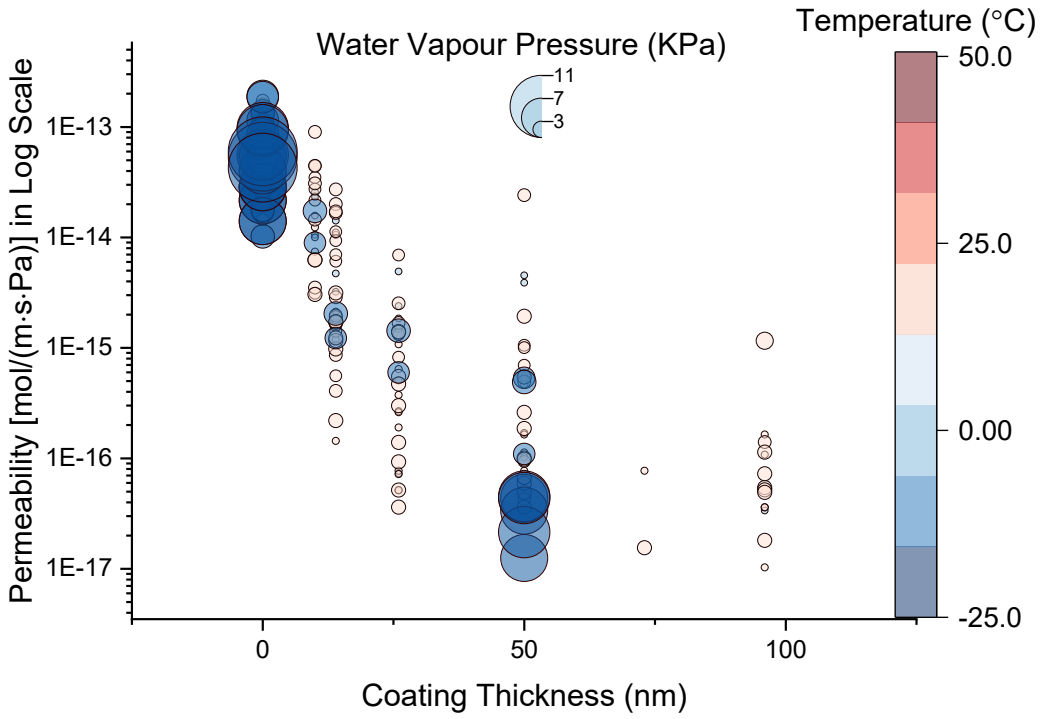


Figure 4-9: Permeability [mol/(m·s·Pa)] versus AlO_x thickness on PET, shown on both linear and logarithmic scales, reveals a consistent decline in permeability with increasing thickness, as observed through the Ca test. This trend holds across varying water vapor pressures, relative humidity, and temperatures. The data spread is like MOCON Aquatran results, with the trend clearly visible despite variations in test conditions and system controls. Note: temperature coverage limitation: some sets only include two temperatures and any Ea inferred from these points would be treated as apparent Ea's and cannot be extrapolated beyond the measured (T, RH), hence in subsequent Ea estimations required at least three temperatures.

4.3.2 ALD – AlO_x and RF Sputtered - Al_2O_3 or (AlOx)

An important comparison for polymer barriers is between ALD AlO_x and PVD alumina like films (*i.e.* RF Sputtered layers). This section explores the value of the Ca test, in revealing whether permeation may be dominated by macro-defects or by a high density of anno-defects. In RF-Sputtered Al_2O_3, Tobin, observed bright spots / lines associated with macro-defects together with progressive background greying across the Ca layer, indicating water-vapour ingress between macro-defects and hence a high

density of nano-defects [11, 194]. By contrast, the studied ALD AlO_x films maintain a dark, stable background with only localised bright features, consistent with far fewer nano-defects and a macro defect-limited regime.

Ca-test comparison

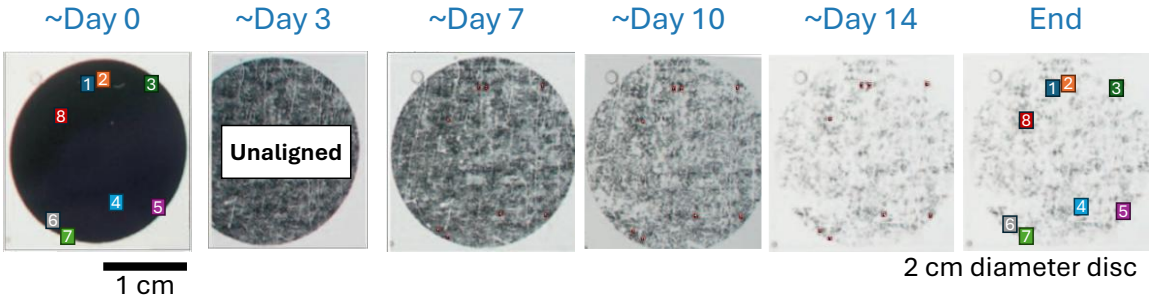
- RF Sputtered Al_2O_3 (literature, re-evaluated in Figure 4-10): BOPP (rough surface, ~ 145 nm Al_2O_3) and PEN (smooth surface, ~ 148 nm Al_2O_3) at 38°C / 85% RH both show pronounced background greying between bright macro-defect sites, consistent with nano-defect assisted transport [11, 194]
- ALD AlO_x (this study): PET with 14 - 100 nm AlO_x tested across different conditions 14 nm at 25°C and 39.5% RH ($MgCl_2$), 50 nm at 50.5°C and 27% RH (LiCl), 50 nm at 48°C and 50% RH ($MgCl_2$), and 100 nm at 25°C and 78.5% RH ($MgCl_2$), shows a near constant background grey level between macro-defects, possibly indicating this type of dominant defect for ALD under these conditions.

Activation energy trends align with these Ca test suggestions; wherein Tobin *et al.* reported WVTR Ea values of 67 kJ/mol for uncoated BOPP and 54 kJ/mol for uncoated PEN. The RF sputtered Al_2O_3 coatings raised these to 104 kJ/mol for BOPP and 84-95 kJ/mol for PEN, suggesting nano defect permeation makes a significant contribution [11, 194]. For ALD, Yoon *et al.*, also using ALD, reported an Ea of 50.8 kJ/mol for 100 nm Al_2O_3 on PET [335]. Similarly, Carcia *et al*, report WVTR for their best ALD alumina film approach the Aquatran detection floor limit (~1×10^{-4} g/m^2·day). For a 25 nm ALD Al_2O_3 film at 60°C / 85% RH measured by the optical Ca method, the steady state behaviour corresponds to a WVTR of around ~ 4×10^{-4} g/m^2·day (from figure and state

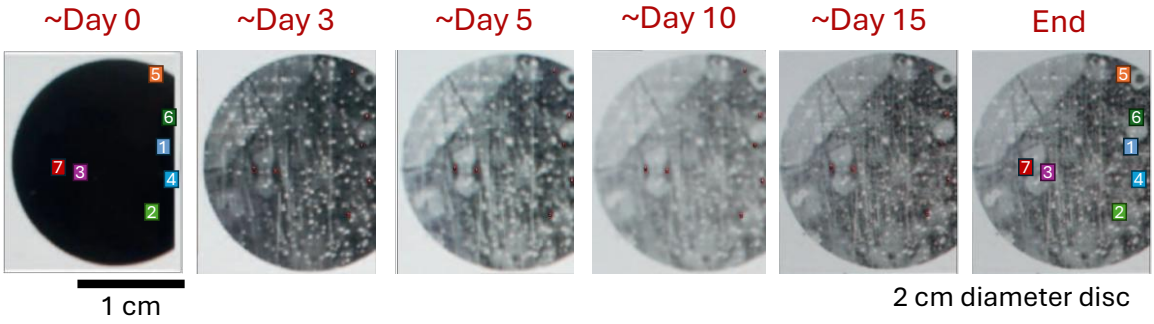
conversion). Using these two temperature as an indicative pair gives an apparent Ea ≈ 50 to 55 kJ/mol, noting that these assumptions were made at 38 °C near detection limit and configurations differ between Aquatran and Ca test [55, 218, 336]. The Ea data of the coated ALD substrates (Figure 4-6 and Figure 4-12) show modest or low apparent Ea reinforcing that permeation may be mostly dominated by microdefects rather than a high density of nano defects. A corresponding particle analysis study is also given in supplementary information: 9.3.8 Particle Analysis on RF Sputtered Films.

On an industrial note: pulsed DC reactive magnetron sputtering is a standard route for depositing AlO_x thin films, providing stable oxide deposition at practical power densities [337]. For polymer web barriers, reactive thermal evaporation of Al in O_2 to form AlO_x / Al_2O_3 is an established roll to roll process on industrial boat type metallisers, with web widths up to ~2450 mm and speeds up to ~840 m/min, and documented barrier or optical performance on PET and BOPP [338, 339]. These PVD / evaporation methods can deliver competitive thickness or optics when parameters (power waveform, duty cycle, pressure, reactive O_2 flow, and substrate temperature) are optimised. However, the line-of-sight geometry and energetic species tend to favour columnar or nano defect pathway making multilayer stacks favourable and used to interrupt any defect propagation for high barrier performance.

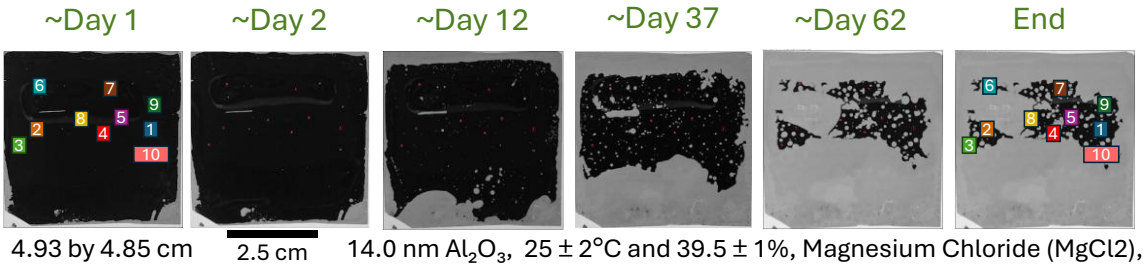
A.1 RF Sputtered: AlOx on Bi-axially Oriented Polypropylene (BOPP)



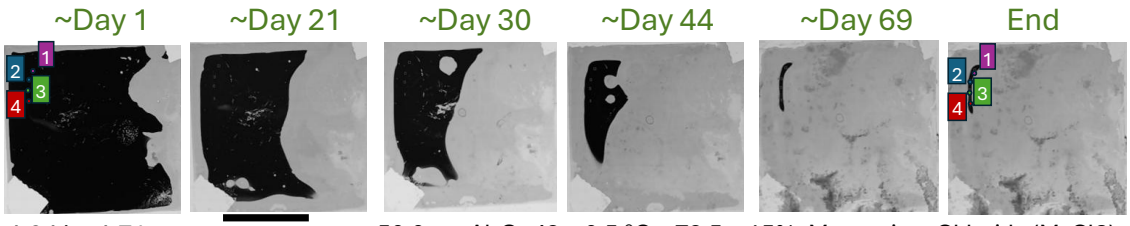
B.1 RF Sputtered: AlOx on Polyethylene Naphthalate (PEN)



C.1 ALD: AlOx on Polyethylene Terephthalate (PET)

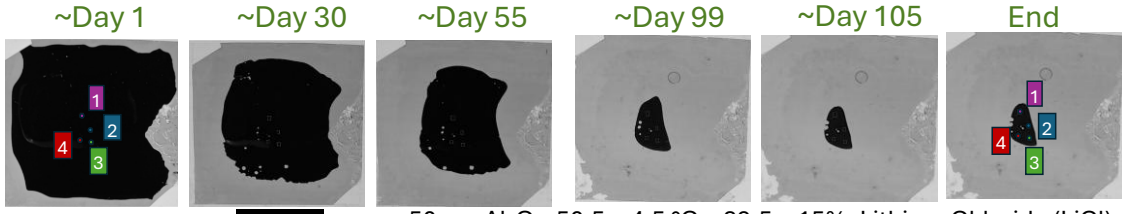


C.2



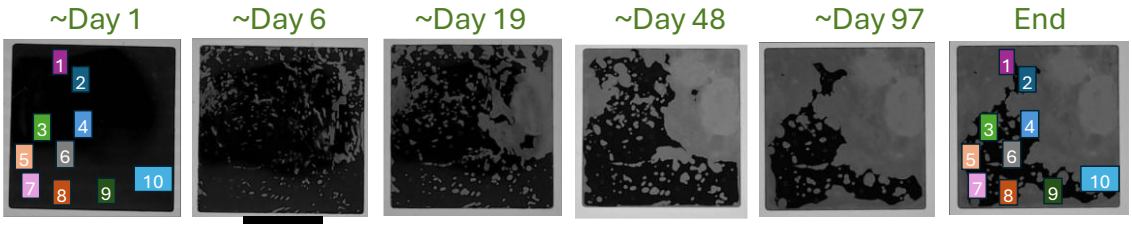
4.94 by 4.71 cm 2.5 cm 50.0 nm Al_2O_3 48 ± 0.5 °C ≈ 78.5 ± 15%, Magnesium Chloride (MgCl2)

C.3



4.95 by 4.78 cm 2.5 cm 50 nm Al_2O_3, 50.5 ± 4.5 °C ≈ 39.5 ± 15%, Lithium Chloride (LiCl),

C.4



3 by 3 cm 1.5 cm 100 nm Al_2O_3, 25 ± 1°C and 78.5 ± 1%, Magnesium Chloride (MgCl2),

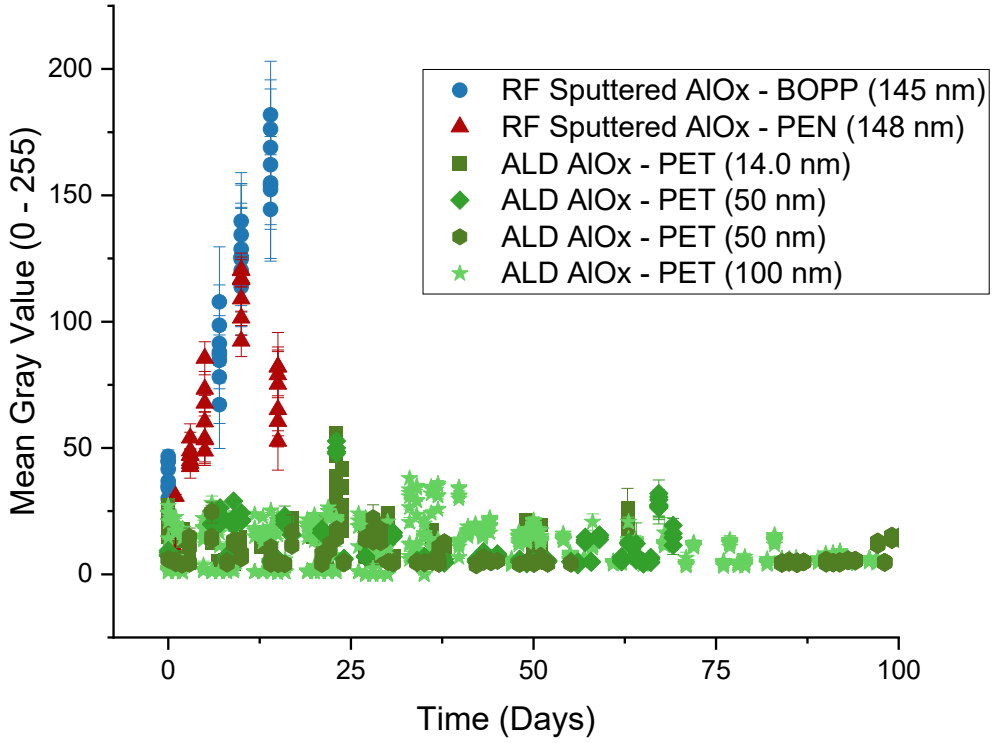


Figure 4-10: Ca test images with marked and pre-labelled points that lie between bright pin-hole-type bright spots used to measure mean grey values at these labelled points, showing the progression of background calcium degradation over time: A.1 and B.1 are RF Sputtered AlO_x on Biaxially Oriented Polypropylene and Polyethylene Naphthalate respectively, 2 cm diameter disc. 145 nm on BOPP and 148 nm on PEN at 38°C and 85% RH, as shown by Tobin et al. with seven randomly selected points around the sample and region of interest. For comparison this studies ALD AlO_x films on PET with varying thicknesses - 14 nm at 25°C, 39.5% RH (Saturated Salt: $MgCl_2$); 50 nm at 50.5°C, 27% RH (Saturated Salt: LiCl); 50 nm at 48°C, 50% RH (Saturated Salt: $MgCl_2$); and 100 nm at 25°C, 78.5% RH (Saturated Salt: $MgCl_2$) – also selected random points to measure mean grey values. These mean grey values at the selected points are plotted against time to allow localized tracking of permeation between macro defects. The results demonstrate significant greying in RF-sputtered films, indicative of nano-defects, while ALD films maintain stable grey values, highlighting better uniformity and barrier properties.

This contrast in optical degradation patterns, the diffuse greying versus discrete spotting, reflects a fundamental divergence in the underlying defect morphologies of the two deposition techniques. To fully attribute these failure modes, it is necessary to distinguish the specific defect mechanisms in these ALD coatings from those typical of PVD.

As reviewed by Kelly and Arnell, RF magnetron sputtered films often suffer from shadowing effects during deposition. In this process, atoms arriving in a straight line cannot fill the gaps behind surface irregularities, creating a structure full of physical nano-defects, specifically voids between columnar grains. These physical voids allow water to permeate the barrier uniformly, causing the widespread background greying seen in the sputtered samples [198].

In contrast the ALD films in this study maintained a stable, black background. Because ALD is a chemical process rather than a line of sight physical one like PVD, it coats the surface conformally and uniformly eliminating any possible physical voids. However this does not mean that ALD films are perfect. The defect landscape in these films consists of two distinct categories:

(1) Intrinsic Chemical Defects: Unlike the physical holes in PVD, defects in ALD are chemical. Gronert *et al*, establish films grown at low temperatures (<100 °C) retain high concentrations of hydrogen (up to 20 atomic percentage), primarily as unreacted hydroxyl (-OH) groups [322]. Carcia *et al.* propose that these hydroxyls act as a chemical pathway, allowing water to move through the film via a chemical exchange reaction rather than through a physical hole [55]. However, since the background remained black in this study, this intrinsic permeation is too slow to be the primary cause of failure.

(2) Extrinsic Macro-Defects: The primary failure mechanism, which created the discrete bright spots observed is extrinsic macro defects. Hanika *et al*, describes how thin barriers on polymer substrates are critically limited by surface irregularities; this can include anti block particles (microscopic additives used to prevent plastic sticking) or atmospheric dust trapped on the surface [201]. Yan *et al.* further confirm that defects originating from surface roughness or particles are the dominant failure mode for single layer inorganic barriers. Although ALD is conformal, these large particles can generate local stress or shadows that disrupt the coating. Consequently the barrier limits observed in this work are more likely caused by possible foreign particle defects rather than an actual failure of ALD chemistry itself [28].

4.4 Edge Permeation in the Calcium Test

Edge permeation, or increased calcium reduction around the outer edges of the sample, is a key issue in the measurement of ultra-low water vapor barriers. In the Ca test

that takes place over long periods, water vapor often enters through the sides of the measurement test piece, likely via the epoxy, meaning WVTR estimates will have a contribution from permeation through the epoxy rather than through the barrier layer itself. In uncoated substrates like PET, this is less evident since their higher permeation rates (and hence shorter Ca tests) make epoxy less of a limiting factor. In the direct contact Ca test used here, the permeation due to the edge effects is clear, as a bright region is seen to 'grow' from the perimeter of the sample. By removing these sections of the sample from the data analysis and using the remaining, central, regions to use for the estimate of water vapor permeation through the sample, edge effects can be accounted for.

A detailed methodology for masking edge regions and isolating the true Ca test area is provided in 9.3.6 Methodology for Addressing Edge Permeation and Barrier Assessment. This includes the rational, visual examples, and implications for spot and WVTR analysis. The next section (4.4.1 Estimating WVTR using Constant Region of Interest and Accounting for Edge Effects (Calcium Region Isolation)) presents the corrected WVTR Values obtained by excluding these edge-affected regions and compares them to uncorrected estimates across samples and thicknesses.

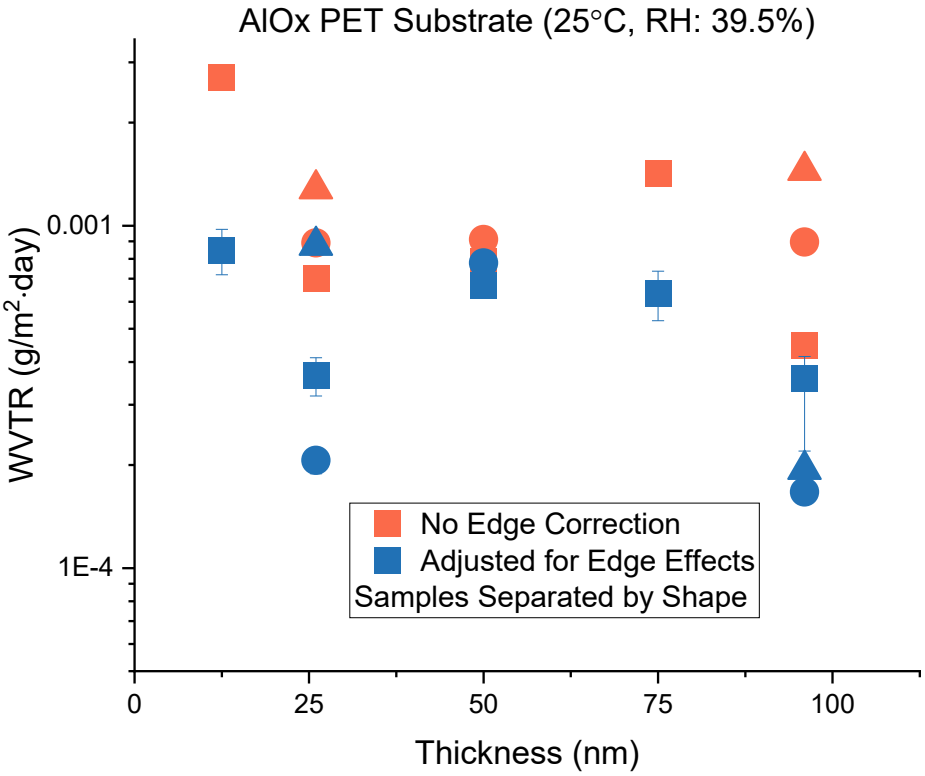
All WVTR values reported in the following sections use data with these edge regions excluded, unless otherwise stated, to ensure better accuracy, especially when comparing barrier performance. WVTR estimates with, and without that edge permeation are compared below to highlight the impact of the edge permeation on overall measured WVTR.

4.4.1 Estimating WVTR using Constant Region of Interest and Accounting for Edge Effects (Calcium Region Isolation)

This sub section further highlights the difference in WVTR estimations or calculations when edge permeation is accounted for compared to assuming a constant region of interest in mean grey measurements which does not account for the possibility of permeation through the edges or epoxy.

Evaluating Figure 4-11, the WVTR of AlO_x coated PET is analysed as a function of thickness, with samples differentiated by shape based on thickness (*e.g.*, square for sample 1, circle – sample 2, etc.). Measurements were performed under two relative humidity conditions: 39.5 ± 1% (Figure 4-11 (a)) and 78.5 ± 1% (Figure 4-11 (b)) at a constant of 25 ± 3.0 °C. The results demonstrate that accounting for edge permeation typically reduces the measured or calculated WVTR for the same sample across all thicknesses, but not to the same degree for all samples, as the amount of edge permeation varies from sample to sample. Removing the edge effects provides a more accurate estimate of the WVTR for the barrier layer.

For instance, in both Figure 4-11 (a) and (b) at ~14.0 nm thickness, accounting for edge effects significantly reduces WVTR estimations across both humidity conditions with corrections lowering values by nearly an order of magnitude. Supporting analysis on the consequences of not accounting for edge permeation is provided in Section 9.3.7.c Percent Error of Not Accounting for Edge Permeation.


AlOx PET Substrate (25°C, RH: 39.5%)
WVTR (g/m2·day)
0.001
1E-4
0
25
50
75
100
Thickness (nm)
No Edge Correction
Adjusted for Edge Effects
Samples Separated by Shape

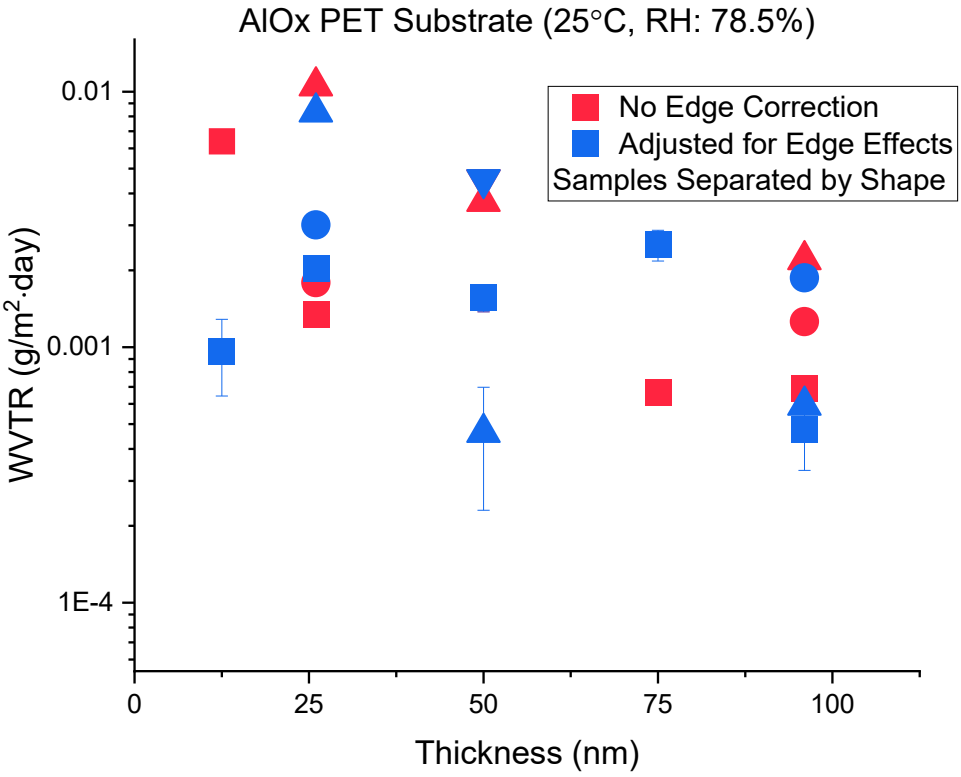

AlOx PET Substrate (25°C, RH: 78.5%)
WVTR (g/m2·day)
0.01
0.001
1E-4
0
25
50
75
100
Thickness (nm)
No Edge Correction
Adjusted for Edge Effects
Samples Separated by Shape

Figure 4-11: WVTR (g/m^2·day) as a function of AlO_x thickness (nm) under two relative humidities (39.5% and 78.5% at a constant temperature of 25°C). Data points are differentiated by shape to represent individual samples (i.e., Sample 1 is square, Sample 2 is circle, Sample 3 is triangle), while they are also colour differentiated by edge correction status (red/orange = uncorrected, blue = corrected). Edge-corrected data consistently show lower WVTR values, highlight the significance of excluding perimeter artefacts like edge permeation in accurately assessing the true barrier performance for certain samples.

4.5 Activation Energy of AlO_x on PET Substrate

4.5.1 Ea of AlO_x Coatings (Ca test) using WVTR

To gain a deeper understanding of the permeation mechanisms, Ea was calculated using edge accounted WVTR values. Figure 4-12 shows the natural log of WVTR plotted against the reciprocal of temperature, examining samples with ALD depositions of 63 cycles (10 nm), 125 cycles (14 nm), 250 cycles (26 nm), and 500 cycles (50 nm).

These samples were tested at approximately -25°C (using a Bosch Series 2 GTV15NWEAG Freezer - 2.4.3 Calcium Test Set-up), 25°C, 35.5°C, and 50.5°C, under relative humidities of ≈ 71% and ≈ 65%. Each thickness was tested at three of the four temperatures listed, depending on the availability and stability of the calcium films during measurement.

The 250-cycle film (≈45.13 kJ/mol) has an Ea indistinguishable from uncaotead PET, indicating that permeation is dominated by macro-defects. In contrast, the 63-cycle (10 nm), 125-cycle (26 nm) have ≈112.95 kJ/mol and ≈71.34 kJ/mol, respectively and 500 cycle (50 nm) - (≈83.62 kJ/mol) coatings give markedly higher Ea values. A higher Ea is often taken as evidence for nano-defect transport, yet the Ca-test background remains uniformly black, unlike the gradual greying seen in sputtered oxides known to contain nano-defects. Nehm et.al provide a plausible alternative: water may diffuse

laterally along the polymer/oxide interface until it locates a sparse macro-defect, and the extra interface step raises the apparent Ea. Thus, the elevated values for the thinner and thickest ALD films may reflect a combination of nano-defect permeation and interface-mediated access to macro-defects, whereas the 26 nm film behaves as a mostly macro-defect limited pathway [258].

When compared to MOCON Aquatran estimates (3.4.5 Activation Energy of Uncoated PET), these values show similar trends. Considering factors such as sample-to-sample variability and that each data point is a single unique sample, the conclusions regarding mechanism should be treated with some caution. Further testing across a broader thickness range, with additional samples and temperatures, is needed for more accurate Ea estimations. A key limitation and caveat of the Ca test is its destructive nature, preventing repeated measurements of the same sample, unlike MOCON Aquatran, which allows testing under varied conditions, complicating direct comparisons of Ea values.

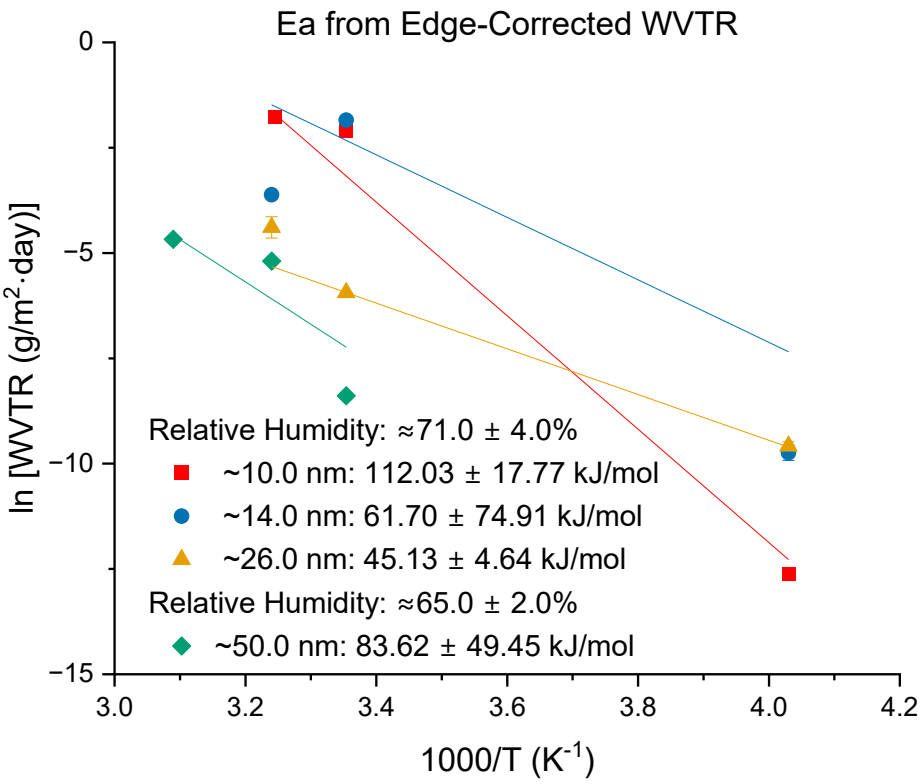


Figure 4-12: Arrhenius plot of ln (WVTR) versus inverse temperature (1/T) for ALD AlO_x films of varying thicknesses, based on edge-corrected WVTR data from the Ca test. The plot accounts for sideways permeation effects and the calculated apparent activation energies E_{app} from slopes are 112.03 ± 17.77 kJ/mol for 63 cycles, 61.70 ± 74.91 kJ/mol for 125 cycles, and 45.13 ± 4.64 kJ/mol for 250 cycles; and 83.62 ± 49.45 for 500 cycles. While linear best-fit lines are applied, the visible scatter (likely due to variations in sample geometry or measurement sensitivity) affects the confidence in assuming a strictly Arrhenius relationship. Wherein, a true non-Arrhenius behaviour may be present if the underlying trend is non-linear, potentially caused by temperature dependent changes in defect geometry (crack opening / closing) or competing transport mechanisms. These values consequently represent the effective temperature sensitivity of the permeation flux over this specific temperature range rather than a single static energy barrier.

4.5.1 Ea of AlO_x Coated PET (Ca test) using Permeability

Figure 4-13 shows Arrhenius plots (ln P vs 1/T) for Ca-test data from PET films coated with AlO_x of varying thickness. Because the dataset is sparse and exhibits appreciable scatter, no robust correlation between Ea and thickness can be claimed.

The variability itself is informative. The 26 nm coating yields an Ea essentially indistinguishable from uncoated PET, implying that large-scale defects still dominate transport. In contrast, the 10 nm and 50 nm films display markedly higher Ea values, illustrating that additional thickness does not automatically improve barrier performance or alter the permeation mechanism. These deviations likely to reflect secondary factors such as stress-induced micro-inhomogeneity, defect coalescence or local changes in water sorption.

Overall, the data suggest that once thickness exceeds ~26 nm, oxide quality rather than thickness per se becomes the primary determinant of water-vapour transport. When flux is limited by through-coating nano defects, Ea therefore reflects the diffusion / solubility balance within the oxide itself. Optimisation should focus on minimising defect density and ensuring film uniformity rather than pursuing ever greater thicknesses.

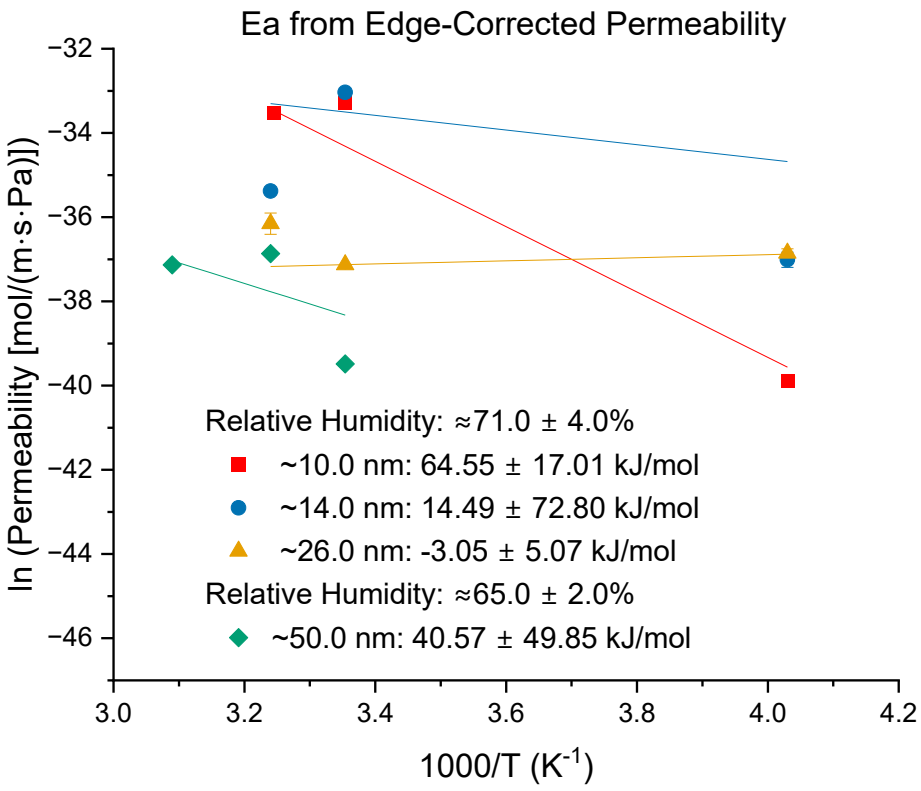


Figure 4-13 Natural logarithm of permeability of Ca tests over the reciprocal of its temperature, considering edge effects. The data illustrates the relationship between diffusion and solubility mechanisms as a function of AlO_x coating thickness. Thinner coatings exhibit diffusion dominated behaviour, where permeability increases with temperature, thicker coatings transition to solubility dominated behaviour, showing reduced permeability with increasing temperature. Showing how increasing thickness influences the balance between diffusion and solubility, impacting overall permeability behaviour.

4.6 Analysis of Defects (Spots) in ALD AlO_x coating

This section focuses on estimating the number of bright spots in the sample area observed during the Ca test, which are assumed to correlate to the number of pin-hole defects in ALD AlO_x films. Various methodologies were explored to identify and count the spots, with the simplest of which used ImageJ. Although ImageJ has certain limitations, its results serve as an essential starting point, providing a foundational understanding and initial estimations of spot counts. These results justified its inclusion

as a baseline for analysis. However, to achieve greater accuracy and precision, a custom Python code was later developed. Each approach contributed valuable insights to the overall defect analysis, illustrating how defects were identified and quantified throughout the study.

4.6.1 Pre-Analysis (Thresholding) of Spots – Using Fiji/ImageJ

Before implementing more advanced analysis techniques, an initial assessment using ImageJ was conducted to establish a baseline for defect estimation. This preliminary step provided a standardized method for detecting and quantifying spots, offering a quick and reproducible means of evaluating relative defect densities. While ImageJ, may not fully capture the nuance and intricacies of isolated spots (misidentification when coalescence occurs, or minor residual artefacts), its ability to provide a broad overview made it a useful tool for comparative analysis. By first utilizing ImageJ, identifiable general trends could be seen before further refinement through more precise computational methods.

Figure 4-14, outlines the standard protocol used for analysing these spots using a 14.0 nm AlO_x on PET substrate tested at 25°C and 39.5% RH as an example:

1. **Calcium Region Selection**: The entire calcium area (5.04 × 4.99 cm) is initially first selected as the region of interest. Over time, edge permeation is accounted for as previously discussed, by focusing on regions unaffected by it and analysing the central region where calcium remains.

2. **Image Conversion**: The selected region and image is then converted to 8-bit grayscale format to simplify the analysis by reducing data complexity while preserving essential intensity variations. This conversion enhances contrast, making it easier to

detect and distinguish defects from the background. It additionally standardizes the image for thresholding and segmentation processes, improving consistent and defect quantification.

3. **Image Segmentation (Weka & Otsu Method)**: The "Trainable Weka Segmentation" (machine learning) tool and Otsu method (Equation 4-2) are used to segment the image into three distinct regions: calcium (red), copper (green), and background (purple/violet), as shown in Figure 4-14. Initially, manual selection was performed to define classification criteria based on intensity differences, establishing a reference range for segmentation. In the processed / segmented images, calcium appears darkest, copper has intermediate intensity, and the backlight makes the background the brightest. Optimizing contrast during segmentation improves defect quantification accuracy and enables clearer differentiation between regions.

4. **Background Removal (Rolling Ball Technique)**: the rolling ball algorithm removes uneven lighting and noise to enhance spot detection. It works by simulating a ball rolling under the image surface, identifying gradual background variations and subtracting them.

For this case a 10-pixel radius was used as the ball size, to determine the scale of the background features to be removed — small enough to preserve fine details while effectively eliminating broad lighting inconsistencies; ensuring only relevant features (calcium and defect spots) are retained.

1. **Spot Analysis**: The image is inverted, and spots are analysed based on size and shape, excluding edge contact artifacts where ImageJ misinterprets boundary noise as defects. Spot characteristics such as size and circularity can be analysed. The circularity,

how closely spot resembles a perfect circle, is defined by Equation 4-1 – where a value of 1 is a perfect circle and closer to 0 is an irregular or elongated shape. Rather than using circularity to exclude spots, it was used to assess the typical shape characteristics, to distinguish possible common defect morphologies (*e.g.*, round vs. elongated) which is used to inform the possible estimated actual defect size, or specifically defect radius (4.7 Calcium Test Defect Size Calculations).

$$Circularity = \frac{4\pi \times Area}{Perimeter^2} \qquad \textit{Equation 4-1}$$

Moreover, camera reflections are often mistaken for defects, inflate spot count and size. While manual thresholding helps, subtle intensity differences between calcium, copper, and the camera outline can still cause errors. To address this, all processed images were visually reviewed to ensure that the counted spots were physically plausible and consistent with expected degradation behaviour. This verification step was essential for distinguishing true defect from artefacts introduced during image acquisition or processing.

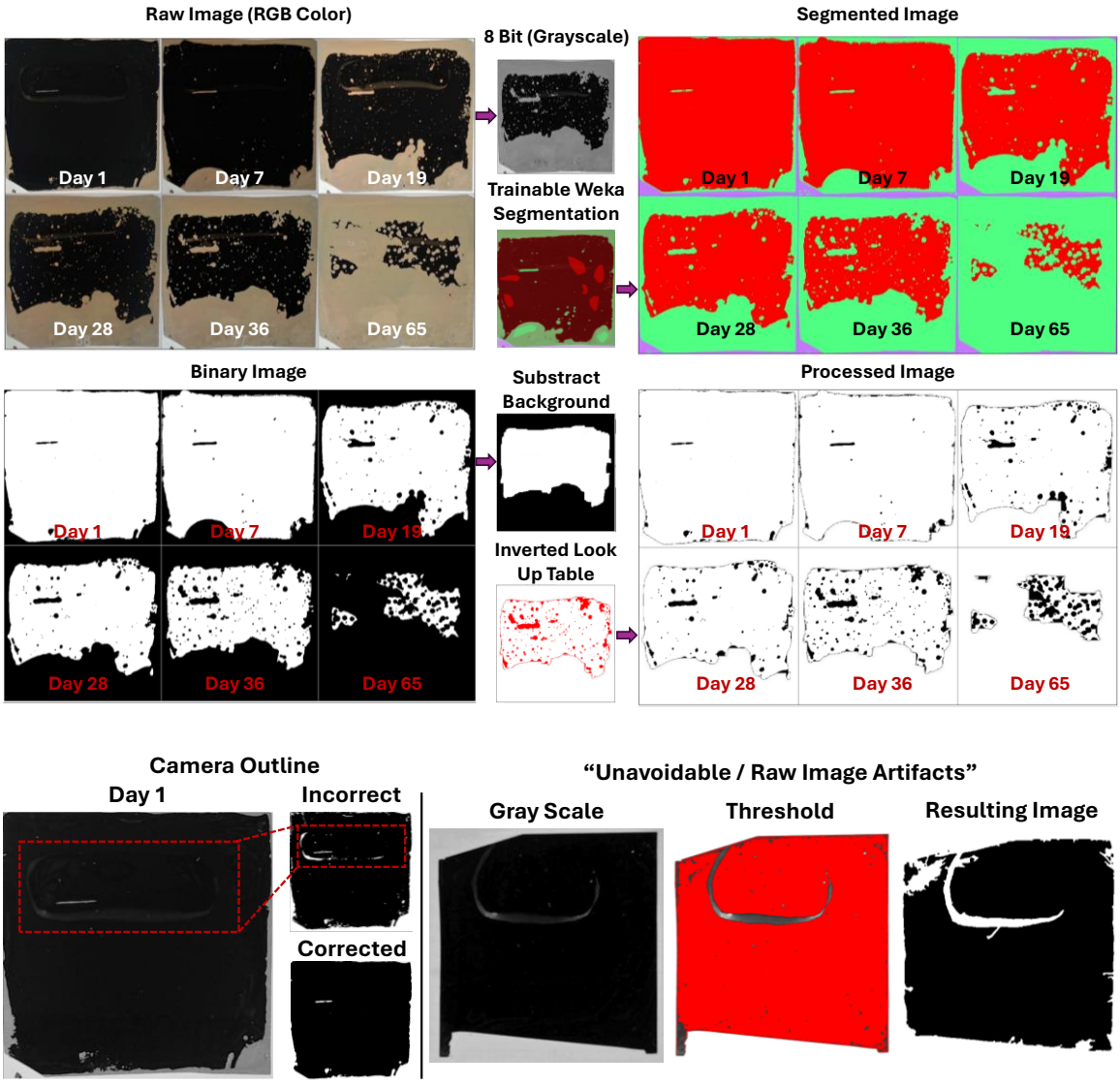


Figure 4-14: Pre-processing of an image from a Ca Test of a Barrier Layer (14.0 nm AlO_x on PET at 25°C, 39.5% RH) starts by converting raw RGB images into an 8-bit grayscale stack for easier identification of calcium, copper, and background regions using Trainable Weka Segmentation. The Otsu method binarizes the image, and background subtraction isolates the spots. The lookup table is inverted to analyse particles, focusing on size and circularity. Caution is to be taken as artifacts from the raw image may affect the grayscale, requiring careful thresholding to avoid overestimating defects or miscounting spots.

Stacked images, in this context, sequential Ca test images taken over time and aligned as a series, are used to track the evolution of calcium degradation and spot formation. These images help visualize the initiation, expansion, and coalescence of

defects, enabling estimations of spot growth rates and spatial distribution across the region of interest.

Figure 4-15, illustrates the progression of defect growth over time due to Ca depletion, indicating areas where water vapor has permeated the barrier and triggered a visible reaction.

- (a) Bright Area boundaries: the progression of Ca depletion and potential defect growth is visualized using pink contour lines which track both the overall recession of the calcium front and the emergence of localized spot formations
- (b) presents a time series of particle analysis images, where individual spots are identified and colour labelled. The outer calcium edges are excluded to focus on internal defect zones and improve classification accuracy.
- (c) a cumulative summary of all detected defects is shown, isolating only the particles/spots used in quantification and highlighting how spot count and size evolve over time.
- (d) visualizes the shrinking perimeter of the Ca region, showing its degradation across testing days as water vapor gradually consumes the calcium.

The resulting defects appear in a variety of shapes (*e.g.* circular or elongated) and provide valuable insight into spatial defect distribution, morphology and possible barrier failure dynamics.

However, some spots coalesce over time, making it important to distinguish between isolated spots and those spots in an image that are now made up of multiple

spots (each thought to be associated with a defect in the barrier), which are referred to as coalesced spots (explored in 4.6.2 Differentiating Isolated and Coalescing Spots (Python)) In brief:

- **Isolated spot**: refers to a feature in a given image that appears for the first time in the image sequence and is spatially separate from other features.
- **Repeated spot:** an isolated spot that persists from earlier timepoints without interacting with adjacent spots – recorded individually and to not double count the spot.
- **Coalesced spot** (joined together): results when two or more spots, either existing isolated or already coalesced spots, merge forming an even larger feature that may no longer reflect individual defect sizes and origins.

This distinction is critical in that coalescence can affect the estimated number, size and spatial distribution of defects, potentially skewing barrier performance analysis. To address this, spots that overlap with others or appear in already depleted (or edge permeated) regions are now counted as new. Instead, the analysis tracks defect growth across a stack of time-lapsed Ca test images, isolating true spot origins and recording their evolution.

As argued, spot formation itself occurs when water vapor permeates through a defect in the barrier layer, reacting with the underlying Ca. The growth rate of each spot depends on the defect size (influenced by coating quality) and environmental condition, particularly humidity and temperature. Hence, by analysing these sequential images, it becomes possible to capture how spots form, grow, merge or coalesce until full calcium depletion is reached.

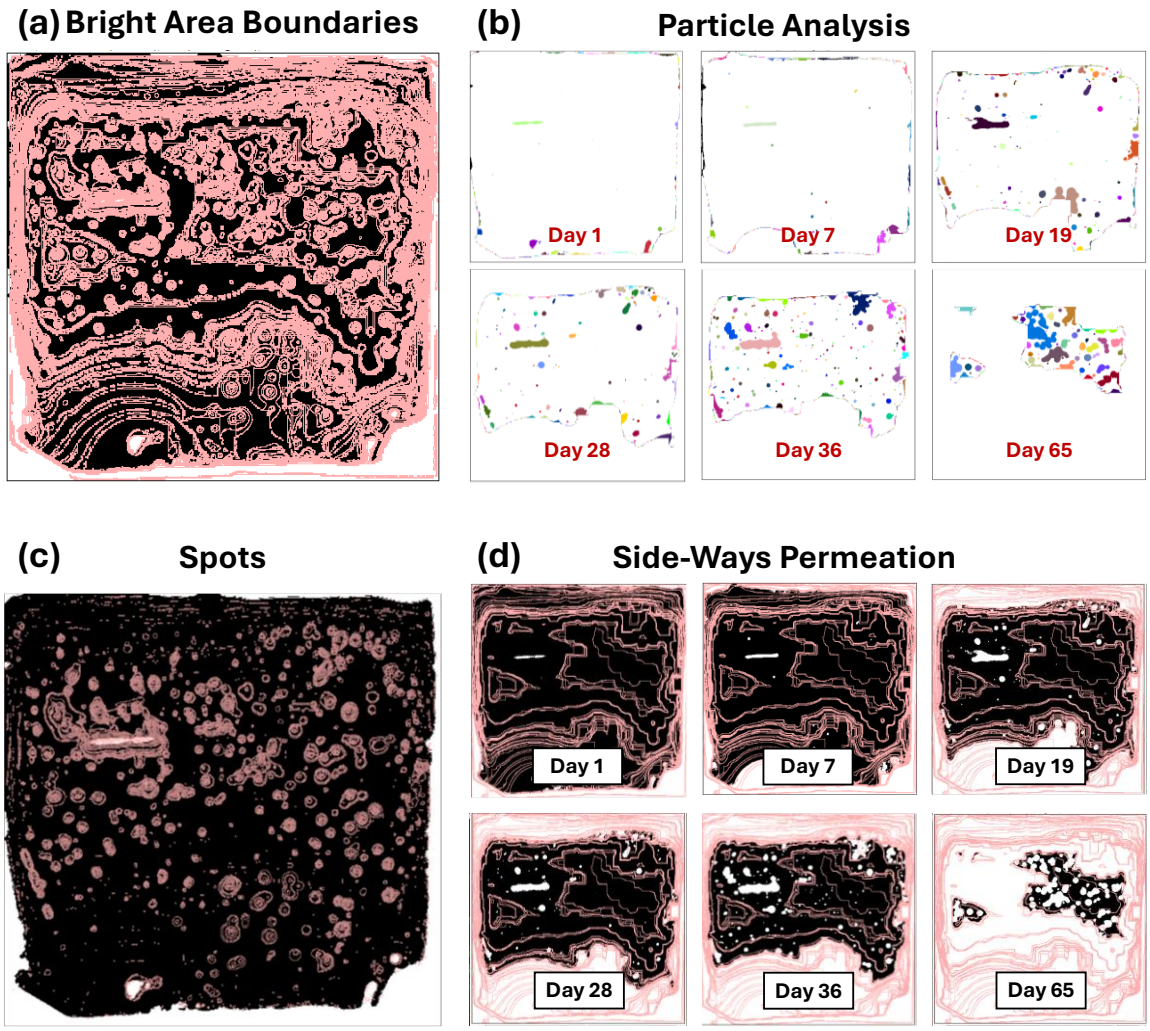


Figure 4-15: Bright area boundaries and particle analysis of a 14.0 nm AlO_x PET substrate (25°C, 39.5% RH), tracking calcium depletion over time using stacked Ca test images. (a) Pink contour lines show the recession of the calcium front and emergence of localized bright spots (water vapour ingress sites). (b) Particle analysis highlights individually detected spots, colour-labelled by appearance time; edge regions have been excluded. (c) Cumulative map showing the isolated internal spots used for defect quantification across the test duration. (d) Perimeter tracking of the active Ca region illustrating degradation and reduction of testable area over time. Spots are classified as isolated, saved as repeated in the memory, or coalesced (joined together), based on their formation and interaction, with spot density (spots per unit area) used to account for changing Ca coverage as the test progresses.

4.6.2 Differentiating Isolated and Coalescing Spots (Python)

Building on the ImageJ thresholding in 4.6.1 Pre-Analysis (Thresholding) of Spots – Using Fiji/ImageJ and 9.3.9 Influence of Thickness and Environmental Conditions on Spot Formation, a short Python routine was added to separate isolated from coalesced bright spots and avoid mis-estimating defect density.

4.6.2.a Methodology for Enhanced Spot Detection (Python Based)

A Python-based algorithm was developed to analyse the same grayscale images, distinguishing isolated spots from coalescing regions, artefacts, and background interference.

For the ImageJ analysis, thresholding using Otsu's method was done. One can imagine that this is like drawing a line ("threshold") in an image to separate: (1) the darker areas representing the calcium layer, including regions of partial calcium depletion, and (2) the background, which are the lighter areas where calcium is entirely absent.

Otsu's method fins an optimal grey-level threshold, *T*, that separates the Ca layer from the background in a grayscale image. It works by testing every possible brightness value to find the one that minimizes the within class variance ($\sigma_w^2(T)$), as this produces the most internally uniform pixel groupings as shown in Equation 4-2. For every candidate grey level in the 8-bit range (0-255), the pixels are divided into two classes, intensity ≤ *T* (calcium) and intensity > T (background). Subsequently the $q_1(T)$ and $q_2(T)$ are the fractions of total pixels assigned to the Ca and background classes, while $\sigma_1^2(T)$ and $\sigma_2^2(T)$ are the variances of grey-level values within those classes that is, the

spread of intensities among Ca pixels and among background pixels, respectively. The threshold that minimises $\sigma_w^2(T)$ yields the best possible separation or the most internally uniform classes and, correspondingly, the greatest contrast between calcium and background.

$$\sigma_w^2(T) = q_1(T)\sigma_1^2(T) + q_2(T)\sigma_2^2(T) \qquad \textit{Equation 4-2}$$

Otsu's Thresholding minimizes overlap between the dark calcium layer and light background, working well with bimodal distributions like the calcium test. However, it struggles with uneven lighting or complex histograms, potentially misidentifying regions.

To improve on this, adaptive Gaussian thresholding sections the image into local regions to account for the difference in uneven lighting which adjusts brightness in smaller sections of the image as described in Equation 4-3, where *x* and *y* are the coordinates of the pixel image, and σ^2 the standard deviation of the Gaussian filter. The block size or the size of the local regions were defined to by 35 by 35 pixels (moderate choice where a smaller block size could have been chosen but computationally would have been taxing and take longer to complete).

$$G(x, y) = \frac{1}{2\pi\sigma^2}\exp\left(-\frac{x^2 + y^2}{2\sigma^2}\right) \qquad \textit{Equation 4-3}$$

Following this, the Canny Edge Detection for finding the boundaries of objects through intensity changes between pixels over the image was applied using a multi-stage approach [340-342]. This method works by the five different process steps: (1) Noise reduction using a Gaussian filter, where a Gaussian kernel is applied to the image (similar to Gaussian smoothing, Equation 4-3; (2) The intensity gradient of the image is

calculated using finite difference approximations (Sobel operator), such that the gradient magnitude (G) and direction (θ) are computed for each pixel as delineated in Equation 4-4, where the G_x and G_y are gradients in the corresponding directions; (3) Non-maximum suppression: where a binary edge map is created to retain only the strongest edges (local maxima of the gradient magnitude); and (4) Double Thresholding: two intensity thresholds (low = 0.2 and high = 0.6, normalized features of 0 darkest image and 1 brightest) were applied to classify strong and weak edges. Finally (5) Edge Tracking by Hysteresis, where weak edges are connected to strong ones and retained, while unconnected weak edges are discarded.

$$G = \sqrt{G_x^2 + G_y^2} \text{ and } \theta = arctan\left(\frac{G_y}{G_x}\right) \qquad \textit{Equation 4-4}$$

After detecting edges, each spot is classified as either isolated or coalescing. An isolated spot is defined as newly detected defect whose centroid lies beyond a set threshold distance from all previously observed spots, indicating it is both spatially and historically distinct. A coalescing spot, in contrast, is one whose centroid lies sufficiently close to a previously identified centroid, to suggest the likelihood coalescence. This classification enables the identification of newly emerging defects and supports the analysis of how existing ones evolve particularly in the context of Ca layer degradation, where spot formation, expansion and interaction are indicative of permeation pathways.

To implement this classification, a cKDTree (k-d tree) structure was used to efficiently compare spot centroids across consecutive image frames. The Euclidean distance between centroids was calculated as defined in Equation 4-5, and a 20-pixel (~0.20 cm) threshold was applied. If the centroid of a newly detected spot lay within this

threshold of any previously recorded centroid, the spot was classified as coalescing. This centroid-based proximity method serves as a practical and computationally efficient proxy for spot continuity or interaction, particularly in time-lapse image sequences. However, it does not directly assess edge or overlap or physical merging of the depleted Ca, and as such it may occasionally misclassify distinct but closely spaced features. For higher precision especially in cases of irregular growth or spot morphology, edge-based or shape-aware approaches may be warranted.

$$d = \sqrt{(x_1 - x_2)^2 + (y_1 - y_2)^2} \qquad \textit{Equation 4-5}$$

After thresholding and classification, spots were counted by identifying the edges detected through Canny's method. The minimum and maximum spot sizes were set at 15 and 30 pixels, respectively, to filter out artifacts. This helped ensure that misidentified features, such as noise or lighting artifacts, were not counted as spots, however it also possibly did not count spots that were outside this range.

Moreover, to account for sideways permeation and edge artifacts, a clear border function was applied to remove bright areas identified near the image boundaries. This helped eliminate misidentified spots caused by the edges of the calcium region, though some valid data near the borders may have been lost as a result.

4.6.2.b Limitations and Challenges of Current Python Workflow

Identifying spots becomes particularly challenging when dealing with large datasets (it is impractical to do an individual inspection of each image) and when linear network structures form such as those seen in coated PVAl substrates (5.6 Defect Analysis of Coated PVAl Films). In ideal cases, such as with coated PET substrates

(example shown in Figure 4-17), the Python based classification algorithm distinguishes isolated and coalescing spots with reasonable accuracy. However as illustrated schematically in Figure 4-16, the current centroid-proximity logic in the workflow struggles once multiple spots begin to merge.

At time 0, four isolated spots are detected (shown in green), consistent with the centroid distance criterion. At time *t*, as two spots begin to merge, a single coalescing region (magenta) is registered, while the two previously detected isolated spots are retained (repeated spot), indicated in white. By 2*t* these repeated spots initially merge and form a coalescing spot, while a newly emerging spot near this coalescing cluster is correctly identified as isolated. By 3*t* further merging results in a single coalescing cluster or spot, collapsing distinct initiation events into one object and obscuring the true number of growth centres involved.

This behaviour where all merged spots are treated as one group, highlights a key limitation of the current workflow. The 20-pixel centroid-based threshold in the cKDTree implementation means that once spots merge, individual histories and contributions are irretrievably lost. Moreover, smaller or later onset defects that nucleate close to a growing coalesced cluster are unlikely to be resolved first as isolated; instead, they are immediately subsumed into the existing cluster. This can result in undercounting and misclassification, especially in the PVAl samples where long crack like structures amplify these merging effects (Figure 5-15).

Additional limitations arise from the fixed size filters (15 to 30 pixels), which discard features that fall outside this range – including legitimate small seed spots and highly coalesced clusters. Similarly, the removal of border touching features risks

excluding valid data near the image boundaries. Combined, these constraints bias the defects statistics towards larger, central areas and under-represent both early stage and edge located defects. This underscores improvements in tracking across timepoints – to maintain a better history of merging events, adaptive size filters that better capture full defect distribution, edge or overlap based criteria to identify true coalescence events beyond simple centroid proximity, and shape aware segmentation to handle linear features in PVAl more robustly. Such improvements would yield a more accurate model and defect density quantification.

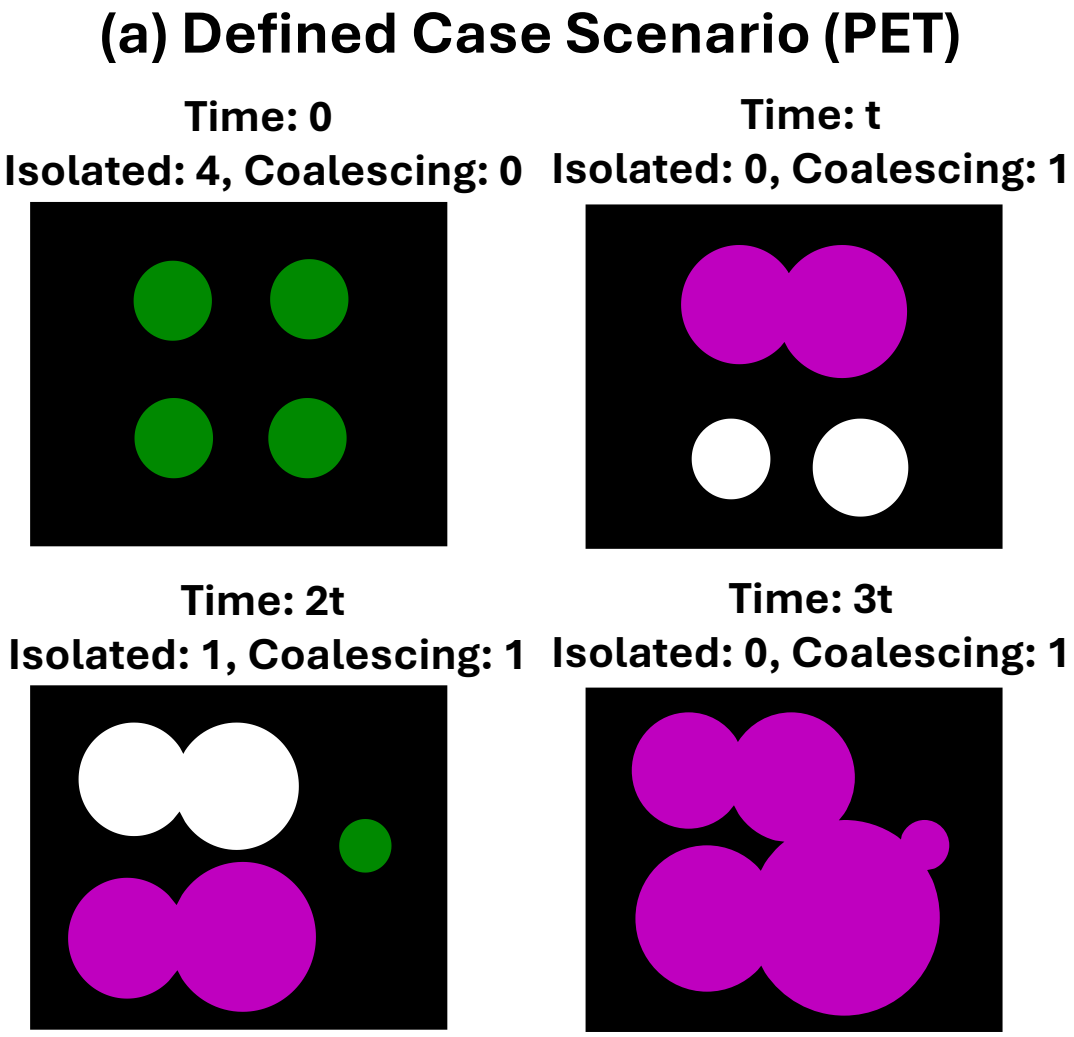


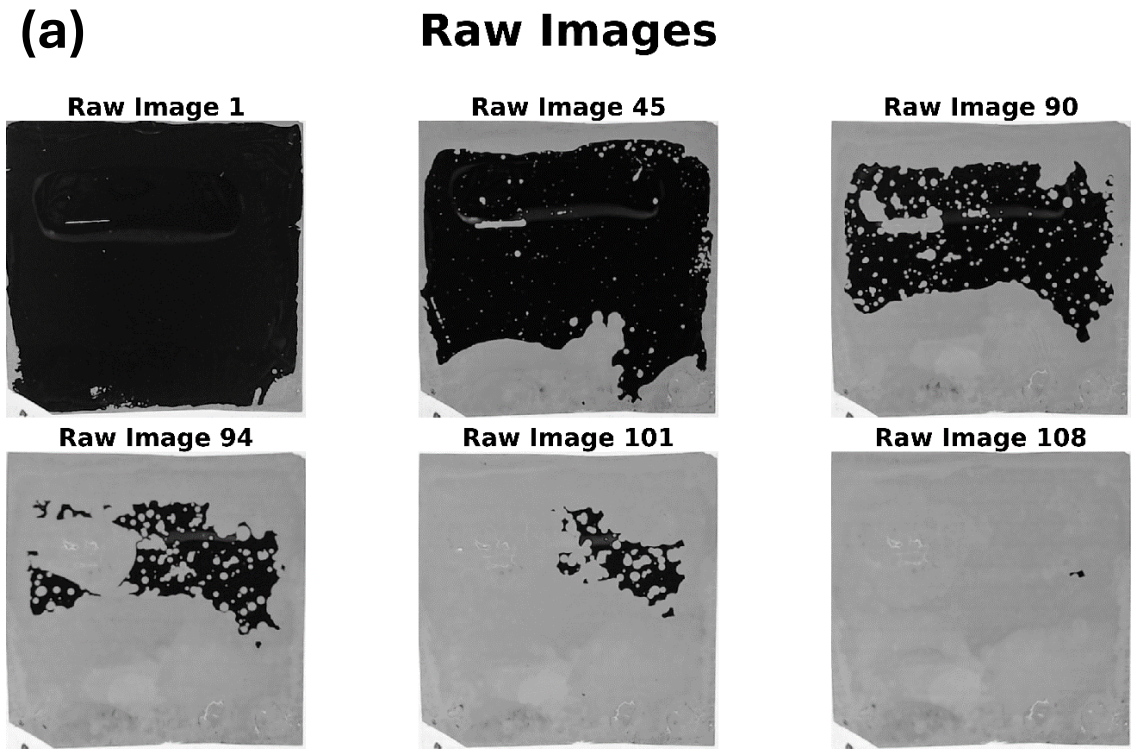
Figure 4-16: Idealized representation of spot classification logic across four timepoints. At time 0, four isolated green spots are identified. At t, two of these merge to form a single coalescing spot (magenta), while the other two isolated spots persist (white). By 2t, previously merged spots remain coalesced, and a newly emerged isolated spot appears near this cluster. At 3t, continued merging results in a single large coalescing cluster, collapsing distinct initiation events into one region. This schematic illustrates the centroid-proximity logic in the Python-based classification and highlights how coalescence and merging can obscure the true number and evolution of defect origins.

4.6.2.c Spot Density Example (14.0 nm AlO_x – PET)

This method was again applied to a 14.0 nm AlO_x coated PET substrate tested at 25°C with 39.5% RH (where relative humidity was fixed using saturated salt solutions – labels such LiCl and $MgCl_2$ in figure panels denote the salt solution used to set the chamber RH (as explained in 2.4.3 Calcium Test Set-up). As seen in Figure 4-17, the (a) raw image was processed through this updated Python pipeline, showing the (b) detected edges, which includes centroid-based tracking and temporal memory and then the (c) classification and spot identification. This led to a more accurate classification of defects by reducing the likelihood of double-counting and more reliably distinguishing newly appearing isolated spots from those coalescing with existing defects. For instance the 4^{th} and 5^{th} frames or (Raw Image 94 and 101) show that in Figure 4-17 (c) several spots are identified as coalesced based on their proximity to previous detected regions, demonstrating the method's ability to account for spatial continuity over time.

In summary, this method improves the precision of defect classification by distinguishing between isolated and coalescing spots, an essential factor for accurately assessing the number of potential defects in a barrier layer, which then informs or can elucidate its barrier properties. This is because only isolated spots represent defects, which indicate breakthrough points through the barrier layer. Misclassifying these would lead to an incorrect estimation of the total defect count. The inclusion of a memory-based

spatial filtering approach, combined with robust handling of lighting variation and edge artefacts, provides a more reliable and reproducible basis for interpreting defect evolution in permeation testing.



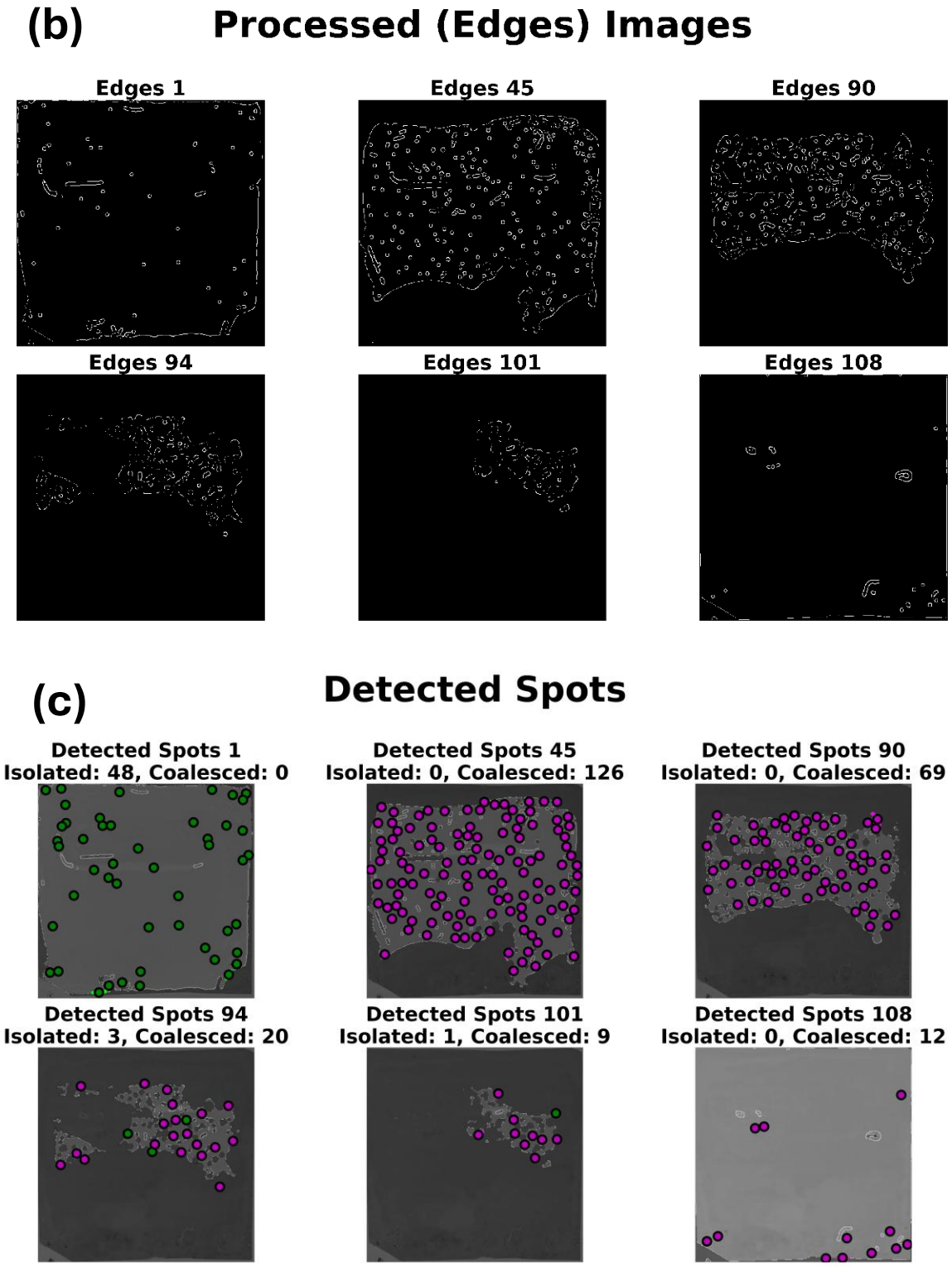


Figure 4-17: Spot detection and classification results for a 14.0 nm AlO_x layer on a coated PET substrate at 25°C and 39.5% RH ($MgCl_2$ salt solution). (a) Raw grayscale images showing the progressive degradation of the Ca indicator layer. (b) Corresponding edge detected images produced via the Canny method. (c) Final spot

classification results based on centroid proximity and temporal memory, distinguishing between isolated (green – blue contours represent estimated size of spot) and coalescing (magenta) spots. The updated Python-based pipeline enables more reliable defect classification by reducing the likelihood of double-counting and tracking spot evolution across frames. This demonstrates the method's ability to account for spatial continuity over time and supports a more accurate assessment of defect development and identification.

4.6.3 Spot Density Estimation Results (Python Code)

This methodology was applied to calcium tests at low (39.5%) and high (78.5%) relative humidity at a constant 25°C, and the total number of newly detected isolated and coalescing spots per frame, normalized by the imaged area, was plotted over time (spots · cm^2 · $frame^{-1}$). This normalization was necessary to account for variations in image size across various Ca test samples, as larger imaged areas would naturally contain more spots simply due to their size, potentially biasing comparisons. By expressing spot counts per unit area, this approach allows for meaningful comparison across different tests and coating conditions A detailed discussion of the spot density in both humidities is found in appendix sections: (9.3.9.dSpot Density (Low RH – 39.5%)) and (9.3.9.e Spot Density (High RH – 78.5%)).

4.6.3.a Summary of Spot Density – Python Estimations

The analysis of defect densities through spot identification in Ca test (~3x3 cm or 5x5 cm) under varying RH (39.5% and 78.5%) and temperatures (25°C and an additional 50.5°C data set) is presented in Figure 4-18; Here, defect density is defined as the total number of isolated spots detected across the full test duration, normalized by the imaged Ca region area (spots · cm^{-2}). This differs from the time-resolved spot count plots shown in (Figure 9-22 and Figure 9-23), which depict normalized spot counts per frame. Results

indicate a mean defect density of 13 ± 3 spots/cm^2, with no clear dependence on RH, temperature or coating thickness. This supports the interpretation that the formation of defects is governed primarily by intrinsic coating irregularities rather than environmental conditions.

While limited literature is available that directly quantifies defect densities of ALD AlO_x, contrasting this with established data for metallic aluminium (Al) coatings provide useful context as a short introduction. Metallic Al coatings deposited via thermal evaporation or sputtering onto PET substrates exhibit significantly higher defect densities, often on the order of 10^3 to 10^4 defects per cm^2. As reiterated an important distinction is that these values specifically refer to metallic aluminium films and not necessarily aluminium oxide (AlO_x or stoichiometrically: Al_2O_3), and were compiled by Park *et al* [61] based on earlier work by Jamieson and Windle [343], and subsequently cited by Chatham [103].

Jamieson and Windle used optical and transmission electron microscopy to analyse vacuum evaporated Al films (10 – 70 nm) on PET, reporting pinhole sizes of 1-10 μm and densities of 2,500 to 40,000 cm^{-2} [343]. Chatham, in a comprehensive review of barrier coatings, reiterated these values and explicitly cited Jamieson and Windle as the primary source. Where it was highlighted that PVD coatings often suffer from defects due to particulate contamination, surface roughness and geometric shadowing, which can cause voids, keyholes, and on-uniform coverage that limit overall barrier integrity [103].

Additionally, Hanika *et al.* conducted a detailed morphological and barrier performance study of aluminium-coated polymer films using a combination of optical microscopy AFM and SEM. They correlated structural observations with oxygen

transmission rate measurements showing that microstructural defects like pinholes and film discontinuities are again the main factors to consider. While they did not employ a Ca test for WVTR, the study did report representative pinhole densities of approximate 20,000 cm^{-2} [201].

Collectively these studies show inherent limitations of PVD techniques like thermal evaporation and sputtering when applied to flexible polymer substrates, due to the line-of-sight nature, PVD methods are more sensitive to surface topography, dust particles and incomplete shadowed growth compared to CVD or ALD, leading to significant variation in defect density and compromised barrier performance.

Turning to ALD-grown Al_2O_3, the central focus. Zhang and colleagues investigated defect density in ultra-thin Al_2O_3 films using electroplating, where copper ions filled defects (pinholes) in the Al_2O_3 layer, making them visible under optical and electron microscopes. Their study, which tested film thicknesses from 2 to 10 nm on Nickel (Ni) and Tungsten (W) substrates, found significant variations in defect density. At 2 nm, Ni had 130,000 defects/cm^2, while W had 90 defects/cm^2. At 5 nm, defect densities dropped to 100 defects/cm^2 on Ni and 70 defects/cm^2 on W. By around 10 nm, both substrates showed similar defect densities of around 10 defects/cm^2, consistent with our observations. Beyond this thickness, remaining defects were attributed to surface contamination rather than substrate quality [344]. The concept of reducing defects with increasing aluminium oxide coating thickness is similarly observed in the defect sealing work by Diaz *et al.* [345].

Plasma-enhanced ALD, as supported by literature, produces denser, defect-free films, especially in thinner layers, compared to thermal ALD. Plasma and deposition

parameters also impact overall film quality [346-348]. As also reiterated by the researchers from the University of Colorado (Zhang and Abdulagatov *et al.*), even in clean room conditions, defects are difficult to prevent. These defects, often caused by substrate contamination rather than the ALD process itself, affect barrier effectiveness [349].

Notably, in this work, increasing coating thickness does not inherently reduce defect density, as spot count remains comparable across thicknesses (further explored in: 4.9 Surface Analysis of AlO_x Barrier Layers on PET). While WVTR data generally correlate lower permeability with greater thickness (up to 50nm), there are differences between individual films such that low WVTR's have been observed at lower thicknesses (4.4.1 Estimating WVTR using Constant Region of Interest and Accounting for Edge Effects (Calcium Region Isolation)). Low defect density does not guarantee improved water vapor barrier properties which also depend on factors such as defect size (discussed: 4.8 Influence of Spots and Defect Sizes to AlO_x Barrier Properties)

While not strictly evidenced, sample trends and experience notes that thinner coatings though capable of good barrier performance were harder to test, as these thinner barriers were more prone to higher WVTR and variability. This may partly reflect the limitations of the Ca test, which struggles to resolve defects in weak barriers due to rapid degradation, making consistent measurement at low thicknesses more challenging.

A related long-term degradation study by Maindron *et al.* reinforces this interpretation. Using a fluorescent sensor (AlQ_3) and UV imaging, they monitored defect formation in 20 nm ALD AlO_x films under 85 °C / 85% RH. Despite their initially pinhole-free character, these coatings exhibited a lag time of ~64 hours, after which

defect density increased linearly at a rate of 0.268 defects/cm²/h, leading to full barrier failure within 520–670 hours. This corresponds to a final defect density of ~600 defects/cm^2. Although the detection method and test structure differ from calcium-based approaches, the work highlights how even nominally dense ALD barriers can accumulate localized moisture ingress points over time. Their findings validate the importance of time-resolved spot tracking and caution against assuming long-term barrier stability based solely on early performance indicators or low initial defect counts [350].

Critically, the distinction between isolated spots and coalesced defects must guide defect analysis. A blanket approach to spot detection risks underestimating true defect counts, as coalesced regions may mask multiple underlying flaws. This differentiation is essential for accurate assessment of barrier coating integrity.

In conclusion, while environmental conditions do not directly govern defect density, thicker coatings statistically favour reproducible, high performance barrier layers. The findings also emphasize the need for nuanced defect classification to avoid erroneous assumptions about coating quality. Additional relevant analysis is given in supplementary information: 9.3.9 Influence of Thickness and Environmental Conditions on Spot Formation.

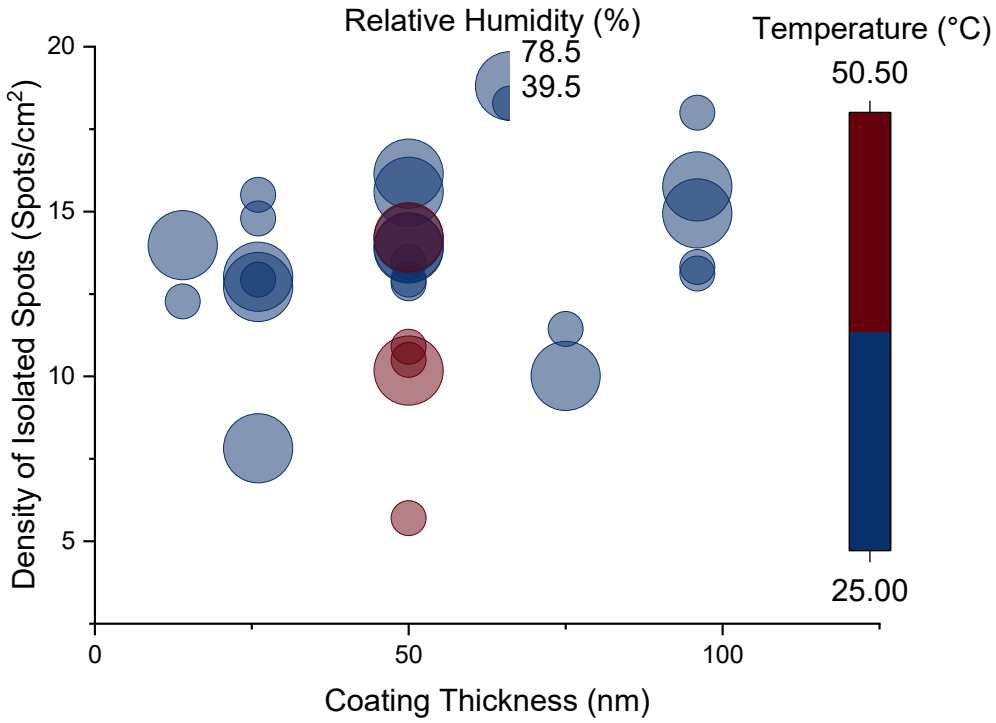


Figure 4-18: The estimated spot density (spots/cm²) is plotted against coating thickness (nm) for multiple calcium test samples, identifying isolated spots as potential defects in the coated film. The average defect density is ***13 ± 3 spots/cm²****, with a maximum of* ***18 spots/cm²*** *and a minimum of* ***5 spots/cm²****. The data suggests that spot density (i.e., the number of defects) remains relatively independent of variations in relative humidity and temperature. However, while thin films can exhibit low defect densities, the probability of creating good films increases with higher coating thicknesses as suggested with previous WVTR and permeability results. Additionally, this analysis provides a more accurate defect estimation, as it focuses exclusively on isolated spots, avoiding potential overestimation caused by coalescence, which was a limitation in previous ImageJ methodologies.*

4.7 Calcium Test Defect Size Calculations

As well as the density of defects, the size of the defects would directly impact the permeability of the barrier layer. Understanding the size of these defects, may also help identify the nature or origin of the macro defects. The schematics of Figure 4-19 illustrate how water-vapour ingress relates to defect geometry.

Figure 4-19 (a) describes the typical circular growth pattern of Ca test spots, on an ALD AlO_x barrier layer on PET substrate. While some spots exhibit distorted shapes due to coalescence or uneven layers, the analysis of individual spots focused on spots exhibiting a consistent circular growth pattern in the period prior to coalescence. This simplification allowed for estimation of the size of the underlying defect, assuming a circular shape, based on the measured area ($A= \pi r^2$).

Over time, as discussed in (4.6.2 Differentiating Isolated and Coalescing Spots (Python)), these circular spots grow radially and eventually coalesce, forming larger depleted regions. While the visible depleted regions grow, the mathematical model employed here assumes a constant physical defect size to estimate the water uptake rate, it is acknowledged that this is an idealisation. Two primary mechanisms that may alter defect geometry during the test:

(1) Moisture Induced Degradation: As water vapor permeates the defect, it interacts with aluminium oxide coating; Maindron *et al.* demonstrated that their ALD Al_2O_3 films suffer from accelerated degradation when exposed to high humidity and high temperatures, eventually leading to barrier failure [350]. This degradation process suggests that the effective barrier properties near a defect may diminish over time.

(2) Substrate Swelling and Stress: This is relevant for the hydrophilic PVAl substrates used in Chapter: 5 Aluminium Oxide (ALD) Coated PVAl. As the substrate absorbs moisture through the initial defect, localized swelling creates hygroscopic stresses. Leterrier *et al.*, established the mismatch in hygroscopic expansion between the coating and substrate generates tensile stress in the

coating. This stress accumulation can drive the propagation of cracks or induce delamination at the interface effectively increasing the physical defect area during the measurement period [219, 220, 268, 351].

Therefore, the defect size calculated here represents an effective hydraulic diameter averaged over the measurement period, rather than a static geometric feature. The assumption of constancy is retained to allow for first order approximations of defect populations but with the caveat that it likely underestimates the maximum defect size reached by the end of the test.

Meanwhile, Figure 4-19 (b) provides a cross-sectional view of the barrier layer, illustrating how water vapour permeates through the multilayer structure eventually reaching the Ca layer (similar to Figure 2-3 on water vapour ingression pathway in Ca test sandwich). Unlike the simplified depiction of vertically aligned defects, defects in the (1) top and (3) bottom barrier layers are randomly distributed and are generally uncorrelated.

Water vapour enters the structure through defects in the top oxide barrier, then diffuses laterally within the (2) polymer substrate, forming a localised vapour reservoir beneath the surface. Only where this vapour encounters a defect in the bottom barrier layer can it penetrate further and reach the Ca film, resulting in the formation of visible degradation spot.

The Ca test therefore only images those under-side defects that receive vapour, and the rate at which a spot grows reflect the flux of water vapour that reaches the defect location. This flux is governed by the WVTR (through the polymer) multiplied by the area of the bottom side defect. As shown, the larger spot area after a certain time (T)

where the spot growth area is proportional to WVTR and will depend on the underlying defect area.

However, the water vapor permeation is not strictly confined to the area directly beneath the hole. Some vapor also diffuses from the surrounding polymer, extending beyond the hole's diameter. This additional influx means that the estimated defect size represents an upper bound—likely larger than the actual defect—since the model assumes all vapor comes solely from the hole area, leads to an overestimation of the defect size.

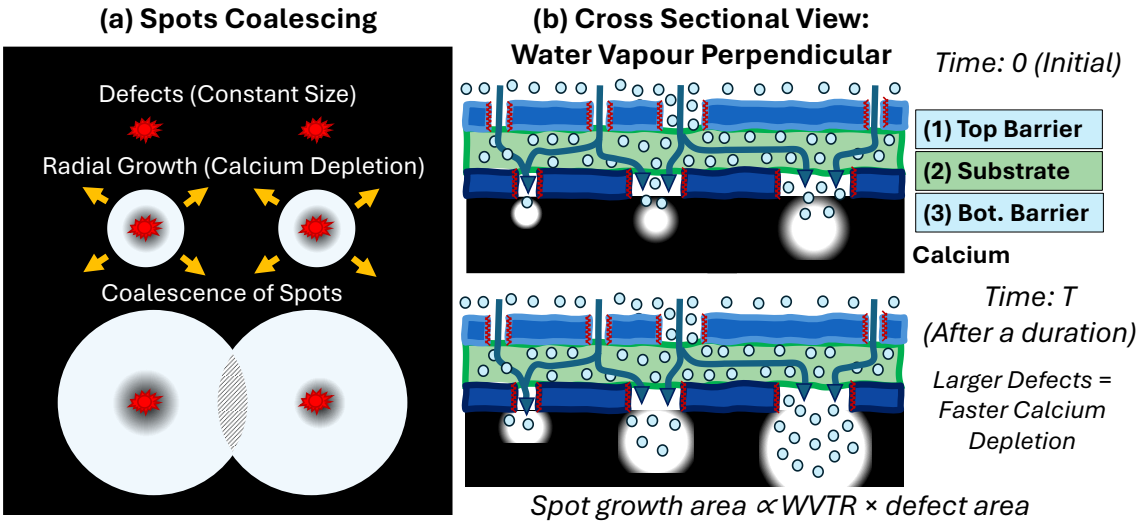


Figure 4-19: (a) Schematic illustrating that the calcium depletion spot (not the defect itself) expands radially over time. For the purpose of the model, the physical defect is idealised as constant in size to calculate an effective hydraulic diameter, though the actual geometry may evolve due to degradative mechanisms. Aside from this the illustration also shows the maximum spot area measured just before the coalescence of the adjacent or neighbouring spot. (b) Cross-section view of water vapour ingress and lateral diffusion within a multilayer barrier structure. Vapour enters through random, unaligned defects in the top barrier, diffuses laterally in the polymer substrate and only reaches the Ca layer where it encounters a defect in the bottom barrier. The Ca test therefore detects only those bottom side defects that allow vapour transmission. After critical time (T) larger defect areas enable greater vapour flux (proportional to WVTR × defect area), leading to faster radial spot growth and more rapid localised Ca degradation.

4.7.1 Defect Size Definition

To estimate the defect size responsible for the growth of a particular spot, one must calculate the mass of water permeating through the barrier layer ($M_{(H_2O)}$) at that defect, modifying and using the fluence equation (Equation 2-2). Where $M_{(H_2O)}$ is the total mass of water vapour that has passed through the defect (up until then) to give rise to the size of spot that it is observed at a particular time as defined in Equation 4-6. It is the molar ratio ($M_{(H_2O)} = 0.9M_{(Ca)}$), calcium density 1.55 g/cm^3, area of the calcium spot ($A_{(ca)}$), and height of the calcium layer when it becomes transparent or opaque ($h_{(Ca)}$) and the average mean grey value.

$$M_{(H_2O)} = 0.9 \cdot \rho_{(ca)} \cdot A_{(ca)} \cdot h_{(Ca)} \cdot (Gray\ Value) \qquad \textit{Equation 4-6}$$

To obtain a reliable approximation of the defect size (as defined in Equation 4-7), it is crucial to have an accurate estimate of the WVTR of the bare substrate under the specified environmental conditions. The defect size is determined by the relationship between the estimated rate of calcium depletion at the specific spot, and the WVTR of the bare substrate as moisture, where the defect size is proportional to the rate of moisture uptake and inversely proportional to the WVTR of the bare substrate.

$$Defect\ Size\ (m^2) = \frac{M_{(H_2O)}\ (\frac{g}{days})}{WVTR_{Bare\ Substratet}\ (\frac{g}{m^2 \cdot days})} \qquad \textit{Equation 4-7}$$

Example calculations, datasets and extended discussion for Ca test defect size calculations are presented in 9.3.10 Example: Defect Size Estimation Calculations.

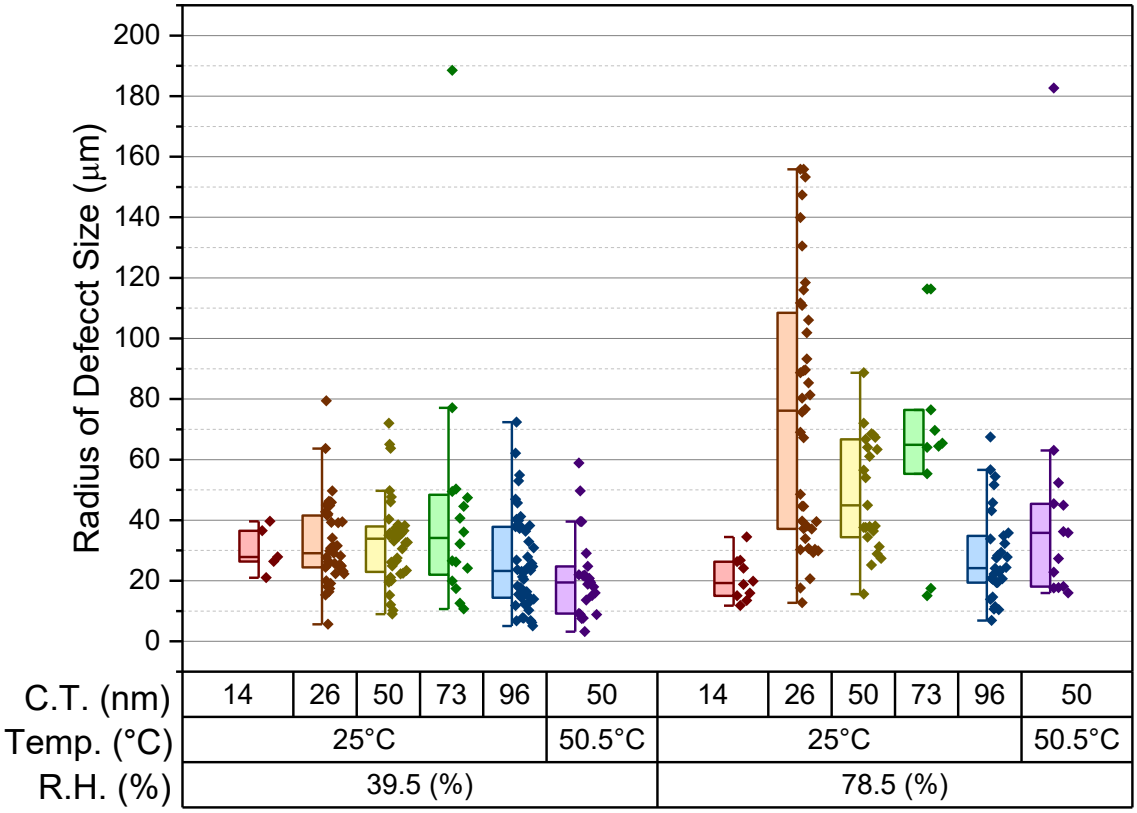
4.7.1.a Summary of Defect Sizes

The different estimated defect sizes are summarized in Figure 4-20 (box and whisker plot) based on coating thickness. Assuming the WVTR of Bare PET is ~2.11 ± 1.40 g/m²·day at 29 ± 3.5°C and 48.2 ± 19.6% humidity, the estimated defect sizes, ranging from 5 μm to 80 μm, are plotted in Figure 4-20. Notably, an outlier in the 73 nm coating (spot no. 1) shows a defect size of 188 ± 74.0 μm, significantly raising the average macro-defect size for this sample. A similar anomaly is seen in the 50 nm sample at 50.5°C and 78.5% RH, highlighting occasional large defects that can skew average estimations, so box and whisker pots are used in the figure to illustrate the spread. The data in this figure do not show a strong trend of defect size with coating thickness.

In comparison to literature, Park *et al* [61] suggests that representative defect radii for inorganic barrier coatings range from 400 to 3000 μm (PECVD- or evaporated film such as SiO_2, Si_3N_4 or Al on PET). This appears inconsistent with earlier studies such as Chatham, which in turn references Jamieson and Windle and others reporting pinhole diameters within the range of 1 to 20 μm range based on optical microscopy of evaporated Al coatings closer to the observed [103]. Chai *et al.* observed clear surface pinholes in 4.5 nm thick Al_2O_3 films on high purity copper, corresponding to porosity of 5.29%. Although Chai does not explicitly report the size of these pinholes, SEM micrographs suggest these are on the order of ~0.025 to 0.25 μm in radius. At a slightly higher thickness of 7.8 nm these pinholes interestingly were no longer visible by SEM and porosity dropped to 0.33% indicating morphological transition to a more continuous pinhole free film [352]

However, caution is necessary when interpreting these results, as the exact WVTR of Bare PET under these conditions is not definitively known, and measurements can vary. Moreover, because the PET substrates in this study are coated on both sides, the effective water-vapour concentration gradient across the film is also unknown. The AlO_x barrier on the side exposed to the environment reduces moisture ingress, meaning the driving force permeation through a defect on the Ca-facing side may be lower than for an uncoated reference. This uncertainty, together with the fact that the WVTR of the same exact bare PET under the same RH/temperature conditions has not been measured here, means that the defect sizes should be regarded as lower bound estimates rather than absolute values.

Additionally, as noted in the table, while multiple points or defects were analysed per sample, only a limited number of samples were collected for each condition. This suggests that the dataset may not be fully representative, and further testing with a larger sample size is needed to strengthen the reliability of these findings. This methodology also selects those point-like defects that are clearly separated from others and may not be fully representative of all means of water vapour permeation across a macroscopic scale.



No. of Samples						
RH (%)	Temp. (°C)	14 nm	26 nm	50 nm	73 nm	96 nm
39.5	25	1	3	3	1	3
39.5	50.5	-	-	2	-	-
78.5	25	1	3	2	1	3
78.5	50.5	-	-	3	-	-

Figure 4-20: Defect Radius (µm) over Coating Thickness (nm), under varying temperature and RH conditions. The plot illustrates the variability in defect sizes across different measurement spots, highlighting the range of defects observed under different environmental conditions. While no clear trend is evident, the data suggests a consistent range of expected defect sizes within AlO_x barrier films. The accompanying table provides an overview of sample distribution across thickness levels, indicating that although multiple defect points were analysed, the limited number of samples may affect the statistic robustness off the findings. Note: The driving force for water-vapour transport may differ from that of an uncoated film because the opposite side of the PET is also covered by an AlO_x barrier.

4.8 Influence of Spots and Defect Sizes to AlO_x Barrier Properties

The relationship between spot density, defect size, WVTR, and permeability is key. A higher number or larger size of defects should increase WVTR and permeability. Blunt *et al.*, concluded that defect size, rather than defect density alone is an important factor influencing WVTR. Larger defects provide direct, high-diffusivity paths for moisture ingress, leading to disproportionate increases in WVTR, even when defect density remains constant; this study says that while smaller defects contribute to moisture permeation, the total permeation is much greater for small number of larger defects than for a higher density of smaller pinhole-type defects over the same area [353]. Klumbies *et al.* demonstrated that WVTR does not always decrease linearly with coating thickness but depends on defect reduction [334], in agreement with the presented experimental data, where even thick coatings fail to reduce WVTR if a large area of defects persist. This also aligns with Yu *et al*, where it was emphasized that barrier performance hinges on defect minimization rather than bulk thickness [72].

4.8.1 Total Defect Area Index

In a simple model, the permeation through the macro defects might be postulated as simply proportional to the total defect area within an area of sample, neglecting any effect of complex concentration profiles in the polymer associated *e.g.* with clusters of defects. The total spot defective area (A_{dspots}) can be estimated using Equation 4-8, as the product of the spot density (D_s) and the average defect size (S_d).

$$\boldsymbol{A_{dspots}} = \boldsymbol{D_s}\left(\frac{\boldsymbol{Spots}}{\boldsymbol{cm^2}}\right) \times \boldsymbol{S_D}\ (\mu\boldsymbol{m^2}) \qquad \textit{Equation 4-8}$$

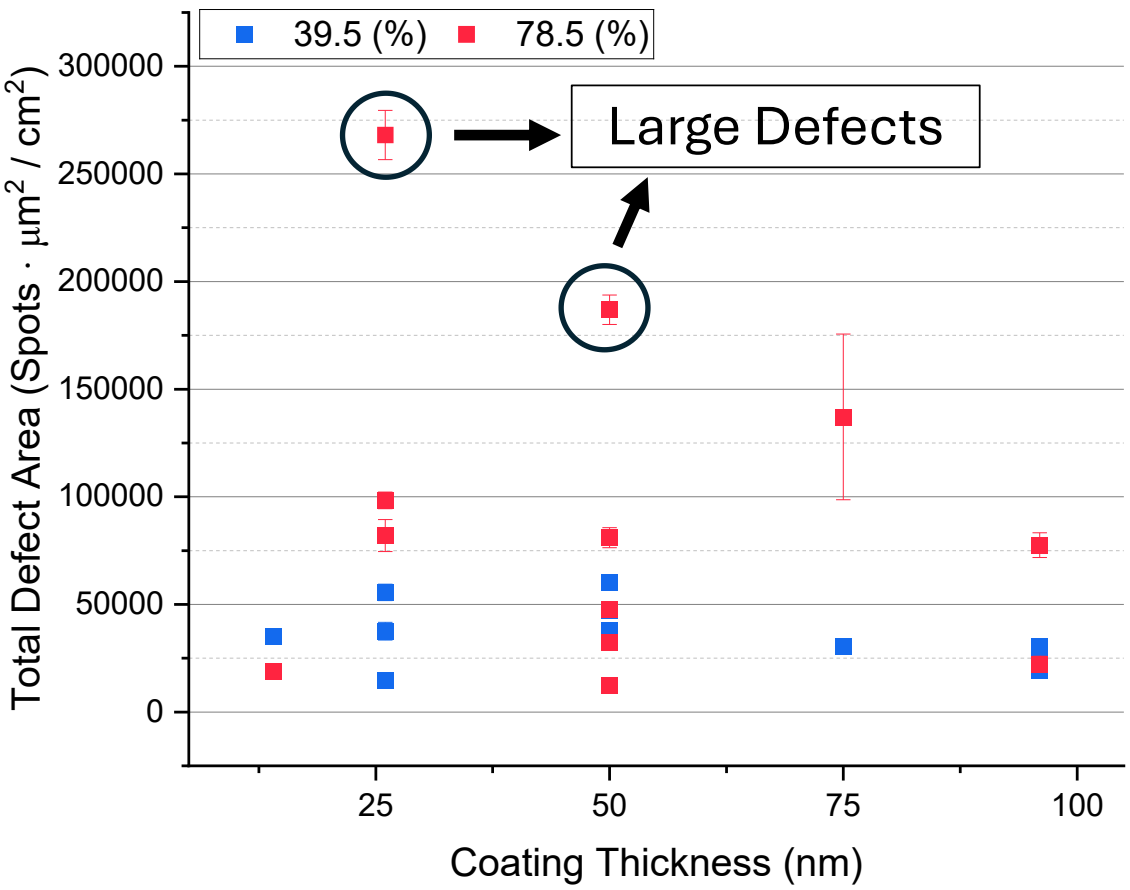
4.8.1.a Total Defect Area over Coating Thickness

Most samples were tested at 25°C and two relative humidities: 39.5% and 78.5%. The total area of defects per unit area of sample plotted against coating thickness, as seen in Figure 4-21, shows no clear difference in the overall defect area with RH, as one would expect. There is also no clear trend in defect area with coating thickness, with only perhaps a hint that the defect area is greater for thinner coatings.

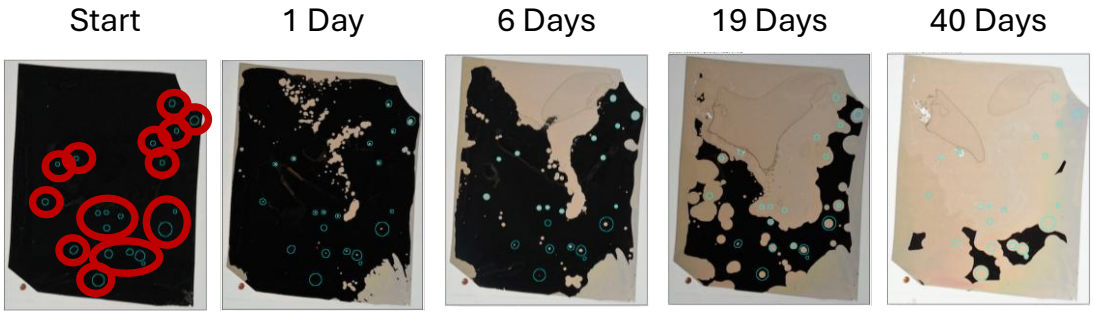
Looking at the data in Figure 4-21, it is noted that there is one sample at each of the (A) 26 nm and (B) 50 nm thicknesses that shows a particularly large defect area. Checking on these specific images shows reveals interesting insights.

For the (A) 26 nm sample (5.09 by 6.40 cm), it was estimated that it had 7.81 spots/cm^2, while 20 spots considered highlighted in red (some are combined in one bubble) have an estimated defect average size of 104.47 ± 21.60 μm, significantly larger than the overall average defect sizes (~40 μm as shown in Figure 4-20). Despite the low spot density, due to the large defect sizes present in this sample the estimated total defect area is large, meanwhile for the (B) 50 nm sample (3.03 by 3.05 cm) that showed large total defect area, a similar observation was made where a considered 9 spots had an estimated defect size of 64.79 ± 12.38 μm. In these cases of higher defect area, the reason for the larger defects, areas seem to be due to larger defect sizes and not high defect counts.

Overall, coating thicknesses between 14 nm and 96 nm resulted in similar defect area estimations, with minor anomalies attributed to specific sample variation (larger defect sizes).



A. 26 nm Large Defect Sample (5.09 by 6.40 cm): 7.81 Spots/cm²
20 Defects Avg. Size: 104.47 ± 21.60 µm



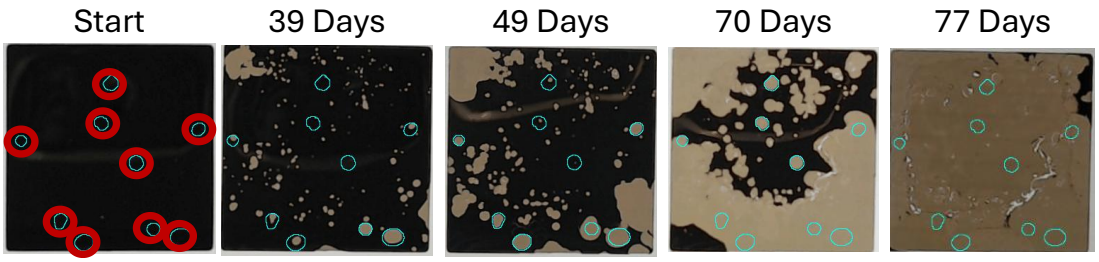


Figure 4-21: The total defect area (Spots·µm²/cm²) plotted against coating thickness for samples tested at 25°C under 39.5% and 78.5% relative humidity shows significant variability with no clear correlation. Outliers at 26 nm, 50 nm, and 73 nm, along with large standard deviations, suggest inconsistencies likely due to sample preparation, measurement errors, or environmental factors.

4.8.1.b Impact of Total Defect Area on WVTR

Figure 4-22 and Figure 4-23 plots WVTR over total defect area, for the various samples at 25°C at two humidities (39.5% and 78.5%), showing specifically the large defects yielding higher WVTR's – agreeing with the physical relationship of more area of defects and higher WVTR's.

To highlight this relationship, Equation 4-9, demonstrates how the WVTR or permeability can be estimated (indicated by purple symbol line in Figure 4-22 and Figure 4-23). Specifically, the estimation considers the ratio of the total known defect area ($A_{def,known}$) to the total barrier layer area (A_{total}) multiplied by the overall average WVTR or Permeability ($\overline{WVTR/Perm.}$). This average value is approximated using a linear fit of bare or uncoated PET Ca test data since exact WVTR values were not measured at the specified RH's. The estimated values at 25°C are approximately 1.86 g/m²·day (9.53E-14 mol/(m·s·Pa)) at 39.5% and 2.89 g/m²·day (7.45E-14 mol/(m·s·Pa)) at 78.5%

$$\boldsymbol{Prediction_{WVTR/Perm.}} = \frac{\boldsymbol{A_{def,known}}}{\boldsymbol{\overline{A_{total}}}} \cdot \boldsymbol{\overline{WVTR/Perm.}} \qquad \textit{Equation 4-9}$$

Figure 4-22, shows the lower humidity (39.5%) condition describing how the experimental data generally fits well with the expected linear trend and predicted data total defect area primarily determines WVTR [334, 353], though there still remains some variability in samples and their assessment such that points do not fit the linear trend within the estimated error.

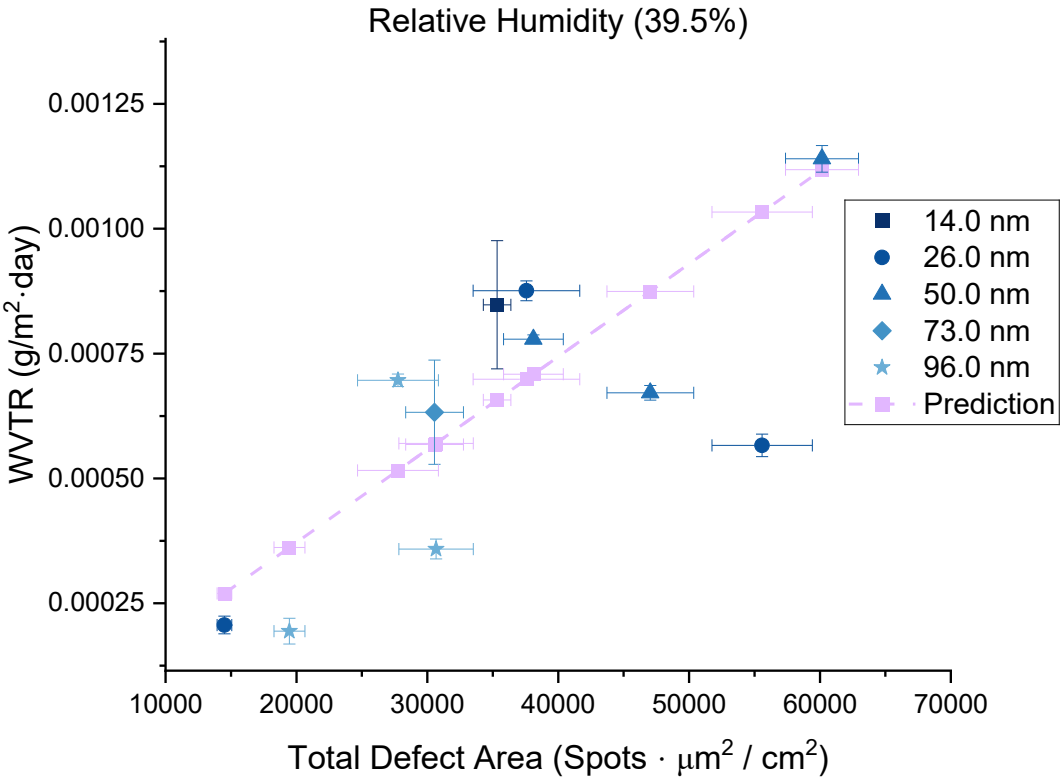


Figure 4-22: WVTR as a function of total defect area for ALD barrier layers at 25°C 39.5%. The data confirms a strong correlation between WVTR and total defect area, with slight deviations likely due to measurement limitations in the Ca test, edge permeation effects or inaccuracies in defect size estimation. The results align with literature predictions from Blunt et. al. and Klumbies et. al. describes how barrier performance is dictated by total defect area, particularly large defects, rather than coating thickness alone. Highlight the critical role on defect minimization strategies in ALD fabrication for

moisture barrier performance. As acknowledged, while there is noticeable scatter and most points do not fall within the estimated error bounds of the linear fit, the overall trend and its quantification remain well supported. The deviations may reflect sample-to-sample variability, limitations in the Ca test measurement of WVTR, or defect area estimation uncertainty.

Moving towards the higher humidity, Figure 4-23, shows the similar trend of WVTR increasing with total defect area. Interestingly the experimental values, despite showing higher total defect area present a lower spread of values from the linear relationship compared to the lower humidity batch.

Moreover, it is also worth noting that the model predicts the WVTR accurately at higher total defect areas, even beyond 100,000 (spots · μm^2 / cm^2). These findings further reinforce the idea that the quality of the ALD AlO_x layer plays a more critical role in determining its barrier properties than thickness alone. However, as previously discussed an optimal thickness may help reduce the likelihood of defects to allow for better coverage while minimizing coating time and source materials.

Another improvement by reducing defect dominated transport is improving oxide nucleation and the oxide-polymer interface through surface pretreatments. A brief oxygen-plasma or UV-ozone pretreatment has been shown to add oxygen containing groups to polymer surface (carboxylic/anhydride and some hydroxyl), making reactive sites on the polymer surface improving ALD nucleation and adhesion. Ozone treatment for PET has shown a 65% increase in pull out adhesion compared to untreated PET [354]. On other polymer substrate like Polypropylene, oxygen plasma pre-treatment is said to be necessary to achieve ALD growth rates with standard precursors, consistent with more reactive surface sites and nucleation [81]. A better bonded and more abrupt oxide to

polymer interface also leaves fewer lateral interfacial channels, sealing this point can extend lag time and reduce apparent WVTR [13, 102, 355].

Furthermore, we can distinguish between “dry adhesion” which is the initial bond strength governed by physical forces in ambient conditions (mechanical interlocking or fixings and Van Der Waals Forces, *i.e.* Gecko or Spiders legs attaching to wall) and, wet adhesion which is defined as the interface’s ability to resist delamination during prolonged moisture exposure, understood as liquid-based adhesives or adhesion using chemical bonds or capillary forces.

In terms of films, a distinction cited by Ortigoza-Diaz *et al.* shows thin-film Parylene systems where coatings may exhibit sufficient dry adhesion via mechanical interlocking and secondary forces (hydrogen bonding, Van der Waals) suffer from catastrophic delamination upon exposure to moisture [356] indicating that these physical interactions are thermodynamically unstable in water. It has been shown that water molecules can diffuse to the interface and compete with adhesive groups breaking these weak bonds and effectively displacing the coating by forming a weak boundary layer (hydrolytic displacement). On the other hand, to achieve high wet adhesion, surface pre-treatments (*e.g.*, plasma) are employed to modify the polymer surface chemistry, typically increasing surface energy and creating polar functional groups. This activation facilitates the formation of strong covalent bonds (chemical links) between the coating and the substrate. Unlike most physical bonds these covalent linkages resist thermodynamic displacement by water molecules, thereby preserving interfacial integrity and ensuring barrier performance over long durations [356-359].

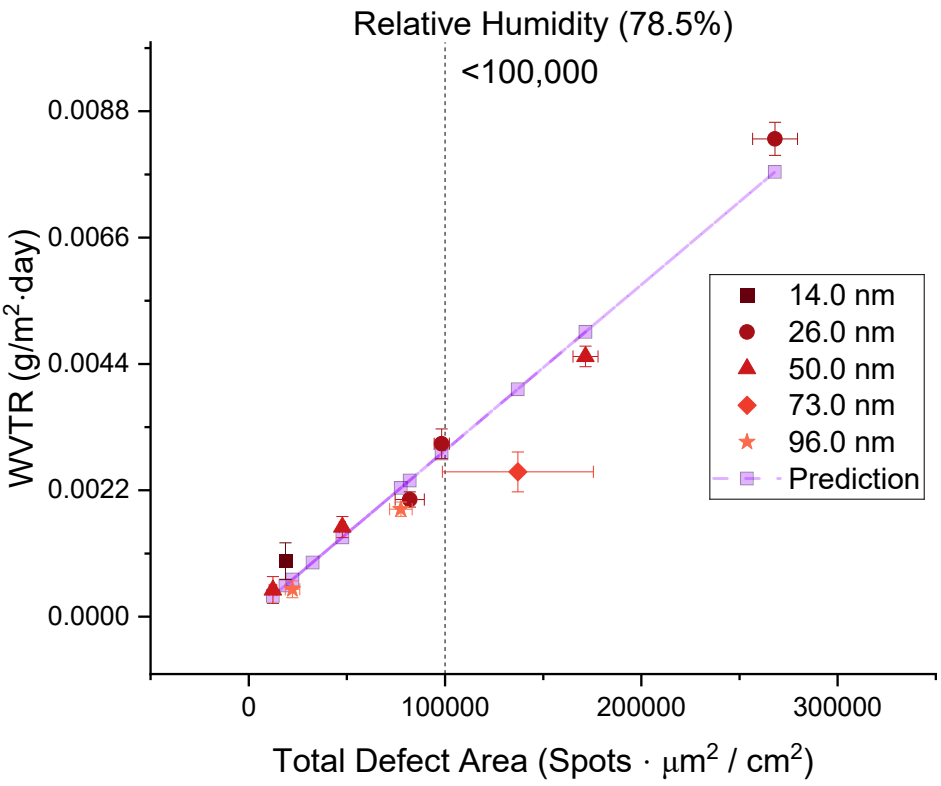


Figure 4-23: WVTR as a function of total defect area for ALD barrier layers at 25°C 78.5%, shows the same predicted relationship – demonstrating the fidelity of the predictive model to experimental data, particularly at higher defects beyond those observed at lower humidity levels. However, the slight deviation in the 73.0 nm sample may be attributed to either an underestimation of defect size (indicating a lower actual total defect area) or an overestimation of edge effects in WVTR estimation. These findings further emphasize the importance of ALD AlO_x quality over thickness alone in achieving superior barrier performance.

Now plotting the data in terms of permeability, Figure 4-24 shows a clear trend where permeability increases with total defect area. When accounting for factors such as thickness and RH in permeability calculations, the data maintains the linear correlation, reinforcing the argument that WVTR and permeability are defect-dependent properties. This further supports the idea that barrier performance is primarily influenced by the

quality of the ALD AlO_x layer, rather than just thickness or external environmental conditions.

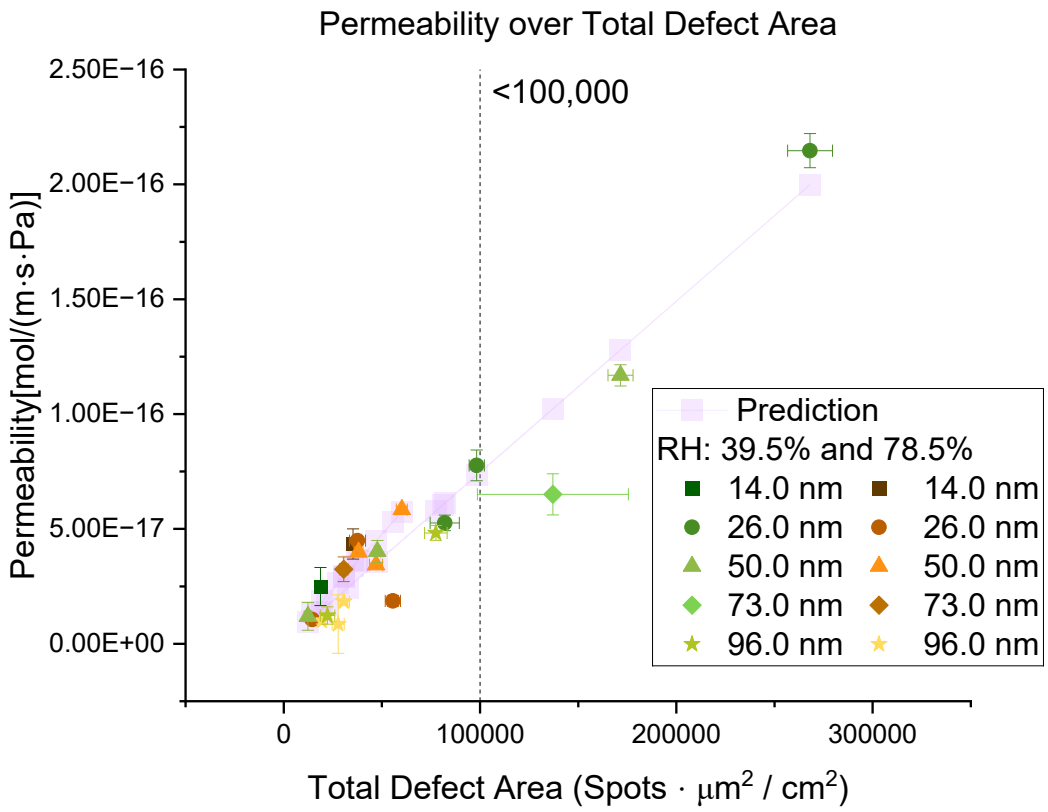


Figure 4-24: Permeability as a function of total defect area, demonstrating a clear increasing trend. This highlight the dependence of ALD AlO_x permeability on the quality of the barrier layer, reinforcing the notion that defect density is the primary determinant of overall permeability–rather than external environmental factors such as RH.

4.9 Surface Analysis of AlO_x Barrier Layers on PET

4.9.1 Film Characterization of Uncoated PET

An important factor that may influence the overall quality of the barrier layer or ALD coating are the characteristics of the substrate onto which it is deposited, in this case PET substrate (DuPont Teijin Films – 100 µm with a 25 µm peel layer). The substrate's

surface can significantly influence the barrier properties of the encapsulation layer, as, for example, particles at the substrate surface can reduce coating uniformity and introduce defects. Although not carried out in this study, surface modifications like plasma or UV exposure can modify the surface of the polymer and improve adhesion between the polymer and the coating and could be explored in future studies. These treatments enhance PET adhesion by removing contaminants, introducing polar functional groups (*e.g.*, hydroxyl, carbonyl, carboxyl), and increasing surface energy. This improves wettability, strengthens adhesive interactions and may slightly alter surface roughness, promoting mechanical interlocking [360].

Figure 4-25 (a) presents optical micrographs of an uncoated PET substrate after its peel layer was removed. The substrate was then placed on a glass (microscope) slide for imaging revealing surface morphology differences. While no defects are visible to the naked eye, at 5x magnification, small scratches or discontinuities are noticeable, likely from processing or handling. The ALD coatings were applied in a clean room environment, which helps reduce the risk of contaminants such as dust or airborne particles during film deposition. However, it is important to note that subsequent sample handling and microscopy imaging were performed outside the cleanroom, which could introduce additional surface features or contamination. While cleanroom conditions cannot eliminate all defects, they do lower the likelihood of contaminated-related permeation pathways that can weaken barrier performance.

Figure 4-25 (b), zooms in on the surface, revealing scratches, discontinuities, and possible contaminants. While defects are still visible, the substrate remains reasonably uniform and suitable for coating. Figure 4-25 (c), an SEM image, shows that at higher

magnification, areas between the blemishes that were observed under the optical microscope appear smooth, confirming that the substrate is generally free of significant surface defects. Figure 4-25 (d), presents an extreme case of PET substrate damage as observed under an optical microscope. Prominent scratches, fractures and non-uniform regions are visible which could significantly impact the quality and performance of a barrier layer coating.

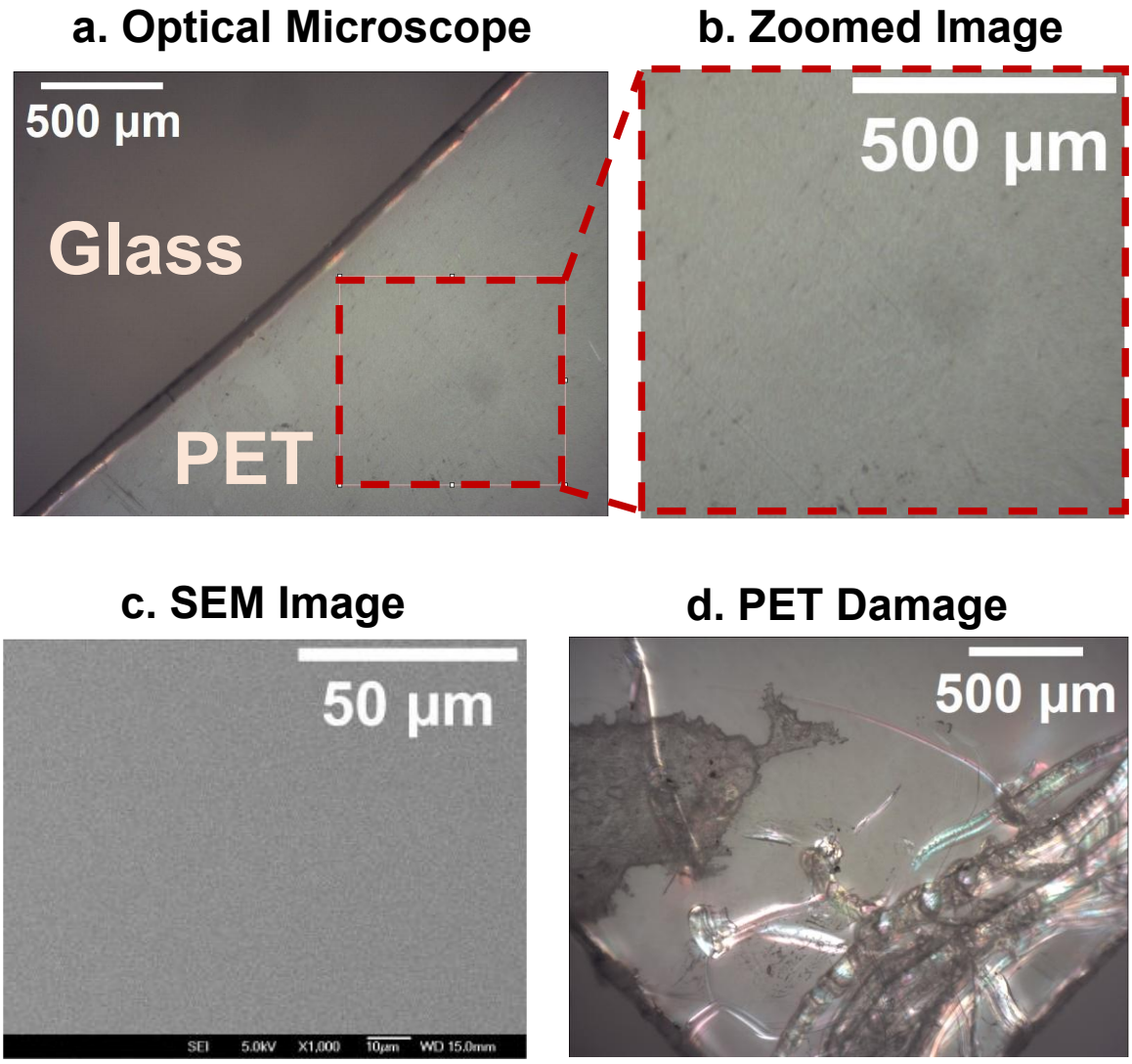


Figure 4-25: (a) Optical microscope image of the peeled side of uncoated PET on a glass slide (Yenway CX40 Upright Microscope), (b) Zoomed 5x image highlighting scratches, discontinuities, or possible contaminants, (c) Scanning Electron Microscope (Jeol 6500F

SEM) image of uncoated PET showing no significant surface defects at higher resolution, indicating the film is generally defect-free, (d) Optical microscope image of damaged PET substrate, revealing sever defects, fractures and possible contaminants. These irregularities can compromise the uniformity and effectiveness of a barrier layer coating.

In addition to imaging the surface of the uncoated PET, the "scratch" features and roughness were analysed. Figure 4-26 (a), an optical profilometer image, shows that despite surface texture, including unidirectional scratches or waves, the uncoated PET remains relatively flat. Across 17 samples, the average surface roughness was 0.14 ± 0.13 μm with a maximum height of 0.50 ± 0.57 μm, as confirmed by contour plots showing a generally flat and uniform surface with only slight peak features.

Figure 4-26 (b) shows Atomic Force Microscope (AFM) data of the uncoated PET, examining a smaller region with higher detail. The rough features observed in the optical microscope and profilometer are visible but remain minimal, with surface variations only on the order of tenths of a micron. Despite localized surface peaks approaching 0.5 μm, the average roughness of PET substrate remains in the tenth of a micron range. Given ALD's conformal nature, this roughness is sufficiently minimal for effective encapsulation, potentially even enhancing adhesion.

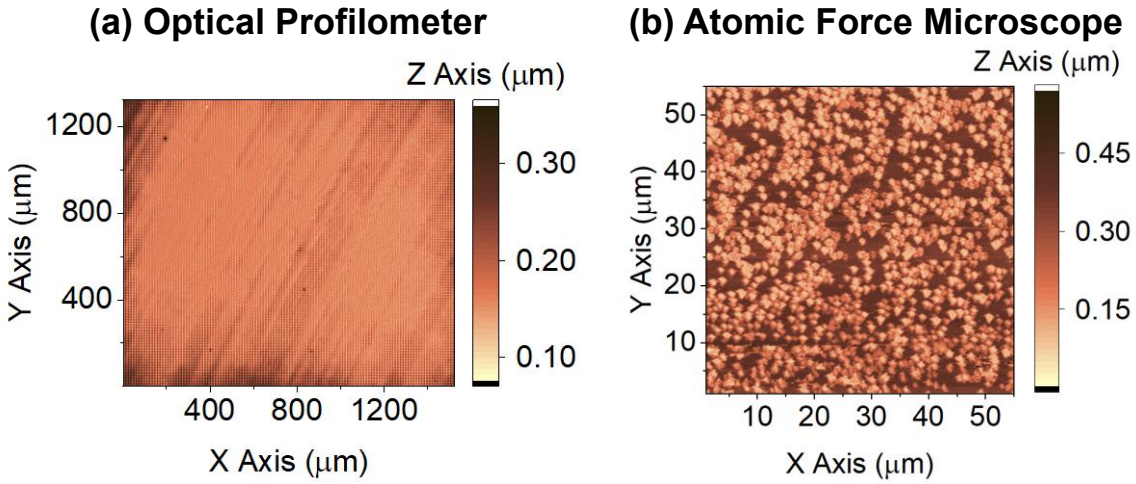


Figure 4-26: (a) Optical Profilometer (3D Optical Profiler by Filmetrics) of an uncoated PET substrate (1,522 µm × 1,323 µm) shows a mean height of 0.18 µm and a maximum height of 0.36 µm, using a non-contact method to analyse surface features over a wide area. (b) Atomic Force Microscope (AFM - Agilent 5400) image of a smaller region (55 µm × 55 µm) confirms surface features within the 0.10 to 0.30 µm range, supporting the profilometer findings.

4.9.2 Film Characterization of Coated AlO_x ALD PET

Aluminium oxide films grown via thermal ALD using TMA and water are inherently amorphous when deposited at temperatures below approximately 600 °C [33, 361]. This observation is also corroborated by Groner *et al.*, who characterized low temperature ALD AlO_x (grown between 33°C and 177°C) as an amorphous material lacking long range crystalline order [217]. Given this expected amorphous state and extreme thinness of these layers, X-ray diffraction (XRD) analysis was not performed, as it would be unlikely to provide useful structural information due to the lack of a crystalline signal. While high-resolution transmission electron microscopy (HR-TEM) would be more effective, albeit technically difficult, method to definitively establish the presence or absence of crystallinity. Consequently the permeation mechanisms in these coatings are not governed by grain boundary diffusion as there are no crystalline grains or associated boundaries present to act as diffusive pathways. Instead, Carcia *et al*, for similar low temperature barrier films, gas transport is governed by the intrinsic free volume or chemical defect structure of the amorphous lattice. Specifically, Carcia *et al.* propose that permeation proceeds via a chemical exchange mechanism along percolating clusters of hydroxyl (-OH) defects, which create localized pathways for moisture transport through the otherwise dense amorphous matrix [218, 336]. Despite the films lacking grain boundaries the high concentration of hydrogen based defects serves as the functional equivalent for any water diffusion through the barrier layer.

4.9.2.a Microscopy Defect Probability Analysis

This analysis aims to quantify defect occurrence probabilities and verify whether observed defect sizes align with theoretical estimates, ensuring that microscopy-based detection reflects expected values. The probability estimates are derived from the Ca test data, which was used to infer defect densities and correlate them with microscopic observations. Figure 4-27 illustrates the probability of detecting at least one defect in a 1 mm × 1 mm region across different coating thicknesses, showing that the likelihood remains relatively consistent regardless of coating thickness.

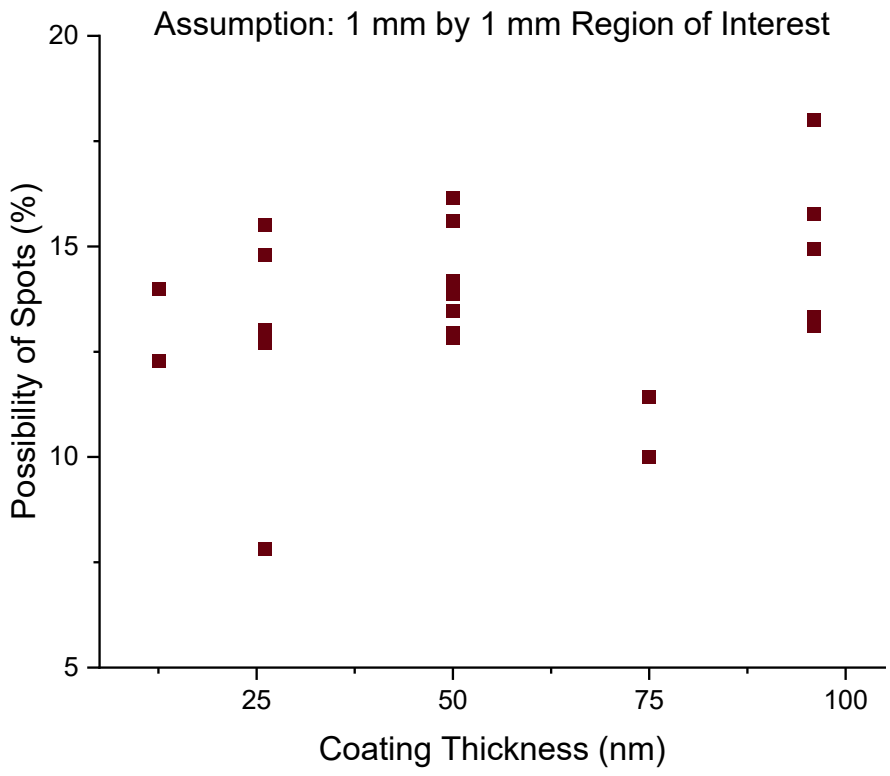


Figure 4-27: Probability of detecting a defect (%) as a function of AlO_x coating thickness (nm) on PET, illustrating the influence of coating thickness on the occurrence of defects within a $1\ mm \times 1\ mm$ *region of interest in coated samples.*

Based on a defect density of ~13 spots / cm^2 (Figure 4-18), the Poisson-estimated probability of detecting at least one defect in a randomly selected 1 mm × 1 mm region is ~12%. Using this information, Figure 4-28 presents a 26 nm AlO_x PET barrier layer observed under different imaging conditions, highlighting the probability of detecting defects at varying magnifications.

- **(a) Optical Microscopy (5 × Magnification, 2,417 µm by 1,810 µm):**
  In this large field of view, the probability of detecting at least one defect is ~43%. Features such as blemishes and spots may indicate potential defects, but the presence of artifacts such as reflections or distortions from the glass slide, could lead to misinterpretation during analysis. These artifacts must be distinguished from actual material defects to ensure accurate defect characterization.
- **(b) Scanning Electron Microscopy (220 µm by 165 µm):**
  At this higher magnification with a smaller field of view, the probability of detecting a defect drops significantly to ~0.5%. However, if a defect is present, it would be highly noticeable, given its average size of 49.67 ± 12.51 µm, as illustrated in the idealized overlay on the SEM image. Additionally, the SEM image reveals surface damage from sample preparation, as well as contaminants and edge degradation, providing deeper insight into coating integrity and structural weaknesses beyond what is visible under optical microscopy.

This comparison demonstrates how field of view and magnification influence defect detection, emphasizing the need for both optical and SEM imaging to aid the

assessment of defects and differentiate between actual material failures and imaging artifacts.

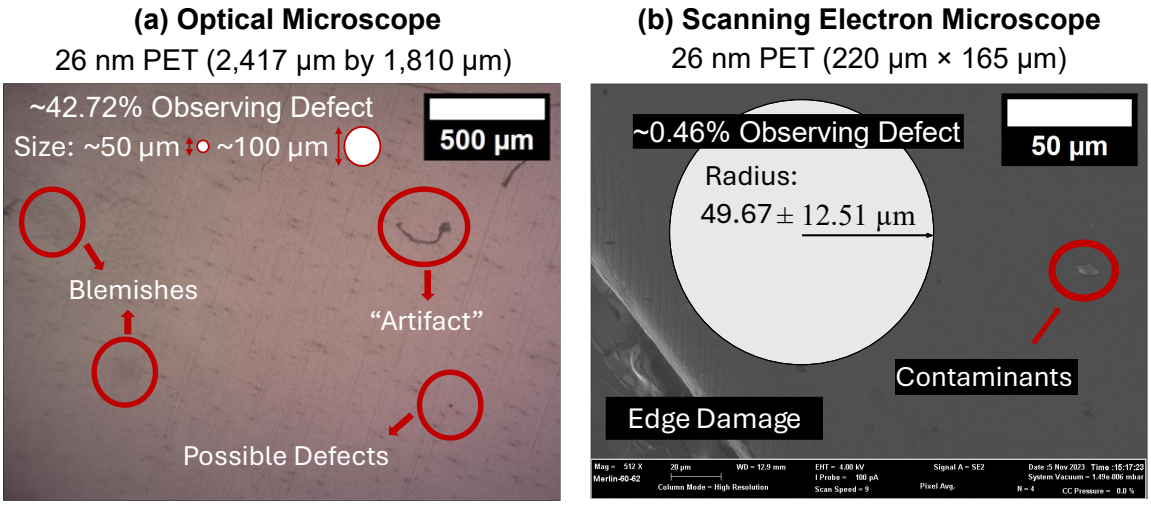


Figure 4-28: (a) Optical Microscopy (5 × Magnification, 2,417 µm by 1,810 µm) shows ~42.72% defect detection probability, with blemishes and possible defects. (b) SEM (220 µm by 165 µm) has a low ~0.46% detection probability, but any defect present would be large and easily recognizable (49.67 ± 12.51), also revealing surface damage, contaminants and edge degradation. Note: As a visualization samples with a smaller area will often appear cleaner or defect free because of the lower chance of a defect entering the field of view is low. However, when a defect as noted is present it should appear with a high contrast and without any possible glass slide artifacts – further explaining possible differences on images between SEM and Optical micrographs even with the same conditions.

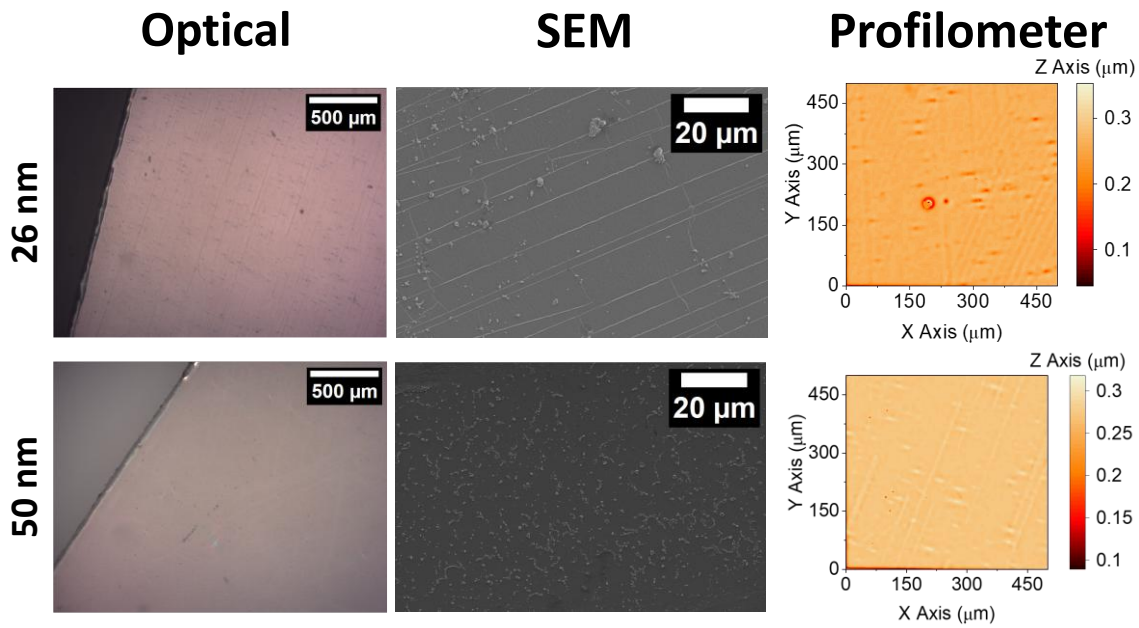
4.9.2.b Surface Morphology and Defects

Figure 4-29, compares the surface morphology of ALD AlO_x coatings on PET at thicknesses of 26 nm, 50 nm, and 96 nm, using optical microscopy, SE, and optical profilometry.

In the optical images, faint processing lines and occasional spots are likely contaminants or substrate-related features, and are apparent at all thicknesses but do not indicate significant damage to the coating. The SEM images similarly reveal subtle line patterns, which appear progressively masked as coating thickness increases from 26 nm

to 50 nm. At 96 nm, however a few localized blemishes become more prominent, suggesting that while thicker coatings can better cover substrate irregularities, they may also introduce or highlight discrete surface defects.

These observations are corroborated by the profilometry data, which show relatively uniform surfaces across all three thicknesses but also capture fine topographical details corresponding to the optical and SEM observations (*e.g.* lines, spots or blemishes). Thus, although all coatings are sufficiently continuous to obscure large-scale substrate flaws, the incremental increase in thickness modifies the visibility of underlying features and may also lead to the appearance of localized defects in the coating, suggesting that as coating thickness increases new morphological changes are observed that directly influence overall moisture resistance and mechanical stability of the barrier.



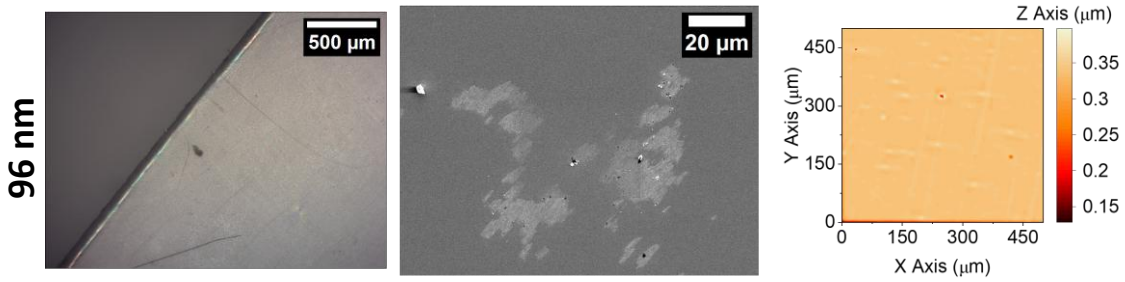


Figure 4-29: Surface analysis images (Optical and SEM) and profilometry data of 26 nm, 50 nm, and 96 nm coatings reveal distinct features, possible defect spots, and surface roughness. The profilometer data highlights the overall uniformity of AlO_x coating on the PET substrate, with thicker coatings showing better coverage and consistency. As noted: optical images were acquired with the sample on a glass microscope slide. Any straight or branched lines seen in transmission that reproduce on the blank slide are slide scratches or fractures and not cracks in the PET/AlO_x film, while SEM (no glass slide) and profilometry do not show any through film fracture features. Note: A possible interpretation of the straight lines seen in 26 nm as suggested would be PET processing lines or substrate marks that are increasingly masked upon coating of AlO_x, and are not interpreted as coating cracks on PET, and possibly progressively masked with increasing AlO_x thickness as it is no longer visible in thicker coatings at 50 nm and 96 nm.

The study of even thicker coatings is seen in Figure 4-30. At a thickness of approximately 250 nm, the ALD AlO_x coating on PET appears to mask the underlying macro-scale features that are present in uncoated PET substrates. Profilometry data confirm a notably reduced surface roughness range, suggesting that features below 100 µm are effectively concealed by the coating. This behaviour indicates that the 250 nm ALD layer is sufficiently robust to smooth out large structural irregularities in the substrate.

In contrast, at 375 nm, the ALD AlO_x coating exhibits signs of structural instability, as evidenced by the appearance of defects visible in both optical and SEM images. These defects may stem from internal stresses or layer collapse within the thicker film. Correspondingly, the profilometry data show an increase in surface roughness range, corroborating the formation of new morphological features rather than simply obscuring existing substrate irregularities.

This progression demonstrates that these very thick ALD coatings can effectively cover macro-scale substrate flaws (not necessary for improvements for moisture barrier resistance), further increases in thickness may introduce new defects as the film undergoes morphological changes, thereby affective the overall surface profile.

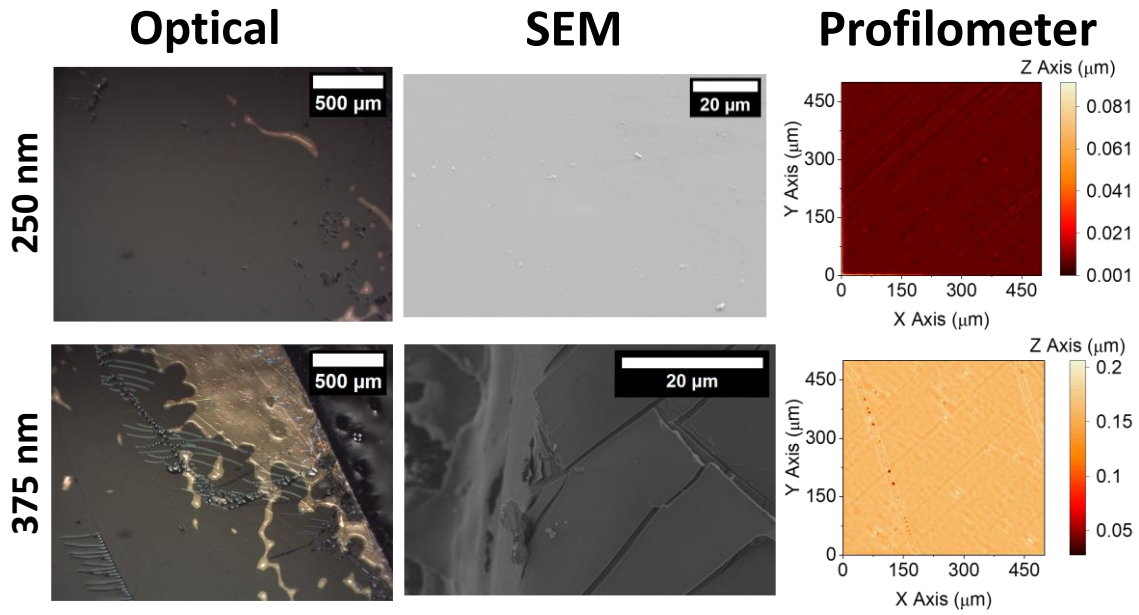


Figure 4-30: Surface analysis images of 250 nm and 375 nm ALD AlO_x under optical, SEM and profilometer data, that shows the coverage of macro scale irregularities of PET that are no longer visible but further coatings show internal stresses and collapse that indicate new defects within the film.

4.10 Conclusions

ALD Coating Effectiveness & Optimization:

- The study extensively explores the use of ALD to create AlO_x coatings on PET substrates as water vapor barriers. It identifies an optimal thickness range of 26-50 nm, where ALD offers the best WVTR reduction, while thicker coatings do not produce further barrier improvements. Although low permeabilities can be achieved even at lower thicknesses, the likelihood of achieving a more effective

barrier generally increases with thicker coatings. Coatings below 26 nm are more susceptible to macro effects, which compromise their performance. Additionally, the findings indicate that higher deposition temperatures further enhance barrier properties.

Temperature, Humidity, and Masking Impact:

- The study also highlights the influence of temperature, humidity on ALD-coated films. While environmental factors such as RH and temperature affect WVTR measurements, the proportional influence is theoretically expected to be similar for both coated and uncoated films if the permeation is governed by macro defects and the coating defines the effect transport area. In coated films, coating thickness can have some influence on barrier performance.

Permeation Mechanisms & Defect Analysis:

- In this work, ALD coated films often showed a relatively low Ea, like the polymer suggesting macro-defect dominated transport, however many samples also showed a higher Ea (Figure 4-6). This contrasts with thick RF sputtered AlO_x but that behaviour is not universal: many studies on thin RF sputtered oxides find low Ea values compared to what is presented in this work. Film thickness and defect morphology rather than the deposition method alone govern apparent transport mechanism [11, 194] . Spot analysis in this study supports that larger defect areas correspond with higher WVTR, affirming macro-defect control as a key design target for improving barrier performance.

5 Aluminium Oxide (ALD) Coated PVAl

5.1 Biodegradable Substrates for Flexible Electronics

Flexible electronics have traditionally relied, for substrates, on non-biodegradable, petroleum-based polymers like Polypropylene (PP), Polyimide (PI), Thermoplastic Polyurethane (TPU), Polyethylene Naphthalate (PEN), Polydimethylsiloxane (PDMS), and Polyethylene Terephthalate (PET), the latter used in this study. However, growing interest in biodegradable polymers, both natural and synthetic, offers a sustainable alternative that can degrade hydrolytically or enzymatically, reducing electronic waste and making them suitable for flexible electronics.

Biodegradable substrates, including biobased polymers, nanocomposites, and paper and other cellulose-based materials, are extensively utilized in conventional packaging due to their potential for environmental sustainability. Their appeal has expanded to emerging applications in flexible electronics (transient medical devices, disposable sensors and short-term protective barriers), owing to their tuneable mechanical properties, lightweight nature and compatibility with optical transparency requirements. However, performance limitations impede widespread adoption in this field. While certain biodegradable materials (*e.g.*, cellulose acetate, polylactic acid films) achieve high optical clarity comparable to conventional plastics, others suffer from inherent opacity or inconsistent light transmission. Additional challenges include elevated surface roughness (hindering precision printing of electronic components), inadequate barrier properties against moisture and oxygen (critical for device longevity), and mechanical fragility under repetitive stress. Addressing these limitations through materials engineering —

such as nanoscale reinforcements, hybrid coatings, or chemical modification — could unlock their potential in next-generation sustainable electronics [362, 363].

Among the various options, the chemically synthesized biodegradable polymer polyvinyl alcohol (PVAl) shows promise for flexible applications because of its excellent film forming ability and optical clarity [363, 364]. PVAl is produced by hydrolysis of polyvinyl acetate (PVAc), and its final properties depend strongly on the degree of hydrolysis and the resulting crystallinity [365, 366]. The abundance of surface hydroxyl (-OH) groups renders PVAl hydrophilic and gives it a typical WVTR of order 10^2 $g/m^2 \cdot day$ at 38°C / 70% RH, rising to $\geq 5 \times 10^2$ $g/m^2 \cdot day$ at 90% RH and falling below 20 $g/m^2 \cdot day$ at 50% RH [367]; These same -OH groups also provide a high density of nucleation sites that promote conformal growth of inorganic barriers during low-temperature ALD [368-370]

This chapter investigates whether an ultrathin AlO_x ALD coating can transform this highly permeable yet compostable substrate into a high-performance moisture barrier. Two commercially available, melt-processed PVAl films from Aquapak Polymers (UK) are evaluated:

- Partially Hydrolysed (85% to 90%) monolayer film (~21 μm), referred to as Thin PVAl (Betol)
- Partially Hydrolysed (85% to 90%) bilayer film (~42 μm), referred to as Thick PVAl (Alpine)

The PVAl films used are commercial melt processed (extruded) grades given as sheets from rolls. It is typical to use solution casting in laboratory scale research for simplicity however using melt processing techniques like extrusion casting and blown

film extrusion are preferred for industrial scale production for higher throughput and efficiency. Using melt processing films shows a directly translatable findings for scalable commercial applications such as roll to roll manufacturing the dominant workflow for flexible large area electronics. Studies show that blown film PVA develops higher in plane orientation and crystallinity than solution-cast films (and some extrusion cast films), which correlates with stronger mechanical properties and significantly better oxygen barrier performance; additionally gel extruded routes also avoid skin core thickness heterogeneity that is often seen in solution cast films [371-374].

An expanded rationale for material selection is further described in detail in 9.4 Aluminium Oxide (ALD) Coated PVAl Supporting Materials of the supporting information, along with supporting information on PVAl substrate and synthesis (9.4.2 to 9.4.3 in pp. 500-501), PVAl properties (9.4.4 in pp. 502 - 506), uncoated PVAl WVTR method/results (9.4.5 in pp. 507 - 513), Ca-test setup and representative plots / features for Thin and Thick PVAl (9.4.6 in pp. 514 - 529), legacy ImageJ defect analysis (9.4.7 in pp. 530 - 533), Python-based defect maps distributions (9.4.8 in pp. 533 - 545), population statistics (9.4.9 in pp. 547 - 552) and defect size data sets (9.4.10 in pp. 557 - 576). Using this information and characterisation methods established in the previous chapters, the barrier performance of the AlO_x coated substrates along with defect mechanisms are analysed and discussed.

5.2 Comparison of Uncoated PVAl MOCON Aquatran Results

There is a wide variation in reported WVTR and permeability values for PVAl (see Table 5-1), likely due to differences in methodologies, film types, and environmental conditions, as well as the challenges to measure the permeation in such a hydrophilic material. The MOCON Aquatran results measured here for uncoated PVAl films show significant discrepancies from literature values, except for those of Mo *et al.* [94], which align closely with these data. A detailed discussion of PVAl material properties and MOCON WVTR measurement challenges, including additional figures and data are presented in 9.4.5.b Discussion on Mocon Aquatran WVTR Results.

Chandio *et al.* (2021) [375] and Xianda *et al.* (1987) [367] reported much higher WVTRs—90 ± 5.2 and 790 g/m²·day respectively—using less controlled methods, while Mo *et al.* (2014) [62], using biaxially oriented PVAl under specialized conditions, reported lower values (0.2 to 24 g/m²·day), similar to our findings.

Park *et al.* (2023) [376] and Sarwar *et al.* (2018) [377] also found higher WVTRs, underscoring the influence of testing methodologies, such as ASTM E96 versus MOCON Aquatran, and differences in film properties. This suggests that controlled testing, and standardized methodologies are critical for achieving consistent and accurate WVTR measurements.

These insights highlight the need for better standardized testing to ensure reliable comparisons across studies.

Table 5-1: Literature Comparison of Uncoated PVAl Results

Film Type	WVTR ($g/m^2 \cdot day$)	Permeability ($mol/(m \cdot s \cdot Pa)$)	Conditions	Thickness (µm)	Methodology
Experiment: Thin (Betol)	4.76	9.68E-15	38°C, 100% RH	21	Mocon Aquatran 2
Experiment: Thick (Alpine)	3.52	1.43E-14	38°C, 100% RH	42	Mocon Aquatran 2
Chandio *et al.* (2021) [375]	90 ± 5.2	2.30E-13	40°C, 85% RH	25	ASTM E96, water cup method
Xianda *et al.* (1987) [367]	790	1.70E-12	38°C, 90% RH	20	GB 1037-70 (Gravimetric Method)
Park *et al.* (2023) [376]	600 (25 $g/h/m^2$)	1.94E-11	22°C, 75% RH (NaCl) and 0% RH ($CaCl_2$)	100	Modified ASTM E96
Mo *et al.* (2014) (Biaxially Oriented PVAl) [94]	0.2	5.57E-15	23°C, 10% RH	12.2	Modified ASTM F1249-90, PERMATRAN-W 3/33
	4.0	1.11E-13	23°C, 60% RH		
	24.0	6.69E-13	23°C, 90% RH		
Sarwar *et al.* (2018) [377]	43.09	9.74E-13	40°C, 24 hours (No RH reported, assumed 100% for permeability calculations)	260	"Water bottle method"

5.3 Activation Energy of PVAl Mocon Aquatran

Most samples did not exhibit the anticipated linear relationship between ln(WVTR) and 1000/T, indicating that the permeation mechanism in PVAl is complex

and inherently non-Arrhenius. Unlike hydrophobic substrates, PVAl acts as a hydrogel like material in the presence of high humidity. The diffusion of water is highly concentration-dependent (free volume theory and diffusion models by Fujita and Crank) [285, 378]. As temperature increases during a test (at constant RH), the relative humidity (and thus chemical potential of water) must be carefully controlled. However, even at constant RH, the molecular mobility of the PVAl chains increases non-linearly as the material approaches its moisture-depressed glass transition temperature.

Consequently, the permeation of water through PVAl is governed by coupled diffusion-relaxation and swelling mechanism. The activation energy of diffusion is not constant but decreases as the free volume of the swollen polymer increases. Concurrently, the exothermic heat of sorption drives a reduction in solubility at higher temperatures. The interplay of these non-linear terms result in the complex curvature in Arrhenius plots. Therefore, any linear fit applied to this data yields only an apparent, path dependent temperature coefficient (E_{app}), valid only for the specific hydration state of the polymer during measurement, rather than a fundamental energy barrier.

For the specific samples that did display a linear trend Thick PVAl (Alpine) and the 50 nm AlO_x coated Thin (Betol) and Thick (Alpine) PVAl, did display this trend, allowing for activation energy estimation in these cases. From these the estimated activation energy for uncoated PVAl films was 31.07 ± 9.60 kJ/mol, which deviates from literature values reported for similar materials, which themselves show large variations:

- PVAl: 2.89 to 7.53 kJ/mol (0.69 to 1.8 kcal/mol) at temperatures between 20 and 160°C [367].

- Radiation-crosslinked PVA membranes: 25.2 – 25.8 kJ/mol (6.03–6.16 kcal/mol), determined using a hyperfiltration system under pressures ranging from 0 to 1000 psi, with permeability measured between 25 and 70°C [379].
- Pure PVA (0% LiCl content, no salt dopant): 70 kJ/mol [380].
- PVA/PSF composite membranes: 35 kJ/mol, applicable to PVA or PVAl films despite composite limitations [381].

The 50 nm AlO_x-coated Thin and Thick PVAl films exhibited similar activation energies to one another of approximately 44 kJ/mol, indicating a consistently slightly higher value than the uncoated polymer. However, these estimates should be interpreted with caution, as the variability and challenges in accurately measuring WVTR introduce potential uncertainties in the results.

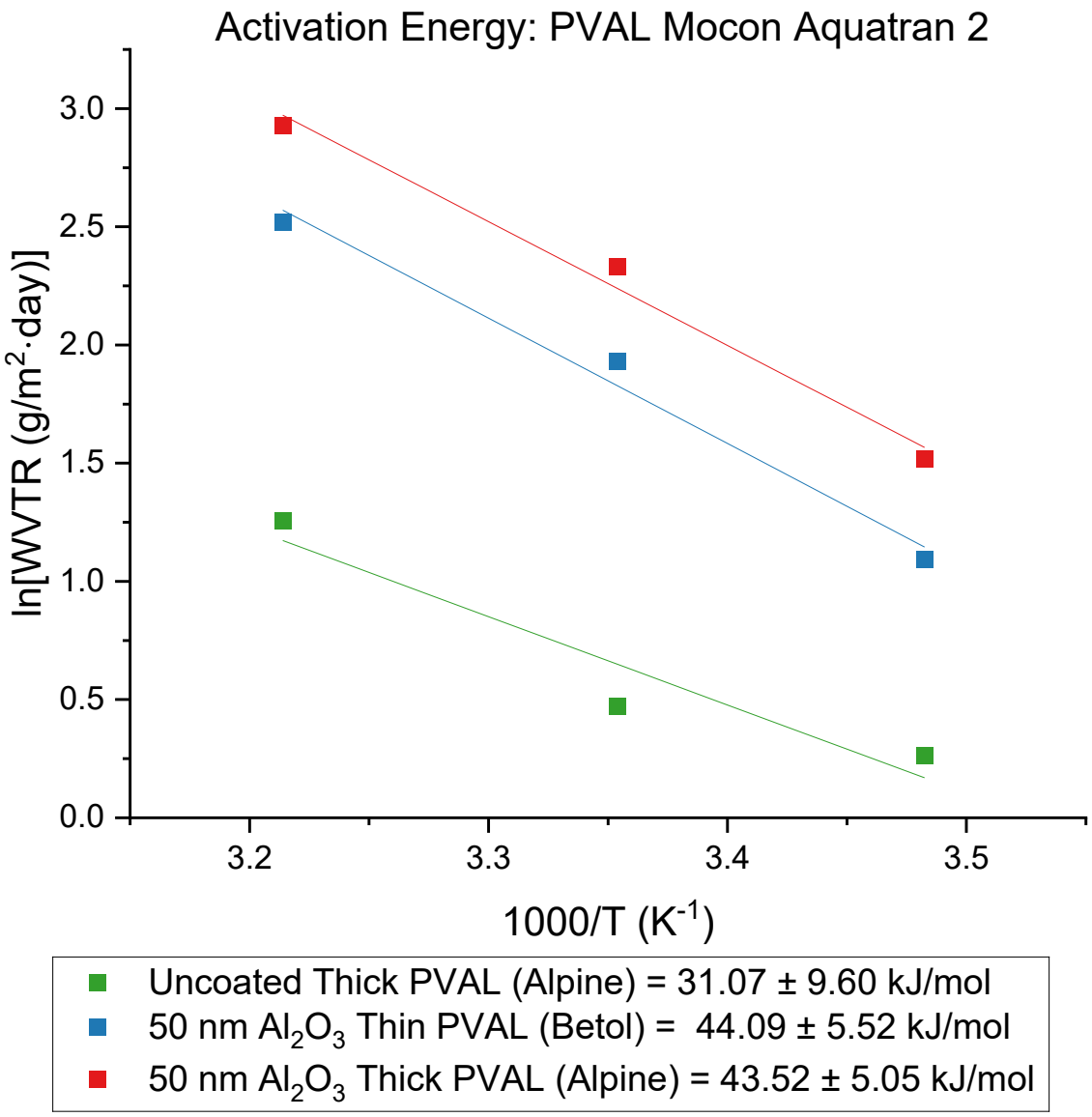


Figure 5-1: Activation Energy Comparison for Defect Analysis in PVAl Films. Arrhenius Plot of ln [WVTR (g/m²·day)] vs. 1000/T (K^{-1}), for uncoated and coated PVAl films. The linear fits provide estimates of the apparent activation energy of the water vapor transmission rate. However, the hydrogel like nature of PVAl implies that transport is governed by couple diffusion-swelling mechanisms, making these values effective temperature coefficients for this hydration state rather than static energy barriers.

5.4 Evaluating WVTR of PVAl Using Ca Test

This section presents the Ca test as a complementary method to evaluate WVTR in both uncoated and ALD AlO_x coated PVAl films addressing known limitations of

MOCON measurements in previous studies. To streamline the main discussion, extended results, including detailed measurements of uncoated and coated PVAl films and representative visual features observed in the coated samples are presented in 9.4.6 Supplementary Ca Test Results for Uncoated and Coated PVAl Films. The potential for nanoscale defects was also explored and concludes with a summary of values for each considered condition and case.

5.4.1 Presence of Nano defects in Coated PVAl Layers

While most of the analysis has focused on macro defects, as evidenced by the visible bright features, nano defect permeation may also be possible. One indication of significant permeation through nano defects would be a greater overall WVTR activation energy, however the coated PVAl samples were not Ca tested at a full range of different temperatures due to time and material constraints. Nevertheless, as demonstrated in 4.3.2 ALD – AlO_x and RF Sputtered - Al_2O_3 or (AlOx), uniform changes in the mean grey value of a region between macro defects can indicate potential nano defect permeation.

The mean grey values at areas between the bright features are measured such that a slow change in these values could indicate permeation through nano defects, where permeation occurs not through visible spots or typical microdefects. Figure 5-2, shows mean grey (average grey intensity within a selected region of interest) values for various coating thicknesses at different points, which still showed significant calcium remaining: Thin PVAl with (a) 26 nm (13 points), (b) 50 nm (12 points), and (c) 96 nm (12 points) coatings were measured. The results generally show no increase in this mean grey value with time, indicating that calcium was retained, and no observable permeation through nano defects occurred at these points over the time scale measured.

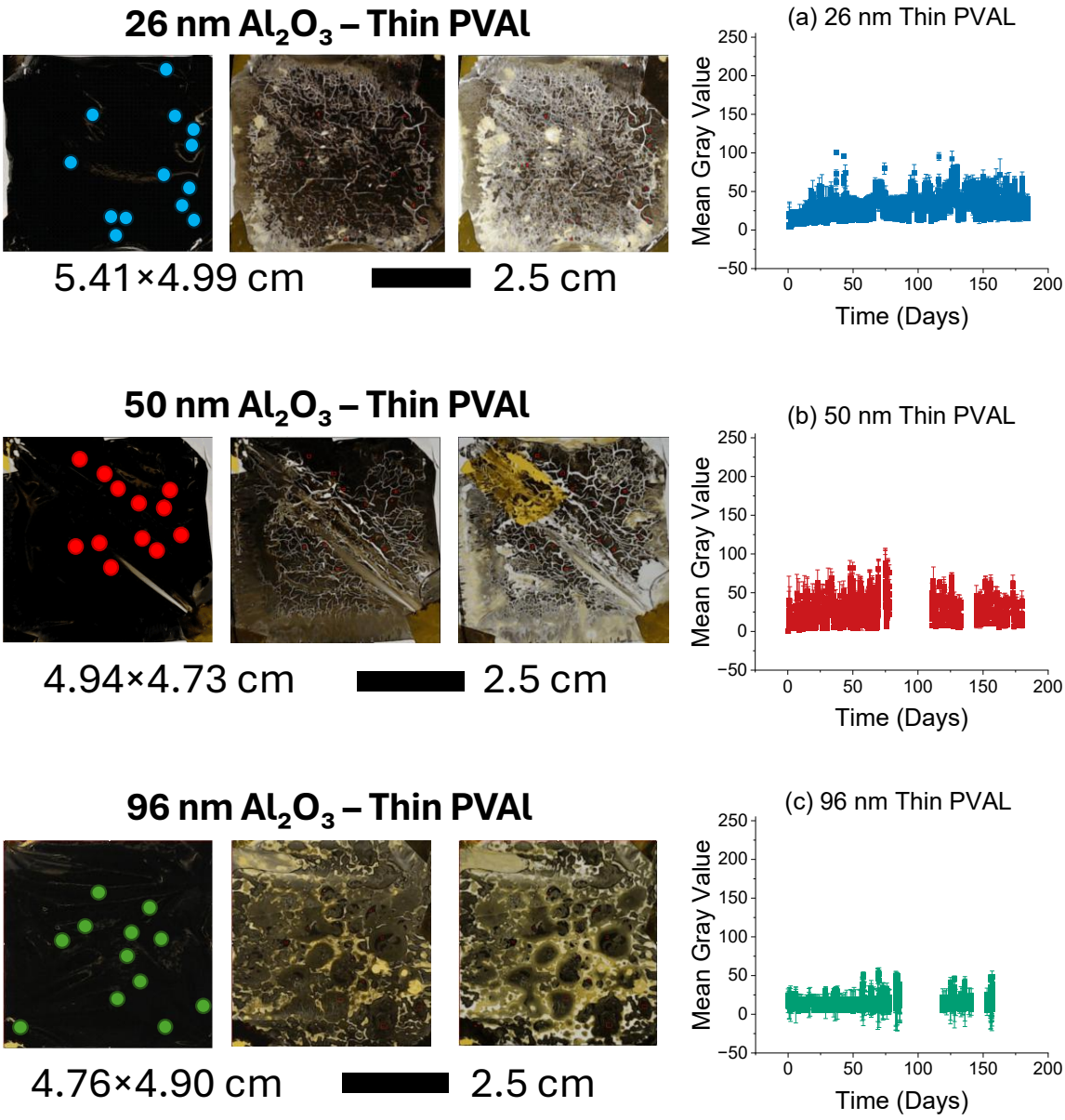


Figure 5-2: Representative samples of Thin PVAl substrates at (a) 26 nm (13 points), (b) 50 nm (12 points), and (c) 96 nm (12 points) show areas with remaining calcium, suggesting no nano defects are present, as indicated by the consistent average mean grey values.

For the Thick PVAl substrate (Figure 5-3), the same methodology was applied, analysing different points in the image where significant unreacted calcium remained: (a) 26 nm (12 points), (b) 50 nm (11 points), and (c) 96 nm (12 points). Unlike the Thin

PVAl, the Thick PVAl showed some change in mean grey value, indicating slow greying and suggesting potential nano defect permeation.

This could be attributed to either the intrinsic surface morphology of the thick PVAl or the nature of the AlO_x coating process. Based on microscopy at the micrometre scale (optical and SEM; see section 5.5 Surface Analysis of Uncoated and AlO_x-Coated PVAl Films), the thicker substrate appears slightly smoother than the thinner one, though the differences are relatively minor. However, the formation of nano-defects in ALD is not typically governed by substrate micro-roughness. The ALD technique is known for producing highly uniform and conformal films that can evenly coat complex topographies [323], and for creating densely packed, virtually pinhole-free layers [33, 350].

Because ALD is so effective at creating a conformal layer, it suggests that if nano-defects are indeed forming on PVAl, their origin is less likely to be the physical roughness of the substrate. Instead, it is more probably that their presence is determined by factors that ALD cannot easily mitigate such as the substrate's surface chemistry, like variations in the density of reactive -OH groups in the PVAl surface or minor inconsistencies in the deposition conditions themselves. Difficulties with initial nucleation on a given substrate are also a known source of pinholes in otherwise high-quality ALD films [382]. IN contrast macroscale defects, typically original from contamination or coating damage, that should be large enough to be possible resolved in some microscopy techniques.

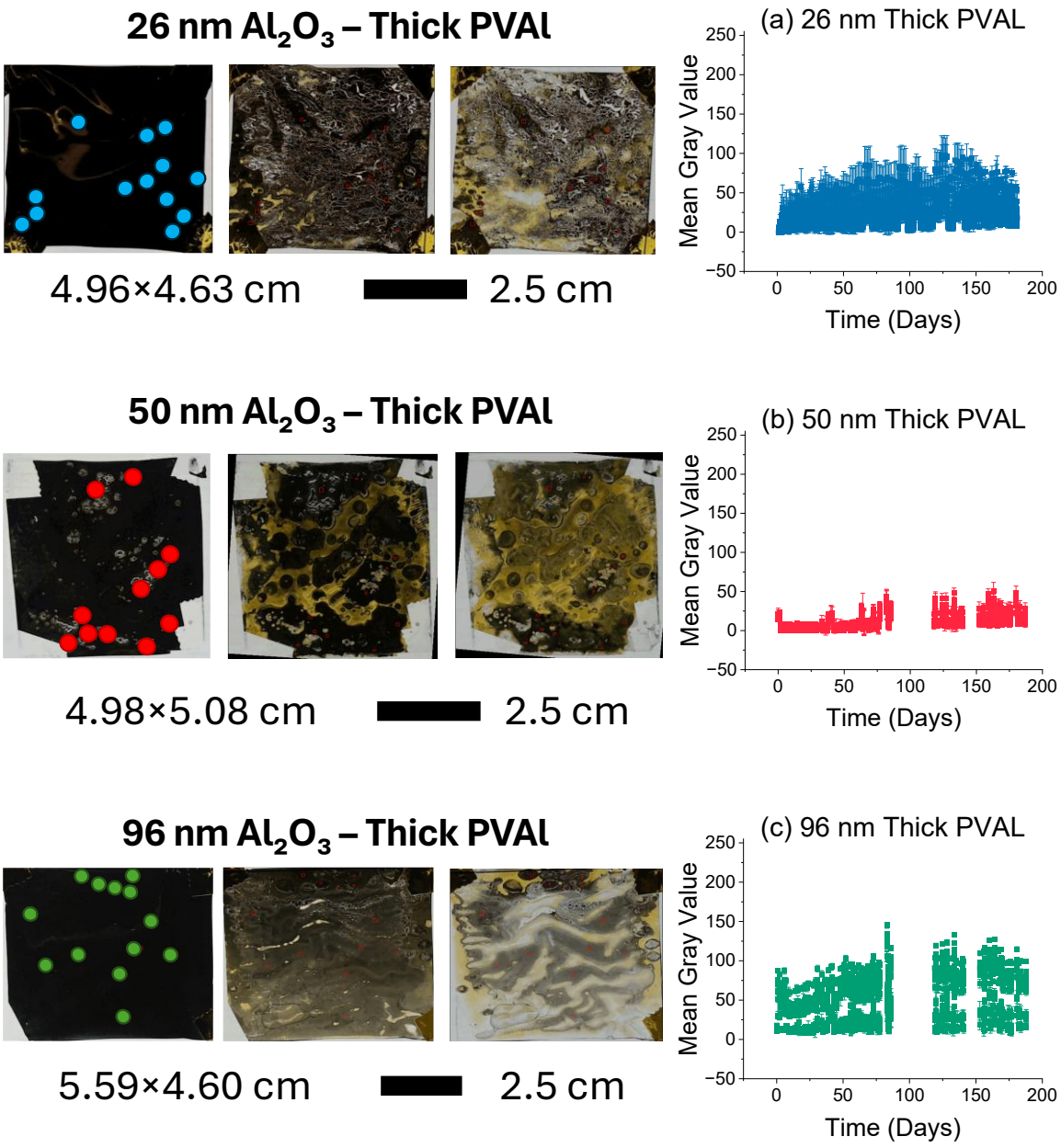


Figure 5-3: Representative sample points in Thick PVAl (a) 26 nm: 12 points, (b) 50 nm: 11 points, (c) 96 nm: 12 points, showing slow greying, indicating potential nano defects. This suggests that nano defects, in addition to microdefects, may be present in AlO_x

5.4.2 Overall Barrier Measurements of Coated PVAl (Ca Test)

Collating all the available coated PVAl samples and their WVTR, the following figures summarize trends on coating thickness, temperature and relative humidity, and their impact on the permeability of thin and thick PVAl coatings.

5.4.2.a WVTR of AlO_x Thin PVAl (Betol)

Figure 5-4, is a grouped scatter plot of the WVTR for AlO_x-coated thin PVAl samples, showing the influence of coating thickness. The large scatter of WVTR for nominally identical T/RH conditions is not just random variation; it shows early suggestions of defect dominated transport on polymer coated substrates (further explored in 5.8 Total Defect Area Calculation of PVAl).

In line with this, environmental factors that are known to influence WVTR. The data reveals two distinct transport regimes determined by the interplay of coating thickness and temperature:

(1) Intrinsic Regime (25°C): At 25°C and 39.5% RH, WVTR decreases noticeably with increasing coating thickness (dropping from ~0.012 to ~0.002 $g/m^2 \cdot day$ as thickness increases). This behaviour is consistent with Fickian diffusion, where the barrier performance is controlled by the bulk film thickness ($J \propto 1/L$), showing some form thickness dependence.

(2) Defect Dominated Regime (50.5°C): In contrast, at 50.5°C (65 to 71%), the values plateau (ranging between 0.001 to 0.004 $g/m^2 \cdot day$) and exhibit no clear inverse relationship with thickness. This indicates a transition in the transport mechanism. As explained by da Silva Sobrinho *et al.* [250] and

> Graff *et al.* [13], once a critical barrier quality is reached residual permeation is controlled by nano-scale defects (pinholes) rather than the bulk lattice. Under these conditions, adding further thickness yields diminishing returns because the flow bypasses the bulk material through these defects.

The variability observed at 50.5°C is characteristic of this defect dominated regime. Instrumental uncertainty for more precise measurements like the MOCON system is around 5% error, thus for a more erratic and less controlled system the observed scatter (20 to 60%) such as in this Ca test possibly originates more from stochastic distribution of defects on the substrate surface. Kempe *et al.* mention that in high sensitivity Ca testing, when permeation is limited by sparse defects rather than bulk material, sample to sample scatter naturally increases [59]. Moreover the lack of thickness dependence at higher temperature of 50.5°C is not a lack of process control but a physical signature that barrier has reached the defect limit of the substrate class.

For perspective, adding the ALD AlO_x significantly reduces WVTR from approximately ~10^2 ($g/m^2 \cdot day$) of uncoated PVAl to coated PVAl to range of ~10^{-1} to 10^{-5} ($g/m^2 \cdot day$), demonstrating that despite the defect-driven scatter, the barrier improvement is substantial.

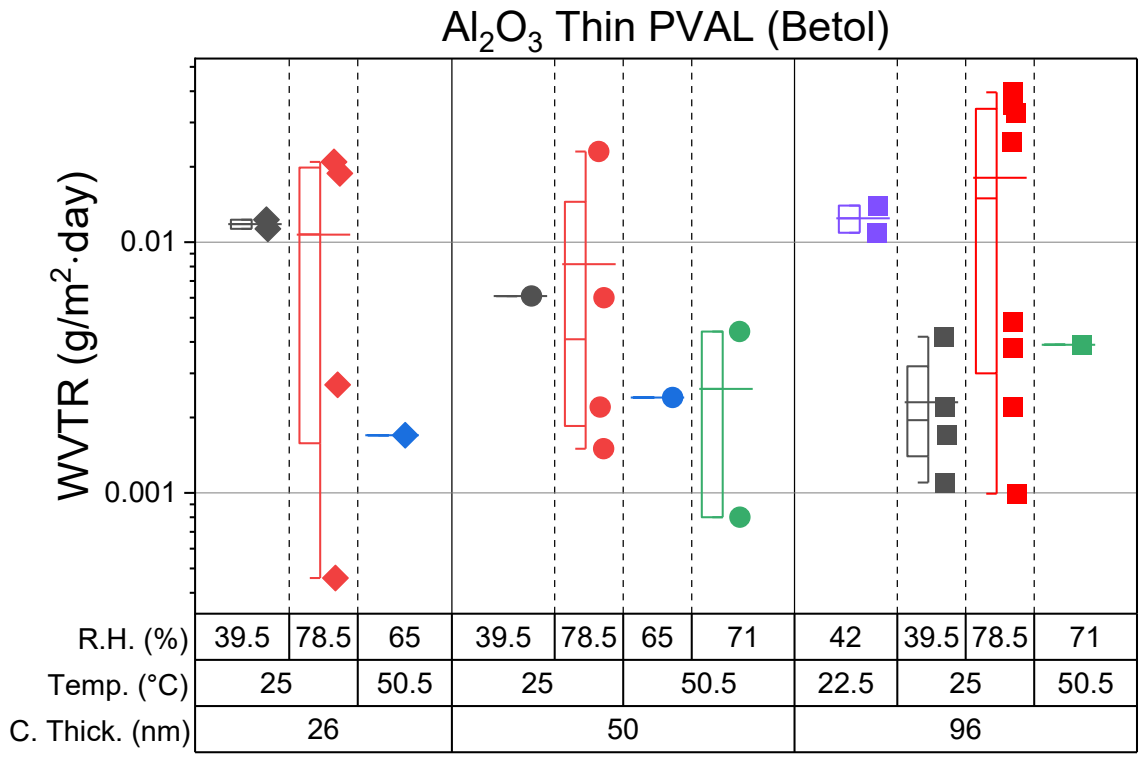


Figure 5-4: Scatter group plot of ALD AlO_x-coated PVAl (Betol) showing the effects of coating thickness, temperature, and relative humidity on estimated WVTR. The plot demonstrates that different coating thicknesses have similar WVTRs, indicating a reduced influence of environmental factors. The broad scatter at fixed T/RH and coating thickness gives the suggestion of defect dominated permeation such that it is the quality of the coating that may be the main determinant of WVTR; as argued local defect size and density along with potential interfacial pathways can overwhelm environmental trends in coated substrates, where thicker coatings can lower the overall median WVTR but residual scatter remains due to defect statistics.

5.4.2.b WVTR of AlO_x Thick PVAl (Alpine)

Using the same concepts as above but with the thicker PVAl (Figure 5-5), the WVTR values are similar to or slightly higher than those of the thin PVAl samples.

On the topic once more of scatter and uniformity, while coating thickness as said drives performance in specific regimes (as seen in Thin PVAl – Betol samples), the thicker PVAl – Alpine samples exhibit high scatter that limits a clear linear correlation with thickness. This scatter is consistent with observed island like degradation spots in

the Ca images for the coated PVAl, in this regime water ingress is not uniform across the sample surface. It instead occurs through discrete larger features (pinholes possibly caused by dust shadows or substrate roughness). The measured WVTR is again governed by the statistical probability of capturing these localized defect populations within the region of interest or test area, rather than by pure systematic environmental or thickness trends.

In terms of data it is peculiar that elevated temperature and higher humidity show a decrease in WVTR or similar results where an increase should be expected; but as argued in a defect dominated system the presence of a single critical macroscopic defect on a sample can skew the measured and estimated WVTR overwhelming the subtle environmental trends. Making the observed variation arise from the discrete nature of defects (extrinsic factors) inherent to non-cleanroom deposition rather than measurement failure.

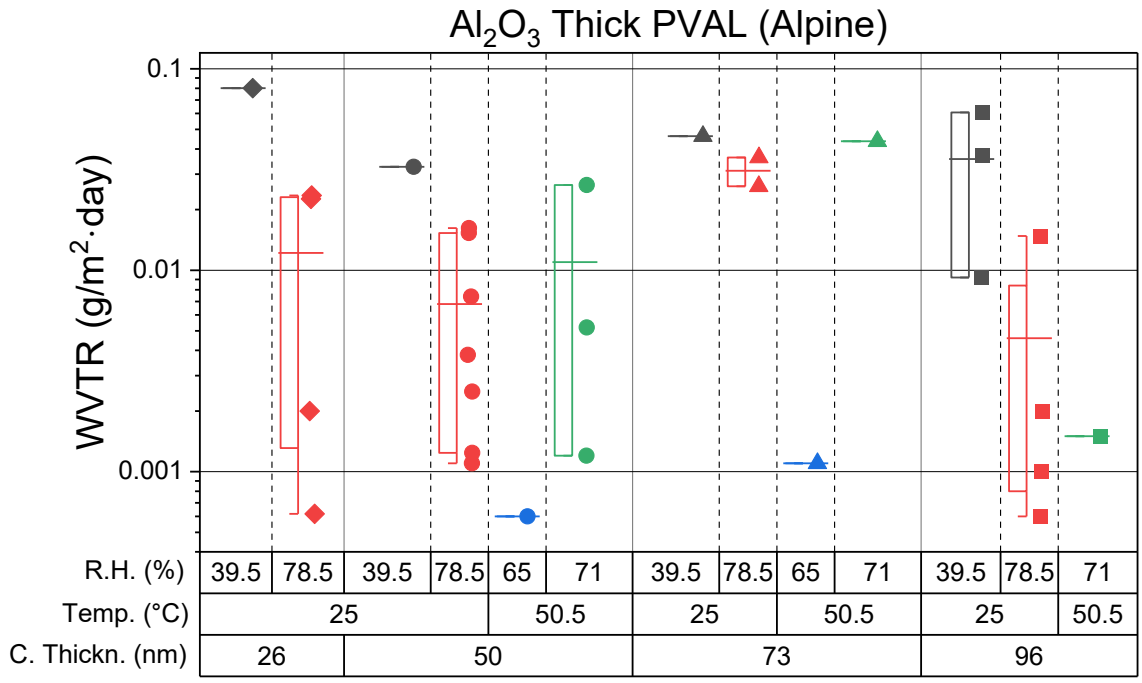


Figure 5-5: Scatter group plot of ALD AlO_x - coated thick PVAl (Alpine) showing the effects of coating thickness, temperature, and relative humidity on estimated WVTR. Like the thin PVAl substrates, environmental factors do not significantly influence WVTR and increasing coating thickness does not greatly improve performance. It is peculiar that elevated temperatures and higher humidity like 25 °C shows a decrease in WVTR where an increase should be expected instead, likely due to scatter rather than systematic effect. Where the observed variation arise more from sample inconsistencies, measurement sensitivity, or localized defect distributions within the coatings. The broad scatter may also confirm that permeation in this system may be governed by randomized defect density (extrinsic factors) rather than intrinsic material properties.

5.4.2.c Permeability of AlO_x Thin PVAl (Betol)

Permeability (Equation 2-3) was calculated using the combined thickness of the PVAl substrate and the ALD coating, as shown for both thin (Figure 5-6) and thick (Figure 5-7) coated PVAl samples. This calculation also normalises for the water vapour partial pressure across the film, allowing comparisons across varying conditions. While the ALD AlO_x layer contributes only nanometres to the micrometre-scale substrate, it was included to ensure methodological consistency across all datasets. Its inclusion has a negligible effect on the numerical value.

The uncoated thin PVAl sample had a permeability of $\sim 10^{-14}$ mol/(m·s·Pa), while coated thin PVAl samples exhibited much lower values in the range of $\sim 10^{-16}$ to 10^{-18} mol/(m·s·Pa). This reduction highlights direct evidence that ALD coating, not the bulk substrate is the rate limiting component in the system. Making the calculate permeability primarily reflect the performance of the AlO_x barrier layer itself. This highlights the substantial barrier enhancement provided by the ALD AlO_x layer, despite its minimal thickness contribution.

However, due to the large scatter between individual samples (nearly two orders of magnitude), no consistent trend with temperature or coating thickness is observed (Figure 5-6 and Figure 5-7). Interestingly, both figures suggest that higher temperatures may

correspond to lower permeability, a trend also seen in bare PET in the MOCON Aquatran data (Figure 3-16) and in ALD-coated PET (Figure 4-9), where samples of the same type and condition tested at higher temperatures appear to show lower permeability compared to those tested at lower temperatures.

This counterintuitive behaviour is consistent with the findings of Matteucci *et al.*, who show that for strongly sorbing vapours such as water, permeability may decrease with increasing temperature if the exothermic heat of sorption outweighs the activation energy of diffusion [383]. Similarly, Crank emphasizes that permeability depends on both diffusivity and solubility; when the decline in sorption with temperature is greater than the increase in diffusion, as is often the case with water in hydrophilic polymers like PET and PVAl the net permeability can decrease as temperature rises [285].

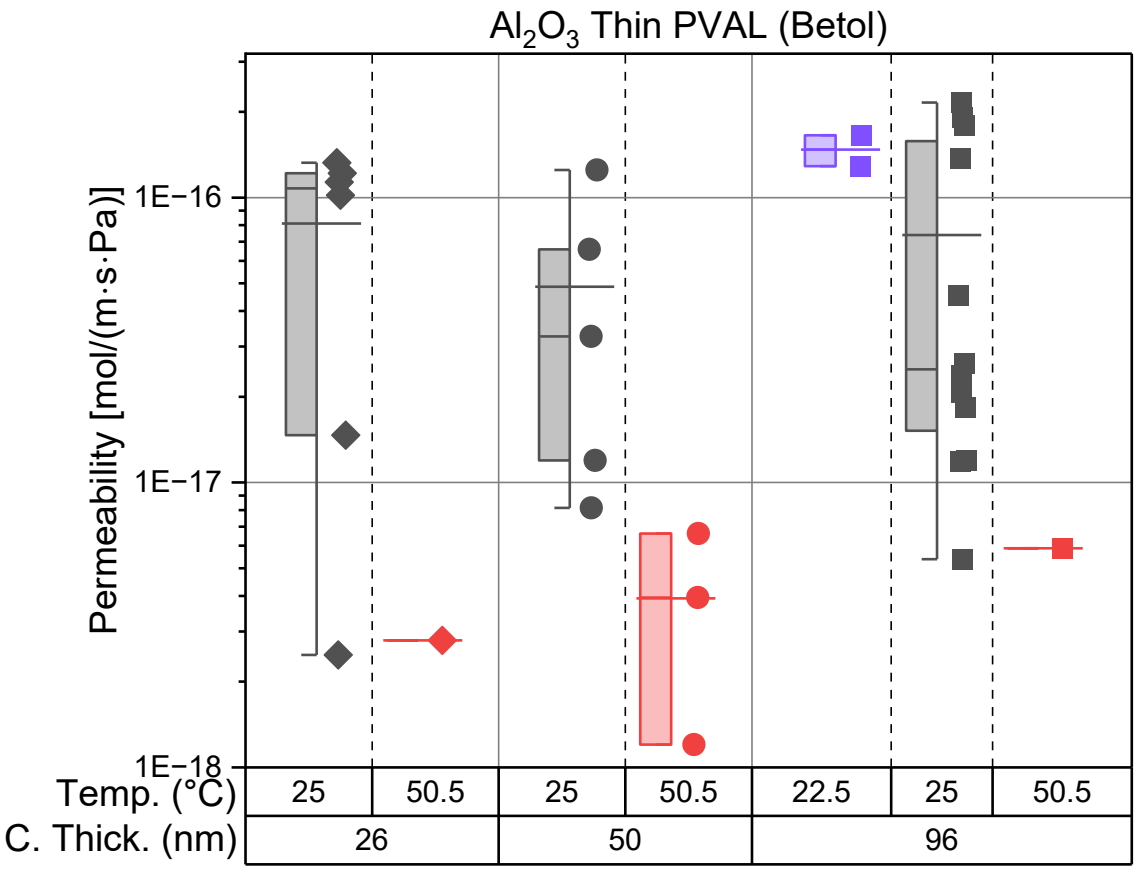


Figure 5-6: Scatter group plot of ALD AlO_x-coated thin PVAl (Betol), grouped by coating thickness and temperature, showing the range of permeability. While some variations and outliers exist, possibly due to sample damage or inconsistencies, the coated thin PVAl generally achieves low permeability regardless of temperature and coating thickness. Interestingly, permeability appears lower at higher temperatures and elevated conditions, following a trend like WVTR. While the exact cause remains unclear, this behaviour may have been influenced by factors such as changes in film morphology, reduced microdefect impact or temporary effects like moisture interaction. Further studies would be needed to determine whether the mechanisms such as defect reduction or structural rearrangement contribute to this trend.

5.4.2.d Permeability of AlO_x Thick PVAl (Alpine)

For the thicker PVAl substrate, the permeability of coated thick PVAl (Figure 5-7) is in the range of ~10^{-15} to 10^{-17} [mol/(m·s·Pa)]. While permeability in some coated thick PVAl samples, is slightly higher than that of coated thin PVAl, it remains overall comparable to coated PET (Figure 4-24). This is a significant result, demonstrating that well-deposited ALD coatings can enable PVAl to reach barrier performance like PET. Although permeability is normalised to total film thickness, comparing thin and thick PVAl still reinforces that substrate thickness is not the dominant factor, once a uniform, defect-minimised ALD layer is formed [370].

Microstructural analysis (5.5 Surface Analysis of Uncoated and AlOx-Coated PVAl Films) shows that while both substrate types exhibit surface irregularities, their characteristics differ: thin PVAl displays more spot-like protrusions and fissures, whereas thick PVAl exhibits cavity-like features and flow lines. These differences may influence coating behaviour, though ALD's conformality allows for reasonable coverage across both surfaces.

In this work, coating thickness does not show a strong trend in determining barrier properties for thick PVAl. While it is expected that beyond a certain alumina thickness, further improvements may plateau or even introduce stress-related defects, no clear

critical thickness was established in this study. The spread of permeability values remains within two orders of magnitude (Figure 5-7), suggesting high variability likely due to defect-related mechanisms, rather than a consistent or narrow distribution.

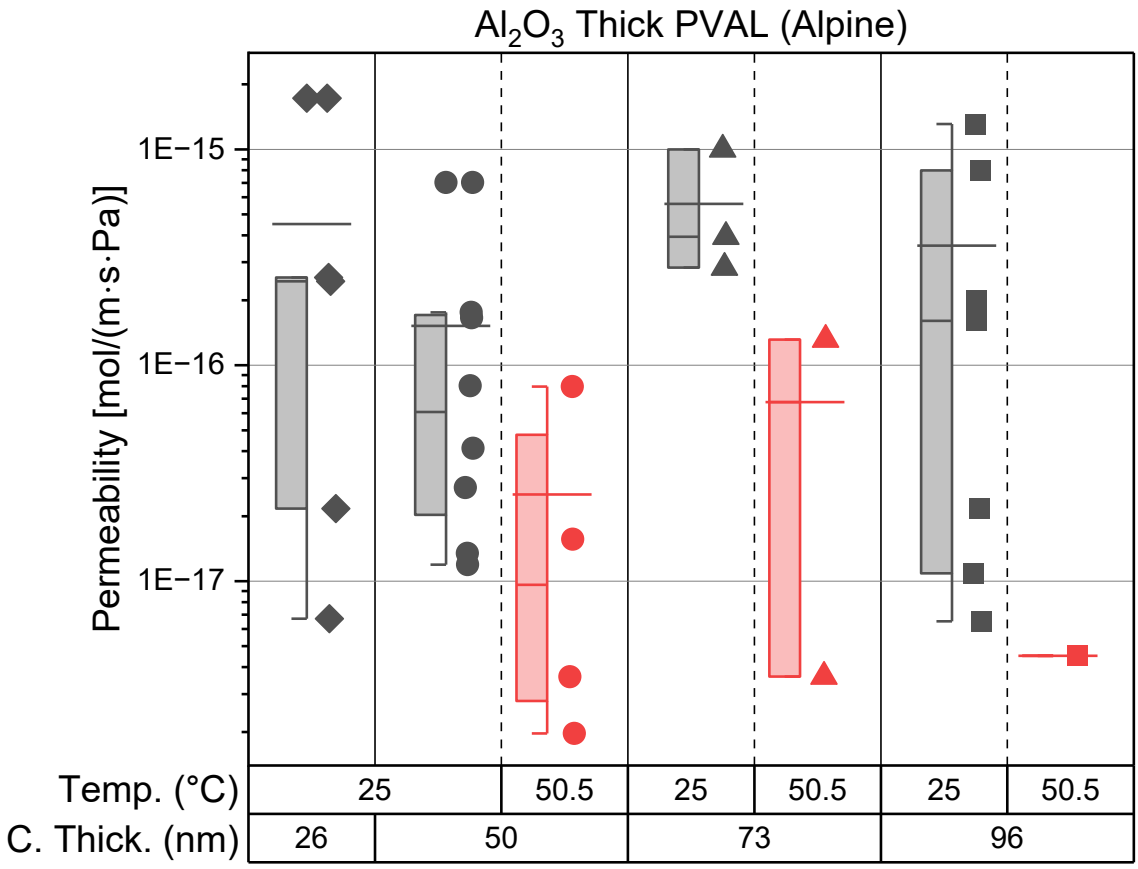


Figure 5-7: Scatter group plot of ALD AlO_x-coated thick PVAl (Alpine), grouped by coating thickness and temperature, showing consistent permeability estimates in the range of ~10^{-15} to 10^{-17} [mol/(m·s·Pa)], slightly lower than thin PVAl but still within a similar range.

5.5 Surface Analysis of Uncoated and AlO_x-Coated PVAl Films

Barrier quality can be heavily influenced by the surface characteristics of the polymer substrate. The substrate polymer impacts surface roughness, film nucleation, and ultimately barrier quality [368]. Study of the surface morphology can reveal potential

defect sites, such as the linear features initially observed in coated PVAl substrates Ca test images (5.4 Evaluating WVTR of PVAl Using Ca Test).

The surface morphology of PVAl films depends on their composition and processing. For instance, solution-cast PVAl films for antibacterial purposes are typically transparent, homogenous, and smooth; Suganthi *et al.* reported a root mean square (RMS) roughness of 10.50 ± 1.03 nm. While the original publication states a scan area of 2 nm × 2 nm, this is physically inconsistent with the roughness magnitude and is interpreted here as a typographical error for 2 μm × 2 μm a standard dimension for such topological analyses [384].

In contrast, irradiating PVAl films increased roughness from 6.6 nm to 9.5 nm. However, adding ZnO nanoparticles had minimal effect, with roughness values of 7.6 nm for non-irradiated and 11.5 nm for irradiated films [385].

Chan, Senin, and Naimah's characterization of PVA films revealed subtle artifacts or possible contaminants in SEM images. PVAl is generally a softer material with a Rockwell Hardness of 37.72, compared to 62.19 for typical commercial plastics [386]. Tsukada, Freddi, and Crighton observed bubble-like structures (4-7 μm) in cast PVA films [387]. Kim *et al.* found that uncoated PVAl had a mean roughness of ~18 nm and a contact angle of 68°, whereas AlO_x-coated PVAl showed reduced roughness (~9 nm) and an increased contact angle of 92°, indicating improved hydrophobicity and water vapor barrier properties [388].

The PVAl films in this study are melt-processed, and to the best of current knowledge, no prior studies have specifically reported the surface characterisation of melt-processed PVAl films. This gap in the literature is likely due to the significant

challenges associated with PVAl melt processing, as its melting temperature is extremely close to its thermal degradation point, necessitating the use of plasticizers such as glycerol to enable processing [389].

Nonetheless, insights drawn from other melt-processed polymers, such as polycaprolactone (PCL), demonstrate that melt-pressing can often produce smoother films than solution casting [390]. In contrast, melt-processing PVAl blends with other materials like zein (largely hydrophobic corn protein) produces phase separated blends where the zein rich domains fail to wet the hydrophilic PVAl matrix. SEM micrographs of these blends reveal interfacial voids and micron scale surface heterogeneity pointing to poor interfacial interactions and limited compatibilization between the two polymers [391]. The PVAl films studied here have a rougher surface compared to the PET films, which may influence the overall quality of the barrier layer.

5.5.1 Uncoated / Bare Thin PVAl and Thick PVAl

The images below depict surface features of uncoated thin (~21 μm, Betol) and thick (~42 μm, Alpine) PVAl films. Figure 5-8, shows low-magnification optical microscopy images, where small dots or spot-like features are visible. Due to the semi-transparent nature of PVAl, it is not immediately clear whether these features are superficial or embedded within the bulk. However, comparison with optical profilometry, which measures actual surface height variation, suggests that these are indeed surface-localized in the Betol film, corresponding to raised protrusions whereas the Alpine film shows shallow cavity-like depressions

Focusing on the SEM analysis in Figure 5-8, reveals the presence of discrete micrometre-scale particulate features distributed across the surface of the thin PVAl

substrate. In the context of non-cleanroom roll to roll processing, these features are identified as extrinsic surface contamination, originating either from environmental dust or anti- block additives inherent to the polymer web [338, 339].

Regarding the nature of these features, it is critical to note that these are not chemically bonded to the bulk polymer but are typically adhered via weak electrostatic or van der Waals forces. This weak adhesion poses a significant threat to the integrity of any subsequent barrier coating (like AlO_x) through a micro masking (or shadowing) mechanism.

1. Deposition Shadowing: Citing Zhang *et al.*, particles present on the substrate surface during ALD physically obstruct the precursor gas flow, preventing film nucleation on the area directly beneath them.
2. Adhesion Failure and Pinhole Formation: Because these particles are mechanically unstable, thermal expansion mismatch during testing (*e.g.*, at 50.5 °C) or web handling stresses can easily dislodge them. Once removed, these particles exposed previously shadowed area are now uncoated voids.

These mechanisms provide physical evidence for defect dominated permeation discussed in the Ca test results, The removal of these loosely attached particles creates direct pinholes, which Elrawemi *et al.*, have identified as the primary failure mode governing WVTR especially in single layer barrier films like the one considered in this work [37].

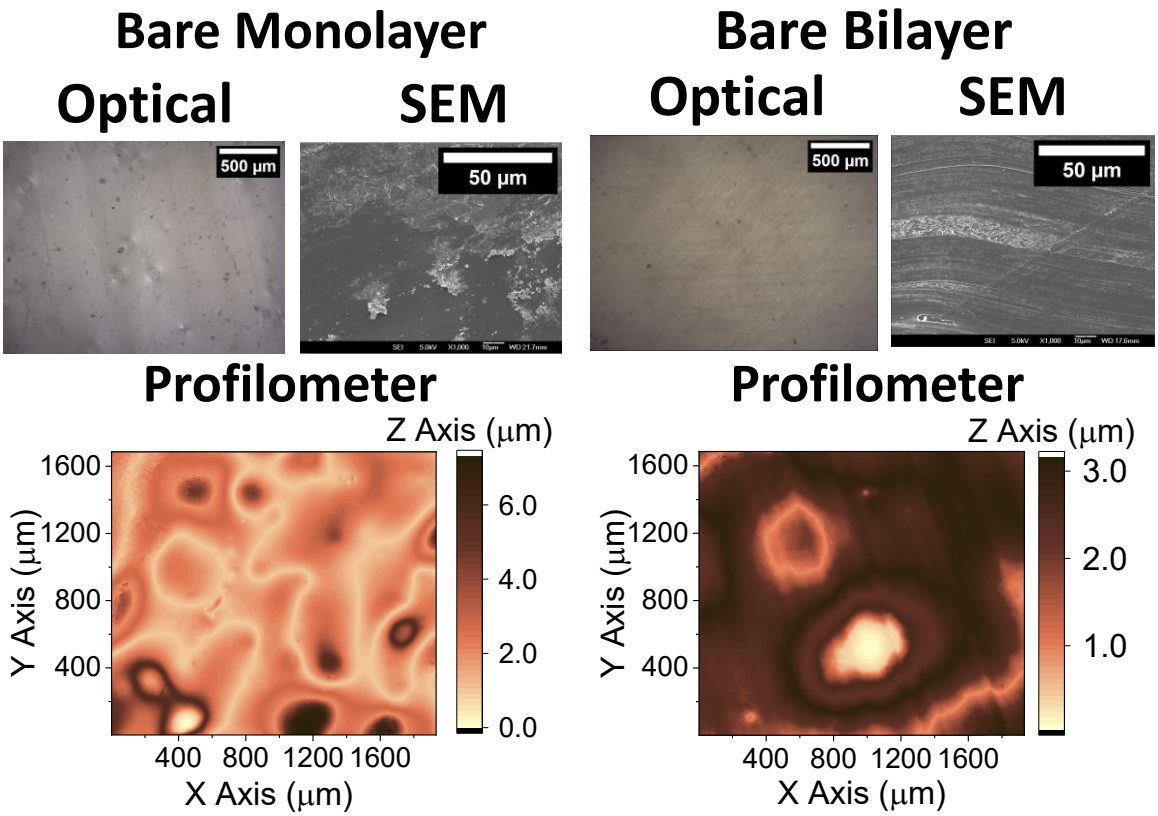


Figure 5-8: Optical, SEM, and optical profilometer images of uncoated thin and thick PVA films reveal a clear film with blob- or spot-like features that could affect coated film characteristics. The surface is rougher compared to bare PET and shows potential dust-like artifacts, which may also be present in the ALD-coated barrier layers. The optical images span a field of approximately 2500 µm × 2000 µm, which is roughly comparable to the 1600 µm × 1600 µm area analysed by profilometry; though not identical, both views are sufficient to capture representative surface features.

5.5.2 Coated AlO_x Thin and Thick PVAl

For coated layers, ALD's highly conformal nature promotes uniform coverage, even on rough surfaces. Figure 5-9 (a), shows the Ca-test sample of a PVAl film coated with 26 nm AlO_x. Four 1 cm × 1 cm sections are highlighted, that illustrate the linear bright features observed in the Ca test at the micrometre scale.

Bright features in this specific Ca-tested sample were used to estimate the number of defects at ~13 per cm^2, based on Python algorithm that counts isolated, non-connected

depletion zones (Figure 5-16). In this context, and as previously defined (4.6 Analysis of Defects (Spots) in ALD AlO_x coating), a defect is the first occurrence of an irregular or depleted region not visibly connected to others. However, this distinction is not always clear-cut. As seen in Figure 5-9, some features appear to grow or merge, making it challenging to classify whether these represent individual or interconnected defects.

This limitation in resolution and contrast within the Ca-test method makes it difficult to consistently quantify true defect density. For example, features that appear as distinct point-like spots under SEM or optical microscopy may manifest as merged or branching structures in the Ca-test image. As a result, the derived number (13 defects/cm^2) reflects only clearly separated, isolated defects, likely underestimating the full irregularity of the landscape (alluded in 4.6.2.b Limitations and Challenges of Current Python Workflow).

The estimated defect density of $\lambda = 0.13$ defects per 1 mm × 1 mm field of view informs the Poisson calculation for the probability of directly observing at least one defect. This assumes defects occur randomly, independently, and at a constant density across small areas. One can estimate the probability of observing at least one defect that can be found using Equation 5-1, where number of defects (k) and X (number of defects seen):

$$P(X = k) = \frac{\lambda^k e^{-\lambda}}{k!} \qquad \textit{Equation 5-1}$$

To find the probability of at least one defect ($P(X \geq 1)$), the complement is used which simplifies it to ($e^{-0.13}$).

$$P(X \geq 1) = 1 - e^{-0.13} \approx 0.122.$$

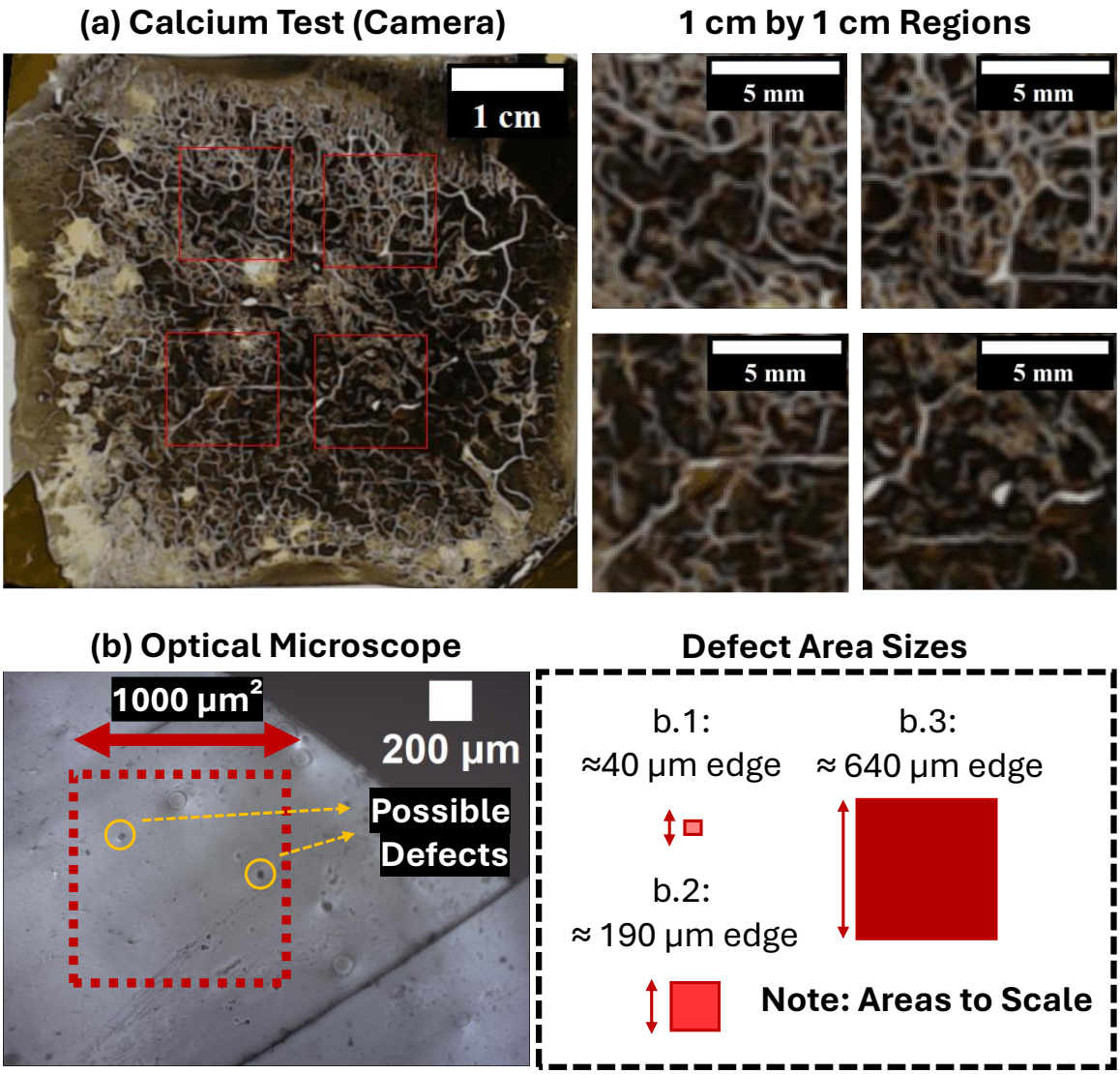
This suggests a ~12.2% chance of finding at least one defect in a 1 mm × 1 mm field of view, consistent with the Ca-test images, though this should be treated as a conservative baseline.

The spatial resolution of the Ca test is relatively low (~tens of microns), which means that microscale clusters of irregularities observed in optical or SEM images may manifest as a single, merged defect in the Ca-based analysis. While the Ca-test provides a reasonable defect estimate, the actual nature of these features remains ambiguous making it challenging to definitively classify them as defects or not.

Figure 5-9 (b) shows an optical microscope image showing possible defects. Estimations made in a later section (5.7 Defect Size / Area Estimation in Coated PVAl Films), show that a modal, or most common, defect size is ~1,600 μm^2 (edge length of ~40 μm) (b.1). For this specific sample the size of the observed defect was estimated to be a bit larger, at around ~36,100 μm^2 (edge length of ~190 μm) (b.2). For contrast the largest detected defect in the Ca test was found to be around ~409,600 μm^2 (edge length of ~640 μm), which would have been obviously visible in the optical microscopy, if it had fallen within the field of view.

The SEM images in Figure 5-9 (c) (two magnifications were considered: c.1: SEM at 100× magnification and c.2: SEM at 1 k× magnification), both reveal linear features. As these are coated samples, these are possible defects in the AlO_x, seen more evidently at higher magnification (c.2), The optical and SEM data (Figure 5-9) suggest a potentially higher density of smaller features than expected from the Ca test, some of which may coalesce or overlap and thus be undercounted in Ca-based analysis.

In summary, while this specific methodology of Ca-testing provides a valuable metric to estimate defect sizes and density, it likely underrepresents defect complexity due to its limited spatial resolution, such that there is difficulty in distinguishing individual vs. clustered features and to resolve all individual defects.



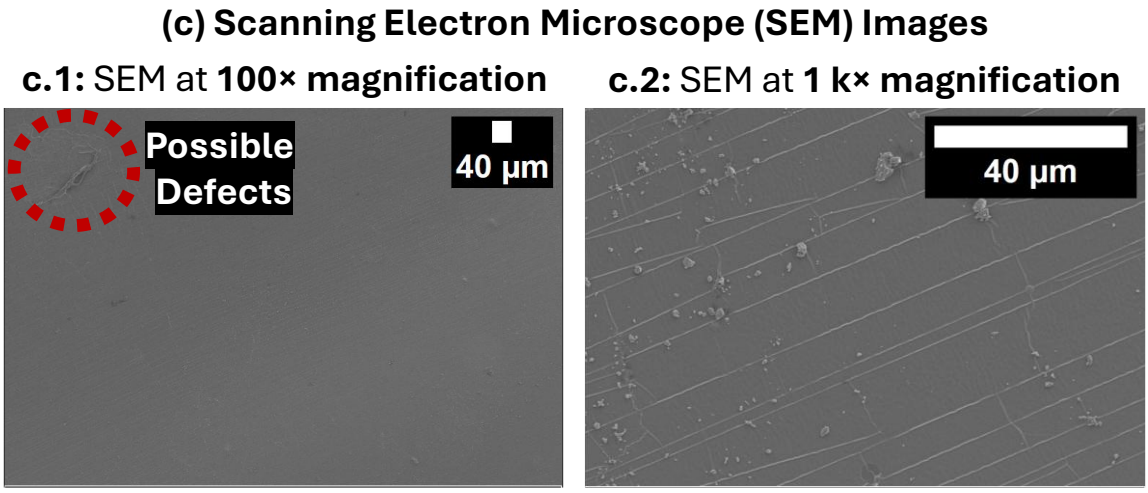


Figure 5-9: Ca-test images (a) of a 26 nm AlO_x coated thin PVAl film, highlighting four 1 cm × 1 cm regions that show perturbations or bright area that are localized increases in grey level relative to the surrounding background between potential macro defects that indicate moisture ingression. These manifest as linear features and irregularities rather than the spot-like defects seen on coated PET substrates. The estimated defect density from these Ca-test images is ~13 defects/cm^2 (Figure 5-16), which translates to a ~12.2% probability of observing at least one defect in a 1 mm by 1mm field of view based on a Poisson analysis. Subsequently, Optical microscope images (b) show possible defect sizes ranging from ~1,600 µm^2 (edge length ~40 µm) to ~36,100 µm^2 (edge length ~190 µm – average defect size of this 26 nm AlO_x thin PVAl sample), where the largest visible defect detected in all the various tested samples in 5.7 Defect Size / Area Estimation in Coated PVAl Films was around ~409,600 µm^2 (edge length ~640 µm). SEM images (c) at two magnifications (c.1 at 100× and c.2 at 1k×) reveal additional straight lines and finer features, some of which may be film processing related or true defects, indicating a higher density of small, possibly interconnected features. These results suggest that Ca test may undercount defects by merging finer structures into larger more prominent features, illustrating the challenge in distinguishing true defects from possible surface irregularities in PVAl films. Moreover, this multi-modal analysis also provides the justification for assigning these perturbations to defects: the bright linear perturbations seen in the Ca-test images in (a) are assigned to defects due to these sites of moisture ingress directly correlate with the physical straight lines and finer features observed in corresponding SEM images (c) these kinds of defects are therefore interpreted as possible micro cracks or linear separations in the AlO_x (potentially associated with stress or substrate shrinkage of the hydrophilic PVAl substrate).

5.5.2.a Coated AlO_x Thin PVAl

Figure 5-10 presents surface analysis using optical, SEM, and optical profilometry images of various coated Thin PVAl samples (26 nm, 50 nm, and 96 nm).

The 26 nm coated PVAl shows similar features to bare PVAl (Figure 5-8) — remaining optically transparent—but SEM inspection reveals possible defects, such as cuts or slashes in the coating. These defects could explain the linear features observed in the calcium test for the 26 nm samples, which are more line-like than spot-like.

The profilometer image also reveals similar features to the uncoated PVAl, indicating that the coating did not significantly alter the surface topography, suggesting that the ALD coating was conformal. This suggests that since the uncoated PVAl naturally has occasional surface protrusions; these are reflected and present even after coating, resulting in a coated thin PVAl surface profile like that of uncoated PVAl substrates.

While the 50 nm AlO_x coated PVAl (twice as thick as the 26 nm coating) may initially appear similar under optical microscopy, closer inspection reveals numerous fine micro fissures alongside persistent defect-like particles. The term “micro-fissures” is used instead of “cracks” to avoid implying stress-induced failure, as “cracks” typically denote fracture caused by mechanical and thermal stress, which has not been confirmed in this case. SEM imaging confirms these features as surface irregularities, rather than flake- or snow- like deposits that would suggest loosely attached material. These observations correlate with the combined spot- and linear- like defects detected in the Ca test, implying that fine cracks seen in the optical microscope correspond to the linear features identified by Ca testing.

The profilometer data for the 50 nm coating reveals more variation in features and height, with scales and protrusions becoming more pronounced, likely due to the increased coating thickness.

For the 96 nm AlO_x - coated PVAl, spot- or island-like features are visible, along with prominent linear features in the optical microscope. These appear more as a network of fine surface discontinuities (micro fissure) rather than “slashes”, suggesting that the barrier layer’s increased thickness may contribute to island-like formations and interconnected pathways leading to significant defects. The SEM image also reveals the fine linear features; however, based on profilometer data, these do not directly correspond to the linear features seen in SEM. Instead, the observed cavities in the profilometer data seem to match the size and density of the spots seen in the optical microscope, indicating a different structural relationship.

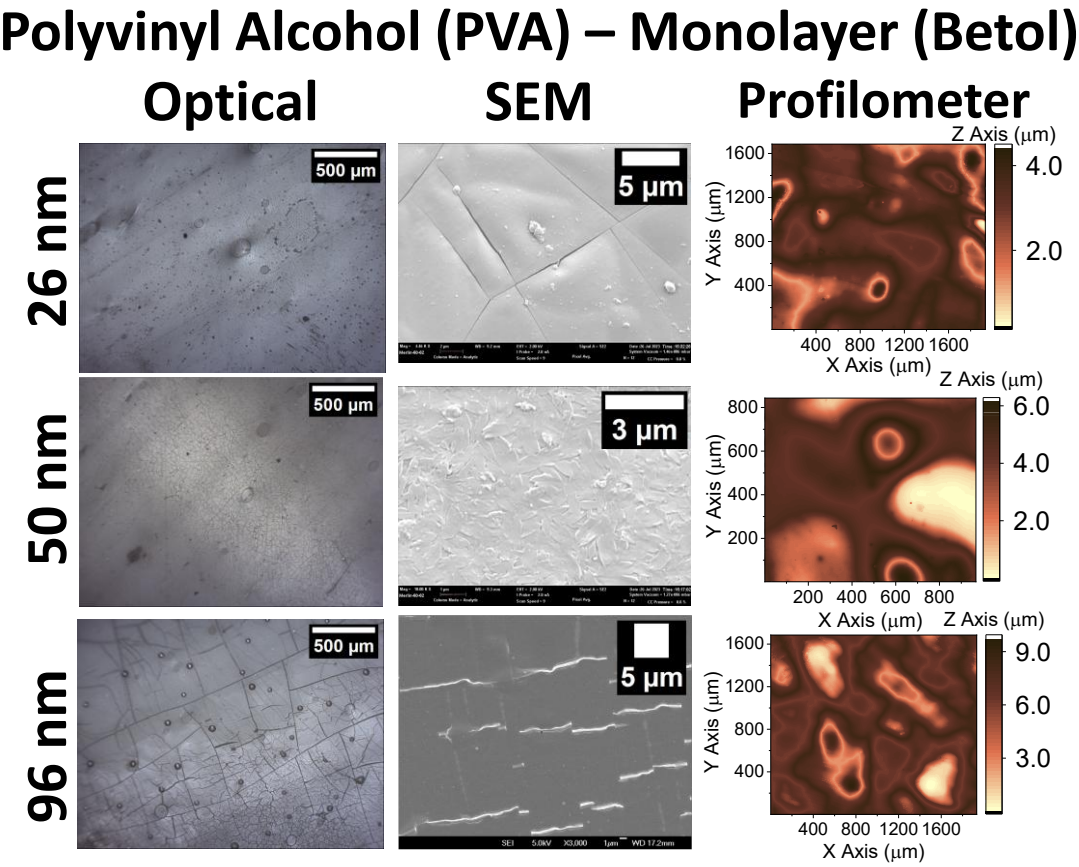


Figure 5-10: Coated Thin PVAl films with AlO_x thicknesses of 26 nm, 50 nm, and 96 nm was analysed using optical, SEM, and profilometer images. The results explain the calcium test observations: linear defects at 26 nm, a mix of spot- and linear-like features

at 50 nm, and island or ravine-like mixed with linear features at 96 nm, likely due to coating collapse at higher thicknesses.

5.5.2.b Coated AlO_x Thick PVAl

Like the observations in section 5.5.2.a, Figure 5-11 shows that for thick PVAl substrates, the 26 nm coating shows no distinct features beyond processing lines and dust. However, SEM images reveal surface discontinuities or micro fissure-like features, like those in the 26 nm coated Thin PVAl films. The profilometer data also mirrors the thin PVAl results, with minor surface variations but no significant deviations, aside from occasional macro-scale protrusions.

The 50 nm coating shows no significant difference between thin and thick PVAl under the optical microscope both retaining rough and plain surfaces, however upon closer inspection, the network of fine discontinuities or micro-fissures are not evident. The SEM images also reveal a similar packed morphology, that appear flake- or snow-like deposited on top of the PVAl layer,

As the coating thickness increasers from 50 nm to 96 nm, fine surface discontinuities (*e.g.*, micro fissures) are more effectively covered or bridged, making them less apparent compared to those on the thinner PVAl (Betol) coatings. The slight linear features or networks seen in thinner films may stem from handling or stress-induced cracks —though not fully verified— whereas the thicker Alpine substrate or thicker film is less prone to bending or cracking, thereby exhibiting fewer visibly stressed defects.

For the thickest coating at 96 nm, the AlO_x-coated PVAl exhibits a rough topography, visible contaminants and processing lines in the optical micrographs, while

SEM imaging reveals distinct lines —potentially macro defects or pinholes encapsulated by the thicker coating.

In the profilometer data, cavity- or dip- like features are observed regardless of coating thickness. However, it's important to note that nanoscale features such as fine cracks or surface changes confined to the thin ALD layer are unlikely to be detected, since the profilometer's vertical (z-axis) resolution operates in the micrometre range, which is significantly larger than the coating thickness. As a result, the presence or absence of the coating may not noticeably alter the surface profile in the profilometer data. The prominent hill- or dip- like features seen are therefore more likely to originate from substrate irregularities or larger-scale defects. This also possibly explains the visibility of at least one linear feature, which is substantial enough to appear consistently across optical, SEM and profilometer imaging.

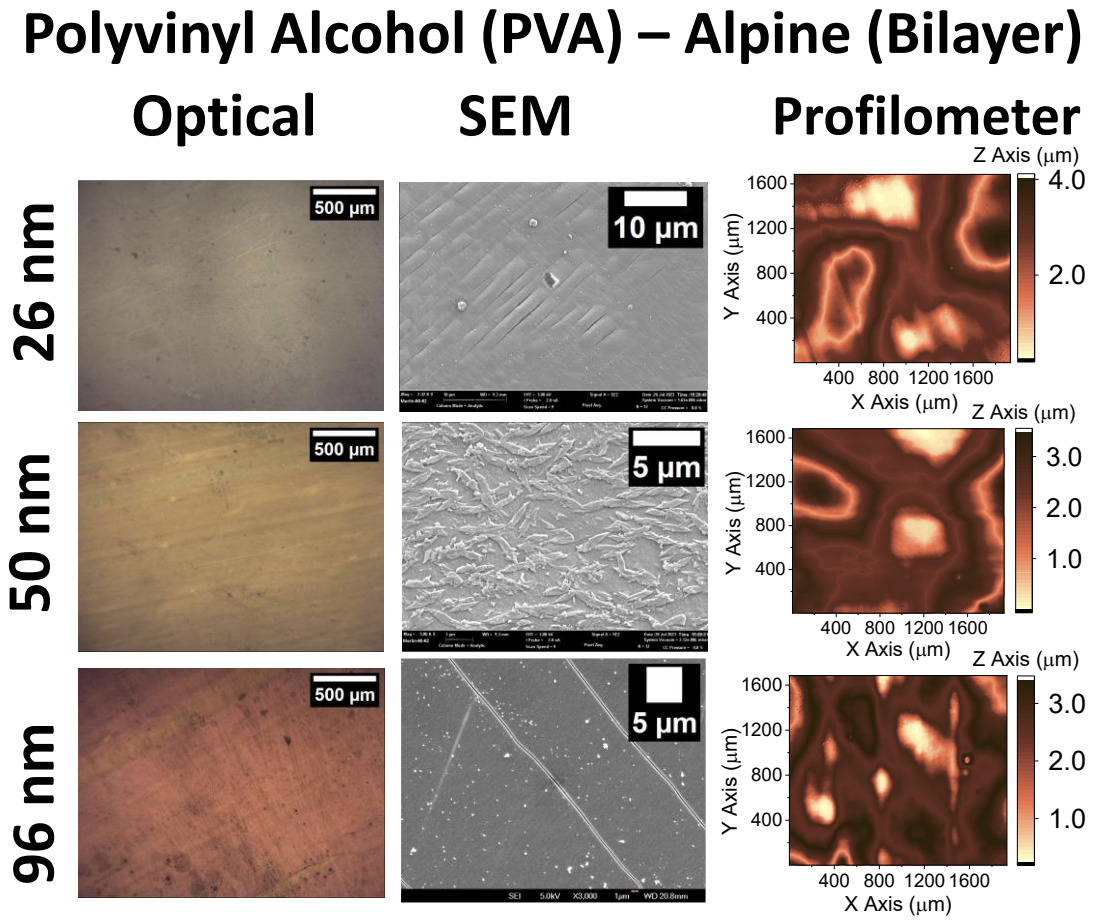


Figure 5-11: Coated thick PVAl films with AlO_x thicknesses of 26 nm, 50 nm, and 96 nm show similar optical, SEM, and profilometer results to the coated thin PVAl samples. These observations suggest that the coating plays a key role in the defects seen in the calcium test, providing insight into the permeation pathways of water vapor through the barrier layer.

5.5.3 Relationship to Calcium Test and Estimated WVTR

The surface morphology of uncoated PVAl samples, both thin and thick, shows a rougher surface with more prominent features than the PET substrates. PET had feature ranges around ~0.1 µm, while PVAl has features from ~1 to 6 µm.

Although ALD is a highly conformal technique, PVAl substrates possess characteristics that could challenge uniform deposition. The combination of high-aspect ratio topographical features, potential surface contaminants, and the absence of an

engineered protection layer are recognised risk factors for creating localised variations in film coverage. While analysis of the coated surfaces did not reveal higher density of discrete defects like micro fissures, the complex topography may nonetheless contribute to subtle non-uniformities that could influence the final film properties.

The recurring appearance of elongated, linear features, such as the slash-like patterns observed in SEM, consistent with the linear bright features in the calcium test images suggests that polymer surface roughness alone is not the sole contributor. These features are more consistent with failure mechanism arising from possible residual stress of the AlO_x film or substrate deformation during or after coating, due to thermal expansion mismatch, water absorption or mechanical relaxation. Compared to PET, PVAl has a higher thermal expansion coefficient and is highly hygroscopic, which can cause swelling or shrinkage under ALD conditions or during post-deposition handling. Such dimensional instability likely contributes to local stress build-up and formation of these discontinuities or defects in the coating.

While notable differences in coated surface morphology are observed across AlO_x thicknesses, these variations only partially explain the measured permeability values. Morphological features evolve distinctly across the coating range —linear, crack-like patterns are prominent at 26 nm; island-like “snowflake” structures emerge at 50 nm; and at 96 nm, re-emerging linear discontinuities or micro-fissures are visible. Despite these clear visual differences, the calculated permeability remains reasonably consistent across thicknesses As illustrated in Figure 5-6 and Figure 5-7, permeability decreases more significantly with increasing temperature than with coating thickness. This may be due to PVAl-specific thermal responses such as stress relaxation or polymer chain mobility,

which can reduce internal stress and improve bonding with the AlO_x layer which can limit vapor transport even in samples with visible surface irregularities.

To investigate the role of substrate topography, materials with distinctly different surface morphologies were compared. PET substrates for example exhibit low surface roughness (~2 – 6 nm RMS) and show uniform ALD AlO_x coverage with few visible defects [81, 82, 260]. In contrast, PVAl substrate have significantly rougher surfaces with more apparent coating irregularities. However, despite these clear differences in surface quality, the resulting WVTR and calculated permeability values remain comparable across the substrates, suggesting that these material systems, initial surface roughness is not the dominant factor controlling the ultimate permeation performance of the ALD barrier layer.

5.5.4 Impact of Humidity on Surface Morphology and Defect Formation in PVAl

Environmental exposure, particularly to moisture or high humidity, can significantly alter the surface morphology of PVAl films prior to coating, potentially influencing subsequent defect formation in the barrier layer. This section investigates how ambient conditions may induce surface changes that lead to failure mechanisms observed in Ca test images.

Figure 5-12 (a.1) shows an undried PVAl film, exposed to humid conditions during transport and laboratory storage. Prominent linear surface features are evident, which may be carried over into subsequent coatings. In contrast, Figure 5-12 (a.2) displays the same film after oven drying (~50 °C overnight) and storage in a desiccator. The surface appears clearer, with only some linear and spot-like features, like the dried samples described in 5.5.1 Uncoated / Bare Thin PVAl and Thick PVAl.

While not all PVAl samples were oven dried immediately before testing, it is important to note that the ALD reactor conditions inherently provide a partial drying or conditioning step. Prior to deposition, all samples experience high vacuum (~300 mTorr) and elevated temperatures (80 – 150 °C), which remove a significant portion of loosely bound surface moisture and volatile adsorbates. As discussed by Spagnola *et al.*, such in situ vacuum conditioning can reduce the water content at or near the polymer surface [368].

Although the ALD process subsequently utilizes water vapor as a co-reactant, this exposure occurs under controlled, low pressure conditions distinct from ambient humidity. The initial vacuum step ensures that all films regardless of prior storage history are brought to a consistent thermodynamic baseline before the film nucleation begins. This slightly minimizes the influence of any uncontrolled atmospheric moisture uptake prior to coating.

However, the re-introduction of moisture during the Ca testing phase (at atmospheric pressure and high humidity) reveals a fundamental instability in PVAl. Regarding the concern that dry PVAl acts as a moisture sink (sponge effect) that might artificially mask barrier failure: diffusion theory reveals that to distinguish between sorption (Water uptake) and permeation (steady-state flow) [285].The scatter observed in the rate of Ca depletion, confirms that variability is not merely an artifact of the time take to re-saturate the PVAl, but also a reflection of physical changes (defects) in the barrier integrity during the test.

Post Ca test exposure coated samples, imaged after undergoing a full Ca test, further illustrate this humidity effect. Figure 5-12 (b.1) shows a 50 nm AlO_x – coated

PVAl film (Betol) after humidity exposure. Crack-like or linear features dominate, similar in appearance to those in the 96 nm coated sample, but less evident in the original 50 nm set (Section 5.5.2 Coated AlO_x Thin and Thick PVAl).

These features are likely to arise from moisture-related changes during the test, though the precise mechanism remains unclear. It is possible that a combination of water uptake, mechanical stress and changes in the polymer structure during testing contributed to the development of these features. As schematized in Figure 5-12 (c), two primary changes to fissures are proposed: (c.1) outward or width-wise expansion, and (c.2) lengthwise propagation. These extended cracks likely act as low-resistance pathways for water vapor diffusion. The latter (c.2) aligns with Ca test data which shows that corroded regions lengthen significantly over time while maintaining constant width.

This degradation behaviour stands in contrast to that seen in PET samples, where failure typically proceeds through the radial growth of circular pinholes. Ca-test studies on AlO_x – coated PET consistently shows distinct round defects that expand in diameter over time – without forming filamentary cracks (see Sections 4.6 Analysis of Defects (Spots) in ALD AlO_x coating and 4.9 Surface Analysis of AlO_x Barrier Layers on PET). This is supported by the cited literature: Kim *et al.* (2016), in a comparable Ca test study on PET, observed bright, circular degradation spots that grew symmetrically, consistent with radial diffusion. Their data showed that spot radius increased with the square root of time ($r \propto \sqrt{t}$), while spot area expanded linearly (this trend is illustrated in Figures 3a–c, 4c–d, and 5 of Kim's publication) [206]. Similarly, Louch *et al.* (2008) reported that planarized PET developed discrete, round pinholes after aging, whereas rougher PET samples showed mostly uniform Ca thinning [392]. In both cases, no long or filamentary

cracks were observed, supporting the conclusion that PET degradation is governed by isolated defect growth, rather than stress driven fracture mechanisms.

These contrasting behaviours can be explained by differences in water uptake and mechanical response. PVAl is highly hygroscopic, capable of absorbing over 10 wt % water at high RH, where it can develop internal stresses upon drying which may lead to micro-crack formation. This phenomenon is well documented: Santanach Carreras *et al.* (2007) observed "mud-crack" networks in alumina films containing PVAl, where higher solids content of alumina particles led to greater drying stress and more extensive cracking [393]. Similarly, Li *et al.* (2024) found that solution cast PVAl films developed a crack surface "skin" during drying, unless plasticisers were used [394].

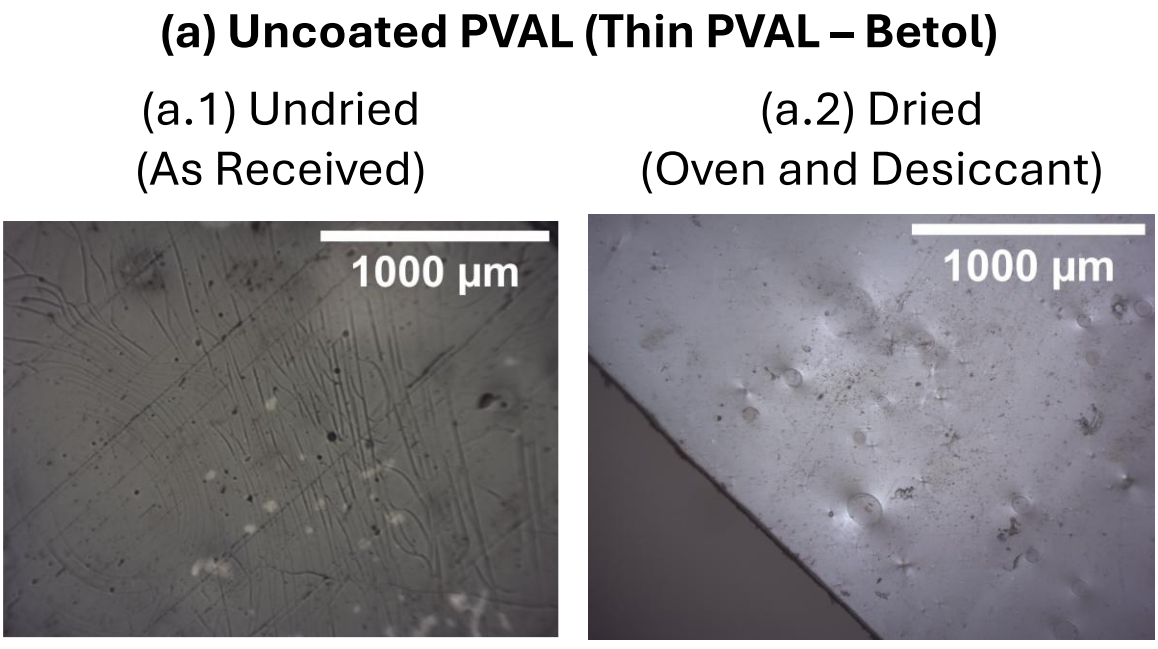
While these features may originate from drying, the continued propagation during the Ca test suggests that polymer swelling may also contribute. As moisture permeates the barrier layer, localized adsorption by the PVAl could induce expansion. This expansion constrained by surrounding dry polymer and the rigid ALD coating may generate stress concentrations that drive crack growth.

As described by Leterrier *et al.*, ceramic coatings are brittle and can only stretch a tiny amount (less than 1%), before breaking. When the underlying PVAl absorbs moisture it swells significantly expanding far beyond what the coating may withstand. This expansion forces the coating to crack, creating these long linear defects observed in the Ca test images. This remains a hypothesis but is consistent with observations of these type of linear defects that extend in length during humidity exposure.

These findings reflect some of the trends observed in this thesis. In Figure 5-12 (b.1), the intersecting cracks observed after humidity exposure and drying are

morphologically consistent with literature reports. Although drying protocols were not systematically tracked, it is reasonable to infer that cycles of ambient exposure, desiccator storage, and occasional oven drying recreated the drying stresses responsible for crack formation. These cracks, while not always deliberately induced, appear to be a natural consequence of PVAl's water-responsive character.

Taken together, the evidence supports that humidity-induced morphological changes are a dominant driver of defect formation in PVAl. These changes promote the development of long, anisotropic cracks that facilitate water vapor ingress. In contrast, PET's low water uptake (<0.5 wt %) and dimensional stability confine degradation to the radial expansion of isolated pinholes. This distinction is critical for interpreting Ca test failure modes across polymer substrates.



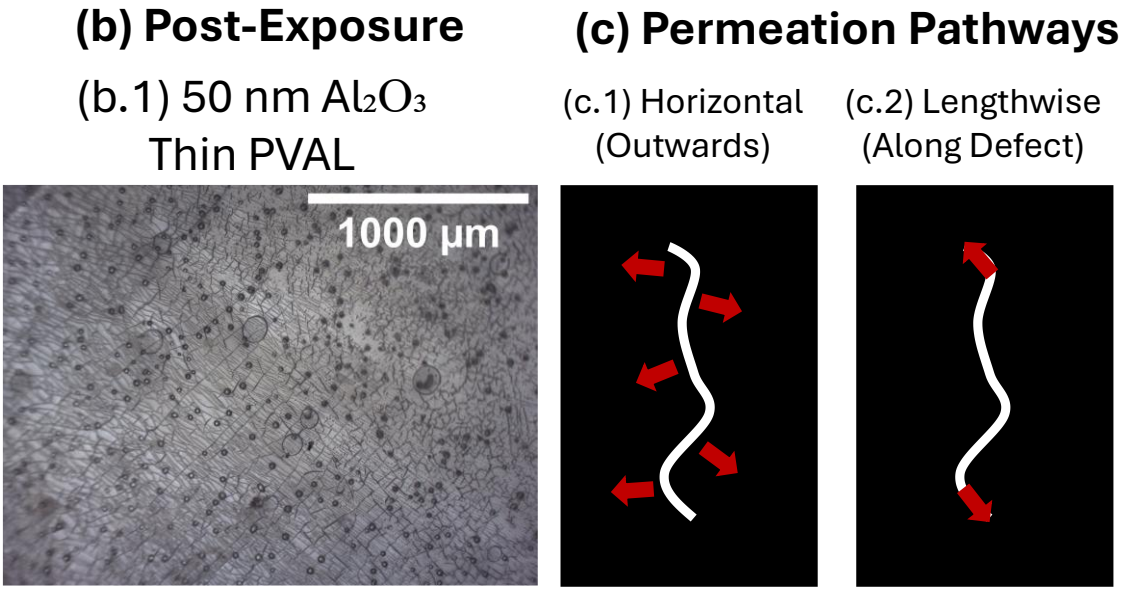


Figure 5-12: (a) Optical microscopy images of uncoated thin PVAl (Betol) films under different storage conditions. (a.1) Undried PVAl sample exposed to ambient humidity shows a dense network of linear features, suggesting shrinkage-induced stress patterns and possible crack nucleation sites. (a.2) A comparable sample after oven drying (~50 °C overnight) and desiccator storage shows a smoother surface with minor linear and dot-like features, consistent with dried samples described in Section 0. These images highlight the impact of environmental humidity on PVAl's surface morphology. (b.1) 50 nm AlO_x – coated PVAl film after ambient humidity exposure, displaying prominent crack-like or linear network features, like those seen in thicker (96 nm) coated samples. These features suggest that moisture ingress, followed by drying-induced shrinkage, can promote crack formation even in coated samples. (c) Schematic representations of proposed permeation pathways for these linear features. (c.1) Outward (width wise) expansion stabilizes, the crack width over time, while (c.2) lengthwise propagation along cracks acts as low-resistance channel for moisture diffusion. This behaviour aligns with Ca test observations, where elongated cracks expand significantly in length rather than width, indicating anisotropic permeation driven by stress localization and drying shrinkage.

5.6 Defect Analysis of Coated PVAl Films

This section analyses defect evolution in ALD AlO_x – coated PVAl films as observed through bright features in Ca test images and their influence on WVTR. The analysis focuses on defect density (defects per cm^2), morphology and the spatial distribution of features across different AlO_x coating thickness.

Two representative cases are presented here: a 26 nm coating showing early-stage, linear defect development, and a 96 nm coating where later-stage fragmentation dominates, illustrating the mechanical response of brittle oxide films under stress, in line with the models of Leterrier and Howells [219, 220, 351].

Supplementary analyses including the preliminary ImageJ-based quantification, the intermediate 50 nm thin PVAl case, and all thick PVAl date are included in appendix: 9.4.7 Supplementary Defect Analysis of ALD-Coated PVAl Films.

5.6.1 Defect Characterization Using Python for Isolation and Coalescing Features

The same methodology used to identify isolated and coalescing defects in coated PET was applied to coated PVAl substrates, with the addition of distribution plots. These plots show where defects, both linear and dot-like, are concentrated by dividing the image into a 50 × 50 grid and counting spots in each cell. The spatial maps used a fixed 50 × 50 binning across the masked or region of interest defined calcium window; the map values are counts per cell (dimensionless). Because the grid spans the whole physical image, the per cell size is equal to (image width/50) × (height/50). For example, for the 26 nm Thin PVAl panel (5.26 × 4.88 cm), one cell is 1.05 × 0.98 mm.

Areas with higher spot densities are visualized with more intense colours, revealing defect patterns. While not perfect, this approach provides more accurate defect estimates, aligning better with literature data. The analysis was repeated for 26 nm, 50 nm, and 96 nm AlO_x coatings on thin and thick PVAl substrates.

5.6.2 Defect Distribution of AlO_x Thin PVAl

The following figures, shows the detection of isolated (green) and coalescing (pink) spots for AlO_x Thin PVAl. Isolated spots are the first to appear and are tracked individually; while coalescing spots are identified when two previously isolated spots merge.

5.6.2.a 26 nm Defect Distribution of AlO_x Thin PVAl

Figure 5-13 (a.1) shows the raw, unprocessed Ca test images over time. Figure 5-13 (b.1) presents the same images with colour-coded classifications of isolated (green) and coalescing (purple) spots, while (c.1) displays the corresponding spatial distribution of these features. Note: The sub-figure labels (a.1, b.1, c.1) are used here and in subsequent sections (*e.g.*, a.2 for 50 nm, a.3 for 96 nm), to consistently identify equivalent views across different coating thicknesses.

Spot classification in (b.1) uses the label "isolated" to denote spots that are first detected independently, *i.e.* not yet merged with neighbouring features. Most of these features appear within the first few image frames (*e.g.*, by image 2), reflecting early-stage degradation, while later-emerging bright regions are typically the result of coalescence with pre-existing spots.

As explained in 4.6.2 Differentiating Isolated and Coalescing Spots (Python), classification occurs algorithmically in three steps: (1) detection of spots identified via Canny edge detection applied to an adaptive-threshold image, with features limited to those within the Ca layer mask; (2) filtering, in which only regions with an area between 15 – 30 pixels (~1.5 to 3.0 mm – assumption) are considered to avoid noise and oversized

artefacts; and (3) classification, in which for each new detected region, its centroid is compared to those from previously detected isolated spots - if the centroid lies more than 20 pixels (~2.1 mm) away from all previous isolated centroids, it is labelled isolated, if it lies within this threshold it is labelled coalescing. Detected regions are visualized with distinct annotations, isolated spots appear as green dots with blue contours; while coalescing spots are shown as purple or magenta dots and contours.

While this method offers a robust and efficient way to track early signs of Ca depletion, it has known limitations. Figure 5-13 (b.1.1) illustrates the pitfalls and concerns using Image 1 and Image 2 as examples. In the raw optical image of Image 1, two potential artifacts, likely due to dust or lighting, are visible (highlighted as orange/yellow box and red circle). In the corresponding detection map, the algorithm correctly excludes the red circle (no features detected) but detects several isolated spots in the orange/yellow region. In Image 2, the artifact in the orange/yellow box is no longer visible, and this is reflected in the detection output (no features detected). Conversely, a new physical feature emerges in the red circled region, which is appropriately identified by the algorithm. This example demonstrates the algorithm's overall reliability but also highlights the importance of validating potential false positives/negatives, especially when artifact presence varies between frames.

These challenges are common to edge-based, threshold-driven methods, and while these do not invalidate overall trends, it necessitates cautious interpretation in regions with high spot density or during late-stage degradation. More advanced approaches such as region mask comparison, pixel-wise tracking, or persistent feature IDs could in theory address these ambiguities but were not implemented here due to the high computational

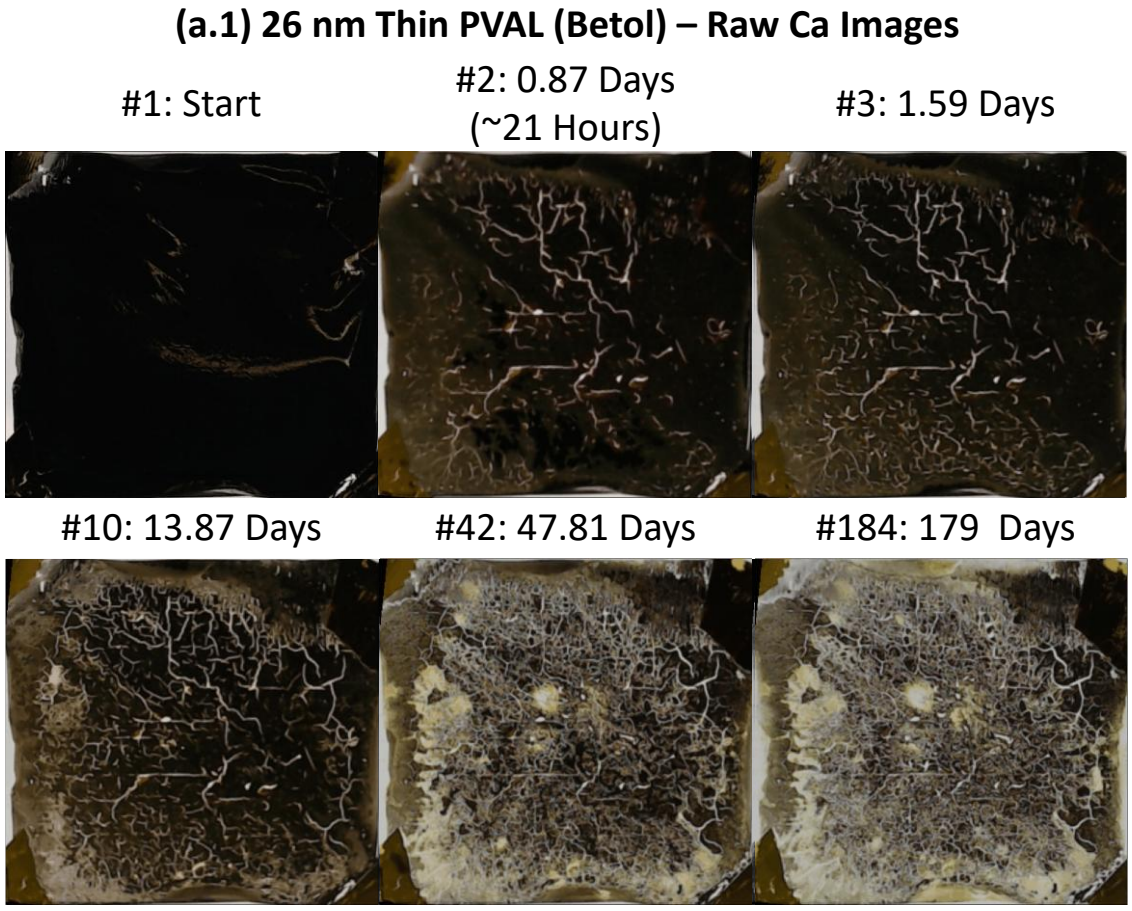
and manual validation requirements they entail. Given the large number of high-resolution frames, the chosen centroid-distance method balances interpretability, consistency and feasibility across the data set.

Moreover, as acknowledged, while coalescing classification may not always yield additional insight beyond what is visible in the raw image series, it does help indicate when a feature is evolving in size or interacting with surrounding features. The distinction is particularly helpful for identifying isolated spots, which are of primary interest in evaluating barrier integrity. That said, it is acknowledged that the distinction may be less critical in later stages of degradation, where widespread coalescence becomes dominant.

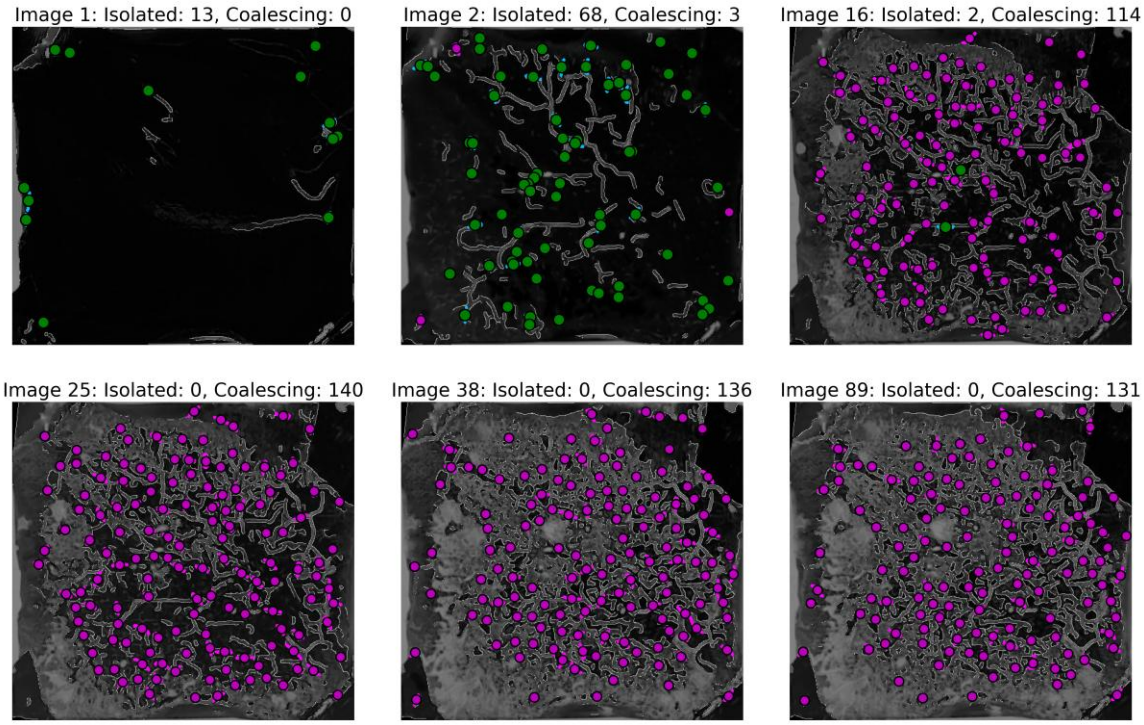
Edge effects, the brightening at the sample edges due to water ingress from the sides rather than through the film, are excluded from the analysis, as these do not reflect intrinsic barrier performance. While edge-related features are clearly observed in PET samples, these appear far less prominently in the PVAl coated films analysed here. This reduced edge effect may also be due to the shorter duration of these experiments, which limits the extent of sideways water permeation.

In PVAl samples, the spot distribution, as shown Figure 5-13 (c.1), appears quite uniform across the sample, indicating that defects and moisture ingression are not confined to specific regions but occur throughout the film area. While occasional bright areas at the edges (*e.g.*, at the left upper side) may still be detected as spots, the overall pattern suggests a broadly distributed defect landscape, rather than localized failure points or dominant edge infiltration. The full defect analysis of the intermediary thickness

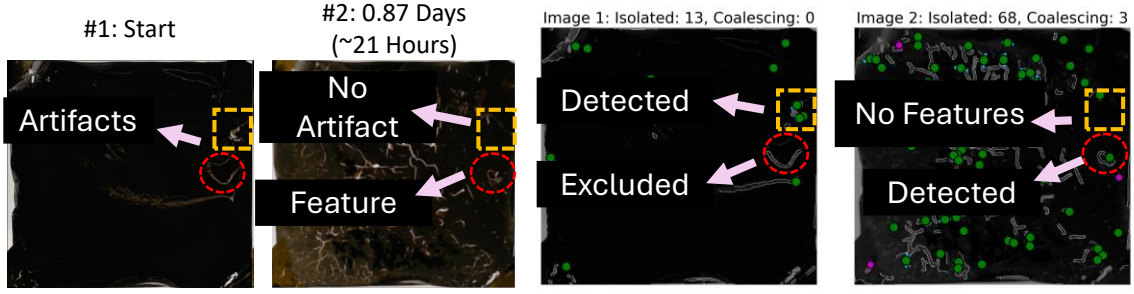
50 nm AlO_x coated thin PVAl including region-specific segmentation and spatial mapping is provided in 9.4.8.a 50 nm Defect Distribution of AlO_x Thin PVAl.



(b.1) 26 nm Thin PVAL (Betol) – Defect Classification Overlay (Green: Isolated with Blue Contour and Purple: Coalesced)



(b.1.1) Limitations on Image Detection (Image 1 and Image 2)



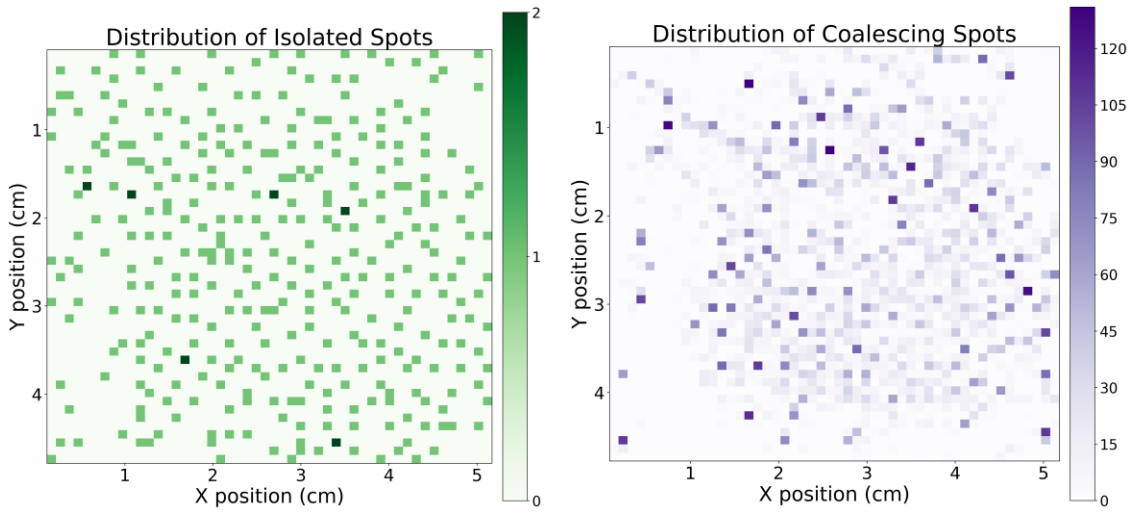


Figure 5-13: Defect evolution and spatial distribution for a 26 nm AlO_x barrier on thin PVAl (5.26 × 4.88 cm – cell size ≈ 1.05 × 0.98 mm). (a.1) Raw Ca-test frames at six representative times, illustrating the progressive dark-to-bright conversion that accompanies calcium depletion. (b.1) Same frames with automated classifications super-imposed: isolated spots are first-appearance features of 15–30 px^2 whose centroids lie > 20 px (~2.1 mm) from any earlier isolated centroid are marked by green dots with blue contours; coalescing spots, new features whose centroids fall within that 20 px radius are marked by magenta dots and contours. Panel titles give the cumulative counts of isolated and coalescing spots detected in each frame. (b.1.1) Two zoom-in examples highlight algorithm behaviour: a dust-/lighting artefact in the yellow dashed box is present in Frame 1 but absent in Frame 2, and the algorithm responds accordingly, whereas a genuine defect (red circle) emerges in Frame 2 and is correctly detected. (c.1) Fixed 50 × 50 grid maps showing the cumulative number of detections per cell over the whole sequence, left, isolated-spot counts (green scale 0–2); right, coalescing-spot counts (purple scale 0 to >120), allowing direct spatial comparison across samples. Counts represent totals accumulated over time (not temporal frequency), and "total detected spots" is therefore omitted from the legend. Brightening at specimen borders caused by lateral water ingress is excluded through the calcium-layer mask, so the maps reflect only intrinsic barrier defects.

5.6.2.b 96 nm Defect Distribution of AlO_x Thin PVAl

Figure 5-14, (a.3) Ca test images of the 96 nm AlO_x coating on thin PVAl, reveals island-like black circles, surrounded by irregular bright fracture paths or linear microdefects. Here the black circular regions are understood as not Ca-depleted zones,

rather these retain calcium indicating that degradation has occurred in the surrounding areas. This morphology contrasts with the finer more linear fissure networks observed in thinner coatings (*e.g.*, 26 nm and 50 nm) and differs from the PET benchmark where pre-existing pinholes produced bright, circular defects on a dark background. Instead, the emergence of these widely spaced rounded features points to possibly a fundamentally different mechanically driven failure mode, not one necessarily dominated by pre-existing flaws.

As the PVAl substrate absorbs moisture it swells, imposing in-plane tensile stress on the overlying brittle AlO_x coating. Early studies by Leterrier *et al.* (2004), on ITO-coated polymers showed that crack onset strain and fragment spacing depended strongly on coating thickness and mechanical mismatch [219]. This stress-transfer model was later applied to barrier oxides by Howells *et al.* (2008), who experimentally demonstrated that thicker SiO_x films on PET exhibit larger inter-crack distances and lower saturation crack densities (CD_{sat}) due to delayed fracture onset and wider fragment formation [351]. These underlying mechanics were further elaborated in the comprehensive review by Leterrier *et al.* (2010), which links CD_{sat} to coating thickness via the stress transfer length and confirms that scaling trend across SiO_x, SiN_x and other brittle coatings on compliant or soft substrates [220].

It is argued that once the critical strain is exceeded, the brittle oxide fractures into discrete segments who spacing scales inversely with coating thickness (h_c) as described in Equation 5-2. Accordingly, the 96 nm AlO_x PVAl film breaks into broader fragments, leaving behind larger calcium rich islands whereas thinner films form denser crack networks and exhibit faster, more uniform Ca depletion. This classical crack-saturation

behaviour is a hallmark of fragmentation driven failure in stiff, brittle coatings on the soft PVAl substrate.

$$CD_{sat} \propto \frac{1}{h_c} \qquad \textit{Equation } 5\text{-}2$$

Additionally, as explored in 9.4.8.b Defect Distribution of AlO_x Thick PVAl, substrate thickness further modulates stress distribution and deformation response. Thicker substrates may have wider buckling or delamination as water is absorbed, leading to early onset brightening across wide areas, while thinner substrate promote more spatially discrete fragmentation before coalescence. Altogether, the observed patterns are characteristic of stress induced fragmentation regime, not wholly controlled by initial coating flaws. In terms of detection (b.3) the tracking algorithm successfully captures newly formed or isolated features with strong visual alignment between the raw Ca test images and overlaid detections, though minor discrepancies persist when features coalesce or nucleate between imaging frames, particularly during early stages leading to occasional undercounting.

Meanwhile, the spatial distribution (c.3) of isolated spots is shown uniformly across the sample (no strong spatial bias), while coalesced spots exhibit distinct clustering in certain regions, suggesting that localized areas experience more advanced or accelerated permeation that may reflection variations in defect distribution or substrate properties.

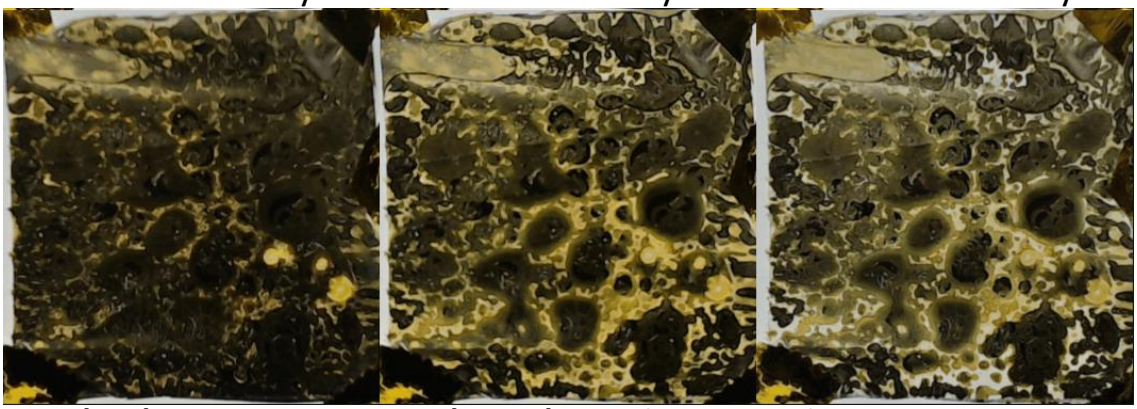
The defect distributions of thick AlO_x coatings (26 nm, 50 nm and 96 nm) on PVAl, show stress dependent evolution from linear cracking to wave-like deformation are discussed 9.4.8.b Defect Distribution of AlO_x Thick PVAl, supporting the role of substrate modulated barrier failure.

(a.3) 96 nm Thin PVAL (Betol) – Raw Ca Images

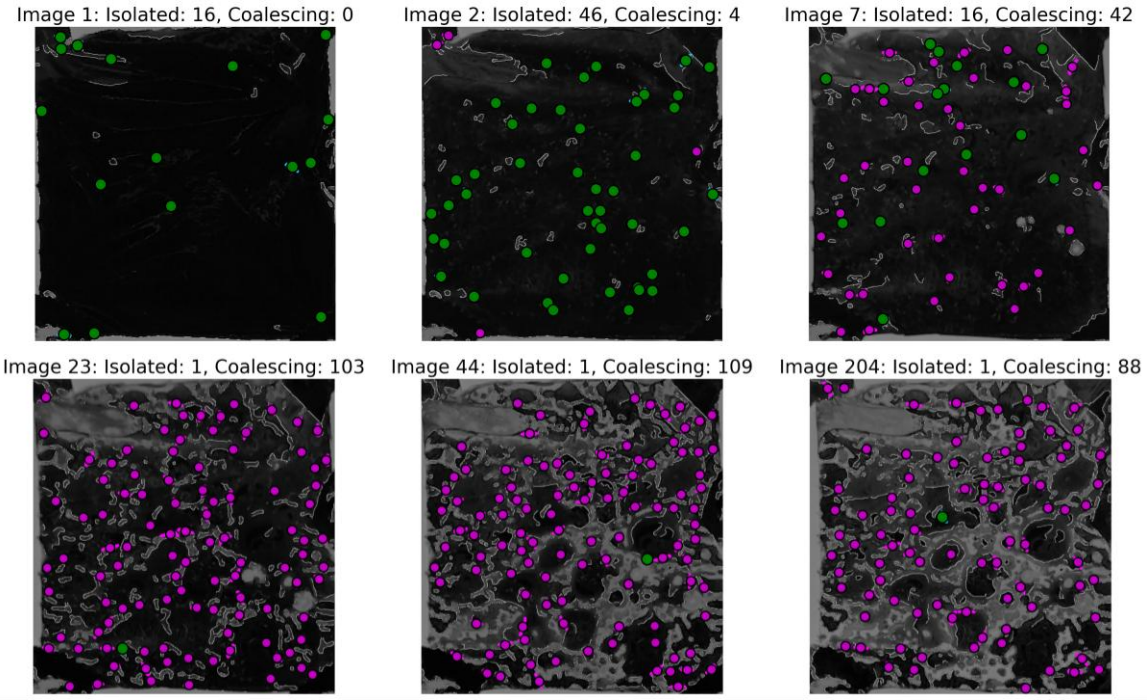
#1: Start #2: 0.90 Days (~21.6 Hours) #7: 6.92 Days



#23: 28.94 Days #44: 51.98 Days #204: 187.87 Days



(b.3) 96 nm Thin PVAL (Betol) – Defect Classification Overlay (Green: Isolated with Blue Contour and Purple: Coalesced)



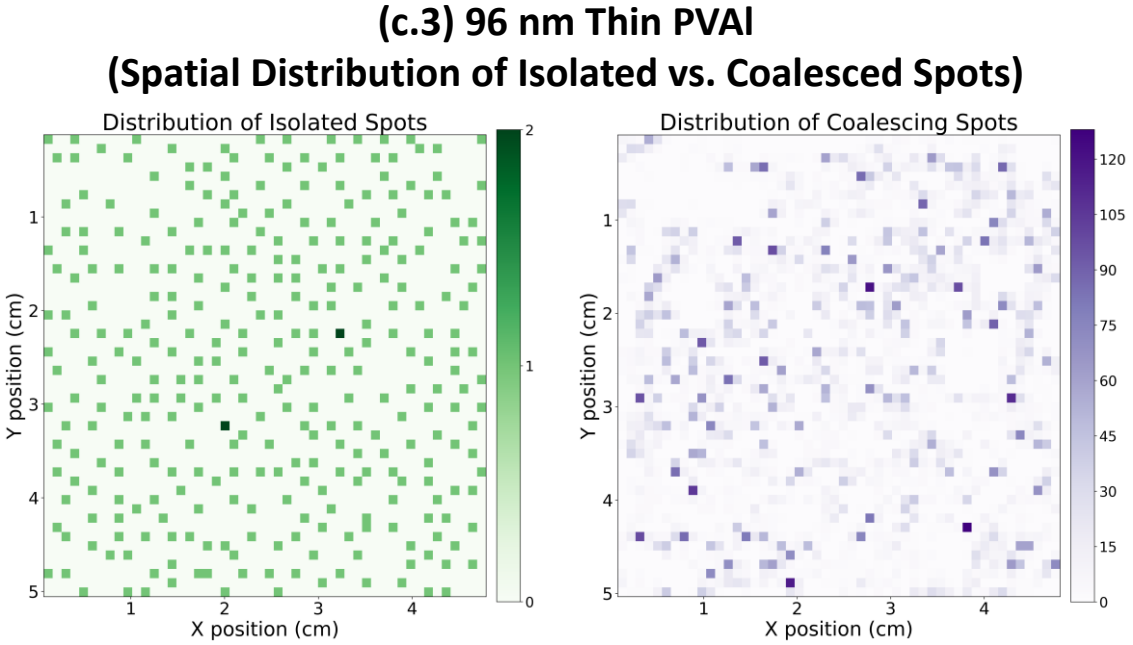


Figure 5-14:Ca-test results for the 96 nm AlO_x coating on thin PVAl (4.91 × 5.13 cm - cell size ≈ 0.98 × 1.03 mm). (a.3) Raw images reveal island-like calcium-depleted zones surrounded by irregular bright microdefects. This morphology contrasts with the finer, linear fissures in thinner coatings (26 nm and 50 nm), and differs from the pinhole-type defects in PET. Instead, the rounded, widely spaced features suggest a stress-induced fragmentation regime. As the PVAl swells under moisture uptake, in-plane tensile stress develops in the oxide. This behaviour aligns with prior work by Leterrier et al. (2004, 2010) [219, 220] and Howells et al. (2008) [351], which showed that thicker brittle films fragment into fewer, broader segments, with saturation crack density scaling inversely with coating thickness ($CD_{sat} \propto 1/h_c$; see Equation 5-2) (b.3) Overlays of detected spots show strong agreement with raw frames. Isolated defects appear early and are later replaced by coalescing features as cracks merge and grow. Minor detection errors arise where features nucleate or merge between frames. (c.3) Spatial maps show isolated spots distributed uniformly, suggesting widespread initial permeation. In contrast, coalescing spots cluster in localized areas, indicating heterogeneous defect growth, possibly influenced by local stress concentrations or coating variability. These patterns support a fragmentation-driven mechanism with spatially variable evolution.

5.6.3 Statistics of Defect Populations in AlO_x on Thin PVAl and Thick PVAl

A key distinction in defect analysis is whether a feature is classified as isolated/unique or coalescing as explained in 4.6.2 Differentiating Isolated and Coalescing Spots (Python), in brief: isolated spot is a new, standalone defect that hasn't

merged yet with other spots, while a coalescing spot forms when two or more spots combine.

This distinction helps track new defect formation and the evolution of existing ones. Coalescence can obscure its estimation as previously distinguishable spots can obscure other spots or defects through coalescence, potentially leading to undercounting of defects.

Although the imaging system captures the precise timestamps of each frame, the temporal resolution is limited by the intervals between image acquisitions. As such, the uncertainty in identifying the exact time a spot is identified and classified is also governed by these time gaps. While the detection algorithm performs reliably, this limitation inherently introduces some degree of uncertainty in the onset of spot formation.

Despite these challenges, credible and consistent results were achieved. The overlay between raw Ca images and the detected spots shows strong visual agreement, confirming the algorithm's general reliability. Furthermore, the quantified defect densities (normalized for area) summarized in Figure 5-16 (more detail is given in the supplementary information in Figure 9-40, Figure 9-41) fall within expected ranges – typically on the order of tens of isolated defects per cm^2, consistent with what is visually observed in early frames. Isolated defect counts are highest at initial timepoints and gradually decline as coalescence increases. This temporal behaviour aligns with visual trends observed in the raw images, reinforcing the validity of results while acknowledging some limitations.

Referencing Section 5.5 Surface Analysis of Uncoated and AlOx-Coated PVAl Films, surface morphology strongly influences defect formation, which directly impacts barrier performance and product reliability. The thin PVAl case explores the feasibility of minimizing both substrate and coating thickness (thinner coating 26 nm). While this thin coating and thin substrate shows promising barrier properties, it remains highly sensitive to surface defects and poses possible challenges for reliable barrier properties for large scale applications.

In line with this, observations of ALD-coatings with 26 nm, 50 nm and 96 nm thicknesses on PVAl substrates (refer: 5.6.2 Defect Distribution of AlOx Thin PVAl, 9.4.8.b Defect Distribution of AlOx Thick PVAl, and 5.5 Surface Analysis of Uncoated and AlOx-Coated PVAl Films) reveal distinct differences in surface morphology and their correlation with defect features as identified in the Ca test.

At 26 nm, both thin and thick PVAl substrates exhibit “slash-like” features in SEM surface images. While it is difficult to precisely quantify the exact shape, size, and orientation of these features, they bear a clear visual resemblance to the linear defects observed in the Ca test, suggesting a possible connection between surface morphology and permeation behaviour at this thickness.

Meanwhile, at 50 nm, a “snow-like” surface texture is observed. However, the island-like defects seen in the calcium test at this thickness are significantly larger than those identified in surface analysis. This mismatch in scale suggests that possible additional mechanisms beyond surface roughness such as localized film failure or not proven but possible stress-induced deformation, may be responsible for the observed defects.

Finally at 96 nm, coated PVAl substrates, especially those on the thick variant, exhibit smoother and more uniform surfaces in SEM analysis. Despite this, the linear features visible in surface images differ notably in size from the island or wave-like defects found in the Ca test. While the features may appear similar in shape, the inconsistency in scale implies that this might originate from different defect formation process.

Figure 5-15 further illustrates the limitations and potential inaccuracies that may arise, not necessarily from the identification process or code itself, but potentially from the nature of the raw data, intrinsic morphological features and the lag time associated with calcium depletion for certain defects.

At time 0, linear features are clearly identifiable, these are defined as elongated, crack-like defects that differ from typical circular spots in both shape and geometry. Rather than being round, square or rectangular, these features exhibit a high aspect ratio, (Further explored in: 5.7 Defect Size / Area Estimation in Coated PVAl Films). These features may intersect, branch, bifurcate, forming complex network-like structures.

As the system evolves over time (*e.g.* at time t), individual features begin to merge or overlap and are classified as coalesced, following the spatial threshold-based definition implemented in the code. At 2t, the pink dashed lines in the schematic illustrate apparent “branching” or defect expansion, representing either the growth of an existing crack or the formation of connecting paths between nearby defects. These connections emphasize how two formerly separate regions may be linked but are still classified as coalesced based on centroid proximity within the algorithm.

This representation underscores a key limitation, where this increased structural complexity and may cause ambiguity when trying to distinguish new isolated features from extension of older ones. By 3t, for instance, the figure shows a case where a newly formed defect may be incorrectly grouped as coalesced simply because it lies close to an existing network or previously identified isolated defect – a scenario illustrated in the dashed red box. This issue is particularly pronounced for linear defects, which unlike compact circular spots, can propagate asymmetrically and form convoluted paths that overlap or nearly touch. Altogether these behaviours highlight the challenge of interpreting evolving geometries using fixed distance thresholds and reinforce the importance of accounting for network connectivity and growth direction when analysing coalescence in anisotropic systems. These networked linear features are hypothesized to possibly represent narrower or evolving defects that resulted in delayed Ca depletion, though the precise nature remains unclear. These networks could reflect additional cracks forming or extending as the polymer swells.

In this context, a key focus of the analysis is how defect geometry, particularly length and evolving width may influence permeation behaviour and the rate of Ca depletion. However, while these factors are discussed conceptually, a full geometric analysis (*e.g.* precise shape, curvature and width profiles) is difficult and not explicitly performed in this study. Such quantitative geometric analysis in future work, would require a computational pipeline based on morphological skeletonization and topological graph analysis that could be used for the binary Ca test masks. Unlike the centroid based tracking used for the circular spots in PET, the complex dendritic and linear features in PVAl require algorithms capable of independently quantifying network connectivity and

crack opening and displacement. This proposed workflow proceeds by applying a medial axis transform (skeletonization to reduce linear features to 1 pixel wide centre lines), allowing for a more precise extraction of crack length and tortuosity, while a Euclidean Distance Transform would map the local width distribution along the propagation path.

This in turns allows the calculation of characteristic defect spacing and saturation crack density, which directly link morphology to barrier physics. Defect spacing controls the variable in tortuosity based permeation models [13], which relate lateral diffusion path length to lag time. Moreover, quantifying evolution of crack density allows the estimation of interfacial shear stress using stress transfer mechanics from frameworks by Leterrier [219] and Howells [351]. While this computational approach quantifies macro scale features from optical data, a representative subset of samples can be characterized by SEM to validate optical width measurements and correlate the macro scale bright spots with possible specific micro-structural failure modes (*e.g.* cohesive fracture and delamination).

This challenge, namely the difficulty of characterizing and consistently analysing interconnected or evolving linear features is more frequently observed in coated PVAl substrates than in coated PET, though it is not exclusive to one material. The emergence of these intersecting or branching features may also arise from coating damage, such as local stress points or contamination during handling, or localized variations in the coating's structural integrity.

The coalescing graphs in this section show that, due to continued growth, the algorithm classifies further additions to existing branch-like structures as new coalescing lines, resulting in a plateau effect. Although no truly new coalescing events may be

forming, the algorithm interprets continued extension as separate events rather than as growth of existing ones. While this could be refined, doing so risks added complexity and potential misclassification.

This issue is less evident in coated PET samples, where individual features are more easily identifiable. This is like due to the absence of branching or bifurcating structures and the fact that defects in PET appear more consistent in size, leading to clearer, more uniform detection. In contrast, coated PVAl exhibits a broader range of defect sizes, where smaller or more irregular cracks may go undetected or overlap with others.

The smoother, more uniform substrate on PET may also reduce stress-induced variability, limiting this linear like propagation and aiding in clearer feature separation. These factors contribute to improved identification accuracy in PET compared to PVAl.

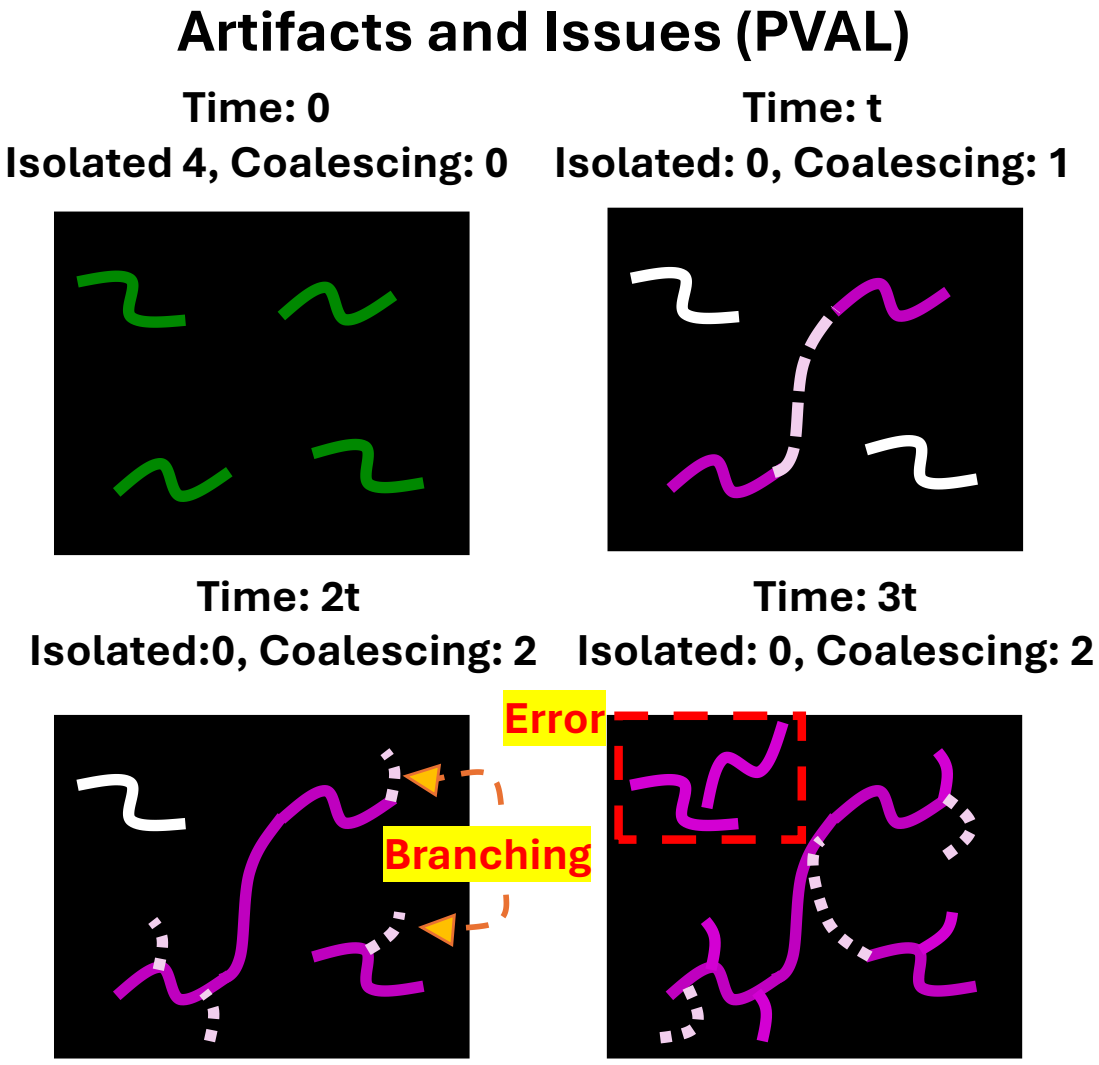


Figure 5-15: Schematic showing the progression and classification challenges of linear defect features over time. At time 0, isolated features are visible as separate entities (green). As time progresses to t, spatial overlap and merging begin, triggering classification as coalesced based on centroid proximity. By 2t, pink dashed lines highlight apparent connections between defects—interpreted here as possible crack growth or joining paths. These are not considered a new class but remain coalesced under the algorithm's distance rule. At 3t, the dashed red box marks an example of a potential misclassification: a newly emerging defect located near a larger network may be wrongly grouped as coalesced. This schematic illustrates how evolving linear geometries especially those that extend or form networks can complicate accurate identification. Because the algorithm relies on a fixed spatial threshold, such features may be joined prematurely, particularly in cases of asymmetric growth or swelling. The result is increased ambiguity when distinguishing isolated defects from extensions, highlighting the need to interpret connectivity and growth behaviour alongside spatial proximity.

5.6.3.a Summary of Spot Densities of Coated PVAl Substrates

To summarize, the total number of isolated spots was divided by the sample area for each sample to calculate the isolated spot density. Figure 5-16 shows a slight effect of substrate type on defect density, though the exact trend remains difficult to confirm. Supporting statistical analysis of these isolated and coalescing spot densities are presented Appendix in 9.4.9 Supporting information - Statistics of Defect Populations in ALD – AlOx PVAl (pp: 547 to 557).

As discussed in 4.6.3.a Summary of Spot Density – Python Estimations, ALD-deposited AlO_x on PET and PEN substrates have been widely studied using Ca tests, electrochemical decoration, and transmission-based barrier methods. Within the commonly studied 20–30 nm thickness range, reported defect densities typically fall between 10 and 50 spots·cm^{-2}, depending on deposition method, substrate preparation, and process conditions. Films thinner than ~20 nm, especially those made via thermal ALD without plasma enhancement or surface activation, often exhibit defect densities exceeding 50 cm^{-2}. In contrast, thicker coatings (≥ 50 nm) or plasma-enhanced films tend to show lower values, generally 10–30 cm^{-2}, or even lower when film densification is optimized [109, 110, 334, 344, 350, 395]

Figure 4-18, however shows no strong trend with increasing AlO_x thickness in PET samples; defect density appears broadly flat, with values clustering between 10 and 15 cm^{-2} across the range tested. While there is a notable local minimum around 50 nm (~5 spots·cm^{-2}), the overall data do not indicate a consistent decrease or increase with thickness.

Against this benchmark, the isolated-spot densities measured on PVAl samples (Figure 5-16) ranging from 9 to 17 spots·cm^{-2} (mean: 13.0 ± 2.0 spots·cm^{-2}) fall well within, and in several cases below, the range typically observed for PET. This supports the conclusion that PVAl is not intrinsically more prone to pinhole defects than PET under the same ALD conditions.

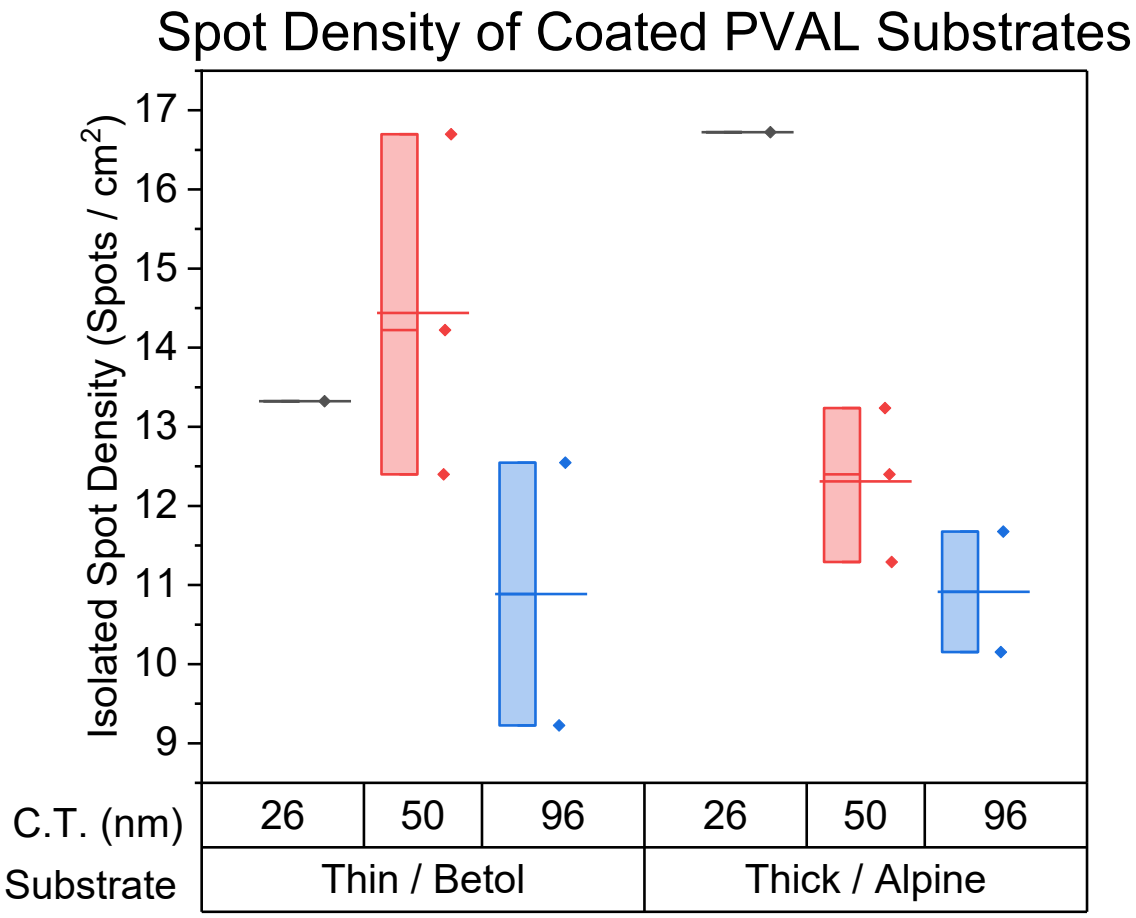


Figure 5-16: Scatter group plot of total isolated spot density versus substrate thickness and AlO_x coating thickness shows the spread and effect of substrate and coating thickness. For thin substrate, no clear trend is observed; 50 nm coatings show higher isolated spot counts, while 26 nm and 96 nm coatings show significantly fewer spots. In contrast, thicker PVAl exhibits a clear trend of decreasing isolated spots with increased thickness.

5.7 Defect Size / Area Estimation in Coated PVAl Films

One can consider whether an approach like that used in section 4.7 Calcium Test Defect Size Calculations, exploiting Equation 4-7, can also be applied to coated PVAl films to estimate the underlying defect size. However, it is important to recognize that the nature of the defects observed in these films differs notably from those in PET. Most of the observed features in PVAl films exhibit aspect ratios between 4.0 and 6.0 (Figure 9-40 and Figure 9-41), suggesting that these defects are more linear or elongated rather than circular.

While the total length of bright linear features appears to increase over time (as seen in the Ca test images), the width or thickness of these lines does not visibly expand over time, which might be expected if more water were permeating through a consistent linear defect. This discrepancy suggests two possibilities: either water transport through the defect is somehow self-limiting after the initial Ca reaction, or water diffusion preferentially occurs along the linear defect rather than perpendicularly to it. If structural changes in the PVAl substrate, such as swelling, or relaxation of residual stresses cause crack propagation in the coating during the Ca test, then the water vapour will permeate through the new crack length (extending the length of the observed spot) much more quickly than it diffusing through the reacted Ca or overlying epoxy to widen the spot and react with the Ca there.

Because of these complexities and the random, elongated morphology of the defects in PVAl, it is more practical to estimate an approximate defect size or area rather than focusing on size and shape. This estimated area can be compared to possible visible features in Section 5.5 Surface Analysis of Uncoated and AlO_x-Coated PVAl Films. The

following section outlines the assumptions behind these area-based estimates and how these reflect the observed defect morphology.

5.7.1 Assumptions of Defect Size / Area

The actual defect area as argued can be calculated using Equation 4-7, that states the rate of water uptake $M_{H_2O}(\frac{g}{day})$ of the specific area divided by the product of bare WVTR ($\frac{g}{m^2 \cdot day}$) polymer film (PVAl) gives an approximation of the defect size or area. For reference the bare WVTR is taken as 2.13 ± 0.004 g/m²·day (Figure 9-30) (a) obtained under similar conditions similar to those of the coated samples (Note: The uncoated samples were tested at milder conditions - 23 °C and 40% RH to prevent instantaneous saturation and ensure the capture of the transition region, whereas the coated PVAl samples were tested at higher humidity at ~25 °C and 78.5% RH to sufficiently drive permeation through the barrier defects within a practical timeframe).

The following section now analyses an example of a coated thin PVAl defect (5.7.2 Example of Defect Size Calculation (26 nm Thin PVAl Substrate Defects)). Other examples are presented in: Appendix 9.4.10 Supporting information - Statistics of Defect Sizes in ALD – AlO_x PVA (pp. 557 to 580).

5.7.2 Example of Defect Size Calculation (26 nm Thin PVAl Substrate Defects)

The first set of analysed samples is the 26 nm Thin PVAl (Betol), with six regions of interest selected (Figure 5-17) ranging in size from 0.41 × 0.46 cm to 1.38 × 1.04 cm. These regions show the model's ability to outline and identify defects over time.

In each region of interest, for simplified detection, the largest visible feature was selected an intentional choice, though it likely means that the estimate only applies to larger defects.

This approach was justified for two reasons: (1) tracking continuous defect growth would be difficult without a clearly defined and isolated feature as seen in the PET, and tracking largest defect typically offers better fidelity for monitoring a single specific defect's progression over time; and (2) it is assumed that the largest defects dominate water permeation behaviour.

The code was configured to isolate these dominant features, enabling consistent analysis of mean grey value over time, which was used to estimate the mass of water permeating through the defect per unit time (M_{H_2O}) as defined in 4.6.2 Differentiating Isolated and Coalescing Spots (Python).

As in previous methodology, images were segmented and converted to binary format (black and white). The largest spot or feature was then identified using the measure.label() function, which assigns a unique ID to each feature, followed by measure.regionprops() to find the maximum feature—all using the scikit-image library (skimage.measure module), which is used in other fields beyond material science (*i.e.* medical science and engineering) [396].

As argued, focusing on the largest defect minimizes misidentification of coalescing or other isolated spots, improving accuracy in spot growth rate calculations. Previous iterations of the code often mischaracterized defects due to interference from surrounding artifacts. Isolating the largest defect ensures consistent size measurements of the same feature.

Figure 5-17, shows a 3 x 2 montage of the six regions of interest, highlighting the largest defect with a red outline and its isolated binary image. The model occasionally misidentifies defects due to artifacts or image quality issues, leading to incorrect classification of the largest defect and inaccuracies in tracking propagation. However, it generally accurately tracks the defect over time and gives a rough approximation of water uptake through that specific spot in the barrier layer.

Defect #1 (26 nm Thin PVAl) shows typical propagation, the bright feature starting small and growing larger over time. It can branch into dendritic structures or coalesce with other defects. Some defects stabilize and stop growing, possibly indicating full saturation, as seen in the pale points beyond the transition region. These dendritic formations may be due to substrate and coating heterogeneity, impurities, geometric discontinuities, or voids, all of which can create pathways for water vapor permeation, reflected by depleted calcium regions.

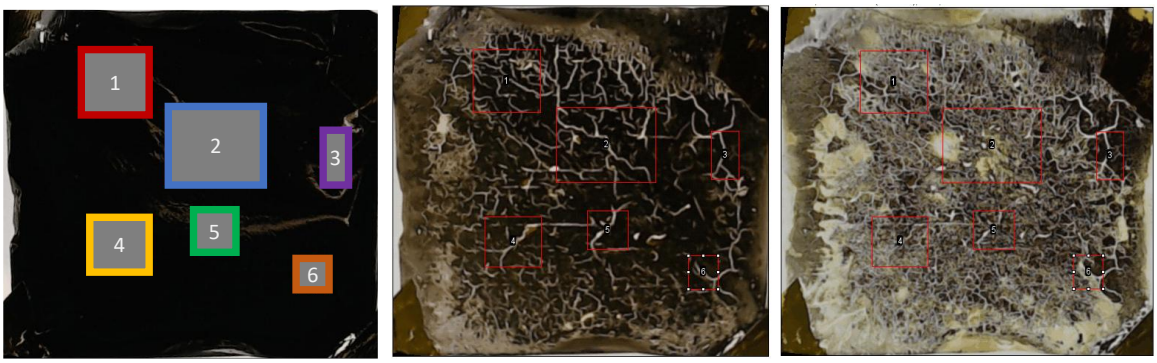
In Defect #2 (26 nm Thin PVAl), a split forms with four branching ends. Defect #3 shows two distinct defects coalescing, complicating isolation and estimation. Defect #4 shows branching within the defect, increasing its area. Defect #5 remains stable before branching in multiple directions, while Defect #6 thickens over time and eventually coalesces, maintaining its shape like other regions.

For water uptake rate, Defect #1 shows the steepest slope (2.31E-07), corresponding to a defect area of 1.09×10^5 μm² ($\pm 1.08 \times 10^4$ μm²). This defect area represents the actual cross-sectional region through which water permeates, a faster rate of spot growth indicates a larger defect and overall size.

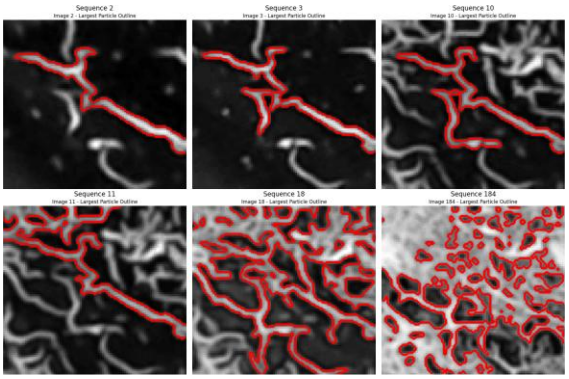
In Defect #2 (1.38 × 1.04 cm), the defect width was not the largest, while Defect #4 (0.78 × 0.69 cm) had a similar of 3.49×10^4 μm^2 ($\pm$ 5.11 $\times 10^3$ μm^2). Despite differences in region size, the defect area was more strongly correlated with the water uptake rate rather than the absolute region size or data quality, as expected. Defect #5 (0.57 × 0.53 cm) had the smallest defect area 4.70×10^3 μm^2 ($\pm$ 1.78 $\times 10^3$ μm^2) highlighting that the defect area estimation depends primarily on the growth rate rather than simply on the ROI size. Ultimately, the observed growth rate is critical for determining the defect area and understanding the overall defect landscape in the barrier film.

Regarding data fidelity, it is concerning that the coefficient of determination (R^2) is low for some defects, with values of 0.10 and 0.22, indicating poor linearity. However, other defects, like Defect #6, show higher R^2 values (0.76), suggesting a better fit. Despite these limitations, the estimations still provide insight into the growth rate, though they are not perfect. This variability is also reflected in the defect size standard deviations, which remain within a realistic range.

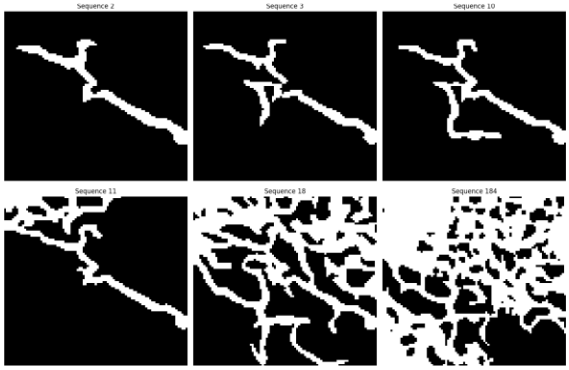
(a) 26 nm Thin PVAL (Betol)



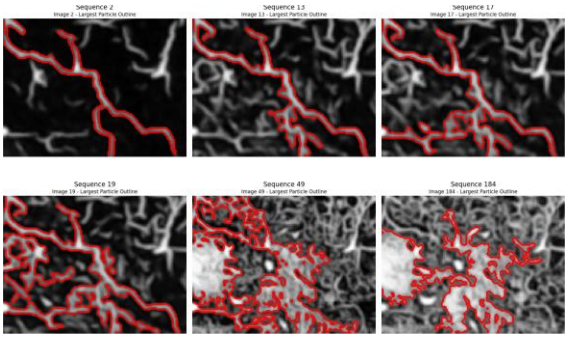
Defect #1 Outline



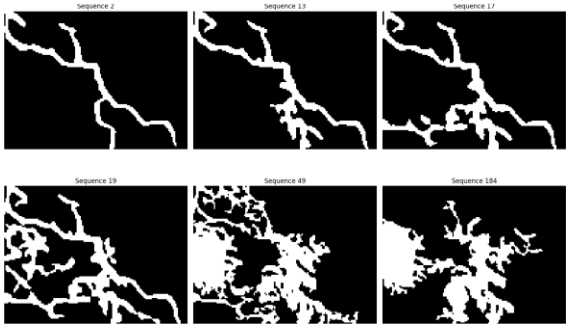
Defect #1 Isolated (Binary)



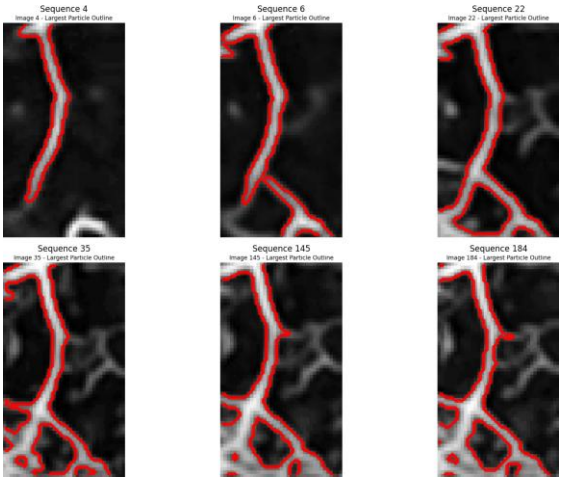
Defect #2 Outline



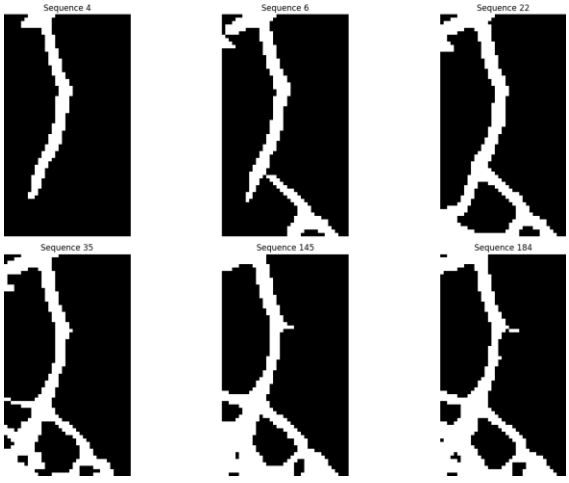
Defect #2 Isolated (Binary)



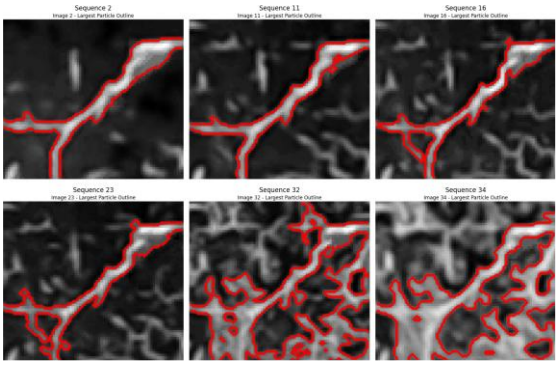
Defect #3 Outline



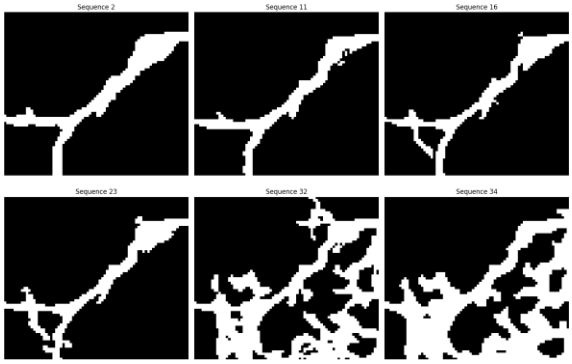
Defect #3 Isolated (Binary)



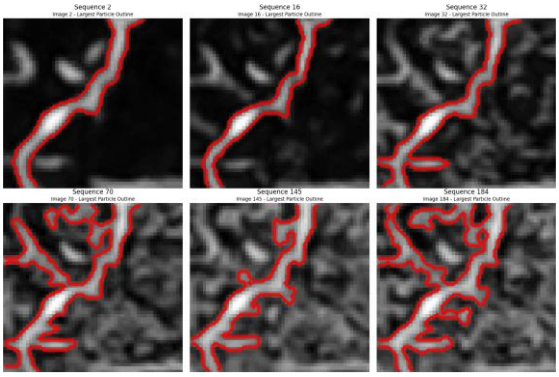
Defect #4 Outline



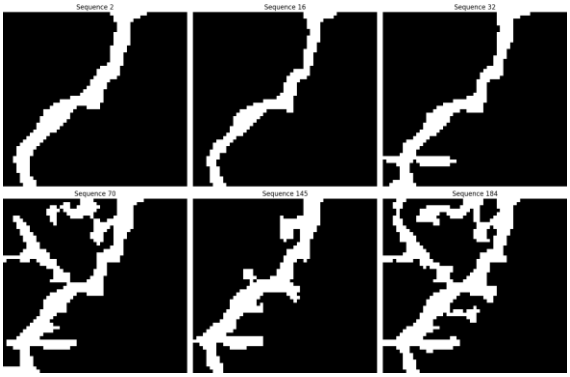
Defect #4 Isolated (Binary)



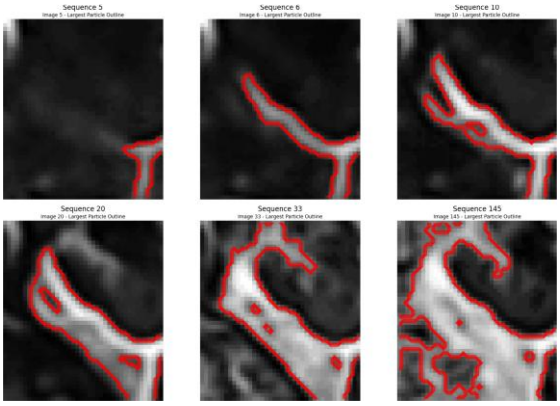
Defect #5 Outline



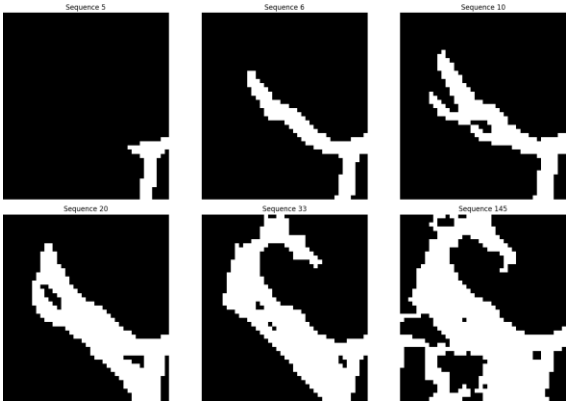
Defect #5 Isolated (Binary)

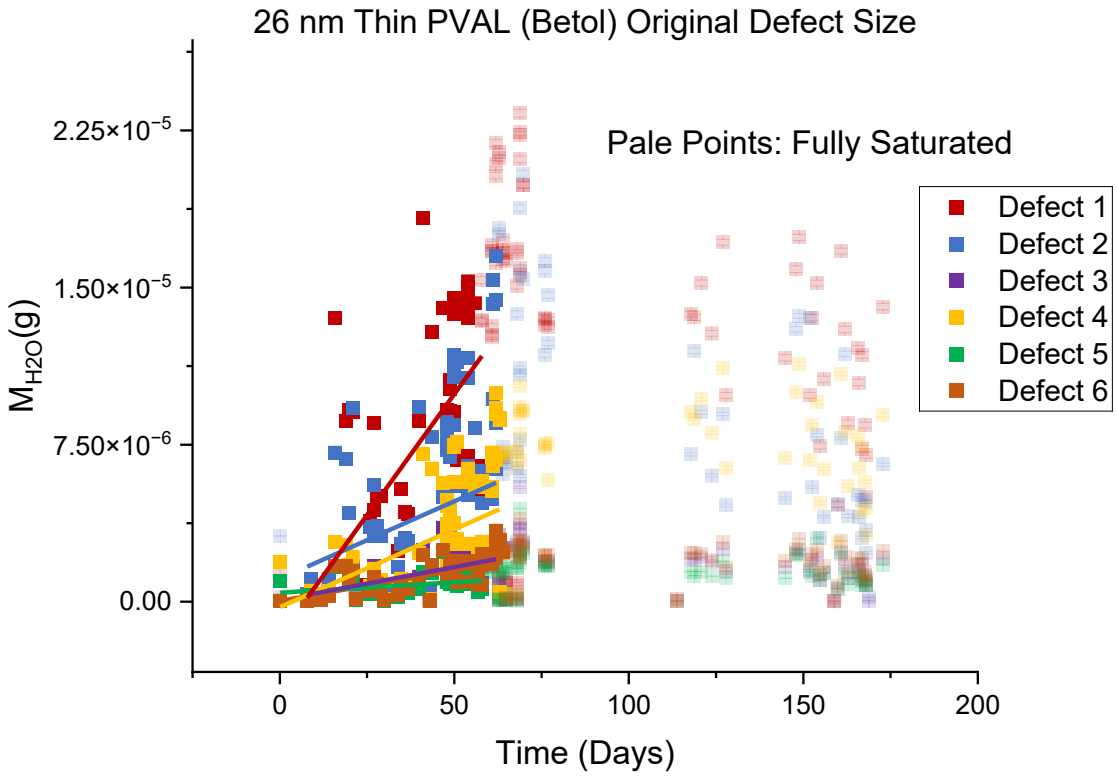


Defect #6 Outline



Defect #6 Isolated (Binary)





Defect	ROI Size (cm)	Slope (g/day)	Slope Std. Dev.	Adj. R. Squared	Defect Total Area (μm²)	Defect Area Std. Dev.
1	0.94 by 0.86	2.31E-07	2.25E-08	0.65	1.09E+05	1.08E+04
2	1.38 by 1.04	7.41E-08	1.64E-08	0.22	3.48E+04	7.73E+03
3	0.38 by 0.67	3.16E-08	4.42E-09	0.42	1.49E+04	2.09E+03
4	0.78 by 0.69	7.43E-08	1.08E-08	0.38	3.49E+04	5.11E+03
5	0.57 by 0.53	1.00E-08	3.79E-09	0.10	4.70E+03	1.78E+03
6	0.41 by 0.46	2.89E-08	1.71E-09	0.79	1.36E+04	8.84E+02

Figure 5-17: Six selected regions of interest from a 26 nm AlO_x ALD-coated thin PVAl substrate, with surrounding outlines and binary image montages, highlighting the dominant defect in each region. These largest defects were chosen to minimize errors from coalescing or interfering features and provide consistent water uptake rate

estimations. The water uptake rate (slope of the grey value change over time) is calculated for each defect, and the corresponding defect area is determined, revealing typical sizes ranging from approximately $4.70 \times 10^3\ \mu m^2\ (\pm\ 1.09\ \times 10^5\ \mu m^2)$. *Despite variation in region sizes, the defect area depends more strongly on growth rate than absolute region size. Variability in fit (R^2 values from 0.10 to 0.79) reflects differences in defect growth behaviour and image fidelity.*

5.7.3 Summary of Defect Size and Area

Figure 5-18, compares estimated defect areas (μm^2) for every PVAl substrate / coating combination. Across all 40 regions of interest, defect areas span nearly six orders of magnitude, from ~1.6×10^3 μm^2 for the smallest considered isolated spot on thin 96 nm PVAl to ~4.2×10^5 μm^2 for the largest dendritic feature on thin 50 nm PVAl. While individual values scatter within this envelope, three observations emerge.

- **Coating Thickness Effect:** Moving from 26 nm to 50 nm AlO_x on thin PVAl, the initially tested region for the latter showed significantly higher defect size estimates. To assess whether this was representative, additional regions of interest were analysed (detailed data presented in 9.4.10.a 50 nm Thin PVAl Substrate Defects). These broader measurements revealed that the 50 nm sample's defect sizes were more consistent with other coating thicknesses, suggesting the originally sampled region may have been an outlier or a locally severe area. However, the outlier region was retained in the dataset to transparently illustrate the stochastic nature of barrier failure. In thin film encapsulation, a localized cluster of large defects often dominates the total WVTR. At 96 nm where linear river features dominate and the median area falls in the mid- 10^4 μm^2 range, occasional macro-defects (*e.g.*, Spot 1 on thick PVAl having a higher estimate at ~1.18×10^5 μm^2) still appear.

- **Substrate-thickness effect:** For every coating thickness, thin (~21 μm) and thick (~42 μm) PVAl substrates show overlapping defect area distributions, indicating that substrate thickness may exert less overall influence and control towards the final defect size. This lack of effect provides some insight towards the failure mechanism of the barrier layer. As previously discussed Leterrier *et al*, and Howells *et al.*, these brittle inorganic coatings on top a relatively soft and flexible PVAl fracture easily. This means that since PVAl which is highly hygroscopic upon exposure to moisture it undergoes significant swelling (exceed 10% expansion) will make the brittle ALD AlO_x possibly crack or fracture [219, 220, 307, 351]. As known both substrate thicknesses generate swelling strains that exceed the critical fracture limit of the brittle AlO_x layer. Because the threshold for fracture is surpassed in both cases, increasing the substrate bulk does not mitigate the damage. The defect formation is therefore governed by fundamental mechanical mismatch between the swelling PVAl polymer and the brittle AlO_x coating, rather than possible macroscopic thickness of the substrate.
- **Morphology:** linking bright features in the Ca test to the morphology as done in 5.5.2 Coated AlO_x Thin and Thick PVAl, supports an interpretation that mid – 10^4 μm^2 defects correspond to linear or dendritic features. It shows that defects of the sizes estimated can be visible as the modal, or most common, defect size is around ~1,600 μm^2 (edge length of around ~40 μm) – showing that these defect features should be visible in the microscopy images.

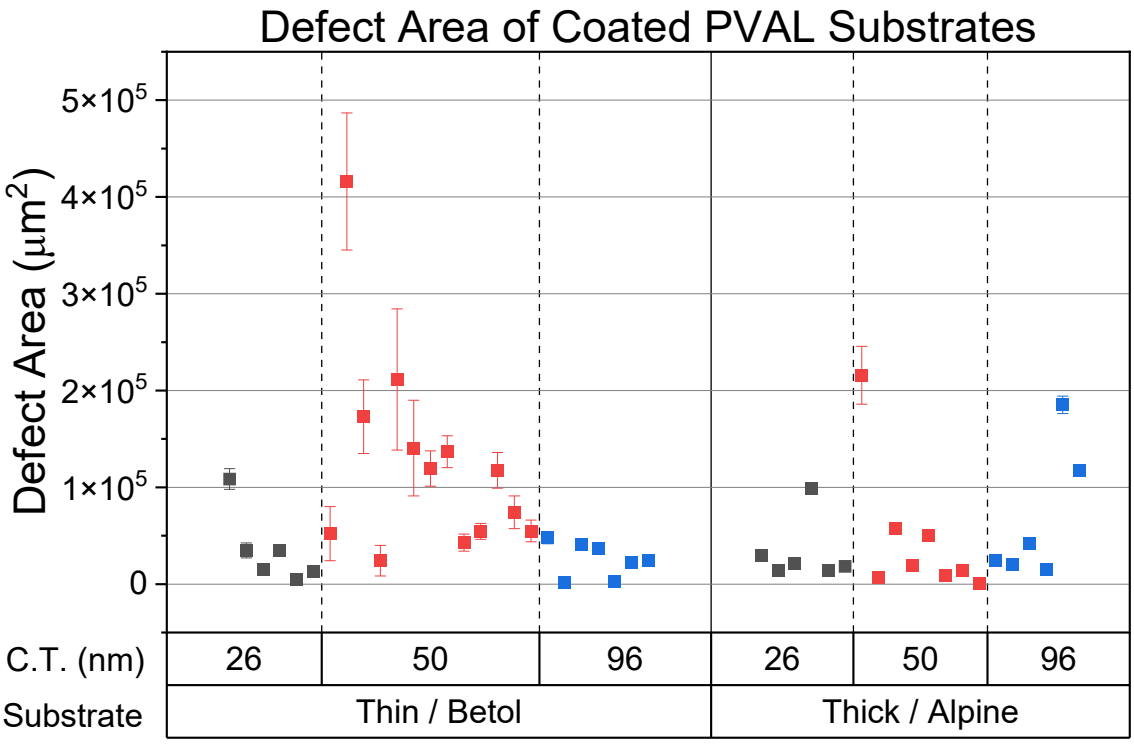


Figure 5-18: Grouped scatter plot comparing estimated defect areas (µm²) for thin and thick PVAl substrates with varying AlO_x coating thicknesses (26 nm, 50 nm and 96 nm). Defect areas span nearly six orders of magnitude, from the smallest isolated spot (~1.6 × 10^3 µm² in thin 96 nm PVAl) to the largest dendritic feature (~4.2 × 10^5 µm² in thin 50 nm PVAl). Data points are coloured by substrate and coating thickness, with error bars reflecting the standard deviation of area estimates.

5.8 Total Defect Area Calculation of PVAl

The next phase of analysis relates average defect area to WVTR or permeability, like the estimations done in the PET. The PVAl total defect area can also be estimated by Equation 4-8, where the total defect area is the product of the spot density and average defect size.

Using the information from the WVTR measurements done in section 9.4.6.b Measuring ALD AlO_x Coated Thin and Thick PVAl Calcium Test (conducted at 25°C, RH: ~78.5%). Results showed that permeation was primarily defect-driven, as increasing coating thickness did not consistently improve performance. On thick PVAl, for example,

the 26 nm coating had a notably lower WVTR than the 50 nm and 96 nm coatings. Ca test images revealed linear or fracture like permeation features, contrasting with the pinholes seen in PET-based samples. Based on this Figure 5-19 plots WVTR predictions against the total detected defect area for each condition.

The general trend shows that higher total defect areas correspond to increased WVTR, consistent with observations in coated PET samples (4.8.1 Total Defect Area Index). However, there are some deviations particularly for the 96 nm (thin and thick) and 50 nm thin PVAl samples, uncertainties in the defect density and size estimations may introduce errors. These discrepancies highlight the challenges of fully capturing the complex interplay between total defect area estimation and overall barrier performance. Nonetheless, the observed trend reinforces the concept of defect driven permeation in coated PVAl films.

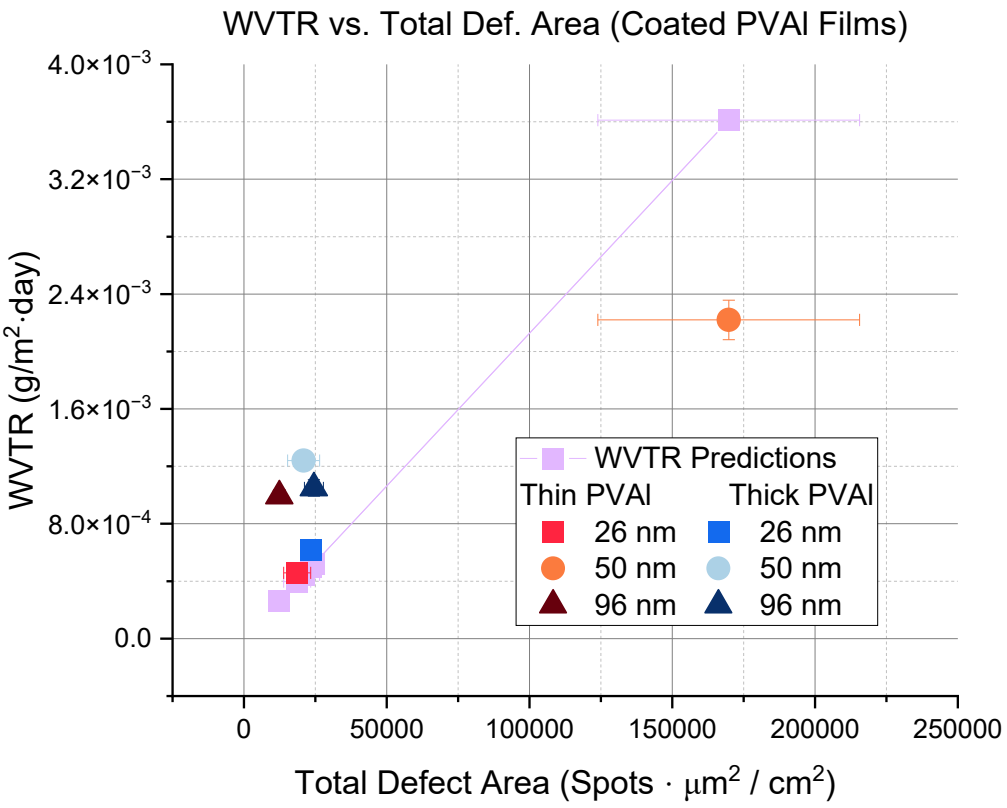


Figure 5-19: The WVTR plotted against total defect area for coated PVAl films, illustrating the general trend that larger defect areas lead to increased permeation rates. Despite some deviations (notably in the 96 nm thin and thick PVAl, and 50 nm thin PVAl samples), the data supports a defect driven permeation mechanism consistent with findings in coated PET substrates.

Examining the same case but now in permeability over total defect area (Figure 5-20), confirms that an increase or decrease in total defect area correlates directly with overall permeability. However, there is a notable deviation in the coated thick PVAl samples, where permeability appears higher than expected based on its corresponding defect areas. This discrepancy could stem from several factors: errors in defect area estimation (*e.g.*, misinterpretation of binarized images and defect size estimations), or inaccuracies in WVTR determination (potentially from the chosen transition region). Despite these deviations, the overall data trend reinforces the conclusion that defect

driven permeation is a key mechanism in coated PVAl films, larger defect areas result in higher permeabilities, while smaller defect areas correlate with better barrier performance.

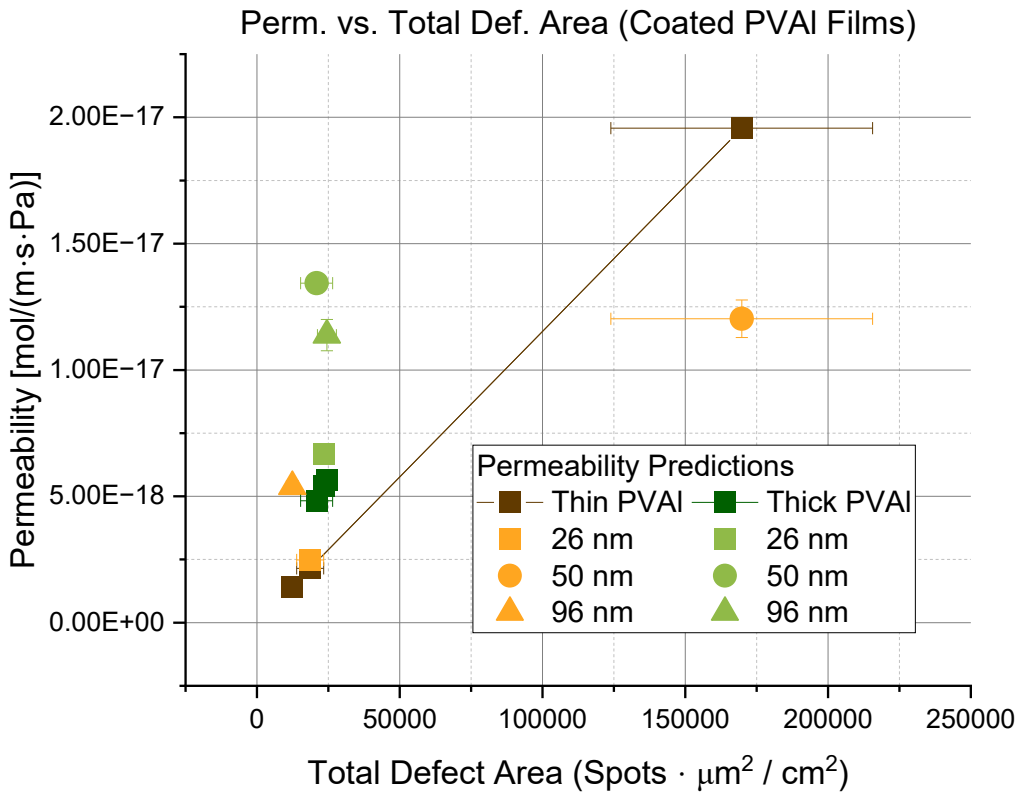


Figure 5-20: Permeability plotted against total defect area for coated PVAl films of two varying substrate thicknesses and AlO_x coating thicknesses. The trend underscores a defect drive permeation mechanism where larger defect areas yield higher permeability, while lower defect areas result in reduced permeation. Although some discrepancies exist (notably in thick PVAl samples), the overall pattern remains clear across the data range.

Overall, it is demonstrated that applying an ALD AlO_x coating improves barrier properties, and that between the linear permeation features that develop, the Ca remains quite dark, suggesting that the coating can provide a good barrier. However, the defect structures, that are possibly developing as the substrate changes shape locally as it absorbs water, greatly limits the barrier properties of the coating. Further enhancement

will depend on reducing this defect density, or reducing the propensity for defects to develop. As known, multilayer dyads Al_2O_3 /SiO_x and multilayer structures can limit the distortion of the coating and can decouple the effect of defects form one layer to the next. Hirvikorpi's study showed significant improvement in water vapor barrier properties by adding a non-toxic polyelectrolyte multilayer (PEM) film, composed of sodium alginate and chitosan, alongside an ALD Al_2O_3 layer on a PLA substrate. This multilayer setup achieved better results than ALD AlO_x or Al_2O_3 alone, likely due to surface morphology changes from the PEM intermediate layer. Results include PLA: 53 ± 4 g/m²·day, PLA + PEM: 106 ± 7 g/m²·day, PLA + 25 nm Al_2O_3: 33 ± 6 g/m²·day, PLA + PEM + 25 nm Al_2O_3: 25 ± 9 g/m²·day, though PEM's benefit may be overstated given the high standard deviations [369]. This suggests that further improvements towards barrier layers may require more than a single layer.

5.9 Conclusions and Insights AlO_x (ALD) Coated PVAl

This chapter explored how ALD AlO_x coatings can transform biodegradable PVAl into a reliable moisture barrier. Two types of PVAl: thin PVAl (Betol) and thick PVAl (Alpine) were evaluated to see if thin coatings could reliably reduce WVTR. Impressively, even the thinnest coatings ~26 nm improve moisture resistance dramatically, with some achieving performance on par with coated PET films.

A key outcome of the study is that defect driven permeation, not simply coating or substrate thickness controls the overall barrier performance. Contrary to a simplistic model in which thicker layers inherently provide better barrier properties, this work shows that performance is not monotonic with thickness in these defect-controlled

systems. While thicker coatings were anecdotally easier to handle, this does not consistently translate to lower WVTR or permeability. Instead, the overall integrity and defect landscape of the coating particularly the total defect area provided to be a dominant factor. Surface analysis reveals that distinct defect patterns evolve with coating thickness, from isolated lines at thinner coatings to interconnected networks at thicker ones.

The findings also highlight how PVAl's inherent roughness and swelling tendency may influence defect evolution in the AlO_x layer. Although no nanoscale cracks were directly observed, the gradual greying seen in the AlO_x coated thick PVAl substrate samples during the Ca test may indicate subtle moisture ingress through distributed microdefects or intrinsic imperfections in the coating. These features were not well captured by MOCON measurements, but became evident in the Ca test, which aided by visual inspected provided a more detailed view of defect driven permeation behaviour.

The practical implications of these results are that coating quality is paramount in achieving low permeability, controlling and reducing defects and preventing crack propagation will improve overall barrier properties. This suggests that improving surface preparation to create a smoother, more planarized PVAl substrate would be a critical step in reducing defect formation in the subsequent barrier layer and hybrid or layered approaches will be necessary to manage the mechanical and swelling mismatch between PVAl and brittle ceramic layer.

Future work should focus on refining surface treatments and ALD processes to produce ultra-low defect densities and sizes to provide resilient barriers. While AlO_x – ALD coatings demonstrate promise in enhancing moisture resistance in the PVAl films,

the performance still hinges on defect control rather than adding thickness, and its future may lie in interface improvements and further advanced coating strategies.

6 Methodological Uncertainty and Limitations

6.1 Introduction

This chapter precedes the conclusion in order to make a critical evaluation of the experimental methodologies employed in this work, identifying specific sources of error and uncertainty that directly influence the results of the barrier performance data. While the previous chapters have established the efficacy of ALD coatings in reducing WVTR and defect driven permeation within these systems, a more rigorous and thorough assessment is required to differentiate or decouple possible intrinsic material properties from extrinsic experimental errors and artifacts that arise during sample preparation and measurement.

This discussion addresses the inherent limitations of the Ca test protocol, that include environmental contamination and edge permeation, and the inability of the Ca test to be used on opaque films or structures. Additionally, uncertainties associated with low temperature ALD growth on polymer substrates as discussed by Groner *et al.* are also reiterated here [55, 217, 218, 322]. It also will touch on theoretical frame work to describe permeation kinetics, clarifying the thermodynamic basis for the observed negative energies. This chapter defines the boundaries of reliability for the experimental data, distinguishing between the concrete conclusions and those that remain indicative.

6.2 Critical Evaluation of Material Synthesis and Deposition Fidelity

This section delves into the assumptions made with the overall ALD process described in 2.5 ALD Parameters and the thickness verification data presented in 9.3.3

ALD AlO_x Thickness (Ellipsometer). While standard deposition parameters were employed, a rigorous retrospective analysis reveals specific uncertainties regarding stoichiometric purity and substrate dependent nucleation that directly affects the interpretation of the barrier performances reported in main Chapters: 4 Aluminium Oxide - AlO_x (ALD) Coated PET and 5 Aluminium Oxide (ALD) Coated PVAl.

6.2.1 Stoichiometry and Structural Limitations of Low Temperature Alumina

As known the self-limiting nature of ALD theoretically yields a precise film via alternating surface half-reactions. However, kinetic limitations at temperatures below 200 °C often prevent the complete removal of methyl ligands and surface hydroxyls during the purge cycle. Heil *et al.*, demonstrate that ligand exchange mechanisms are highly temperature-dependent, although their work focuses on plasma assisted ALD, the principle that reduced thermal activation impedes ligand removal might also be expected to apply to a thermal ALD deposition [397].

In terms of stoichiometry, Kim *et al.*, report that films grown at low temperatures (<100 °C) deviate significantly from the ideal Al:O ratio of 2:3. Their work showed that O/Al ratios increasing to ≈ 2.0 for ozone based processes, and as high as 2.3 for water-based processes at 100 °C, attributing the latter to the insufficient purging of surface-adsorbed water [398]. Comparatively, Groner *et al.*, reports O/Al ratios for thermal ALD typically in the range of 1.35 (oxygen deficiency) to 1.70 across a 33 °C to 177 °C window. Crucially, these ratios were achieved in a viscous flow reactor using extended purge times (up to 180 seconds for water at 33 °C) to strictly enforce self-limiting ALD growth. This variability underscores that film stoichiometry is not intrinsic but is also highly sensitive to the specific purging efficiency and kinetics of the deposition reactor.

This incomplete ligand exchange has profound structural implications and consequences towards the density and hydrogen content and thus impact the barrier density. Groner *et al.*, established that ALD alumina density drops linearly with deposition temperature, falling from ~ 3.0 g/cm^3 at 177 °C to as low as 2.5 g/cm^3 at 33 °C. This reduction is not merely a packing inefficiency but is also directly correlated with the incorporation of unreacted hydrogen. Forward recoil spectrometry data from the same study confirms that hydrogen content increases inversely with temperature, reaching > 20 atomic percentage at deposition temperature near 33 °C [322].

Recent X-ray scattering and Pair Distribution Function analysis by Pugliese *et al.*, confirms that low temperature ALD alumina lacks long range order. The local structure is more analogous to molten alumina, dominated by 4- and 5- coordinate aluminium species rather than the stable 6- coordinate species found in α-alumina [399].

Light element impurities like hydrogen, introduces a specific uncertainty regarding the intrinsic permeability of the barrier. The hydration and lower density (2.5 g/cm^3 vs 3.9 g/cm^3 for bulk sapphire) effectively increase the free volume of the lattice. Therefore, the WVTR values reported in this thesis likely reflect permeation through a looser, hydrogen rich amorphous network rather than intrinsic diffusion through a dense ceramic lattice [400].

Throughout the study, the barrier layers are nominally defined as Aluminium Oxide (AlO_x). A distinction between AlOx (unspecified stoichiometry) and to Al_2O_3 where the latter's nomenclature, standard for the TMA and water process described in 2.5 ALD Parameters, implies a stoichiometric purity and crystallinity. However at a low temperature window (80°C to 150°C) for deposition, as is utilised in this work; it is said

to be kinetically restricted such that a preference for using AlO_x would be more accurate than Al_2O_3. This is particularly evident at the lower deposition temperature such as 80°C which will typically yield a non-crystalline AlO_x [322], which may influence the barrier properties of the AlO_x on the PVAl films.

6.2.2 Nucleation Delay and Substrate Dependent Growth

A significant methodological constraint identified 9.3.3 ALD AlO_x Thickness (Ellipsometer) is the reliance on Si witness samples to estimate the thickness of coatings on polymer substrates. A retrospective analysis of the ellipsometry data in Figure 9-9 reveals that at low cycle counts (63 cycles) the measured thickness on silicon deviated from the expected linear trend by 61.82%. This discrepancy is attributed to the dependence of the refractive index on film density during the initial nucleation stages. As mentioned by Puurunen and Groner *et al.*, ALD growth on non-ideal surfaces often begins with an island-growth (Volmer-Weber) regime where the film is initially discontinuous and porous [176, 322]. Because the standard Cauchy model used in this study assumes a dense film with a constant RI, the fit returns a systematically biased thickness estimate for the transient nucleation phase.

This finding is critical when transferred to polymer substrates such as PET and PVAl. Unlike silicon's native oxide, these polymers lack a dense, uniform field of reactive hydroxyl groups, leading to a significant physical nucleation delay or latency. On these polymer surfaces, the TMA molecules may initially diffuse into the polymer subsurface, a soak in effect or react only with sparse functional groups further delaying the formation of a closed surface film [322].

Consequently, the 10 nm nominal thickness assigned to samples throughout this thesis including the data in Sections: 4.2 AlO_x on PET – MOCON Aquatran, 4.3 AlO_x on PET (ALD) – Ca Test and 5.4 Evaluating WVTR of PVAl Using Ca Test, represents the growth potential on an ideal witness surface rather than the actual morphology on the polymer. In reality, these coatings were likely thinner and discontinuous, as a true barrier layer is only established once isolated clusters grow large enough to merge into a pinhole-free sheet. This systematic overestimation explains the anomalously high WVTR and low activation energies consistently observed for the thinnest samples in various test methods [400].

6.2.3 Extrinsic Defect Sources and Process Control Variability

A rigorous analysis of the WVTR data in Chapter 5 (*e.g.* Figure 5-4) reveals a high degree of scatter or variability between samples, even those produced under identical conditions, this builds up on error analysis 5.4.2 Overall Barrier Measurements of Coated PVAl (Ca Test). While ALD is chemically reproducible, the deficiencies in controlling growth as argued can be stochastic (random) extrinsic factors rather than a failure of the ALD chemistry. To ensure consistency, the primary or intrinsic contributors (arise from polymers or the mismatch between polymer and coating system), and secondary stochastic contributors (handling and reactor history) should be considered.

1. Particulate Contamination (Shadowing Mechanism): The dominant cause of defect variability in this study is said to be the presence of particulates like micron-scale dust or anti-block particles on the substrate surface; as confirmed by SEM analysis in Section 5.5.1 Uncoated / Bare Thin PVAl and Thick PVAl, in the absence of a cleanroom environment or an automated

load-lock system ambient dust can settle on the polymer prior to or during the loading phase, introducing the particulates that constitute as defects.

- Panjan *et al.*, mentions that a particle resting on the surface acts as a physical mask during deposition [401]. Even in conformal ALD, a particle blocks the precursor from reaching the substrate surface directly underneath its contact point, creating a localized shadow or defect where no film nucleates.
- During the Ca test observation the samples were heated to around 50°C for some cases. A significant mismatch of the coefficient of thermal expansion between the polymer substrate, brittle alumina coating, and dust particle can create possible interfacial stresses. This stress may dislodge loosely adhered particles, removing the alumina and exposing an uncoated pinhole underneath. This is supported by Zhang *et al.*, who attribute the persistence of pinhole defects in ultra-thin ALD films to similar substrate surface contamination mechanisms [344]. The AlOx has a CTE: 7.2 – 10.3 (10^{-6} / °C), PET: 20 – 80 (10^{-6} / °C), and PVAl: 70 – 100 (10^{-6} / °C), showing a significant mismatch between AlO_x and the polymer substrate that induces high thermal stresses that will lead to buckling and cracking of AlO_x during thermal cycling [402-405].
- Because of the stochastic nature and randomness of dust particles, one sample might have no large particles (high performing barrier layer), while another sample would have more or a lot of large

particles (low performing barrier layer). This would explain how coating thickness is independent with barrier performance, such that a single large dust for example at a thick 50 or 96 nm film can easily compromise its barrier properties while a 26 nm film without any dust particles can have better barrier properties or lower WVTR. Barrow and Dickey, also experimentally demonstrate this sensitivity, showing ALD barrier layers on flexible substrates exhibit this exact performance loose with the density of substrate defects and particles [406, 407].

2. Reactor Conditioning (Memory Effects or Reactor Cleanliness): A secondary source of variation comes from the manual loading protocol and methodology described in 2.5 ALD Parameters. Opening the reactor chamber to the humid laboratory atmosphere (despite being in a clean room environment) between runs can introduce possible unwanted contaminants like moisture or particles to the chamber walls.
    - It is known that adsorbed background moisture may act as a parasitic reactant during the first few cycles of the next ALD run or process, altering the partial pressure of precursors that reach the substrate. Van Ommen and Goulas note that reactor consistency and reproducibility rely heavily in controlling these background interactions, as adsorbed species directly influence nucleation behaviour [408]. This can lead to unquantified variable in the early

stage of film density contributing to performance differences between batches.

The variability in barrier performance is also limited by a mixture of intrinsic and extrinsic process control (cleanliness) of the material. Future works need to control and prioritize contact cleaning of substrates and steps that mitigate particulates like the use of load locked reactors to possibly reduce these extrinsic errors from the true material performance. Material compatibility also needs to be further considered and how it matches with the intended coating process and method.

6.2.4 Clarification on Negative Activation Energy

The temperature-dependent data presented in Chapter 3 Uncoated Polyethylene Terephthalate (PET) Substrates, Chapter 4 Aluminium Oxide - AlOx (ALD) Coated PET and 5 Aluminium Oxide (ALD) Coated PVAl require a reinterpretation of the negative activation energy values. In strict kinetic theory, a negative energy is not physically meaningful. Therefore, these values should be treated as negative apparent activation energies extracted from the Arrhenius-type fits over a limited temperature window, rather than as intrinsic material parameters.

In the context of polymer permeation, the apparent activation energy reflects the combined temperature dependence of both diffusion and sorption processes, consistent with the solution-diffusion model discussion (Section: 1.4 Background on Permeation Theory), where $P = D \cdot S$ (Equation 1-6). In many polymers, diffusion coefficient increases with temperature, whereas the equilibrium solubility coefficient for water can decrease with temperature because sorption is often exothermic (water uptake is thermodynamically favoured at lower temperature). When the temperature driven

decrease in solubility coefficient outweighs the increase in diffusion coefficient, the net permeability can decrease with increasing temperature; producing a negative apparent activation energy from an Arrhenius-style fit.

For uncoated PET, the negative apparent energy indicates that over the tested temperature range (14 to 50 °C), the temperature dependence of water solubility in PET dominates the net temperature dependence of permeability. This is consistent with PET sorption literature showing that the solubility coefficient decreases sharply with temperature and that dissolution is strongly exothermic (negative enthalpy of dissolution) [234, 282]. Distinctively, it is interpreted as negative temperature coefficient of permeability or negative apparent activation energy and not a negative kinetic barrier.

Furthermore, the application of linear Arrhenius fits represents an idealisation that may not fully capture the transport in hygroscopic polymer substrates, particularly PVAl. Two dynamic factors are especially relevant: (1) water plasticisation and concentration dependence, where water acts as a plasticizer causing the diffusion coefficient to depend on both temperature and water concentration rather than remaining constant [285, 378]; (2) methodological effects during ex-situ Ca testing, where intermittent sample removal for imaging and re-introduction to the test environment can introduce temperature excursions and handling variability. For coated samples, this may also change stress states in the brittle oxide layer and potentially alter defect pathways, contributing to non-linear deviations from ideal Arrhenius behaviour.

Consequently, as reiterated here, the activation energies reported in this work should be viewed as effective temperature coefficients for the specific environmental window tested, rather than static material constants.

6.3 Calcium Test Methodology Analysis

6.3.1 Calcium Film Purity and Deposition Artefacts

The reliability (precision and accuracy) of the Ca test is based on the assumption that the sensor layer is pure, where metallic calcium that reacts instantly and uniformly with incoming water vapor. However, a critical evaluation of the experimental protocols in 2.4.4 Calcium Deposition Caveats and Contamination. Identifies two specific sources of contamination: (1) storage conditions of the Ca source pellets and the (2) configuration of the thermal evaporator.

Despite being placed with desiccants and low moisture box or environment, the pellet surface still reacted with residual atmospheric moisture. Ca source pellets arguably should have been stored in an inert glove box environment instead. Cros *et al.*, demonstrated using ion beam analysis that Ca surfaces degrade rapidly even upon brief exposure to ambient moisture forming a skin of Calcium Hydroxide ($Ca(OH)_2$) and oxide [107].

Moreover, in the aged but reliable Edwards 306 thermal evaporator used in the study without a proper load lock system, this surface contamination becomes even more evident and presents a specific problem. When the source boat is heated, the surface oxide/hydroxide layer is often the first material to evaporate. Although a shutter was used to define the deposition time, if the source was not sufficiently “soaked” (held at high heat with the shutter closed to burn off impurities) prior to deposition, this initial contaminated fraction would be deposited onto the barrier substrate first.

This deposition may have created a pre-oxidized or dead layer at the interface between the barrier coating and the bulk Ca sensor. If a continuous or near-continuous calcium oxide (CaO) layer were deposited below the metallic Ca, this would introduce the following errors in the measurement of permeation:

- Lag Time Extension (Artefact): Physically there might be a slight lag time extension (hard to fully quantify), because water vapor permeating through the barrier must diffuse through this dead layer before it reaches the fresh reactive metallic calcium. This effect may be further exacerbated by non-uniform Ca thickness during the early stages of deposition. Literature notes that oxidation kinetics of Ca films are highly sensitive to surface conditions [202]. A native passivation layer can introduce a non-linear incubation period or lag time. But because diffusivity was not calculated from lag time in this work, this does not affect the WVTR approximations or the barrier performance analysis.
- Steady State WVTR (Robustness): An important observation as shown in 3.4.3.b Other Factors that Influence Onset Time (Ca and Cu layer) and Figure 3-7 that this contamination does not invalidate the steady state WVTR. Once the water vapor breaches the dead layer and establishes a reaction front, the rate of Ca consumption is limited only by the flux of water arriving through the barrier film. Therefore, while the start time of the signal may be delayed (an artifact), the linear depletion slope used to calculate the WVTR remains valid and reliable measure of the intrinsic barrier performance.

Recognizing this limitation, the analysis in Chapter 4 Aluminium Oxide - AlO_x (ALD) Coated PET, prioritizes the steady state slope WVTR over lag time based

diffusion calculations; where the scatter observed in the onset times of uncoated PET samples likely reflect the variable thickness of this initial oxide layer (due to differences in pellet condition or soak times) and possible deposited Ca thickness, rather than intrinsic variability in PET substrate itself. While this initial surface contamination introduces a measurable lag for highly permeable films (where the test duration is short), its relative impact is negligible for ultra-low WVTR ALD barriers, in these high performance systems the measurement timescale is governed by the limiting flux through the barrier coating, rendering the brief initial artefact insignificant relative to the total observation period. However future protocols must mandate an extended pre-soak of the Ca source behind a closed shutter to sublime any surface oxides before exposing the sample.

6.3.2 UV Induced Substrate Degradation during Epoxy Encapsulation

A critical methodological constraint in the sample preparation protocol described in Section: 2.4.3 Calcium Test Set-up is the exposure of polymer substrates to high intensity ultraviolet radiation during the curing of the epoxy sealant. As detailed in Section 9.1.3.d Cleanliness Protocol and Epoxy Curing Time, the encapsulation process requires exposing the sample to a 250W UV source for approximately 5 minutes to cure the ELC-2500 epoxy. While essential for sealing the Ca sensor, this exposure presents a risk of photo-oxidative degradation for both PET and PVAl substrates, potentially altering the barrier interface or mechanical integrity of the film.

Although the exposure duration is relatively short as noted, the intensity of the curing lamp can accelerate degradation mechanisms that typically require prolonged ambient weathering.

- Polyethylene Terephthalate (PET): Research by Rostampour *et al.*, shows that PET is highly sensitive to UV radiation. The light energy breaks the chemical bonds (specifically the ester linkages) in the polymer backbone (chain scission) [409]. This reaction creates unstable atoms (free radicals) that react oxygen, ultimately shortening the polymer chains at the surface [409, 410]. Falkenstein *et al.*, demonstrate that this damage makes the surface brittle and changes its texture. If this brittleness occurs right where the barrier coating sits, it could cause the coating to peel or lift (delaminate). This could create a sideways path for water to leak in, causing the test to report a falsely high WVTR [410].
- Polyvinyl Alcohol (PVAl): PVAl is also vulnerable but degrades in a different way. Vijayalakshmi and Madras report that UV light breaks the main polymer chains and disrupts the material's internal structure [411]. This damage often leads to crosslinking, where the molecular chains stiffen and link together abnormally. The result is often visible yellowing and a loss of flexibility. Sri Aprilia *et al.*, confirm that UV exposure makes PVAl significantly weaker and more likely to snap when stretched [412]. For a flexible electronic substrate or barrier layer substrate, this is critical such that a brittle sample makes it more prone to cracking and creates defects in the fragile barrier coating.

The samples in this study did not show obvious signs of damage (like severe yellowing), but invisible chemical changes could still affect the results. To confirm whether this would happen in future work, one can use various material characterisations to determine any possible damage:

1. Chemical Check (Spectroscopy): A non-destructive method like FTIR can be used to identify whether the 5-minute UV cure chemically altered the polymer substrates. FTIR can be used to assess the molecular fingerprint of the substrate, detecting the chemical bond breakage before visible damage may occur.
    - PET: As detailed by Rostampour *et al.*, UV induced degradation leaves a specific spectral signature. The ester bond cleavage (chain scission) causes the peak at 1713 cm^{-1} (C=O stretching) to decrease, while a new peak typically emerges or grows around 1685 cm^{-1}, indicating the formation of carboxylic acid end groups from the broken chains [409]. Comparing the ratio for these peaks before and after the 5-minute cure provides a definitive chemical check for damage.
    - PVAl: The degradation mechanism involves chain scission and crosslinking. Sri Aprilia *et al.*, used FTIR to track the intensity changes in the broad hydroxyl (-OH) band at 3350 cm^{-1}, which reflects the changes in hydrogen bonding network due to UV exposure [412]. While no new peaks were observed in the specific timeframe, in the work by Vijaylakshmi and Madras confirm that extensive photodegradation leads to the formation of carbonyl groups, detectable as new peaks. It may be possible to monitor the hydroxyl band and checking for any emerging carbonyl peaks

(around 1710 – 1735 cm^{-1}) would signal that UV dose may have chemically altered the substrates structure [411].

- PET/PVAl (UV-Vis / XPS as complementary checks): While FTIR can identify changes in functional groups, it may primarily be sensitive to relatively pronounced bond changes and may not detect subtle early stage oxidation or surface limited modifications. Complementary techniques like UV-Vis (for yellowing / optical adsorption changes) and/or XPS (for surface oxidation and new chemical states, where an increase O/C ratio and new carbonyl or oxidized carbon components would be key indicators of change). These additional techniques should also be considered.

2. Mechanical Verification (Tensile Testing): These chemical changes often lead to physical embrittlement; a mechanical test can confirm if the substrate's integrity has been compromised.
    - Dummy samples of uncoated PET or PVAl, can be exposed to the UV – light (5 minutes or more) typical for the UV curing cycle in this experiment, and then subjected to a standard tensile test until failure. Then one can use elongation at break to determine if any difference occurs by comparing the un-exposed and exposed UV substrate.
    - PET: UV induced chain scission should shorten the polymer chains, drastically reducing the material's ability to stretch. A drop in elongation should be observed if UV light damages the substrate, confirming embrittlement.

- PVAl: UV exposure causes crosslinking and chain stiffening. Sri Aprilia *et al.*, showed that UV exposure can significantly also reduce the elongation at break, making the material significantly more brittle and prone to micro-cracking [412]. If the UV-exposed PVAl snaps sooner than the unexposed control; it can be an indicator the curing process has compromised the overall mechanical flexibility of the PVAl substrate.

6.3.3 Assumptions in WVTR Estimation (Stoichiometry and Chemical Specificity)

The calculation of WVTR presented in Section 2.4.5 Measuring WVTR, Permeability and Activation Energy relies on the stoichiometric assumption that the metallic Ca sensor reacts exclusively and completely with permeating water vapor to form $Ca(OH)_2$, as defined in Reaction 1-1. While this reaction model is the standard for optical and electrical Ca tests, a critical assessment of the chemical specificity reveals two potential sources of uncertainty regarding the reaction species.

(1) The question on if Ca also reacts with oxygen, as it can leak through the barrier and consume some of the Ca sensor ($2Ca + O_2 \rightarrow 2CaO$) is a potential problem. The calculation assumes that all Ca loss is caused by water, if oxygen is also reacting the calculated WVTR would be overestimated because the test cannot distinguish between Ca lost to water versus Ca lost to oxygen. However, Cros *et al*, showed that using isotope labelling that at room temperature, Ca reacts almost exclusively with water vapor and has little or negligible reactivity with dry oxygen – confirming that a standard lab environment where the Ca consumption is driven by moisture making the

water-based calculation valid [107]. This is also supported and cited in the Introduction: “oxygen at room temperature does not react with metallic calcium” [11, 14, 85, 107].

(2) Secondly, on whether the reaction always forms a hydroxide is also an assumption, such that the whole reaction with water is always $Ca(OH)_2$. In dry conditions it is theoretically possible for the reaction to stop at Calcium Oxide (CaO), which consumes only one water molecule per calcium atom instead of two. If this reaction stops at CaO, the amount of water permeating would be overstated by a factor of 2. However, Higgs *et al.*, confirms that when there is a continuous supply of water vapor (Ca test box, or in high humidity testing conditions especially 85 to 90% RH used in the thesis), the final stable product is indeed $Ca(OH)_2$. Thus, assuming that the hydroxide form is chemically correct for these accelerated aging tests. One may also argue that even if side reactions of CaO formation or O_2 reaction did occur, these would both lead to an overestimation of the WVTR. Signifying, that the values reported in the study are conservative upper bounds and that the actual barrier performance of the substrate or ALD films are likely better than what is calculated.

6.3.4 Effect Ex-Situ Observation (Intermittent Measurement) in Ca Test

A unique limitation of the optical Ca test used in this study specifically for the ALD coated barrier layers are the significantly long time frames – more than one year (4 Aluminium Oxide - AlO_x (ALD) Coated PET and 5 Aluminium Oxide (ALD) Coated PVAl), making it impractical to continuously monitor them with the limited resources. At

the same time, the ability to store samples in a controlled oven environment and perform year-long tests represents a strength of the method for evaluating very high performance barriers, as such extended durations would not typically be feasible in a standard MOCON configuration. As explained in section 2.4.3 Calcium Test Set-up, the samples classified as high barrier or good barriers had to be physically removed from the controlled oven environment to be imaged or scanned. Unlike the continuous electrical Ca test or standard MOCON measurement that monitor permeation without disturbing the sample, this method introduces a slight stop and start or discontinuity, despite small relative to the entire time frame it is still a case for discussion.

Every time the sample was taken out of the test chamber and placed onto the viewing dock or ambient lab environment (~20 °C / ~40% RH) for imaging. This abrupt change alters the water concentration gradient across the film and temporarily disrupts the steady-state diffusion profile within the barrier. In particular, the sudden drop in external humidity can induce transient desorption from the polymer and modify the internal water concentration distribution before steady-state conditions are re-established upon return to the chamber. As argued by MOCON Inc., a critical source of error in manual gravimetric testing (ASTM E96), is removing samples from the controlled environment disrupts the steady state equilibrium and causes transient fluctuations [413]. By analogy, the manual handling in this optical Ca test introduces similar desorption artefacts that are absent in automated systems, such as the *in-situ* method for bad barriers.

The rapid cooling between the room and chamber may cause the plastic substrate to shrink faster than the brittle oxide coating (especially possible in PVAl due to the larger thermal expansion coefficient compared to AlO_x). This mismatch can create stress,

even though the scanning or imaging takes less than 5 minutes, this constant cycling could theoretically cause micro-cracks in the coating and create defects that wouldn't exist in a steady, undisturbed test. Moreover, this suggests that the reported WVTR values may again be slightly higher or worse than the true steady state performance.

Despite this drawback, removing the samples was necessary to get the high-resolution images of defect growth. As Nisato *et al.*, and Louch *et al.*, reiterates that while electrical tests are more sensitive and continuous, the true value is in the defect imaging and the crucial information of how the barrier fails (*e.g.*, distinguishing pinholes from edge leaks and characterizing overall barrier failure), that bulk electrical data misses or in standard MOCON instrument [414, 415]. This can also be mitigated by having dedicated resources or cameras where one can observe *in-situ* despite being less economical it does directly alleviate and solve the problem as done in this works poor barrier Ca test set-up. Klumbies *et al.*, notes that the optical tests are also less prone to bottleneck artifacts that can skew electrical measurements of localized defects [416]. The fact that the Ca depletion curves (e.g Figure 9-16) remain linear suggests that the barrier recovered quickly or any possible effects are minimal after each scan and did not suffer any catastrophic failure from thermal shock.

The WVTR values especially for the ALD results are considered to reflect barriers performance under conditions that include periodic thermal cycling.

6.4 Future Strategies for Defect Characterization

This work identified that dust particles and nucleation issues as some likely causes of barrier inconsistency (6.2 Critical Evaluation of Material Synthesis and Deposition

Fidelity), but these were largely inferred from indirect permeation data. To move from guessing and measuring, future work could expand beyond Ca test imaging or the micrographs from Optical microscope, SEM or Profilometry.

(1) Visualizing defects can also be done with fluorescent tags, as known optical microscope often cannot resolve nanoscale pinholes or cracks in transparent ALD films, (*i.e.* Abbe diffraction limit of 400 – 700 nm). Zhang *et al.*, resolved this by applying a fluorescent tag or glowing dye to the surface of ALD coated polymers. The dye preferentially accumulates in the surface-accessible cracks or pinholes and washes off smooth, intact coated areas. Under a fluorescence microscope, the defects light up as bright spots against a dark background. This method was able to image defects as small as ~200 nm in 25 nm thick Al_2O_3 films [417]. This would provide a spatial map of defect density (defects/cm^2) on the barrier layer, allowing correlation of defect populations with the observed variability in WVTR, although fluorescence contrast alone does not confirm that the detected features are through thickness permeation pathways.

(2) Electrochemical defect detection can also be conducted to investigate the island growth and nucleation issues (6.2.2 Nucleation Delay and Substrate Dependent Growth), require a conductive substrate. Electrical methods offer higher sensitivity than the optical ones. Copper plating or defect decoration by Zhang *et al.*, showed that one can use an ALD coated substrate as an electrode in a copper solution, the copper highlights these faint and invisible defects [344]. Electrochemical Impedance Spectroscopy

(EIS) is also another possible option, Perrotta *et al.*, show that EIS is highly sensitive to both nano porosity (tiny voids between islands) and macro defects (pinholes). This technique could possibly distinguish between water vapour passing through few big holes versus water soaked through the generally porous film, helping to identify if the 10 nm films failed due to dust or poor nucleation [418].

(3) Conductive Atomic Force Microscopy (C-AFM) done by Panjan *et al.*, highlighted how growth defects can often start at the nanoscale. C-AFM scan on the surface of an ALD barrier layer with an atomic scale conductive tip can map out electrical current, which would reveal if the barrier is truly continuous or if it leaks at the edges of possible defects or islands formed during nucleation, proving supporting evidence on the growth mechanisms [401].

Adopting these direct visualization techniques would transform the analysis of how much a barrier leaks to further understanding exactly where and why it fails. By isolating extrinsic dust defects from intrinsic nucleation limits, this also provides a feedback loop needed to engineer a truly defect free encapsulation method or barrier layer.

7 Conclusion

Advancements in the application of flexible electronics using water-sensitive materials have been largely constrained by the water vapor barrier limitations of protective layers. This study employs a novel defect imaging calcium test (Ca test) with a copper backing layer to explore and characterize defects that act as permeation pathways, potentially leading to device failure. Methodological groundwork was established by comparing estimated WVTR from the Ca test with conventional values from the Mocon Aquatran 2, using a standard PET substrate. After validating the Ca test with uncoated PET samples, the study addressed inconsistencies in WVTR measurements by calculating permeability coefficients and apparent activation energies were derived. It was determined that negative apparent activation energy values reflect a solubility dominated transport mechanism (characteristic of the bare substrate), whereas positive values indicate a diffusion dominated regime (characteristic of effective barrier layers).

This work utilized ALD to deposit AlO_x coatings on PET substrates, demonstrating a significant enhancement in water vapor barrier properties and, revealing optimal coating thickness and process parameters, though the resultant barriers are still below the stringent requirements for flexible electronics. Spatial density and defect analyses provided insights into spot density and defect size across varying coating thicknesses on PET, clarifying limitations in achieving ultra-low WVTR. Although the ALD coating reduced the proportion of water vapor permeation through intrinsic nano defects compared to RF magnetron-sputtered films, extrinsic macro defects, likely due to contamination, inclusions, or coating damage, continued to impact overall barrier effectiveness.

The thesis also investigates ALD-coated PVAl substrates to enhance the barrier properties of biodegradable materials with rough surfaces. The ALD coating was able to improve barrier performance, but this study provided valuable insights into the defect structures observable from the localised permeation of water. Notably, thinner AlO_x (26 nm) showed very promising low permeabilities, despite linear defects and sizes (low total defect area estimations), contrasting with the higher spot-like defects in ALD-coated PET substrates. Extensive coding and spot identification analyses, with broader applications beyond defect identification, were conducted.

An important result found in this study is the relationship between total defect area of coated substrate and corresponding predictions which show a directly proportional relationship showing that, indeed, permeation is defect driven in coated barrier layers. This study has shown a way to estimate total defect area through the calcium test using a mixture of defect density and size estimations.

This work advances the field of flexible electronics by enhancing the understanding of permeation mechanisms through use of the imaging Ca test, improving its fidelity, and using statistical analysis and coding to obtain spatial density information in coated PET and PVAl substrates. It provides a strong foundation for future research on alternative barrier layers, coating methods, substrates, and multi-layer structures that require ultra-low water vapor permeation rates.

7.1 Future work and Recommendations

The thesis demonstrates strong potential in establishing a reliable basis for the defect calcium imaging test, validating it against the Mocon Aquatran (industry

standard). However, further work is needed to improve the process, particularly in environmental control (temperature and humidity within the calcium test box), data capture quality, and *in-situ* observations (minimizing fogging, alignment issues, and lighting inconsistencies) where these compounding effects can directly affect the WVTR estimations (and consequently permeability calculations). Further improvements, in image calibration and noise reduction, through consistent use of the calibration bar were found to help reduce variability in WVTR estimation. While earlier analyses, literature and studies remain valuable, incorporating these enhancements can increase confidence in the accuracy and consistency of the measured WVTR. Additionally, obtaining a more accurate verification that the 145 nm calcium layer corresponding to the threshold at which the film becomes fully opaque under the specific light source and imaging set-up would improve reliability of thickness to opacity correlation used in the analysis. Optimizing Ca test sample preparation can also reduce contamination and further minimize compounded errors, improving overall test robustness.

Testing a broader range of materials to confirm observed trends and activation energy estimates against literature values would also be an interesting extension.

For ALD coating optimization, exploring processing temperatures and conditions could further enhance barrier quality. While the spot analysis and detection algorithm were effective, image quality was a limiting factor; continuous *in-situ* observation could have mitigated this. Additionally, refining spot detection for each individual image would enhance precision.

Testing alternative biodegradable materials, particularly those that are less hydrophilic, could help overcome a key limitation in current studies. In addition,

increasing the number of repeat measurements for the same materials would improve statistical significance and reduce variability in observed trends.

Exploring a broader range of PVAl thicknesses, especially substrates of comparable thickness to the PET studied here may also bring a new perspective to the analysis, as these samples could be more comparable and exhibit different barrier behaviours while being generally easier to handle. This would further aid in refining comparisons across materials and support more reliable interpretation of the results.

Further work on integrating the encapsulation layers with device testing and consideration of multilayer encapsulations is recommended to advance research in flexible electronics. Specifically, inorganic nanolaminates (AlO_x / Al_2O_3 / SiO_x) can interrupt defect percolation pathways between adjacent layers, *i.e.*, increasing tortuosity, and balance residual stress. Along with better advancements in total defect area detection with machine learning, this would also be overall beneficial to improving the performance and lifetime of these moisture sensitive devices.

8 Bibliography

[1] D. Siegel, S. Shivakumar, The Flexible Electronics Opportunity, National Academy of Sciences (The National Academic Press), Washington, District of Columbia, 2014.

[2] D.X.H.a.D.K.G. Raghu Das, Flexible, Printed and Organic Electronics 2019-2029: Forecasts, Players & Opportunities. https://www.idtechex.com/en/research-report/flexible-printed-and-organic-electronics-2019-2029-forecasts-players-and-opportunities/639.

[3] M.R.P. Ltd, Flexible Electronics & Circuit Market with COVID-19 Impact Analysis by Structure Type (Single Sided Flex Circuit, Multilayer Flex Circuit), Application (Displays, Printed Sensors), Vertical (Consumer Electronics), and Geography - Global Forecast to 2026, 2021. https://www.marketsandmarkets.com/Market-Reports/flexible-electronics-market-50634885.html.

[4] S.W. Ruchal Humbare, Vineet Kumar, lexible Electronics Market By Component (Flexible Display [OLED, E-paper, and LCD], Flexible Battery, Flexible Sensor [Bio Sensors, CMOS Hybrid Sensors, Photo Detectors, Piezo Resistive, and Others], Flexible Memory, and Flexible Photovoltaics) and Application (Consumer Electronics, Automotive, Medical & Healthcare, Energy & Power, Aerospace & Defense, and Others): Global Opportunity Analysis and Industry Forecast, 2020–2027, 2020. https://www.alliedmarketresearch.com/flexible-electronics-market.

[5] R.a. Markets, Global Flexible Display Market Report 2019-2025 - Samsung Electronics and LG are the Market's Forerunners, 2020. https://www.prnewswire.com/news-releases/global-flexible-display-market-report-2019-2025---samsung-electronics-and-lg-are-the-markets-forerunners-300991429.html.

[6] W.S. Wong, A. Salleo, Flexible electronics: materials and applications, Springer Science & Business Media2009.

[7] S.R. Forrest, The path to ubiquitous and low-cost organic electronic appliances on plastic, Nature 428(6986) (2004) 911–918.

[8] B.A. Morris, The science and technology of flexible packaging: multilayer films from resin and process to end use, William Andrew2016.

[9] M.B. Tucker, Some mechanics challenges and solutions in flexible electronics, 2009.

[10] H. Ardebili, J. Zhang, M.M. Pecht, Encapsulation technologies for electronic applications, William Andrew2018.

[11] V. Tobin, Roll-to-roll deposition of highly flexible organic-inorganic barrier layers for printed electronics and photovoltaics, University of Oxford, 2018.

[12] J. Lewis, Material challenge for flexible organic devices, Materials today 9(4) (2006) 38–45.

[13] G.L. Graff, R.E. Williford, P.E. Burrows, Mechanisms of vapor permeation through multilayer barrier films: Lag time versus equilibrium permeation, Journal of Applied Physics 96(4) (2004) 1840–1849.

[14] A.G. Erlat, M. Yan, A.R. Duggal, Substrates and thin-film barrier technology for flexible electronics, Flexible Electronics, Springer2009, pp. 413–449.

[15] F. So, D. Kondakov, Degradation mechanisms in small-molecule and polymer organic light-emitting diodes, Advanced Materials 22(34) (2010) 3762–3777.

[16] C.J. Brabec, J.A. Hauch, P. Schilinsky, C. Waldauf, Production aspects of organic photovoltaics and their impact on the commercialization of devices, MRS bulletin 30(1) (2005) 50–52.

[17] S. Li, L. Lan, M. Li, Z. Gao, X. Yan, D. Fu, X. Sun, Thin-Film Encapsulation for OLEDs and Its Advances: Toward Engineering, Materials 18(13) (2025) 3175.

[18] Y. Jeon, H. Lee, H. Kim, J.-H. Kwon, A review of various attempts on multi-functional encapsulation technologies for the reliability of OLEDs, Micromachines 13(9) (2022) 1478.

[19] G. Wang, Y. Duan, Efforts of implementing ultra-flexible thin-film encapsulation for optoelectronic devices based on atomic layer deposition technology, SmartMat 5(6) (2024) e1286.

[20] B.-H. Kwon, C.W. Joo, H. Cho, C.-m. Kang, J.-H. Yang, J.-W. Shin, G.H. Kim, S. Choi, S. Nam, K. Kim, Organic/inorganic hybrid thin-film encapsulation using inkjet printing and PEALD for industrial large-area process suitability and flexible OLED application, ACS Applied Materials & Interfaces 13(46) (2021) 55391–55402.

[21] G.V. Research, Flexible Electronics Market (2023 - 2030), 2023. https://www.grandviewresearch.com/industry-analysis/flexible-electronics-market.

[22] A.M. Research, Flexible Electronics Market, by Application (Consumer Electronics, Automotive, Medical and Healthcare, Energy and Power, Aerospace and Defense, Others), by Component (Flexible display, Flexible battery, Flexible sensors, Flexible memory, Flexible photovoltaics): Global Opportunity Analysis and Industry Forecast, 2022 - 2032, 2024. https://www.alliedmarketresearch.com/flexible-electronics-market.

[23] D.B.M. Research, Global Flexible Electronics Market – Industry Trends and Forecast to 2030, 2023. https://www.databridgemarketresearch.com/reports/global-flexible-electronics-market.

[24] A.M. Research, Potting compound Market Expected to Reach $4.1 Billion by 2027, 2020. https://www.alliedmarketresearch.com/potting-compounds-

market#:~:text=The%20global%20potting%20compound%20market,3.9%25%20from%202020%20to%202027.

[25] J. Fahlteich, M. Fahland, W. Schönberger, N. Schiller, Permeation barrier properties of thin oxide films on flexible polymer substrates, Thin solid films 517(10) (2009) 3075–3080.

[26] H. Li, Y. Ma, Y. Huang, Material innovation and mechanics design for substrates and encapsulation of flexible electronics: a review, Materials Horizons (2020).

[27] P.E. Burrows, G.L. Graff, M.E. Gross, P.M. Martin, M.-K. Shi, M. Hall, E. Mast, C. Bonham, W. Bennett, M.B. Sullivan, Ultra barrier flexible substrates for flat panel displays, Displays 22(2) (2001) 65–69.

[28] M. Yan, T.W. Kim, A.G. Erlat, M. Pellow, D.F. Foust, J. Liu, M. Schaepkens, C.M. Heller, P.A. Mcconnelee, T.P. Feist, A transparent, high barrier, and high heat substrate for organic electronics, Proceedings of the IEEE 93(8) (2005) 1468–1477.

[29] T. Kinkeldei, N. Munzenrieder, C. Zysset, K. Cherenack, G. Tröster, Encapsulation for Flexible Electronic Devices, IEEE - Electron Device Letters, Vol. 32 No. 12, (2011) 1743 – 1745.

[30] G. Nisato, H. Klumbies, J. Fahlteich, L. Müller-Meskamp, P. van de Weijer, P. Bouten, C. Boeffel, D. Leunberger, W. Graehlert, S. Edge, Experimental comparison of high-performance water vapor permeation measurement methods, Organic Electronics 15(12) (2014) 3746–3755.

[31] S.-W. Seo, E. Jung, C. Lim, H. Chae, S.M. Cho, Water permeation through organic–inorganic multilayer thin films, Thin Solid Films 520(21) (2012) 6690–6694.

[32] C.Y. Park, J.S. An, H.J. Jang, J.H. Lee, B.H. Choi, Growth behavior and improved water–vapor-permeation-barrier properties of 10-nm-thick single Al2O3 layer grown via cyclic chemical vapor deposition on organic light-emitting diodes, Organic Electronics 15(8) (2014) 1717–1723.

[33] S.M. George, Atomic layer deposition: an overview, Chemical reviews 110(1) (2010) 111–131.

[34] U. Diebold, The surface science of titanium dioxide, Surface science reports 48(5-8) (2003) 53–229.

[35] L. Moro, N.M. Rutherford, R.J. Visser, J.A. Hauch, C. Klepek, P. Denk, P. Schilinsky, C.J. Brabec, Barix multilayer barrier technology for organic solar cells, Organic Photovoltaics VII, International Society for Optics and Photonics, 2006, p. 63340M.

[36] T. Ahmadzada, D.R. McKenzie, N.L. James, Y. Yin, Q. Li, Atomic layer deposition of Al2O3 and Al2O3/TiO2 barrier coatings to reduce the water vapour permeability of polyetheretherketone, Thin Solid Films 591 (2015) 131–136.

[37] M. Elrawemi, L. Blunt, L. Fleming, D. Bird, D. Robbins, F. Sweeney, Modelling water vapour permeability through atomic layer deposition coated photovoltaic barrier defects, Thin Solid Films 570 (2014) 101–106.

[38] J.I. Larruquert, Optical properties of thin film materials at short wavelengths, Optical Thin Films and Coatings, Elsevier2018, pp. 291–356.

[39] M. Lamberti, F. Escher, Aluminium foil as a food packaging material in comparison with other materials, Food Reviews International 23(4) (2007) 407–433.

[40] J. Kerry, Aluminium foil packaging, Packaging technology (2012) 163–177.

[41] M.D. Steven, J.H. Hotchkiss, Comparison of flat film to total package water vapour transmission rates for several commercial food wraps, Packaging Technology and Science: An International Journal 15(1) (2002) 17–27.

[42] P. Charlier, G. Sjöberg, Recycling of aluminum foil from post-consumer beverage cartons, Minerals, Metals and Materials Society, Warrendale, PA (United States), 1995.

[43] M. Gökelma, A. Vallejo-Olivares, G. Tranell, Characteristic properties and recyclability of the aluminium fraction of MSWI bottom ash, Waste Management 130 (2021) 65–73.

[44] T. Li, Z. Huang, Z. Suo, S.P. Lacour, S. Wagner, Stretchability of thin metal films on elastomer substrates, Applied physics letters 85(16) (2004) 3435–3437.

[45] D. Georgiou, S. Logothetidis, High-barrier films for flexible organic electronic devices, Handbook of Flexible Organic Electronics: Materials, Manufacturing and Applications (2014) 123.

[46] S. Castro-Hermosa, M. Top, J. Dagar, J. Fahlteich, T.M. Brown, Quantifying Performance of Permeation Barrier—Encapsulation Systems for Flexible and Glass-Based Electronics and Their Application to Perovskite Solar Cells, Advanced Electronic Materials 5(10) (2019) 1800978.

[47] J.S. Lewis, M.S. Weaver, Thin-film permeation-barrier technology for flexible organic light-emitting devices, IEEE Journal of selected topics in quantum electronics 10(1) (2004) 45–57.

[48] I.-C. Cheng, S. Wagner, Overview of flexible electronics technology, Flexible Electronics, Springer2009, pp. 1–28.

[49] M.D.J. Auch, O.K. Soo, G. Ewald, C. Soo-Jin, Ultrathin glass for flexible OLED application, Thin Solid Films 417(1-2) (2002) 47–50.

[50] P. Kofinas, R.E. Cohen, A.F. Halasa, Gas permeability of polyethylene/poly (ethylene-propylene) semicrystalline diblock copolymers, Polymer 35(6) (1994) 1229–1235.

[51] V. Siracusa, Food packaging permeability behaviour: A report, International Journal of Polymer Science 2012 (2012).

[52] S. Mrkić, K. Galić, M. Ivanković, S. Hamin, N. Ciković, Gas transport and thermal characterization of mono-and di-polyethylene films used for food packaging, Journal of applied polymer science 99(4) (2006) 1590–1599.

[53] P.S. Maydannik, T.O. Kääriäinen, K. Lahtinen, D.C. Cameron, M. Söderlund, P. Soininen, P. Johansson, J. Kuusipalo, L. Moro, X. Zeng, Roll-to-roll atomic layer deposition process for flexible electronics encapsulation applications, Journal of Vacuum Science & Technology A: Vacuum, Surfaces, and Films 32(5) (2014) 051603.

[54] S. Iwamori, Y. Gotoh, K. Moorthi, Characterization of silicon oxynitride gas barrier films, Vacuum 68(2) (2002) 113–117.

[55] P. Carcia, R. McLean, M. Groner, A. Dameron, S. George, Gas diffusion ultrabarriers on polymer substrates using Al 2 O 3 atomic layer deposition and SiN plasma-enhanced chemical vapor deposition, Journal of Applied Physics 106(2) (2009) 023533.

[56] S. Cho, K. Lee, A.J. Heeger, Extended Lifetime of Organic Field-Effect Transistors Encapsulated with Titanium Sub-Oxide as an 'Active'Passivation/Barrier Layer, Advanced materials 21(19) (2009) 1941–1944.

[57] H. Ye, H.-J. Kwon, X. Tang, D.Y. Lee, S. Nam, S.H. Kim, Direct Patterned Zinc-Tin-Oxide for Solution-Processed Thin-Film Transistors and Complementary Inverter through Electrohydrodynamic Jet Printing, Nanomaterials 10(7) (2020) 1304.

[58] D.-w. Choi, S.-J. Kim, J.H. Lee, K.-B. Chung, J.-S. Park, A study of thin film encapsulation on polymer substrate using low temperature hybrid ZnO/Al2O3 layers atomic layer deposition, Current Applied Physics 12 (2012) S19–S23.

[59] M.D. Kempe, M.O. Reese, A.A. Dameron, Evaluation of the sensitivity limits of water vapor transmission rate measurements using electrical calcium test, Review of Scientific Instruments 84(2) (2013) 025109.

[60] M. Klopffer, B. Flaconneche, Transport properties of gases in polymers: bibliographic review, Oil & Gas Science and Technology 56(3) (2001) 223–244.

[61] J.-S. Park, H. Chae, H.K. Chung, S.I. Lee, Thin film encapsulation for flexible AM-OLED: a review, Semiconductor science and technology 26(3) (2011) 034001.

[62] *E.G.* Jeong, J.H. Kwon, K.S. Kang, S.Y. Jeong, K.C. Choi, A review of highly reliable flexible encapsulation technologies towards rollable and foldable OLEDs, Journal of Information Display 21(1) (2020) 19–32.

[63] S. Logothetidis, Polymeric substrates and encapsulation for flexible electronics: bonding structure, surface modification and functional nanolayer growth, Rev. Adv. Mater. Sci 10(5) (2005) 387–397.

[64] W. Su, Encapsulation Technology for Organic Electronic Devices, Printed Electronics: Materials, Technologies and Applications (2016) 287.

[65] T.-H. Lee, J.-S. Kim, J.-H. Lee, H.-J. Kim, Pressure-Sensitive Adhesives for Flexible Display Applications, Hybrid Nanomaterials-Flexible Electronics Materials, IntechOpen2019.

[66] J.A. Hauch, P. Schilinsky, S.A. Choulis, S. Rajoelson, C.J. Brabec, The impact of water vapor transmission rate on the lifetime of flexible polymer solar cells, Applied Physics Letters 93(10) (2008).

[67] C. Lungenschmied, G. Dennler, G. Czeremuzskin, M. Latrèche, H. Neugebauer, N.S. Sariciftci, Flexible encapsulation for organic solar cells, Photonics for Solar Energy Systems, SPIE, 2006, pp. 258–265.

[68] M.-C. Choi, Y. Kim, C.-S. Ha, Polymers for flexible displays: From material selection to device applications, Progress in Polymer Science 33(6) (2008) 581–630.

[69] J.S. Limkaichong, Flexible Electronics Encapsulation in Thin Polyester Films, University of Massachusetts Lowell, 2020.

[70] I.A. Channa, A. Distler, C.J. Brabec, H.-J. Egelhaaf, Solution-coated barriers for organic electronics, Organic Flexible Electronics, Elsevier2021, pp. 249–303.

[71] L. Moro, R.J. Visser, Barrier films for photovoltaics applications, Organic Photovoltaics (2008) 491–510.

[72] D. Yu, Y.-Q. Yang, Z. Chen, Y. Tao, Y.-F. Liu, Recent progress on thin-film encapsulation technologies for organic electronic devices, Optics Communications 362 (2016) 43–49.

[73] M. Schaer, F. Nüesch, D. Berner, W. Leo, L. Zuppiroli, Water vapor and oxygen degradation mechanisms in organic light emitting diodes, Advanced Functional Materials 11(2) (2001) 116–121.

[74] J.H. Kwon, Y. Jeon, S. Choi, H. Kim, K.C. Choi, Synergistic gas diffusion multilayer architecture based on the nanolaminate and inorganic-organic hybrid organic layer, Journal of Information Display 19(3) (2018) 135–142.

[75] M.K. Tripp, C. Stampfer, D.C. Miller, T. Helbling, C.F. Herrmann, C. Hierold, K. Gall, S.M. George, V.M. Bright, The mechanical properties of atomic layer deposited alumina for use in micro-and nano-electromechanical systems, Sensors and Actuators A: Physical 130 (2006) 419–429.

[76] G. Krautheim, T. Hecht, S. Jakschik, U. Schröder, W. Zahn, Mechanical stress in ALD-Al2O3 films, Applied surface science 252(1) (2005) 200–204.

[77] V. Jambur, M. Molina-Ruiz, T. Dauer, D. Horton-Bailey, R. Vallery, D. Gidley, T. Metcalf, X. Liu, F. Hellman, I. Szlufarska, Temperature effects on the structure and mechanical properties of vapor deposited a-SiO2, Journal of Non-Crystalline Solids 587 (2022) 121588.

[78] A. Bulusu, A. Singh, C.-Y. Wang, A. Dindar, C. Fuentes-Hernandez, H. Kim, D. Cullen, B. Kippelen, S. Graham, Engineering the mechanical properties of ultrabarrier films grown by atomic layer deposition for the encapsulation of printed electronics, Journal of Applied Physics 118(8) (2015).

[79] M. Nasim, Y. Li, M. Wen, C. Wen, A review of high-strength nanolaminates and evaluation of their properties, Journal of materials science & technology 50 (2020) 215–244.

[80] A. Rückerl, R. Zeisel, M. Mandl, I. Costina, T. Schroeder, M.H. Zoellner, Characterization and prevention of humidity related degradation of atomic layer deposited Al2O3, Journal of Applied Physics 121(2) (2017).

[81] M. Gebhard, L. Mai, L. Banko, F. Mitschker, C. Hoppe, M. Jaritz, D. Kirchheim, C. Zekorn, T. de Los Arcos, D. Grochla, PEALD of SiO2 and Al2O3 thin films on polypropylene: investigations of the film growth at the interface, stress, and gas barrier properties of dyads, ACS applied materials & interfaces 10(8) (2018) 7422–7434.

[82] V. Chawla, M. Ruoho, M. Weber, A.A. Chaaya, A.A. Taylor, C. Charmette, P. Miele, M. Bechelany, J. Michler, I. Utke, Fracture mechanics and oxygen gas barrier properties of Al2O3/ZnO nanolaminates on PET deposited by atomic layer deposition, Nanomaterials 9(1) (2019) 88.

[83] J. Robertson, High dielectric constant gate oxides for metal oxide Si transistors, Reports on progress in Physics 69(2) (2006) 327–396.

[84] J. Fischer, Permeation and Measurement Techniques, in: M. Inc. (Ed.) PLACE Conference, St. Louis Missouri, 2007.

[85] M.D.K. Matthew O. Reese, Arrelaine A. Dameron, Calcium Test – Different test methods for WVTR on barriers, with an emphasis on ultrabarriers, sources of errors/irreproducibility, limits, etc. – basically why it's hard to do it right, in: N.R.E. Laboratory (Ed.) 2017.

[86] R. Paetzold, D. Henseler, K. Heuser, V. Cesari, W. Sarfert, G. Wittmann, A. Winnacker, High-sensitivity permeation measurements on flexible OLED substrates, Organic Light-Emitting Materials and Devices VII, International Society for Optics and Photonics, 2004, pp. 73–82.

[87] P. Burrows, V. Bulovic, S. Forrest, L.S. Sapochak, D. McCarty, M. Thompson, Reliability and degradation of organic light emitting devices, applied physics letters 65(23) (1994) 2922–2924.

[88] A. Fick, Ueber diffusion, Annalen der Physik 170(1) (1855) 59–86.

[89] W. Henry, III. Experiments on the quantity of gases absorbed by water, at different temperatures, and under different pressures, Philosophical Transactions of the Royal Society of London (93) (1803) 29–274.

[90] K. Vouilloz, Beginner's Guide to the Calcium Test, in: H. Assender (Ed.) University of Oxford, Oxford, 2019.

[91] A.A. Gokhale, I. Lee, Recent advances in the fabrication of nanostructured barrier films, Journal of nanoscience and nanotechnology 14(3) (2014) 2157–2177.

[92] G. Matsui, Characterisation of Gas Barrier Polymer Films, Materials, University of Oxford, Oxford, 2020, p. 98.

[93] C.S. Deng, H. Assender, F. Dinelli, O. Kolosov, G.A.D. Briggs, T. Miyamoto, Y. Tsukahara, Nucleation and growth of gas barrier aluminium oxide on surfaces of poly (ethylene terephthalate) and polypropylene: effects of the polymer surface properties, Journal of Polymer Science Part B: Polymer Physics 38(23) (2000) 3151–3162.

[94] C. Mo, W. Yuan, W. Lei, Y. Shijiu, Effects of temperature and humidity on the barrier properties of biaxially-oriented polypropylene and polyvinyl alcohol films, Journal of Applied Packaging Research 6(1) (2014) 5.

[95] Z. Zhang, I.J. Britt, M.A. Tung, Permeation of oxygen and water vapor through EVOH films as influenced by relative humidity, Journal of Applied Polymer Science 82(8) (2001) 1866–1872.

[96] Z. Song, H. Xiao, Y. Zhao, Hydrophobic-modified nano-cellulose fiber/PLA biodegradable composites for lowering water vapor transmission rate (WVTR) of paper, Carbohydrate polymers 111 (2014) 442–448.

[97] S. Iizuka, K. Murata, M. Sekine, C. Sato, A novel cup with a pressure-adjusting mechanism for high-temperature water vapor transmission rate measurements, Polymer Testing 50 (2016) 73–78.

[98] R.L. Kovács, L. Daróczi, P. Barkóczy, E. Baradács, E. Bakonyi, S. Kovács, Z. Erdélyi, Water vapor transmission properties of acrylic organic coatings, Journal of Coatings Technology and Research (2020) 1–12.

[99] M. Stevens, S. Tuomela, D. Mayer, Water vapor permeation testing of ultra-barriers: Limitations of current methods and advancements resulting in increased sensitivity, Society of Vacuum Coaters 48 th Annual Technical Conference Proceedings, 2005, pp. 189–191.

[100] B. Visweswaran, Encapsulation of organic light emitting diodes, Princeton University, 2014.

[101] P. Mandlik, A novel hybrid inorganic-organic single layer barrier for organic light-emitting diodes, Princeton University2009.

[102] A. Roberts, B. Henry, A. Sutton, C. Grovenor, G. Briggs, T. Miyamoto, M. Kano, Y. Tsukahara, M. Yanaka, Gas permeation in silicon-oxide/polymer (SiOx/PET) barrier films: role of the oxide lattice, nano-defects and macro-defects, Journal of Membrane Science 208(1-2) (2002) 75–88.

[103] H. Chatham, Oxygen diffusion barrier properties of transparent oxide coatings on polymeric substrates, Surface and Coatings Technology 78(1-3) (1996) 1–9.

[104] J. Felts, Thickness effects on thin film gas barriers: silicon-based coatings, Society of Vacuum Coaters, 34th Annual Technical Conference Proceedings, 1991, pp. 99–104.

[105] G. Nisato, P. Bouten, P. Slikkerveer, W. Bennett, G.L. Graff, N. Rutherford, L. Wiese, Evaluating high performance diffusion barriers: the calcium test, Proc. Int. Display Workshop/Asia Display, 2001.

[106] G. Nisato, M. Kuilder, P. Bouten, L. Moro, O. Philips, N. Rutherford, Society for information display, 2003 International Symposium, Digest of Technical Papers, 2003, p. 88.

[107] S. Cros, M. Firon, S. Lenfant, P. Trouslard, L. Beck, Study of thin calcium electrode degradation by ion beam analysis, Nuclear Instruments and Methods in Physics Research Section B: Beam Interactions with Materials and Atoms 251(1) (2006) 257–260.

[108] R. Paetzold, A. Winnacker, D. Henseler, V. Cesari, K. Heuser, Permeation rate measurements by electrical analysis of calcium corrosion, Review of Scientific Instruments 74(12) (2003) 5147–5150.

[109] H. Klumbies, L. Müller-Meskamp, T. Mönch, S. Schubert, K. Leo, The influence of laterally inhomogeneous corrosion on electrical and optical calcium moisture barrier characterization, Review of Scientific Instruments 84(2) (2013) 024103.

[110] S. Schubert, H. Klumbies, L. Müller-Meskamp, K. Leo, Electrical calcium test for moisture barrier evaluation for organic devices, Review of Scientific Instruments 82(9) (2011) 094101.

[111] A. Sim, Characterization of Gas Barrier Polymer Films, Materials, University of Oxford, Oxford, 2017, p. 85.

[112] H. Assender, Sim, Ashley, Tobin, Vincent, Water Vapour Permeation (EP3669168A1), European Patent Office, 2020.

[113] Z. Pan, M. Bora, R. Gee, R.H. Dauskardt, Water vapor transmission rate measurement for moisture barriers using infrared imaging, Materials Chemistry and Physics 308 (2023) 128289.

[114] H. Asgarimoghaddam, Q. Chen, F. Ye, A. Shahin, O.A.C. Marchione, B. Song, K.P. Musselman, Spatial atomic layer deposition of nitrogen-doped alumina thin films for high-performance perovskite solar cell encapsulation, Nano Energy 127 (2024) 109782.

[115] J. Lin, Metal oxide nanoparticles as carrier transport layer in perovskite solar cells application, HKU Theses Online (HKUTO) (2023).

[116] A. Roos, Water Vapour Permeation Testing of Ultra-Barriers: Limitations of Current Methods and Advancements Resulting in Increased Sensitivity, in: MOCON (Ed.) 2013.

[117] A.-. MOCON, A Comparison Of ASTM Test Standards F3299 vs. F1249, in: I.N.A. MOCON (Ed.) 2018.

[118] A.-. MOCON, Aquatran Model 3: Water Vapor Permeation Analyzer, MOCON Inc. , Minneapolis, Minnesota, 2020.

[119] A.-. MOCON, ASTM F3299 AMETEK MOCON Welcomes Another WVTR Standard Test Method to the Family, Ametek - MOCON, 2018.

[120] H. Norenberg, V. Burlakov, Recent developments in measuring permeation through barrier films and understanding of permeation processes, Society of Vacuum Coaters 47 th Annual Technical Conference Proceedings, 2004, pp. 164–167.

[121] D. Wang, J. Li, X. Wang, J. Li, Measurement of gas permeation through packaging materials of OLED by mass spectrometry, 5th International Symposium on Advanced Optical Manufacturing and Testing Technologies: Optoelectronic Materials and Devices for Detector, Imager, Display, and Energy Conversion Technology, International Society for Optics and Photonics, 2010, p. 76583T.

[122] R. Dunkel, R. Bujas, A. Klein, V. Horndt, A new method for measuring ultra-low water-vapor permeation for OLED displays, Journal of the Society for Information Display 13(7) (2005) 569–573.

[123] B.D. Vogt, H.-J. Lee, V.M. Prabhu, D.M. DeLongchamp, E.K. Lin, W.-l. Wu, S.K. Satija, X-ray and neutron reflectivity measurements of moisture transport through model multilayered barrier films for flexible displays, Journal of applied physics 97(11) (2005) 114509.

[124] P.M. Martin, Handbook of deposition technologies for films and coatings: science, applications and technology, William Andrew2009.

[125] R.F. Bunshah, D.M. Mattox, Applications of metallurgical coatings, Physics Today 33(5) (1980) 50–55.

[126] L. Quintino, Overview of coating technologies, Surface Modification by Solid State Processing, Elsevier2014, pp. 1–24.

[127] A. Bashir, T.I. Awan, A. Tehseen, M.B. Tahir, M. Ijaz, Chapter 3 - Interfaces and surfaces, in: T.I. Awan, A. Bashir, A. Tehseen (Eds.), Chemistry of Nanomaterials, Elsevier2020, pp. 51–87.

[128] D.M. Mattox, V. Mattox, Vacuum coating technology, Springer2003.

[129] J. Koskinen, Cathodic-arc and thermal-evaporation deposition, Reference Module in Materials Science and Materials Engineering, Elsevier Ltd.2014, p. 3—55.

[130] N. Hardy, What is Thin Film Deposition By Thermal Evaporation?, 2013. http://www.semicore.com/news/71-thin-film-deposition-thermal-evaporation. (Accessed April 20 2021 2021).

[131] R.J. Martín-Palma, A. Lakhtakia, Chapter 15 - Vapor-Deposition Techniques, in: A. Lakhtakia, R.J. Martín-Palma (Eds.), Engineered Biomimicry, Elsevier, Boston, 2013, p. 383—398.

[132] D. Depla, S. Mahieu, J.E. Greene, Chapter 5 - Sputter Deposition Processes, in: P.M. Martin (Ed.), Handbook of Deposition Technologies for Films and Coatings (Third Edition), William Andrew Publishing, Boston, 2010, pp. 253–296.

[133] J.E. Greene, Tracing the recorded history of thin-film sputter deposition: From the 1800s to 2017, Journal of Vacuum Science & Technology A: Vacuum, Surfaces, and Films 35(5) (2017) 05C204.

[134] D.M. Mattox, Chapter 4 - Physical Sputtering and Sputter Deposition, in: D.M. Mattox (Ed.), The Foundations of Vacuum Coating Technology (Second Edition), William Andrew Publishing2018, pp. 87–149.

[135] M. Dawber, 2 - Sputtering techniques for epitaxial growth of complex oxides, in: G. Koster, M. Huijben, G. Rijnders (Eds.), Epitaxial Growth of Complex Metal Oxides, Woodhead Publishing2015, pp. 31–45.

[136] M.M. Zagho, H.D. Dawoud, N. Bensalah, T.M. Altahtamouni, A brief overview of RF sputtering deposition of boron carbon nitride (BCN) thin films, Emergent Materials 2(1) (2019) 79–93.

[137] F. Lévy, Film Growth and Epitaxy: Methods, Reference Module in Materials Science and Materials Engineering, Elsevier2016.

[138] A. Zhou, 2 - Methods of MAX-phase synthesis and densification – II, in: I.M. Low (Ed.), Advances in Science and Technology of Mn+1AXn Phases, Woodhead Publishing2012, pp. 21–46.

[139] T.T. Nan Jokerst, Introduction to Sputter, in: D.U.-. SMIF (Ed.) Thin Film Deposition, YouTube, Durham, North Carolina, 2020, pp. https://www.youtube.com/watch?v=GgD6G3B–2WU&ab_channel=DukeUniversity–SMIFDukeUniversity–SMIF.

[140] I. Semicore Equipment, What Is PVD Sputtering?, 2013, p. https://www.youtube.com/watch?v=L6ZIkmIVm6c&t=66s&ab_channel=SemicoreEquipment.

[141] J.E. Greene, Tracing the recorded history of thin-film sputter deposition: From the 1800s to 2017, Journal of Vacuum Science & Technology A 35(5) (2017).

[142] S. Rossnagel, Thin film deposition with physical vapor deposition and related technologies, Journal of Vacuum Science & Technology A: Vacuum, Surfaces, and Films 21(5) (2003) S74–S87.

[143] A.H. Simon, Chapter 7 - Sputter Processing, in: K. Seshan, D. Schepis (Eds.), Handbook of Thin Film Deposition (Fourth Edition), William Andrew Publishing2018, pp. 195–230.

[144] A. Iles, N. Pamme, Sputtering for Film Deposition, in: D. Li (Ed.), Encyclopedia of Microfluidics and Nanofluidics, Springer US, Boston, MA, 2013, p. 1—9.

[145] I.V. Tudose, F. Comanescu, P. Pascariu, S. Bucur, L. Rusen, F. Iacomi, E. Koudoumas, M.P. Suchea, Chapter 2 - Chemical and physical methods for multifunctional nanostructured interface fabrication, in: V. Dinca, M.P. Suchea (Eds.), Functional Nanostructured Interfaces for Environmental and Biomedical Applications, Elsevier2019, p. 15—26.

[146] S.T. Mileiko, Chapter XI - Hot Pressing, in: S.T. Mileiko (Ed.), Composite Materials Series, Elsevier1997, p. 475—515.

[147] D. Vacuum, Weighing the Benefits of Sputtering vs. Evaporation, 2021. https://www.dentonvacuum.com/weighing-the-benefits-of-sputtering-vs-evaporation/.

[148] EESemi, Physical Vapor Deposition (PVD) by Sputtering, 2004. https://www.eesemi.com/sputtering.htm.

[149] A. Technologies, PHYSICAL VAPOR DEPOSITION – Sputtering vs. Electron Beam Evaporation, 2010. https://abrisatechnologies.com/2012/09/physical-vapor-deposition-sputtering-vs-electron-beam-evaporation/.

[150] A. Behera, P. Mallick, S.S. Mohapatra, Chapter 13 - Nanocoatings for anticorrosion: An introduction, in: S. Rajendran, T.A.N.H. Nguyen, S. Kakooei, M. Yeganeh, Y. Li (Eds.), Corrosion Protection at the Nanoscale, Elsevier2020, pp. 227–243.

[151] M.B. Tahir, M. Rafique, M.S. Rafique, T. Nawaz, M. Rizwan, M. Tanveer, Chapter 8 - Photocatalytic nanomaterials for degradation of organic pollutants and heavy metals, in: M.B. Tahir, M. Rafique, M.S. Rafique (Eds.), Nanotechnology and Photocatalysis for Environmental Applications, Elsevier2020, pp. 119–138.

[152] K.V. Madhuri, 10 - Thermal protection coatings of metal oxide powders, in: Y. Al-Douri (Ed.), Metal Oxide Powder Technologies, Elsevier2020, pp. 209–231.

[153] L. Xia, 2 - Importance of nanostructured surfaces, in: A. Osaka, R. Narayan (Eds.), Bioceramics, Elsevier2021, pp. 5–24.

[154] S. Barua, X. Geng, B. Chen, Chapter 3 - Graphene-based nanomaterials for healthcare applications, in: S.k. Choi (Ed.), Photonanotechnology for Therapeutics and Imaging, Elsevier2020, pp. 45–81.

[155] K. Choy, Chemical vapour deposition of coatings, Progress in materials science 48(2) (2003) 57–170.

[156] R. Wang, R. Ma, Kinetics of halide chemical vapor deposition of silicon carbide film, Journal of Crystal Growth 308(1) (2007) 189–197.

[157] J. Carlsson, P. Martin, Chemical vapor deposition Handbook of Deposition Technologies for Films and Coatings, Science, Technology and Applications (2010) 444–445.

[158] J.-H. Park, T. Sudarshan, Chemical vapor deposition, ASM international2001.

[159] A. Pattanaik, V. Sarin, Basic principles of CVD thermodynamics and kinetics, Chemical Vapor Deposition, ASM International2001, pp. 23–43.

[160] S.O. Mbam, S.E. Nwonu, O.A. Orelaja, U.S. Nwigwe, X.-F. Gou, Thin-film coating; historical evolution, conventional deposition technologies, stress-state micro/nano-level measurement/models and prospects projection: a critical review, Materials Research Express 6(12) (2019) 122001.

[161] L. Sun, G. Yuan, L. Gao, J. Yang, M. Chhowalla, M.H. Gharahcheshmeh, K.K. Gleason, Y.S. Choi, B.H. Hong, Z. Liu, Chemical vapour deposition, Nature Reviews Methods Primers 1(1) (2021) 5.

[162] W. Bryant, The fundamentals of chemical vapour deposition, Journal of Materials science 12(7) (1977) 1285–1306.

[163] H.O. Pierson, Handbook of chemical vapor deposition: principles, technology and applications, William Andrew1999.

[164] I. Sayago, E. Hontañón, M. Aleixandre, 9 - Preparation of tin oxide nanostructures by chemical vapor deposition, in: M.O. Orlandi (Ed.), Tin Oxide Materials, Elsevier2020, pp. 247–280.

[165] J. Creighton, P. Ho, Introduction to chemical vapor deposition (CVD), Chemical vapor deposition 2 (2001) 1–22.

[166] Y.B. Pottathara, Y. Grohens, V. Kokol, N. Kalarikkal, S. Thomas, Chapter 1 - Synthesis and Processing of Emerging Two-Dimensional Nanomaterials, in: Y. Beeran Pottathara, S. Thomas, N. Kalarikkal, Y. Grohens, V. Kokol (Eds.), Nanomaterials Synthesis, Elsevier2019, pp. 1–25.

[167] S. Senapati, P. Maiti, 9 - Emerging bio-applications of two-dimensional nanoheterostructure materials, in: S. Jit, S. Das (Eds.), 2D Nanoscale Heterostructured Materials, Elsevier2020, pp. 243–255.

[168] Y. Zhang, L. Zhang, C. Zhou, Review of chemical vapor deposition of graphene and related applications, Accounts of chemical research 46(10) (2013) 2329–2339.

[169] D.L. Chandler, Explained: chemical vapor deposition, 2015. https://news.mit.edu/2015/explained-chemical-vapor-deposition-0619.

[170] R.L. Puurunen, A short history of atomic layer deposition: Tuomo Suntola's atomic layer epitaxy, Chemical Vapor Deposition 20(10-11-12) (2014) 332–344.

[171] Chapter 6 - Thin Films on Silicon, in: M. Tilli, T. Motooka, V.-M. Airaksinen, S. Franssila, M. Paulasto-Kröckel, V. Lindroos (Eds.), Handbook of Silicon Based MEMS Materials and Technologies (Second Edition), William Andrew Publishing, Boston, 2015, pp. 124–205.

[172] T. Suntola, Atomic layer epitaxy, Materials Science Reports 4(5) (1989) 261–312.

[173] M. Leskelä, J. Niinistö, M. Ritala, 4.05 - Atomic Layer Deposition, in: S. Hashmi, G.F. Batalha, C.J. Van Tyne, B. Yilbas (Eds.), Comprehensive Materials Processing, Elsevier, Oxford, 2014, pp. 101–123.

[174] T.-M. Pan, S. Mondal, Structural Properties and Sensing Characteristics of Sensing Materials, (2014).

[175] A. Pakkala, M. Putkonen, Chapter 8 - Atomic Layer Deposition, in: P.M. Martin (Ed.), Handbook of Deposition Technologies for Films and Coatings (Third Edition), William Andrew Publishing, Boston, 2010, pp. 364–391.

[176] R.L. Puurunen, Surface chemistry of atomic layer deposition: A case study for the trimethylaluminum/water process, Journal of applied physics 97(12) (2005) 9.

[177] S.-J. Cho, M.-J. Uddin, P. Alaboina, Review of nanotechnology for cathode materials in batteries, Emerging nanotechnologies in rechargeable energy storage systems, Elsevier2017, pp. 83–129.

[178] R.W. Johnson, A. Hultqvist, S.F. Bent, A brief review of atomic layer deposition: from fundamentals to applications, Materials today 17(5) (2014) 236–246.

[179] M. Tilli, M. Paulasto-Kröckel, M. Petzold, H. Theuss, T. Motooka, V. Lindroos, Handbook of silicon based MEMS materials and technologies, Elsevier2020.

[180] J. Dini, Properties of coatings: Comparisons of electroplated, physical vapor deposited, chemical vapor deposited, and plasma sprayed coatings, Material And Manufacturing Process 12(3) (1997) 437–472.

[181] B.-Y. Kim, S.-H. Lee, S.-G. Park, K.-Y. Oh, J. Song, D.-H. Kim, Comparison study for TiN films deposited from different method: chemical vapor deposition and atomic layer deposition, MRS Online Proceedings Library 672(1) (2001) 1–6.

[182] K. Wada, T. TERAO, T. MIYASE, T. HORI, H. DOI, M. FURUMAI, High-Quality 6-inch SiC Epitaxial Wafer “EpiEra”, SEI TECHNICAL REVIEW 87 (2018) 54–58.

[183] X. Han, J. Ma, A. Tian, Y. Wang, Y. Li, B. Dong, X. Tong, X. Ma, Surface modification techniques of titanium and titanium alloys for biomedical orthopaedics applications: A review, Colloids and Surfaces B: Biointerfaces 227 (2023) 113339.

[184] M. Gagné, D. Therriault, Lightning strike protection of composites, Progress in Aerospace Sciences 64 (2014) 1–16.

[185] D.M. Mattox, Physical vapor deposition (PVD) processes, Metal Finishing 100 (2002) 394–408.

[186] A. Baptista, F. Silva, J. Porteiro, J. Míguez, G. Pinto, Sputtering physical vapour deposition (PVD) coatings: A critical review on process improvement and market trend demands, Coatings 8(11) (2018) 402.

[187] T.B.S. Institution, BS EN ISO 15106-3:2005, Plastics. Film and sheeting. Determinaktion of water vapour transmission rate - Electrolytic detection sensor method, 2005.

[188] T.B.S. Institution, BS ISO 15106-7:2015, Plastics. Film and sheeting. Determination of water vapour transmission rate - Calcium corrosion method, 2015.

[189] B. Duncan, J. Urquhart, S. Roberts, Review of measurement and modelling of permeation and diffusion in polymers, (2005).

[190] A. F-13, Standard test method for water vapor transmission rate through plastic film and sheeting using a modulated infrared sensor, (2020).

[191] I.N.A. MOCON, AQUATRAN® Model 2 - Brochure Code: 0113, MOCON, US Headquarters Offices Worldwide, 2013.

[192] Plastics — Film and sheeting — Determination of water vapour transmission rate — Part 7: Calcium corrosion method, (2015).

[193] H. Assender, A. Sim, V. Tobin, Water Vapour Permeation, European Patent Office, 2020.

[194] V.R. Tobin, H. Suttle, H.E. Assender, Nanodefect-controlled permeation in AlOx/polymer gas barrier films, Thin Solid Films 642 (2017) 142–150.

[195] P.F. Carcia, R.S. McLean, M.H. Reilly, M.D. Groner, S.M. George, Ca test of Al2O3 gas diffusion barriers grown by atomic layer deposition on polymers, Applied Physics Letters 89(3) (2006) 031915.

[196] A.T.X.S. Hazel Assender, Vincent Tobin, Water Vapour Permeation, in: W.I.P.O.I. Bureau (Ed.) United Kingdom, 2019.

[197] L. Marsh, R. Lasky, D. Seraphim, G. Springer, Moisture solubility and diffusion in epoxy and epoxy-glass composites, IBM Journal of Research and Development 28(6) (1984) 655–661.

[198] P.J. Kelly, R.D. Arnell, Magnetron sputtering: a review of recent developments and applications, Vacuum 56(3) (2000) 159–172.

[199] W. Keuning, P. Van de Weijer, H. Lifka, W. Kessels, M. Creatore, Cathode encapsulation of organic light emitting diodes by atomic layer deposited Al2O3 films and Al2O3/a-SiNx: H stacks, Journal of Vacuum Science & Technology A: Vacuum, Surfaces, and Films 30(1) (2012) 01A131.

[200] G. Valette, Hydrophilicity of metal surfaces: silver, gold and copper electrodes, Journal of Electroanalytical Chemistry and Interfacial Electrochemistry 139(2) (1982) 285–301.

[201] M. Hanika, H.C. Langowski, U. Moosheimer, W. Peukert, Inorganic layers on polymeric films–influence of defects and morphology on barrier properties, Chemical Engineering & Technology: Industrial Chemistry-Plant Equipment-Process Engineering-Biotechnology 26(5) (2003) 605–614.

[202] D.J. Higgs, M.J. Young, J.A. Bertrand, S.M. George, Oxidation kinetics of calcium films by water vapor and their effect on water vapor transmission rate measurements, The Journal of Physical Chemistry C 118(50) (2014) 29322–29332.

[203] J.A. Bertrand, Gas diffusion barriers using atomic layer deposition: a new calcium test and polymer substrate effects, University of Colorado at Boulder, 2012.

[204] P. Boldrighini, A. Fauveau, S. Thérias, J.L. Gardette, M. Hidalgo, S. Cros, Optical calcium test for measurement of multiple permeation pathways in flexible organic optoelectronic encapsulation, Review of Scientific Instruments 90(1) (2019).

[205] H.L. Brown, The properties and performance of moisture/oxygen barrier layers deposited by remote plasma sputtering, University of Surrey (United Kingdom)2015.

[206] H. Kim, A.K. Singh, C.-Y. Wang, C. Fuentes-Hernandez, B. Kippelen, S. Graham, Experimental investigation of defect-assisted and intrinsic water vapor permeation through ultrabarrier films, Review of Scientific Instruments 87(3) (2016).

[207] Z. Li, Z. Wang, Z. Chen, J. Feng, L. Shangguan, J. Wang, H. Sun, Y. Duan, Novel optical and electrical combined calcium corrosion test: An industrial application of the barrier permeability of spotless water vapor, Measurement 196 (2022) 111264.

[208] T.W. Kim, M. Yan, A.G. Erlat, P.A. McConnelee, M. Pellow, J. Deluca, T.P. Feist, A.R. Duggal, M. Schaepkens, Transparent hybrid inorganic/organic barrier coatings for plastic organic light-emitting diode substrates, Journal of Vacuum Science & Technology A 23(4) (2005) 971–977.

[209] S. Hergert, M. Linkor, M. Korny, N. Fruehauf, Process development and accurate low-cost characterization for OLED sealants by using a calcium test, Journal of the Society for Information Display 15(6) (2007) 421–429.

[210] A. Hogg, T. Aellen, S. Uhl, B. Graf, H. Keppner, Y. Tardy, J. Burger, Ultra-thin layer packaging for implantable electronic devices, Journal of Micromechanics and Microengineering 23(7) (2013) 075001.

[211] D. Paul, W. Koros, Effect of partially immobilizing sorption on permeability and the diffusion time lag, Journal of Polymer science: Polymer physics edition 14(4) (1976) 675–685.

[212] T.G. Mayerhöfer, S. Pahlow, J. Popp, The Bouguer-Beer-Lambert law: Shining light on the obscure, ChemPhysChem 21(18) (2020) 2029–2046.

[213] A. Mendoza-Galván, J. Méndez-Lara, R. Mauricio-Sánchez, K. Järrendahl, H. Arwin, Effective absorption coefficient and effective thickness in attenuated total reflection spectroscopy, Optics Letters 46(4) (2021) 872–875.

[214] A.-M. Andringa, A. Perrotta, K. de Peuter, H.C. Knoops, W.M. Kessels, M. Creatore, Low-temperature plasma-assisted atomic layer deposition of silicon nitride moisture permeation barrier layers, ACS applied materials & interfaces 7(40) (2015) 22525–22532.

[215] S. Potts, W. Keuning, E. Langereis, G. Dingemans, M. Van de Sanden, W. Kessels, Low temperature plasma-enhanced atomic layer deposition of metal oxide thin films, Journal of The Electrochemical Society 157(7) (2010) P66.

[216] M. Alexander, G. Thompson, G. Beamson, Characterization of the oxide/hydroxide surface of aluminium using x-ray photoelectron spectroscopy: a procedure for curve fitting the O 1s core level, Surface and Interface Analysis: An International Journal devoted to the development and application of techniques for the analysis of surfaces, interfaces and thin films 29(7) (2000) 468–477.

[217] M. Groner, S. George, R. McLean, P. Carcia, Gas diffusion barriers on polymers using Al2O3 atomic layer deposition, Applied Physics Letters 88(5) (2006).

[218] P.F. Carcia, R. McLean, M. Reilly, M. Groner, S. George, Ca test of Al2O3 gas diffusion barriers grown by atomic layer deposition on polymers, Applied physics letters 89(3) (2006).

[219] Y. Leterrier, L. Medico, F. Demarco, J.-A. Månson, U. Betz, M. Escola, M.K. Olsson, F. Atamny, Mechanical integrity of transparent conductive oxide films for flexible polymer-based displays, Thin Solid Films 460(1-2) (2004) 156–166.

[220] Y. Leterrier, A. Mottet, N. Bouquet, D. Gilliéron, P. Dumont, A. Pinyol, L. Lalande, J. Waller, J.-A. Månson, Mechanical integrity of thin inorganic coatings on polymer substrates under quasi-static, thermal and fatigue loadings, Thin Solid Films 519(5) (2010) 1729–1737.

[221] G.N. Parsons, S.E. Atanasov, E.C. Dandley, C.K. Devine, B. Gong, J.S. Jur, K. Lee, C.J. Oldham, Q. Peng, J.C. Spagnola, Mechanisms and reactions during atomic layer deposition on polymers, Coordination Chemistry Reviews 257(23-24) (2013) 3323–3331.

[222] W.A. MacDonald, New advances in poly (ethylene terephthalate) polymerization and degradation, Polymer international 51(10) (2002) 923–930.

[223] A.L. Andrady, Plastics and environmental sustainability, John Wiley & Sons2015.

[224] H. Köpnick, M. Schmidt, W. Brügging, J. Rüter, W. Kaminsky, Polyesters, Ullmann's encyclopedia of industrial chemistry (2000).

[225] M. Caironi, Y.-Y. Noh, Large area and flexible electronics, John Wiley & Sons2015.

[226] W.A. MacDonald, Latest advances in substrates for flexible electronics, Large Area and Flexible Electronics (2015) 291–314.

[227] V. Zardetto, T.M. Brown, A. Reale, A. Di Carlo, Substrates for flexible electronics: A practical investigation on the electrical, film flexibility, optical, temperature, and solvent resistance properties, Journal of Polymer Science Part B: Polymer Physics 49(9) (2011) 638–648.

[228] I. Yakimets, D. MacKerron, P. Giesen, K.J. Kilmartin, M. Goorhuis, E. Meinders, W.A. MacDonald, Polymer substrates for flexible electronics: achievements and challenges, Advanced Materials Research 93 (2010) 5–8.

[229] S.M. Ho, Synthesis of Thin Films on Flexible Substrates: A Review, Middle-East Journal of Scientific Research 24(7) (2016) 2235–2238.

[230] K.L. Jarvis, P.J. Evans, N.A. Cooling, B. Vaughan, J. Habsuda, W.J. Belcher, C. Bilen, G. Griffiths, P.C. Dastoor, G. Triani, Comparing three techniques to determine the water vapour transmission rates of polymers and barrier films, Surfaces and Interfaces 9 (2017) 182–188.

[231] K. Fukuda, K. Yu, T. Someya, The future of flexible organic solar cells, Advanced Energy Materials 10(25) (2020) 2000765.

[232] S. Wang, T. Chinnasamy, M.A. Lifson, F. Inci, U. Demirci, Flexible substrate-based devices for point-of-care diagnostics, Trends in biotechnology 34(11) (2016) 909–921.

[233] L. Li, L. Han, H. Hu, R. Zhang, A review on polymers and their composites for flexible electronics, Materials Advances (2023).

[234] A. Launay, F. Thominette, J. Verdu, Water sorption in amorphous poly (ethylene terephthalate), Journal of applied polymer science 73(7) (1999) 1131–1137.

[235] T. Homola, L.Y. Wu, M. Černák, Atmospheric plasma surface activation of poly (ethylene terephthalate) film for roll-to-roll application of transparent conductive coating, The Journal of Adhesion 90(4) (2014) 296–309.

[236] M.A. Fadel, N.A. Kamel, M.M. Darwish, S.L.A. El-Messieh, K.N. Abd-EL-Nour, W.A. Khalil, Preparation and characterization of polyethylene terephthalate–chamomile oil blends with enhanced hydrophilicity and anticoagulant properties, Progress in Biomaterials 9 (2020) 97–106.

[237] L. MatWeb, Overview of materials for Polyethylene Terephthalate (PET), Unreinforced, 1996–2023. https://www.matweb.com/search/DataSheet.aspx?MatGUID=a696bdcdff6f41dd98f8eec3599eaa20&ckck=1.

[238] M. Tolan, O. Seeck, J.-P. Schlomka, W. Press, J. Wang, S. Sinha, Z. Li, M. Rafailovich, J. Sokolov, Evidence for capillary waves on dewetted polymer film surfaces: A combined X-ray and atomic force microscopy study, Physical review letters 81(13) (1998) 2731.

[239] K. Iwakura, Y. Wang, M. Cakmak, Effect of biaxial stretching on thickness uniformity and surface roughness of PET and PPS films, International Polymer Processing 7(4) (1992) 327–333.

[240] A.R. Kolahchi, A. Ajji, P. Carreau, Improvement of PET surface hydrophilicity and roughness through blending, AIP Conference Proceedings, AIP Publishing, 2015.

[241] D.T. Films, Melinex (Polyester Film) PCS/PCSUV, 2021.

[242] B. Demirel, A. Yaraş, H. Elcicek, Crystallization Behavior of PET Materials, Baü Fen Bil. Enst. Dergisi 13(1) (2011) 26–35.

[243] F. DuPont Teijin, Melinex® PCS: Unique Peelable Clean Surface Film for Electronics, 2018.

[244] W.A. MacDonald, Engineered films for display technologies, Journal of Materials Chemistry 14(1) (2004) 4–10.

[245] A. Grüniger, A. Bieder, A. Sonnenfeld, P.R. von Rohr, U. Müller, R. Hauert, Influence of film structure and composition on diffusion barrier performance of SiOx thin films deposited by PECVD, Surface and Coatings Technology 200(14) (2006) 4564–4571.

[246] C.M. Samaniego-Esguerra, G.L. Robertson, Development of a mathematical model for the effect of temperature and relative humidity on the water vapour permeability of plastic films, Packaging Technology and Science 4(2) (1991) 61–68.

[247] L. Murray, P. McCarry, Effect of test conditions and PET surface treatment on moisture barrier of multilayer metallized film structures, Journal of Plastic Film & Sheeting 19(1) (2003) 55–67.

[248] J. Burst, W. Rance, D. Meysing, C. Wolden, W. Metzger, S. Garner, P. Cimo, T. Barnes, T. Gessert, M. Reese, Performance of transparent conductors on flexible glass and plastic substrates for thin film photovoltaics, 2014 IEEE 40th Photovoltaic Specialist Conference (PVSC), IEEE, 2014, pp. 1589–1592.

[249] L. Piergiovanni, P. Fava, A. Siciliano, A mathematical model for the prediction of water vapour transmission rate at different temperature and relative humidity combinations, Packaging Technology and Science 8(2) (1995) 73–83.

[250] A. da Silva Sobrinho, G. Czeremuszkin, M. Latreche, M. Wertheimer, Defect-permeation correlation for ultrathin transparent barrier coatings on polymers, Journal of Vacuum Science & Technology A: Vacuum, Surfaces, and Films 18(1) (2000) 149–157.

[251] C. Ascione, Development of high performance moisture barrier coating for PET bottles.

[252] B. Henry, F. Dinelli, K.-Y. Zhao, C. Grovenor, O. Kolosov, G.A.D. Briggs, A. Roberts, R. Kumar, R. Howson, A microstructural study of transparent metal oxide gas barrier films, Thin Solid Films 355 (1999) 500–505.

[253] B. Henry, A. Erlat, C. Grovenor, C. Deng, G. Briggs, T. Miyamoto, N. Noguchi, T. Niijima, Y. Tsukahara, The permeation of water vapor through gas barrier films, PROCEEDINGS OF THE ANNUAL TECHNICAL CONFERENCE-SOCIETY OF VACUUM COATERS, 2001, pp. 469–475.

[254] A. Erlat, B. Henry, J. Ingram, D. Mountain, A. McGuigan, R. Howson, C. Grovenor, G. Briggs, Y. Tsukahara, Characterisation of aluminium oxynitride gas barrier films, Thin solid films 388(1-2) (2001) 78–86.

[255] S. Mahmood, C. Kant, A. Raj, H.-C. Lin, M. Katiyar, Evaluation of encapsulation strategies for solution-processed flexible organic light-emitting diodes, Materials Chemistry and Physics 292 (2022) 126808.

[256] T. Hanada, T. Negishi, I. Shiroishi, T. Shiro, Plastic substrate with gas barrier layer and transparent conductive oxide thin film for flexible displays, Thin Solid Films 518(11) (2010) 3089–3092.

[257] K. Saitoh, R. Kumar, S. Chua, A. Masuda, H. Matsumura, Estimation of moisture barrier ability of thin SiNx single layer on polymer substrates prepared by Cat-CVD method, Thin Solid Films 516(5) (2008) 607–610.

[258] F. Nehm, F. Dollinger, J. Fahlteich, H. Klumbies, K. Leo, L. Müller-Meskamp, Importance of interface diffusion and climate in defect dominated moisture ultrabarrier applications, ACS Applied Materials & Interfaces 8(30) (2016) 19807–19812.

[259] G. Abbas, P. Papakonstantinou, T. Okpalugo, J. McLaughlin, J. Filik, E. Harkin-Jones, The improvement in gas barrier performance and optical transparency of DLC-coated polymer by silicon incorporation, Thin Solid Films 482(1-2) (2005) 201–206.

[260] K.L. Jarvis, P.J. Evans, G. Triani, Influence of the polymeric substrate on the water permeation of alumina barrier films deposited by atomic layer deposition, Surface and Coatings Technology 337 (2018) 44–52.

[261] G.D. Barber, G.J. Jorgensen, K. Terwilliger, S. Glick, J. Pern, T. McMahon, New barrier coating materials for PV module backsheets, Conference Record of the Twenty-Ninth IEEE Photovoltaic Specialists Conference, 2002., IEEE, 2002, pp. 1541–1544.

[262] N. Chen, P. Kovacik, R.M. Howden, X. Wang, S. Lee, K.K. Gleason, Low substrate temperature encapsulation for flexible electrodes and organic photovoltaics, Advanced Energy Materials 5(6) (2015) 1401442.

[263] I.-C. Cheng, S. Wagner, Overview of Flexible Electronics Technology, Flexible Electronics: Materials and Applications, Springer Science, Business Media, LLC, New York, 2009, pp. 1–28.

[264] S. Kiese, E. Kücükpinar, M. Reinelt, O. Miesbauer, J. Ewender, H.-C. Langowski, A systematic approach for the accurate and rapid measurement of water vapor transmission through ultra-high barrier films, Review of Scientific Instruments 88(2) (2017).

[265] S. Qin, S. Xiang, B. Eberle, K. Xie, J.C. Grunlan, High moisture barrier with synergistic combination of SiOx and polyelectrolyte nanolayers, Advanced Materials Interfaces 6(16) (2019) 1900740.

[266] D. Wuu, W. Lo, C. Chiang, H. Lin, L. Chang, R.-H. Horng, C. Huang, Y. Gao, Plasma-deposited silicon oxide barrier films on polyethersulfone substrates: temperature and thickness effects, Surface and Coatings Technology 197(2-3) (2005) 253–259.

[267] H. Low, Y. Xu, Moisture barrier of AlxOy coating on poly (ethylene terephthalate), poly (ethylene naphthalate) and poly (carbonate) substrates, Applied surface science 250(1-4) (2005) 135–145.

[268] M. Mariello, K. Kim, K. Wu, S.P. Lacour, Y. Leterrier, Recent advances in encapsulation of flexible bioelectronic implants: Materials, technologies, and characterization methods, Advanced Materials 34(34) (2022) 2201129.

[269] P. Hülsmann, G. Wallner, Permeation of water vapour through polyethylene terephthalate (PET) films for back-sheets of photovoltaic modules, Polymer Testing 58 (2017) 153–158.

[270] S. Schubert, H. Klumbies, L. Müller-Meskamp, K. Leo, Electrical calcium test for moisture barrier evaluation for organic devices, Review of Scientific Instruments 82(9) (2011).

[271] K. Lahtinen, J. Kuusipalo, Prediction of WVTR with general regression models, Tappi European Place Conference, 2007, pp. 1023–1054.

[272] H. Norenberg, M. Percy, Water vapor permeation through polymer films at elevated temperatures, Society of Vacuum Coaters 49 th Annual Technical Conference Proceedings, 2006, pp. 664–666.

[273] D.W. Green, R.H. Perry, Perry's chemical engineers' handbook, McGraw-Hill Education2008.

[274] R. Shogren, Water vapor permeability of biodegradable polymers, Journal of environmental polymer degradation 5 (1997) 91–95.

[275] L.W. McKeen, Film properties of plastics and elastomers, William Andrew2017.

[276] D. Ravens, I. Ward, Chemical reactivity of polyethylene terephthalate. Hydrolysis and esterification reactions in the solid phase, Transactions of the Faraday Society 57 (1961) 150–159.

[277] Omnexus, Comprehensive Guide on Polyethylene Terephthalate (PET), 2023. https://omnexus.specialchem.com/selection-guide/polyethylene-terephthalate-pet-plastic#:~:text=It%20has%20a%20Tg%20of,Tg%20of%2065%C2%B0C.

[278] C.-T.T. Ltd, Glass Transition Temperature of PET, 2016. https://ctherm.com/resources/newsroom/thermal-analysis-labs/determining-glass-transition-temperature-of-pet/.

[279] J. Jog, Crystallization of polyethyleneterephthalate, Journal of Macromolecular Science, Part C: Polymer Reviews 35(3) (1995) 531–553.

[280] L. De Vos, B. Van de Voorde, L. Van Daele, P. Dubruel, S. Van Vlierberghe, Poly (alkylene terephthalate) s: From current developments in synthetic strategies towards applications, European Polymer Journal 161 (2021) 110840.

[281] T. Shigetomi, H. Tsuzumi, K. Toi, T. Ito, Sorption and diffusion of water vapor in poly (ethylene terephthalate) film, Journal of applied polymer science 76(1) (2000) 67–74.

[282] H. Yasuda, V. Stannett, Permeation, solution, and diffusion of water in some high polymers, Journal of Polymer Science 57(165) (1962) 907–923.

[283] E. Pons, B. Yrieix, L. Heymans, F. Dubelley, E. Planes, Permeation of water vapor through high performance laminates for VIPs and physical characterization of sorption and diffusion phenomena, Energy and Buildings 85 (2014) 604–616.

[284] W.J. Koros, W.C. Madden, Transport properties, Encyclopedia of polymer science and technology (2002).

[285] J. Crank, The mathematics of diffusion, Oxford university press1979.

[286] J. Ferry, Viscoelastic Properties of Polymers, Wiley1980.

[287] L. Masaro, X. Zhu, Physical models of diffusion for polymer solutions, gels and solids, Progress in polymer science 24(5) (1999) 731–775.

[288] S. Buchwalder, F. Bourgeois, J.J.D. Leon, A. Hogg, J. Burger, Parylene-AlOx Stacks for Improved 3D Encapsulation Solutions, Coatings 13(11) (2023) 1942.

[289] D.T. Films, MYLAR® HS, 2011. https://www.ukinsulations.co.uk/pdfs/MYLAR_HS.pdf.

[290] R. Wolf, K. Wandel, C. Boeffel, Moisture barrier films deposited on PET by ICPECVD of SiNx, Plasma Processes and Polymers 4(S1) (2007) S185–S189.

[291] S. Lian, J. Zhang, J. Wang, C. Xu, H.C. Swart, J.J. Terblans, A Model for adsorption and diffusion in water vapor barrier films, physica status solidi (b) 258(6) (2021) 2000609.

[292] Y.G. Tropsha, N.G. Harvey, Activated rate theory treatment of oxygen and water transport through silicon oxide/poly (ethylene terephthalate) composite barrier structures, The Journal of Physical Chemistry B 101(13) (1997) 2259–2266.

[293] J. Brandrup, Polymer Handbook, John Wiley & Sons, Inc, 1999.

[294] ASTM, Standard Test Method for Determining Gas Permeability Characteristics of Plastic Film and Sheeting, Designation: D1434 − 23, 2023.

[295] T. Padfield, Equations describing the physical properties of moist air 1, 2019. https://www.conservationphysics.org/atmcalc/atmoclc2.pdf.

[296] M.G. Lawrence, The relationship between relative humidity and the dewpoint temperature in moist air: A simple conversion and applications, Bulletin of the American Meteorological Society 86(2) (2005) 225–234.

[297] W.D. Callister Jr, Materials science and engineering an introduction, 2007.

[298] R.B. Cassel, Physical Aging and Fragility of Amorphous Polyethylene Terephthalate, TA Instruments TA299 (2002) 1–7.

[299] A.S. Jones, T.E. Long, S.S. Wells, Poly (ethylene terephthalate)(PET) copolymers containing both 1, 4-cyclohexanedimethanol and isophthalic acid moieties, Google Patents, 2000.

[300] D.R. Paul, Polymeric gas separation membranes, CRC press2018.

[301] J. Vrentas, C.M. Vrentas, Sorption in glassy polymers, Macromolecules 24(9) (1991) 2404–2412.

[302] X. Fan, Mechanics of moisture for polymers: fundamental concepts and model study, EuroSimE 2008-International Conference on Thermal, Mechanical and Multi-Physics Simulation and Experiments in Microelectronics and Micro-Systems, IEEE, 2008, pp. 1–14.

[303] R.M. Barrer, Diffusion in and through Solids, Рипол Классик1941.

[304] Y. Yampolskii, Polymeric gas separation membranes, Macromolecules 45(8) (2012) 3298–3311.

[305] P. Bernardo, E. Drioli, G. Golemme, Membrane gas separation: a review/state of the art, Industrial & engineering chemistry research 48(10) (2009) 4638–4663.

[306] W.R. Vieth, Diffusion in and through polymers: principles and applications, American Scientist;(United States) 81(1) (1991).

[307] N.A. Peppas, E.W. Merrill, Crosslinked poly (vinyl alcohol) hydrogels as swollen elastic networks, Journal of Applied Polymer Science 21(7) (1977) 1763–1770.

[308] N.L. Thomas, A. Windle, A theory of case II diffusion, Polymer 23(4) (1982) 529–542.

[309] J. Vrentas, J. Duda, Diffusion in polymer—solvent systems. I. Reexamination of the free-volume theory, Journal of Polymer Science: Polymer Physics Edition 15(3) (1977) 403–416.

[310] A. El Aissaoui, A. El Afif, Non-Fickian mass transfer in swelling polymeric non-porous membranes, Journal of Membrane Science 543 (2017) 172–183.

[311] G. Billovits, C. Durning, Penetrant transport in semicrystalline poly (ethylene terephthalate), Polymer 29(8) (1988) 1468–1484.

[312] C. Sammon, J. Yarwood, N. Everall, A FTIR–ATR study of liquid diffusion processes in PET films: comparison of water with simple alcohols, Polymer 41(7) (2000) 2521–2534.

[313] S.K. Burgess, D.S. Mikkilineni, B.Y. Daniel, D.J. Kim, C.R. Mubarak, R.M. Kriegel, W.J. Koros, Water sorption in poly (ethylene furanoate) compared to poly (ethylene terephthalate). Part 2: Kinetic sorption, Polymer 55(26) (2014) 6870–6882.

[314] C. Bishop, Vacuum deposition onto webs, films and foils, William Andrew2011.

[315] S.O. Pehkonen, S. Yuan, The inorganic film coatings for corrosion protection, Interface Science and Technology, Elsevier2018, pp. 185–255.

[316] C. Li, B. Wei, J. Zhang, Encapsulation of organic light-emitting devices for the application of display, 2008 International Conference on Electronic Packaging Technology & High Density Packaging, IEEE, 2008, pp. 1–4.

[317] Q. Lu, Z. Yang, X. Meng, Y. Yue, M.A. Ahmad, W. Zhang, S. Zhang, Y. Zhang, Z. Liu, W. Chen, A review on encapsulation technology from organic light emitting diodes to organic and perovskite solar cells, Advanced Functional Materials 31(23) (2021) 2100151.

[318] A. Ghosh, L. Gerenser, C. Jarman, J. Fornalik, Thin-film encapsulation of organic light-emitting devices, Applied physics letters 86(22) (2005).

[319] H. Lifka, H. Van Esch, J. Rosink, 50.3: Thin Film Encapsulation of OLED Displays with a NONON Stack, SID symposium digest of technical papers, Wiley Online Library, 2004, pp. 1384–1387.

[320] S.-H.K. Park, J. Oh, C.-S. Hwang, J.-I. Lee, Y.S. Yang, H.Y. Chu, Ultrathin film encapsulation of an OLED by ALD, Electrochemical and solid-state letters 8(2) (2005) H21.

[321] E. Langereis, M. Creatore, S. Heil, M. Van de Sanden, W. Kessels, Plasma-assisted atomic layer deposition of Al2O3 moisture permeation barriers on polymers, Applied physics letters 89(8) (2006).

[322] M. Groner, F. Fabreguette, J. Elam, S. George, Low-temperature Al2O3 atomic layer deposition, Chemistry of materials 16(4) (2004) 639–645.

[323] M. Ritala, M. Leskelä, J.P. Dekker, C. Mutsaers, P.J. Soininen, J. Skarp, Perfectly conformal TiN and Al2O3 films deposited by atomic layer deposition, Chemical Vapor Deposition 5(1) (1999) 7–9.

[324] A. Yersak, Roll-to-Roll Atomic Layer Deposition for Ultrabarriers, University of Colorado at Boulder, 2016.

[325] A.A. Dameron, S.D. Davidson, B.B. Burton, P.F. Carcia, R.S. McLean, S.M. George, Gas diffusion barriers on polymers using multilayers fabricated by Al2O3 and rapid SiO2 atomic layer deposition, The Journal of Physical Chemistry C 112(12) (2008) 4573–4580.

[326] M. Leskelä, J. Niinistö, M. Ritala, Atomic layer deposition, (2014).

[327] E. Marin, L. Fedrizzi, Atomic layer deposition an innovative technology to improve corrosion and surface functionalities of alloys, Encyclopedia of Interfacial Chemistry: Surface Science and Electrochemistry, Elsevier2018, pp. 79–89.

[328] F. Grillo, J.A. Moulijn, M.T. Kreutzer, J.R. van Ommen, Nanoparticle sintering in atomic layer deposition of supported catalysts: Kinetic modeling of the size distribution, Catalysis Today 316 (2018) 51–61.

[329] A.J. Elliot, C. Ma, R. Lu, M. Xin, S. Han, J.Z. Wu, R. Sakidja, H. Yu, Controlling the thickness of Josephson tunnel barriers with atomic layer deposition, arXiv preprint arXiv:1408.3077 (2014).

[330] E. Schilirò, R.L. Nigro, S. Panasci, F. Gelardi, S. Agnello, R. Yakimova, F. Roccaforte, F. Giannazzo, Aluminum oxide nucleation in the early stages of atomic layer deposition on epitaxial graphene, Carbon 169 (2020) 172–181.

[331] A.W. Weimer, Particle atomic layer deposition, Journal of Nanoparticle Research 21(1) (2019) 9.

[332] Y.-W. Yeh, S.-H. Lin, T.-C. Hsu, S. Lai, P.-T. Lee, S.-Y. Lien, D.-S. Wuu, G. Li, Z. Chen, T. Wu, Advanced atomic layer deposition technologies for Micro-LEDs and VCSELs, Nanoscale Research Letters 16 (2021) 1–14.

[333] V. Cremers, R.L. Puurunen, J. Dendooven, Conformality in atomic layer deposition: Current status overview of analysis and modelling, Applied Physics Reviews 6(2) (2019).

[334] H. Klumbies, P. Schmidt, M. Hähnel, A. Singh, U. Schroeder, C. Richter, T. Mikolajick, C. Hoßbach, M. Albert, J.W. Bartha, Thickness dependent barrier performance of permeation barriers made from atomic layer deposited alumina for organic devices, Organic Electronics 17 (2015) 138–143.

[335] K.H. Yoon, H.S. Kim, K.S. Han, S.H. Kim, Y.-E.K. Lee, N.K. Shrestha, S.Y. Song, M.M. Sung, Extremely high barrier performance of organic–inorganic nanolaminated thin films for organic light-emitting diodes, Acs Applied Materials & Interfaces 9(6) (2017) 5399–5408.

[336] P. Carcia, R. McLean, M. Reilly, Permeation measurements and modeling of highly defective Al2O3 thin films grown by atomic layer deposition on polymers, Applied physics letters 97(22) (2010).

[337] M. Sridharan, M. Sillassen, J. Bøttiger, J. Chevallier, H. Birkedal, Pulsed DC magnetron sputtered Al2O3 films and their hardness, Surface and Coatings Technology 202(4-7) (2007) 920–924.

[338] C. Struller, P. Kelly, N. Copeland, Aluminum oxide barrier coatings on polymer films for food packaging applications, Surface and Coatings Technology 241 (2014) 130–137.

[339] C. Struller, P. Kelly, N. Copeland, V. Tobin, H. Assender, C. Holliday, S. Read, Aluminium oxide barrier films on polymeric web and their conversion for packaging applications, Thin Solid Films 553 (2014) 153–156.

[340] J. Canny, A computational approach to edge detection, IEEE Transactions on pattern analysis and machine intelligence (6) (1986) 679–698.

[341] W. Rong, Z. Li, W. Zhang, L. Sun, An improved CANNY edge detection algorithm, 2014 IEEE international conference on mechatronics and automation, IEEE, 2014, pp. 577–582.

[342] W. McIlhagga, The canny edge detector revisited, International Journal of Computer Vision 91 (2011) 251–261.

[343] E. Jamieson, A. Windle, Structure and oxygen-barrier properties of metallized polymer film, Journal of Materials Science 18 (1983) 64–80.

[344] Y. Zhang, D. Seghete, A. Abdulagatov, Z. Gibbs, A. Cavanagh, R. Yang, S. George, Y.-C. Lee, Investigation of the defect density in ultra-thin Al2O3 films grown using atomic layer deposition, Surface and Coatings Technology 205(10) (2011) 3334–3339.

[345] B. Díaz, E. Härkönen, J. Światowska, V. Maurice, A. Seyeux, P. Marcus, M. Ritala, Low-temperature atomic layer deposition of Al2O3 thin coatings for corrosion protection of steel: Surface and electrochemical analysis, Corrosion science 53(6) (2011) 2168–2175.

[346] S. Potts, L. Schmalz, M. Fenker, B. Díaz, J. Światowska, V. Maurice, A. Seyeux, P. Marcus, G. Radnóczi, L. Tóth, Ultra-thin aluminium oxide films deposited by plasma-enhanced atomic layer deposition for corrosion protection, Journal of The Electrochemical Society 158(5) (2011) C132.

[347] E. Jia, C. Zhou, W. Wang, Uniformity and passivation research of Al 2 O 3 film on silicon substrate prepared by plasma-enhanced atom layer deposition, Nanoscale Research Letters 10 (2015) 1–6.

[348] G.l. Dogan, S.O. Demir, R. Gutzler, H. Gruhn, C.B. Dayan, U.T. Sanli, C. Silber, U. Culha, M. Sitti, G. Schütz, Bayesian machine learning for efficient minimization of defects in ald passivation layers, ACS Applied Materials & Interfaces 13(45) (2021) 54503–54515.

[349] A. Abdulagatov, Y. Yan, J. Cooper, Y. Zhang, Z. Gibbs, A. Cavanagh, R. Yang, Y. Lee, S. George, Al2O3 and TiO2 atomic layer deposition on copper for water corrosion resistance, ACS applied materials & interfaces 3(12) (2011) 4593–4601.

[350] T. Maindron, T. Jullien, A. André, Defect analysis in low temperature atomic layer deposited Al2O3 and physical vapor deposited SiO barrier films and combination of both to achieve high quality moisture barriers, Journal of Vacuum Science & Technology A 34(3) (2016).

[351] D. Howells, B. Henry, Y. Leterrier, J.-A. Månson, J. Madocks, H. Assender, Mechanical properties of SiOx gas barrier coatings on polyester films, Surface and Coatings Technology 202(15) (2008) 3529–3537.

[352] Z. Chai, Y. Liu, J. Li, X. Lu, D. He, Ultra-thin Al 2 O 3 films grown by atomic layer deposition for corrosion protection of copper, RSC Advances 4(92) (2014) 50503–50509.

[353] L. Blunt, M. Elrawemi, L. Fleming, F. Sweeney, Correlation of micro and nano–scale defects with WVTR for aluminium oxide barrier coatings for flexible photovoltaic modules, International Journal of Precision Technology 3(3) (2013) 290–302.

[354] L. Ferreira, M.B. Evangelista, M.C.L. Martins, P.L. Granja, J.L. Esteves, M.A. Barbosa, Improving the adhesion of poly (ethylene terephthalate) fibers to poly (hydroxyethyl methacrylate) hydrogels by ozone treatment: Surface characterization and pull-out tests, Polymer 46(23) (2005) 9840–9850.

[355] D.-Y. Su, Y.-H. Kuo, M.-H. Tseng, F.-Y. Tsai, Effects of surface pretreatment and deposition conditions on the gas permeation properties and flexibility of Al2O3 films on polymer substrates by atomic layer deposition, Journal of Coatings Technology and Research 16(6) (2019) 1751–1756.

[356] J. Ortigoza-Diaz, K. Scholten, E. Meng, Characterization and modification of adhesion in dry and wet environments in thin-film Parylene systems, Journal of Microelectromechanical Systems 27(5) (2018) 874–885.

[357] L. Carrino, W. Polini, L. Sorrentino, Ageing time of wettability on polypropylene surfaces processed by cold plasma, Journal of Materials Processing Technology 153 (2004) 519–525.

[358] M.L. Abel, J.F. Watts, Examination of the interface of a model adhesive joint by surface analysis: a study by XPS and ToF-SIMS, Surface and Interface Analysis: An International Journal devoted to the development and application of techniques for the analysis of surfaces, interfaces and thin films 41(6) (2009) 508–516.

[359] A. Kinloch, C. Korenberg, K.T. Tan, J. Watts, Durability of structural adhesive joints, Applied Science Publication: London, UK (1983).

[360] K. Gotoh, A. Yasukawa, Y. Kobayashi, Wettability characteristics of poly (ethylene terephthalate) films treated by atmospheric pressure plasma and ultraviolet excimer light, Polymer journal 43(6) (2011) 545–551.

[361] S. Prokes, M. Katz, M. Twigg, Growth of crystalline Al2O3 via thermal atomic layer deposition: Nanomaterial phase stabilization, APL Materials 2(3) (2014).

[362] A.K. Jaiswal, V. Kumar, E. Jansson, O.H. Huttunen, A. Yamamoto, M. Vikman, A. Khakalo, J. Hiltunen, M.H. Behfar, Biodegradable cellulose nanocomposite substrate for recyclable flexible printed electronics, Advanced Electronic Materials 9(4) (2023) 2201094.

[363] Y.H. Jung, T.-H. Chang, H. Zhang, C. Yao, Q. Zheng, V.W. Yang, H. Mi, M. Kim, S.J. Cho, D.-W. Park, High-performance green flexible electronics based on biodegradable cellulose nanofibril paper, Nature communications 6(1) (2015) 7170.

[364] Z.W. Abdullah, Y. Dong, I.J. Davies, S. Barbhuiya, PVA, PVA blends, and their nanocomposites for biodegradable packaging application, Polymer-Plastics Technology and Engineering 56(12) (2017) 1307–1344.

[365] F. Khoerunnisa, E. Septiani, H. Hendrawan, Y. Sonjaya, Effect of SWCNT Filler on Mechanical Properties and Electrical Conductivity of PVA/CS/GA/SWCNT Nanocomposite Thin Film, Key Engineering Materials 840 (2020) 441–447.

[366] S. Aruldass, V. Mathivanan, A. Mohamed, C. Tye, Factors affecting hydrolysis of polyvinyl acetate to polyvinyl alcohol, Journal of Environmental Chemical Engineering 7(5) (2019) 103238.

[367] Y. Xianda, W. Anlai, C. Suqin, Water-vapor permeability of polyvinyl alcohol films, Desalination 62 (1987) 293–297.

[368] J.C. Spagnola, B. Gong, S.A. Arvidson, J.S. Jur, S.A. Khan, G.N. Parsons, Surface and sub-surface reactions during low temperature aluminium oxide atomic layer deposition on fiber-forming polymers, Journal of Materials Chemistry 20(20) (2010) 4213–4222.

[369] T. Hirvikorpi, M. Vähä-Nissi, A. Harlin, M. Salomäki, S. Areva, J.T. Korhonen, M. Karppinen, Enhanced water vapor barrier properties for biopolymer films by polyelectrolyte multilayer and atomic layer deposited Al2O3 double-coating, Applied Surface Science 257(22) (2011) 9451–9454.

[370] T. Hirvikorpi, R. Laine, M. Vähä-Nissi, V. Kilpi, E. Salo, W.-M. Li, S. Lindfors, J. Vartiainen, E. Kenttä, J. Nikkola, Barrier properties of plastic films coated with an Al2O3 layer by roll-to-toll atomic layer deposition, Thin Solid Films 550 (2014) 164–169.

[371] S. Zeng, L. Li, Q. Wang, Structure-property correlation of polyvinyl alcohol films fabricated by different processing methods, Polymer Testing 126 (2023) 108143.

[372] S. Mohanty, A. Arya, D. Jena, S. Guhathakurata, N.B. Manik, G. Ahmad, S. Mallik, Potential soluble substrates for transient electronics applications: A review, Aip Advances 12(5) (2022).

[373] N. Mittal, T.-M. Jang, S.-W. Hwang, M. Niederberger, PVA–FeCl 3 composites as substrate and packaging materials for the controlled degradation of non-degradable metals in transient electronics, Journal of Materials Chemistry A 11(24) (2023) 12999–13006.

[374] U.S.D.o. Energy, Roll-to-Roll (R2R) Processing Technology Assessment, Quadrennial Technology Review: Technology Assessment, U.S. Department of Energy, Washington, DC, 2015.

[375] A.D. Chandio, I.A. Channa, M. Rizwan, S. Akram, M.S. Javed, S.H. Siyal, M. Saleem, M.A. Makhdoom, T. Ashfaq, S. Khan, Polyvinyl alcohol and nano-clay based solution processed packaging coatings, Coatings 11(8) (2021) 942.

[376] N. Park, M.A. Friest, L. Liu, Enhancing the Properties of Polyvinyl Alcohol Films by Blending with Corn Stover-Derived Cellulose Nanocrystals and Beeswax, Polymers 15(21) (2023) 4321.

[377] M.S. Sarwar, M.B.K. Niazi, Z. Jahan, T. Ahmad, A. Hussain, Preparation and characterization of PVA/nanocellulose/Ag nanocomposite films for antimicrobial food packaging, Carbohydrate polymers 184 (2018) 453–464.

[378] H. Fujita, Diffusion in polymer-diluent systems, Fortschritte Der Hochpolymeren-Forschung, Springer2006, pp. 1–47.

[379] M.G. Katz, T. Wydeven Jr, Selective permeability of PVA membranes. I. Radiation-crosslinked membranes, Journal of Applied Polymer Science 26(9) (1981) 2935–2946.

[380] D.T. Bui, A. Nida, K.C. Ng, K.J. Chua, Water vapor permeation and dehumidification performance of poly (vinyl alcohol)/lithium chloride composite membranes, Journal of Membrane Science 498 (2016) 254–262.

[381] Y.M. Wei, Z.L. Xu, F.A. Qusay, K. Wu, Polyvinyl alcohol/polysulfone (PVA/PSF) hollow fiber composite membranes for pervaporation separation of ethanol/water solution, Journal of applied polymer science 98(1) (2005) 247–254.

[382] J.C. Gertsch, E. Sortino, V.M. Bright, Deposit and etchback approach for ultrathin Al, (2021).

[383] B. Freeman, Y. Yampolskii, I. Pinnau, Materials science of membranes for gas and vapor separation, John Wiley & Sons2006.

[384] S. Suganthi, S. Vignesh, J. Kalyana Sundar, V. Raj, Fabrication of PVA polymer films with improved antibacterial activity by fine-tuning via organic acids for food packaging applications, Applied Water Science 10(4) (2020) 1–11.

[385] D. Fernandes, A.W. Hechenleitner, S. Lima, L. Andrade, A. Caires, *E.G.* Pineda, Preparation, characterization, and photoluminescence study of PVA/ZnO nanocomposite films, Materials Chemistry and Physics 128(3) (2011) 371–376.

[386] K. Chan, H. Senin, I. Naimah, Structural and mechanical properties of polyvinyl alcohol (PVA) thin film, AIP Conference Proceedings, American Institute of Physics, 2009, pp. 366–369.

[387] M. Tsukada, G. Freddi, J.S. Crighton, Structure and compatibility of poly (vinyl alcohol)-silk fibroin (PVA/SA) blend films, Journal of Polymer Science Part B: Polymer Physics 32(2) (1994) 243–248.

[388] S.W. Kim, M.M. Rehman, M. Sajid, M.M. ur Rehman, J. Gul, J. Dai Jo, K.H. Choi, Encapsulation of polyvinyl alcohol based flexible temperature sensor through spatial atmospheric atomic layer deposition system to enhance its lifetime, Thin Solid Films 673 (2019) 44–51.

[389] C. Thellen, S. Cheney, J.A. Ratto, Melt processing and characterization of polyvinyl alcohol and polyhydroxyalkanoate multilayer films, Journal of applied polymer science 127(3) (2013) 2314–2324.

[390] K.R. Ammann, M. Li, S. Hossainy, M.J. Slepian, The influence of polymer processing methods on polymer film physical properties and vascular cell responsiveness, ACS applied bio materials 2(8) (2019) 3234–3244.

[391] S.J.V. Torres, G.B. Medeiros, F. Rosário, F. Yamashita, L.H.C. Mattoso, E. Corradini, Mechanical and water absorption properties and morphology of melt processed Zein/PVAl blends, Polímeros 30(4) (2020) e2020042.

[392] R. Adam, the Calcium test as a tool for Evaluating the Performance of Flexible barrier Films, (2008).

[393] E.S. Carreras, F. Chabert, D. Dunstan, G. Franks, Avoiding "mud" cracks during drying of thin films from aqueous colloidal suspensions, Journal of colloid and interface science 313(1) (2007) 160–168.

[394] Y. Li, X. Liu, D. Lv, S. Hou, X. Yu, Y. Han, Suppression of the Skin-Core Structure of Poly (vinyl alcohol) Films by Adding Urea/Diethanolamine to Improve the Mechanical and Optical Properties, Macromolecules 57(13) (2024) 6109–6122.

[395] Y. Zhang, J.A. Bertrand, R. Yang, S.M. George, Y. Lee, Electroplating to visualize defects in Al2O3 thin films grown using atomic layer deposition, Thin Solid Films 517(11) (2009) 3269–3272.

[396] S. Van der Walt, J.L. Schönberger, J. Nunez-Iglesias, F. Boulogne, J.D. Warner, N. Yager, E. Gouillart, T. Yu, scikit-image: image processing in Python, PeerJ 2 (2014) e453.

[397] S. Heil, J. Van Hemmen, M. Van De Sanden, W. Kessels, Reaction mechanisms during plasma-assisted atomic layer deposition of metal oxides: A case study for Al2O3, Journal of Applied Physics 103(10) (2008).

[398] S.K. Kim, S.W. Lee, C.S. Hwang, Y.-S. Min, J.Y. Won, J. Jeong, Low temperature (< 100 C) deposition of aluminum oxide thin films by ALD with O3 as oxidant, Journal of The Electrochemical Society 153(5) (2006) F69.

[399] A. Pugliese, B. Shyam, G.M. Repa, A.H. Nguyen, A. Mehta, E.B. Webb III, L.A. Fredin, N.C. Strandwitz, Atomic-layer-deposited aluminum oxide thin films probed with X-ray scattering and compared to molecular dynamics and density functional theory models, ACS omega 7(45) (2022) 41033–41043.

[400] M. Putkonen, T. Sajavaara, L. Niinistö, J. Keinonen, Analysis of ALD-processed thin films by ion-beam techniques, Analytical and bioanalytical chemistry 382(8) (2005) 1791–1799.

[401] P. Panjan, A. Drnovšek, P. Gselman, M. Čekada, M. Panjan, Review of growth defects in thin films prepared by PVD techniques, Coatings 10(5) (2020) 447.

[402] E. Ease.

[403] A. Huntz, L. Maréchal, B. Lesage, R. Molins, Thermal expansion coefficient of alumina films developed by oxidation of a FeCrAl alloy determined by a deflection technique, Applied surface science 252(22) (2006) 7781–7787.

[404] A. Noorjahan, P. Choi, Thermodynamic properties of poly (vinyl alcohol) with different tacticities estimated from molecular dynamics simulation, Polymer 54(16) (2013) 4212–4219.

[405] J. Shih-Hui, Alucone Interlayers to Minimize Stress Caused by Thermal Expansion Mismatch between Al2O3 Films and Teflon Substrates, (2013).

[406] W.A. Barrow, E.R. Dickey, The Effects of Substrate Defects and Particles on ALD Barrier Layer Water Vapor Transmission Performance, Proceedings of the 54th Annual Technical Conference of the Society of Vacuum Coaters, Society of Vacuum Coaters, Chicago, IL, 2011, pp. 1–6.

[407] E. Dickey, W.A. Barrow, High rate roll to roll atomic layer deposition, and its application to moisture barriers on polymer films, Journal of Vacuum Science & Technology A 30(2) (2012).

[408] J. Van Ommen, A. Goulas, Atomic layer deposition on particulate materials, Materials Today Chemistry 14 (2019) 100183.

[409] S. Rostampour, R. Cook, S.-S. Jhang, Y. Li, C. Fan, L.-P. Sung, Changes in the chemical composition of polyethylene terephthalate under UV radiation in various environmental conditions, Polymers 16(16) (2024) 2249.

[410] P. Falkenstein, D. Gräsing, P. Bielytskyi, W. Zimmermann, J. Matysik, R. Wei, C. Song, UV pretreatment impairs the enzymatic degradation of polyethylene terephthalate, Frontiers in Microbiology 11 (2020) 689.

[411] S. Vijayalakshmi, G. Madras, Photodegradation of poly (vinyl alcohol) under UV and pulsed-laser irradiation in aqueous solution, Journal of applied polymer science 102(2) (2006) 958–966.

[412] N. Sri Aprilia, A.K. HPS, N. Olaiya, A. Amin, C. Abdullah, S. Kamarazaman, Z. Zuhra, K. Rahmah, F. Fitriani, D.A. Gopakumar, Ultraviolet light exposure degradation effect on the properties of nanocrystalline cellulose-reinforced polyvinyl alcohol composite film, Progress in Rubber, Plastics and Recycling Technology 38(1) (2022) 21–37.

[413] M. Inc., ASTM E96 vs F1249: Which Provides More Accurate Test Results?, MOCON Incorporated, 2017.

[414] S. Louch, *et al.*, The Calcium Test as a Tool for Evaluating the Performance of Flexible Barrier Films, Society of Vacuum Coaters Annual Technical Conference Proceedings, 2008, pp. 803–807.

[415] G. Nisato, *et al.*, Experimental comparison of high-performance water vapor permeation measurement methods, Organic Electronics 15 (2014) 3746–3755.

[416] H. Klumbies, *et al.*, Diffusion Barriers for Organic Devices and their Evaluation with Calcium Corrosion Tests, Society of Vacuum Coaters Annual Technical Conference Proceedings, 2010.

[417] Y. Zhang, Y.-Z. Zhang, D.C. Miller, J.A. Bertrand, S.-H. Jen, R. Yang, M.L. Dunn, S.M. George, Y. Lee, Fluorescent tags to visualize defects in Al2O3 thin films grown using atomic layer deposition, Thin Solid Films 517(24) (2009) 6794–6797.

[418] A. Perrotta, S.J. García, J.J. Michels, A.-M. Andringa, M. Creatore, Analysis of nanoporosity in moisture permeation barrier layers by electrochemical impedance spectroscopy, ACS applied materials & interfaces 7(29) (2015) 15968–15977.

9 Appendix

9.1 Methodology Supporting Material

9.1.1 Sample Masks

For highly permeable samples such as the uncoated polymer substrates (*e.g.* BOPP, PET, or PVA), an essential step in preparing a MOCON Aquatran test is the application of an impermeable aluminium foil mask to limit the area of permeation (Figure 9-1). This is necessary to prevent damage to the MOCON sensors, which can occur if more than 5 $g/m^2 \cdot day$ of water vapour permeates through the sample. The masks were fabricated in-house using aluminium foil with an adhesive backing (3M Scotch™ Pressure-Sensitive Adhesive Tape). The foil was punched with 1 cm^2 holes and applied appropriately onto the sample.

These masks also enable testing of smaller sample areas, as the maximum sample area (without masking) for the MOCON Aquatran is 50 cm^2. The mask, in this case, also acts as a sample holder, especially relevant for coated samples, where producing large-coated areas may be impractical, or where areas of a sample *e.g.* with large visible defects should appropriately be excluded.

A key concern is the potential error introduced by using a mask and how this affects the comparability between data extracted from a full-size sample, which would better represent the barrier properties, and a smaller masked sample that may not be representative of the large-area barrier performance. To address this, several uncoated substrates, including Biaxially Oriented Polypropylene (BOPP) and Polyethylene

Terephthalate (PET) from Lotus Films, as well as PET films with a peel layer (Melinex Polyester) from DuPont Teijin Films, were tested to evaluate the fidelity of the masks.

With the masked samples, as well as water that permeates perpendicular to the plane of the film, water can also move sideways, into and out of the polymer under the mask, and so the concentration gradient (and hence, flux) of water in the polymer will be more complex than for the unmasked sample. In addition, any possible defects in the sample in the substrate or relevant coating, may not be properly represented in the smaller area of permeation in the masked sample leading to larger variations and potential inaccuracies in the measured values.

For the samples studied, both sides were masked to reduce the likelihood of contamination (*e.g.*, dust or handling-induced damage) and to ensure that only the defined test aperture (typically 1 cm^2) was exposed for permeation measurements. Although thinner films can be masked on a single side, double-sided masking was used for consistency across repeated tests, preventing inadvertent contact or surface damage on the reverse side and confining vapor transport strictly to the aperture. Contamination risks, such as particulate intrusions, scratches or unintended deposition (coated barriers), are further minimized when both sides are secured. To achieve proper alignment, the masks were positioned visually then fastened in a fixed, stationary set-up to prevent leakage around the aperture or sample misalignment during handling [419].

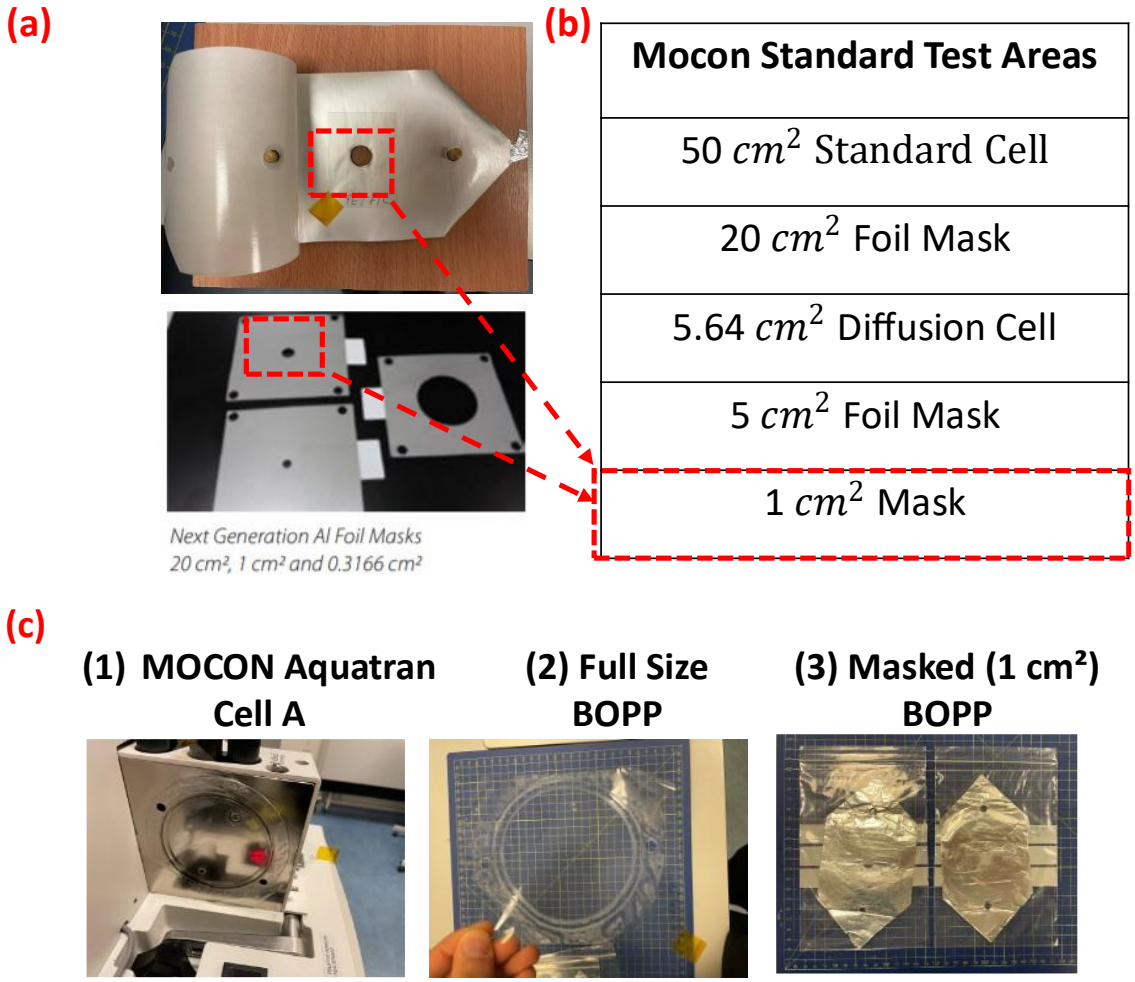


Figure 9-1: (a) Punched aluminium foil masks with adhesive backing, (b) standard mask sizes used in the MOCON Aquatran, and images depicting (c-1) the interior of a MOCON Aquatran cell, (c-2) a full-size BOPP film, and (c-3) masked 1 cm² samples

Table 9-1 presents the effect of using different mask sizes (1 cm^2 and 0.79 cm^2) and a full-size (50 cm^2) sample on WVTR measurements at ~25 °C and ~100% RH. Two samples on the dual cells available in the MOCON Aquatran 2 were used and averaged. The results show that slight variations are present with the addition of the mask but may be more due to sample-to-sample variation rather than intrinsic material or the mask itself. The WVTR's also fit within literature range (PET: 18 $g/m^2 \cdot$day for a 25 µm thick

film, around 4.5 g/m^2·day for 100 µm at ~23–25 °C at 90% RH, while BOPP: 3.9 and 6.2 g/m^2·day for 25.4 µm or 1 mil film ~38 °C at 90% RH) [420-423].

Table 9-1: Summary of WVTR – Mask Sizes on Different Uncoated Substrates

Material	Test Area (cm²)	Thickness (µm)	WVTR (g/(m²·day))	Permeability (mol/(s·m·Pa))
PET	50	100	2.68 ± 0.04	$\mathbf{5.42 \times 10^{-14} \pm 7.1 \times 10^{-16}}$
	1	125	1.83 ± 0.02	$\mathbf{4.62 \times 10^{-14} \pm 4.1 \times 10^{-16}}$
	0.79	125	2.15 ± 0.23	$\mathbf{5.43 \times 10^{-14} \pm 4.2 \times 10^{-15}}$
BOPP	50	48	1.16 ± 0.54	$\mathbf{1.12 \times 10^{-14} \pm 4.9 \times 10^{-15}}$
	1	48	1.10 ± 0.03	$\mathbf{1.07 \times 10^{-14} \pm 2.9 \times 10^{-16}}$
	0.79	48	1.78 ± 0.27	$\mathbf{1.73 \times 10^{-14} \pm 3.6 \times 10^{-15}}$

9.1.2 Calcium Test Negative and Positive Control

In developing the calcium test, preliminary studies were conducted to assess the quality of test sample encapsulation materials like ELC-2500 UV Epoxy and glass structures. A negative control (glass encapsulation on both sides, no permeation expected) and a positive control (uncoated polymer, rapid calcium depletion expected) were tested, as shown in Figure 9-2, establishing a baseline for future experiments.

Preliminary tests revealed issues with copper layer thickness: the negative control had an overly thick layer or insufficient calcium deposition, while the positive control's copper was too thin, leading to rapid calcium depletion. These results underscore the need for a sufficiently thick, uniform copper layer to prevent premature calcium exposure before epoxy encapsulation and testing (discussed: 2.4.2 Copper Thickness). Despite

these issues, the findings were crucial in assessing epoxy suitability and refining the test set-up for more reliable measurements.

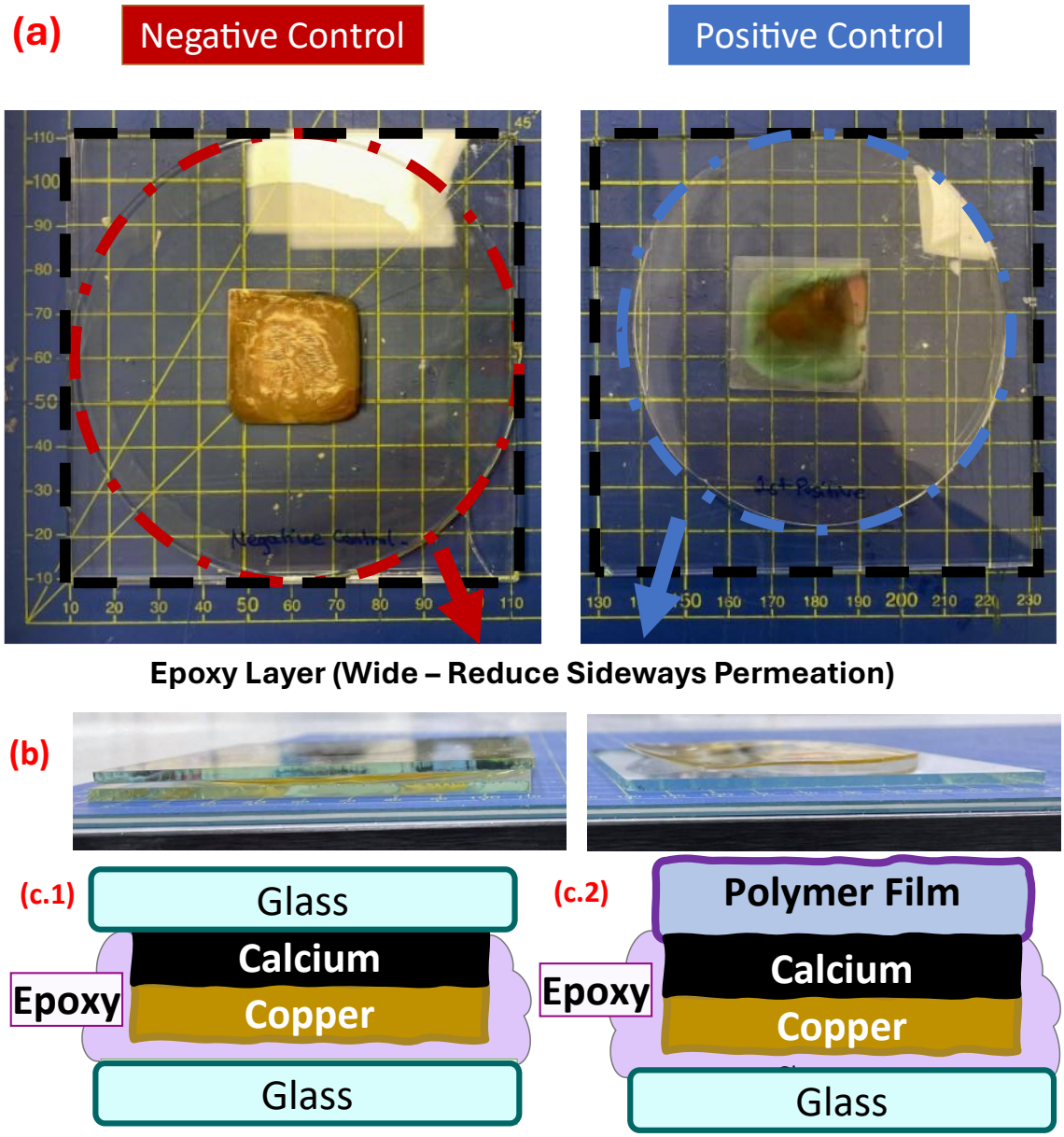


Figure 9-2: Control calcium tests to establish baseline settings and verify sample preparation. (a) Top view of the negative control (glass slides) and positive control (DuPont PET film), (b) front view of the specimens (positive control unhinged), and (c.1 and c.2) schematics of the negative and positive controls. The epoxy layer is illustrated extending around the edges to reduce sideways permeation. Samples were stored at room temperature (~23–25 °C) and 40% relative humidity for approximately one year.

9.1.3 Miscellaneous Improvements

9.1.3.a Temperature Profile and Issue of Fogging

Throughout the project, several improvements were made, as shown in Figure 9-3, these include developing a temperature profile to compare the hotplate's set temperature with the actual environment temperature inside the calcium test box. Additionally, solutions were implemented to prevent fogging on the test box window, which obstructed the camera's view and caused blurry images of the calcium test specimens.

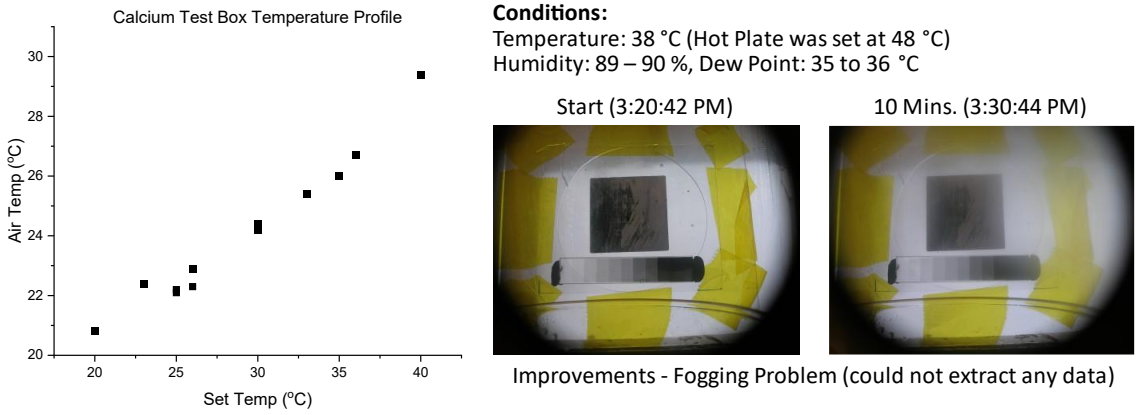


Figure 9-3: The Calcium Test Box Temperature Profile shows the air temperature inside the test box (measured by a data logger with a thermocouple) plotted against the hotplate's-controlled set temperature. While slight variations occur due to uneven heating on the hotplate, the ambient temperature typically remains within a degree or two of the target range. Another challenge is condensation or fogging on the glass window, caused by the warm air inside the test box meeting the cooler surface of the window. This fogging can obstruct visibility and affect image clarity.

9.1.3.b Solutions to Fogging

Fogging occurs when warm air condenses on the cooler surface of the window. Figure 9-16 illustrates two methods used to prevent condensation: (1) applying a hydrophobic coating and (2) heating the glass. The first method involved applying hydrophobic coatings to a glass slide (0.8 to 1.0 W/m·K) [424] or an acrylic/PMMA slide (0.1 to 0.2 W/m·K) [425], reduces the surface energy and limits droplet formation on the

windows. The second method used 5-volt heater pads around the window to raise its temperature and prevent condensation.

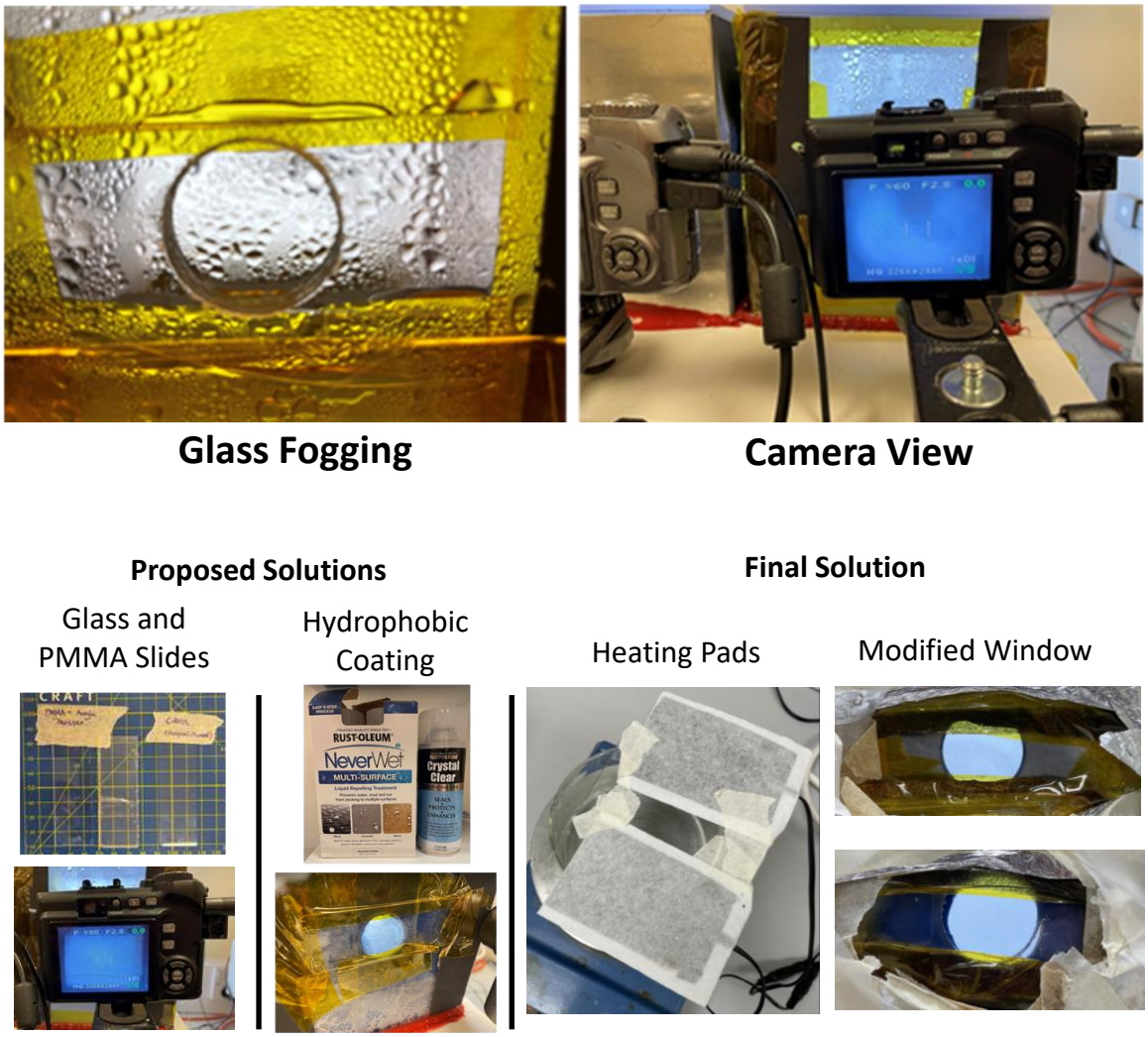


Figure 9-4: The issue of glass fogging at higher ambient temperatures, which caused condensation on the window walls, was resolved using two methods: (1) applying a hydrophobic coating to increase the contact angle and reduce condensation, and (2) heating the window walls to prevent warm air inside the calcium test box from condensing on the cooler surface.

9.1.3.c Calibration Bar

To reduce image-to-image variations, a crucial addition is the calibration strip shown in Figure 9-5 (a), This strip consists of eleven distinct shades, providing a reference for comparing the sample across frames (*i.e.* for this example the Max or lightest portion of the 11 shades is measured to be 202.0 which acts as the maximum normalized value of 100, and the minimum or assumed darkest region to be 19.0 or normalized to the minimum or 0). The mean grey values of the region of interest are measured using tools like ImageJ or MATLAB and allow for the creation of a calibration plot that serves as a reference for intensity shifts between images. The calibration strip compensates for changes in lighting or image capture timing, ensuring consistency in measured grey values. Without this calibration, variations in intensity between images could introduce significant errors.

The effect of the calibration strip is demonstrated in Figure 9-5 (b). Without calibration strip, the calculated fluence graph does not account for environmental lighting changes, leading to inaccuracies. The calibration strip serves as a reference, that is subject to the same environmental changes, but maintains constant transmittance, so can be used to normalize mean intensity values. By using a linear forecast function, the corresponding reference value is predicted based on the measured intensity of the region of interest. This calibrated fluence value is then plotted over time, ensuring accuracy and consistency.

In this example, a shift in mean intensity occurs midway through the dataset, as seen between images 23 and 24 in Figure 9-5 (c). This change can be corrected using the calibration plot, shown in Figure 9-5 (d). By forecasting or interpolating normalized values for each image relative to the reference bar, the variation in mean grey values due to lighting differences is effectively adjusted; where the light portion represents the

calibration plots or average mean intensity values and corresponding normalized values of the first 23 images, and the latter darker portion represents the calibration plots for when the sets of images reduced in mean intensity or average calibration plot of the subsequent images (24th and further). The graph shows that for certain sections or significant shifts in lighting one can group or compensate for the shift average mean grey value change.

For reference, initial frame #1 has intensity 19.42, which would correspond to a normalized value of 0, atypical for as it is opaque, and light has not yet transmitted through the calcium layer. Upon reaching frame #75 where all the calcium has been depleted, it now has a mean intensity of 69.24 and may correspond to a normalized value around 30; accounting and compensating for the difference in mean intensity shifts.

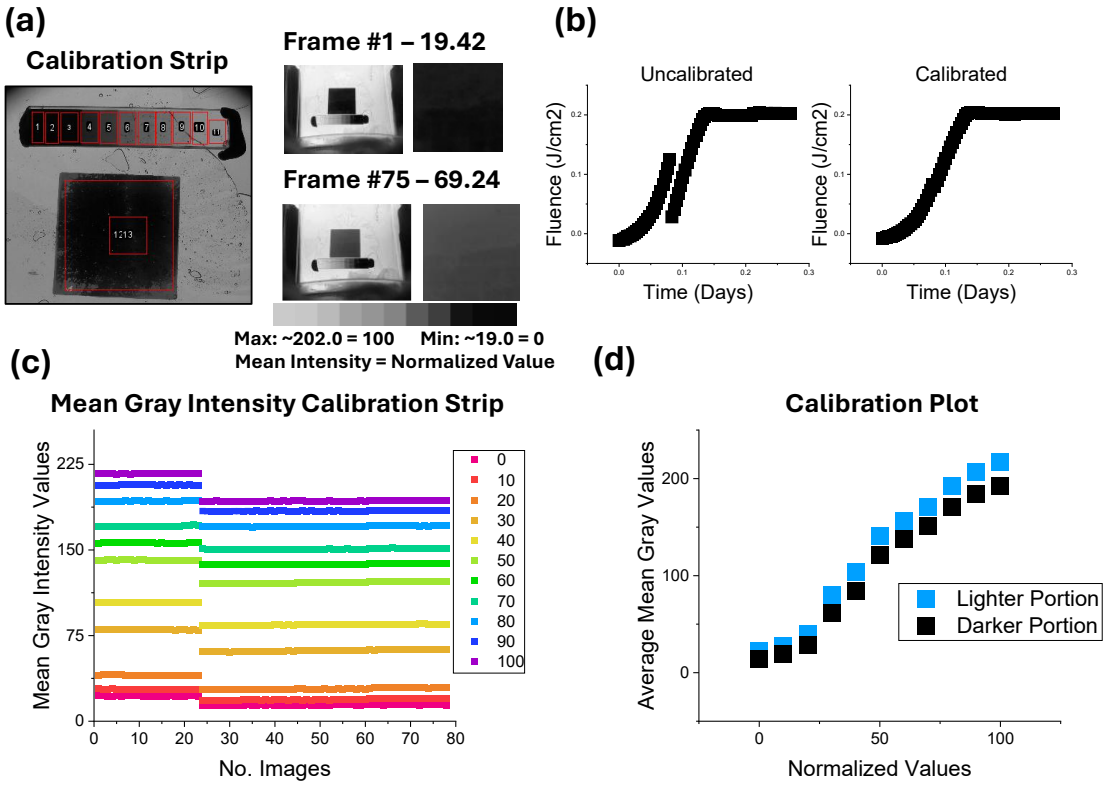


Figure 9-5: (a) Influence of Calibration Strip on fluence calculations, showing regions of interest and changes in mean grey values (reference max for calibration strip mean intensity of 202.0 = 100 normalized, darkest shade mean intensity at 19.0 = 0 normalized; measured initial frame opaque at Frame #1: 19.42, the mean or final mean intensity value when all of the calcium has been depleted at Frame #75: 69.24). (b) Uncalibrated vs. calibrated calculated fluence over time, highlighting how shifts in mean grey values impact fluence calculations, corrected by normalizing with the calibration strip. (c) Calibration strips mean intensity values, illustrating the downshift between images 23 and 24 and constant grey values across the eleven regions of interest. (d) Average normalized mean grey values of the calibration strip, grouped into "lighter" (pre-shift) and "darker" (post-shift) portions, used to correct fluence plots for each calcium test sample.

9.1.3.d Cleanliness Protocol and Epoxy Curing Time

A major issue with early calcium test samples was contamination. It was observed that every step, particularly during thermal evaporation and deposition of the calcium and copper layers, required strict surface cleanliness, as shown in Figure 9-6. To address this, aluminium foil was added to the substrate holder of the thermal evaporator (Edwards 306), which was heavily prone to contamination before deposition for easier cleaning. A dedicated test box lined with lint free paper was used to transport the samples between the thermal evaporator and appropriate Ca test box location. Additionally, another step that could have introduced contamination and sample damage was during the sealing of the sample onto the glass substrate using the UV-cured epoxy, careful attention was needed to not introduce contaminants and keeping the area clean to avoid possible permeation paths for the water vapor which before full enclosure.

Calcium Test Sample Preparation Observation – Clean Protocol.



Dirty Mask

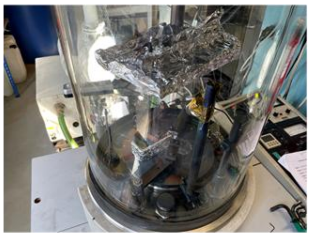


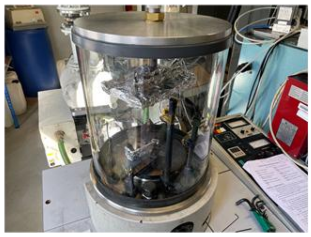
Cleaned



Aluminum Foil (Easier Cleanup)

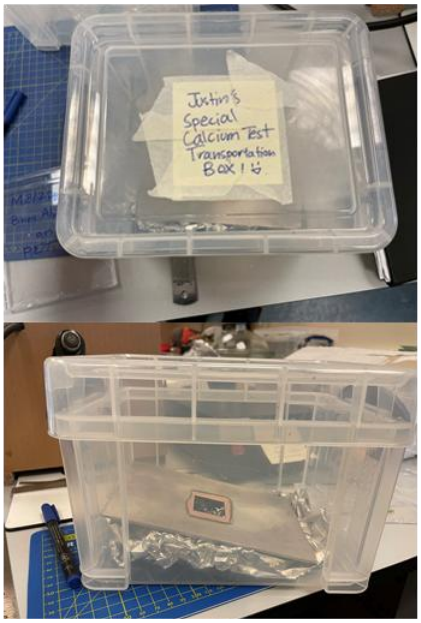
Noticed that this should reduce the number of contaminants while depositing the Calcium and Copper or less pinhole defects.





Current Setup

"Special Ca Test Box" – Seems to help in minimizing human contact and pre-reaction of calcium so far.



Different Curing Times of Epoxy - No significant difference from 5 mins. to 20 mins. (adhere) to glass.

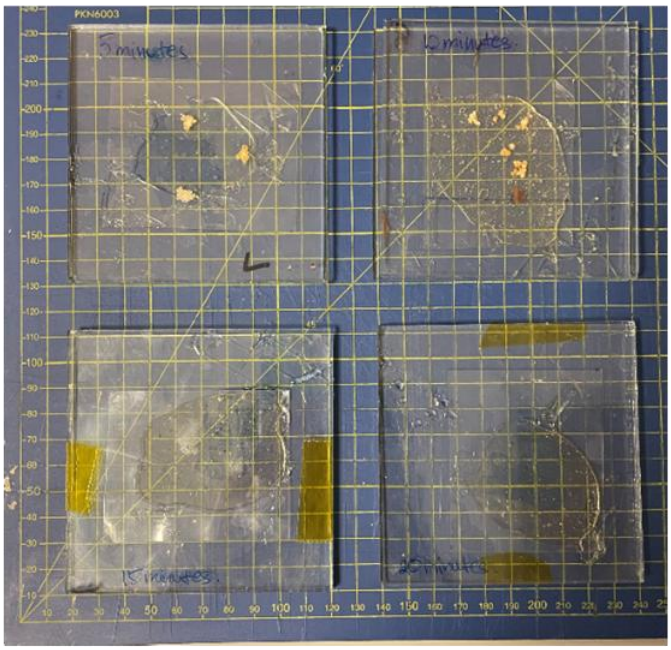


Figure 9-6: A cleanliness protocol was developed to prevent contamination and reduce dust artifacts during calcium testing, particularly during the deposition of calcium and copper. A dedicated container was introduced for transporting samples between the thermal evaporator and the calcium test box to limit contamination, it was also observed that varying epoxy curing times had no significant effect after five minutes of curing reducing the time of cure would reduce the amount of possible exposure to any possible impurities within the surrounding environment.

9.2 Uncoated PET Substrate Supporting Materials

9.2.1 Linear Dependence of Permeation on WVPP: Influence of Temperature and Experimental Variability

Permeation as a function of WVPP is illustrated in Figure 9-7, encompassing various datasets such as MOCON Aquatran 2 measurements, Calcium test data, and literature values. A generally linear relationship, consistent with Henry's Law, suggests that permeation scales proportionally with WVPP. Nevertheless, subtle differences among datasets and the impact of temperature deserve further analysis.

MOCON Aquatran 2 data (Figure 9-7, a) demonstrates a relatively clean, linear trend with minimal scatter, suggesting consistent experimental conditions and well-controlled temperature. When data are plotted with the different temperatures indicated, three slightly different gradients in the trends may be observed for the three different temperatures.

Calcium Test data (Figure 9-7, b) display more pronounced scatter and deviations from a neat linear pattern, making it challenging to determine if the slope remains uniform across different temperature conditions. This variability could stem from measurement sensitivity, less stringent temperature control, or other experimental factors. Without clearer resolution, it is difficult to ascertain whether similar trends observed in the Mocon data hold true. However, it is seen that it is closer in absolute value towards other literature in comparison to the MOCON Aquatran 2 data.

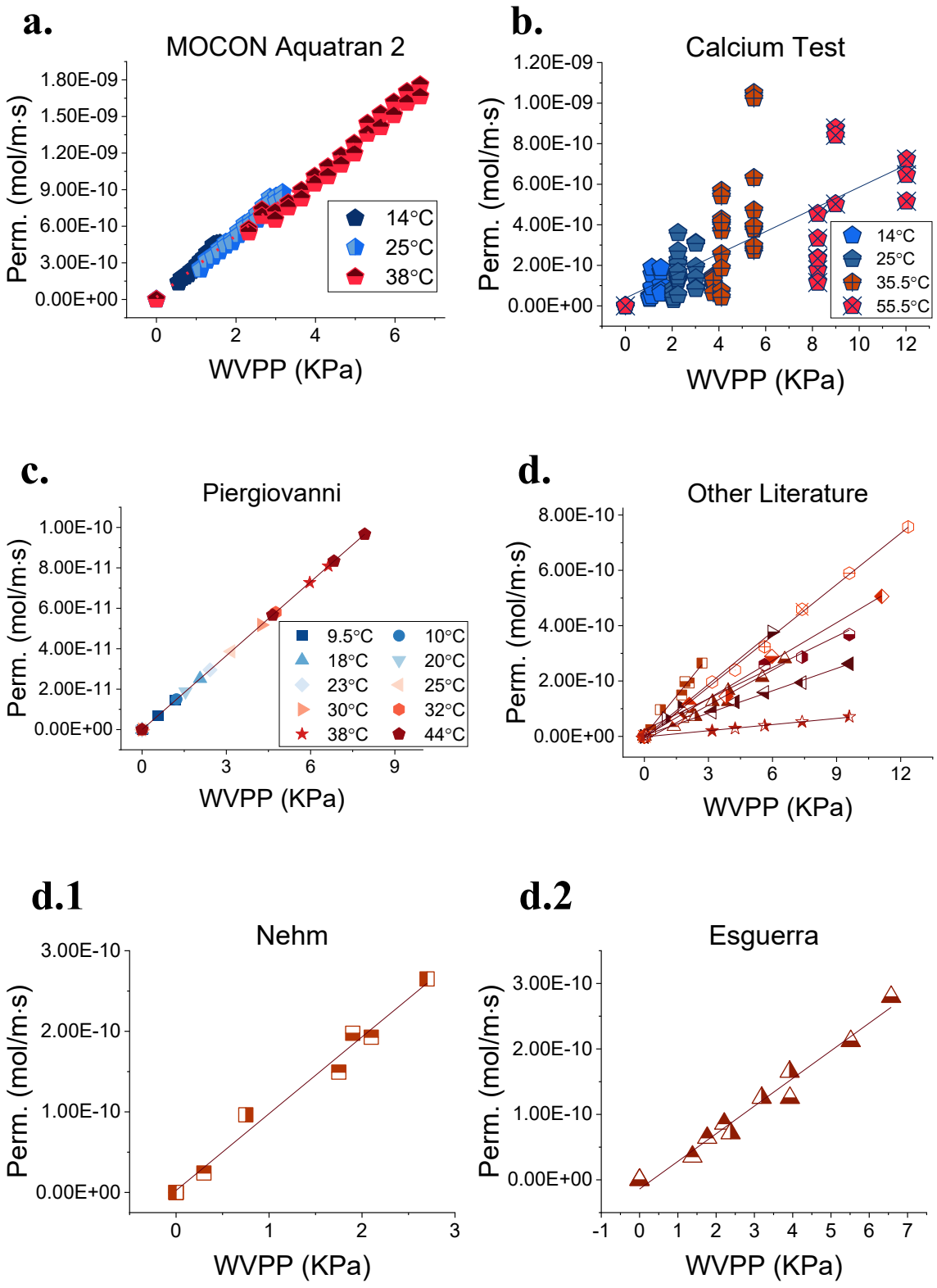
Literature values, Figure 9-7 **(c-d)** generally follow the expected linear relationship, especially at lower WVPP, but their slopes vary. This likely reflects

differences in experimental methods, material properties, and environmental controls, including temperature. Digging deeper into these various studies.

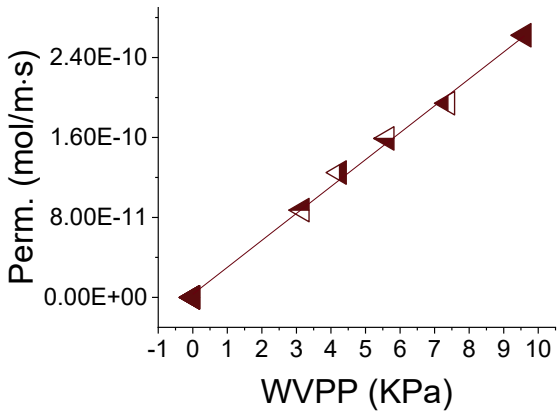
- Figure 9-7 **(c)**: Piergiovanni's study on 19 μm PET under different conditions demonstrates a strong linear relationship between permeation, and WVPP, as predicted by Henry's law. This relationship appears independent of temperature, indicating that WVPP predominantly governs permeation rates. Piergiovanni further explored the predictability of water vapor permeation rates, showing an almost straight line with respect to water vapor pressure and temperature. [249].
- Figure 9-7 **(d)**: Multiple studies on uncoated PET confirm a generally linear relationship between permeation and WVPP. These studies include:
    - (d.1) Nehm's data using 75 μm Melinex PET and an electrical calcium test, showing Henry's law "linear dependency" across a wide temperature range (20°C to 68°C) [258].
    - (d.2) Esguerra's WVTR prediction model tested at three temperatures (20°C, 30°C, and 40°C) and relative humidity (55% to 90%) using a 12 μm PET film. The study demonstrates having closer absolute value of permeation rates with temperature but exhibits the linear relationship [246].
    - (d.3) Erlat's data using 50 μm optical grade PET and Permatran W3/31, showing an activation energy of 40.6 KJ/mol with linear trends between permeation and WVPP [254].
    - (d.4) Schubert's e-Ca test on 125 μm Melinex ST 504, confirmed with Brugger WDDG, also shows a linear relationship [110].

- (d.5) Deng's data on 12 μm uncoated PET with silica particles, tested with MOCON Permatran W3/31 at 30°C to 45°C, shows permeation values that do not pass through the origin (as would be expected) but exhibit linearity between pressures [93].
- (d.6) Sobrinho's data on 13 μm biaxially oriented PET (ICI 800) tested at 25°C to 50°C shows a linear relationship up to 35°C, but deviations occur at higher temperatures [250].
- (d.7) Fahlteich's 75 μm PET (DuPont Teijin Melinex 400) tested with Brugger WDDG permeation tester across 15°C to 50°C shows a linear relationship, but reports lower activation energy (3.6 ± 1 KJ/mol) likely due to calculation methods [25].
- (d.8) BM Henry's data on 50 μm PET using MOCON Permatran W3/31 at 25°C to 45°C, reporting an activation energy of 49 ± 2 KJ/mol, shows a linear relationship relative to each other, though not passing through the origin [252].

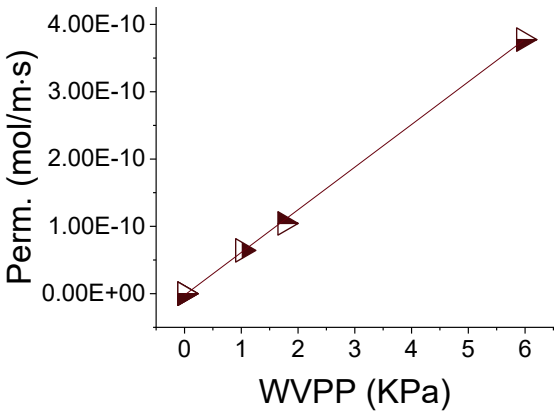
These results highlight the generally linear relationship between permeation and WVPP, though some variability is introduced by differences in material thickness, test methods, and conditions.


a.
MOCON Aquatran 2
Perm. (mol/m·s)
1.80E-09
1.50E-09
1.20E-09
9.00E-10
6.00E-10
3.00E-10
0.00E+00
0
2
4
6
WVPP (KPa)
14°C
25°C
38°C
b.
Calcium Test
Perm. (mol/m·s)
1.20E-09
1.00E-09
8.00E-10
6.00E-10
4.00E-10
2.00E-10
0.00E+00
0
2
4
6
8
10
12
WVPP (KPa)
14°C
25°C
35.5°C
55.5°C
c.
Piergiovanni
Perm. (mol/m·s)
1.00E-10
8.00E-11
6.00E-11
4.00E-11
2.00E-11
0.00E+00
0
3
6
9
WVPP (KPa)
9.5°C
10°C
18°C
20°C
23°C
25°C
30°C
32°C
38°C
44°C
d.
Other Literature
Perm. (mol/m·s)
8.00E-10
6.00E-10
4.00E-10
2.00E-10
0.00E+00
0
3
6
9
12
WVPP (KPa)
d.1
Nehm
Perm. (mol/m·s)
3.00E-10
2.00E-10
1.00E-10
0.00E+00
0
1
2
3
WVPP (KPa)
d.2
Esguerra
Perm. (mol/m·s)
3.00E-10
2.00E-10
1.00E-10
0.00E+00
-1
0
1
2
3
4
5
6
7
WVPP (KPa)

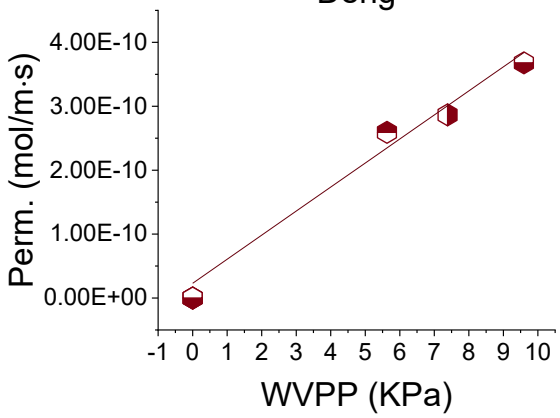
d.3



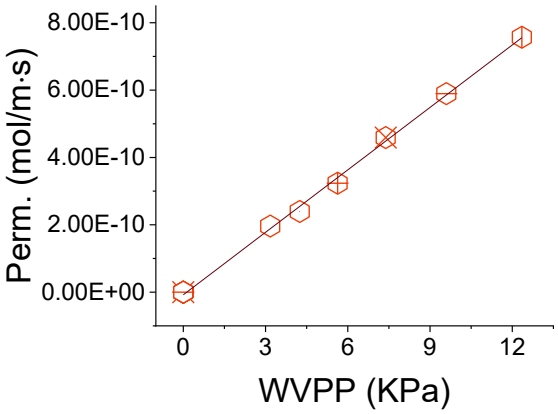
d.4



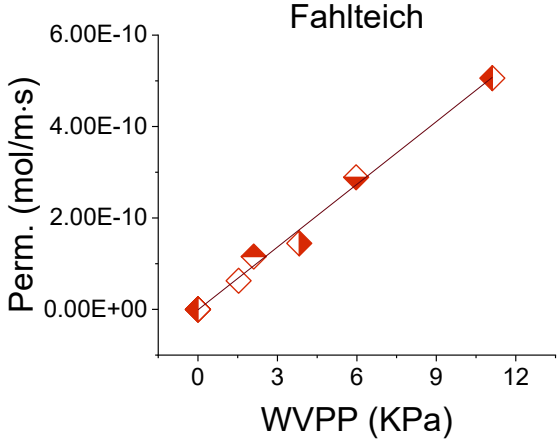
d.5



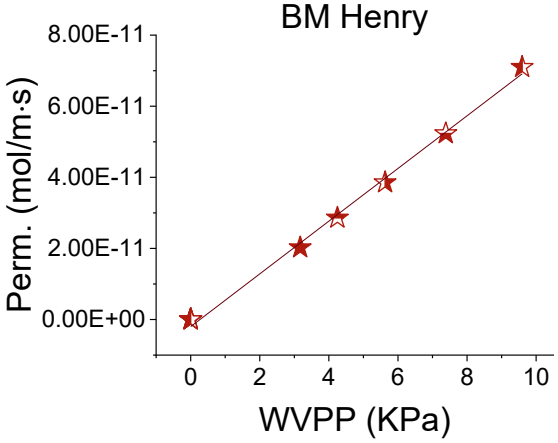
d.6



d.7



d.8



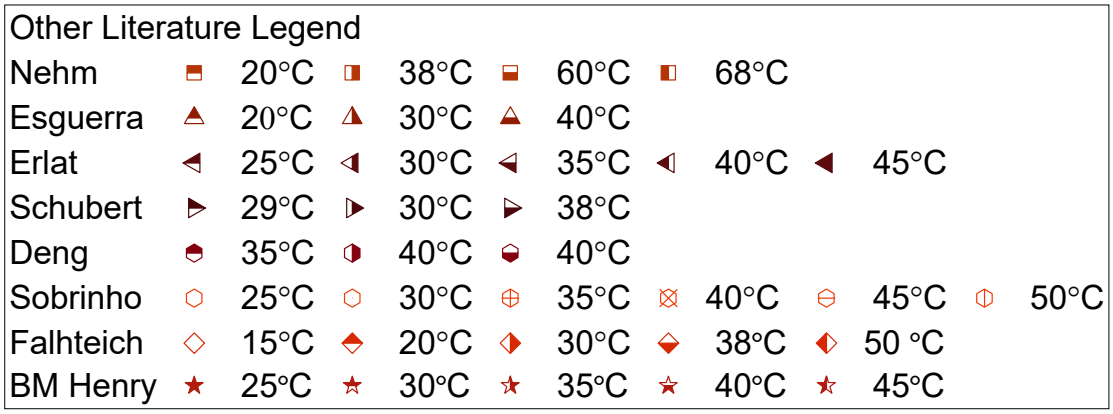


Figure 9-7: Permeation plots over water vapor pressure highlight factors affecting the applicability of Henry's law and its linear relationship. (a) MOCON Aquatran 2 data shows permeation rates clustering by temperature, displaying a clear linear trend. (b) Calcium test data aligns with the general trend observed in the MOCON data and literature. (c) Piergiovanni's data reports numerous WVTRs under varying conditions, showing a strong linear trend originating from the origin [249]. (d) A compilation of literature data on uncoated PET substrates at various temperatures shows consistent linear trends, though variations increase with different methods, parameters, and film types [25, 93, 110, 246, 250, 254, 258].

9.3 Aluminium Oxide (ALD) Coated PET Supporting Materials

9.3.1 Relevant Literature Summary on ALD AlO_x Barrier Coatings

Previous studies have demonstrated the effectiveness of ALD-deposited Al_2O_3 coatings as barrier layers. Ghosh *et al.* (2005) reported lifetimes exceeding 1000 hours at 85°C and 80% relative humidity using 180 nm of Al_2O_3 for cathode encapsulation [318]. Similarly, Park *et al.* showed an increase in device lifetime from 72 hours (uncoated) to 320 hours with ALD-deposited Al_2O_3 [320].

Lei *et al.* used Plasma-Assisted ALD (PE-ALD) to deposit Al_2O_3 on 12 µm PET, with plasma enhancing reactivity and allowing lower deposition temperatures. This significantly reduced oxygen transmission rates (OTR), attributed to the tightly packed

Al_2O_3 nuclei. The study linked the OTR improvement to pinhole defects and interfacial groups on the PET surface [426].

In line with this, Park *et al.* also studied ALD polymer encapsulation on polyether sulfone (PES) substrates with various coatings, process parameters, and thicknesses. They deposited 30 nm of AlOx on PES, reporting a WVTR of 0.062 g/m²·day at 38°C and 100% RH. With both sides coated, the film exhibited excellent barrier properties even at low thicknesses. A single-sided coating showed higher WVTR, with values of 0.409 g/m²·day for 30 nm, 0.141 g/m²·day for 40 nm, and 0.102 g/m²·day for 50 nm. Higher processing temperatures further improved barrier performance [61].

Complementary to the work above, Choi's work supports the finding that higher processing temperatures for ALD Al_2O_3 coatings result in better barrier properties. Choi tested 100 nm Al_2O_3 on PES substrates, showing that films processed at 200°C had a higher mass density of 2.82 g/cm³ and a lower WVTR of 5.0×10^{-4} g/m²·day. In contrast, films processed at 50°C had a lower density of 2.50 g/cm³ and a much higher WVTR of 2.1×10^{-2} g/m²·day. This difference is attributed to the lower O-H ratio at 200°C (25.8%) compared to 50°C (38.1%). Surface morphology remained unaffected, with all films having a root mean square roughness of 0.35 ± 0.15 nm [427].

Other work by Groner *et al.* investigated Al_2O_3 ALD at temperatures as low as 33°C and observed that although film density decreased from 3.0 to 2.5 g/cm^3 as temperature dropped, surface morphology remained consistent with a root mean square roughness of 4 ± 1 Å across all conditions [322]. These findings support earlier observations that lower temperature films are less dense but not necessarily rougher.

DuPont research by Carcia and colleagues showed that ALD-produced Al_2O_3 films provide better moisture barriers when made thicker and at higher temperatures. They attributed the lower activation energy of films made at lower temperatures to increased hydrogen and oxygen defects, which result in a more permeable barrier [428].

Carcia and colleagues emphasized the importance of chemical defects in ALD Al_2O_3 films, proposing that moisture permeation occurs through percolating OH-defect clusters rather than pinholes. Using the Ca test, the measured WVTR in Al_2O_3 films deposited on PET substrates coated on only one side. Results show that films grown at 100 °C exhibited WVTR's at or below the glass control limit approximately (~5×10^{-5} g/m^2·day at 38 °C / 85% RH) indicating highly effective barrier performance, though these values may also reflect the Ca test's detection limits. Notably the ~ 7 nm films grown at 50 °C, fully oxidized within seven days, which contrasts with the more rapid degradation in the ~10 nm films in this thesis under similar conditions [336].

Additionally, Carcia's earlier work reported ultra-low WVTRs for Al_2O_3 coatings: 1.7×10^{-5} g/m^2·day at 38°C and 6.5×10^{-5} g/m^2·day at 60°C, with an Ea of 52 kJ/mol for a 25 nm layer on PET. The glass control, with an Ea of 58 kJ/mol, raised concerns about epoxy permeation, suggesting that the observed Ea was likely due to the epoxy rather than the glass, which is impermeable [218].

It is cautioned that edge defects and lateral permeation may have influenced the Ea measurements. The epoxy used to seal the samples (Brominated Bisphenol A with a dicyandiamide curing agent and TMBDDA catalyst) has reported Ea of only 4.5 kJ/mol, which is significantly lower than that of ALD Al_2O_3 coatings reported by Carcia *et al* [197, 218]. This discrepancy raises questions about whether the measured Ea reflects

permeation through the barrier layer alone, or whether interfacial or lateral transport such as through the epoxy and then the P*Et al*so contributed. As such, these values may reflect complex interfacial transport phenomena rather than intrinsic barrier diffusion properties.

Multilayers have proven effective in achieving lower WVTRs. Dameron *et al.* created Al_2O_3 and SiO_2 ALD multilayers on polyimide and PEN substrates, showing that while Al_2O_3 alone deteriorated under H_2O and HTO vapor exposure, adding SiO_2, which resists hydration, reduced WVTR from ~1×10^{-3} g/m²·day to ~5×10^{-5} g/m^2·day [325, 429]. Dameron *et al.* discusses the barrier performance of single-layer Al_2O_3 and SiO_2/Al_2O_3 bilayers, with WVTR values reaching ≤5×10^{-5} g/m^2·day. However, adding more than two bilayers offers no measurable improvement and may degrade performance due to film brittleness and cracking. At very low permeation rates, performance appears to be limited by intrinsic material or substrate properties, making subtle differences in barrier effectiveness increasingly difficult to detect [325].

On another hand, literature by Abdulagatov *et al.* found Al_2O_3 to be fragile against water corrosion, and improved barrier properties by adding a TiO_2 capping layer [349]. This incorporation of additional inorganic materials into alumina (Al_2O_3) layers has significantly enhanced their performance as barrier encapsulants, reportedly extending the shelf life of organic photovoltaics (OPVs) to nearly 7000 hours [430]. Techniques like plasma treatment and surface modification of alumina nanoparticles have also been shown to improve dispersion and compatibility of Al_2O_3 based barriers [431].

Groner *et al.* studied Al_2O_3 ALD deposition on PEN and polyimide substrates, varying thicknesses from 1 to 26 nm at temperatures of 100 to 175 °C. Their results revealed: (1) OTR values below 5×10^{-3} cc/m^2·day MOCON Detection limit, were

achieved showing exceptional barrier performance of these thin coatings, (2) Al_2O_3 ALD films show significant WVTR improvements from 10 nm ($\approx 2 \times 10^{-3}$ g/m²·day) with no further gains beyond a critical thickness of 25 nm, (3) Al_2O_3 ALD films (25 nm) on polyimide (Kapton) maintained a WVTR of 1×10^{-3}g/m²·day after repeated flexing to ~2 cm, showing no cracking or performance degradation [217].

Klumbies emphasized the significance of defect densities and sizes in controlling barrier properties. They noted that low-temperature atomic layer deposition (ALD) can lead to high defect densities, which depend on the substrate's surface roughness, potentially causing water ingress and device failure due to the oxidation of π-conjugated bonds by moisture [73, 255]. The study identified an Al_2O_3 thickness of 25 nm for optimal barrier performance, while thinner layers (5 to 10 nm) failed to provide a consistently pinhole-free barrier. Additionally, defect density decreased by approximately half with every 23 nm increase in Al_2O_3 thickness (from 15 to 100 nm). The research also highlighted the importance of compatibility between the Al_2O_3 coating and the glass substrate, as significant cracking was observed in 100 nm thick coatings, likely due to differing thermal expansion coefficients between coating and substrate [334].

Jarvis *et al.* studied PET and PEN substrates coated with 24 nm of ALD Al_2O_3, measuring WVTR using an HTO permeation method. Their findings aligned with the idea that thicker coatings and substrates reduced WVTR consistent with previous literature. However, WVTR values 10^{-1} g/m^2·day were reported, higher than those typically seen in literature. The HTO permeation measurement method, defects due to surface contamination, or the coating thickness used may be factors contributing to the reported higher WVTR. Notably it is mentioned that O_2 plasma treatment improves the

WVTR, with a lowest WVTR observed to be 3.1×10^{-3} g/m^2·day with a 125 μm PEN substrate, illustrating the critical role of substrate properties and surface preparation in barrier performance [260].

Another common concern was the high processing temperature (200°C) typically required for ALD to achieve continuous, pinhole-free films, which could degrade most polymer substrates [33]. However, Meyer *et al.* demonstrated that excellent barrier films could be produced at a much lower temperature of 80°C, with their 130 nm Al_2O_3/ZrO_2 nanolaminate achieving a WVTR of $4.7 \times 10^{-5}\mathrm{g/m^2 \cdot day}$ at 70°C and 70% relative humidity, with an activation energy of 92 kJ/mol [429, 432].

Langereis *et al.* challenged the notion that lower deposition temperatures yield inferior barriers by using plasma assisted ALD (PE-ALD) to deposit Al_2O_3 PEN substrates, achieving WVTR of $2 \times 10^{-2}\mathrm{g/m^2 \cdot day}$ at 10 nm to $5 \times 10^{-3}\mathrm{g/m^2 \cdot day}$ at 20 nm (~75% reduction in WVTR with the increased thickness). This performance was attributed to the PE-ALD process enhancing film uniformity and increasing hydroxyl content to improve the overall moisture resistance [321].

Mahmood's more recent work examined OLED encapsulation with low-temperature (85°C) ALD-grown Al_2O_3 layers. Using an electrical Ca test, Mahmood found that barrier properties improved with thickness up to a critical point (~43 nm), beyond which internal stress cracks could reduce WVTR performance. Mahmood also highlighted concerns raised by Carcia regarding edge effects and adhesive permeation pathways [55, 197, 255]. The study by Mahmood concluded that barrier to device (B2D) encapsulation set-up, where thin Al_2O_3 layer is directly deposited onto an OLED device without additional glue or barrier films, outperform barrier to barrier (B2B) encapsulation

which uses an additional glued barrier film. This improved performance was attributed to the B2D configuration's reduced overall thickness and the elimination of glue layers, which can introduce mechanical stress, delamination risks, and reduced flexibility. As a result, B2D encapsulation offers enhanced mechanical stability, flexibility and barrier performance [255].

In summary, several studies have been made in using ALD-coated Al_2O_3 as an encapsulation method, both as single and multilayer barriers. However, gaps remain in understanding the permeation mechanisms and factors influencing transmission rates in barrier films. The following sections will address these issues and explore potential solutions.

9.3.2 Sample Preparation

As detailed in the Methodology Section (MOCON Aquatran 2 Sample Preparation: Section 2.3 and ALD Deposition: Section 2.4.8), PET substrates were coated with various thicknesses of AlO_x via ALD. The films were cut to fit a 1 cm^2 foil mask for MOCON Aquatran testing. They were tested at temperatures of 14°C, 25°C, and 38°C with 100% relative humidity (controlled by saturated sponges).

Each sample was independently condition in both Cell A and Cell B for at least 8 hours prior to testing, with no transfer between cells. This preconditioning ensured that the samples reached environmental equilibrium within their respective cells. WVTR measurements were only initiated once a stable, steady-state signal was observed which is consistent with MOCON's recommended convergence criteria for high-barrier films.

9.3.3 ALD AlO_x Thickness (Ellipsometer)

To verify the thickness of the AlO_x layer on the PET substrate, a 10 x 10 mm silicon (Si) chip was included during each deposition. Thickness was measured using an Ellipsometer (Film Sense FS1 4-Wavelength Fixed Angle Ellipsometer). The Ellipsometer measures the ratio of reflected light amplitudes (Psi, ψ) and phase difference (Delta, Δ) after polarized light is reflected from the sample. A theoretical model, based on refractive index and initial thickness estimates, is adjusted to match the measured ψ and Δ values. For this study, a Cauchy model, suited for weakly absorbing dielectric layers, provided the best fit, outperforming the Lorentz or Drude models used for higher absorption materials [433-435].

Figure 9-8 (a), shows a half-coated Si chip, with polyimide tape covering one side during deposition, highlighting the visual difference measured in the ellipsometer. Despite ALD's reputation for uniform coatings, Figure 9-8 (b) reveals some variation in coating thickness, indicating that substrate location and placement in the chamber can affect uniformity.

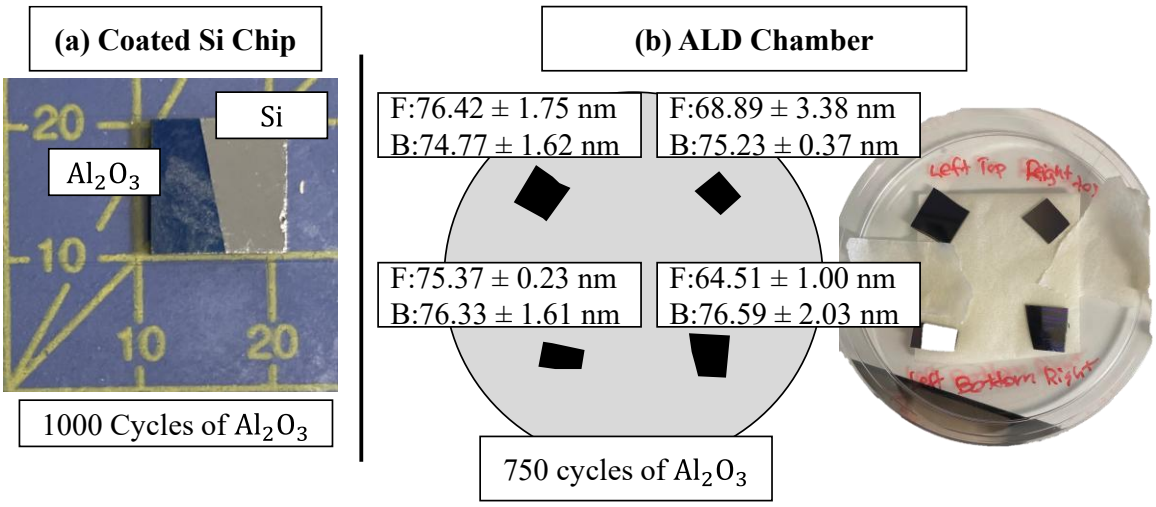


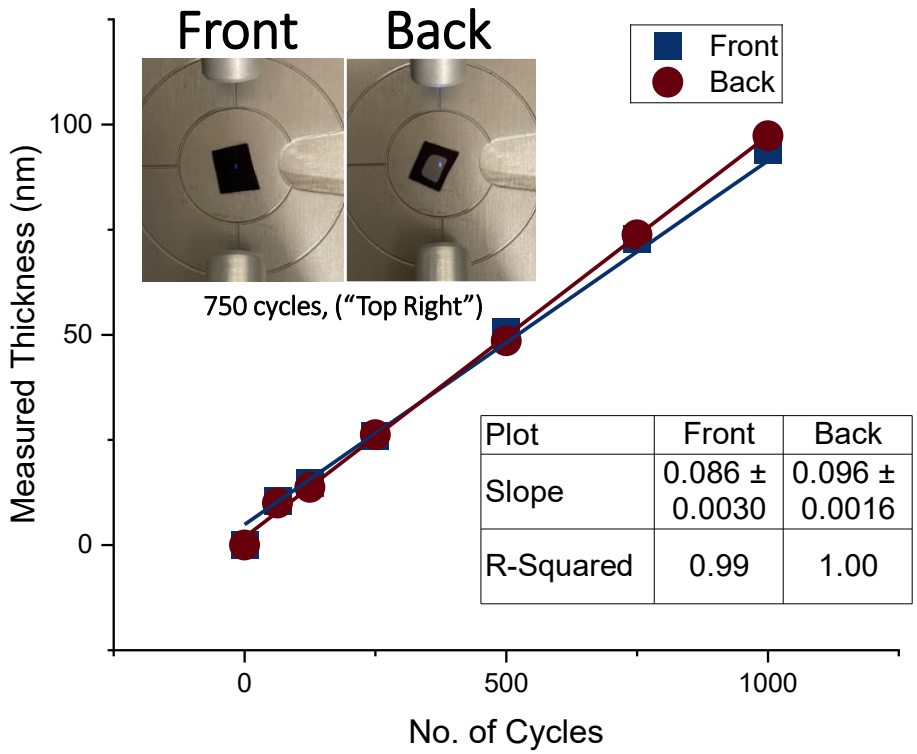
Figure 9-8: (a) A half-coated Si chip (10 x 10 mm) with 1000 cycles of AlO_x shows a clear visual contrast between the coated side (left) and the uncoated Si surface (right). (b) Four Si chips were placed at equidistant corners inside the ALD chamber to assess thickness variation. Ellipsometer measurements from both front (F) and back (B) sides after 750 cycles showed an average AlO_x thickness of ~73.51 ± 4.45 nm across the chips.

Figure 9-9 presents the measured thicknesses on both sides of Si chips after various numbers of ALD-AlO_x cycles, which theoretically should yield growth rates of 0.90 to 1.0 Å/cycle at 150°C (with similar results at 80°C). As calculated, the estimated growth rate agrees in both sides of the silicon chip with around (Front: 0.86 and Back 0.96 Å/cycle).

For lower cycle counts, such as 63 and 125 cycles, the measurements deviated significantly from the expected thicknesses of ~6.3 nm and ~12.5 nm – showing errors of 61.82% and 14.49%, respectively. This discrepancy is attributed to the dependency of the Refractive Index (RI) on the film density during the initial nucleation stages of ALD growth. As established by Puurunen and Groner *et al.*, low temperature ALD growth begins with an island growth mode where the film is discontinuous and porous [176, 322]. This porosity can lower the effective RI compared to the bulk oxide. Because the standard Cauchy model used here assumed a denser film (or higher RI), the regression analysis compensated for the phase shift by overestimating the physical thickness. Therefore this possible large discrepancy, at low cycles may be a signature of the microstructural transition from a low density nucleation layer to a continuous dense bulk film rather than a failure of the deposition rate. While independent verification (*e.g.*, via TEM or X-ray Reflectivity) would be required to decouple the thickness from the RI definitively, the observed optical deviation is consistent with the widely reported behaviour of ALD nucleation on polymers.

For higher cycles, the discrepancies were less significant. At 250 cycles, the measured thicknesses were 26 ± 0.26 nm (front) and 26.26 ± 1.57 nm (back), close to the expected 25 nm. A similar accuracy was observed at 500 cycles (50.56 ± 1.54 nm front, 48.58 ± 1.65 nm back), 700 cycles (72.69 ± 2.69 nm front, 73.74 ± 1.73 nm back), and 1000 cycles (93.92 ± 2.47 nm front, 97.33 ± 1.19 nm back), indicating uniform coating on both sides.

However, larger errors emerged at 750 and 1000 cycles, with deviations of 2 nm and ~5 nm from the expected thicknesses of 75 nm and 100 nm, respectively. In contrast, the 250 and 500 cycle measurements were off by just 1 nm. These results suggest that while the coating is uniform across both sides, small deviations in the growth rate may accumulate over many cycles, resulting slightly greater thickness discrepancies at higher cycle counts. This corresponds to an approximately constant percentage error across the tested range, consistent with typical ALD process variability. Coating both sides of the substrate, as demonstrated by Park *et al.*, improves barrier performance by reducing overall defect-related permeation. This configuration lowers the effective defect density and provides additional resistance paths for moisture ingress [61].



Cycle	Front		Back	
	Value (nm)	Std. Dev (nm)	Value (nm)	Std. Dev (nm)
63	10.39	0.07	10.00	0.00
125	14.88	0.48	13.74	0.71
250	26.08	0.26	26.26	1.57
500	50.56	1.54	48.58	1.65
750	72.69	2.69	73.74	1.73
1000	93.92	2.47	97.33	1.19

Figure 9-9: Ellipsometer measurements of AlO_x-coated Si chips (front and back) over various ALD cycles show significant deviations at lower cycles (63 and 125) and underestimations at higher cycles (750 and 1000), while 250 and 500 cycles yielded optimal growth. Interestingly, at 750 cycles, the back side (75.23 ± 0.37 nm) was more consistent with the predicted 75.0 nm than the front (68.89 ± 3.38 nm), despite appearing less coated. This suggests visual inspection of the Si chip alone may be misleading in assessing coating quality or deposition for barrier films.

For all cycles, the average measured thickness was reported: 250 cycles (26 nm), 500 cycles (50 nm), 750 cycles (73 nm), and 1000 cycles (96 nm) which align closely

with the expected linear growth trend. In contrast, lower cycle counts at 63 cycle and 125 cycles deviated from the expected values of ~6.3 nm and 12.5 nm (based on the nominal growth rate of 1 Å/cycle) and were instead measured at 10 nm and 14 nm, respectively. This discrepancy suggests greater variability or possible overestimation in thickness measurements at low cycle numbers.

Although similar amounts of AlO_x were deposited on both sides of the PET substrate, differences in adhesion between PET and silicon likely introduced measurement errors. Since ALD was performed on both sides, the total thickness reflects the combined barrier layer. In the Ca test, however, only one side (the Ca-facing side or unexposed side) is directly exposed to the environment, while the reverse side is shielded by the PET.

Nonetheless the exposed coating may be more susceptible to mechanical damage or thinning, potentially modulating the rate of water vapor uptake, it is more likely that sharp defect spots seen in the Ca test result from permeation through the defects on the unexposed side, where water vapor ultimately exits the PET and reaches the Ca. This supports the idea that water vapor migrates laterally within the PET and passes only through discrete defect sites in the unexposed AlO_x coating, resulting in localized Ca oxidation. The coating on the exposed side, while not directly imaged, could still influence the rate and onset of permeation by controlling the gradient across the substrate.

For MOCON measurements, in which both sides of the sample are exposed, coating damage or non-uniformities on either side of the coating can more directly impact WVTR performance, making surface integrity critical in those tests.

9.3.4 ALD Processing Temperature and Sample Masking Considerations

9.3.4.a Influence of ALD Processing Temperature

Chamber temperature plays a crucial role in the creation of barrier layers, as high temperatures can degrade certain substrates, and very low temperatures can result in incomplete reactions, poor film quality and adhesion. An optimal processing temperature window is needed to produce excellent barrier layers. To assess the impact of temperature during barrier layer deposition on the resulting WVTR of the barrier material, a comparison was made between typical (150°C) and lower (80°C) processing temperatures.

Figure 9-10 (log scale) shows the WVTR values of four 96 nm AlO_x samples (1000 cycles) on PET, processed at 80°C and 150°C, and tested with the MOCON Aquatran (50 cm^2 full-size samples without an Al mask).While overall variation in WVTR is small, one sample processed at 80°C exhibited higher WVTR values (0.8 ± 0.005 g/m^2·day at 38°C), compared to the other to the other 80°C processed sample (0.16 ± 0.003 g/m^2·day) and to the high-temperature 150°C processed samples (0.25 ± 0.006 g/m^2·day and 0.04 ± (4.3×10^{-4}) g/m^2·day). This slight increase in WVTR, suggests potential coating damage in sample as this sample consistently incurs a higher WVTR across all temperatures used during barrier testing. More importantly it shows that despite slightly lower WVTR's are produced at 150°C processed samples, the 80°C processed samples are highly comparable and similar in terms of overall barrier properties or WVTR.

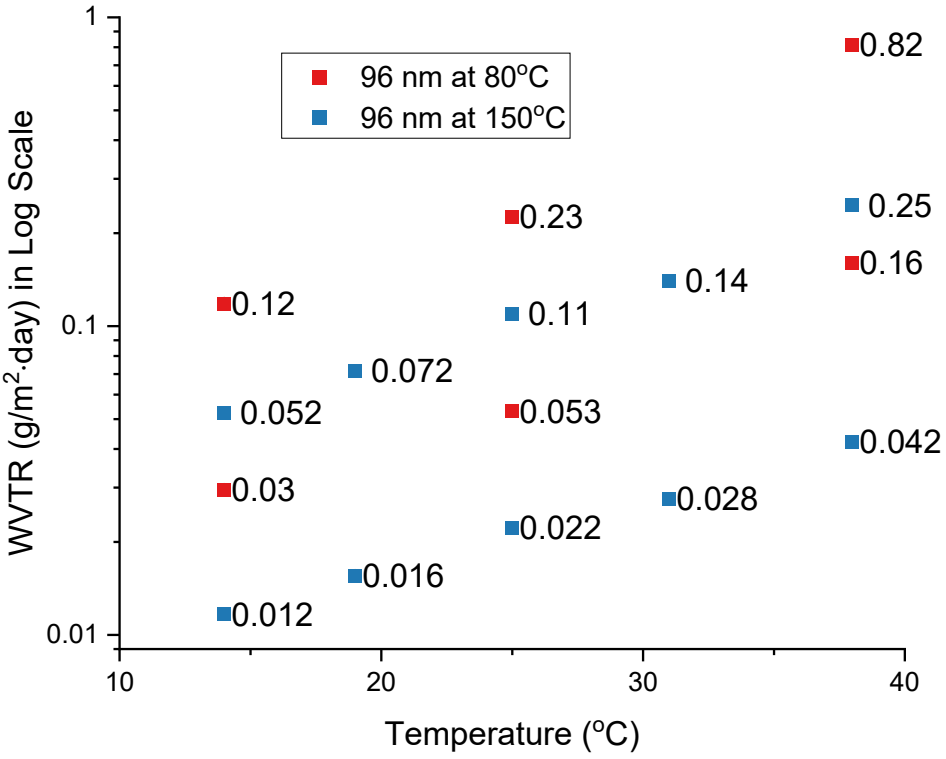


Figure 9-10: WVTR values (log scale) of 96 nm AlO_x barriers (1000 cycles) on PET, processed at 80°C and 150°C, tested with the Mocon Aquatran. The results show low WVTRs overall, with minimal variation except for one outlier at 80°C processed sample, likely due to damage on the exposed side during testing. ***Note:*** *50 cm² full-size samples were tested without an Al mask.*

Activation energy calculations (Figure 9-11) show higher values for low-temperature films (59.97 ± 9.88 KJ/mol and 52.57 ± 8.05 KJ/mol) compared to high-temperature films (46.67 ± 2.58 KJ/mol and 38.85 ± 1.64 KJ/mol). The higher activation energy after low temperature deposition suggests nano-defects may have a greater contribution to permeation, while high temperature deposition led to more macro-defects, with activation energy comparable to that of the bare substrate (~42 KJ/mol). The lower temperature (80°C) is near the PET substrate's glass transition temperature (69–85°C [277-279]), while the higher temperature (150°C), being significantly above it, may

soften the polymer, increasing micro-defects in the barrier layer. This softening, noted when placing the substrate in the heated ALD chamber, is consistent with reports that PET retains its mechanical properties only up to 175°C [279, 436]. Thus, processing at higher temperatures may have increased micro-defects in the barrier layer.

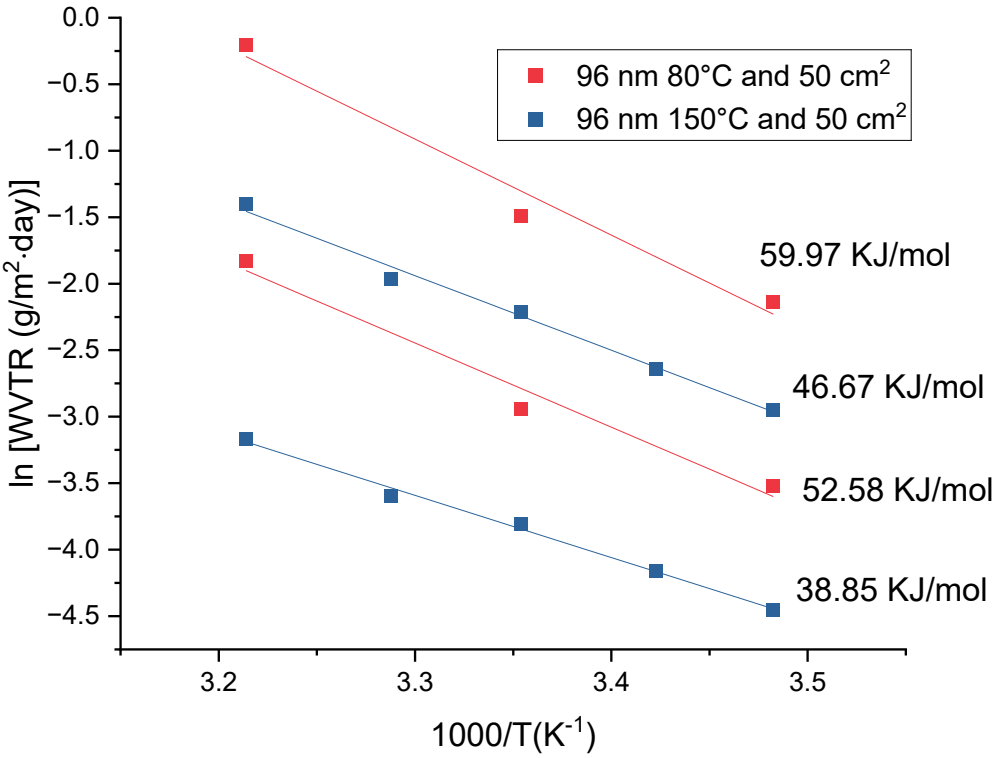


Figure 9-11: Natural log of WVTR vs. reciprocal temperature, using the Arrhenius Equation to estimate activation energy in barrier samples, illustrating slight variations due to different film production temperatures and their effect on defects and overall barrier properties.

9.3.4.b Masking and Sample Defects in ALD AlO_x WVTR

Due to the cost of creating full-size ALD samples (50.0 cm^2) for the MOCON Aquatran, smaller samples using a mask (1.0 cm^2) were utilized. Figure 9-12 compares the WVTR values measured with the Aquatran using full sized-samples and the small

(masked) samples, for the cases of 750-cycle (73 nm) and a 1000-cycle (96nm) AlO_x samples, deposited at 80°C.

Masked samples generally exhibited greater variability in WVTR measurements compared to unmasked ones (Figure 9-12). This is likely due to the smaller area being measured in masked tests, where any local defects can disproportionately impact the result. In contrast, unmasked measurements average over a larger surface area, which can help smooth out the influence of isolated imperfections.

Although some masked samples recorded higher WVTR values, such as in the 750-cycle case, the variability observed across replicate masked samples suggest that masking amplifies the effect of local film heterogeneities, rather than producing a consistently higher barrier permeability. Additionally, the masking process may introduce additional handling steps that risk damaging the barrier film, further contributing to measurement scatter.

As argued beforehand, masking has minimal impact on the WVTR values of uncoated samples or substrates (Table 9-1), This is because, in the absence of a barrier layer, the substrate itself is the primary determinant of permeation behaviour.

In contrast, when an ALD AlO_x coating is applied the barrier layer becomes the dominant control on WVTR, and is highly sensitive to localized damage, defects or surface irregularities. As a result, any non-uniformities introduced during masking or handling have a much greater impact on the measured WVTR of coated samples, amplifying the variability and leading to more pronounced differences compared to uncoated substrates.

In conclusion, masking appears to influence WVTR measurements due to sample specific factors such as defects in barrier coating which are amplified with a smaller tested area.

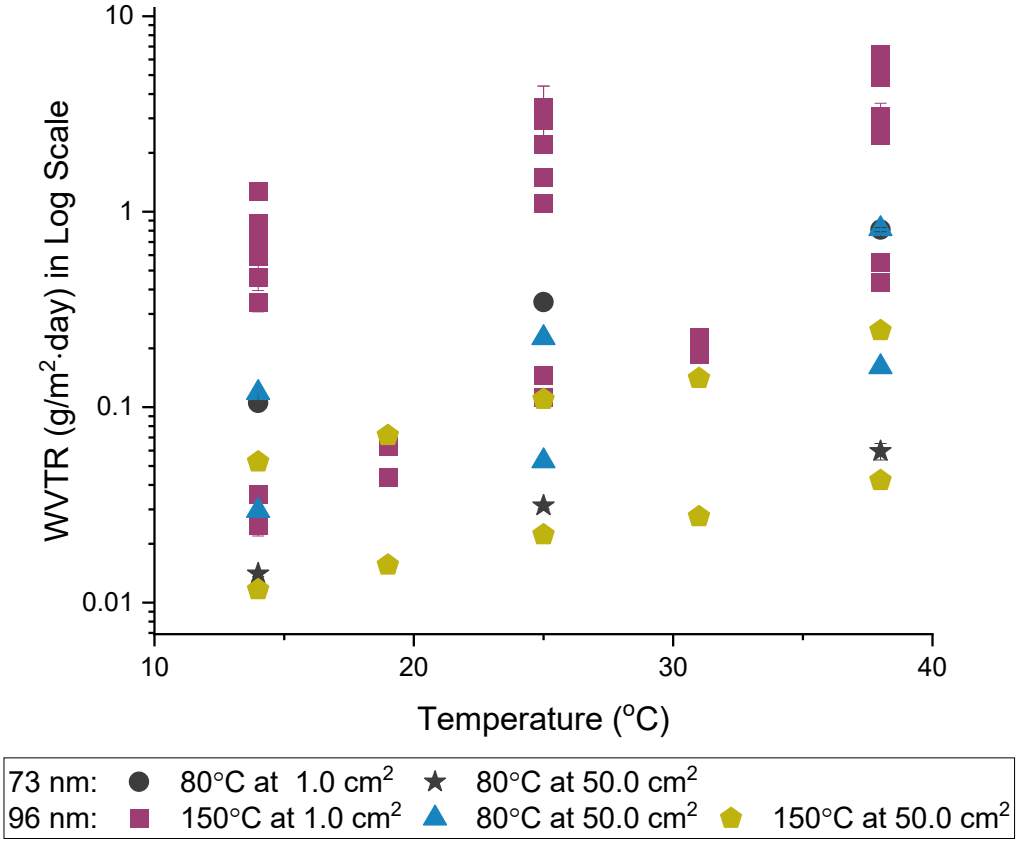


Figure 9-12: Effect of masking on WVTR values for 73 nm (750 cycles) and 96 nm (1000 cycles) with both masked (1.0 cm^2) and unmasked (50 cm^2) AlO_x, showing the slight variation of adding a mask which may increase the overall measured WVTR respective to the same thickness and condition.

9.3.4.c Summary of Processing Temperature and Masking in ALD

Processing temperature and masking of ALD samples can influence the WVTR values measured by the MOCON Aquatran. While masking, in most cases, increased the measured WVTR, in general, the two tested processing temperatures generally produced

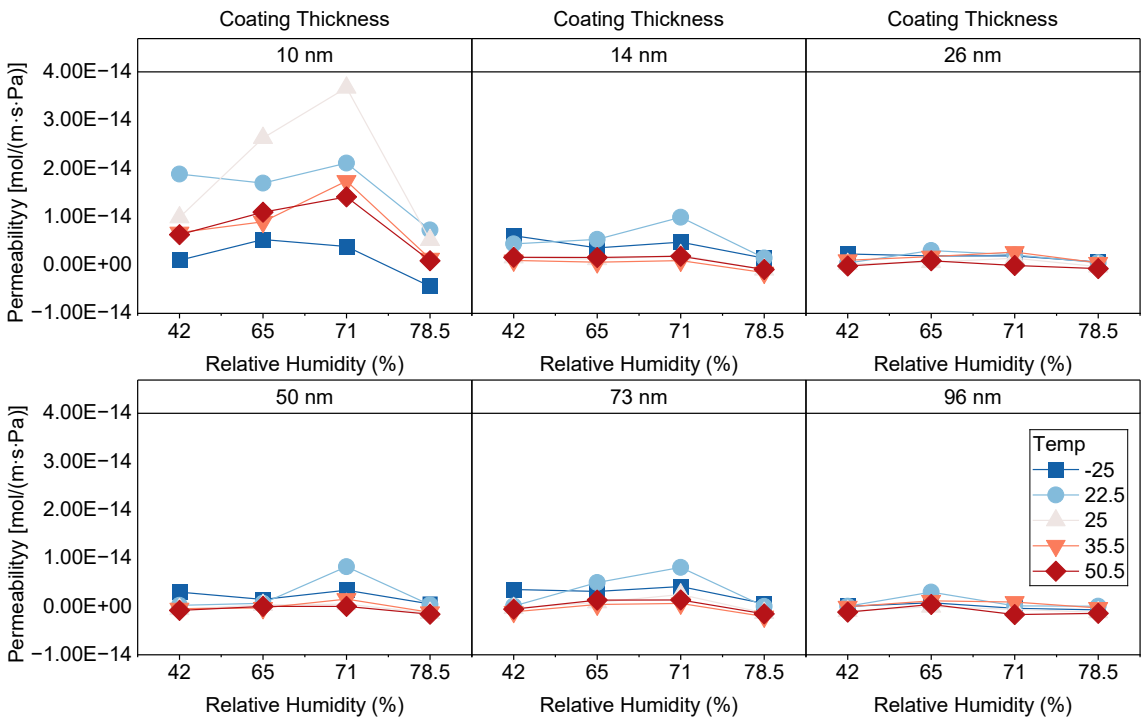
films with WVTR's within a similar spread of values, so the processing temperature is not observed to have a strong effect in this range. In all cases the trend in WVTR with measurement temperature was similar, suggesting that the differences in WVTR between samples reflects a different population density of defects of the same nature. This said, most of the samples were masked, and most were deposited at 150°C, as this condition consistently yielder lower WVTR values and more effective barrier performance.

9.3.5 Statistically Verifying Influence of Temperature and Relative Humidity Towards Permeability of AlO_x films on PET Substrate.

The relationship between temperature, relative humidity, coating thickness, and permeability is unclear from Figure 9-12, necessitating ANOVA analysis. Figure 9-13 illustrates these effects on permeability (linear and logarithmic scales).

The results show that coating thickness as dominant factor ($P = 3.36 \times 10^{-06}$), and that interactions between coating thickness and temperature ($P = 0.905$) and RH ($P = 0.318$), as well as isolated environmental factors lack statistically significant.

This suggests that environmental conditions during Ca testing are less critical to permeability than intrinsic substrate properties, such as uncoated bare PET. Consequently, permeability estimates depend more on coating thickness than environmental variability, improving the accuracy of WVTR assessments under fluctuating conditions.


Coating Thickness
10 nm
14 nm
26 nm
50 nm
73 nm
96 nm
Permeabilityy [mol/(m·s·Pa)]
4.00E−14
3.00E−14
2.00E−14
1.00E−14
0.00E+00
−1.00E−14
42
65
71
78.5
Relative Humidity (%)
Temp
-25
22.5
25
35.5
50.5

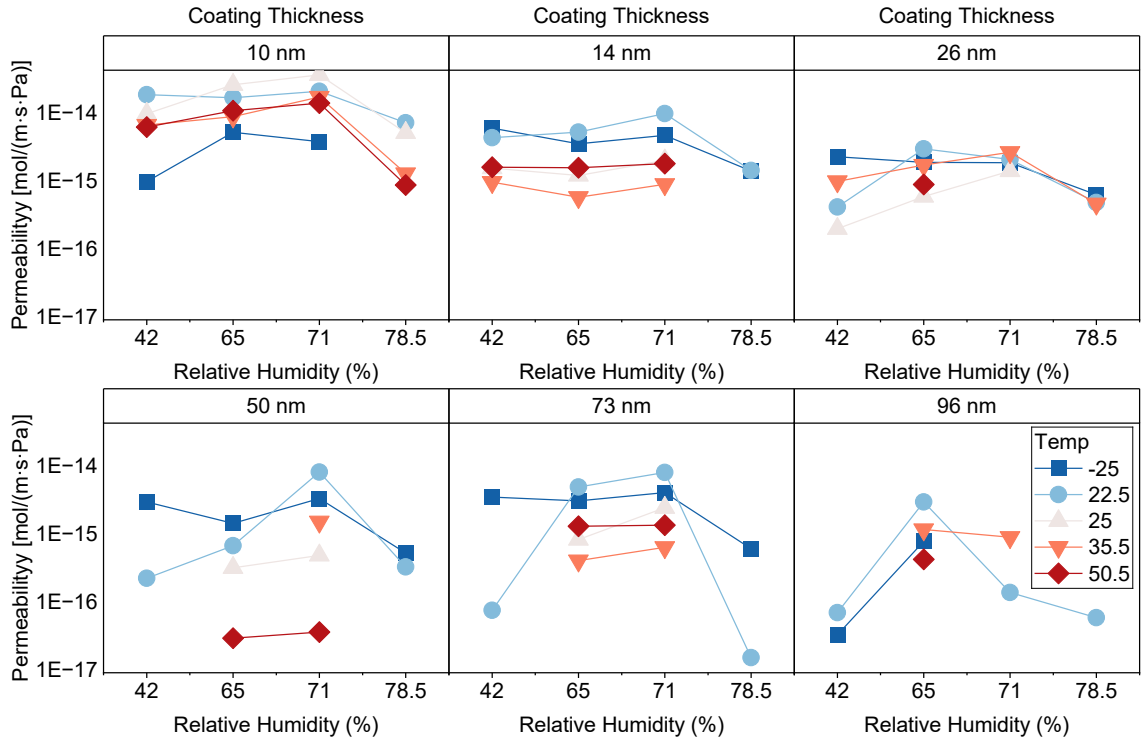

Coating Thickness
10 nm
14 nm
26 nm
50 nm
73 nm
96 nm
Permeabilityy [mol/(m·s·Pa)]
1E−14
1E−15
1E−16
1E−17
42
65
71
78.5
Relative Humidity (%)
Temp
-25
22.5
25
35.5
50.5

Figure 9-13: Summary of ALD AlO_x coating thickness, temperature, and relative humidity on permeability, highlighting coating thickness as the primary factor in barrier performance. Indicating that environmental conditions, such as humidity and temperature, influence WVTR but become less significant after a critical thickness (e.g., above 14.0 nm), where defects or holes in the substrate are sufficiently covered.

9.3.6 Methodology for Addressing Edge Permeation and Barrier Assessment

Edge permeation and ingress through epoxy must be accounted for when calculating Ca test results. This section outlines a methodology to distinguish the true barrier performance from edge effects, ensuring a more accurate analysis.

An important definition in this is identifying the "Ca test region", in brief it is identified as the areas where calcium remains visibly intact (apart from *e.g.* point defects) in the central portion of the sample, distinguished by a clear hue or mean grey value difference from regions where calcium has depleted at the edges exposing the copper background. By only taking measurement from this central region, that is unaffected by edge permeation the analysis isolates barrier performance, minimizing the artifact caused by edge permeation.

As an example, a 14.0 nm AlO_x coating on PET tested at 25°C and 39.5% RH ($MgCl_2$ solution, image size: 4.95 by 4.90 cm) is analysed as shown in Figure 9-14. In this figure, the Ca test region — the area that is measured as the mean grey value to get the overall barrier performance — is isolated (indicated by the red outline) to leave the central area of the sample while excluding edges where permeation through epoxy or side ingress dominates. This ensures the mean grey values accurately reflect the barrier layer's performance, free from the influence of these edge effects. Note that as the fluence is measured in g/cm^2, as the area shrinks the change in area is considered in the fluence measurement. This results in an estimated WVTR: $0.0023 \pm (5.66 \times 10^{-4})$ $g/m^2 \cdot day$

removing these edge effects compared to a higher estimation at $0.026 \pm (2.45 \times 10^{-4})$ $g/m^2 \cdot day$ if the whole square sample area is included.

Additionally, edge permeation can also impact defect characterization by artificially inflating the number of detected spots. Spot analysis is first introduced in Section 4.6 (Analysis of Defects (Spots) in ALD AlO_x coating), where the methodology of counting spots and estimating density of spots is discussed in detail.

Further supporting data and expanded discussion on the influence of sideways permeation are provided in Appendix (Chapter 8), specifically Section 9.3.7.a Whole Region: Impact of Sideways Permeation and Potential Errors).

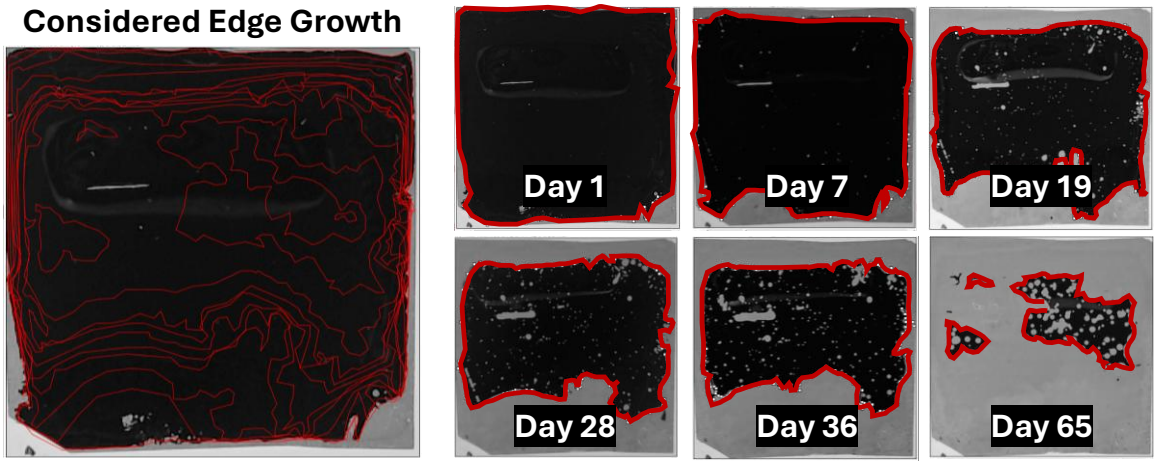
In Figure 9-15, analysing the entire sample, including edge affected regions, results in up to 324 spots on day 1. In contrast, Figure 9-14 shows only 27 spots when the analysis is restricted to the central calcium region unaffected by visible edge permeation. By excluding the perimeter where water vapor ingress is most likely the spot count is reduced to a more accurate reflection of defects within the barrier layer itself, with a revised maximum of 226 spots observed by around Day 28. Although this approach improves the accuracy of defect quantification, it comes at the cost of a reduced analysis area, which may impact statistical robustness.

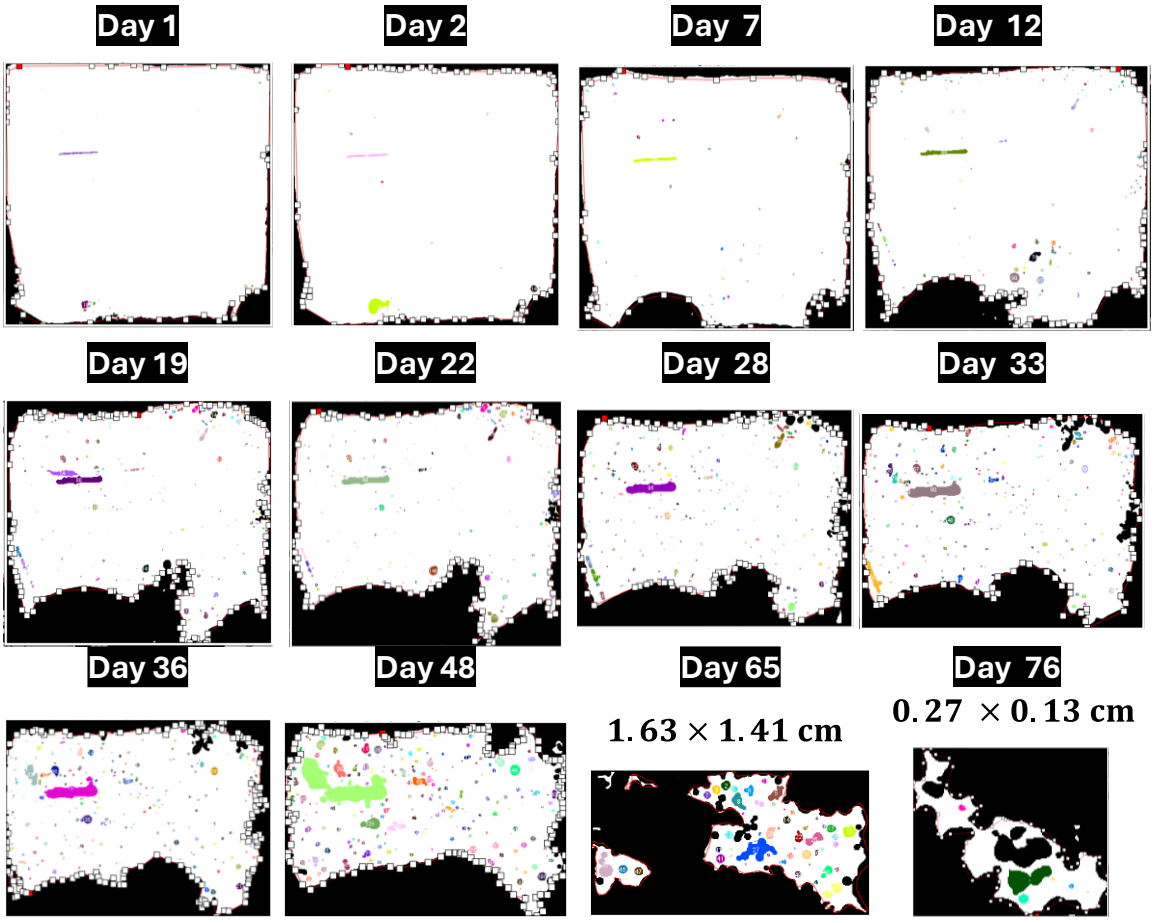
These differences highlight how edge effects, if not properly handled, may influence the estimation of both WVTR and defect densities, with important implications for barrier performance analysis.

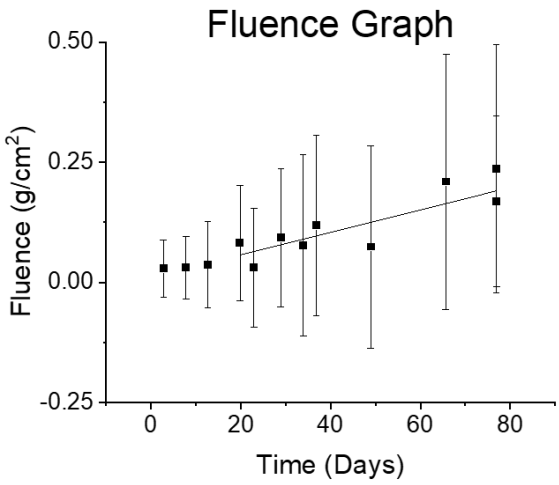
Initially analysing the results, Figure 9-14 the number of detected spots increases with fluence, and while the average spot size remains stable, it artificially grows due to edge effects and spot coalescence over time.

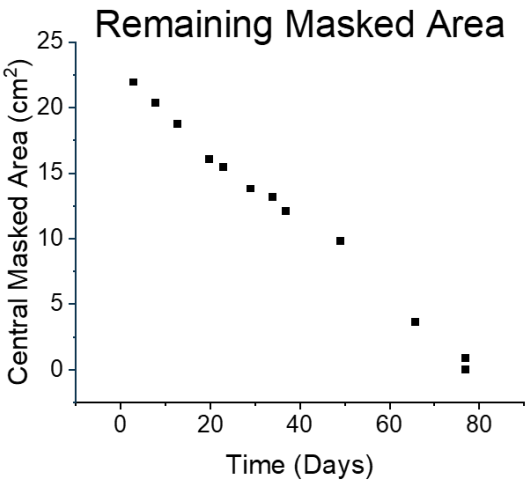
Referring to Figure 9-15 shows an analysis without accounting for edge permeation, in contrast to Figure 9-14 that does, shows that it does affect spot statistic as well, like the average spot size in Figure 9-15 is approximately 0.0042 ± 0.0027 cm^2, while as shown in Figure 9-14 0.0055 ± 0.0059 cm^2; in line with this the both figures do show that the maximum number of spots is typically in the transition region as well (for a detailed discussion of sideways leakage and methodology, in Appendix 9.3.7.a Whole Region: Impact of Sideways Permeation and Potential Errors, with correlations and trends, and calculations of spot density explored, in pp. 466 to 471).

Caution is to be taken as these observations are based on a single sample under specific conditions. To ensure these trends are consistent further testing across multiple samples, with varying thicknesses and environments is needed, as coating properties and conditions could influence overall defect behaviour ad WVTR.




Day 1
Day 2
Day 7
Day 12
Day 19
Day 22
Day 28
Day 33
Day 36
Day 48
Day 65
Day 76
1.63 × 1.41 cm
0.27 × 0.13 cm


Fluence Graph
Fluence (g/cm²)
0.50
0.25
0.00
-0.25
0
20
40
60
80
Time (Days)


Remaining Masked Area
Central Masked Area (cm²)
25
20
15
10
5
0
0
20
40
60
80
Time (Days)

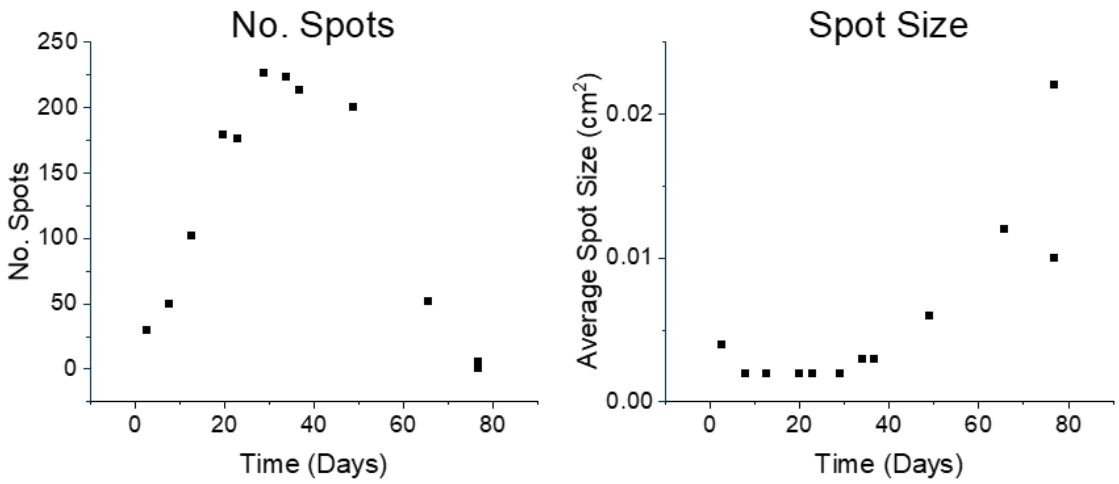


Figure 9-14: Analysis of the remaining Ca region for the 14.0 nm AlO_x on PET sample at 25°C with 39.5% RH ($MgCl_2$ solution) illustrates the impact of accounting for edge permeation (sideways ingress) on both spot count and average spot size. Edge effects are likely caused by epoxy ingress or layer delamination, can artificially inflate WVTR values and introduce errors in the detected number of spots. When edge affect regions are not excluded and the whole sample is considered as shown in Appendix: Figure 9-15 the measured WVTR increases significantly (e.g. 0.026 ± (2.45 × 10^{-4}) g/m^2·day) compared to the corrected value obtained by excluding edge regions 0.0023 ± (5.66 × 10^{-4}) g/m^2·day. Focusing solely on the central calcium region, as done here in this figure, also reduces the estimated spot count showing 27 spots on Day 1 and a maximum of 226 by Day 27, compared to the inflated counts when edge effects are included. Although the absolute values differ, the overall degradation trends remain consistent. The relationship between exposure time, decreasing central masked area (used here as a proxy for remaining calcium – however this also includes spots or areas within this region), and spot size remains evident across both data sets.

9.3.7 Impact of Edge Permeation on ALD AlO_x-Coated PET: Whole-Region and Localized Error Analysis

9.3.7.a Whole Region: Impact of Sideways Permeation and Potential Errors on WVTR and Particle Analysis

This section examines the errors that arise when analysing without accounting for edge permeation. The discussion focuses on quantitatively visualizing the difference if sideways permeation were included in WVTR and particle analysis as referenced in 4.4

Edge Permeation in the Calcium Test – which provides a more accurate calculation of the barrier layer.

Considering the entire Ca region as shown as in Figure 9-15 yields a WVTR: $0.0026 \pm 2.45\ E^{-4}$ g/m²·day, and a permeability of $1.33\ E^{-17} \pm 1.26\ E^{-18}$ [mol/(m·s·Pa)]. Images at specific intervals are highlighted (Days 1, 7, 19, 28, 36, 65) reveal the growth and coalescence of defects. Initial estimates showed ~139 spots are observed, increasing to 161 on Day 7, 272 on Day 19, and peaking at 307 on Day 36, before dropping to 124 on Day 65 due to coalescence. Over this period, the average spot size grew from 0.002 cm² to 0.011 cm², likely due to coalescence or merging — highlighting the importance of considering these effects in defect analysis.

The data consistently indicates increasing spot size over time, reflecting progressive water vapor permeation through localized defects. Once through a defect, water spreads outward and reacts with new Ca. Despite minor errors from data quality and estimations. Figure 9-15 shows constant increase in fluence until saturation, corresponding to defect growth.

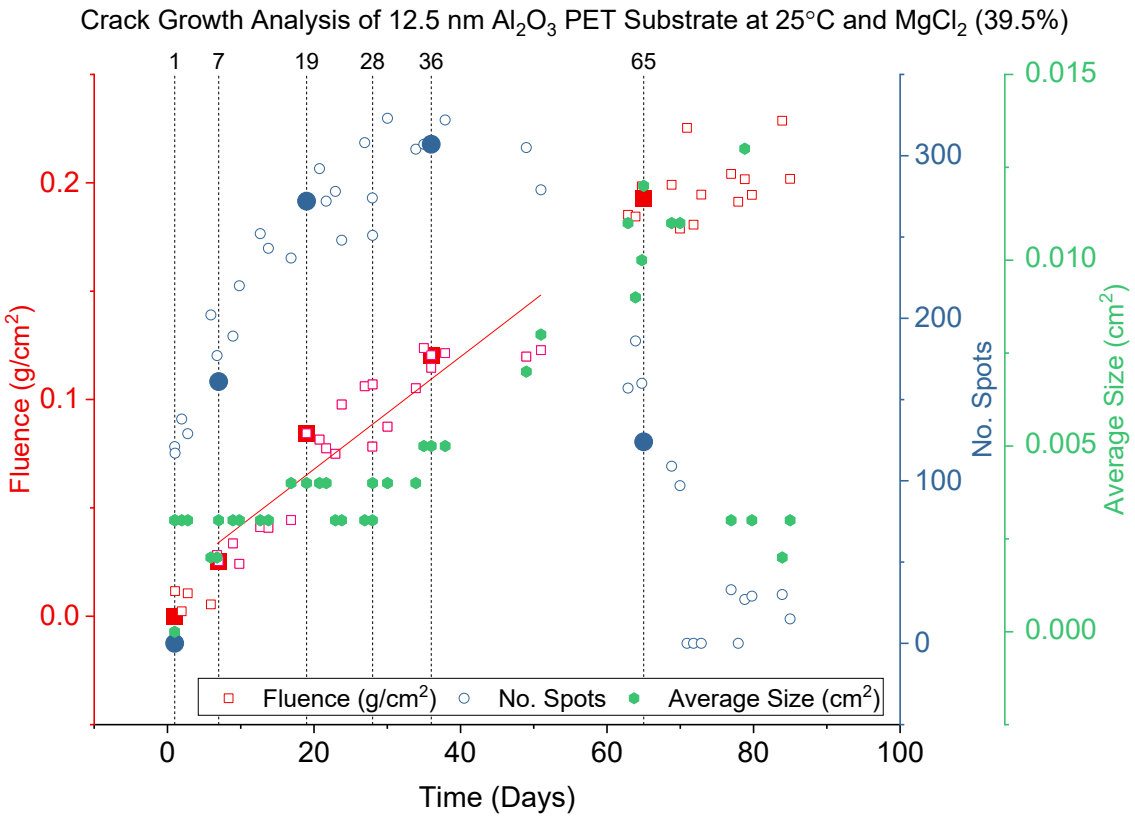


Figure 9-15: Spot growth analysis for a 14.0 nm AlO_x layer on PET substrate at 25°C and 39.5% RH ($MgCl_2$ solution). The chart illustrates the progression of fluence, which increases approximately linearly (WVTR: 0.0026 ± 2.45E^{-4} g/m²·day, Permeability: 1.33 E^{-16} ± 1.26 E^{-17} [mol/(m·s·Pa)]). Spot growth is tracked at specific intervals (Days 1, 7, 19, 28, 36, and 65, showing an increase of average spot size from 0.002 cm² to 0.011 cm².

9.3.7.b Particle Analysis and Regional Variability in Permeation Dynamics

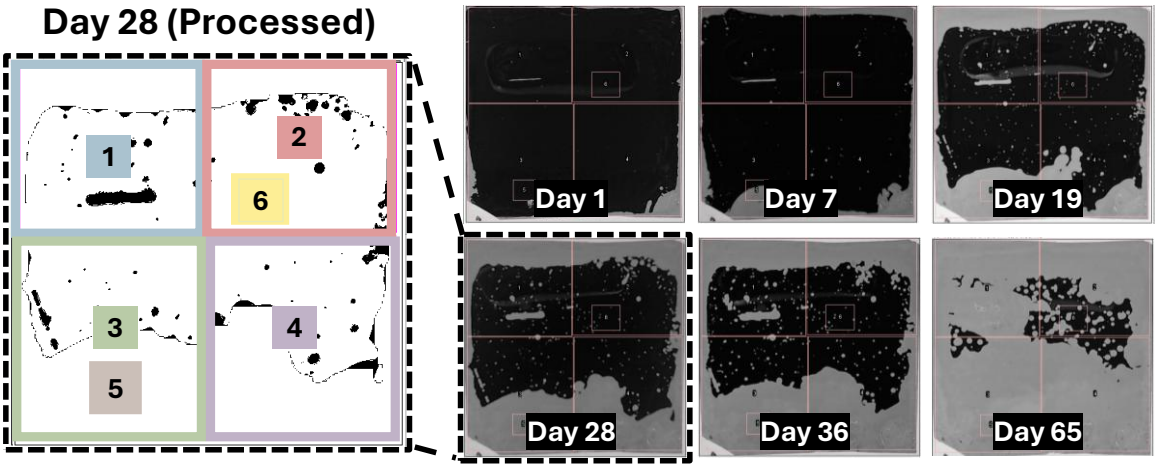
A strength of the Ca test lies in the ability analysing specific regions within the barrier film. Figure 9-16 shows the Ca test from a 14.0 nm AlO_x PET substrate, held at 25°C and 39.5% RH, divided into six regions of interest (ROIs). ROIs 1-4 are larger rectangular sections, while ROIs 5 and 6 are smaller subregions.

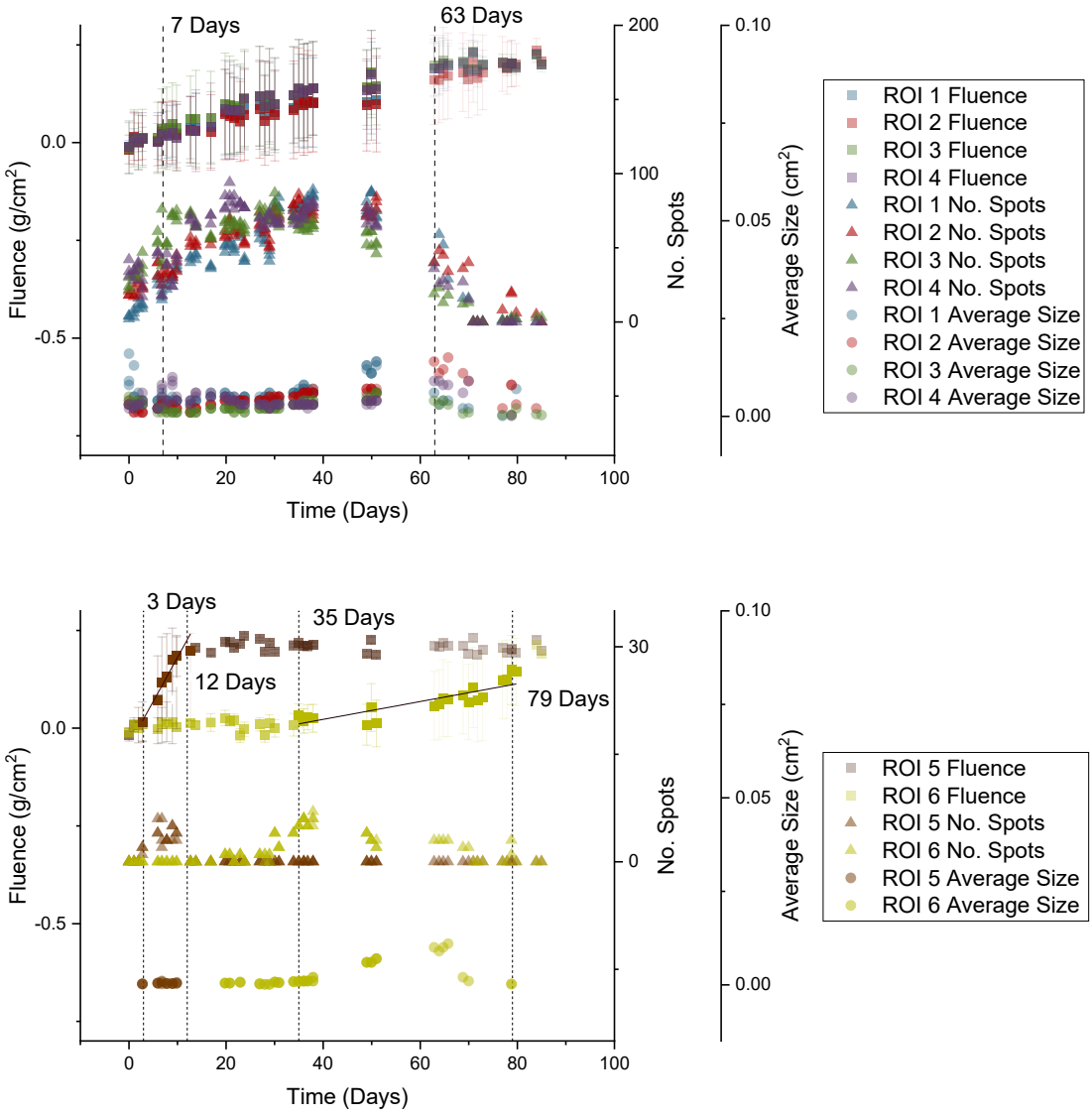
It is important to note that ROIs 1-4 cover substantial portions of the sample, meaning that edge permeation may have a partial influence on the observed results. However, this does not diminish the validity of the regional analysis but rather highlights

the variability in permeation dynamics across different areas of the sample. On the other hand, ROI 5 exhibits faster calcium depletion, suggesting higher localized permeation, whereas ROI 6 depletes more gradually, indicating better barrier performance at that specific arear of the barrier layer.

For ROIs 1-4, the WVTR (0.0027 ± 0.00045 g/m²·day) and permeability ($6.90 \times 10^{-17} \pm 1.16 \times 10^{-17}$ mol/(m·s·Pa)) are close to the overall calcium region, with minor differences due to varying defect counts. The number of spots increases during the test, peaking around the transition region (Day 20-37), but coalescing spots reduce the total count later. Average spot size grows around Day 50 before dropping as calcium depletes.

The contrasting behaviour of ROI 5 (high WVTR, many small spots) and ROI 6 (low WVTR, underscores a correlation between defect count and permeation dynamics. While edge permeation may contribute to variations in results, the key takeaway remains the regional variability in defect behaviour, emphasizing the importance of localized analysis.





Region of Interest (ROI)	1 (2.37 × 2.21 cm)	2 (2.51 × 2.20 cm)	3 (2.42 × 2.62 cm)	4 (2.47 × 2.59 cm)	5 (0.51 × 0.48 cm)	6 (0.65 × 0.57 cm)
WVTR ($g/m^2 \cdot day$)	0.0024	0.0023	0.0027	0.0033	0.0226	0.0023
%Diff. WVTR	14.29	17.86	3.57	17.86	707.14	17.86
Permeability [mol/(m·s·Pa)]	6.19E-17	5.94E-17	6.97E-17	8.52E-17	5.83E-16	5.94E-17
%Diff. Permeability	56.87	58.67	51.48	40.70	306.14	58.67

Figure 9-16: Six Regions of Interest (ROIs) were identified on a 14.0 nm AlO_x PET substrate at 25°C with an $MgCl_2$ solution at 39.5% RH. ROIs 1-4, divided into equal rectangular areas, were analysed for permeation behaviour. Fluence plots, combined

with defect counts and average sizes, showed a clear correlation between defect size/quantity and fluence. ROI 5, which reached full saturation in a week, and ROI 6, which took two months, highlight contrasting WVTRs. These regions suggest that defect size plays a significant role in barrier performance, with the timing of maximum spot count indicating the onset of increased fluence.

9.3.7.c Percent Error of Not Accounting for Edge Permeation

This analysis raises the question of how significantly edge effects can distort the WVTR estimations as illustrated in Figure 9-17. The data reveal that failing to account for sideways permeation or epoxy ingress can result in substantial overestimations of WVTR. In some cases, the difference between corrected and uncorrected values ranges from approximately 20% to over 1000%, reinforcing the need to exclude edge-affected regions for accurate, thickness-independent WVTR assessment.

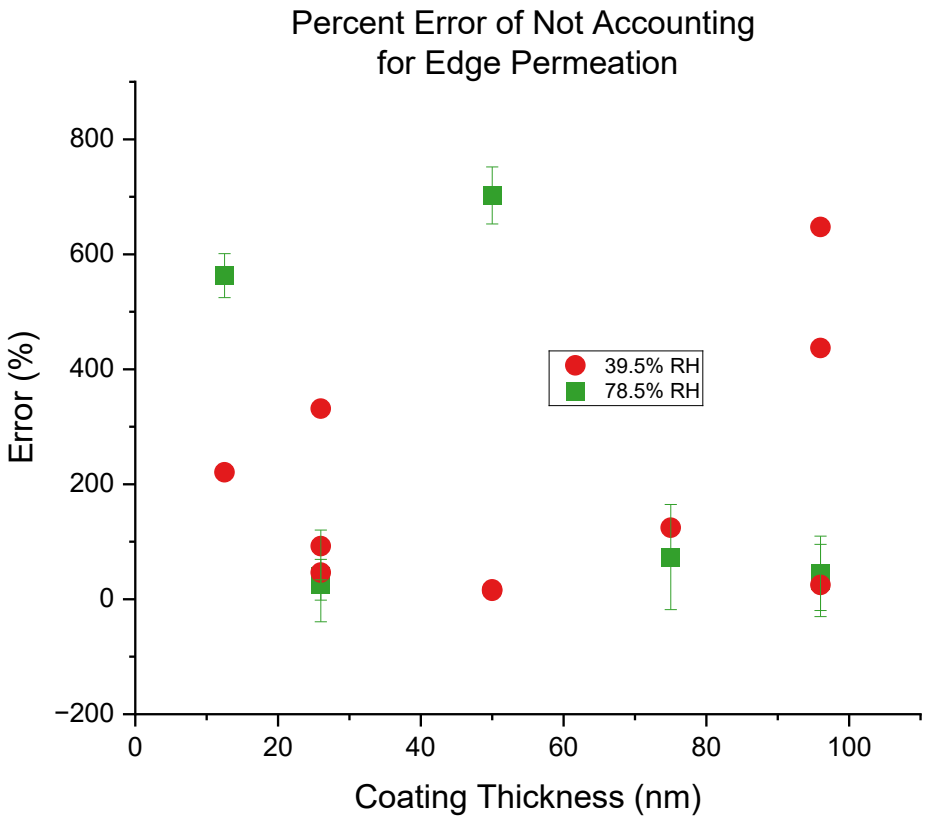


Figure 9-17: Absolute Percent Difference (%) WVTR calculations between non-edge accounted and edge accounted estimations for various thicknesses, based on the data presented in Figure 4-11. The figure reveals substantial discrepancies in WVTR values resulting from water permeation through edge defects, with differences ranging from significant to critical, affirming the necessity of accounting for edge effects.

9.3.8 Particle Analysis on RF Sputtered Films

This methodology and analysis now considers RF magnetron reactive sputtered Al_2O_3 / AlO_x films shown in Figure 9-18 using data from Tobin *et al.* [194]. The samples, 2 cm diameter discs, were manually thresholded due to image inconsistencies and the lack of calibration bars. As done with all samples and results, defect density was calculated based on area to account for incomplete images (cut off) and the limited number of images.

Figure 9-18 (a) shows fluence calculations and from it one can derive the permeabilities; the rougher BOPP substrate (RMS roughness: 24 nm) leads to more defects in the AlO_x layer and higher permeability ($1.30\ E^{-16} \pm 1.81\ E^{-17}$ [mol/(m·s·Pa)]), than the smoother PEN substrate (RMS roughness: 3.5 nm, permeability: $1.14\ E^{-16} \pm 1.32\ E^{-17}$ [mol/(m·s·Pa)]) at 38°C and 85% RH. Importantly, these estimates are lower than MOCON Permatran W 3/31 (ASTM F-1249) their permeability estimations: (BOPP: $3.32\ E^{-15}$ [mol/(m·s·Pa)], PEN: $4.71\ E^{-16} – 6.63\ E^{-16}$ [mol/(m·s·Pa)]); where these permeability values represent the overall permeation of the material though differences in measurement method and sample variation itself could be attributed to the discrepancy between the two permeability estimates.

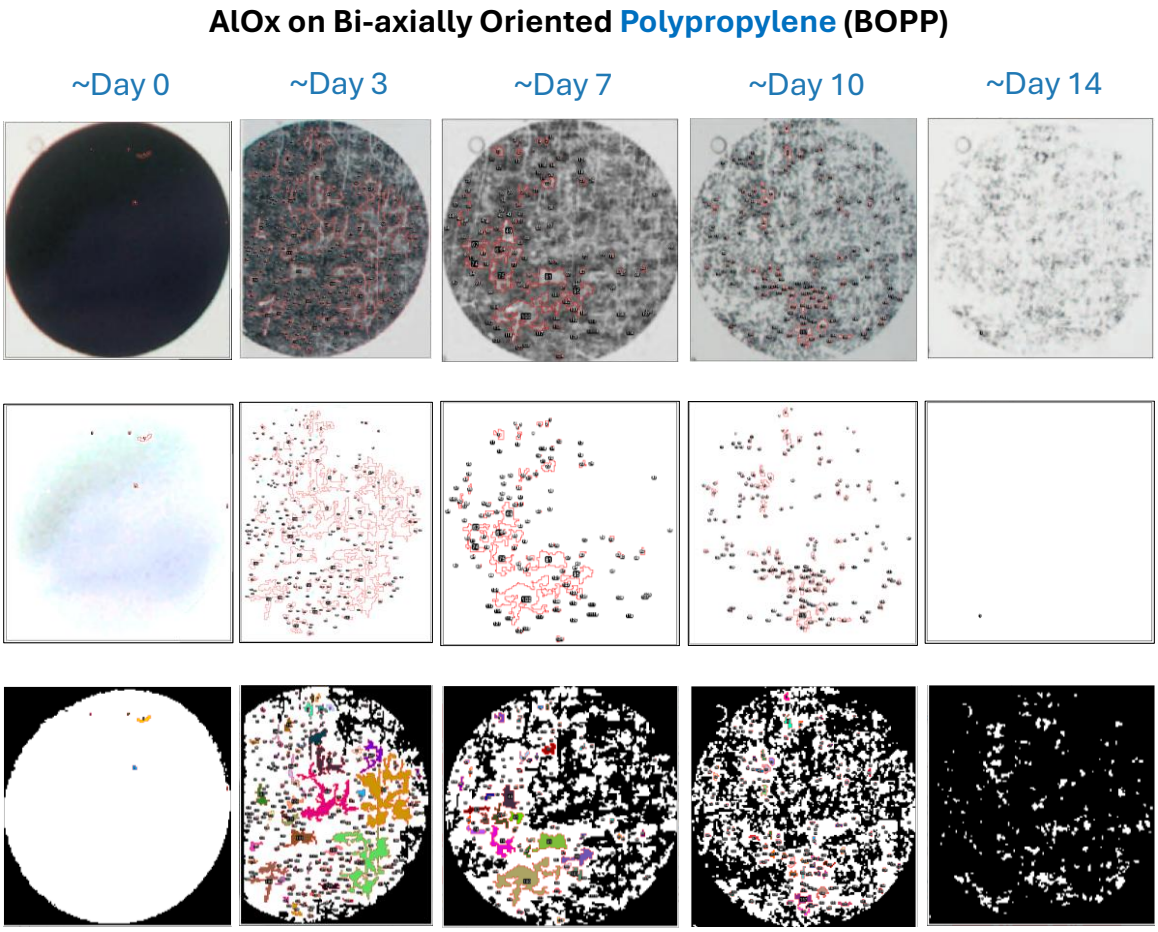
As observed in Figure 9-18, the discrepancy between the calculated permeabilities and the MOCON measurements are likely due to nano-defect permeation. In the Ca test images, this permeation manifests as background greying rather than distinct defect spots.

While the MOCON method captures both visible defects and nano-defect background permeation, the particle analysis performed here only accounts for discrete defect spots. Poor image quality, low contrast and significant noise further complicate thresholding, making it difficult to consistently distinguish isolated spots from possible background noise; wherein adjustments to threshold settings could either exclude or include real spots further introducing additional uncertainty.

For example, in the BOPP images (top row), patchy greying of the Ca layer is observed over time, which indicates permeation. However, it is unclear whether all thresholded regions in the particle analysis (second row) accurately correspond to actual permeation sites. Minor errors in the particle identification are likely, as the thinning of the Ca layer over time reduces the contrast between permeated and non-permeated areas, making segmentation and spot analysis less reliable. Notably, by Day 14, most of the Ca has disappeared, and although some isolated points with defined borders remain, it becomes increasingly difficult to confidently distinguish discrete permeation spots from background Ca thinning.

In the PEN images, a brighter region is observed is observed at the upper left edge of the sample, likely due to edge permeation or sample delamination. To maintain consistency, areas affected by edge effects were excluded from the analysis, as was done for the BOPP samples. Additionally, contrast inconsistencies over time, with images at Day 10 appearing unexpectedly dim compared to Day 15, where Ca appears darker and more refined, suggest that variations in camera settings, lighting, or contrast may have led to underestimation of the number of spots or misclassification of permeated areas as background.

Despite these challenges, the analysis still reveals key observations. BOPP's uneven surface likely led to more defects, whereas PEN's smoother surface exhibited fewer defects as seen in Figure 9-18 (b). Regarding the average spot size Figure 9-18 (c); there is nothing to suggest that the average spot sizes are significantly different between the two materials, suggesting that the defects with which they are associated may be of similar size. A more continuous data set capturing the growth process over time, along with better calibration and normalization would provide a more representative analysis.



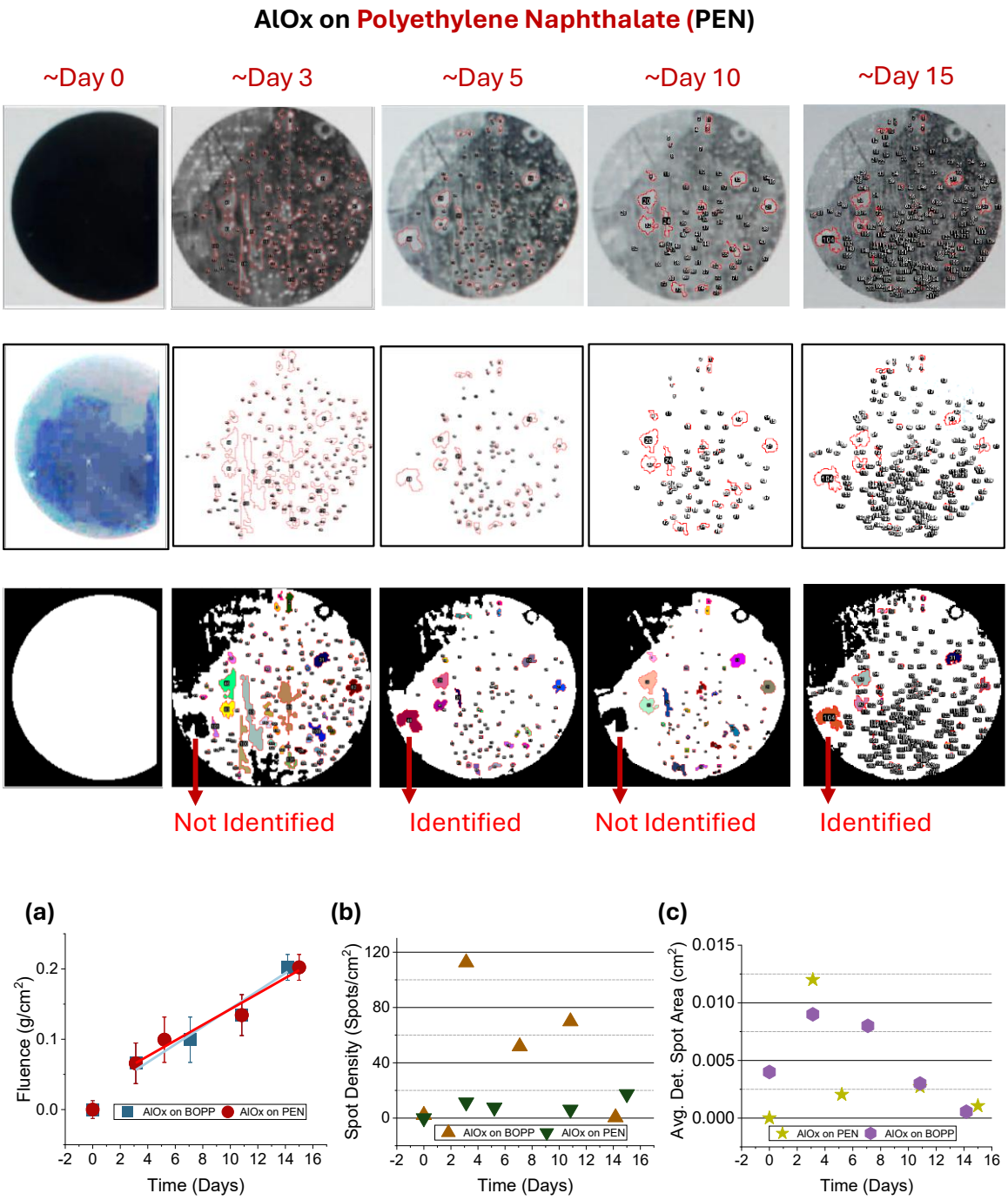


Figure 9-18: Defect analysis of images from Tobin, Suttle, and Assender [194]; comparing Ca tests of RF sputtered AlOx films on BOPP (145 nm) and PEN (148 nm), tested at 38°C and 85% RH. Raw images, identified defect spots, and coloured overlays are shown alongside the grayscale Ca images. Limited data and image quality introduce uncertainties in WVTR measurements. Thresholding challenges due to low contrast and noise make it difficult to differentiate true defects from artifacts and background noise, leading to variations in defect identification (e.g., undetected or misidentified spots on

PEN). (a) Fluence-over-time graph for BOPP and PEN, with WVTR estimates: 0.01265 ± 0.00176 g/m²·day for BOPP and 0.01112 ± 0.00129 g/m²·day for PEN. These values are lower than the MOCON-reported literature values at 38°C and 100% RH (BOPP: 0.38 g/m²·day, PEN: 0.054-0.076 g/m²·day), Data points were selected from the first detected permeation until saturation or the final recorded image. (b) Defect spot density analysis, showing that rougher BOPP exhibited a maximum of 112 spots/cm², while smoother PEN had a maximum of 11 spots/cm². (c) Average detected spot area over time, including both individual or isolated and coalesced spots; coalescence of spots was difficult to fully differentiate in the analysis, potentially leading to a slight overestimation of the average spot size.

9.3.9 Influence of Thickness and Environmental Conditions on Spot Formation

Returning now to the ALD-deposited coatings that form this basis of this work, as seen in 4.2.1 Key Factors in Measuring WVTR of AlO_x Using MOCON Aquatran and 4.3 AlO_x on PET (ALD) – Ca Test, coating thickness influences barrier performance, with optimal thickness minimizing defects and enhancing water vapor resistance (reduced WVTR/permeability). While thicker coatings theoretically reduce defect density, this section investigates whether Ca testing can empirically confirm, this relationship by analysing spot formation dynamics (count, morphology) – where spots represent defects enabling water vapor permeation.

Additionally, the study evaluates whether elevated temperature, and RH merely accelerate spot formation (unchanged defect density / nature) or alter the defects themselves. If environmental conditions solely affect the kinetics of permeation, identical coatings under varying environment should yield comparable average spot counts, with differences only in formation speed. However, practical challenges arise due to rapid spot coalescence at high temperature or RH, which may obscure detection (*e.g.* coalescence or overlapping spots), whereas slower progression at lower temperature and RH allows clearer observation of distinct defects.

Acknowledging limitations (small sample size, incomplete Ca-test timelines), selected samples under the same controlled conditions were analysed to identify preliminary trends, advancing understanding of defect driven permeation mechanisms

9.3.9.a Low Relative Humidity (39.5% $MgCl_2$ at 25°C)

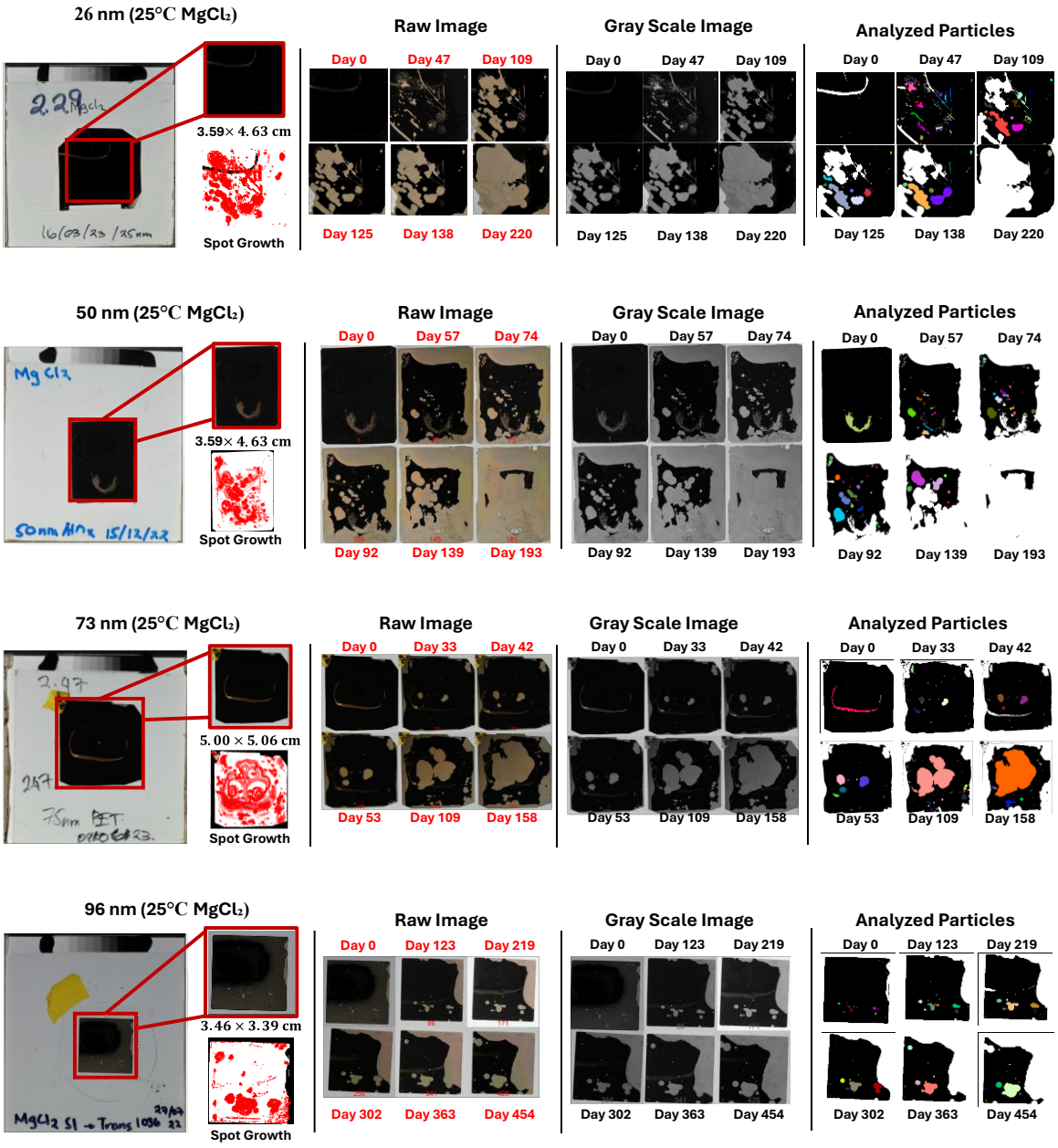
Figure 9-19 shows the spot density detected on ALD AlO_x PET substrates with varying coating thicknesses (14.0 nm (n=1), 26 nm (n=4) 50 nm (n=3), 73 nm (n=1), and 96 nm (n=4)). The samples were tested at 25°C and 39.5% using a $MgCl_2$ salt solution.

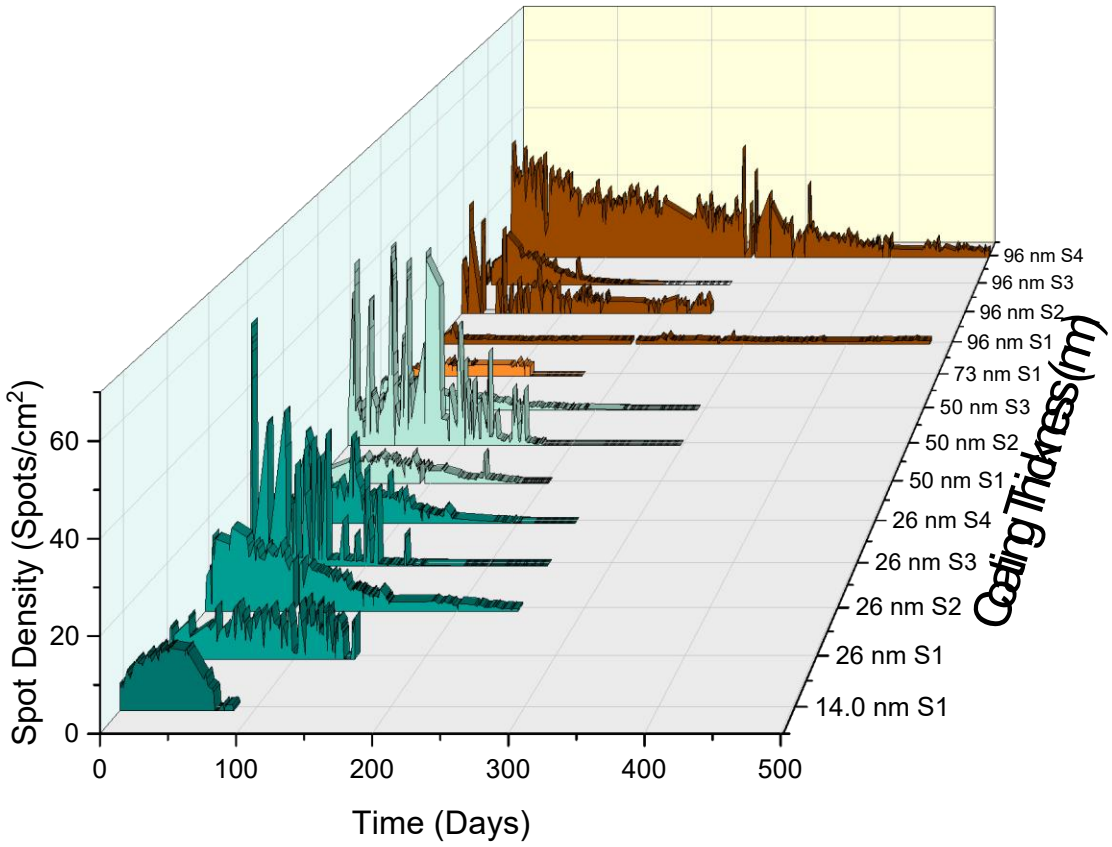
The results indicate that, regardless of coating thickness, the spot density will initially rise as new spots become visible from sufficient water vapour passing through the underlying defect, and then the spot density declines again as spots begin to coalesce. As seen in Figure 9-19 spot density plots are adjusted to have axes cross at zero to clearly show that at long times the density approaches near zero values across all samples. Notably, spot estimations appear slightly higher than expected based on the calculated WVTR values, likely because the analysis includes both isolated and coalesced spots without differentiation (see section 4.6.2 Differentiating Isolated and Coalescing Spots (Python)), potentially leading to some over-counting.

At this stage, no substantial difference in spot density is observed between coatings of different thicknesses. Although some sample-to-sample variation is present, there is no clear trend suggest that thickness alone controls defect formation under these conditions. But there is some suggestion that films with moderate thickness coating may tend to have a lower spot density than the thin (14 nm) and thick (96 nm) coatings.

Furthermore, under these constant conditions, piercing through the images no single pattern governs defect formation across different coating thickness is observed.

The relative slow permeation rates also allowed clear tracking of defect growth over time, enabling high-quality data collection with well-separated spot evolution. For most samples, substantial progression of Ca depletion could be observed within the experimental timeframe. However, in some cases, such as 96 nm S2 and S4, a portion of the Ca layer remained intact by the end of testing. As a result, a small number of potential defects may not yet have been detected.





Thickness (nm)	*14 nm*	*26 nm*	*50 nm*	*73 nm*	*96 nm*
WVTR ($g/m^2 \cdot day$)	*8.48E-04 ± 1.28E-04*	*2.25E-04 ± 0.28E-04*	*4.26E-04 ± 0.86E-04*	*6.32E-04 ± 1.04E-04*	*4.96E-04 ± 1.40E-04*
Permeability [mol/(m·s·Pa)]	*43.4E-18 ± 6.58E-18*	*11.6E-18 ± 1.57E-18*	*21.9E-18 ± 4.38E-18*	*32.5E-18 ± 5.36E-18*	*3.25E-18 ± 7.18E-18*

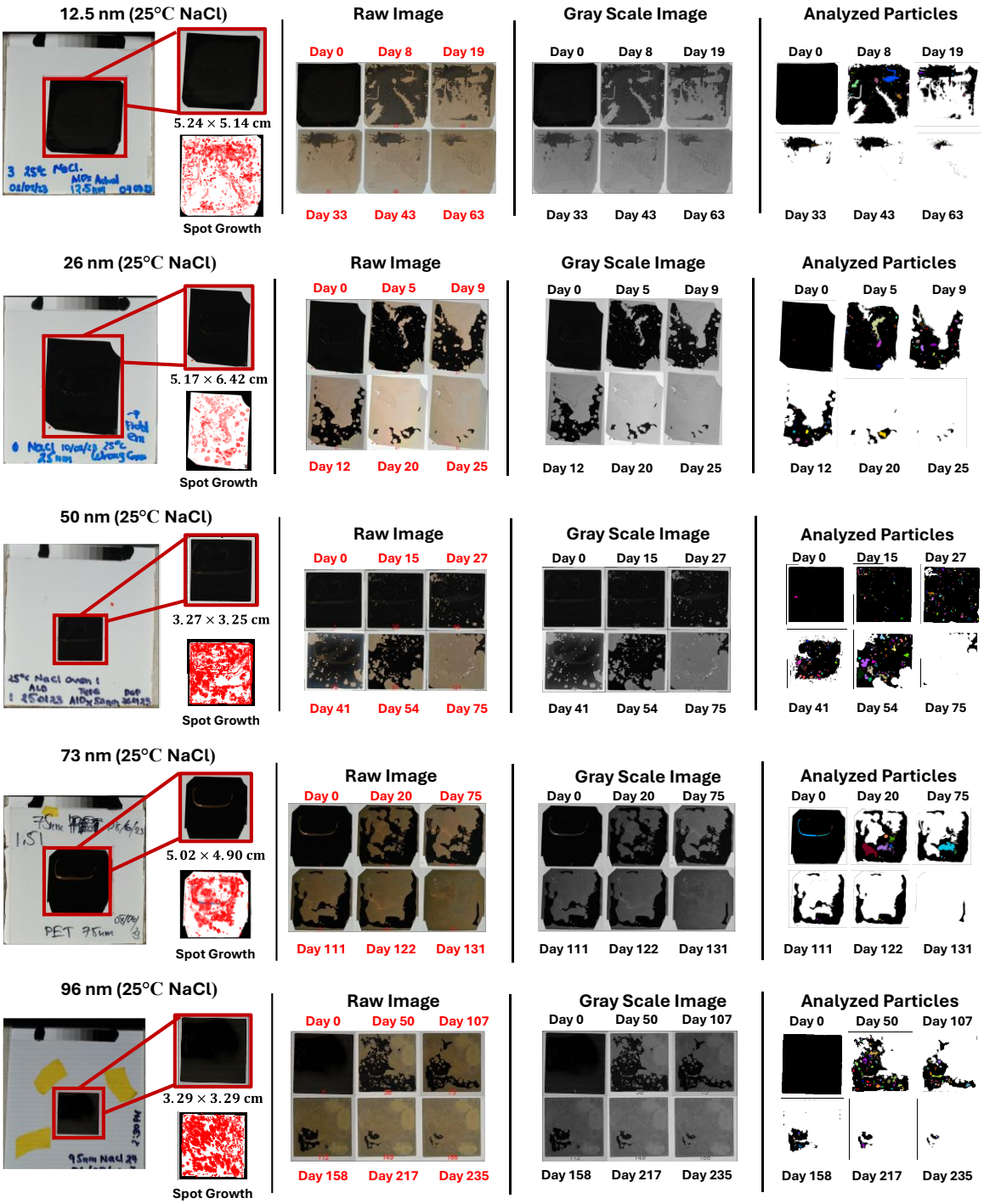
Figure 9-19: Representative raw, grayscale, and analysed images of 26 nm, 50 nm, 73 nm 96 nm ALD AlO_x coatings on PET, tested at 25°C and 39.5% RH ($MgCl_2$ solution). Images show the progression of permeation-induced defects over time with coloured regions marking identified spots. Such that spots are defined as areas of local Ca depletion located within the intact Ca region, excluding areas near the sample edges or classified as background. White regions in the thresholded images represent depleted Ca and/or background or possible edge effects, as known there may occur some errors where Ca intact may not have been classified as spot. Most initial defects appear circular in shape, though this becomes less apparent in coalesced regions where adjacent spots merge and form irregular structures. Below, spot density is plotted over time across samples, revealing similar growth and saturation behaviours. Axes cross at zero to show that spot densities approach near-zero values at long durations. These observations align

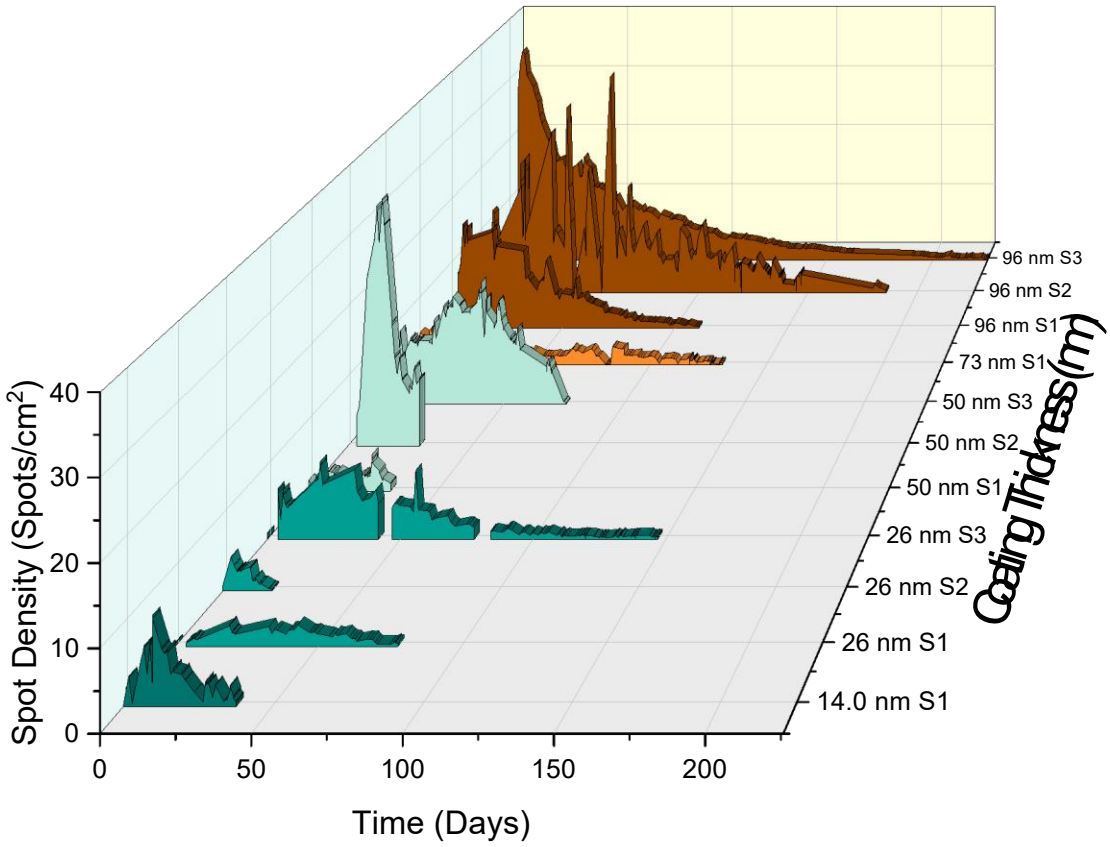
with the WVTR, and permeability values presented, with edge permeation effects excluded.

9.3.9.b High Relative Humidity (78.5% $MgCl_2$ at 25°C)

The same coating thicknesses (14.0 nm (n=1), 26 nm (n=3), 50 nm (n=3), 73 nm (n=1), and 96 nm (n=3)) were tested under slightly different conditions in Figure 9-20. This time, experiments were conducted at 25°C with higher humidity (78.5% RH) using a NaCl solution. Under higher humidity, samples reached full saturation faster (*e.g.*, 14.0 nm in ~23 days, 96 nm in ~125-154 days) compared to lower humidity (39.5% RH). Spot formation and growth were quicker, with fewer distinct spots detected due to coalescence.

As expected, the WVTR values, calculated from the Ca test with edge effects accounted for are higher under high humidity conditions (NaCl, 78.5% RH), while corresponding permeability values remain broadly similar. However, the range of observed spot densities is notably reduced compared to the lower humidity condition ($MgCl_2$, 39.5%). This narrower distribution is not due to a lower number of defects, but rather a detection limitation caused by faster water permeation. Under high RH, individual defects evolve and coalesce more quickly which obscures discrete spot growth and leads to a compressed spot density range. In contrast the slower permeation at lower RH allows for more distinct and prolonged spot development, resulting in a broader and higher spread of measurable spot densities over time.


12.5 nm (25°C NaCl)
5.24 × 5.14 cm
Spot Growth
Raw Image
Day 0 Day 8 Day 19
Day 33 Day 43 Day 63
Gray Scale Image
Day 0 Day 8 Day 19
Day 33 Day 43 Day 63
Analyzed Particles
Day 0 Day 8 Day 19
Day 33 Day 43 Day 63
26 nm (25°C NaCl)
5.17 × 6.42 cm
Spot Growth
Raw Image
Day 0 Day 5 Day 9
Day 12 Day 20 Day 25
Gray Scale Image
Day 0 Day 5 Day 9
Day 12 Day 20 Day 25
Analyzed Particles
Day 0 Day 5 Day 9
Day 12 Day 20 Day 25
50 nm (25°C NaCl)
3.27 × 3.25 cm
Spot Growth
Raw Image
Day 0 Day 15 Day 27
Day 41 Day 54 Day 75
Gray Scale Image
Day 0 Day 15 Day 27
Day 41 Day 54 Day 75
Analyzed Particles
Day 0 Day 15 Day 27
Day 41 Day 54 Day 75
73 nm (25°C NaCl)
5.02 × 4.90 cm
Spot Growth
Raw Image
Day 0 Day 20 Day 75
Day 111 Day 122 Day 131
Gray Scale Image
Day 0 Day 20 Day 75
Day 111 Day 122 Day 131
Analyzed Particles
Day 0 Day 20 Day 75
Day 111 Day 122 Day 131
96 nm (25°C NaCl)
3.29 × 3.29 cm
Spot Growth
Raw Image
Day 0 Day 50 Day 107
Day 158 Day 217 Day 235
Gray Scale Image
Day 0 Day 50 Day 107
Day 158 Day 217 Day 235
Analyzed Particles
Day 0 Day 50 Day 107
Day 158 Day 217 Day 235



Thickness (nm)	*14.0 nm*	*26 nm*	*50 nm*	*73 nm*	*96 nm*
WVTR ($g/m^2 \cdot day$)	*9.65E-04 ± 3.21E-04*	*11.6E-04 ± 5.24E-04*	*21.4E-04 ± 4.51E-04*	*4.21E-04 ± 3.44E-04*	*6.38E-04 ± 1.05E-04*
Permeability [mol/(m·s·Pa)]	*24.9E-18 ± 8.28E-18*	*29.9E-18 ± 13.5E-18*	*55.3E-18 ± 11.7E-18*	*10.9E-18 ± 8.87E-18*	*16.5E-18 ± 2.71E-18*

Figure 9-20: Spot Density Analysis of AlO_x Coatings at 25°C and 78.5% RH. This figure presents representative images and spot density measurements for coatings of varying thicknesses (14.0 nm, 26 nm, 50 nm, 73 nm, and 96 nm) subjected to a high humidity environment (controlled by Saturated NaCl solution). The corresponding WVTR and permeability values are provided in the table. While higher WVTR and permeability suggest a greater number of defects, the observed spot density (spots/cm²) estimations, do not fully correlate with this trend. This discrepancy is attributed to the increased water vapor permeation rate at high humidity, which leads to spot coalescence and blurring, hindering accurate spot detection and potentially underestimating the actual defect density. The challenges in accurately characterizing spot density under these conditions highlight the complex interplay between humidity, permeation, and defect visualization.

9.3.9.c Influence of Temperature on Spot Density

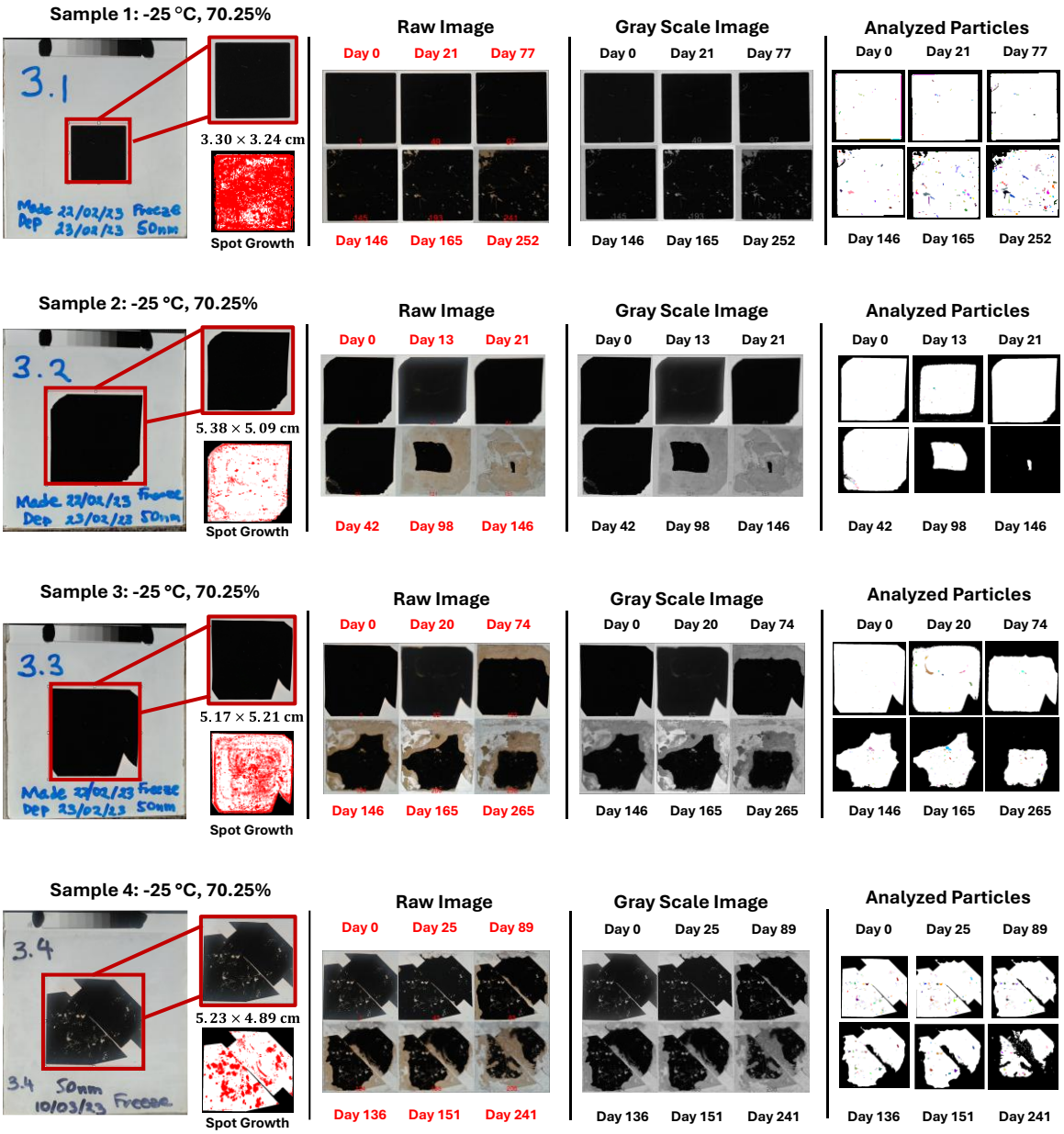
This investigation now shifts and explores how temperature influences spot formation and detection, if the underlying defect density remains constant and unaffected by the environment, one should be able to observe similar average spot densities regardless of temperature.

This idea is explored in Figure 9-21 shows four conditions for a 50 nm AlO_x coating: Sample A (-25°C, 70.25% RH, freezer), Sample B (25°C, 71% RH, $MgCl_2$), Sample C (35.5°C, 71% RH, $MgCl_2$), and Sample D (50.5°C, 71% RH, $MgCl_2$). While the raw images suggest similar underlying defects population regardless of temperature, spot appearance and growth vary with time [437].

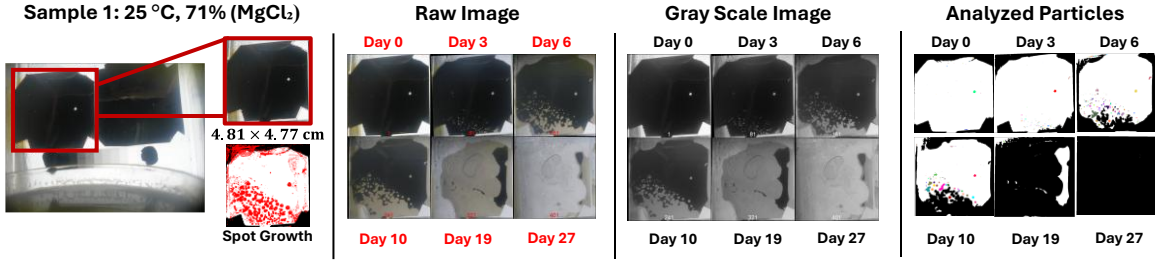
In Sample A (-25°C), calcium depletion was minimal even after 252 days, with most activity due to sideways permeation. Sample B (25°C) showed spot formation. At 35.5°C (Sample C), faster depletion was observed, with higher spot density and larger spot size. Sample D (50.5°C) exhibited early calcium depletion, with noticeable spot growth but a shorter test timeline.

The analysis suggests that temperature affects the timing of spot appearance, with faster growth at higher temperatures. However, it is difficult to detect spots at very high temperatures, similarly to the problem with high relative humidity. While lower temperatures may be an option if time permits, they can be too slow for practical purposes. To address this issue, shorter time intervals for data collection may be used, especially at higher temperatures, to improve spot observation.

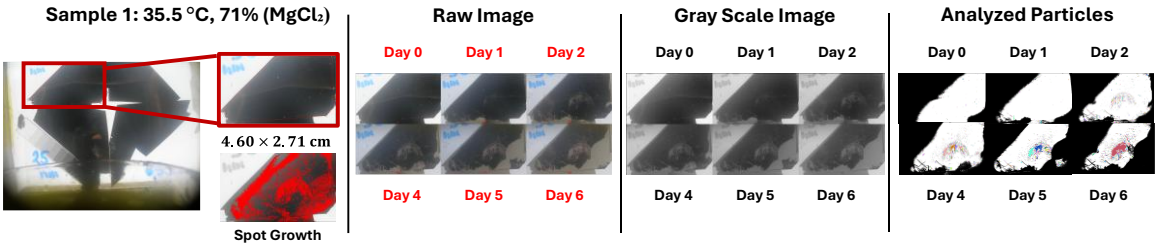
Batch Sample A (1 – 4), -25°C, 70.25%, Freezer Environment



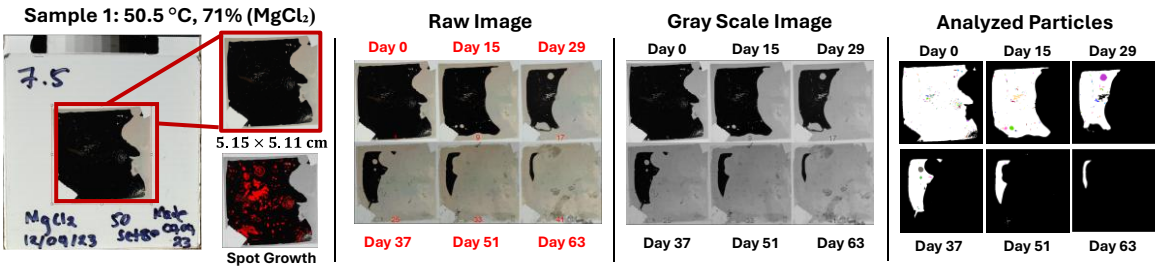
Batch B: Sample (1), 25°C, 71%, $MgCl_2$

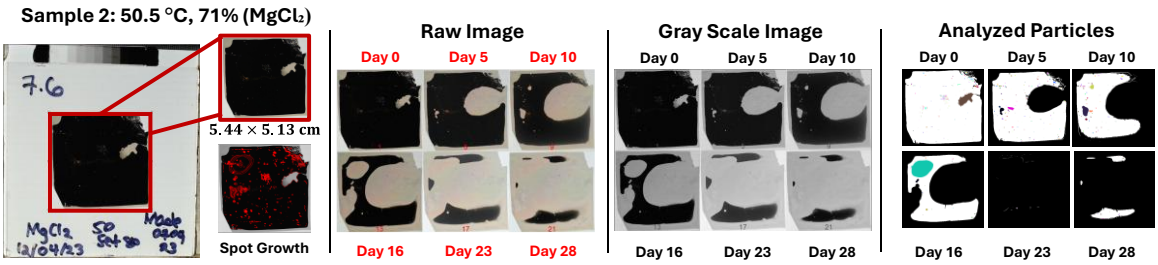


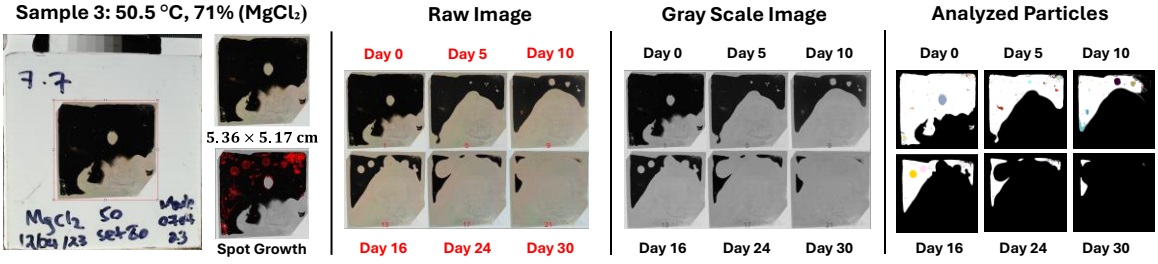
Batch C: Sample (1), 35.5°C, 71%, $MgCl_2$

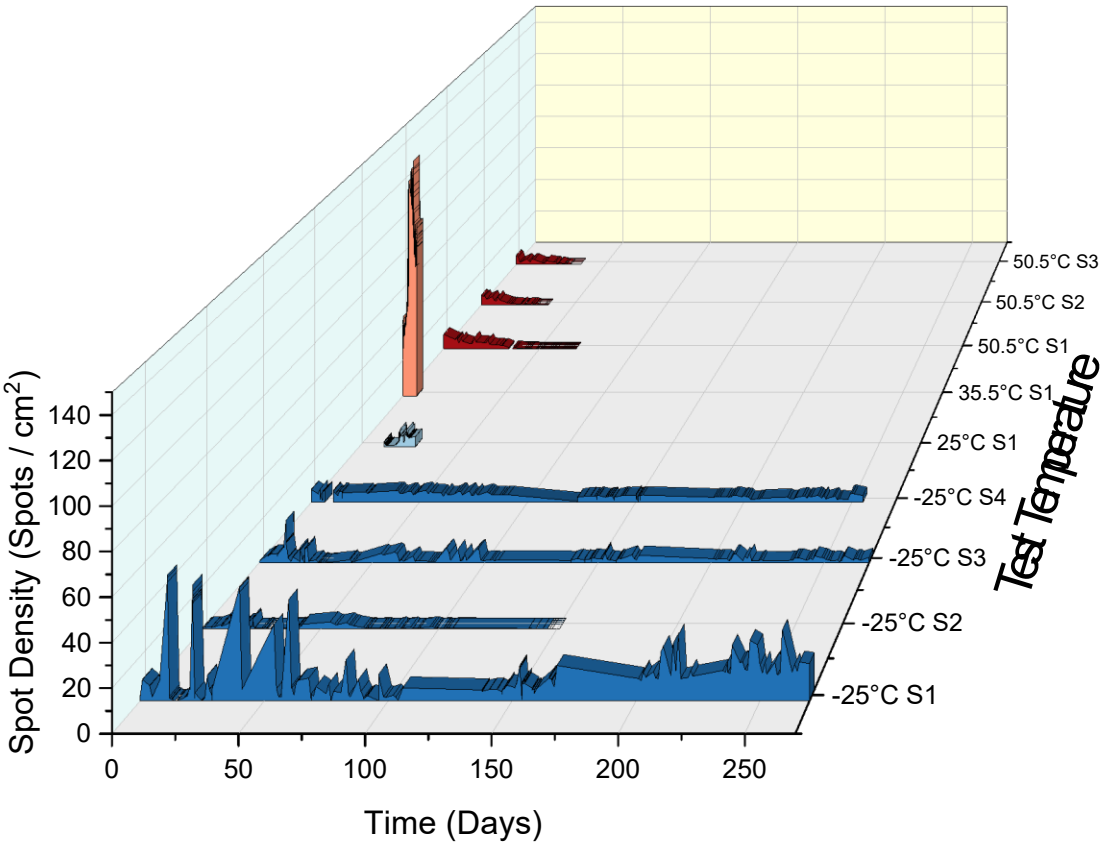


Batch D: Sample (1 - 3), 50.5°C, 71%, $MgCl_2$









Sample	A - #1	A - #2	A - #3	A - #4	B - #1	C - #1	D - #1	D - #2	D - #3
WVTR (g/m2·day)	0.002 ± 3.19E-4	0.002 ± 3.72E-5	0.001 ± 1.99E-5	0.001 ± 2.40E-5	0.015 ± 9.00E-5	0.017 ± 0.44E-5	0.003 ± 0.21E-5	0.006 ± 0.43E-5	0.006 ± 0.41E-5
Adj. R-Square	0.52	0.93	0.93	0.95	0.40	0.92	0.91	0.91	0.94
Permeability [mol/(m·s·Pa)]	2.25 E-15	1.70 E-15	97.3 E-15	1.23 E-15	42.4 E-15	26.9 E-15	236.0 E-15	400.0 E-15	397.0 E-15

Figure 9-21: The influence of temperature on spot density of 50 nm AlO_x ALD coating at constant humidity (~70.25%-71%) was studied across four batches (A: -25°C, B: 25°C, C: 35.5°C, D: 50.5°C). Raw images, grayscale, and particle analysis were used to track spot growth and count predictions. Spot density was plotted according to temperature over time, highlighting how temperatures affect spot formation where at cold

temperatures spot formation takes a substantial amount of time versus a faster spot formation at higher temperatures. Moreover, a table summarizing WVTR, coefficient of determination, and permeability was also included; showing that all the 50 nm samples showed very similar WVTR's and permeabilities; asserting that the number of defects should be the same, and the change in spot detection and growth is due to temperature, underscoring the need for precise environmental control for accurate spot detection.

9.3.9.d Spot Density (Low RH – 39.5%)

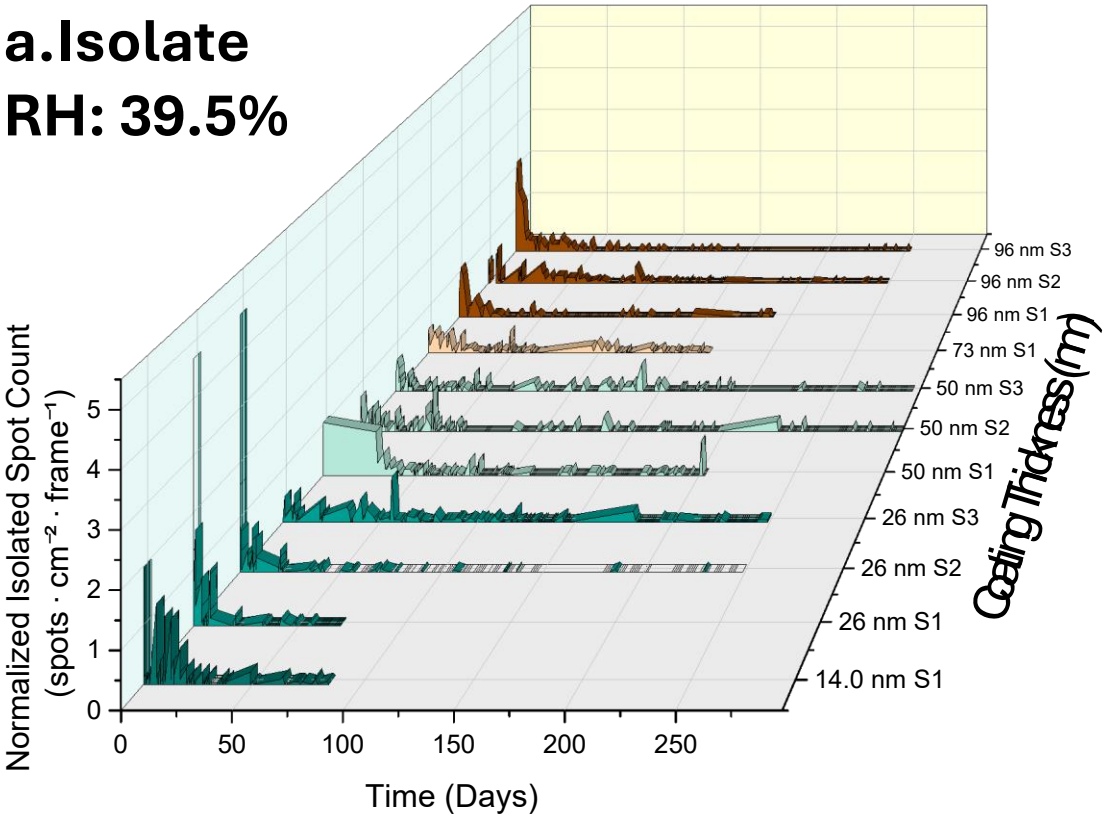
As previously observed in the ImageJ results (9.3.9.a Low Relative Humidity (39.5% $MgCl_2$ at 25°C)) distinguishing between isolated and coalescence spots was challenging, however at lower humidity, more isolated spots were detected, as the slower growth rate prevents rapid coalescence compared to higher RH conditions.

Figure 9-22 (a), illustrates the number of new isolated spots detected over time; Initially, a higher number of isolated spots appear, but this count decreases as the test progresses. These newly detected isolated spots represent defects, with the majority emerging at the beginning of the test. This suggests that prolonged observed, which occurs usually in ultra-low water vapour permeation barriers – take many months to years, may be unnecessary for quantifying overall spot density beyond a certain point. Once the maximum number of isolated spots is reached, the appearance of new spots declines significantly, indicating that most isolated spots due to defects have already been observed. Consequently, the proportion of additional spots detected after this peak corresponds to the area under the curve beyond the maximum, showing that extended observation at later stages contributes minimally to the overall defect quantification.

This finding supports the idea that full calcium depletion process may not be required for identifying spot density but would still be needed for permeation analysis (the fluence over time will depend not only on the number of spots but how they grow over time).

Regarding the effect of coating thickness, the samples appear to have similar estimated values of defect density, however a closer analysis is necessary and is discussed in 4.6.3.a Summary of Spot Density – Python Estimations.

Figure 9-22 (b) depicts the density of coalescing spots over time, showing that coalescence events occur consistently throughout the experiment, even at early time points. This highlights the importance of distinguishing between newly detected, isolated spots and those that result from the merging of previously identified regions. Unlike the ImageJ approach, which does not incorporate spatial history or differentiate between isolated and coalescing spots, the present method uses temporal memory and centroid proximity to reduce overcounting and improve classification accuracy. In this plot, each coalesced spot corresponds to the first time a merged region is detected and classified as coalescing, based on the assumptions embedded in the Python pipeline. However, these regions may contain one or more isolated spots that were already counted individually in earlier frames. While the method minimizes, redundancy by referencing prior centroid positions, some interpretive ambiguity may persist in densely populated areas where spot overlap is more likely or high. This reinforces the value of spatial-temporal tracking in spot analysis for distinguishing between the initial formation of defects and their subsequent growth through coalescence, thereby enhancing the reliability of barrier performance assessments.


a.Isolate
RH: 39.5%
Normalized Isolated Spot Count
(spots · cm⁻² · frame⁻¹)
0
1
2
3
4
5
0
50
100
150
200
250
Time (Days)
96 nm S3
96 nm S2
96 nm S1
73 nm S1
50 nm S3
50 nm S2
50 nm S1
26 nm S3
26 nm S2
26 nm S1
14.0 nm S1
Coating Thickness (nm)

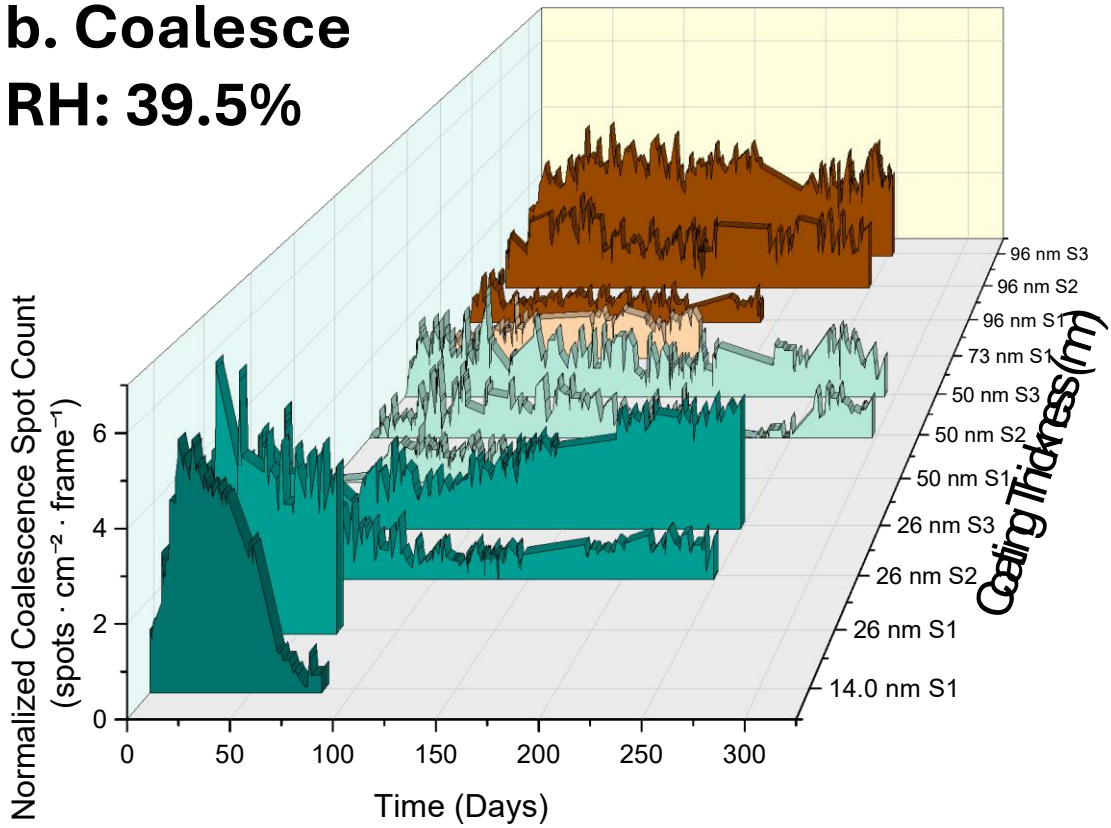

b. Coalesce
RH: 39.5%
Normalized Coalescence Spot Count
(spots · cm⁻² · frame⁻¹)
0
2
4
6
0
50
100
150
200
250
300
Time (Days)
96 nm S3
96 nm S2
96 nm S1
73 nm S1
50 nm S3
50 nm S2
50 nm S1
26 nm S3
26 nm S2
26 nm S1
14.0 nm S1
Coating Thickness (nm)

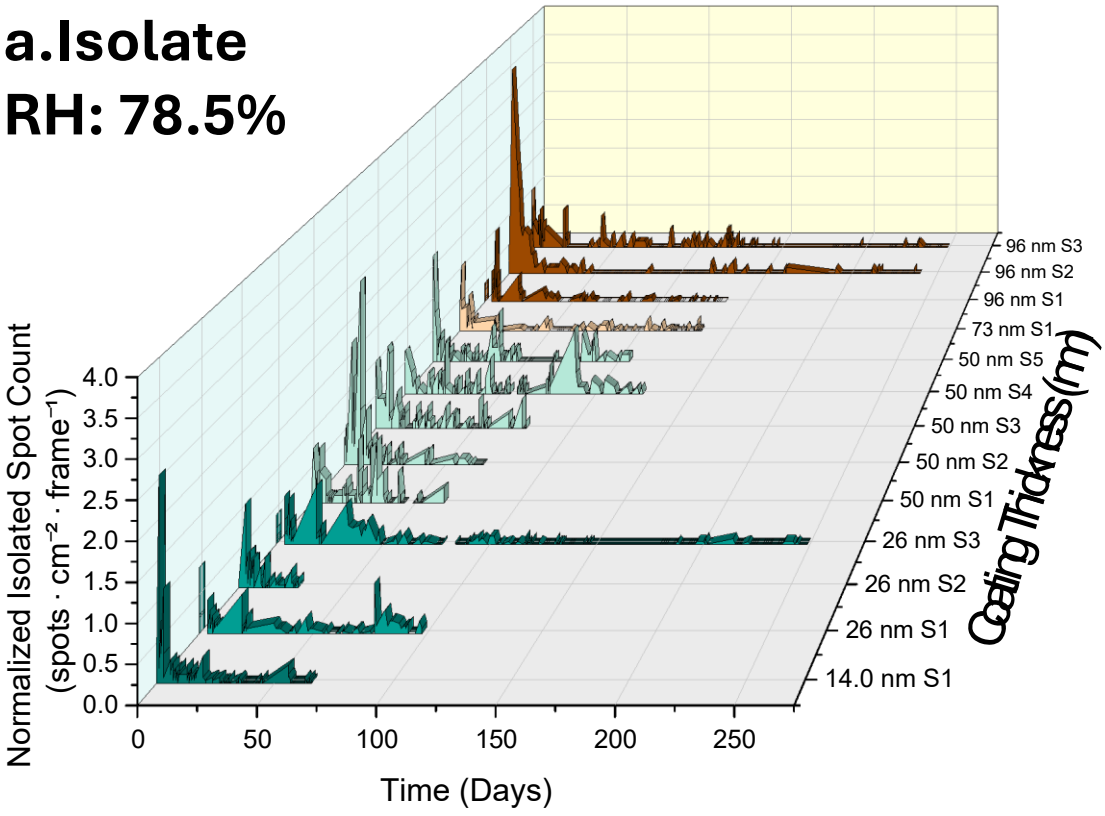
Figure 9-22: (a) ***Isolated Spots*** *and (b)* ***Coalescence Spots*** *(where spots merge) over time for various samples with different coating thicknesses at lower relative humidity (39.5%). The number of spots per frame has been normalized by the imaged area (spots · cm^{-2} · $frame^{-1}$) to account for differences in Ca test image sizes, enabling valid comparisons across samples. The data shows that most isolated spots are detected within the first few days, emphasizing the importance of distinguishing between isolated and coalesced spots. Failure to account for coalescence can significantly impact the estimated number of spots, as merging continues throughout the entire calcium test timeline.*

9.3.9.e Spot Density (High RH – 78.5%)

At higher humidity levels, as noted using the ImageJ methodology (9.3.9.b High Relative Humidity (78.5% $MgCl_2$ at 25°C)), faster permeation made it more challenging for the program to accurately identify and distinguish all possible spots. Some spots began coalescing before they could be individually observed, complicating the characterization process.

As revealed in Figure 9-23 (a), the method used for distinguishing spots provided more consistent characterization and spot count, once again plotted as the total number of newly detected spots per frame normalized by the imaged area (spots · cm^{-2} · $frame^{-1}$). Given the dataset and the increased permeation rate, the spot detection results appear comparable to those at lower humidity. This suggests that coating defects remain largely unaffected by environmental conditions or permeation kinetics.

In Figure 9-23 (b), a similar trend is observed, confirming that coalescence persists across conditions and reinforces the need for time-resolved analysis in spot tracking.


a.Isolate
RH: 78.5%
Normalized Isolated Spot Count
(spots · cm⁻² · frame⁻¹)
Time (Days)
Coating Thickness (nm)
96 nm S3
96 nm S2
96 nm S1
73 nm S1
50 nm S5
50 nm S4
50 nm S3
50 nm S2
50 nm S1
26 nm S3
26 nm S2
26 nm S1
14.0 nm S1

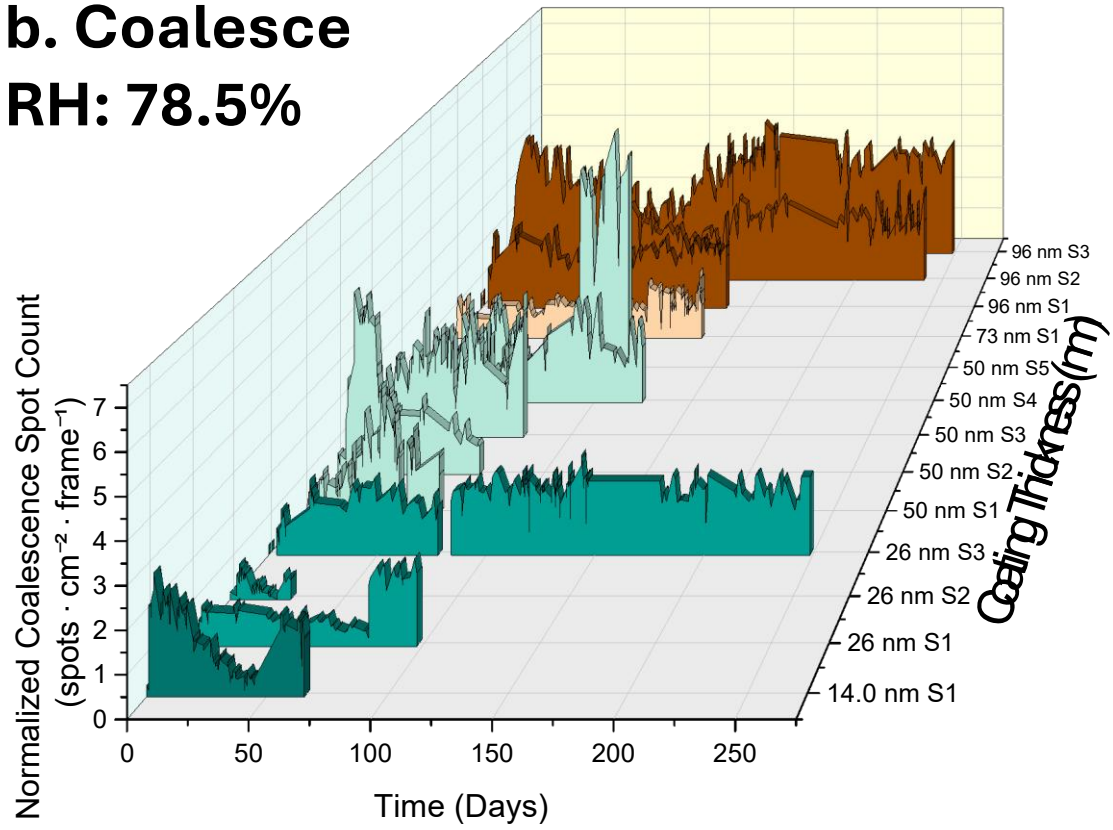

b. Coalesce
RH: 78.5%
Normalized Coalescence Spot Count
(spots · cm⁻² · frame⁻¹)
Time (Days)
Coating Thickness (nm)
96 nm S3
96 nm S2
96 nm S1
73 nm S1
50 nm S5
50 nm S4
50 nm S3
50 nm S2
50 nm S1
26 nm S3
26 nm S2
26 nm S1
14.0 nm S1

Figure 9-23: (a) ***Isolated Spots*** *and (b)* ***Coalescence Spots*** *are tracked over time for various samples with different coating thicknesses at higher relative humidity (78.5%); where number of spots per frame has been normalized by the imaged area (spots · cm^{-2} · $frame^{-1}$). The results reveal trends like those observed at lower humidity, where most isolated spots are detected within the first few days. Despite the faster permeation rate, the method demonstrates improved confidence in accurately characterizing and counting spots across the dataset. Additionally, the findings indicate that coalescence begins relatively early and continues throughout the entire test duration, reinforcing the need for careful differentiation between isolated and merged spots.*

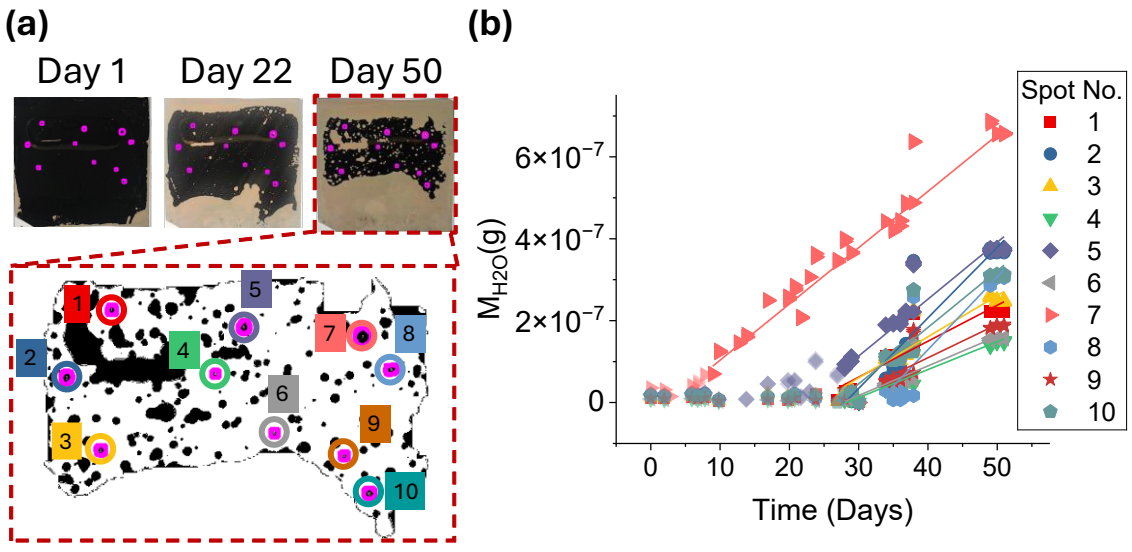
9.3.10 Example: Defect Size Estimation Calculations

The same sample as discussed in previous sections—14.0 nm AlO_x on PET at 25°C and 39.5% RH—was analysed using a value of the average bare PET WVTR ≈ 2.11 g/m²·day. This value represents the mean WVTR across all uncoated PET samples tested under the same conditions, as detailed in section 0 In short, WVTR, in polymers like PET increase with temperature as shown in the Arrhenius type relationship, attributed to enhanced molecular mobility and reduced polymer density [284, 285]. Higher RH elevates the partial pressure of water vapour, increasing the driving force for diffusion [286] and, in some cases can result in polymer swelling, creating additional free volume for permeation [287]. However, the Ea, an intrinsic property of the polymer, remains relatively constant across RH levels, as shown in Figure 3-4, suggesting that RH primarily influences WVTR by enhancing the thermodynamic driving force for permeation rather than significantly altering the diffusion energy barrier or path. While some literature suggests that polymer hydration may affect chain flexiblilty or free volume, such effects are not clearly reflected in the Ea trends observed in this study.

Calcium Test: Uncoated PET film Substrate, full data set seen in 9.6 Calcium Test Data Set for Uncoated PET) Ten distinct spots, before coalescence occurred, were chosen

from the Day 50 image and the growth of each was tracked on images between day 1 and 50, (Figure 9-24).

These selected spots were unaffected by edge permeation *i.e.* they were contained within the remaining calcium region until at least day 50. The spots had a circularity of 0.94 ± 0.06, which refers to the shape of the visible spots themselves; this does not imply that the underlying defect was circular. Spot No. 7 had appeared earlier (around Day 10) than the others, but its rate of increase in area was like others. Two of the spots (2 & 8) had a greater rate of water flow through the underlying defect. The spot growth across the ten spots suggested an average defect radius of 42.03 ± 6.41µm. Further example calculations for various thicknesses are found in 9.3.10.a Defect Calculations for Various Thicknesses.



Plot	1	2	3	4	5	6	7	8	9	10
Circularity	0.99	0.90	0.98	0.88	0.99	1.00	0.93	0.81	0.98	0.96
Slope	91.2 E-10 ±	179 E-10 ±	105 E-10 ±	68.2 E-10 ±	128 E-10 ±	73.0 E-10 ±	142 E-10 ±	192 E-10 ±	91.2 E-10 ±	134 E-10 ±

	2.95 E-10	4.73 E-10	2.50 E-10	2.03 E-10	2.49 E-10	1.44 E-10	2.58 E-10	6.60 E-10	1.48 E-10	2.07 E-10
No. Images (Slope)	34	34	34	34	34	34	66	25	27	30
Adj. R-Square	0.97	0.98	0.98	0.97	0.99	0.99	0.98	0.97	0.99	0.99
Defect Radius (μm)	37.08 ± 6.67	51.95 ± 8.45	39.87 ± 6.14	32.07 ± 5.53	43.90 ± 6.13	33.18 ± 4.65	46.34 ± 6.24	53.79 ± 9.97	37.09 ± 4.72	44.99 ± 5.58

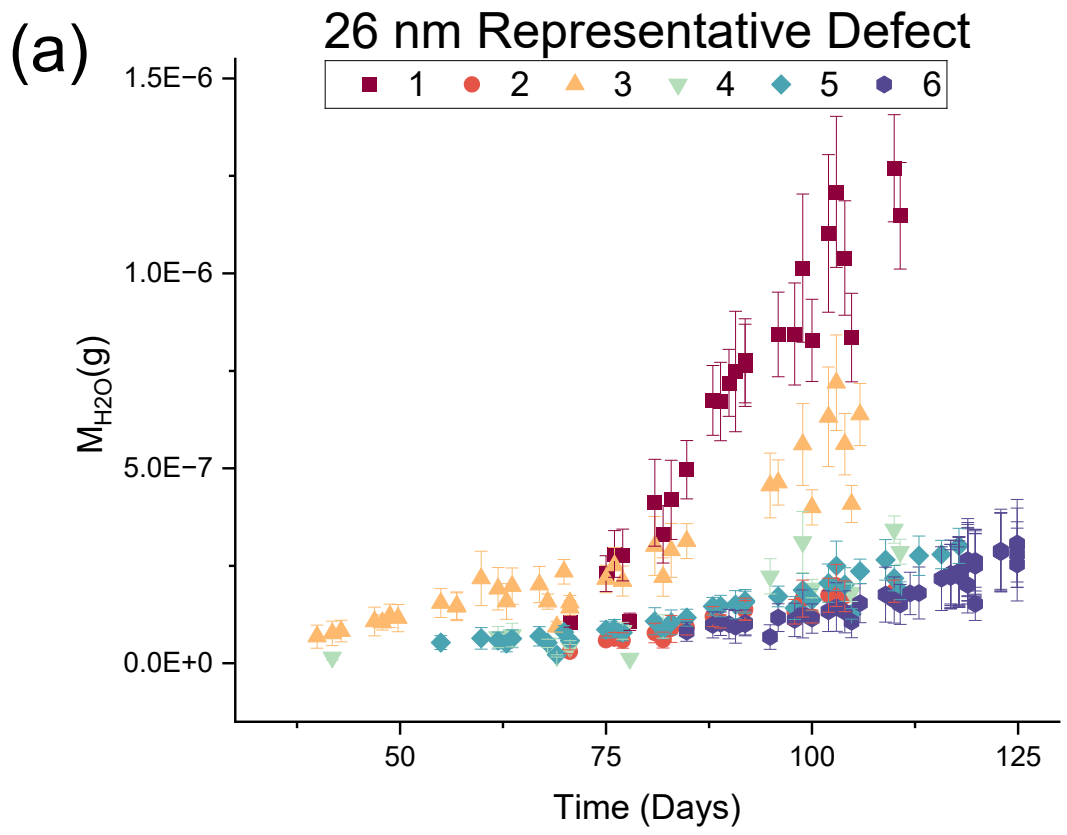
Figure 9-24: (a) Representative images of a coated PET film at Day 1, Day 22, and Day 50 showing the progression of water ingress at selected defect sites (highlighted in magenta). The bottom panel shows a binarized defect map from Day 50 with ten selected spot locations labelled for tracking. (b) Cumulative water mass uptake over time for the ten selected defects. The pale data points indicate the equilibration period before the onset of noticeable water ingress, highlighting the transition point at which each defect begins to grow significantly. By analysing uptake trends and dividing by the experimentally measured bare PET WVTR (~2.11 ± 1.40 g/m²·day at 29 ± 3.5°C and 48.2 ± 19.6% RH), the original defect areas were estimated. Assuming most defects are approximately circular ($r = \sqrt{(A/\pi)}$), defect sizes were inferred to lie in the micrometre range.

9.3.10.a Defect Calculations for Various Thicknesses

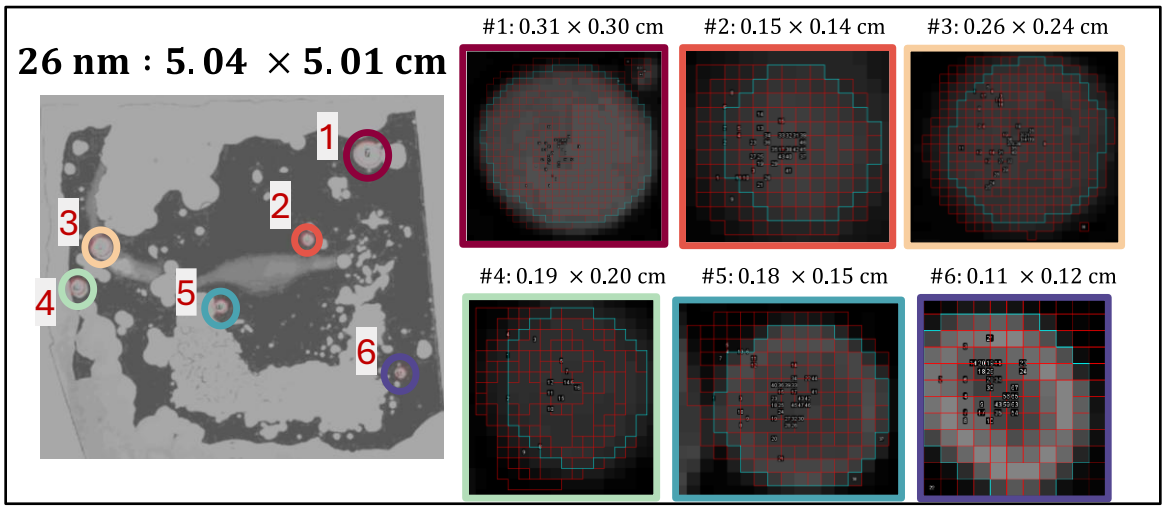
The next step involves applying this defect size estimation method to coatings ranging from 26 nm to 96 nm in thickness by isolating a defect separated from others before it merges with adjacent spots, where its growth is tracked over time to determine its calcium depletion and fluence.

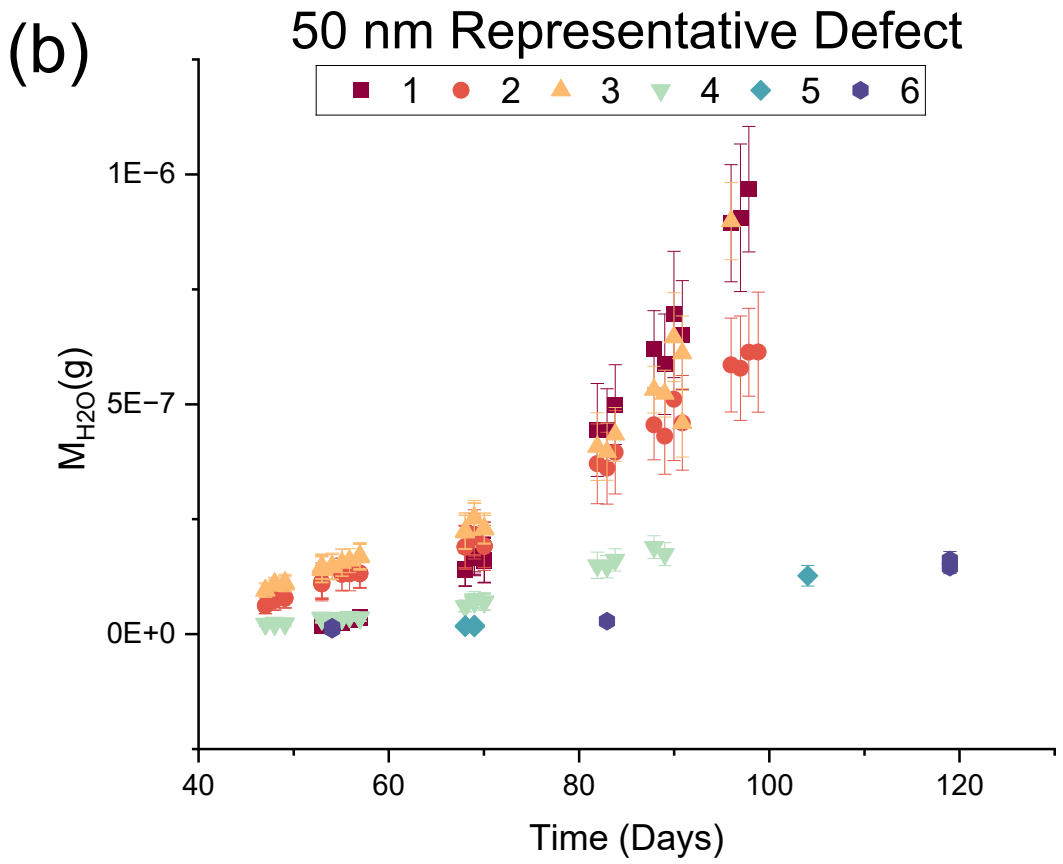
Representative results for 26 nm to 96 nm coatings are shown in Figure 9-25 (a) to (d). For each thickness, at least 5 distinct spots were analysed to estimate water uptake over time. The analysis reveals that different spot within the same sample exhibit varying water uptake rates, indicating differences in defect sizes.

Figure 9-25 (a) shows 26 nm coatings that show defect sizes ranging from around 15 µm to as large as 64 µm. For the 50 nm coating Figure 9-25 (b), indicates a similar range of defects size from 15 µm to 40 µm. The data from the 73 nm coated sample, shown in Figure 9-25 (c), contains one spot that showed a more significant spot growth rate, suggesting a defect size over 100 µm for this spot, but the other spots indicated a more typical defect size. Finally, at 96 nm Figure 9-25 (d) indicates the smallest measured defect size at ~6.0 µm for one of the spots.

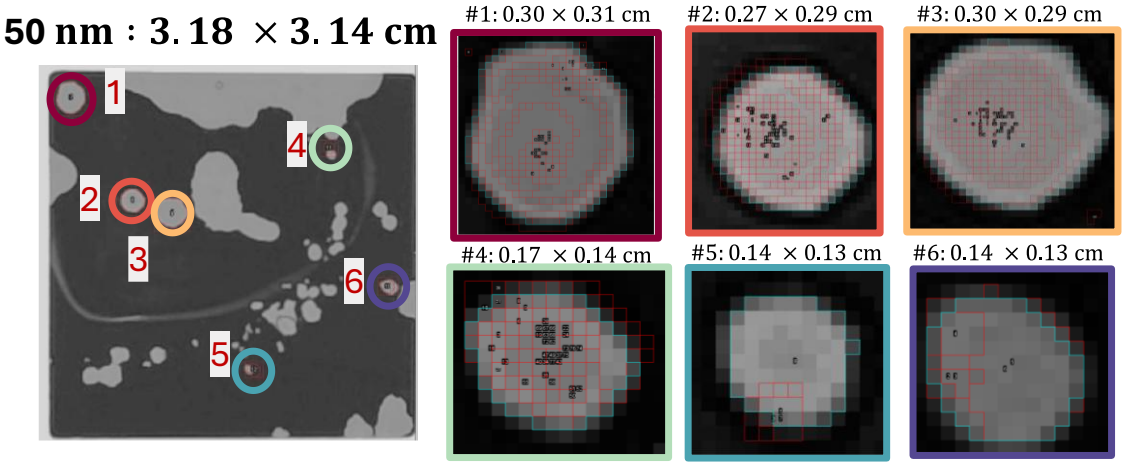


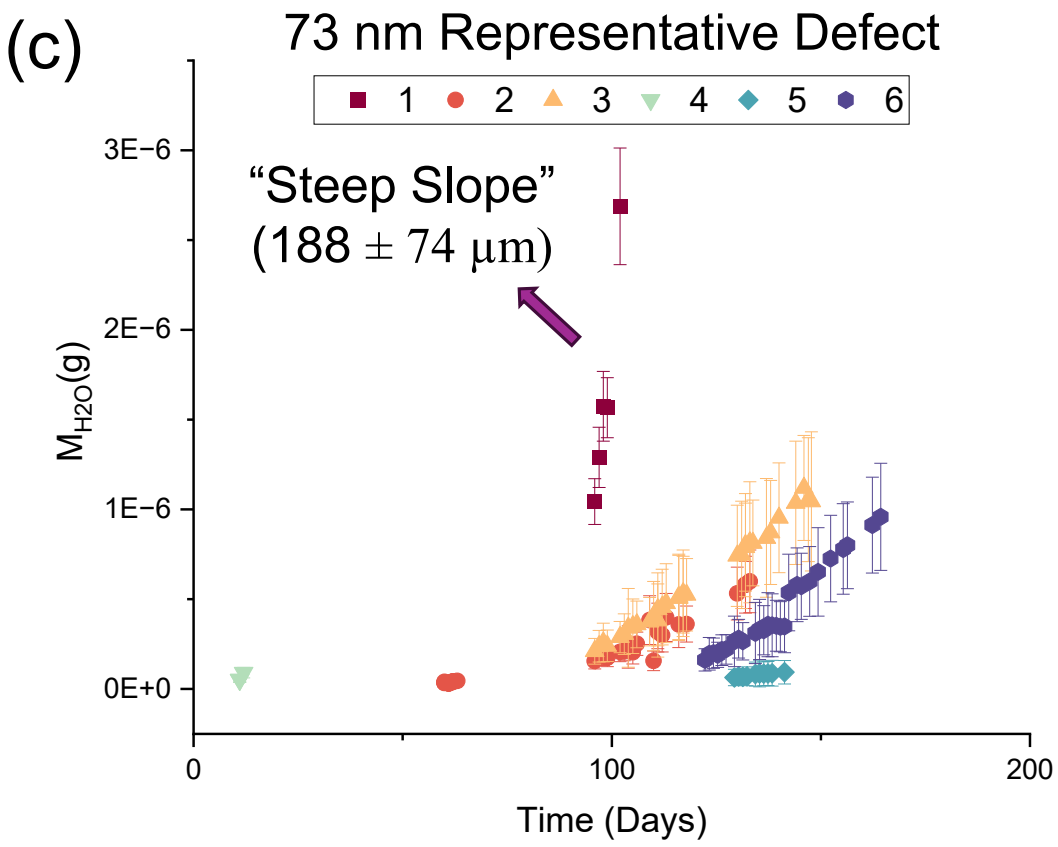
Plot	1	2	3	4	5	6
Defect Radius (µm)	63.64 ± 18.29	24.43 ± 6.00	27.75 ± 10.35	15.26 ± 11.32	25.13 ± 7.54	26.24 ± 6.62





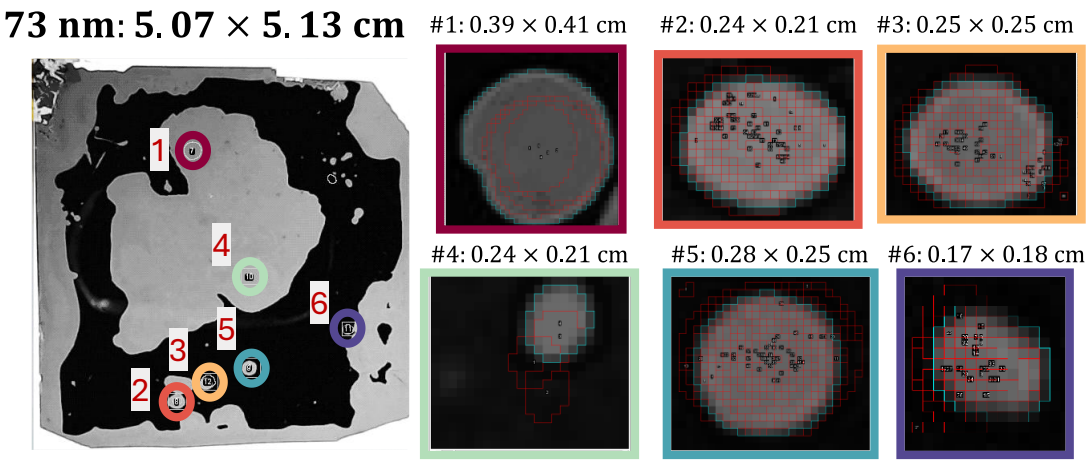
Plot	1	2	3	4	5	6
Defect Radius (μm)	40.32 ± 11.84	34.99 ± 7.16	35.65 ± 8.47	19.54 ± 5.12	21.06 ± 7.23	15.23 ± 7.82

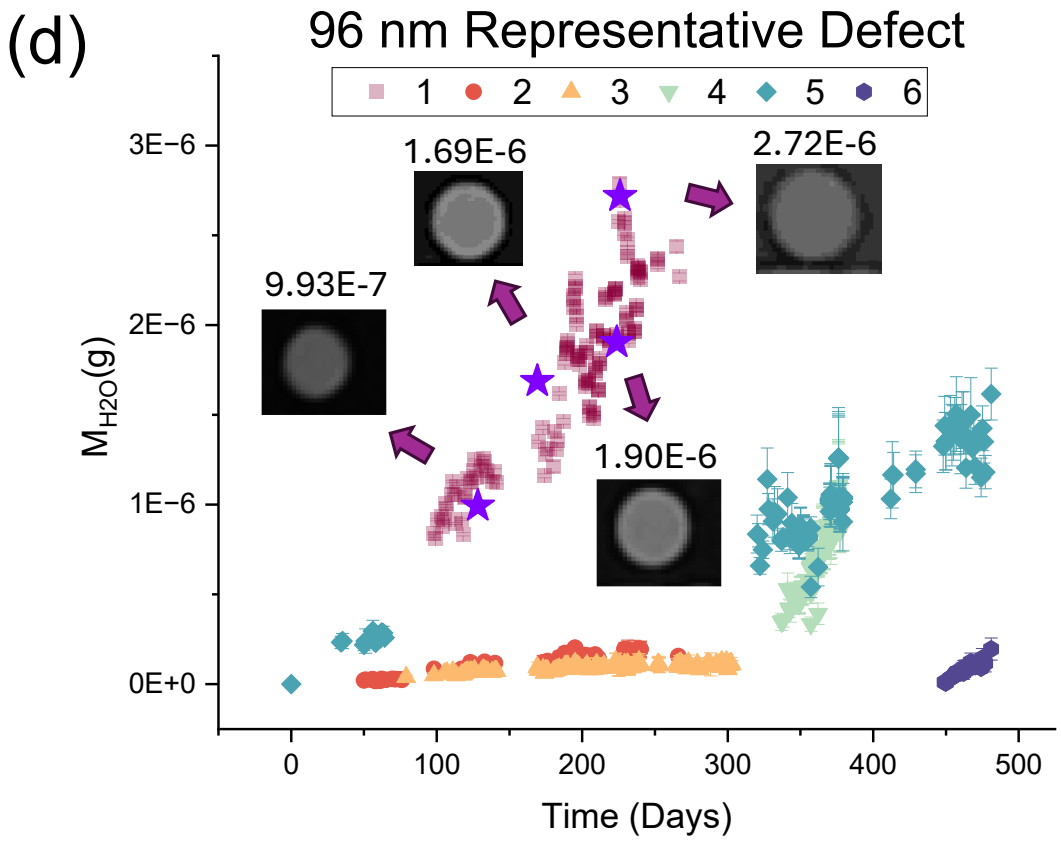

50 nm : 3.18 × 3.14 cm
1
2
3
4
5
6
#1: 0.30 × 0.31 cm
#2: 0.27 × 0.29 cm
#3: 0.30 × 0.29 cm
#4: 0.17 × 0.14 cm
#5: 0.14 × 0.13 cm
#6: 0.14 × 0.13 cm


(c)
73 nm Representative Defect
1 2 3 4 5 6
"Steep Slope"
(188 ± 74 μm)
3E−6
2E−6
1E−6
0E+0
M_{H2O}(g)
0
100
200
Time (Days)

Plot	1	2	3	4	5	6

Defect Radius (μm)	188.55 ± 73.99	26.51 ± 6.35	49.44 ± 6.82	77.07 ± 13.32	19.88 ± 6.26	50.27 ± 11.85





Plot	1	2	3	4	5	6
Defect Radius (µm)	37.80 ± 6.76	11.78 ± 1.94	6.74 ± 1.57	46.88 ± 11.06	18.23 ± 2.89	26.79 ± 7.44

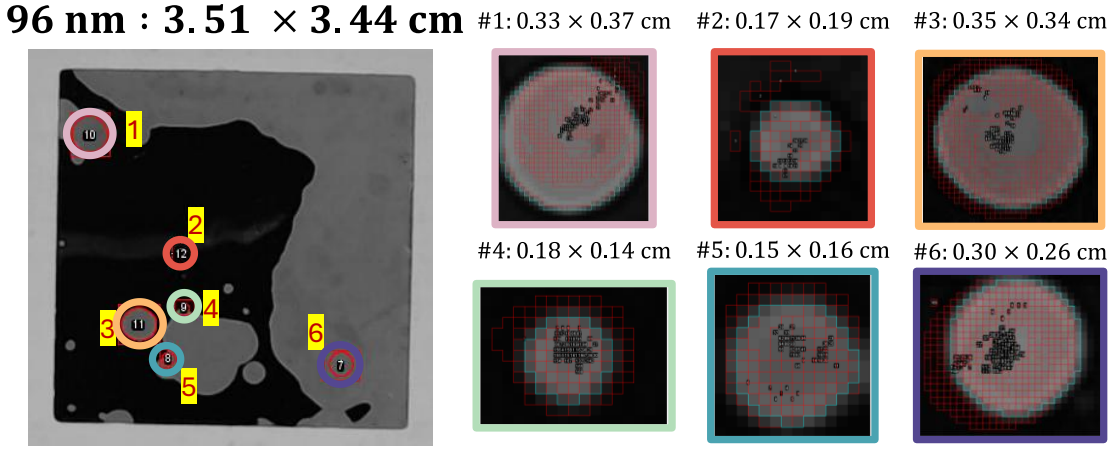


Figure 9-25: Representative samples of spots for varying thicknesses (a) 26.0 nm, (b) 50.0 nm, (c) 73.0 nm, and (d) 96.0 nm, tested at 25°C and 39.5% RH ($MgCl_2$). The graphs display water uptake (fluence) over time, with corresponding images of sample spots for each thickness, showing different defect sizes.

9.4 Aluminium Oxide (ALD) Coated PVAl Supporting Materials

9.4.1 Biodegradable Substrates for Flexible Applications

Cellulose-based substrates like cellulose acetate (CA), methyl cellulose (MC), hydroxypropyl methylcellulose (HPMC), and carboxymethylcellulose (CMC) have garnered attention for applications such as printed sensors and organic transistors, though improvements in moisture resistance and surface smoothness are needed [438].

Natural biopolymers like starch [439, 440] and chitosan provide solutions to issues like stretchability and brittleness, but their high water absorption remains a limitation. Starch films, for example, are used in printed sensors and supercapacitors, but require hydrophobic modifications for use in humid environments. Silk-based substrates have

been explored for OFETs and RFID circuits [441], while regenerated cellulose films have been applied in OLEDs for their flexibility and transparency [442].

Chemically synthesized biodegradable polymers, including polybutylene adipate terephthalate (PBAT) [268], polyvinyl alcohol (PVAl) [364], show potential in packaging and flexible electronics. Although bio-PET [443] is chemically identical to synthetic PET and therefore not biodegradable, it is considered more sustainable due to its plant-based origin. PVAl-based substrates are promising for biodegradable sensors and flexible displays, though they require enhanced moisture barriers. While many biodegradable materials lack intrinsic electronic functionality, conductive hydrogels and polymers like polyaniline and PEDOT are gaining attention for use in wearable devices due to their flexibility, conductivity and biocompatibility[444]. Integrating such materials with biodegradable platforms remains a key challenge for the development of fully sustainable flexible electronics.

Other biopolymers, like polylactic acid (PLA) and biodegradable polyimide substrates [445], are increasingly studied for implantable electronics and despite the promise of biodegradable polymers, challenges like surface roughness, thermal stability, and water vapor permeability persist. Materials like starch and PVAl still face moisture sensitivity issues, which can degrade their mechanical properties in flexible electronics. [364, 443, 446, 447].

9.4.2 Polyvinyl Alcohol (PVAl) Substrate

Polyvinyl alcohol (PVAl, also can be abbreviated as: PVOH, “PVA” – chemical formula $[CH_2CH(OH)]_n$), first prepared by Hermann and Haehnel, is a semicrystalline synthetic polymer, typically derived from oil-based feedstocks [448]. It receives interest

as a water-soluble, biocompatible, and biodegradable vinyl polymer. For example, PVAl, degrades through microorganisms like Pseudomonas, achieving 75% degradation within 46 days, making it suitable for sustainable applications in packaging and flexible electronics due to its non-toxic and odourless nature [364, 449-453]

PVAl has a high-water vapor permeability of about 10^2 g/m²·day. In contrast, polymers like PET, polysulfone, and PVDF have lower permeability values around 10 g/m²·day. Slightly hydrophilic polymers, such as polyimides, nylon (polyamide 6), and polycarbonate, fall between these ranges [422, 454]. It is an attractive substrate for ALD deposition *e.g.* using a TMA and water precursor mix because of the presence of a significant number of reactive or nucleation sites in PVAl due to its hydroxyl groups. Thus, PVAl is a promising substrate to create uniform and defect free coatings, significantly improving its barrier properties [221].

9.4.3 Synthesis of PVAl

Unlike many polymers, PVAl cannot be synthesized through direct polymerization of the repeating unit, in this case vinyl alcohol monomers as these are unstable (they tautomerize to acetaldehyde), but rather it is produced by hydrolysing polyvinyl acetate (PVAc) [364, 451, 455].

PVAc is synthesized via free radical polymerization of vinyl acetate and then hydrolysed using a strong base (NaOH) in an alcohol solution (methanol) through a process known as alcoholysis. This process removes the acetate groups from PVAc, yielding PVAl through hydrolysis [456, 457].

The resulting polymer, PVAl, consists mainly of vinyl alcohol repeat units with hydroxyl groups capable of forming hydrogen bonds, allowing PVAl to achieve high levels of crystallinity despite its atactic configuration [364, 455, 458] (Figure 9-26).

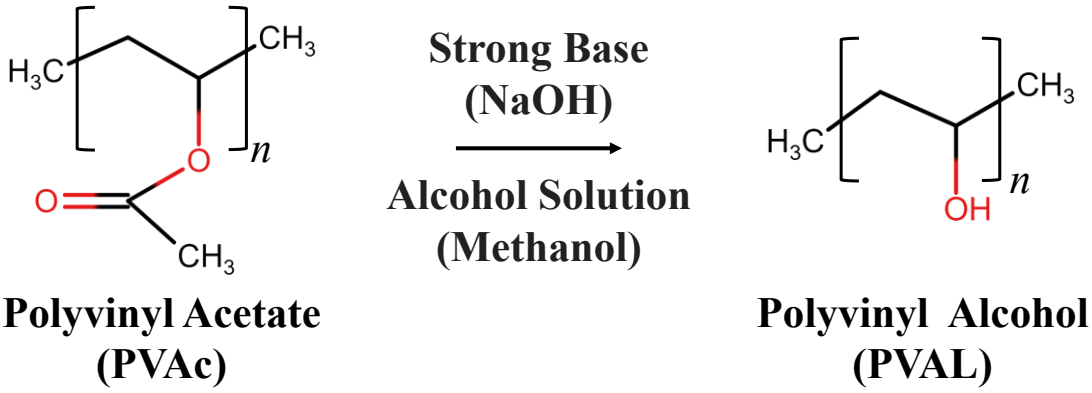


Figure 9-26: Polyvinyl Alcohol prepared by base catalysed trans-esterification reaction of polyvinyl acetate where it is hydrolysed in a strong base (NaOH) in a alcohol solution (methanol) [457, 458].

9.4.4 Properties of PVAl

Polyvinyl Alcohol (PVAl) films are generally categorized based on their degree of hydrolysis, which affects their water solubility and mechanical properties. Partially hydrolysed PVAl (approximately 87-89% hydrolysed) is highly water-soluble and is used in applications, such as water-soluble films and adhesives. In contrast, fully hydrolysed PVAl (approximately 98-99% hydrolysed) is less water-soluble and is utilized where water resistance is important [459].

The properties and performance of PVAl are highly dependent on its water content and degree of hydrolysis, which influence its mechanical properties, degradation behaviour, and crosslinking potential. Water acts as a plasticizer, affecting flexibility and tensile strength, and plays a crucial role in the polymer's biodegradation and chemical modification processes.

9.4.4.a Mechanical Properties Dependent on Water Content:

PVAl's mechanical behaviour is directly influenced by humidity and the degree of hydrolysis. In high-humidity environments, PVAl is plasticised by the absorbed water, becoming soft, flexible, and tough. In contrast, under low-humidity conditions, PVAl becomes hard and brittle. Additionally, PVAl can swell and dissolve in humid or aqueous environments [456, 460, 461].

The hydroxyl groups on PVAl's backbone form hydrogen bonds between chains, creating a physically crosslinked network that enhances mechanical stability. However, these bonds are reversible in water leading, ultimately, to dissolution. For permanent crosslinking (*i.e.* that resists dissolution), covalent bonds must be introduced via external agents (*e.g.*, borax, aldehydes) or energy input (*e.g.*, heat, UV irradiation). PVAl typically has a molecular weight range of 20,000 to 400,000, depending on the length of the precursor vinyl acetate chains, and usually has a degree of hydrolysis between 80% and 99% [364, 453, 455]. Its physical properties include a density of 1.19 g/cm³ [462], a glass transition temperature of approximately 85 °C (358 K) [365], and a melting point around 180 °C (453 K) [463, 464], tensile strength at break 30 – 100MPa, elongation at break 100 – 600% and oxygen transmission (38 micron, 0%RH): 0.2 to 5 $cm^3/day/m^2/bar$ [465].

The degree of hydrolysis significantly affects the mechanical strength and solubility of PVAl [366, 456, 457, 459, 466-471]:

Fully Hydrolysed PVAl (98–99% hydrolysis): Nearly all acetate groups are removed, leading to high crystallinity, higher strength (~80 MPa), and reduced solubility. It dissolves at temperatures above 70°C and is more stable in organic solvents, making it ideal for applications requiring high strength and low solubility.

Partially Hydrolysed PVAl (80–89% hydrolysis): Retains some acetate groups, resulting in lower crystallinity and higher solubility at lower temperatures. Its weaker mechanical properties and higher solubility make it suitable for adhesives, coatings, and applications where solubility is prioritized. It also has lower film-forming ability.

9.4.4.b Degradation:

PVAl is known for its excellent barrier properties against gases such as oxygen, carbon dioxide, and nitrogen, comparable to those of ethylene-vinyl alcohol (EVOH). It also resists oils and organic solvents. However, its structural integrity diminishes significantly under moist conditions due to the presence of hydrophilic hydroxyl groups, which absorb moisture and weaken the material [456, 457, 459, 466]. The degradation of PVAl is influenced by factors such as the degree of polymerization, degree of hydrolysis, and environmental conditions.

PVAl is biodegradable under appropriate conditions, primarily through the action of microorganisms capable of metabolizing the polymer, such as Pseudomonads [472, 473] or Sphingomonas [474]. Partially hydrolysed PVAl degrades more rapidly because its higher solubility in water facilitates microbial access. In contrast, fully hydrolysed PVAl degrades more slowly due to its higher crystallinity and lower solubility, making it less accessible to microbial enzymes [475, 476].

Environmental factors, including temperature (PVAl fibres turn “yellowish” at 220°C and soften at 230 – 250°C), moisture content, and pH, play a significant role in modulating the biodegradation process of PVAl, either accelerating or retarding it. In soil or compost environments, clay particles can inhibit microbial access to PVAl by limiting exposure, thereby reducing the degradation rate. Conversely, high moisture conditions

can enhance the degradation rate by increasing the solubility and availability of PVAl to microbial action [475, 477, 478]

9.4.4.c Crosslinking:

Enhancing the water resistance of PVAl, can be achieved through chemical crosslinking, the incorporation of nanomaterials, and polymer co-blending. Crosslinking forms chemical bonds between hydroxyl groups that create a stable network that reduces water solubility. However this process presents challenges due to difficulty in (1) controlling crosslink density, (2) harsh reaction conditions, and the risk of (3) non-uniform or inhomogeneous network formation [377, 384, 458, 459, 479, 480]. Optimizing reaction parameters (*e.g.*, pH, temperature and crosslinker concentration) is crucial to balancing water resistance with mechanical integrity.

The addition of nanomaterials – such as silver nanoparticles, nano-TiO_2, nanocellulose and cellulose nanofibers – modifies PVAl's microstructure in several ways. These additives can act as physical crosslinking or nucleating sites, that can influence crystallinity depending on its interaction with PVAl chains. As known some nanofillers like nanocellulose have highly ordered domains that can act as templates for PVAl crystallization, increasing the degree of crystallinity in specific conditions, or graphene oxide that can introduce hydrophilic functional groups, facilitating additional hydrogen bonding between PVAl chains and the filler, where this enhanced interfacial interaction can improve mechanical strength and barrier properties by improving the polymer matrix. However, these effects depend on nanoparticle dispersion, concentration and surface functionalization [459, 481-485].

Co-blending PVAl with polymers like chitosan also can introduce additional intermolecular hydrogen bonding further reinforcing the polymer network. Chitosan contains hydroxyl (-OH) and amino ($-NH_2$) groups that form strong hydrogen bonds with PVAl chains. That leads to a more diverse and interconnected network enhancing water resistance and improving film integrity [486]. Notwithstanding this, synergistic modifications that combine crosslinking and nanomaterial addition have also been explored to enhance PVAl's performance in demanding environments [459].

9.4.4.d Applications:

Due to its versatile properties, PVAl is used in a wide range of applications, including consumer packaging (anti-microbial food packaging), household products (detergent capsules or contact lens lubricants), textiles, fused deposition modelling (3D Printing), flexible electronics, and medical products [463, 465, 487-491]

This study evaluated two types of partially hydrolysed (85-90%) PVAl films from Aquapak Polymers (UK) that are melt-processed materials formed into films for packaging and coating applications. The two materials will be referred to as "Thin" (Monolayer PVAl, Betol, ~21 μm) and "Thick" (Bilayer PVAl, Alpine, ~42 μm). The objective was to assess their water vapor barrier properties and determine if adding AlO_x via Atomic Layer Deposition (ALD) could address the challenges in enhancing these properties.

9.4.5 WVTR Measurement for uncoated PVAl MOCON Aquatran

9.4.5.a Challenges in Measuring PVAl WVTR with Mocon Aquatran

Due to its hydrophilic nature, PVAl has high water solubility (S), and hence high-water permeability, which made it challenging to obtain reliable MOCON Aquatran measurements. Measurements often exceeded the machine's 5-gram limit, compromising accuracy. Similar issues have been reported in the literature with failed tests using equipment like the Permatran-W 3/33 MA from Mocon Inc., Minnesota, USA [480].

To mitigate these complications, experiments were conducted using samples masked with a standardized area of 1 cm^2, to reduce the volume of water being measured.

Despite using the mask, the reduced water volume measurements remained high and often erroneous. However, the raw A/D signal data allowed an estimate of WVTR to be made by utilizing previous PET measurements, where A/D turns are well characterized.

Figure 9-27: shows the correlation between A/D turns and WVTR for various materials, including uncoated PET at different humidity levels, AlO_x-coated PET, and a commercial packaging film with high water vapour permeability (from Crown Brand Building Packaging) used as a comparative sample.

The linear regression line, with an adjusted R^2 of 0.892, indicates a strong correlation, allowing estimation of WVTR from A/D turns. WVTR can be estimated using the Equation 9-1:

$$WVTR \approx 4.96 \times \left(\frac{A}{D} Turns\right) - 1.72$$

Equation 9-1

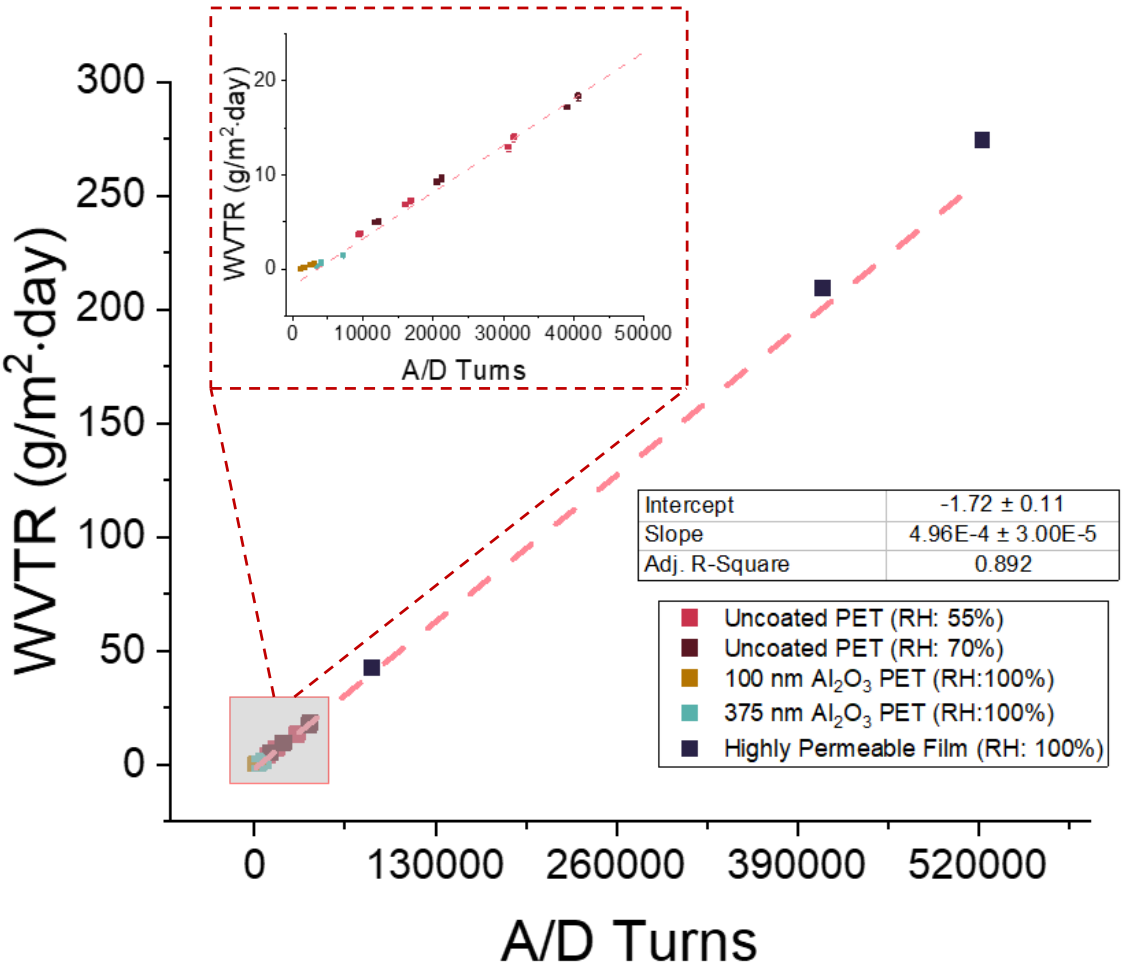


Figure 9-27: The WVTR vs. A/D Turns model demonstrates a linear relationship, allowing estimation of PVA's WVTR using A/D turns from the Mocon Aquatran raw data.

9.4.5.b Discussion on Mocon Aquatran WVTR Results

The uncoated and ALD-coated PVAl substrates (with coatings identical to those used on the PET substrate) were tested for A/D turns, and their estimated Water Vapor Transmission Rate (WVTR) was calculated using Equation 9-1. The results, as shown in Figure 9-28 and Figure 9-29, depict the estimated trends of WVTR over varying coating

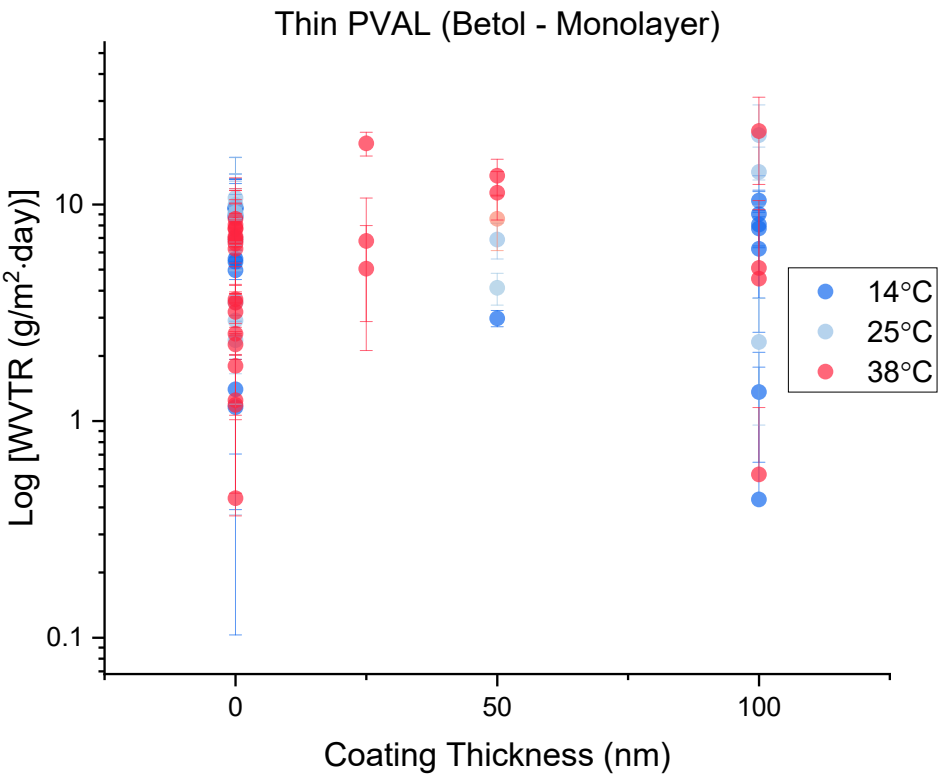
thicknesses. All tests were conducted at 100% relative humidity with varying temperatures.

9.4.5.c Thin PVAl (Betol) Mocon Aquatran

Figure 9-28 shows that uncoated substrates had average WVTR values (4 to 7 $g/m^2 \cdot day$), with no consistent temperature-dependent trend, possibly due to sample variation, mechanical damage or measurement inaccuracies.

For coated samples, WVTR improvements were inconsistent and statistical analysis (ANOVA) found no significant differences in WVTR across coating thicknesses ($p = 0.67$) or temperatures ($p = 0.30$), suggesting the variations were likely random. The high variability in results, especially in thicker coatings, points to potential issues with the measurement process or coating application. It is also notable that the coated samples should record lower WVTR than uncoated specimens regardless of condition, however this was not the case noting that there are other factors at play like possible coating degradation and similarly sample that was masked may have inflated WVTR.

When comparing PVAl to PET, the WVTR variability in PVAl was significantly higher, especially in coated samples. This suggests greater instability in the Mocon Aquatran measurements for PVAl, which may require further investigation to ensure consistent results, or perhaps significant variability in the PVA films.



Coating Thickness (nm)	Temperature (°C)	Mean WVTR (g/m²·day)	Std. Deviation
0 nm	14	6.78	4.24
	25	6.82	3.39
	38	4.76	2.88
26 nm	38	10.32	3.14
50 nm	14	2.98	0.26
	25	6.89	1.29
	38	12.44	2.23
96 nm	14	6.19	2.65
	25	12.44	5.26
	38	8.00	5.96

Figure 9-28: WVTR (on logarithmic scale) for thin PVAl (21 µm), with AlO_x coatings pf varying thicknesses at different temperatures. Error bars represent the standard deviation of measurements, reflecting variability across replicates, likely due to PVAl's high permeability, errors in A/D estimation, and averaging inconsistencies. No consistent trend was observed with coating thickness beyond an initial reduction in WVTR, but notably, at higher temperatures, PVAl sometimes recorded lower average WVTR values

than at lower temperatures. For instance, uncoated PVAl at 38°C showed an average WVTR of 4.76 ± 2.88 g/m²·day, which is lower than the 6.78 ± 4.24 g/m²·day at 14°C. Similarly, for 96 nm AlO_x-coated PVAl, the average WVTR at 38°C was 8.0 ± 5.96 g/m²·day, compared to 6.19 ± 2.65 g/m²·day at 14°C. The relatively high standard deviations indicate substantial variability across measurements, suggesting possible inconsistencies in barrier performance or experimental conditions.

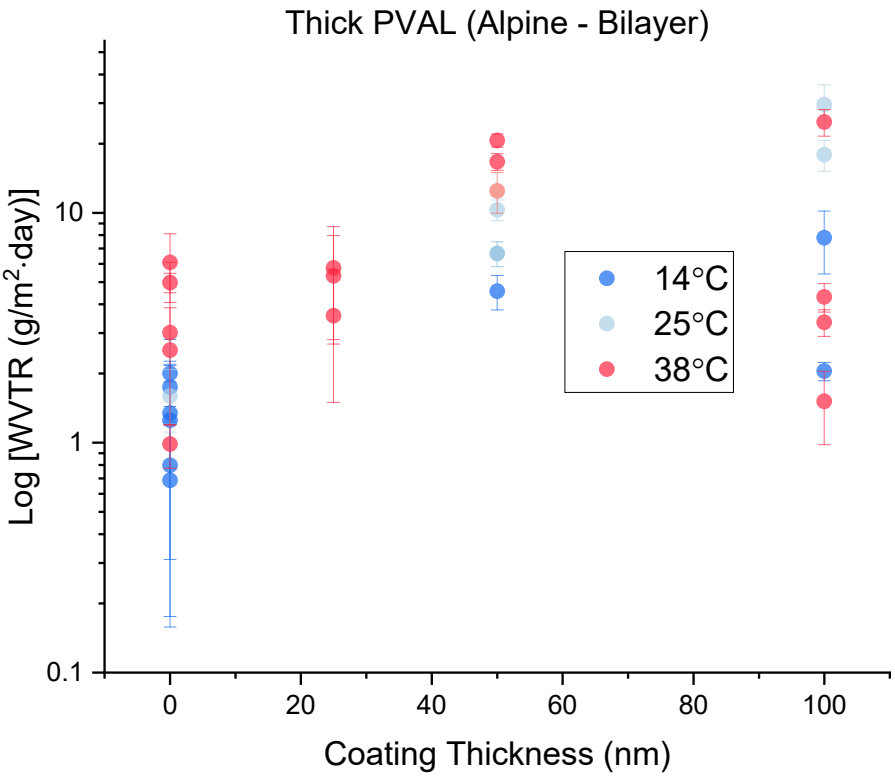
9.4.5.d Thick PVAl (Alpine) Mocon Aquatran

As Fick's law predicts, increasing the substrate thickness reduces WVTR, Figure 9-29. In this case, thicker PVAl (42 μm) showed significantly lower WVTR than thinner PVAl (21 μm), with reductions of ≈ 81% at 14°C and ≈ 77% at 25°C. At 38°C, the reduction was smaller, at ≈ 26%.

While increasing film thickness generally enhances barrier properties at low temperatures, this effect diminishes at higher temperatures. It is possibly due to the hydrophilic nature of PVAl which leads to increased water absorption at elevated temperatures that result in polymer plasticization and network swelling. This disrupts the polymer matrix, increasing permeability and reduces effectiveness of thickness in controlling WVTR as evidenced by loss of barrier properties under high temperature and humidity conditions [367, 492-494].

In line with this, there is no indication from these measurements that the coating reduces the WVTR. Statistical analysis shows no significant differences in WVTR based on coating thickness ($p = 0.35$) or temperature ($p = 0.44$), suggesting the variations may be random. Standard deviations are lower than those seen in thin PVAl, indicating more consistent measurements. However, the expected trend of increasing WVTR with higher temperatures isn't always observed. The same comment on reduction in WVTR with coated samples is also not seen which should be evident.

In summary, while greater substrate thickness improves PVAl barrier properties, inconsistencies and deviations from expected trends, especially at higher temperatures, suggest that factors like the high permeability as well as sample quality, potential defects, and PVAl's hydrophilic nature affect WVTR measurements using this Mocon technique. Further investigation is needed to improve coating reliability and measurement consistency.



Coating Thickness (nm)	Temperature (°C)	WVTR (g/m²·day)	Std. Deviation
0 nm	14	1.30	0.82
	25	1.60	0.49
	38	3.52	1.76
26 nm	38	4.88	2.58
50 nm	14	4.56	0.78
	25	10.31	1.06
	38	18.68	1.37

96 nm	14	4.92	1.69
	25	23.77	4.95
	38	8.51	1.71

Figure 9-29: WVTR (on logarithmic scale) for thick PVAl (42 µm), with AlO_x coatings pf varying thicknesses at different temperatures. Compared to thinner samples, the thicker PVAl exhibited lower standard deviation, suggesting greater uniformity and improved measurement reliability. This may be due to thicker PVAl having better barrier properties (less permeable) and it being thicker was easier to test and handle, especially for cases like PVAl or highly permeable films where detection limits were over exceeded in the MOCON Aquatran. As with thinner samples, a directly proportional relationship between temperature and WVTR is not consistently observed, like trends seen in PET substrates. For example, for 96 nm AlO_x - coated thick PVAl, WVTR at 38°C was 8.51 ± 1.71 g/m²·day, compared to 23.77 ± 4.95 g/m²·day at 25°C. This suggests that factors beyond temperature alone have influenced WVTR estimations in these systems.

9.4.5.e Estimations of coated PVAl Samples at Diff. Humidities.

Additionally, another set of PVAl films was tested at different humidity levels at a constant temperature of 38°C. Table 9-2, summarizes the results for 26 nm and 73 nm thick PVAl films, showing an increase in WVTR with higher relative humidity. Notably, the 26 nm film at 80% RH exhibits a particularly high standard deviation (9.12 ± 18.39 g/m²·day), possibly due to sample damage or high permeation rates at elevated humidity, which is not atypical for PVAl films observed.

Table 9-2: Estimated WVTR's of Coated PVAl samples at Different Humidities.

Coating Thickness (nm)	Relative Humidity (%)	Mean WVTR (g/m²·day)
26 nm	35%	1.19 ± 0.37
26 nm	80%	9.12 ± 18.39
73 nm	35%	1.97 ± 0.77
73 nm	80%	2.62 ± 2.44

9.4.6 Supplementary Ca Test Results for Uncoated and Coated PVAl Films

9.4.6.a Measuring Uncoated Thin and Thick PVAl Ca Test

A key challenge in Ca testing is determining whether calcium depletion accurately reflects permeation through the barrier layers, or if it is significantly influenced by sideways permeation through the epoxy layer. Similar methodologies to isolate permeation are employed to those in previous, PET, chapter: 4.4 Edge Permeation in the Calcium Test;

This is particularly relevant for coated PVAl, where the barrier is much better and longer time scales that even small incremental edge effects can compound and significantly distort the measured WVTR. In contrast, for highly permeable films like uncoated PVAl, edge effects are less critical as water vapor passes readily through the bulk film. These results are presented in Figure 9-30 for uncoated PVAl samples.

In the first experiment, thin PVAl (Betol) films were evaluated at room temperature (23 °C) and 40% RH, Figure 9-30 (a). Slightly uneven permeation was observed, likely due to variations in film thickness or substrate damage, with arrows in Figure 9-30 (a) indicating permeation progressing from right to left. However, unlike the distinct brightness changes seen in previous cases of sideways permeation, the observed permeation pattern here appears different more gradual and diffuse. While the measured WVTR of 2.13 ± 0.004 g/m²·day is relatively low, this alone does not rule out sideways permeation. Instead, the absence of significant sharp, directional front and arguably uniformity in the calcium image suggest that sideways permeation was a dominator factor in the estimation.

Calcium depletion began at approximately 110 minutes and became more pronounced by 165 minutes, with near-complete depletion observed at 220 minutes. The residual “black” spots are likely regions where calcium remained unreacted, although it is also plausible that some of these dark features arise from surface contamination or other artifacts. Notably some of these areas faded over time, while others persisted long suggesting a mixture of origins or variability in local exposure conditions. These differences may result from non-uniform moisture exposure rather than bulk permeation. Where previous Studies have shown that uneven film thickness can lead to differential permeability zones leading to varied calcium degradation patterns [214, 392]. Additionally, contaminants or surface residues may have also altered local permeability by either shielding certain areas from moisture ingress or accelerating degradation at specific sites.

Environmental factors, such as humidity gradients caused by imperfect humidity control within the test box, condensation effects or even microbial growth (though less likely and cannot be entirely excluded) [495], may have contributed to these localized variations. If this were the case, it would suggest that the dark patches result from selective moisture exposure rather than an inherent barrier defect which has direct implications for WVTR interpretation.

In the subsequent experiment, the same thin PVAl substrate was subjected to elevated temperature and humidity (Figure 9-30 (b)). Under these conditions, calcium depletion occurred significantly faster, with nearly half of the calcium layer depleted within 10-15 minutes and near complete depletion by 20 minutes. The sharply defined bright and dark regions observed suggest a distinct permeation behaviour, potentially

influenced by lateral moisture ingression from the sample edges rather than uniform or top-down diffusion the PVAl itself [496].

It is important to acknowledge that this might be a non-barrier related effect: the permeation pattern is consistent with possible sideways migration of water vapor into the sample through pathways such as delamination, capillary flow along the epoxy interfaces, or transport through the hydrophilic domains of the PVAl are known to swell and facilitate in plane diffusion [497].

Accounting for these effects, by excluding the bright regions migrating inward from the edges during analysis as also done in previously in PET samples (see section: 4.4 Edge Permeation in the Calcium Test), still shows a significantly higher WVTR of 25.8 ± 1.10 g/m^2·day.

For the thicker PVAl layer (42 μm) tested at an elevated temperature of 45 °C and under two relative humidity levels (65% and 71%). As shown in the image sequence of Figure 9-30 (c), the optical photographs reveal asymmetric Ca depletion, with bright regions gradually expanding inward from edges. This visible directionality in the depletion pattern suggests some lateral moisture ingression, likely through the epoxy, and was considered during WVTR estimation.

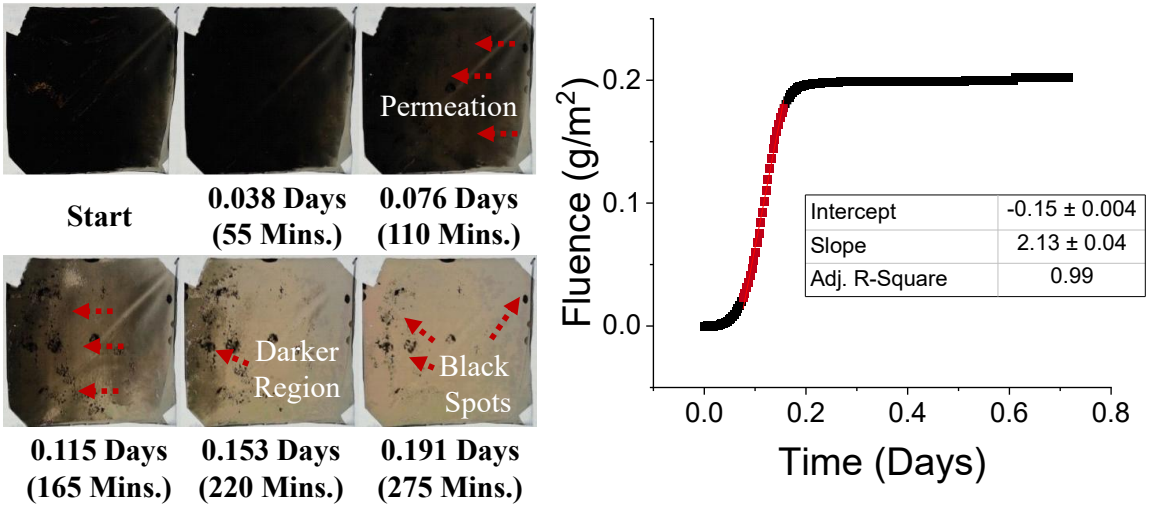
As expected, following Fick's law which predicts that increased thickness results in lower permeability, a reduction in WVTR is observed, where the measured values are 20.3 ± 1.62 g/m^2·day at 65% RH, and 21.1 ± 2.11 g/m^2·day at 71% RH.

Additionally, the optical images of the thicker substrate reveal localized "black spots", indicating areas where Ca persists longer than in the surrounding film. These features are like those observed in Figure 9-30 (a) and are likely caused by non-uniform

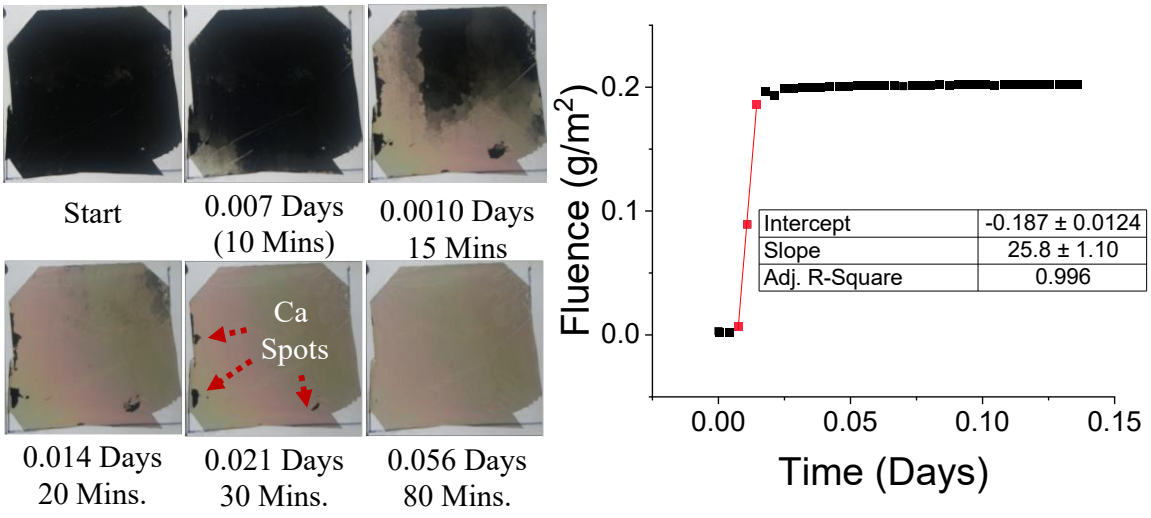
permeation of water vapor due to micro-scale variations in the polymer film, such as localized defects, uneven thickness, or slight inhomogeneities. As observed the main Ca layer depletes first, while these discrete pockets remain intact, highlighting an uneven oxidation patter of the Ca layer.

While thicker polymers generally lead to a reduction in overall WVTR, these findings illustrate how localized diffusion pathways can undermine uniform protection, where achieving a sufficiently low WVTR with coated samples may be more challenging as ensuring perfect encapsulation requires precise control over substrate uniformity which directly impacts defect mitigation.

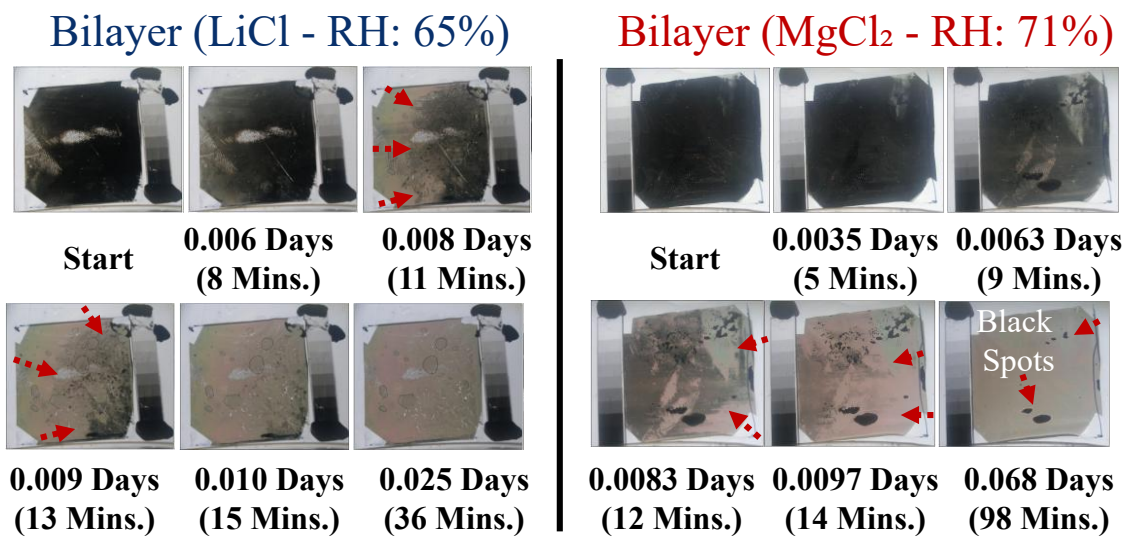
(a) . Thin PVAL (Monolayer Betol) 23 °C, 40% RH



(b) . Thin PVAL (Monolayer Betol) 45 °C, 65% RH



(c) . Thick PVAL (Bilayer Alpine), 45 °C.



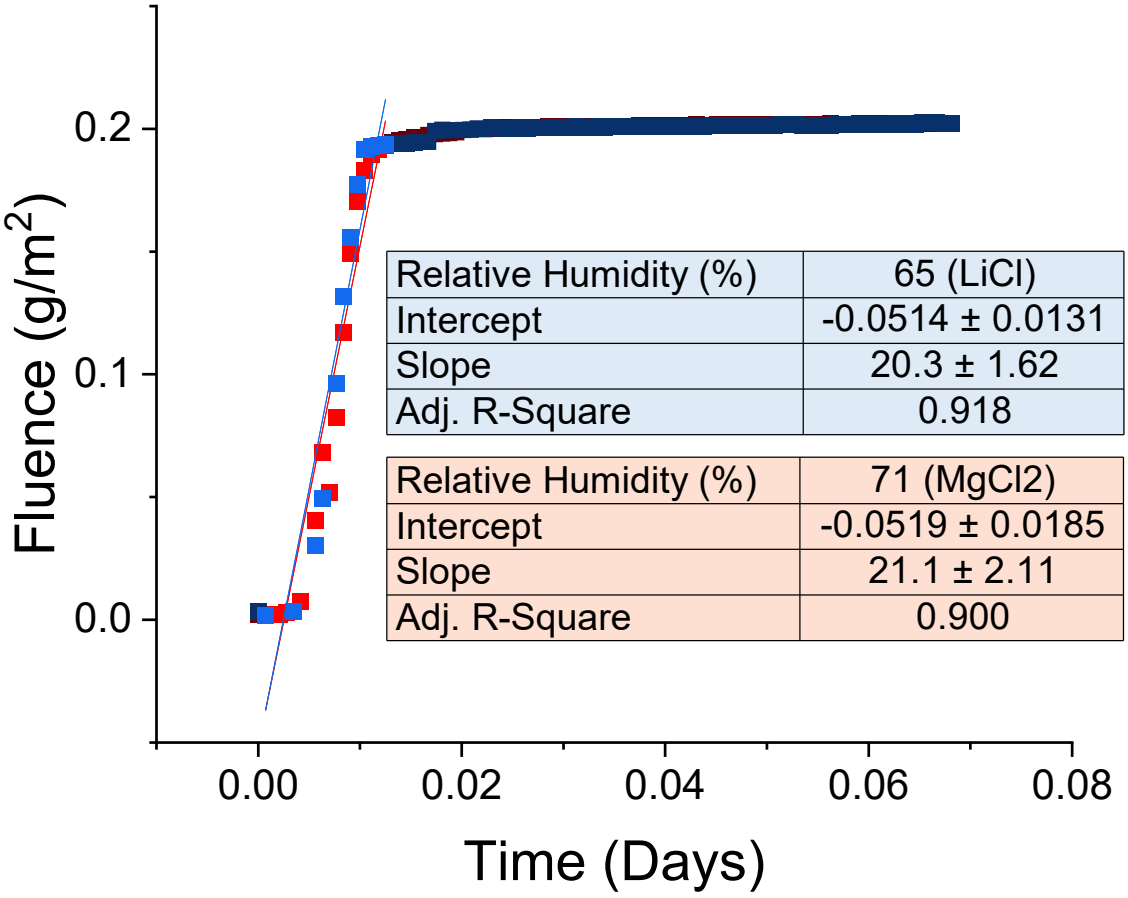


Figure 9-30: (a) Calcium depletion in thin PVAl tested at 23 °C and 40% RH. Red arrows indicate uneven permeation from right to left, likely due to variations in film thickness or substrate imperfections. (b) Calcium depletion in thin PVAl tested at 45 °C and 65% RH, showing accelerated depletion compared to (a), highlighting the influence of elevated temperature on WVTR. The difference in WVTR is approximately ~23 g/m²·day between these conditions. Notably, this estimate is considerably also higher than those obtained from MOCON Aquatran System, which may be due to systematic overestimation in the Ca test (particularly for coated ALD samples). However, at lower conditions, the MOCON Aquatran values align more closely with the results from (a). (c) Thicker PVAl film (42 µm) tested at 45 °C under 65% RH (LiCl) and 71% RH ($MgCl_2$) further highlights discrepancies between measurement techniques. The Ca test estimates for the WVTR of uncoated PVAl are significantly higher compared to MOCON values. While increased thickness results in a slight reduction in WVTR (20.3 ± 1.62 g/m²·day at 65% RH, and 21.1 ± 2.11 g/m²·day at 71% RH), localized permeation effects remain evident. The primary film layer depletes, yet isolated calcium spots persist, suggesting a more complex WVTR transport mechanism than what is typically observed in PET or other conventional barrier substrates.

9.4.6.b Measuring ALD AlO_x Coated Thin and Thick PVAl Calcium Test

This analysis measures the WVTR of ALD AlO_x-coated PVAl samples as measured with the Ca test, which also highlights features that indicate defects within the coating. These defects help in the understanding of permeation rates and mechanisms for coated barriers as they signify permeation pathways. To aid this relationship, the WVTR is first estimated; where the following sections present representative samples and plots of coated thin PVAl (Figure 9-31) and thick PVAl (Figure 9-32), tested at 25 °C and 78.5% RH. These plots show fluence over time and corresponding calcium status or appearance through accompanying montage images.

9.4.6.c Thin PVAl (Betol) Representative Plots Over Thickness

Figure 9-31 (a), shows the degradation of the thinnest tested coating, a 26 nm AlO_x layer on PVAl, which experienced rapid degradation and "linear-like" defects within the first 3 hours of testing. These defects continued to grow until fully propagating throughout the sample by day 48. The WVTR for this sample is $(4.58 \pm 0.857) \times 10^{-4}$ $g/m^2 \cdot day$, significantly lower than the MOCON Aquatran estimates.

The error bars for the calculated fluence, also observed in the PET Ca test results, are derived from the standard deviation reported by ImageJ or Python, when measuring mean grey value across the selected Ca region in a single image. This standard deviation quantifies the pixel-to-pixel variation in grey intensity within the ROI, reflecting the internal variability of each image rather than measurement repeatability or sample-to-sample differences. It accounts for factors such as image noise, local surface inhomogeneities, background illumination non-uniformity or thresholding differences.

Although a calibration bar is used to standardize measurements, these sources of error can persist, leading to slight variations in WVTR.

Figure 9-31 (b) (50 nm coating) and Figure 9-31 (c) (96 nm coating) illustrate the effect of increasing coating thickness. The 50 nm coating still exhibits defects, though they appear later, becoming fully visible only after 21 hours.

It was initially theorized that increasing coating thickness would consistently improve WVTR performance. However, this is not always the case due to defect-controlled permeation (as further discussed Section 5.8). While thicker coatings are generally easier and more reliable to test, allowing for more sample replicated and being less prone to handling damage, they do not necessarily guarantee a lower defect density.

Here, the discussion refers more broadly to thin-film barrier coatings, such as ALD-grown AlO_x on polymer substrates. As previously shown, there appears to be an optimal or critical thickness that minimizes WVTR, particularly in PET-based coatings (section 4.3.1 Permeability Estimations of AlO_x on PET). This does not imply, however, that thinner coatings cannot achieve excellent water vapor barrier performance, provided the coating process yields a defect-free or low-defect microstructure. This was also demonstrated in Section (4.4.1 Estimating WVTR using Constant Region of Interest and Accounting for Edge Effects (Calcium Region Isolation)), where high barrier performance was observed even in thinner films.

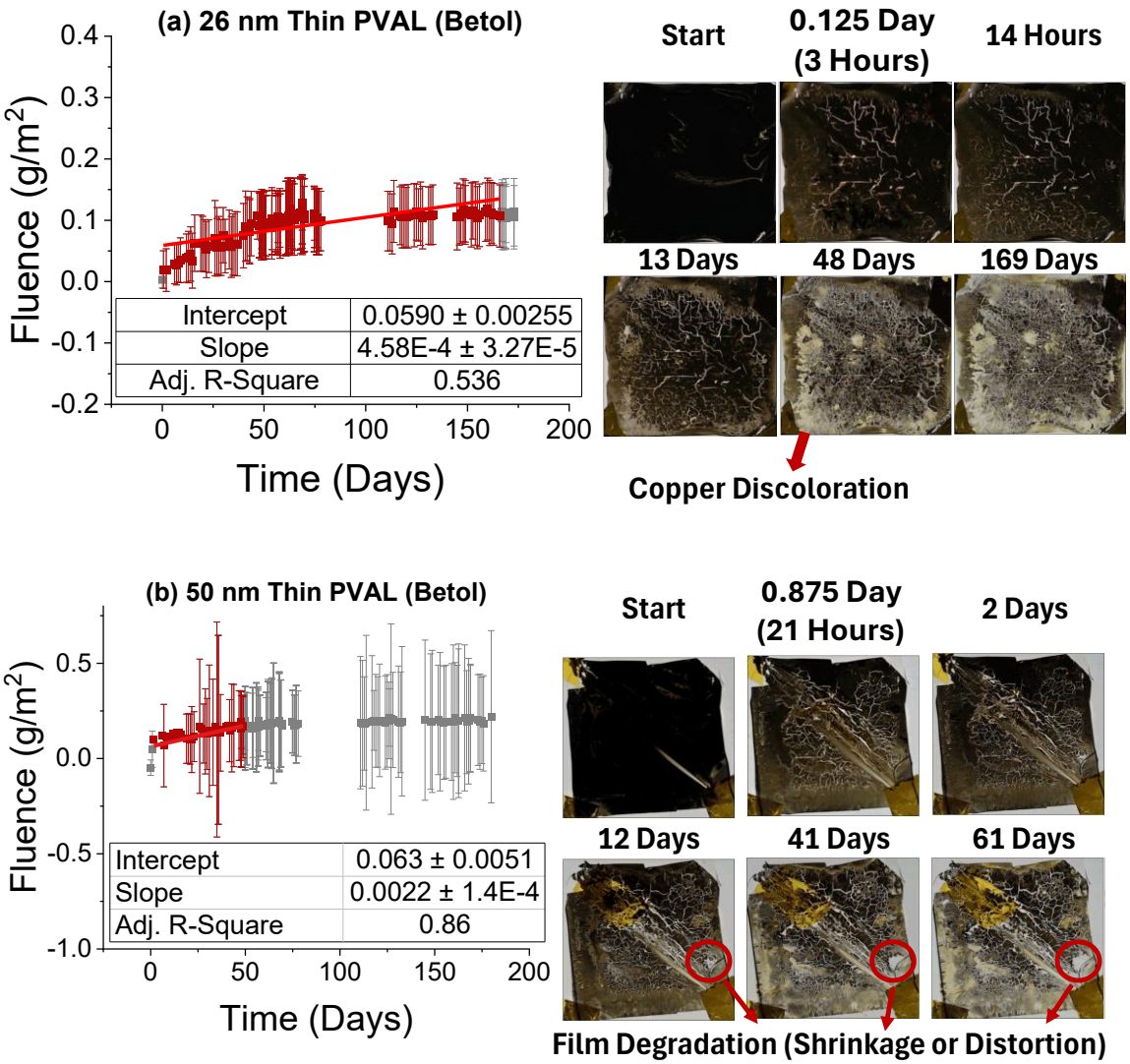
For the 50 nm coating, a WVTR of $(2.22 \pm 0.14) \times 10^{-3}$ g/m²·day was observed while the 96 nm coating shows a WVTR of $(9.93 \pm 0.44) \times 10^{-4}$, this indicates that although the 50 nm coating performed relatively well, the 96 nm coating achieved a more significantly reduced WVTR, demonstrating better barrier performance.

The 96 nm coating shows fewer "linear-like" defects compared to thinner coatings, suggesting that at a certain thickness, the observed defect population is reduced, which helps reduce permeability, as reflected in the lower WVTR. It is also important to clarify that these defects are likely introduced during the deposition process, rather than forming during permeation. While thicker coatings may reduce the likelihood of surface defects or partially cover pre-existing ones, as this is not a case of defects forming in situ under test conditions.

Some regions where calcium is still present by the end of the testing period are observed in these 50 nm and 96 nm coatings, suggesting that there are localized areas in which the coating continues to provide a sufficient barrier to protect the Ca over the test duration. Whether these regions are distinct from the “black spots” previously seen in Figure 9-30 (a) is unclear; while similar in appearance, the linear features in this case appear to persist throughout the test and may originate from a different mechanism. The presence of visible Ca in these regions also suggest that saturation had not yet been fully achieved in the WVTR estimation, as reflected in the corresponding calculations.

Another important observation is the distortion and wrinkling of the film, which appears as non-uniform deformation in the optical images. In several cases, the underlying glass substrate becomes partially exposed, further supporting the conclusion that the film has undergone shrinkage or lateral contraction. One possible explanation is the relaxation of residual strain introduced during the initial film formation; when exposed to humidity, the absorbed water may plasticise the film, allowing molecular chains to reorganise and relax. While hydrolysis has also been proposed as a contributing factor, this has not been directly confirmed.

Notably, as the film undergoes these structural changes, a concurrent change in the underlying copper layer is observed, manifesting as discoloration (*e.g.*, uneven yellowing) and apparent degradation. This suggests a potential interaction between the film's physical changes and the copper backing layer a combined phenomenon of shrinkage-induced distortion and film–substrate interaction not observed in the PET films.



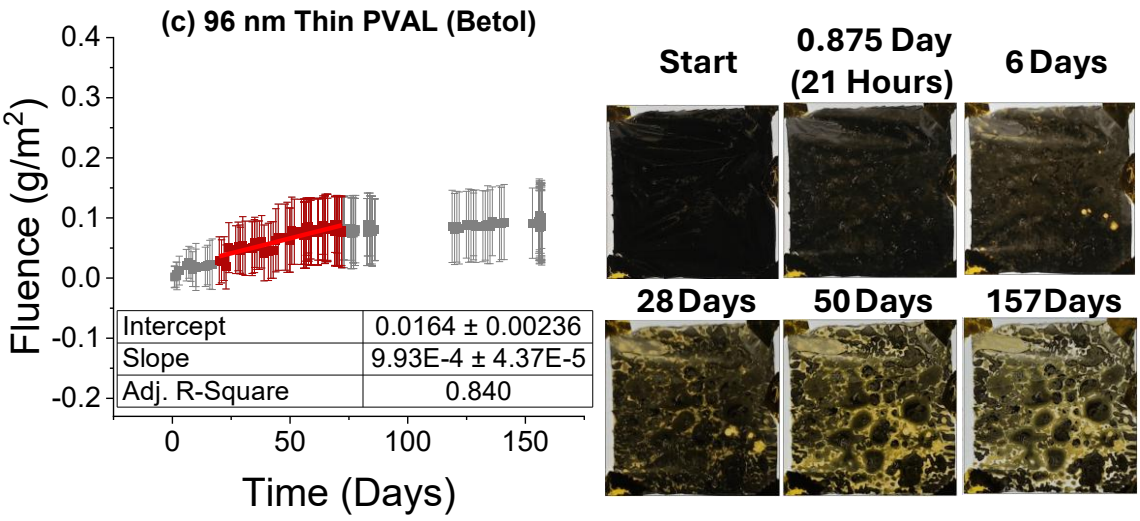


Figure 9-31: Representative Thin PVAl (Betol) coated samples with three varying thicknesses of AlO_x (a) 26 nm - (4.58 ± 0.857) $\times 10^{-4}$ g/m^2·day, (b) 50 nm - (2.22 ± 0.14) $\times 10^{-3}$ g/m^2·day, (c) 96 nm - (9.93 ± 0.44) $\times 10^{-4}$ g/m^2·day, showing that a decrease in WVTR is not always observed in increasing thickness (defect controlled permeation); accompanying images of the calcium depletion and sample during the analysis – showing the defect like features that indicate permeation and the degradation or possible presence of hydrolysis upon reaction with water as suggested by the change and disappearance of copper backing layer.

9.4.6.d Thick PVAl (Alpine) Representative Plots Over Thickness

In general, an increase in substrate thickness would be expected to decrease WVTR. However, this was not clearly observed in the Mocon Aquatran and Ca test results comparing the thicker (Alpine) PVAl and thinner (Betol). Significant sample-to-sample variations became evident, and it is plausible that the increase in substrate thickness was insufficient to induce a measurable difference in barrier performance. In any case, for coated films the population of defects in the barrier, which is likely strongly influenced by the surface properties of the substrate, will be a major factor in controlling WVTR.

Figure 9-32 presents representative Ca test measurements of coated thick PVAl samples. The ALD AlO_x-coated thick PVAl demonstrates once more that it is defect

controlled permeation where a thicker coating does not necessarily lead to a lower WVTR. In fact, the thinner coating at 26 nm showed the lowest WVTR estimation as shown:

- **26 nm**: $(6.18 \pm 0.27) \times 10^{-4}$ g/m²·day
- **50 nm**: $(1.24 \pm 0.04) \times 10^{-3}$ g/m²·day
- **96 nm**: $(1.05 \pm 0.06) \times 10^{-3}$ g/m²·day

These values suggest that increasing the coating thickness does not necessarily lead to improved barrier properties. While a slight improvement is observed from the 50 nm to 96 nm, the difference is minimal, especially when compared to the significantly better performance of the 26 nm sample, which shows a WVTR two orders of magnitude lower.

In terms of features, in the case of the 26 nm thick PVAl sample (Figure 9-32 (a)), the onset of 'linear-like' defects occur significantly later, at 20 hours, than with the thin PVAl (3 hours). PVAl has known is significantly more susceptible to hydrolytic degradation than PET, due to its hydroxyl-rich, hydrophilic backbone which promotes water absorption and chain scission even under moderate humidity. In contrast, PET's polyester backbone is chemically more stable, with hydrolytic degradation typically requiring elevated temperature, acidic conditions, or prolonged exposure to high humidity [498]. While this study was conducted at ~25 °C, the intrinsic moisture sensitivity of PVA remains relevant under ambient conditions [499].

Copper layers, often used in Ca-based WVTR tests as electrode backings, can oxidize under heat and humidity. However, significant oxidation—especially formation of CuO—only occurs at higher temperatures (≥90 °C), and even after days at 60–80 °C,

oxide layers typically remain thin (<40 nm) [500]. At room temperature, discoloration is more plausibly due to mechanical effects like shrinkage or delamination of the hydrophilic PVA layer, rather than substantial copper oxidation.

In Ca-based WVTR testing, “full saturation” refers to the complete conversion of metallic calcium into $Ca(OH)_2$ upon reaction with permeating moisture [392]. Thus, the visible presence of unreacted Ca after extended exposure suggests that the barrier is still effective at limiting moisture ingress, and the system has not yet reached its moisture capacity.

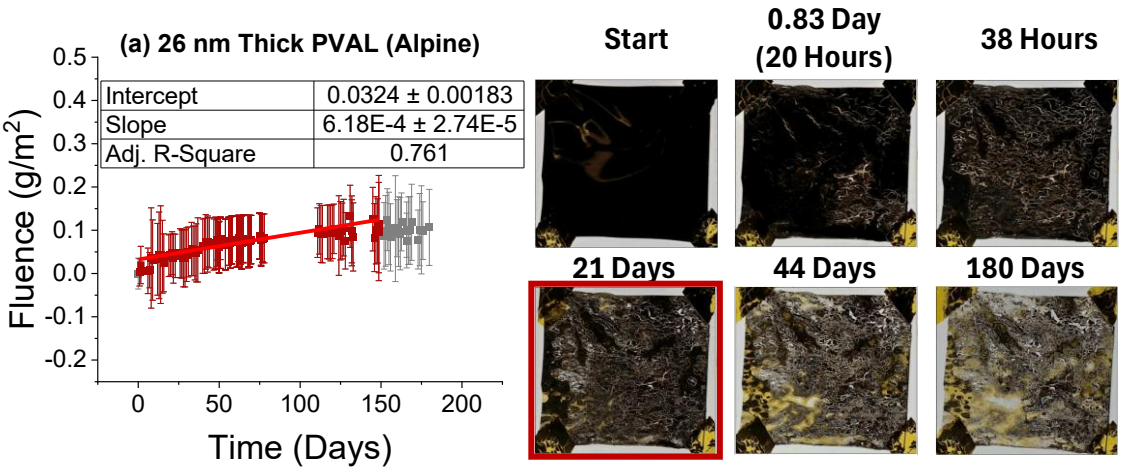
In the thicker AlO_x coatings (50 nm and 96 nm), bright linear structures are still visible in the Ca test images ((Figure 9-32 (b) and (c) respectively and emphasize in (d)). These wide, ravine-like bright lines may indicate macro defect regions where water has permeated through the barrier and reacted with the calcium layer underneath. These paths appear to broaden and intensify over time, particularly evident in the fifth frame of each sample. In between these permeation zones, island-like calcium regions persist, suggesting that the barrier layer remains intact in those areas, effectively preventing water ingress. These dark regions correspond to retained calcium. In contrast, coated PET samples (Figure 9-19, Figure 9-20, Figure 9-21) exhibit bright circular spots with surrounding dark halos, indicating more localized water ingress and reaction with calcium.

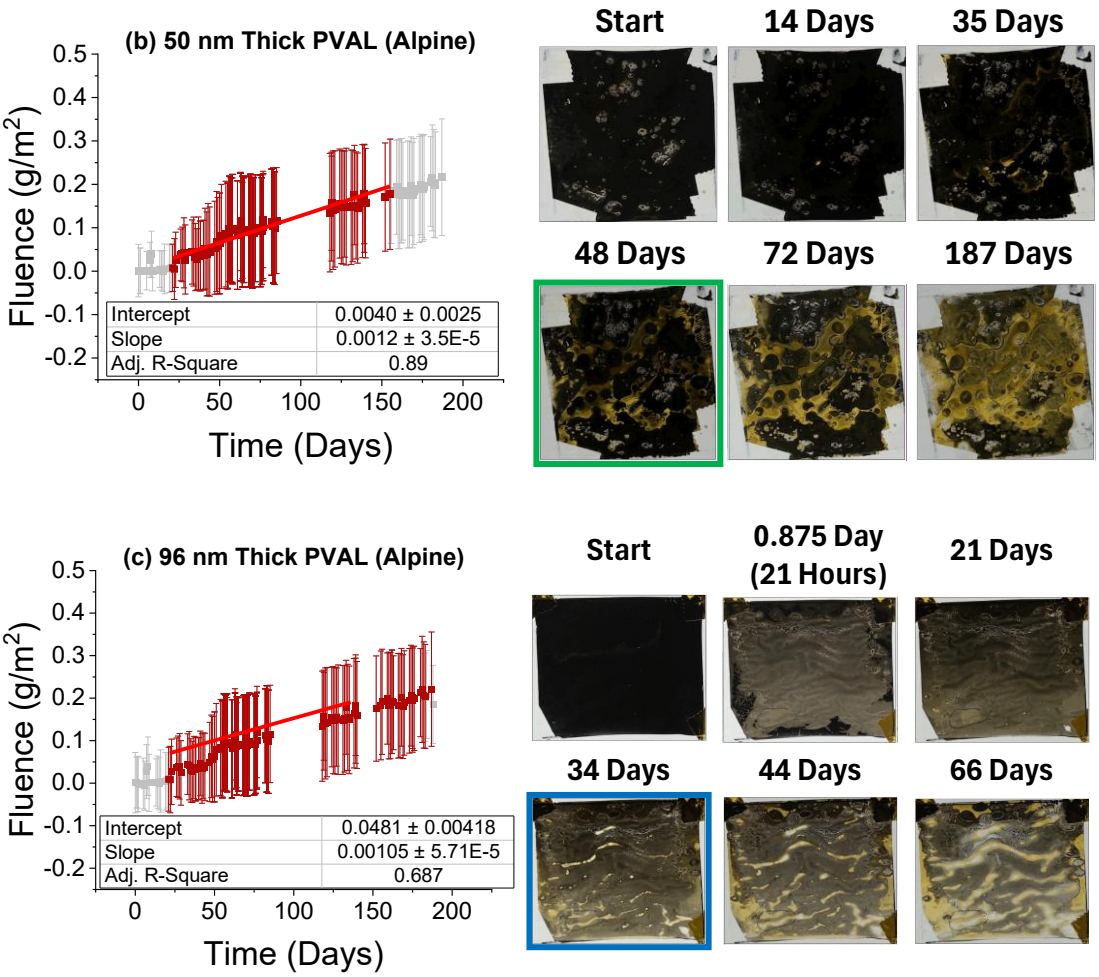
The presence of linear defects (observed in the coated PVAl films) rather than isolated spots (observed in the coated PET) may possibly be attributed to the surface roughness of the substrate PVAl and consequent non-uniformities in both the coating and substrate. Variations in coating uniformity could lead to different stress distributions

across the barrier coating, resulting in linear defects (possible cracks in the coating for example). The PET is less hydrophilic, so will absorb less water so will be less prone to any change in shape as the sample is exposed to water vapour, and the thicker PET substrate is easier to handle and may have reduced the likelihood of coating damage during transportation or testing compared to the thinner, more flexible PVAl substrates.

Another observation is the appearance of "wave-like" features in the 96 nm sample, possibly due movement of thin layers during encapsulation of the sample on the glass *e.g.* with the spreading and curing of the epoxy. This could influence the formation of defects in the coating, particularly in very thin substrates or coatings.

An important observation is the absence of noticeable sideways water ingression, which was common in coated PET substrates even within a few days of testing in some cases. It is possible that the thinner, softer PVAl allows for a superior encapsulation of the sample onto the glass, reducing the effect of water ingress from the sides.





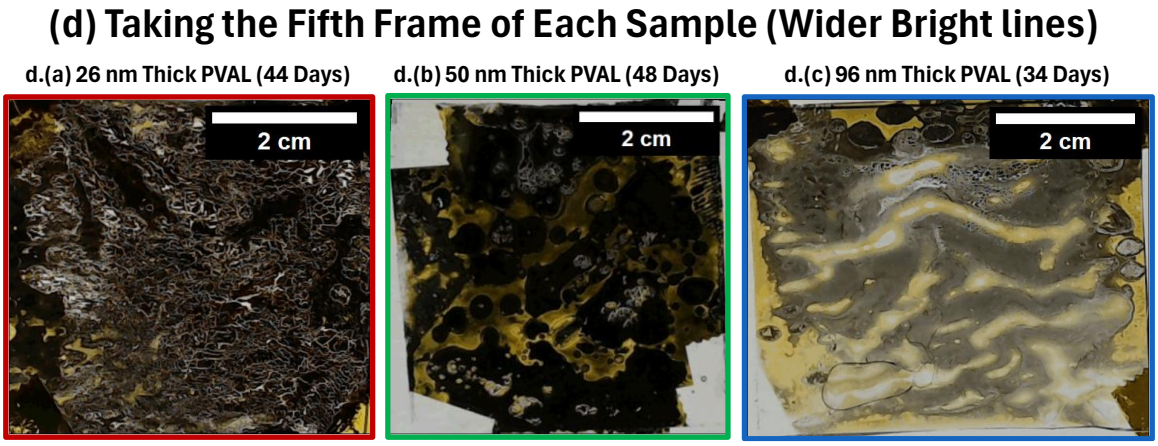


Figure 9-32: Representative thick PVAl samples coated with AlO_x at varying thicknesses: (a) 26 nm - (6.18 ± 0.27) × 10^{-5} g/m²·day, (b) 50 nm - (1.24 ± 0.04) × 10^{-3} g/m²·day, (c) 96 nm - (1.05 ± 0.06) × 10^{-3} g/m²·day. (d) The fifth frame of each sequence (highlighted) shows the development of broad, ravine-like bright features, especially prominent in thicker coatings. These features suggest progressive permeation along macro defect

pathways, while dark island-like areas reflect regions of effective barrier protection. It also shows that thin coatings can achieve low WVTR's and possibly fewer defects. While degradation of the copper layer upon hydrolysis is still observed in all cases.

9.4.6.e Representative Features in Coated PVAl Layers

To assess the typicality of morphological features in coated PVAl layers, Figure 9-33 presents additional Ca test images of selected thin and thick PVAl samples coated with 50 nm and 96 nm of AlO_x. While these images are taken from single samples at progressive timepoints, they consistently exhibit characteristic features observed across multiple experiments and deposition conditions.

For the thin PVAl samples, the 50 nm coating displays prominent spot-like features with granular, uneven textures, suggesting localized water ingress or material aggregation. In contrast, the 96 nm coating reveals more continuous, island-like calcium regions, indicating improved barrier uniformity with increased thickness.

In the thick PVAl samples, the 50 nm coating shows broad, river-like permeation paths, like those seen in representative samples earlier, while the 96 nm coating exhibits smaller, more discrete spot-like features.

While some variation in feature morphology is expected, these examples support the observation that thicker substrates and coatings tend to show fewer fine defects and instead develop larger-scale features.

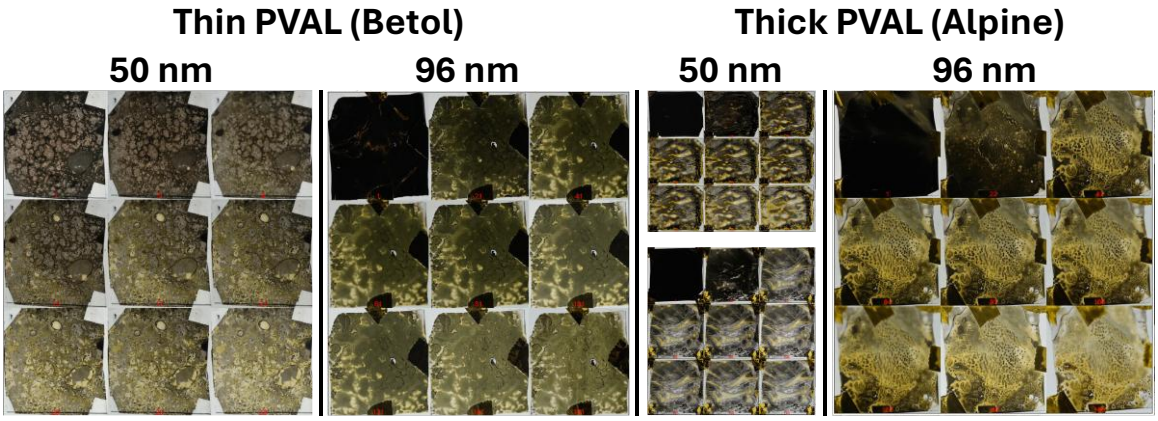


Figure 9-33: Thin and Thick PVAl samples coated with AlO_x (50 nm and 96 nm) show characteristic permeation morphologies captured at progressive timepoints. Though taken from individual samples, the spot-like, island-like, and river-like features are representative of those seen across different conditions. These images illustrate the typical defect patterns that emerge depending on coating thickness and substrate type.

9.4.7 Supplementary Defect Analysis of ALD-Coated PVAl Films

9.4.7.a Initial Methodology Estimations (Image J) - Imprecisions

The initial method involved quantifying defects through particle analysis using ImageJ. However, as seen in PET-coated samples, distinguishing between isolated and coalescing spots is challenging, particularly in PVAl-coated samples due to the interconnected networks and higher permeation rates, that may affect the accuracy of overall defect quantification. As a disclaimer, in this study “spots” broadly refer to any visually distinguishable bright feature in the Ca-test images, including linear or irregularly shaped regions of calcium depletion. The coated PVAl “spots” often appear as elongated or linear features, unlike the circular or dot like features in coated PET, the term is retained for consistency across quantification workflows.

9.4.7.b Defect Density Estimations – Initial Methodology (Image J)

Figure 9-34 shows the initial ImageJ spot density over time for two PVAl substrates with varying AlO_x coating thicknesses. Initially, a rise in spots is seen, followed by a decrease likely due to coalescence, highlighting the challenge of distinguishing distinct defects giving rise to growing, and coalescing, spots. Overall, thick PVAL tends to show fewer spots than thin PVAL at longer times, though there is no clear or consistent effect of coating thickness. These observations are based on single time series per sample, and values are presented to illustrate general trends rather than statistical comparisons.

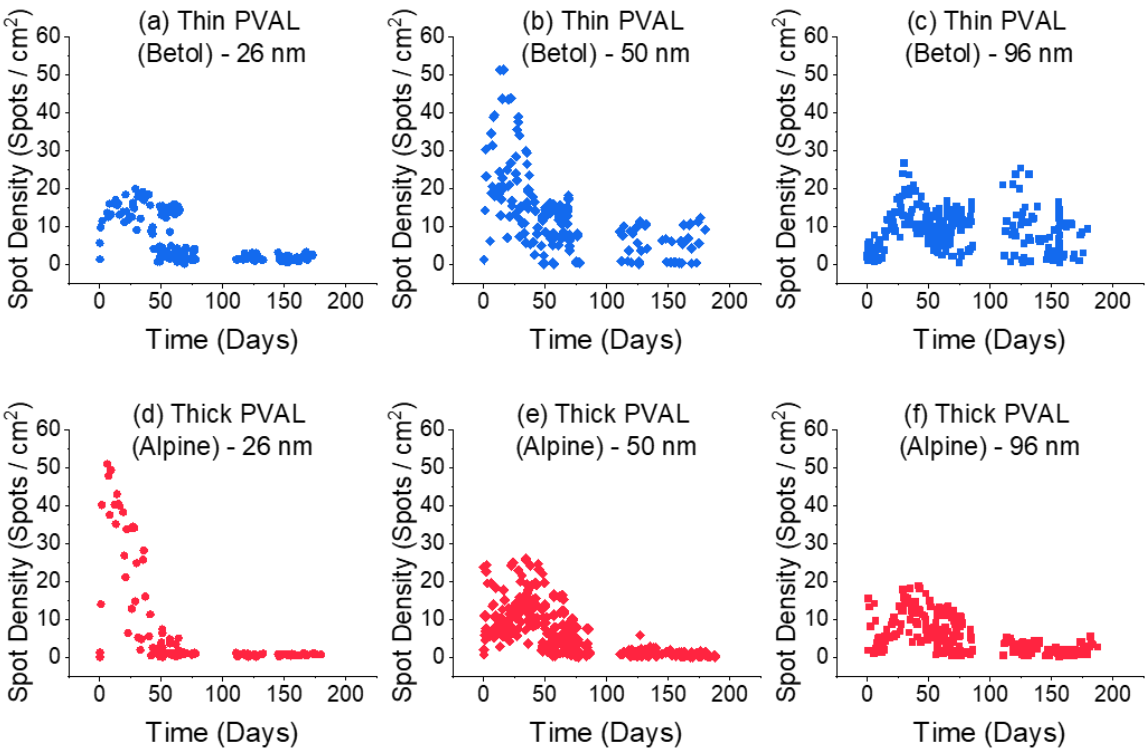


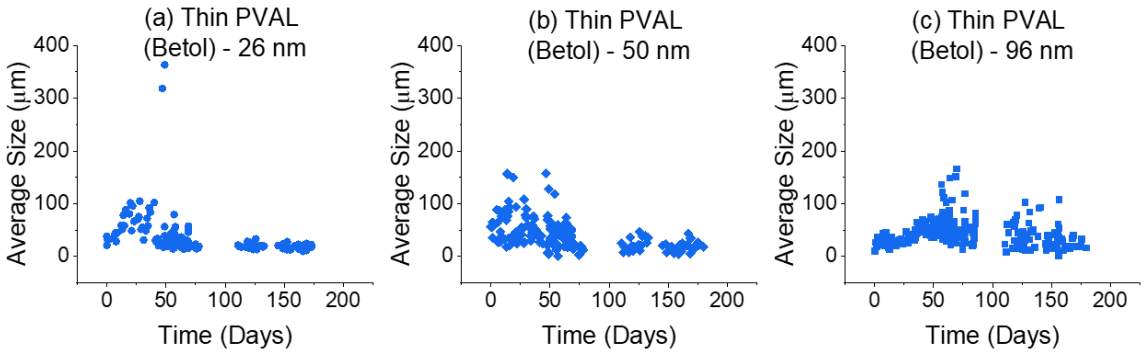
Figure 9-34: ImageJ-estimated number of defect features ("spots") over time for thin and thick PVAL samples with varying AlO_x thicknesses (26, 50, and 96 nm). Trends show an initial increase followed by a decrease in spot count, likely due to coalescence. Thick

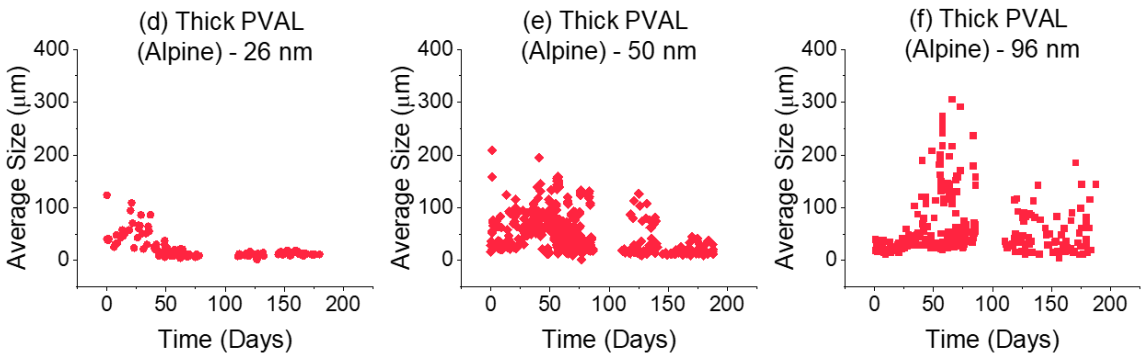
PVAL tends to show fewer spots than thin PVAL over time, but no consistent trend is observed with coating thickness.

9.4.7.c Average Defect Spot Size of Coated PVAl Films Initial Methodology (Image J)

Figure 9-35, shows the average spot size, defined as the major axis length of each detected feature in the Ca-test images, for thin and thick PVAl samples with varying AlO_x thicknesses. While referred to as "spots" for consistency, many features, especially in PVAl, are elongated or irregular, not circular. Sizes (~30–60 µm) reflect linear dimensions, not area.

Although spot size remains relatively stable, occasional outliers above 100 µm, likely from coalescence or overlapping, image artifacts, highlight the challenge of accurate detection using basic thresholding and data quality. This limitation motivated the adoption of more advanced image analysis techniques in later stages of the study and refinement of data.





Coating Thickness (nm)	Thin PVAl (µm)		Thick PVAl (µm)	
	Mean	Std. Dev.	Mean	Std. Dev.
26	34	38	20	20
50	39	28	50	46
96	45	22	60	50

Figure 9-35: Spot size trends over time for thin and thick PVAl samples with varying AlO_x thicknesses (26, 50, and 96 nm). Spot size is defined as the major axis length of each detected feature. While referred to as "spots," features are often elongated or irregular, especially in PVAl. Occasional outliers above 100 µm, likely due to merging or image artifacts, illustrate the limitations of early thresholding methods.

9.4.7.d Initial Methodology (Image J) – Main Points

Though the methodology isn't robust enough to reliably distinguish isolated from coalescing spots, it provides a rough indication that the substrate type (thin vs. thick PVAl) does not have a significant impact on spot density or spot size, at least within the resolution limits and variability of the calcium test.

9.4.8 Spot Density and Identification of Defects (Python Code)

The previous ImageJ methodology had limitations in accurately counting defects and determining average defect size. While it offered a basic comparison, it failed to capture the complexity of defect structures in PVAl films, requiring a more advanced approach.

9.4.8.a 50 nm Defect Distribution of AlO_x Thin PVAl

Figure 9-36 (a.2), shows the Ca test images for the 50 nm AlO_x coating on thin PVAl. A portion of the Kapton / Polyimide tape used during mounting was not fully removed, partially obscuring the top left section of the sample. As this affected defect detection, the data was divided into two sections, also highlighting the Ca test's spatial resolution, allowing localized exclusion of artefacts and region-specific analysis.

Moving to the specific sections Figure 9-36, panels (a.2.1) and (a.2.2) show the raw Ca test images for Sections 1 and 2, respectively. Panels (b.2.1) and (b.2.2) display the overlaid results from the spot detection algorithm, while (c.2.1) and (c.2.2.) present the corresponding spatial distribution of detected features.

Despite Section 1 covering nearly twice the area of Section 2, the algorithm performs consistently across both, successfully identifying spots varying size and shape.

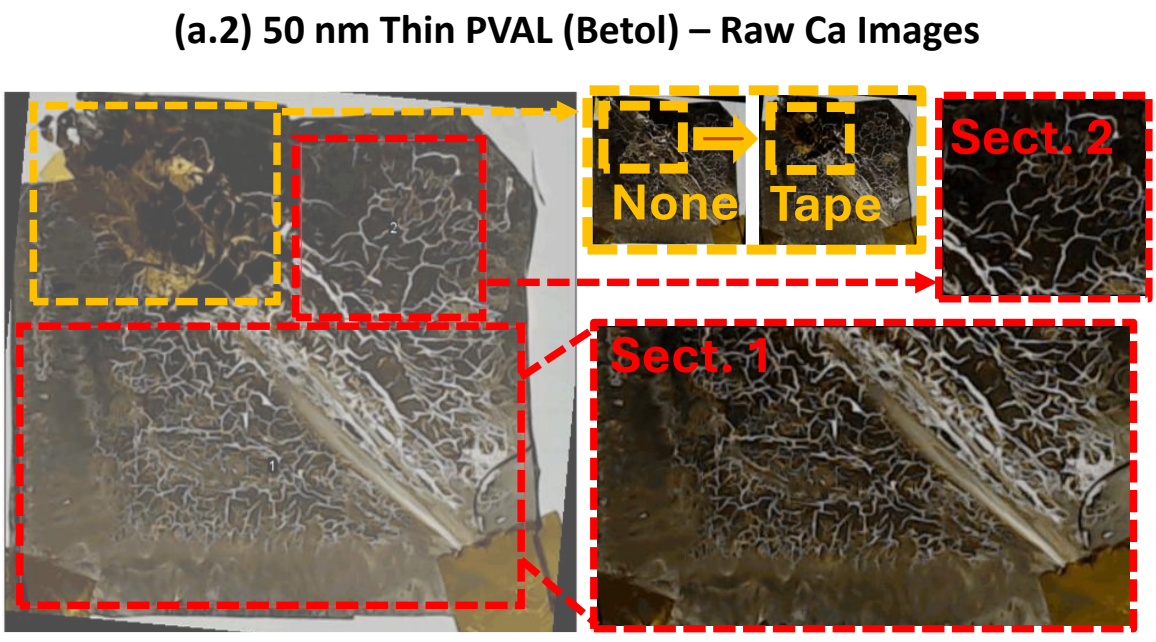
The accuracy of this analysis is influenced by the quality and continuity of raw image data, defined here as consistent illumination, minimal occlusion, and the presence of intermediate image frames that allow progressive tracking of spot formation. This is evident from the smooth transition in detected spot count and morphology across frames, particularly in Section 1.

A key limitation arises if coalescence occurs before the initial appearance of isolated spots. In such cases, newly appearing regions are already merged, bypassing isolated classification altogether. This can affect both quantitative counts and spatial interpretation. The data suggest this may occur more frequently in higher-permeability regions, where faster calcium consumption can lead to earlier merging, especially if

image capture intervals are too wide. Addressing this requires sufficiently high temporal resolution and stable image quality.

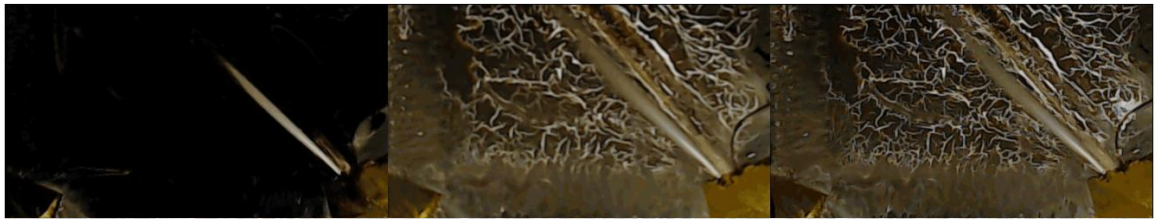
Focusing on (a.2.1) shows larger linear features forming quickly, with a significant increase in linear cracks within less than a day, correctly identified by the code seen in (b.2.1). By 1.6 days, almost all isolated spots have been detected, with many beginning to coalesce. Meanwhile, in (b.2.2), most isolated spots are identified after image 2.

In the spot distributions shown in (c.2.1) and (c.2.2), both regions show a relatively uniform spread of newly formed isolated spots across the sample area. In contrast, coalescing spots appear more concentrated toward the right side of the sample, particularly in Section 1. This asymmetric clustering may reflect localized variations in barrier performance or permeation rate, with faster calcium consumption leading to earlier merging events in certain regions.

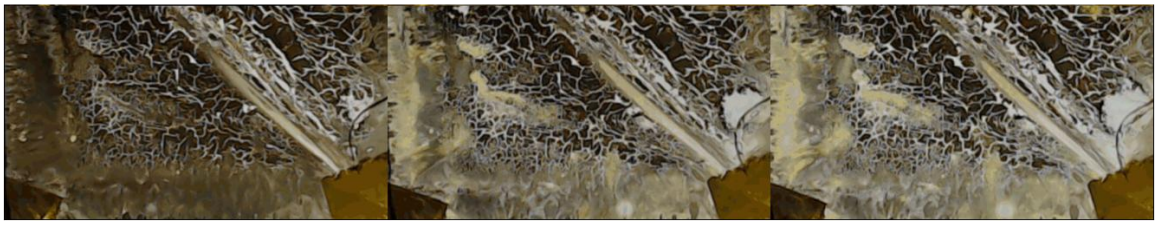


(a.2.1) 50 nm Thin PVAL (Betol) – Raw Ca Images

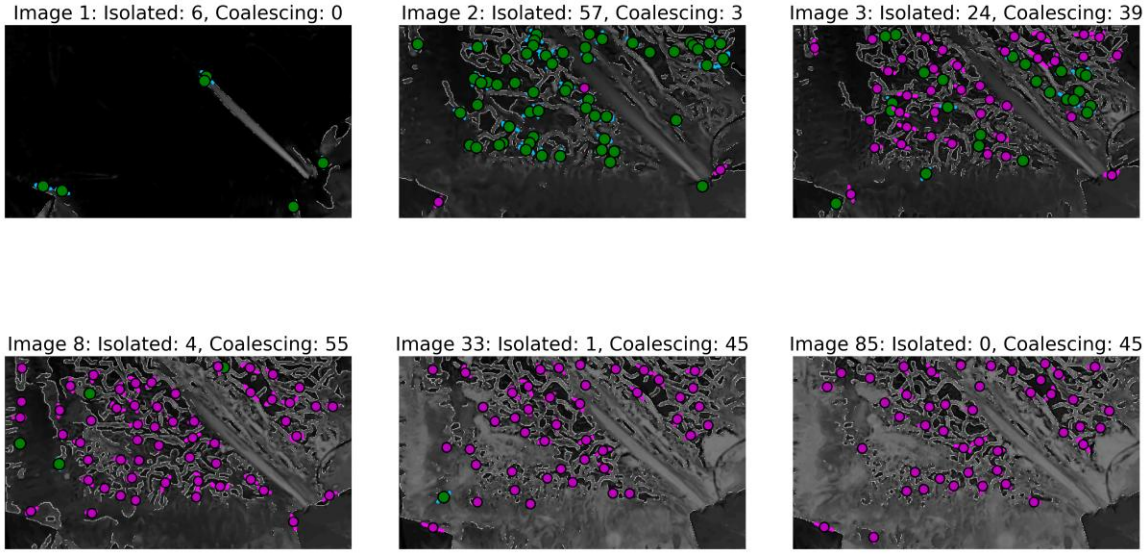
#1: Start | #2: 0.87 Days (~21 Hours) | #3: 1.60 Days



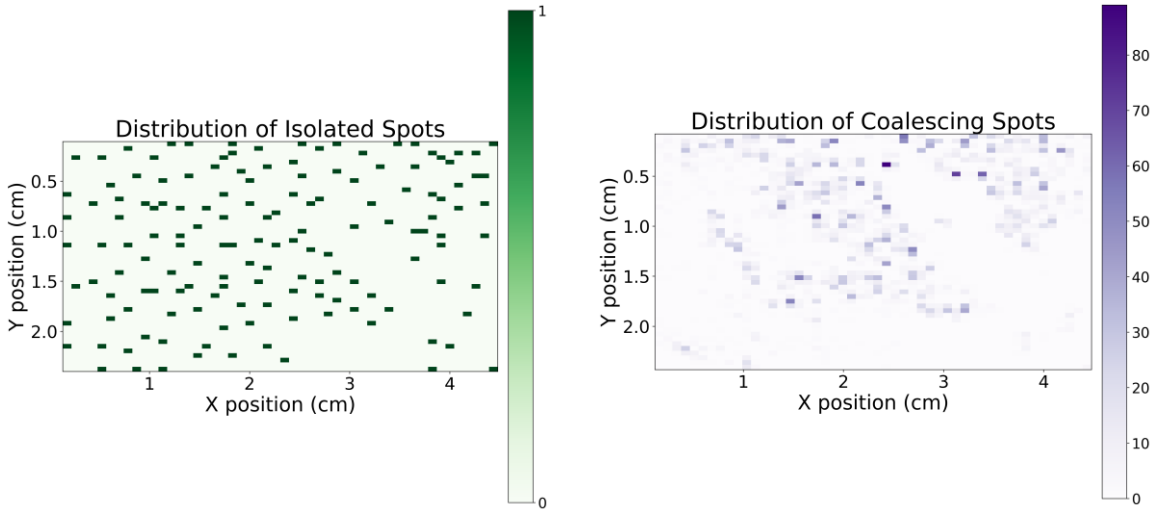
#8: 11.9 Days | #33: 40.95 Days | #85: 60.95 Days



(b.2.1) 50 nm Thin PVAL (Betol) – Defect Classification Overlay (Green: Isolated with Blue Contour and Purple: Coalesced)

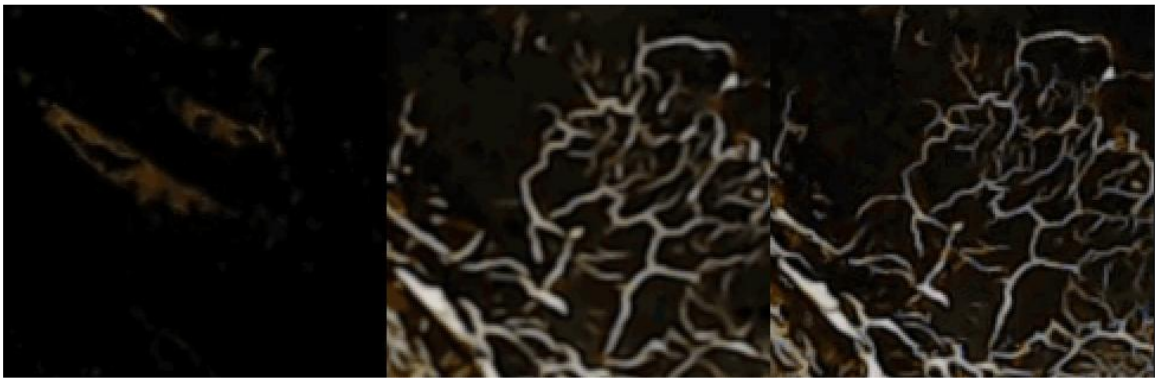


(c.2.1) 50 nm Thin PVAl
(Spatial Distribution of Isolated vs. Coalesced Spots)

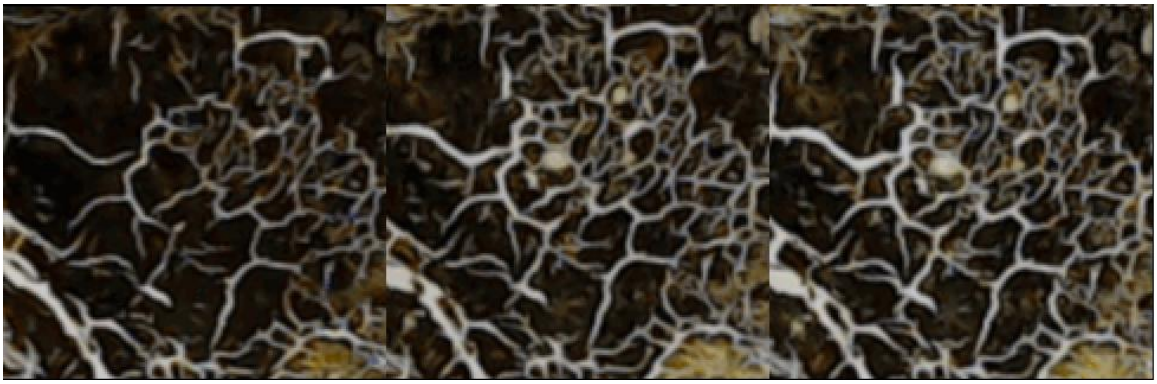


(a.2.2) 50 nm Thin PVAL (Betol) – Raw Ca Images

#1: Start | #2: 0.87 Days (~21 Hours) | #3: 1.60 Days



#8: 11.9 Days | #33: 40.95 Days | #85: 60.95 Days



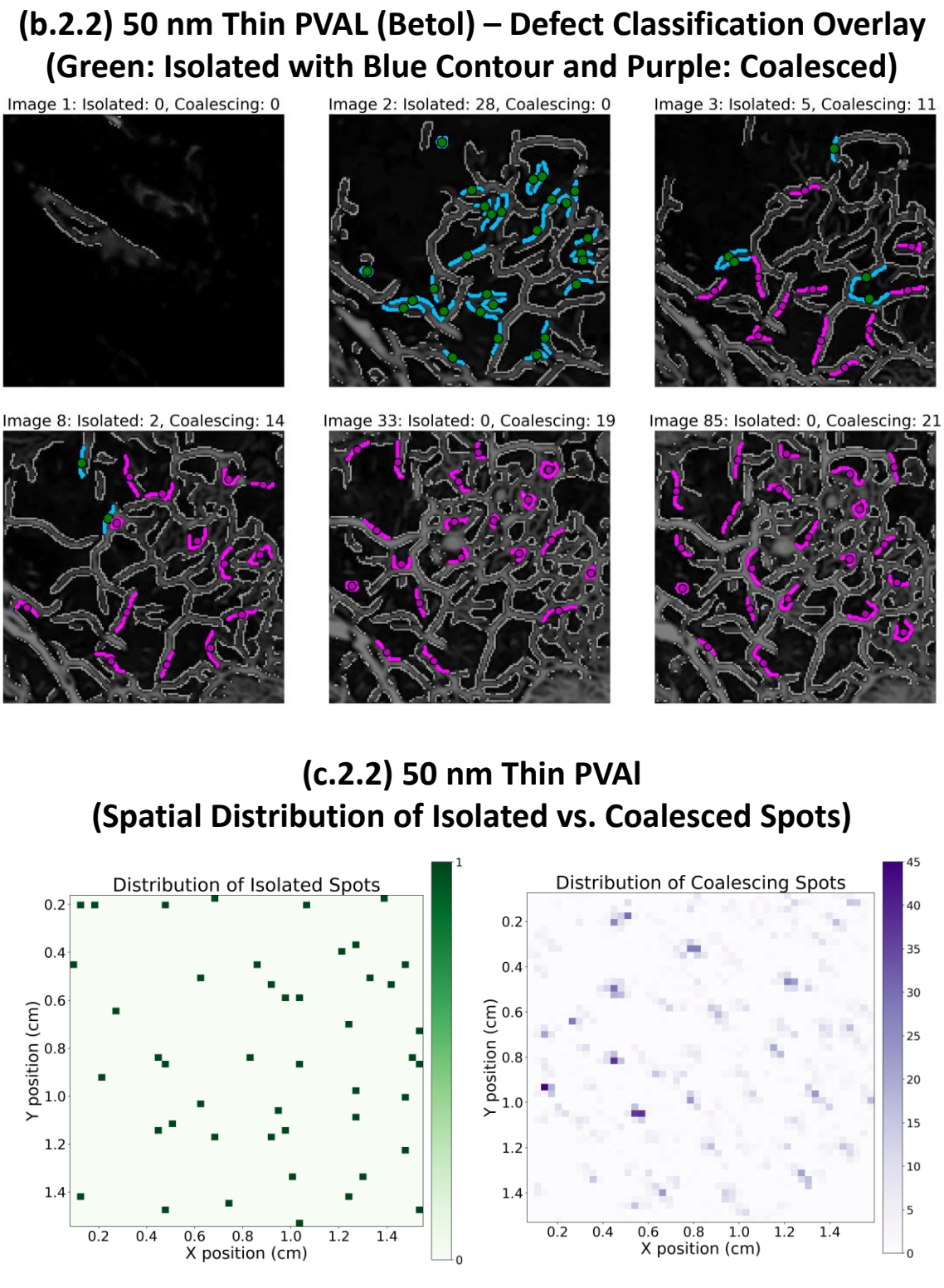


Figure 9-36: Ca test results for 50 nm AlO_x on thin PVAl (5.21 x 5.00 cm), divided into two sections to exclude regions obscured by Kapton tape. (a.2.1) Section 1 (4.60 x 2.56 cm): Raw image showing gradual crack growth. (b.2.1) Detected features include large, coalescing spots identified by the algorithm. (c.2.1) Spatial distribution indicates a

relatively uniform spread of isolated spots across the section and a slight bias on top right for coalescing spots. (a.2.2) Section 2: Raw image reveals defects resembling a "turtle shell" pattern. (b.2.2) Algorithm relatively successfully identifying the defects and features, with (c.2.2) showing a consistent and uniform spatial distribution of the features across the region of interest for both isolated and coalescing. These results also highlight the Ca test's ability to resolved localized defect populations and maintain reliable detection across varying sample regions.

9.4.8.b Defect Distribution of AlO_x Thick PVAl

This section tests the earlier prediction (briefly introduced in 5.6.2.b 96 nm Defect Distribution of AlOx Thin PVAl) that substrate thickness influences stress response during failure specifically, that thicker substrates may lead to broader buckling or delamination, while thinner ones promote more discrete fragmentation. Ca-test results for thick PVAl with 26 nm, 50 nm, and 96 nm coatings (Figure 9-37, Figure 9-38 and Figure 9-39 respectively) are examined to assess this.

9.4.8.c 26 nm Defect Distribution of AlO_x Thick PVAl

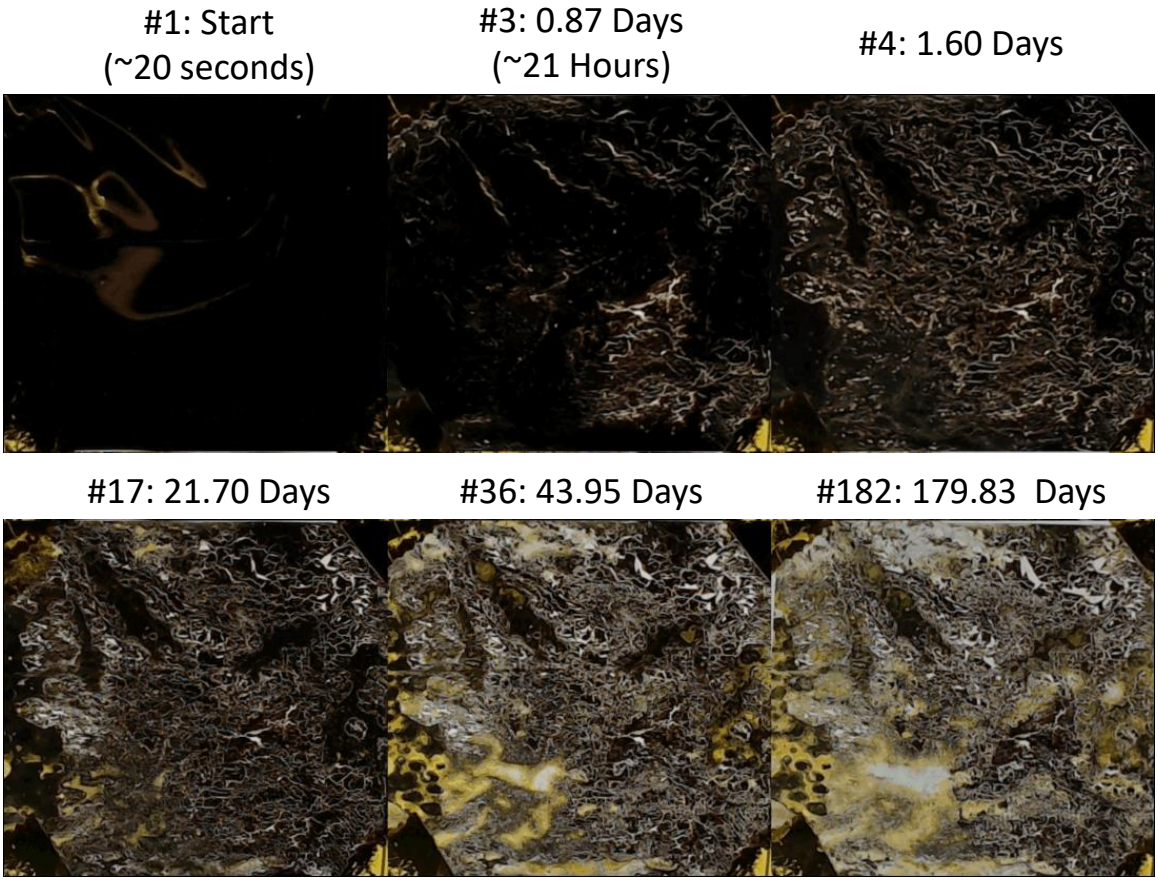
Figure 9-37 (a.4) shows the raw Ca-test images for the 26 nm AlO_x coating on thick PVAl (Alpine), capturing the progressive development of linear or fracture-like features across the surface. Starting around Image #3, it becomes evident that defect emergence is sequential rather than simultaneous, with new features continuing to appear in subsequent frames.

While the lower-left region initially appeared to retain calcium slightly longer, closer inspection particularly of Image #4 reveals wavy, dark regions across a broader area, consistent with the "waviness" or out-of-plane deformation seen in other thicker coatings. As noted, this could reflect subtle "crumpling" of the film: elevated ridge areas

experience local tensile stress and crack earlier, while valley regions remain in compression and delay crack formation, appearing darker for longer.

Panel (b.4) confirms the staggered timing of defect growth, with isolated spots forming early and coalescing ones appearing later. Meanwhile, the spatial maps in (c.4) show that isolated spot distribution is broadly uniform, but coalescing features are less frequent in the lower-left region. This does not imply an absence of permeation but suggests that defect evolution in this region may be delayed or proceeds via different mechanisms, potentially influenced by local stress states or geometric effects. Rather than a lack of defects, the difference likely reflects variations in the timing or mode of barrier breakdown.

(a.4) 26 nm Thick PVAL (Alpine) – Raw Ca Images



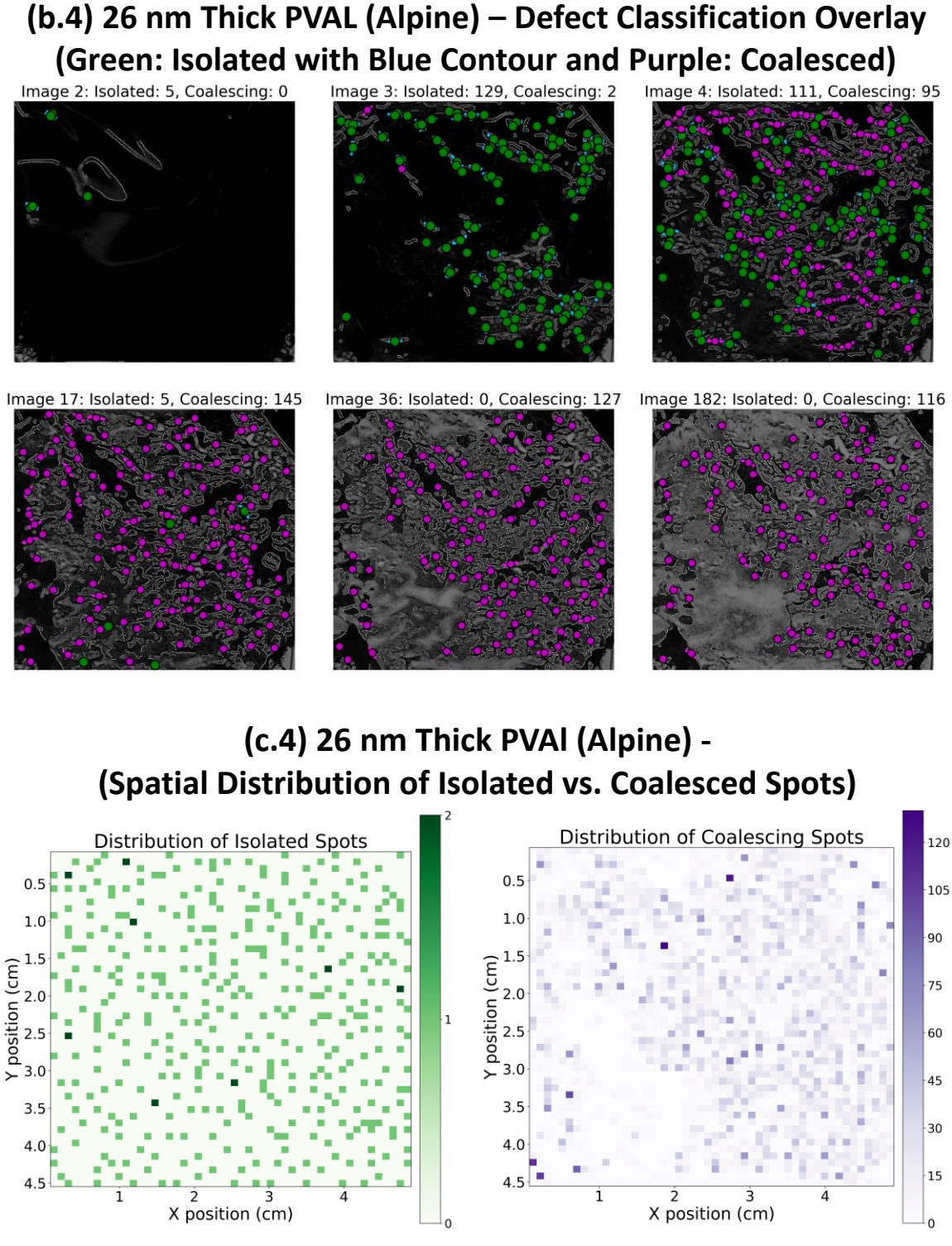


Figure 9-37: (a.4) Raw Ca test images of 26 nm AlO_x on thick PVAl (5.00 x 4.64 cm), showing prominent linear or crack-like features similar to those observed in coated thin PVAl samples. (b.4) The defect detection overlays reveal a staggered appearance of spots, indicating that defects do not emerge simultaneously across the sample. (c.4)

Despite this temporal variation, the spatial distribution of isolated spots is uniformly present the film, but the coalescent spots do suggest a slight bias towards the right-hand side of the barrier layer.

9.4.8.d 50 nm Defect Distribution of AlO_x Thick PVAl

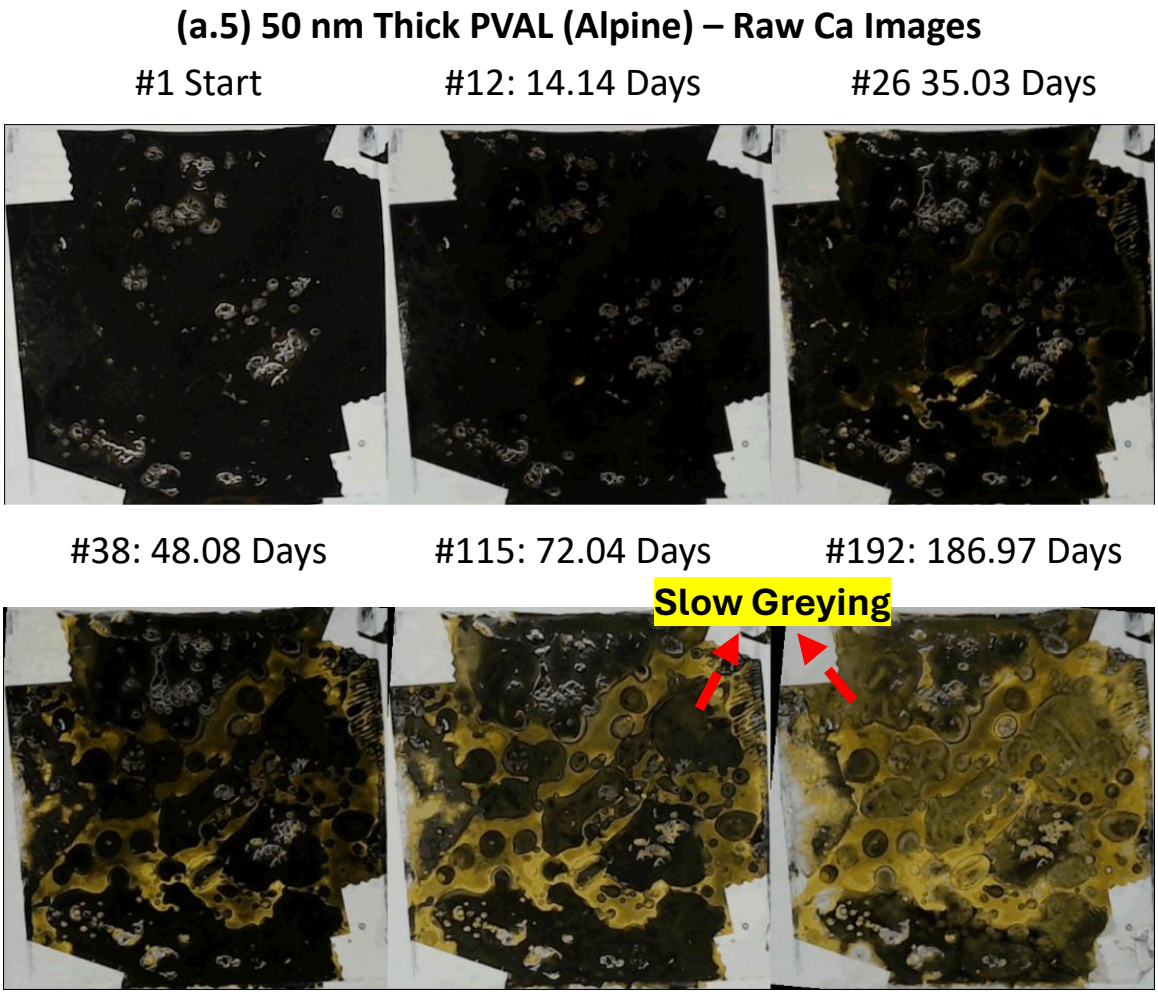
Going to thicker coatings, Figure 9-38 (a.5) shows the raw Ca test images for the 50 nm AlO_x coating on thick PVAl (Alpine). Compared to the more linear or crack-like defects observed in the thinner 26 nm coatings (Figure 5-13 and Figure 9-37), this sample displays more distinct, spot-like features. This shift in observed defects suggests that coating thickness may influence the nature of defects formed with thicker coatings reducing fracture like driven features (in comparison to 50 nm AlO_x observations on thinner PVAl – Betol, Figure 9-36).

Furthermore, a similar spot-dominant pattern is also observed in the thinner PVAl - Betol substrate, but only at the thickest coating of 96 nm (Figure 5-14), indicating that both substrate type and coating thickness can play a role in defect evolution.

Additionally, close inspection of panels 5 and 6 in (a.5), images #115 and #192 shows regions where the film transitions gradually from dark (calcium-intact) to grey, rather than abruptly depleting. These slow greying areas (annotated in Figure 9-38 (a.5)) indicate partial calcium loss, where the background remains darker than fully depleted regions but is lighter than unaffected zones. As argued in sections 4.3.2 ALD – AlO_x and RF Sputtered - Al_2O_3 or (AlOx) and Figure 9-33 this may reflect nano-scale defects or diffuse permeation paths, too subtle to fully deplete calcium in the timeframe of the test but does slowly react and erode calcium layer indicating permeation.

In contrast, other regions retain full darkness suggesting minimal permeation. These observations still imply that macro-defects dominate water ingress, while nano-defects may contribute more subtly without causing total depletion.

(b.5), shows the overlaid defect detections. isolated defects were still observed up to day 48, but by day 72, all detected features had coalesced, though calcium remained visible in some regions. This suggests that the test may not have captured all visually distinct isolated pots, potentially due to coalescence timing or frame resolution. (c.5) Shows that defect distribution in both isolated and coalescence appears to be relatively uniform across the sample surface.



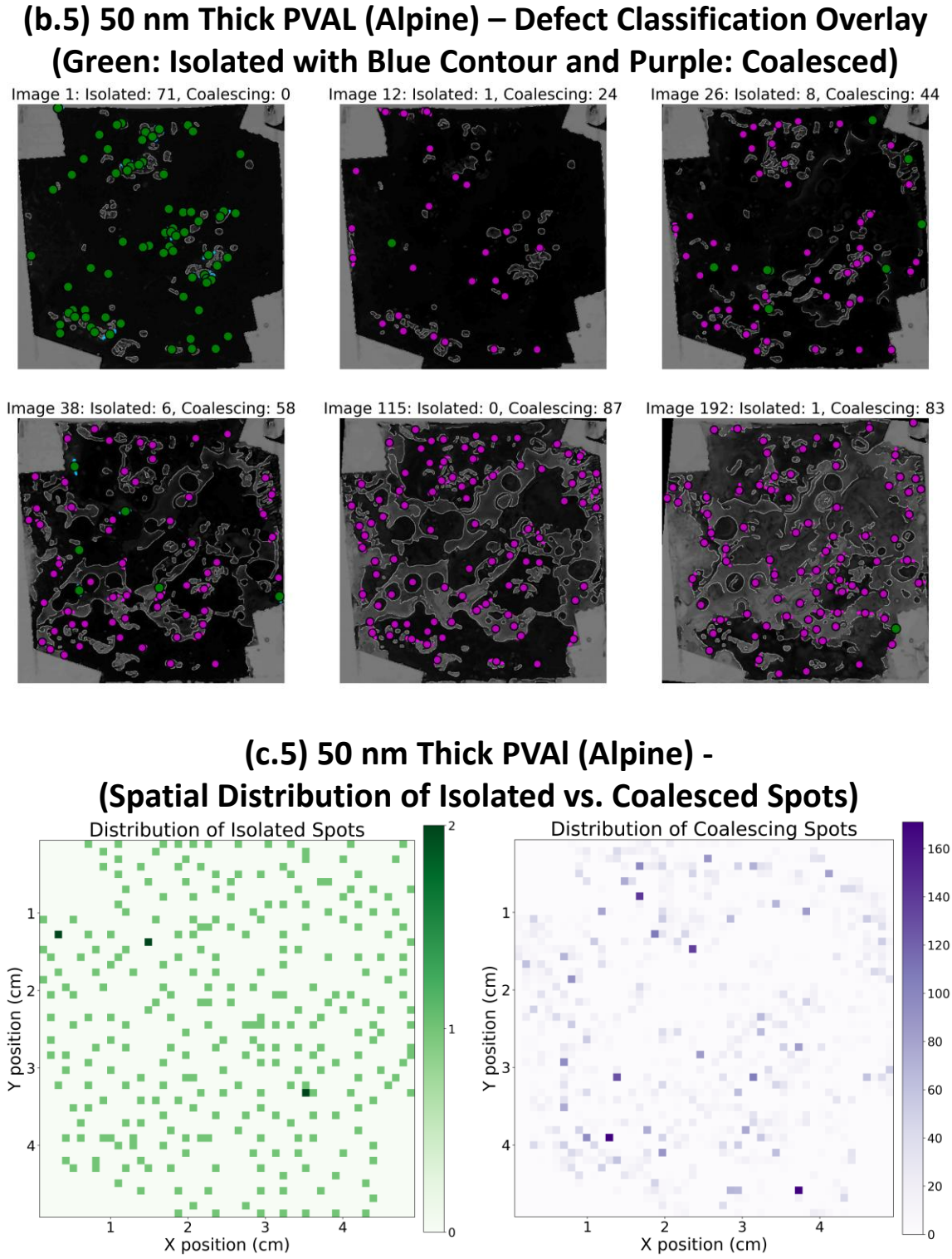


Figure 9-38: (a.5) Raw Ca test images of 50 nm AlO_x on thick PVAl (5.03 x 5.00 cm) show a shift from linear to more spot-like defects compared to thinner 26 nm coatings, suggesting coating thickness influences defect types. (b.5) Overlaid detection results

reveal that isolated defects persist up to day 48 with full coalescence by day 72. However, calcium remains in some regions, indicating partial or delayed permeation. (c.5) Spatial distribution maps show for both isolated and coalescing spots are uniformly spread across the sample, rather than concentrated in specific regions.

9.4.8.e 96 nm Defect Distribution of AlO_x Thick PVAl

Figure 9-39 (a.6) shows unfiltered Ca test images of 96 nm AlO_x on thick PVAl (Alpine), revealing prominent wave-like linear features spanning several millimetres. These large-scale features are visually distinct from the finer surface patterns seen in the SEM of uncoated PVAl (Figure 5-8), which exhibit a much smaller wavelength (~100 μm). This suggests that the observed structures in the Ca test are unlikely to originate from the initial surface roughness and may instead reflect macro-scale deformation phenomena such as stress relaxation, delamination, or water-induced swelling under prolonged permeation.

In (b.6), the broader, wave-like features make it more difficult to distinguish between newly formed (isolated) defects and those that have already coalesced, particularly in later images were overlapping patterns obscure boundaries. However, the Python-based algorithm —fine-tuned using adaptive thresholding, spot tracking, and temporal memory— effectively minimizes error and yields visually consistent results between the raw and overlaid images. The spatial distribution (c.6) of isolated spots is relatively uniform across the sample aligning with trends observed in thinner coatings, further supporting the interpretation that defects are present all through the barrier layer. However, the coalescent spots seem to show an upper side bias, indicating that sample have more coalescing spots on top possibly more occurrences of permeation.

(a.6) 96 nm Thick PVAL (Alpine) – Raw Ca Images

#1: Start

#2: 0.90 Days
~21.6 Hours

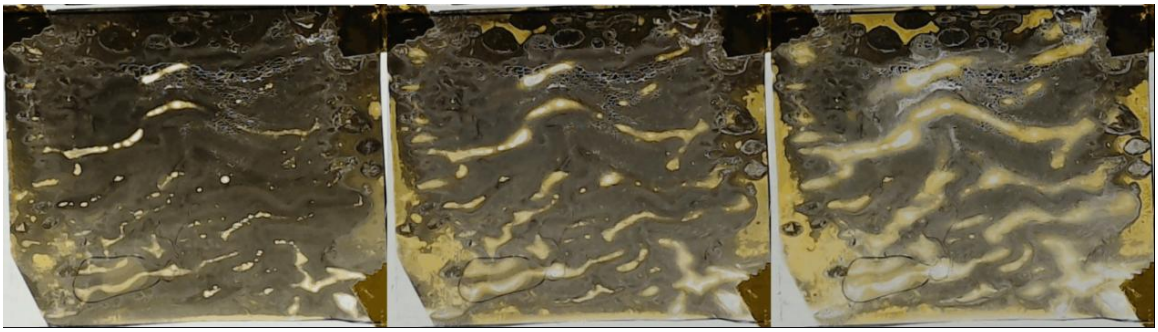
#16: 20.93 Days



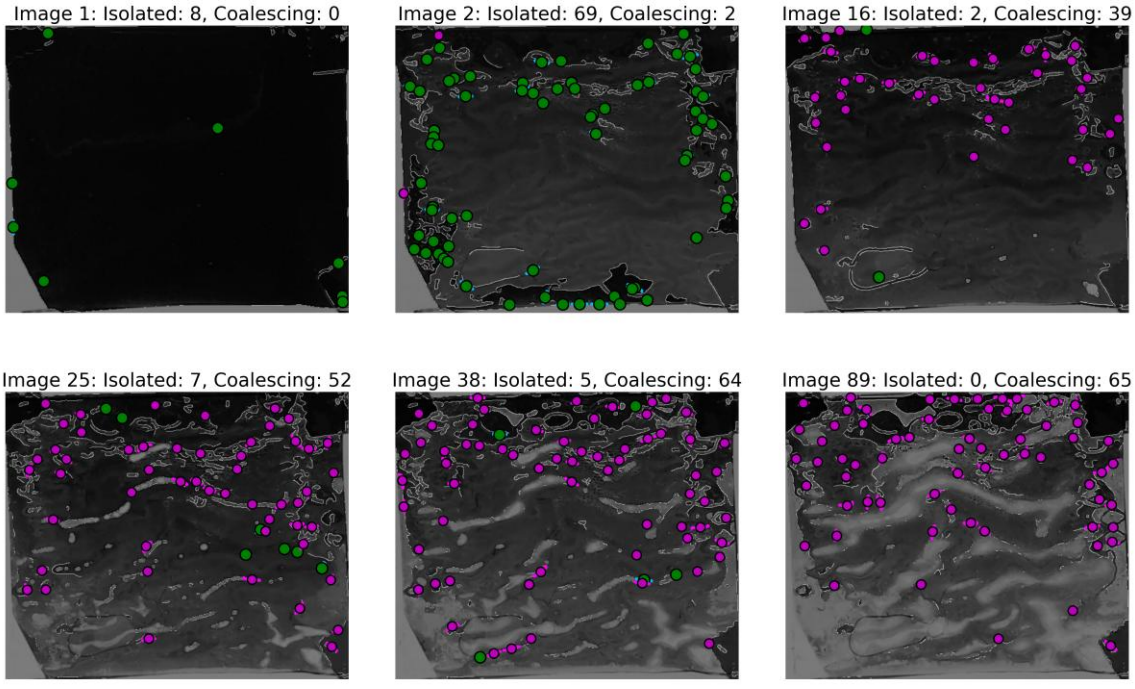
#25: 33.93 Days

#38: 47.93 Days

#89: 65.89 Days



(b.6) 96 nm Thick PVAL (Alpine) – Defect Classification Overlay (Green: Isolated with Blue Contour and Purple: Coalesced)



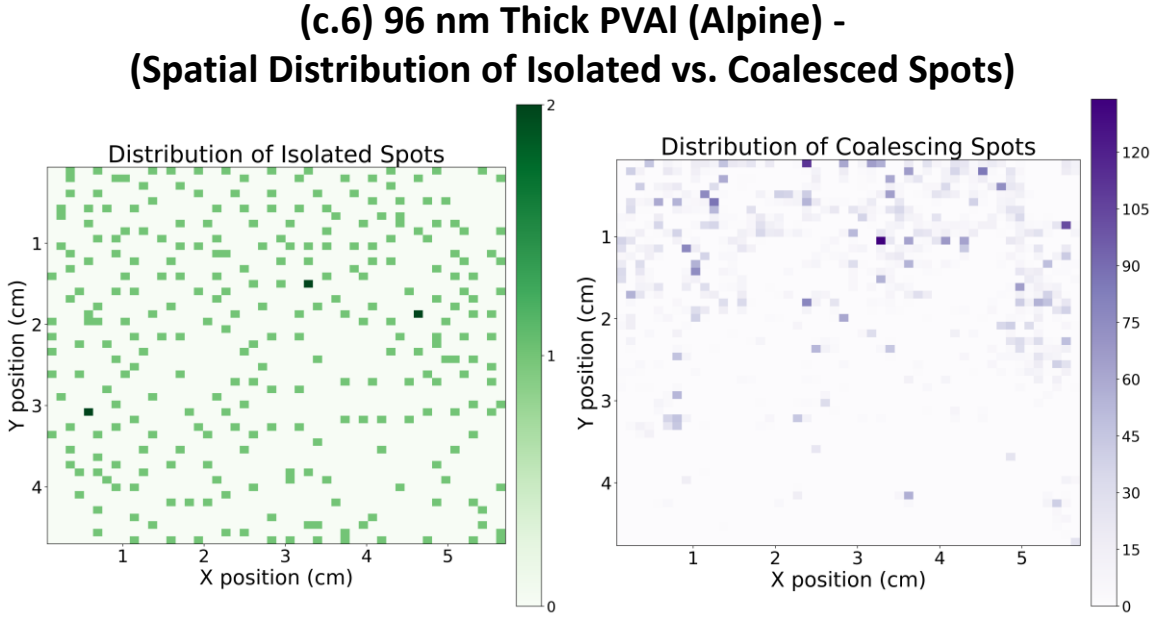


Figure 9-39: Ca-test results for 96 nm AlO_x (5.78 x 4.84 cm), (a.6) Raw images reveal prominent, wave-like features spanning millimetres, distinct from the finer-scale surface roughness of uncoated PVAl, suggesting macro-scale deformation (e.g. swelling or delamination) rather than imprinting from initial topography. (b.6) Spot detection overlays show strong visual correspondence to raw images, despite challenges posed by overlapping patterns in later frames. The Python-based algorithm effectively distinguishes isolated and coalescing features. (c.6) Spatial maps confirm a relatively uniform distribution of isolated spots, while coalescing spots exhibit a bias toward the upper region possibly indicating preferential permeation pathways or uneven stress response.

9.4.9 Supporting information - Statistics of Defect Populations in ALD – AlO_x PVAl

9.4.9.a AlO_x PVAl Thin PVAl Statistics

Analysing the results in Figure 9-40; the density of spots or defects on thin PVAl coatings of different thicknesses—approximately 26 nm (1 sample), 50 nm (2 regions from 1 sample), and 96 nm (2 samples)—was tracked over time, showing spot growth and when they typically appear.

Figure 9-40 (a) shows that most isolated spots appear almost immediately. This does not suggest uniform permeation. If water vapour were permeating uniformly through the barrier, one would expect gradual, diffusion across the entire film, not distinct, early forming spots at localized regions. The rapid appearance of numerous isolated features clearly points to localized defects, areas of higher permeability, through which vapour ingress and calcium depletion occur much faster than in the surrounding material.

The timing of isolated spot appearance appears largely independent of coating thickness with visible defects forming within the same window from the initial uptake up to around 50 days. After this period, few new isolated defects are detected.

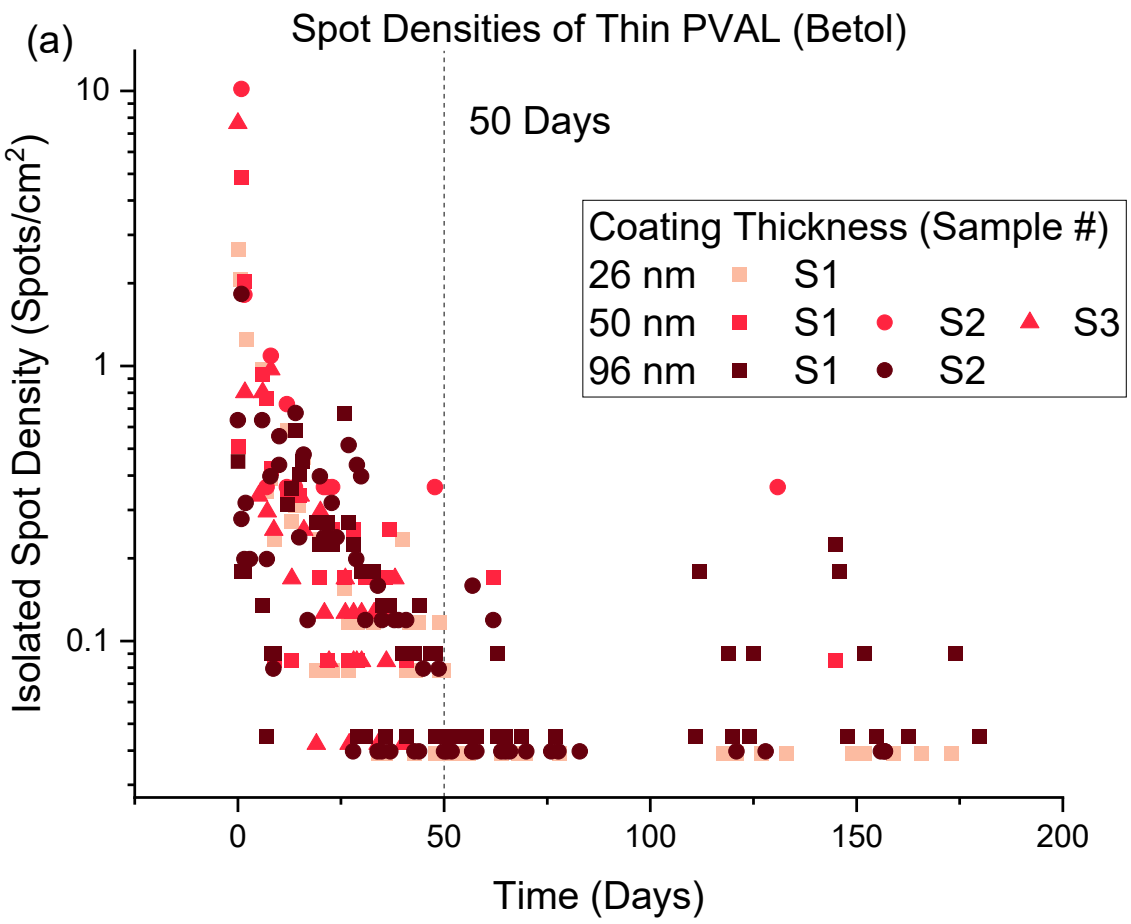
Looking at the coalescent data in Figure 9-40 (b), most coalescence begins after approximately 20 days. Beyond this point, newly emerging isolated spots may be under-detected due to overlap with growing or already coalesced defects. The likelihood of detecting new spots decreases as more of the image becomes occupied.

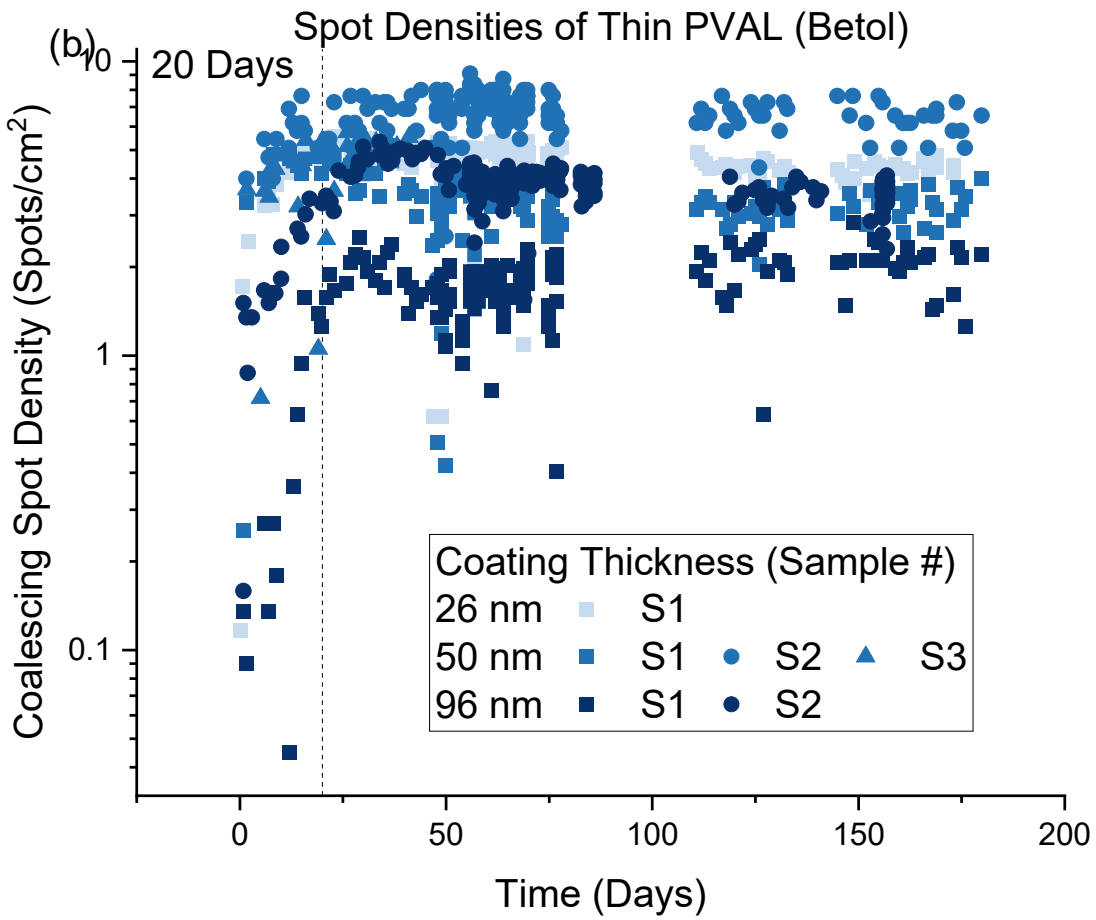
While this analysis normalizes by a fixed total image area, a more accurate approach may be plotting new isolated and coalesced spots per unit of remaining uncovered (bright) area, would better reflect detection probability. However, dynamically tracking the covered area is challenging, as it changes continuously with spot growth and merging. Incorporating such adaptive normalization would improve accuracy but requires further segmentation and tracking and is noted here as a potential refinement for future analysis.

Focusing on the coating thickness, interestingly, it appears to slightly influence the number of detected coalescing spots, with thinner coatings (26 nm and 50 nm) showing

slightly higher plateaus coalescing spots, may indicate the final number of coalescing spots.

Moreover, identifying the exact shape of each defect by eye is difficult, but aspect-ratio analysis provides a clearer picture. For every isolated spot, the aspect ratio is calculated by dividing its major-axis length by its minor-axis length. As shown in Figure 9-40 and the accompanying table, the isolated spots across all PVAl thicknesses exhibit average aspect ratios of 3.4 to 4.2, indicating that these defects begin as slender, elongated features, in contrast to the nearly circular AlO_x blisters seen in PET substrates (AR ~1.0). While aspect ratio cannot fully capture the later, interconnected networks, this early-stage value highlights the elongated nature of the possible initial spots or defects. These isolated features are typically 0.5–0.8 cm long and 1.5–2.5 μm wide. After nearby defects merge, the resulting coalesced regions widen to ~22 μm, forming the broader channels and networks observed at longer test durations.


(a)
Spot Densities of Thin PVAL (Betol)
50 Days
Coating Thickness (Sample #)
26 nm S1
50 nm S1 S2 S3
96 nm S1 S2
Isolated Spot Density (Spots/cm2)
10
1
0.1
0
50
100
150
200
Time (Days)



Thickness (nm)	Avg. Length (cm)	Avg. Aspect Ratio	Isolated Width (µm)	Coalescing Width (µm)
25	0.53 ± 0.21	3.4 ± 0.45	1.5 ± 4.9 µm	21 ± 2.9 µm
50	0.81 ± 0.48	3.7 ± 0.34	2.5 ± 4.4 µm	22 ± 4.6 µm
100	0.45 ± 0.18	4.2 ± 0.56	2.4 ± 5.6 µm	22 ± 4.3 µm

Figure 9-40: (a) Isolated and (b) Coalescing Spot Densities over time for ALD AlO_x - coated thin PVAl films with coating thicknesses of 26 nm, 50 nm, and 96 nm. Isolated spot counts initially rise but gradually plateau after ~50 days, suggesting that no new, distinguishable defects form beyond this point. In contrast, coalescing spot density increases significantly after ~20 days as existing isolated features merge, ultimately stabilizing as saturation is reached. The accompanying table summarizes geometric characteristics of these defects. Isolated spots typically measure ~ 0.53 – 0.81 cm in length and exhibit high aspect ratios (3.4 – 4.2), indicating the elongated, slit-like geometry in early stages. Upon coalescence, defect widths increase markedly from ~ 1.5 – 2.5 µm to ~22 µm, supporting the hypothesis of lateral swelling or active permeation during prolonged exposure. These evolving morphologies highlight the importance of early-stage spot detection in assessing barrier integrity.

9.4.9.b AlO_x PVAl Thick PVAl Statistics

Moving to the thicker PVAl substrate, it should be noted that increased thickness does not inherently reduce the number of unique spots but rather makes the samples easier to handle and potentially less prone to mechanical damage during preparation, distinct from defects that are introduced in the coating process.

For uncoated PVAl, thicker films generally exhibit lower WVTR due to a longer permeation path (There is a wide variation in reported WVTR and permeability values for PVAl (see Table 5-1), likely due to differences in methodologies, film types, and environmental conditions, as well as the challenges to measure the permeation in such a hydrophilic material. The MOCON Aquatran results measured here for uncoated PVAl films show significant discrepancies from literature values, except for those of Mo *et al.* [94], which align closely with these data. A detailed discussion of PVAl material properties and MOCON WVTR measurement challenges, including additional figures and data are presented in 9.4.5.b Discussion on Mocon Aquatran WVTR Results.

Chandio *et al.* (2021) [375] and Xianda *et al.* (1987) [367] reported much higher WVTRs—90 ± 5.2 and 790 g/m²·day respectively—using less controlled methods, while Mo *et al.* (2014) [62], using biaxially oriented PVAl under specialized conditions, reported lower values (0.2 to 24 g/m²·day), similar to our findings.

Park *et al.* (2023) [376] and Sarwar *et al.* (2018) [377] also found higher WVTRs, underscoring the influence of testing methodologies, such as ASTM E96 versus MOCON Aquatran, and differences in film properties. This suggests that controlled testing, and standardized methodologies are critical for achieving consistent and accurate WVTR measurements.

These insights highlight the need for better standardized testing to ensure reliable comparisons across studies.

Table 5-1, Figure 9-28, Figure 9-30). However, in coated samples, this relationship becomes more complex due to factors like coating conformity, defect density, and local delamination (Figure 9-31 and Figure 9-32). These nuances highlight that while thickness reduces baseline permeability, local features dominate in Ca-based assessments. Figure 9-41, presents isolated (a) and coalescing (b) spot densities (number per cm^2) for AlO_x-coated thick PVAl films of varying thicknesses: 26 nm (1 sample), 50 nm (3 samples), and 96 nm (2 samples).

Trends like those in thin PVAl are observed, including initial detection of isolated spots followed by continued growth over approximately 50 days. As noted, misidentifications may occur, and depending on the coating thickness, lag time of defects within the calcium test may also influence the number of detected isolated and coalescing spots.

There is a suggestion that fewer isolated spots are detected in thicker PVAl-coated samples, as shown in Figure 9-41, at least for the 50nm and 96nm thick coatings.

Additionally coalescing spots in thick PVAl appear to develop more slowly, with the plateau in coalescence occurring around 40 days, compared to 20 days in thin PVAl. While this could be due to a lower effective defect density, making coalescence less

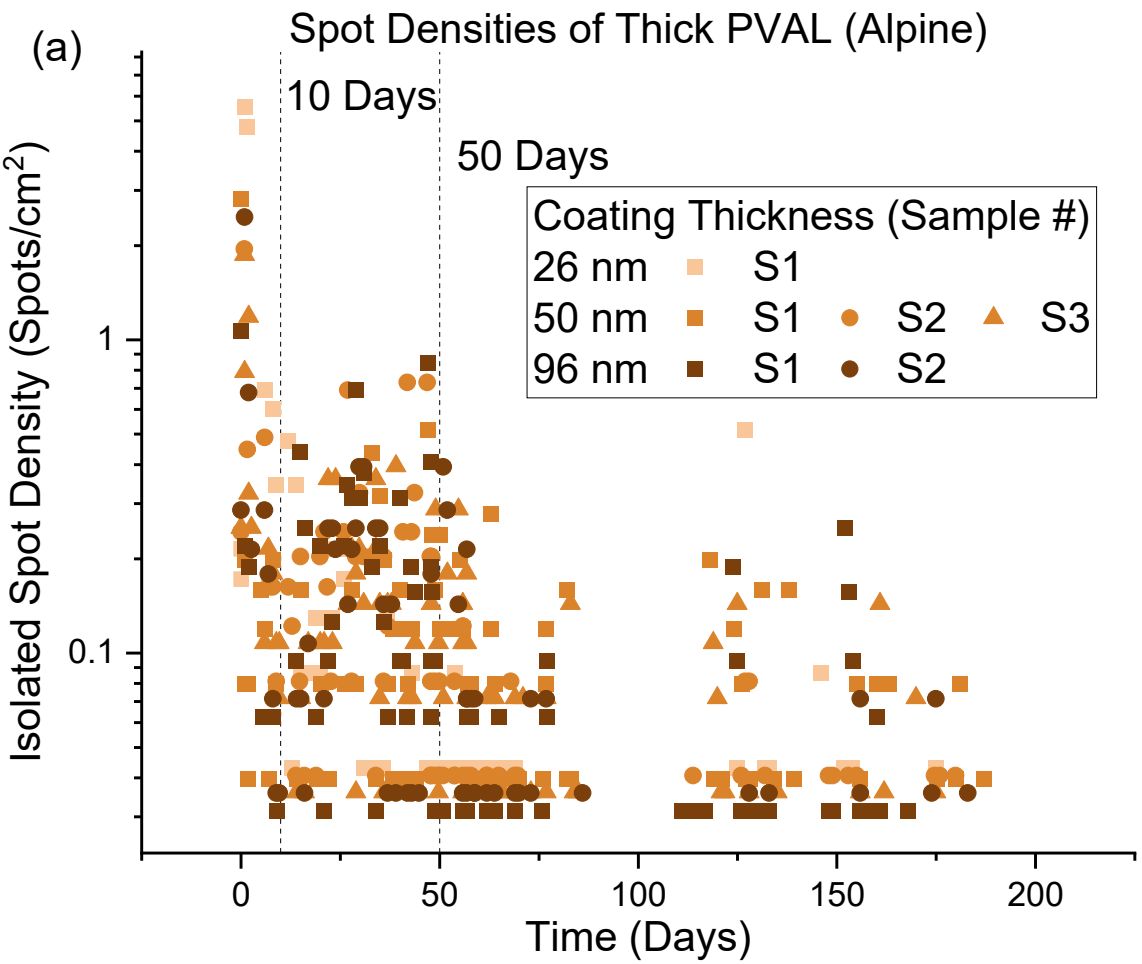
frequent, this is not definitely confirmed, since the total number of isolated spots appears broadly similar across thicknesses (Figure 5-16).

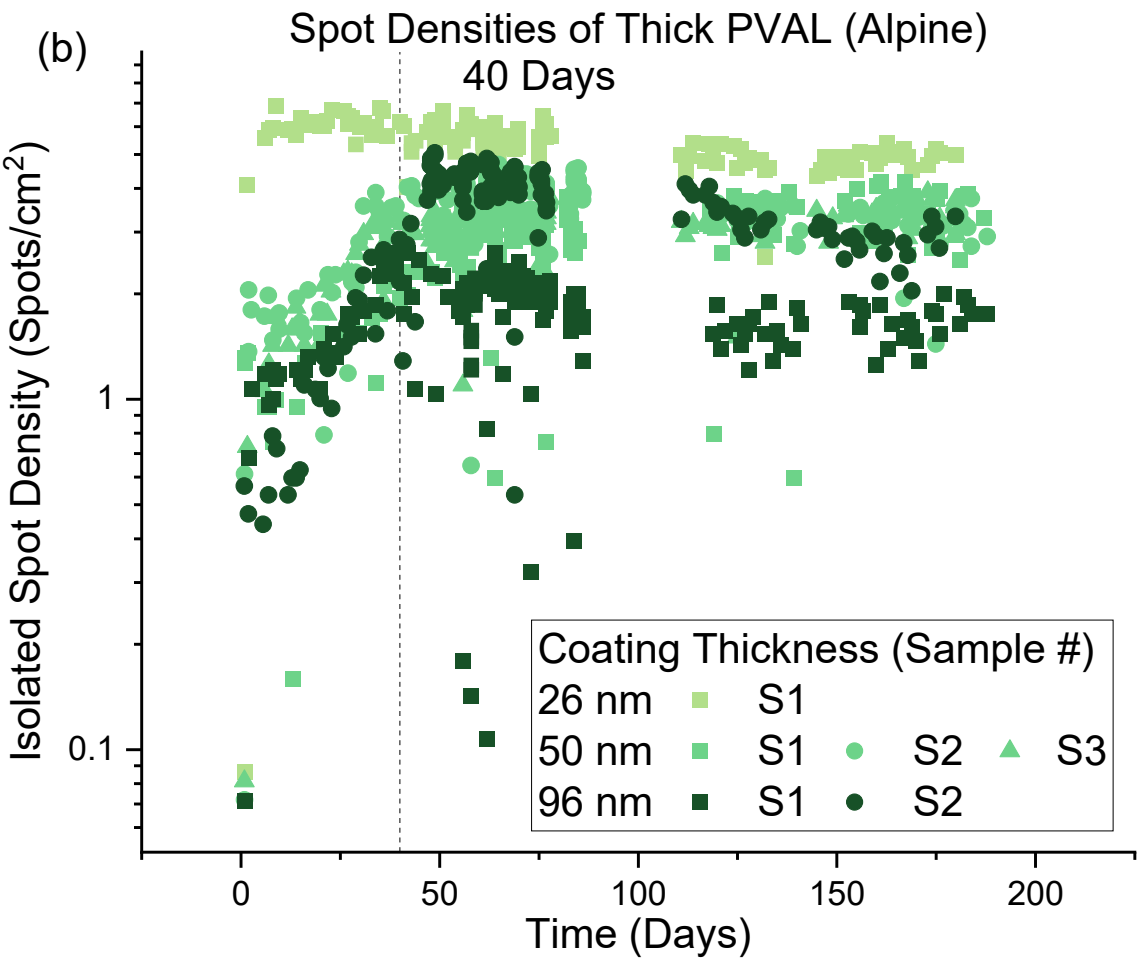
It is also possible that spot growth is slower in thicker PVAl, potentially due to differences in defect sizes, though the summary of defect widths appears relatively comparable (Figure 5-18); where other mechanisms may contribute like variations in diffusion pathways or defect connectivity.

Calculating the aspect ratio based on associated table of Figure 9-41 confirms that these defects start out as predominantly linear, with average values ranging from 3.3 to 4.2. These aspect ratios refer only to isolated features, as reiterated is calculated by dividing the major axis length by the minor axis length. While a high aspect ratio indicates that the defects are elongated rather than circular, it does not imply that they are interconnected, that occurs only later during coalescence.

The average length of defects also increases with coating thickness, from 0.31 cm at 25 nm to 1.30 cm at 50 nm, before slightly decreasing to 1.00 cm at 100 nm. This trend is not likely to be due to sample size limitations, as the image area is consistent across samples. Instead, longer defects in thicker coatings may reflect stress-driven mechanical effects — consistent with previous literature showing that thicker AlO_x barriers on PVAL tend to develop larger or longer flaws, possibly due to strain accumulation or relaxation effects during drying and ageing.

In terms of width, isolated features remain relatively narrow around 1–2 µm, with large variation across samples (high standard deviation), while coalescing defects grow wider with thickness, from 17 µm at 25 nm to 24 µm at 100 nm, indicating lateral merging and network formation over time.


(a)
Spot Densities of Thick PVAL (Alpine)
10 Days
50 Days
Coating Thickness (Sample #)
26 nm S1
50 nm S1 S2 S3
96 nm S1 S2
Isolated Spot Density (Spots/cm2)
1
0.1
0
50
100
150
200
Time (Days)



Thickness (nm)	Avg. Length (cm)	Avg. Aspect Ratio	Isolated Width (µm)	Coalescing Width (µm)
25	0.31 ± 0.18	3.3 ± 0.55	1.4 ± 7.0 µm	17 ± 3.2 µm
50	1.30 ± 0.72	4.1 ± 0.48	2.3 ± 5.0 µm	24 ± 4.2 µm
100	1.00 ± 0.70	4.2 ± 0.71	2.2 ± 4.7 µm	24 ± 4.7 µm

Figure 9-41: Spot densities in thick PVAl films coated with AlO_x at different thicknesses (26 nm, 50 nm, and 96 nm). Panel (a) shows the evolution of isolated spot densities over time, while panel (b) shows coalescing spots. As observed in thin PVAl films, isolated spot counts initially increase and then decline as defects begin to merge. Coalescing spot densities continue to rise until reaching a plateau. Although the total number of isolated spots appears lower in thicker films, the final number of coalescing spots remains comparable to those in thinner PVAl. Defect size trends seem to be also slightly influenced by coating thickness. Average spot lengths increase with coating thickness from 0.31 ± 0.18 cm at 25 nm to 1.30 ± 0.72 cm at 50 nm, while aspect ratios remain high (3.3–4.2), consistent with elongated morphologies. Notably, the average width of isolated defects is much smaller than that of coalescing ones (e.g., 1.4 ± 7.0 µm vs. 17–24 µm), which is expected as the network continues to grow.

9.4.10 Supporting information - Statistics of Defect Sizes in ALD – AlO_x PVA

9.4.10.a 50 nm Thin PVAl Substrate Defects

The next step is to analyse the thicker coatings. Increasing the AlO_x coating thickness to 50 nm (Figure 9-42) shows significant improvement in water vapor barrier properties, likely related to defect sizes as number of defects seem relatively similar and there was even an increase in terms of defect density (Figure 5-16).

Like the analysis of the 26 nm Thin PVAl, six distinct regions of interest from a representative 50 nm sample were selected and analysed. Regions covered by Kapton tape were excluded, and the largest defect from each region was identified for analysis, as in the previous study.

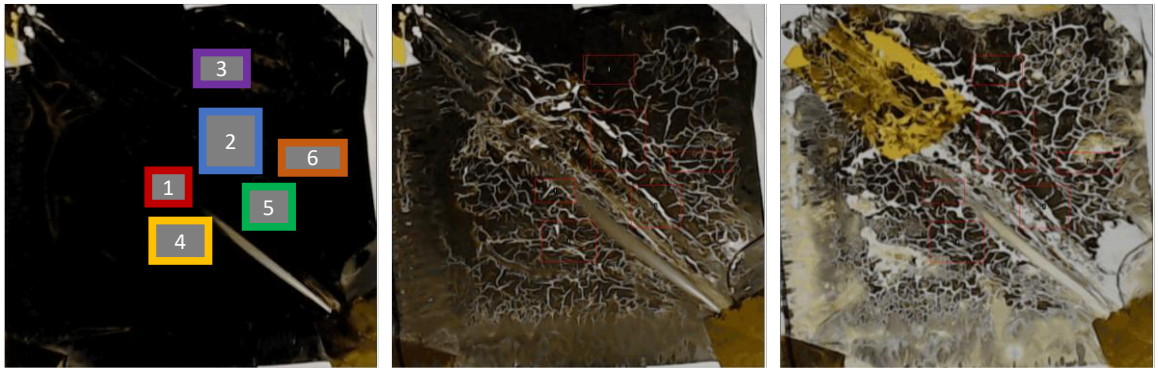
The general shapes of the defects are still complex and random, noting that taking total defect area approach is a better method to assuming a shape like rectangle or square. For example, Defect #1 grows into an inverted "U," while Defects #2, #4, #5, and #6 show dendritic-like features, and Defect #3 resembles a branching structure. These variations highlight how using total defect area avoids systematic over- or underestimation that could arise of a particular shape were assumed.

More precise shape-based analyses such as using elliptical or polygonal correction models, were not pursued here to simplify calculations and to maintain consistency across large datasets. Although the defect area approach may still introduce some error, it provides a reliable estimate of defect size and a useful trend for damage evolution in the barrier layer. Averaging numerous data samples further minimized random errors.

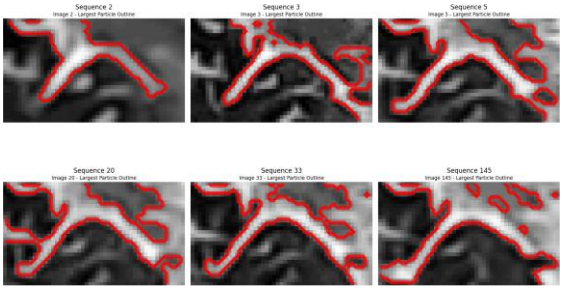
Maindron's work reports defect sizes ranging from a few microns to several hundred microns, with larger defects often linked to deposition processes [350]. The estimated defect areas in this study fall within that range, providing some validity to the assumptions made.

The regions of interest for the 50 nm AlO_x coated PVAl samples are generally smaller than those for the 26 nm samples, but this does not consistently result in smaller defect areas. In fact, the 50 nm samples display not only larger estimated defect areas, some reaching over $4.0 \times 10^5\ \mu m^2$ compared to a maximum of $1.09 \times 10^5\ \mu m^2$ in the 26 nm samples, but also a higher number of visible possible defects within each region. This correlates with the higher water uptake slopes (M_{H2O}) and WVTR values measured for the 50 nm samples. These observations suggest that while thicker coatings can reduce defect density overall, these can still develop more and larger isolated defects. Such defects dominate water permeation behaviour and highlight the complexity of achieving uniform barrier performance for these materials.

(b) 50 nm Thin PVAL (Betol)



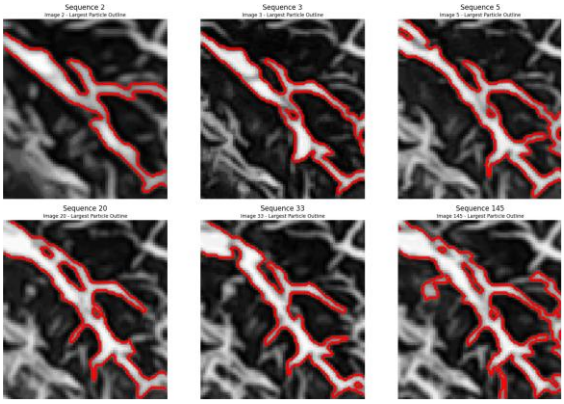
Defect #1 Outline



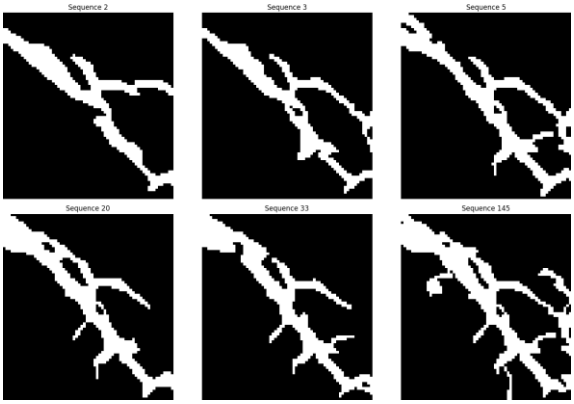
Defect #1 Isolated (Binary)



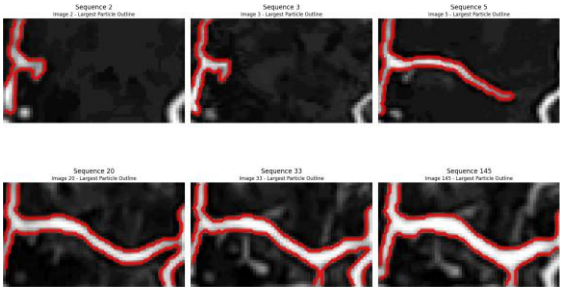
Defect #2 Outline



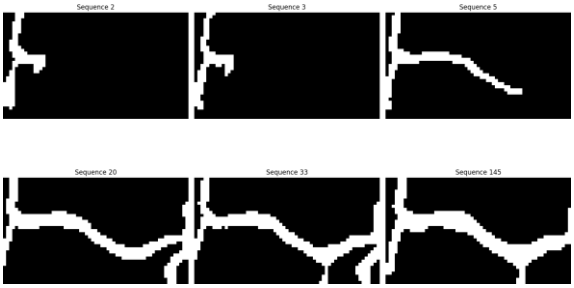
Defect #2 Isolated (Binary)



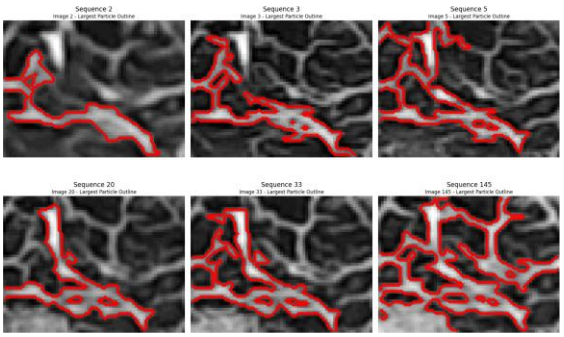
Defect #3 Outline



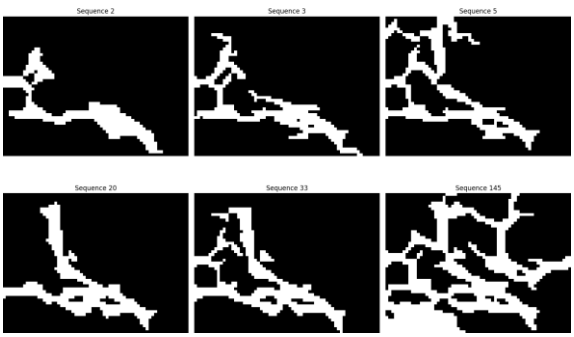
Defect #3 Isolated (Binary)

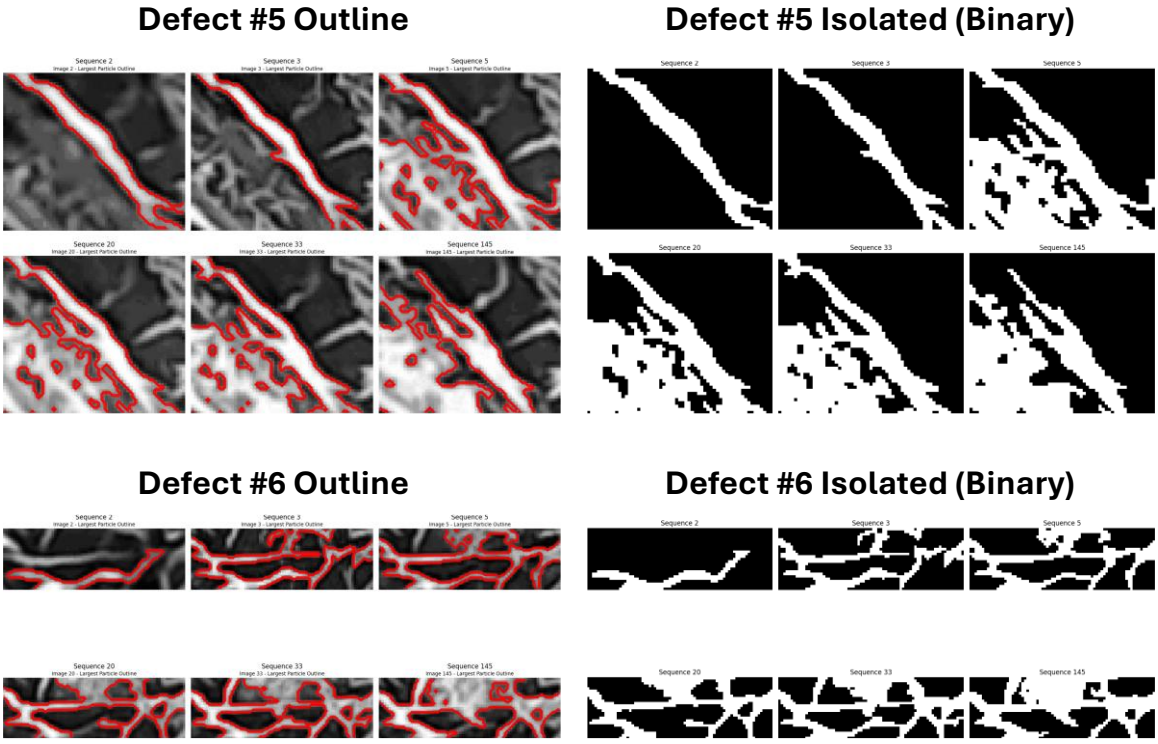


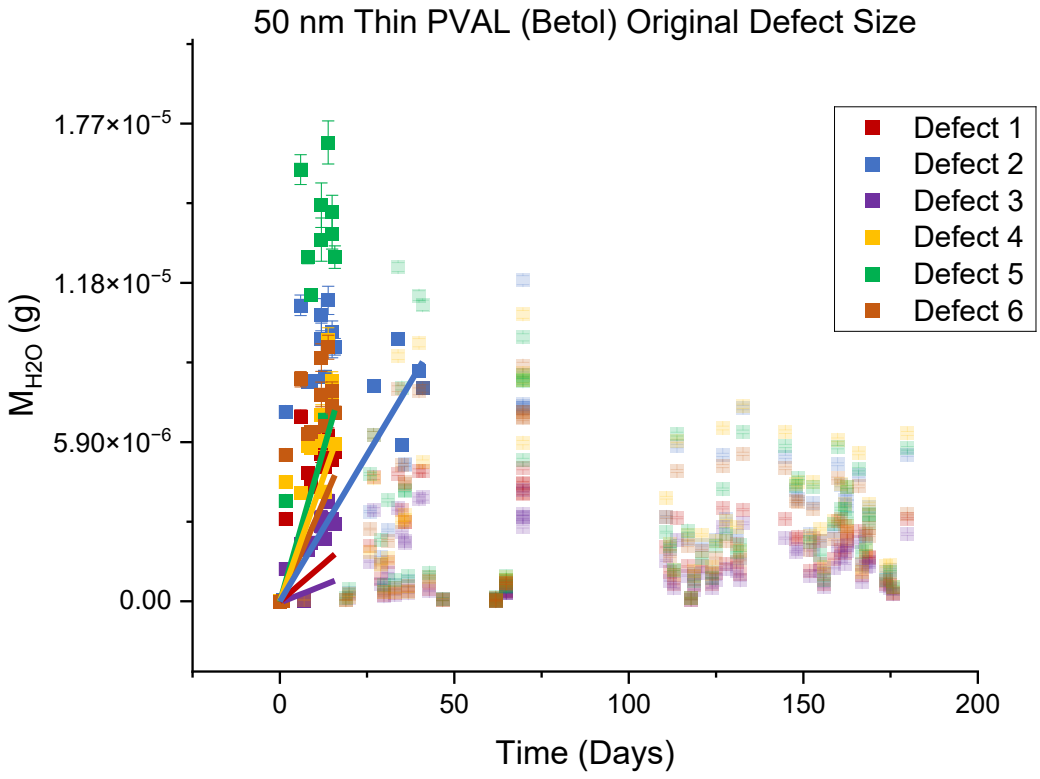
Defect #4 Outline



Defect #4 Isolated (Binary)




Defect #5 Outline
Defect #5 Isolated (Binary)
Defect #6 Outline
Defect #6 Isolated (Binary)


50 nm Thin PVAL (Betol) Original Defect Size
Defect 1
Defect 2
Defect 3
Defect 4
Defect 5
Defect 6
1.77×10⁻⁵
1.18×10⁻⁵
5.90×10⁻⁶
0.00
M_H2O (g)
0
50
100
150
200
Time (Days)

Defect	ROI Size (cm)	Slope (g/day)	Slope Std. Dev.	Adj. R. Squared	Defect Total Area (μm²)	Defect Area Std. Dev.
1	0.50 by 0.29	1.11E-07	5.95E-08	0.16	5.22E+04	2.80E+04
2	0.68 by 0.74	2.17E-07	3.25E-08	0.72	4.16E+05	7.09E+04
3	0.63 by 0.36	3.68E-07	8.06E-08	0.62	1.73E+05	3.80E+04
4	0.67 by 0.50	5.15E-08	3.35E-08	0.10	2.42E+04	1.58E+04
5	0.61 by 0.52	4.5E-07	1.55E-07	0.38	2.12E+05	7.30E+04
6	0.77 by 0.26	2.99E-07	1.05E-07	0.37	1.41E+05	4.94E+04

Figure 9-42: Six selected regions of interest from a 50 nm AlO_x ALD-coated thin PVAl substrate, with the largest defects in each region highlighted by the red outlines and binary segmentation images. These defect areas range from approximately $2.42 \times 10^4\ \mu m^2$ *to over* $4.16 \times 10^5\ \mu m^2$*, consistent with higher water uptake rates and slopes in this sample compared to the 26 nm coatings. Despite the smaller ROI sizes in the 50 nm samples, these larger defect areas along with more numerous visible features, correlate with higher WVTR values and suggest that thicker coatings can still develop more and larger isolated defects. This emphasizes the challenges in achieving a uniform barrier performance in thin film encapsulation applications.*

9.4.10.b 96 nm Thin PVAl Substrate Defects

The same analysis was performed for the 96 nm Thin PVAl substrate (Figure 9-43). Interestingly, not only linear defects were observed, but also spot-like or circular defects similar in appearance to the Ca test spots typically seen in PET substrates, which were also analysed in this study (4.6 Analysis of Defects (Spots) in ALD AlO_x coating).

Five distinct linear defects and two distinct spots were identified, each represented in montages with outlines of surrounding defects and isolated binary images. Unlike thinner coatings, the defects here are less distinct and lack the finer dendritic structures.

Notably, defect #1 shows some distinct coalescence, but the rest are more circular and "spot-like."

The 96 nm Thin PVAl samples show features that resemble island-like structures, with surrounding regions of depleted calcium, rather than distinct spot defects. There are also typical dots where calcium is depleting, like those seen in PET substrates. This may be due to the thicker AlO_x coating being less brittle, resulting in different structures compared to thinner coatings.

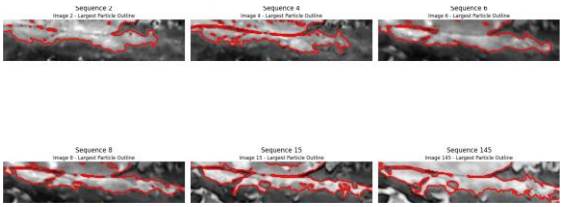
This observation is also reflected in the water uptake rate of the selected regions, which is significantly lower. Consequently, the estimated defect areas are smaller, as the defects appear more "spot-like" rather than other branch or linear like defect structures.

Instead, two distinct spots like defects were also analysed. While their shapes differ from the dominant linear or dendritic features, the total defect areas remain significant with Spot 1 measuring 2.26×10^4 μm^2 and Spot 2 measuring 2.45×10^4 μm^2. These large areas help explain why PVAl, even with a thicker 96 nm AlO_x coating, can still exhibit relatively high WVTR: large, isolated macro-defects compromise barrier integrity even if these appear as circular features in the images.

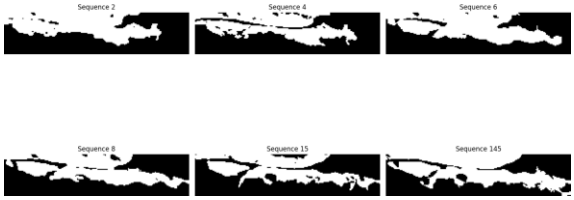
(c) 96 nm Thin PVAL (Betol)



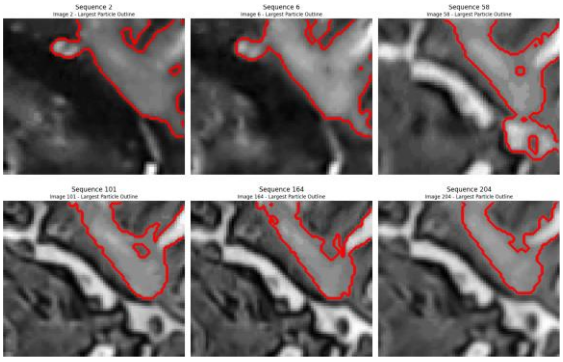
Defect #1 Outline



Defect #1 Isolated (Binary)



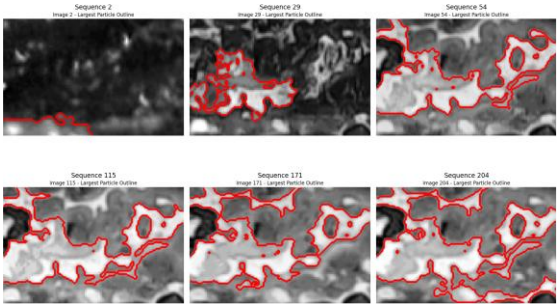
Defect #2 Outline



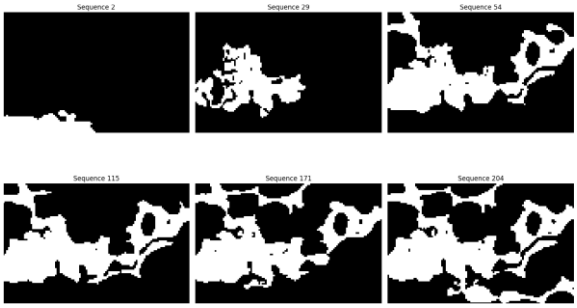
Defect #2 Isolated (Binary)



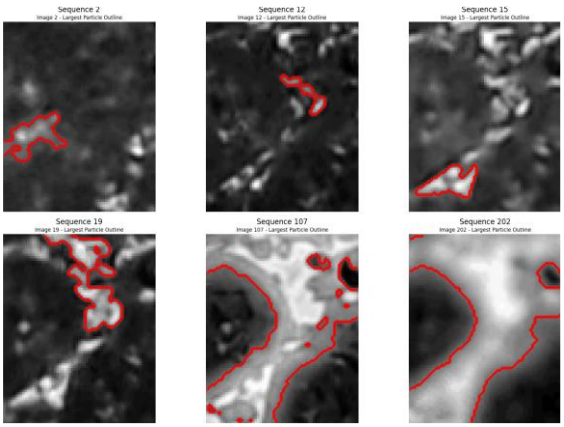
Defect #3 Outline



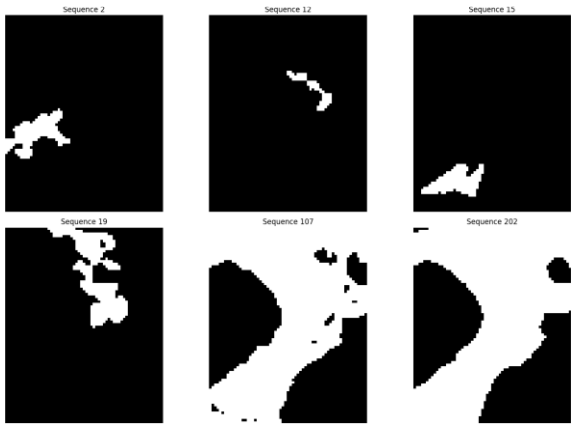
Defect #3 Isolated (Binary)



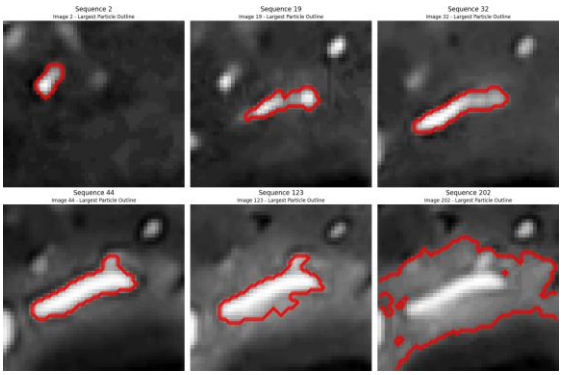
Defect #4 Outline



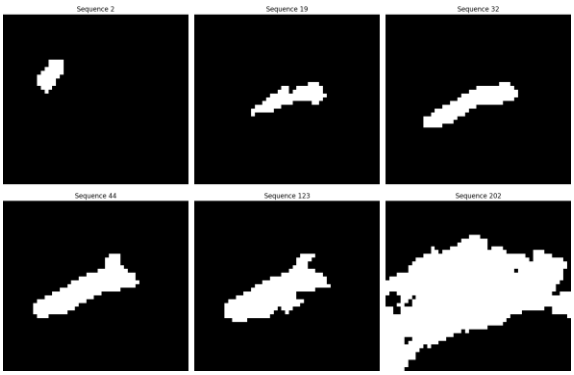
Defect #4 Isolated (Binary)



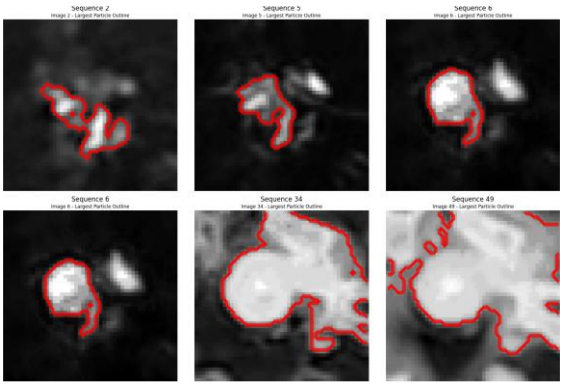
Defect #5 Outline



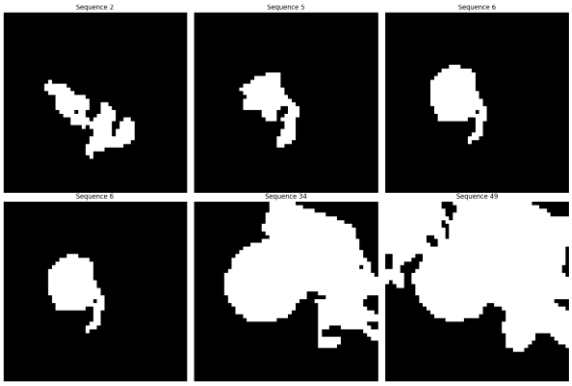
Defect #5 Isolated (Binary)



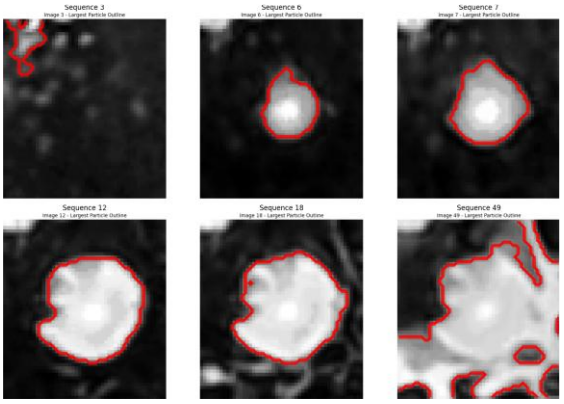
Spot #1 Outline



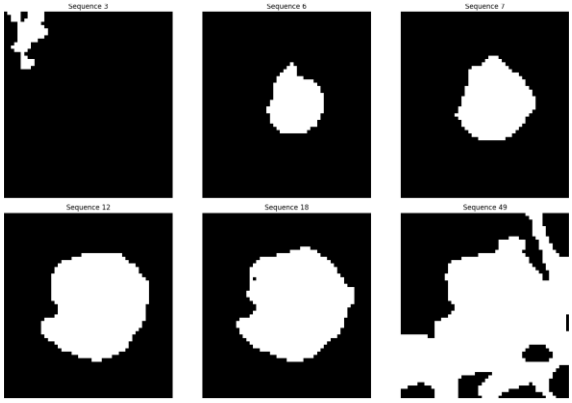
Spot #1 Isolated (Binary)

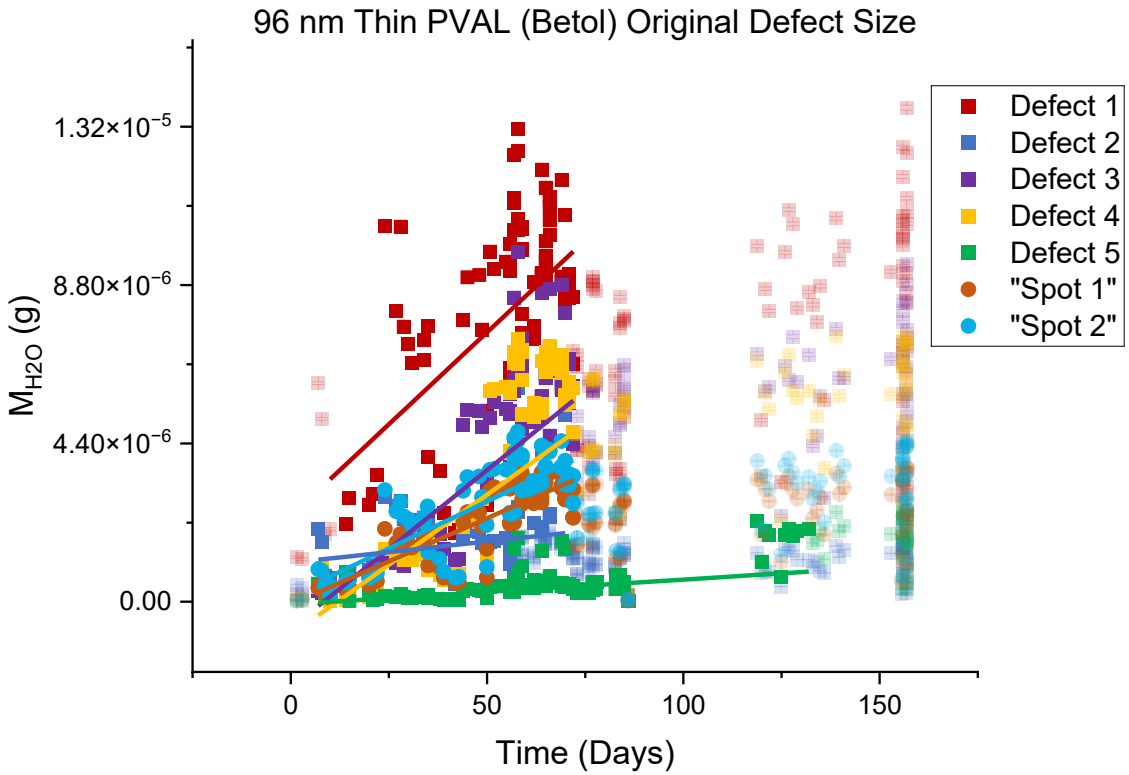


Spot #2 Outline



Spot #2 Isolated (Binary)





Defect	ROI Size (cm)	Slope (g/day)	Slope Std. Dev.	Adj. R. Squared	Defect Total Area (µm²)	Defect Area Std. Dev.
1	2.06 by 0.46	1.02E-07	1.3E-08	0.39	4.80E+04	6.17E+03
2	0.73 by 0.63	3.46E-09	3.78E-09	0.03	1.63E+03	1.78E+03
3	1.18 by 0.76	8.79E-08	4.07E-09	0.82	4.13E+04	2.05E+03
4	0.65 by 0.80	7.79E-08	4.86E-09	0.72	3.66E+04	2.37E+03
5	0.50 by 0.46	6.87E-09	4.69E-10	0.58	3.23E+03	2.28E+02
Spot 1	0.50 by 0.49 cm	4.8E-08	2.09E-09	0.84	2.26E+04	9.98E+02
Spot 2	0.51 by 0.57	5.21E-08	2.98E-09	0.75	2.45E+04	1.43E+03

Figure 9-43: Five linear defects and two distinct circular or spot-like defects in the 96

nm AlO_x ALD-coated thin PVAl substrate, each outlined in red and shown as isolated binary images. These features differ from the finer dendritic structures seen in thinner coatings and instead resemble island-like or "spot" structures with surrounding Ca depletion. While defects areas in these thicker samples are generally smaller – range from $1.6 \times 10^3\ \mu m^2$ *to* $4.8 \times 10^4\ \mu m^2$ *for linear defects, the two circular spot-like features have significant total areas of* $2.26 \times 10^4\ \mu m^2$ *and* $2.45 \times 10^4\ \mu m^2$*, respectively. This supports a possibility that even thicker coatings, large isolated macro-defects can form and compromise barrier performance, explaining the relatively high WVTR observed in these PVAl substrates.*

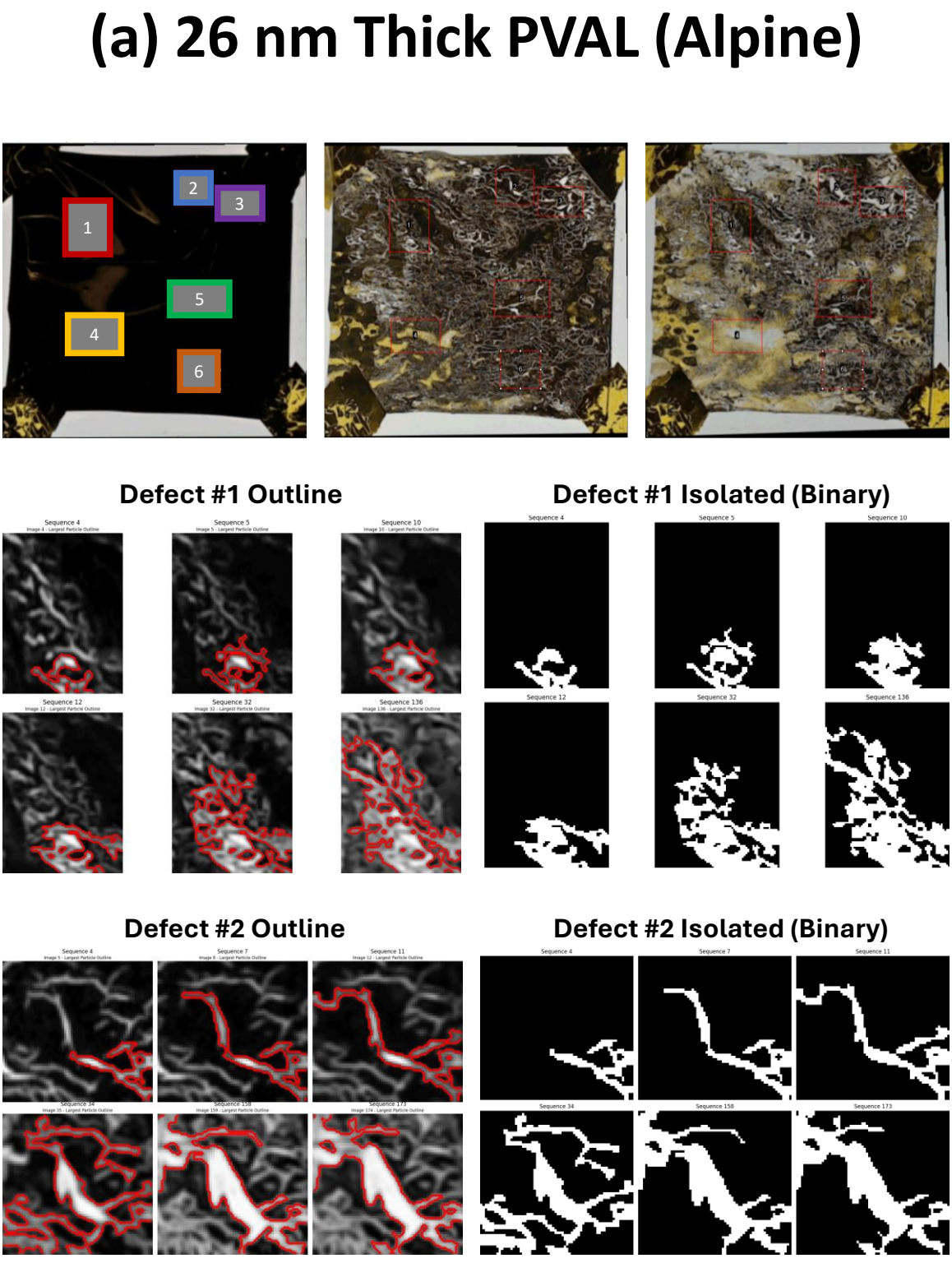
9.4.10.c 26 nm Thick PVAl Substrate Defects

The next investigation focuses on Thick PVAl (~42 µm), double the thickness of thin PVAl. Three AlO_x coating thicknesses were again analysed: 26 nm, 50 nm, and 96 nm, which showed significant improvements in barrier properties. The first analysis deals with the 26 nm coating, predicted to exhibit dendritic and defect-like features like the thinner PVAl substrate.

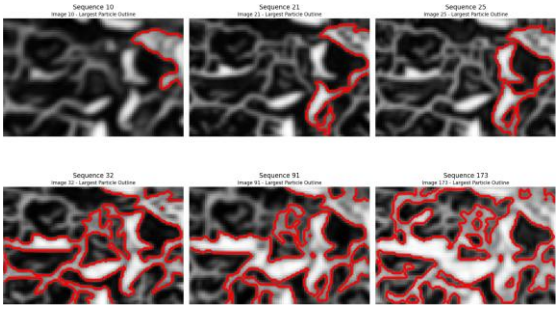
Figure 9-44 shows six regions of interest of varying sizes. Like thin PVAl, the defects do not have distinct shapes. Defect #1 appears as an amalgamation or blob, while Defects #2, #3, #5, and #6 display typical dendritic structures, resembling branches or corals. Defect #4 uniquely shows significant growth or widening, which is less evident in the other defects.

Defect growth appears random but typically extends outward in multiple directions, resulting in defect areas that vary significantly across the six analysed regions. Defect #4 has the steepest slope and the largest estimated total defect area of $9.92 \times 10^4\ \mu m^2$, while Defects #1, #2, #3, #5 and #6 have total areas generally around 1.37 to $2.95 \times 10^4\ \mu m^2$ ($\pm\ 3.0 \times 10^3\ \mu m^2$). Compared to the thinnest PVAl coating (26 nm), these defect area estimates are quite similar, indicating that substrate thickness does not significantly influence the ultimate size of the defect areas. However, in these thicker

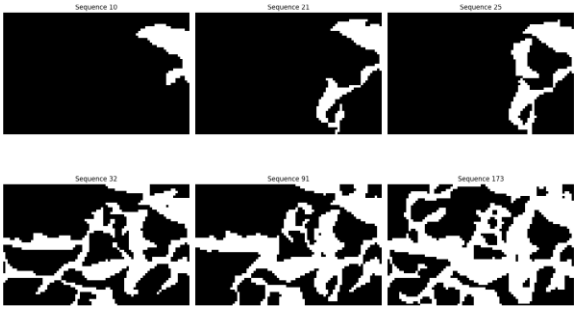
PVAl samples, the defects appear more blob-like, with larger total defect areas than in the thin PVAl substrates.



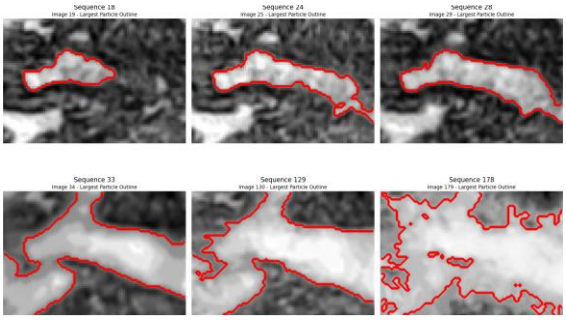
Defect #3 Outline



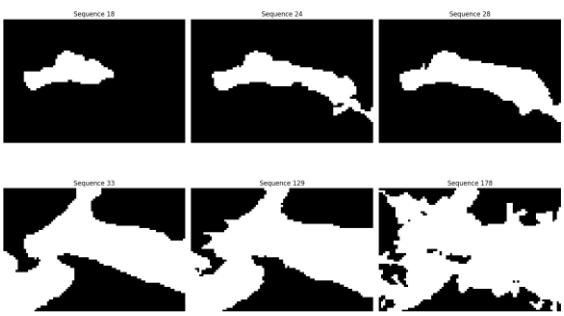
Defect #3 Isolated (Binary)



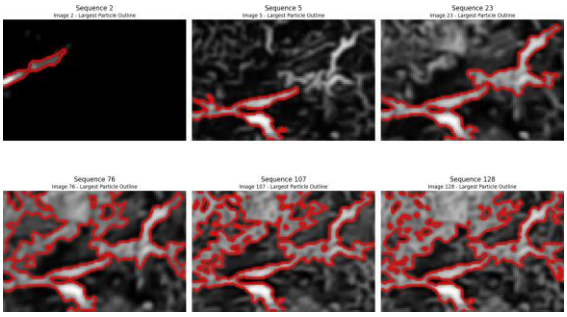
Defect #4 Outline



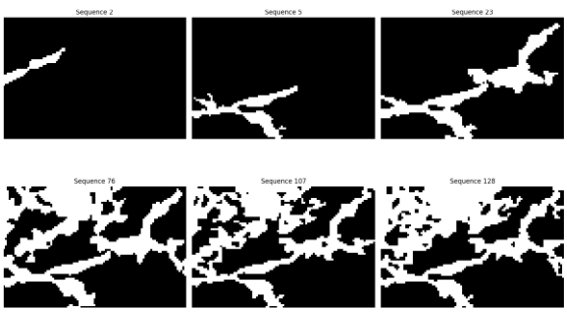
Defect #4 Isolated (Binary)



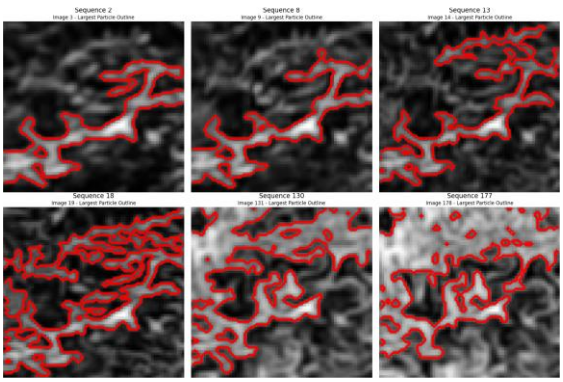
Defect #5 Outline



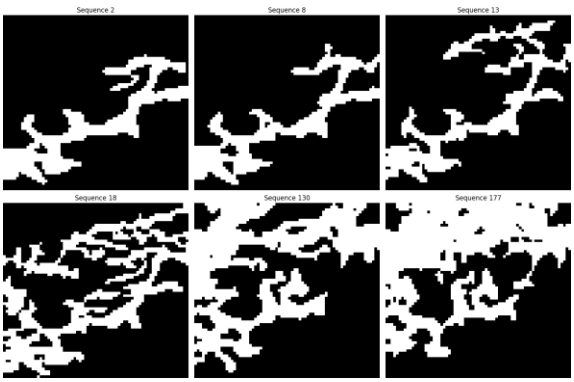
Defect #5 Isolated (Binary)

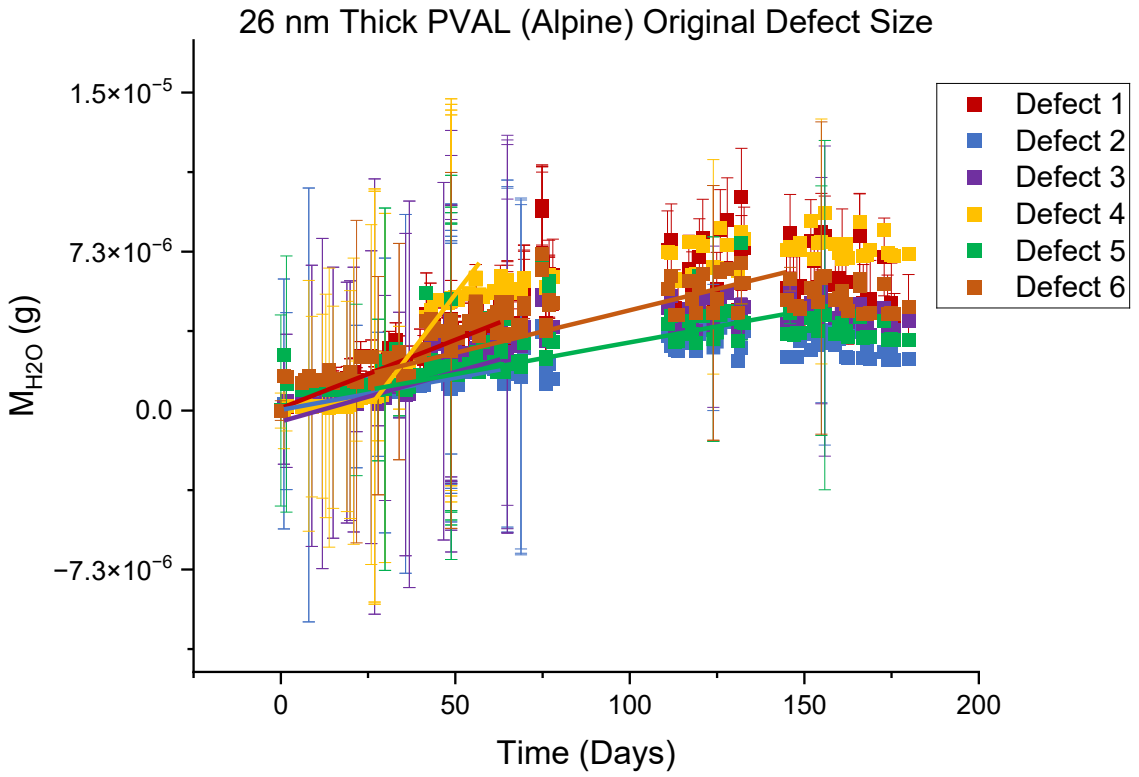


Defect #6 Outline



Defect #6 Isolated (Binary)





Defect	ROI Size (cm)	Slope (g/day)	Slope Std. Dev.	Adj. R. Squared	Defect Total Area (μm²)	Defect Area Std. Dev.
1	0.72 by 0.96	6.27E-08	2.22E-09	0.90	2.95E+04	1.17E+03
2	0.68 by 0.64	2.95E-08	2.76E-09	0.56	1.39E+04	1.32E+03
3	0.82 by 0.53	4.54E-08	5.65E-09	0.41	2.13E+04	2.68E+03
4	0.89 by 0.61	2.11E-07	1.00E-09	0.99	9.92E+04	1.81E+03
5	1.00 by 0.66	2.92E-08	2.15E-10	0.99	1.37E+04	2.62E+02
6	0.73 by 0.69	3.91E-08	7.77E-10	0.95	1.84E+04	4.12E+02

Figure 9-44: Six regions of interest from a 26 nm AlO_x ALD-coated thick PVAl substrate show dendritic, or blob-like defect features similar to those observed in thinner PVAl films. The calculated defect total areas range from $1.39 \times 10^4\ \mu m^2$ to $9.92 \times 10^4\ \mu m^2$, comparable to the 26 nm thin PVAl data. This suggests that while the substrate thickness

does not strongly influence the overall defect size, the defect morphology in thick PVAl substrates tends to appear more blob-like and with larger defect areas compared to the thinner samples.

9.4.10.d 50 nm Thick PVAl Substrate Defects

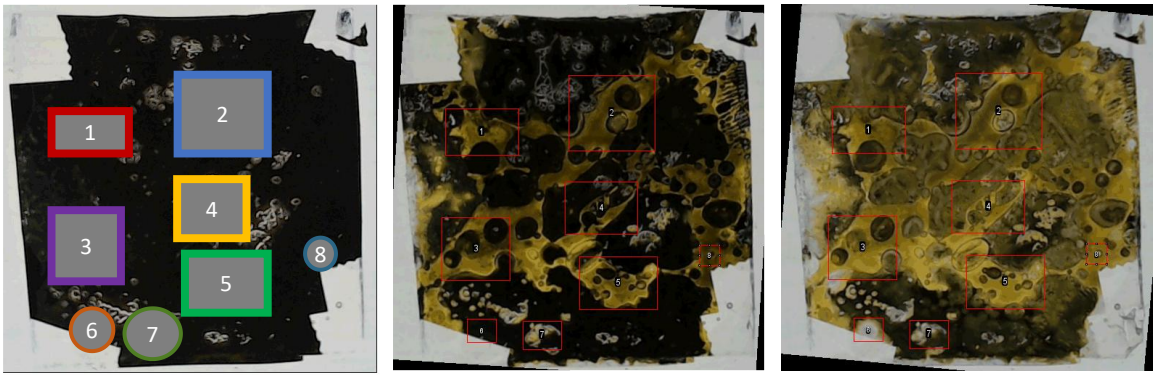
Doubling the initial AlO_x coating to 50 nm results in significant changes in features, as seen in Figure 9-45. The selected regions of interest reveal a transition from stress-induced defects in the thinner coating to more spot-like defects, similar to those seen in PET substrates. This spot-like nature was not initially observed in the 50 nm thin PVAl but is more evident in the thick PVAl. The defects in thick PVAl are generally thicker, with river-like structures rather than the finer defects seen in 26 nm coatings. Defects #1 and #5 display calcium "islands" surrounded by depleted regions ("river or sea"), indicating lateral permeation through these larger, blob-like defects. The random growth and unpredictable coalescence also result in random sand various shapes. Defects #2, #3, and #4 exhibit some dendritic structures but quickly transition into river- or sea-like formations, with calcium deposits surrounded by depleted regions. These were analysed as "spots" like previous samples.

Calculating water uptake rates revealed that Defect #1 had the highest rate and the largest estimated defect area (2.16×10^5 μm^2 $\pm$ 3.00×10^4 μm^2), while the other defects showed similar rates and defect areas generally in the mid- to low- 10^4 μm^2 range. Both thin and thick PVAl substrates with 50 nm coatings showed a similar trend: fewer but potentially larger defect areas, transitioning towards more spot-like or circular formations.

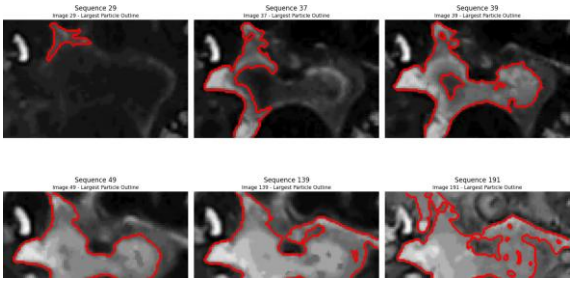
For regions classified as spots, Spot #1 resembles those seen in ALD-coated PET substrates, though edge permeation at the copper-calcium border was noted. To avoid

this, Spots #2 and #3 were selected within boundaries to minimize later permeation effects. Spot #2 appears more dot-like, while Spot #3 resembles the growth patterns of coated PET substrates. Statistically, Spot #1 and Spot #2 have notably large defect areas (8.62×10^3 µm^2 and 1.39×10^4 µm^2, respectively), while Spot #3, though not a perfect circular feature, shows a smaller defect area of 4.86×10^2 µm^2.

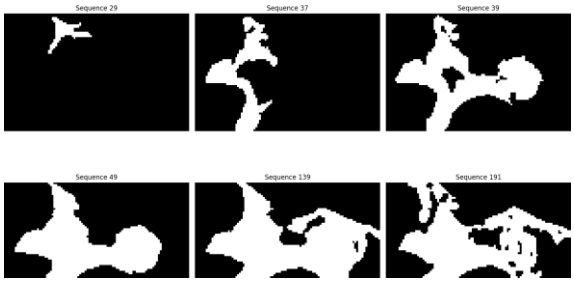
(b) 50 nm Thick PVAL (Alpine)



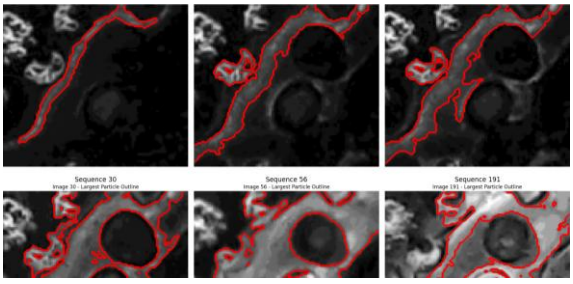
Defect #1 Outline



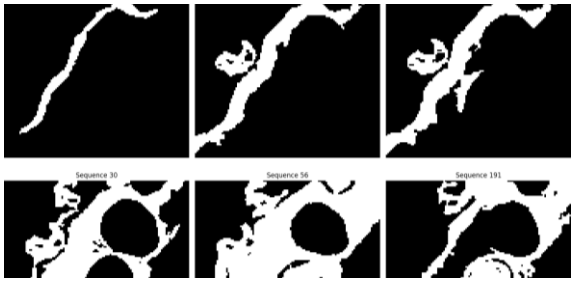
Defect #1 Isolated (Binary)



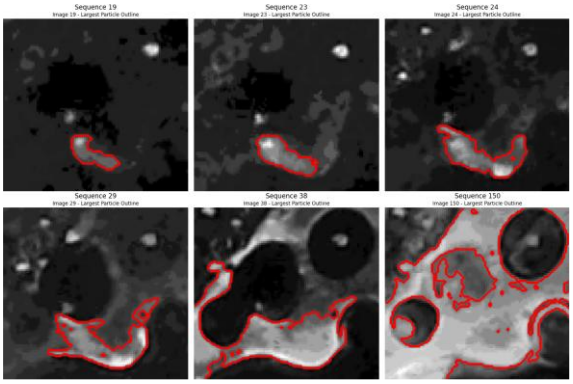
Defect #2 Outline



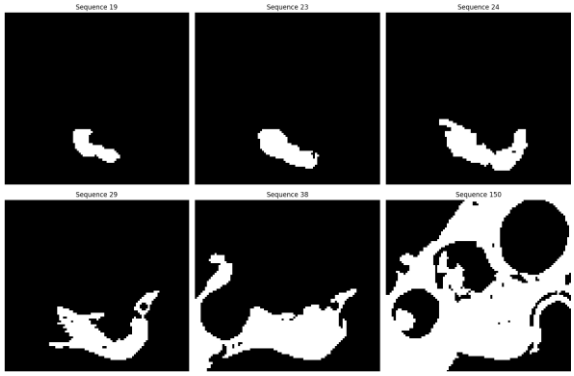
Defect #2 Isolated (Binary)



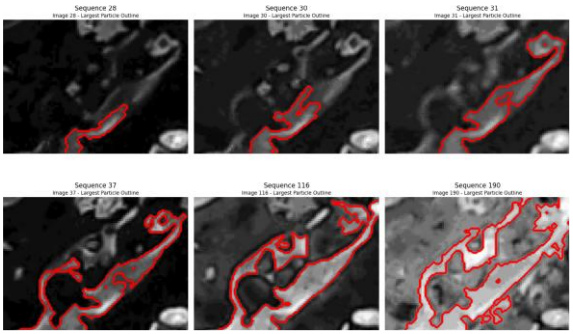
Defect #3 Outline



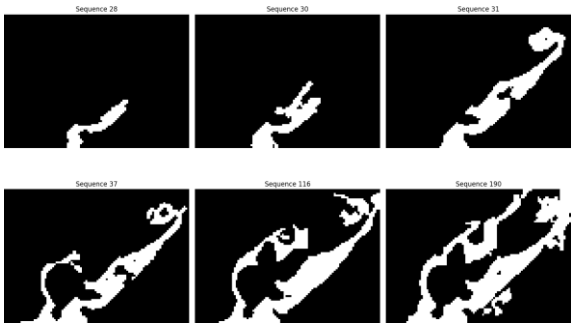
Defect #3 Isolated (Binary)



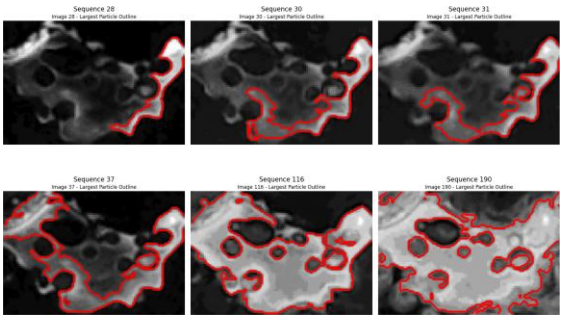
Defect #4 Outline



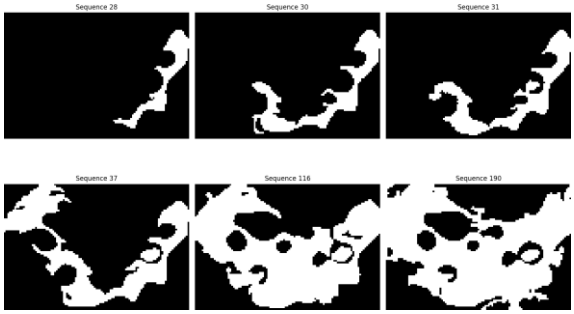
Defect #4 Isolated (Binary)



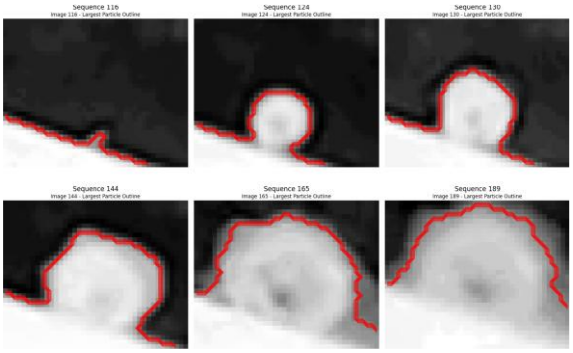
Defect #5 Outline



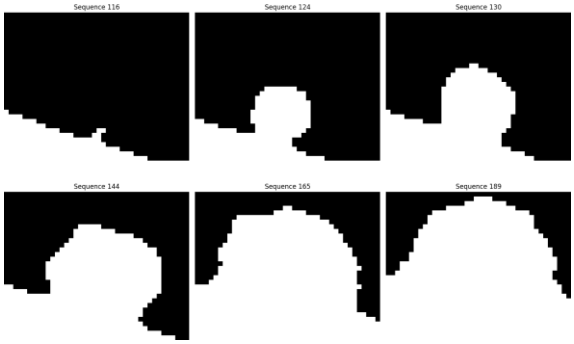
Defect #5 Isolated (Binary)



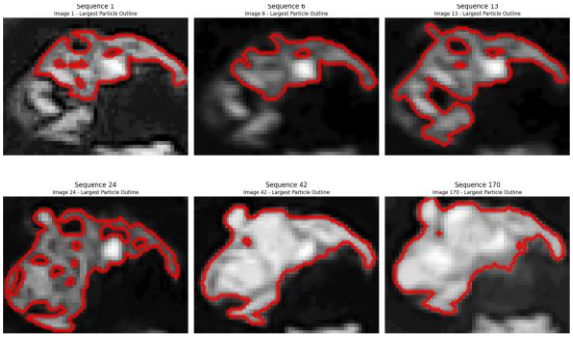
Spot #1 Outline



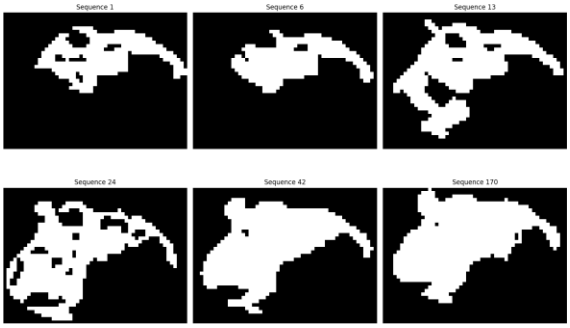
Spot #1 Isolated (Binary)



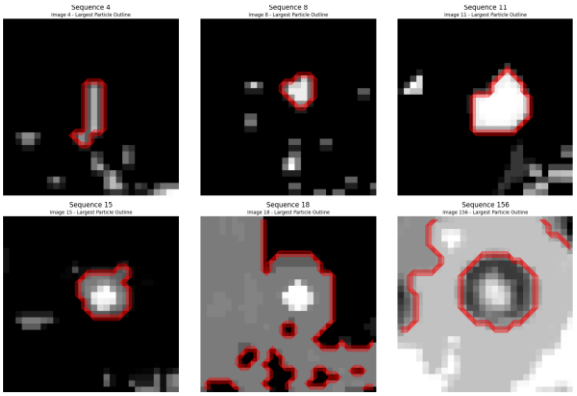
Spot #2 Outline



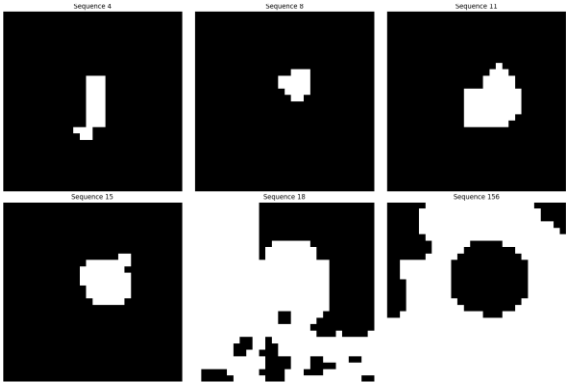
Spot #2 Isolated (Binary)

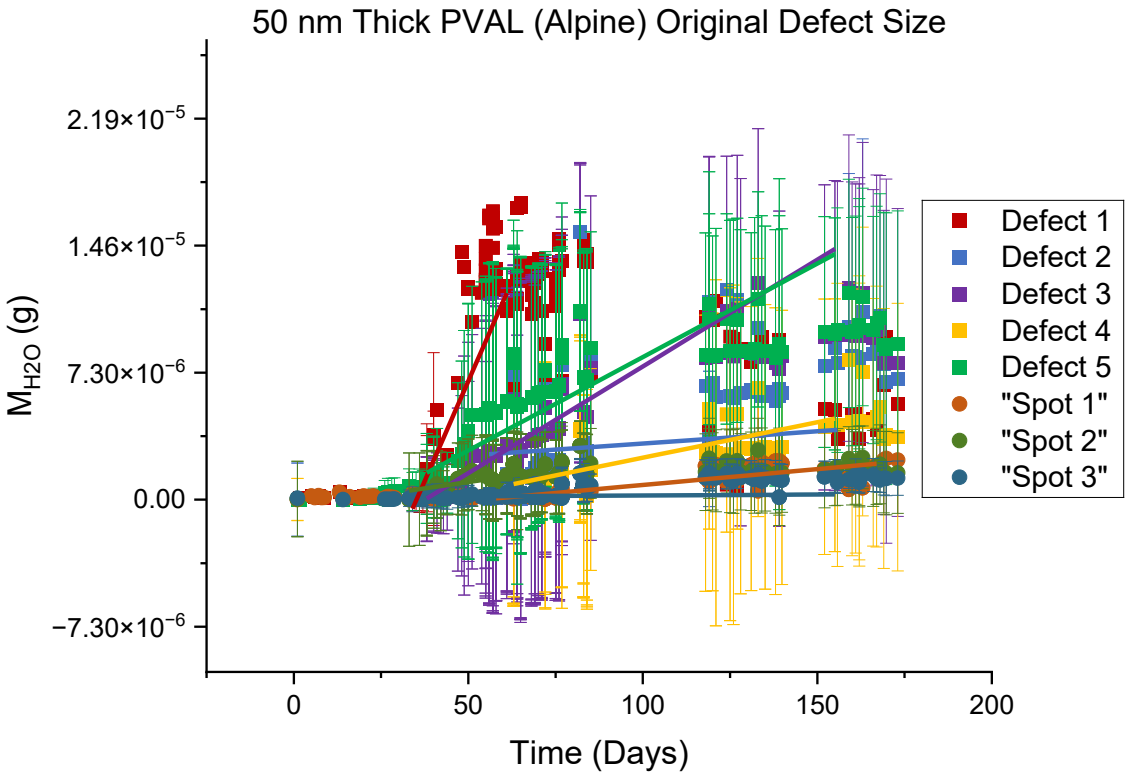


Spot #3 Outline



Spot #3 Isolated (Binary)





Defect	ROI Size (cm)	Slope (g/day)	Slope Std. Dev.	Adj. R. Squared	Defect Total Area (μm²)	Defect Area Std. Dev.
1	1.04 by 0.66	4.59E-07	6.32E-08	0.55	2.16E+05	3.00E+04
2	1.22 by 1.07	1.40E-08	7.59E-09	0.02	6.58E+03	3.57E+03
3	0.97 by 0.89	1.23E-07	4.84E-09	0.82	5.78E+04	2.49E+03
4	1.03 by 0.74	4.08E-08	7.25E-09	0.38	1.92E+04	3.43E+03
5	1.10 by 0.75	1.07E-07	5.46E-09	0.73	5.03E+04	2.72E+03
Spot 1	0.41 by 0.33	7.16E-07	5.90E-08	0.72	8.62E+03	5.27E+02
Spot 2	0.55 by 0.40	1.40E-08	7.59E-09	0.42	1.39E+04	1.77E+03
Spot 3	0.29 by 0.29	1.23E-07	4.84E-09	0.01	4.86E+02	3.61E+02

Figure 9-45: Fiver regions of interest from a 50 nm AlO_x ALD-coated thick PVAl substrate reveal a transition from a linear or dendritic defects to larger, more spot-like formations, with some resembling features seen in ALD-coated PET substrates. The largest defect areas such as Defect #1 $2.16 \times 10^5\ \mu m^2\ \pm 3.00\ \times 10^4\ \mu m^2$*, indicate a trend towards fewer but larger defects in the thicker PVAl, compared to the thinner 26 nm samples. Three additional spots, Spots #1 – 3, show variable sizes, with Spot #1 and Spot #2 having notably larger areas (*$8.62 \times 10^3\ \mu m^2$ *and* $1.39 \times 10^4\ \mu m^2$*) respectively, compared to Spot #3's smaller* $4.86 \times 10^2\ \mu m^2$ *area. These defect area measurements highlight the complex and evolving defect morphology in thicker coatings, demonstrating thicker PVAl samples can still develop significant isolated defects that contribute to water vapour permeation.*

9.4.10.e 96 nm Thick PVAl Substrate Defects

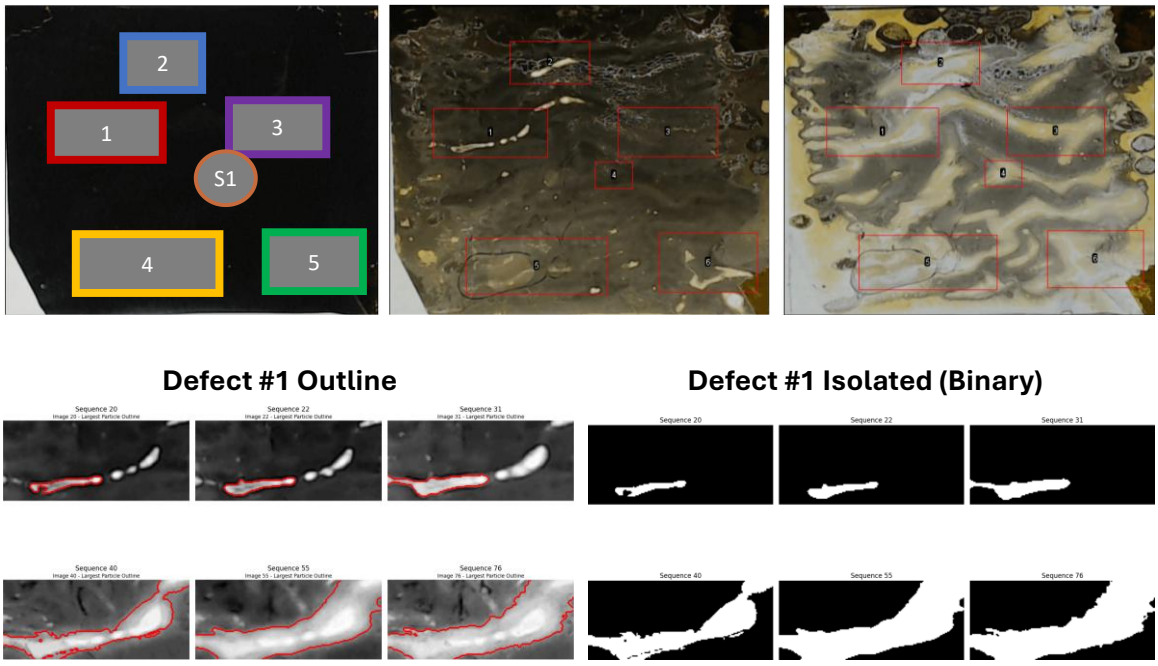
The thickest coating, at 96 nm, is re-examined in Figure 9-46, showing the same set of images with regions of interest, including five defect areas and one spot. Observing the images, it is notable that depleted calcium appears in a wave- or river-like pattern. This may be attributed to its surface as seen in Figure 5-11: results suggest that these linear or river-like structures may stem from overcoated defect lines observed in the barrier layer. Unlike in other samples, the typical dots or blobs are less prominent here, while wave-like features stand out, perhaps also hinting at multiple defects contributing to these formations.

Examining defect #1 reveals slow growth, with typical widening; however, the code interprets the coalescence as a single large defect, potentially combining multiple defects. Defect #2, in contrast, is a single entity that begins to exhibit dendritic-like structures, a pattern mirrored in Defects #3 and #4, where branching also occurs. Defect #5 shows the dot-like structure anticipated in previous assumptions.

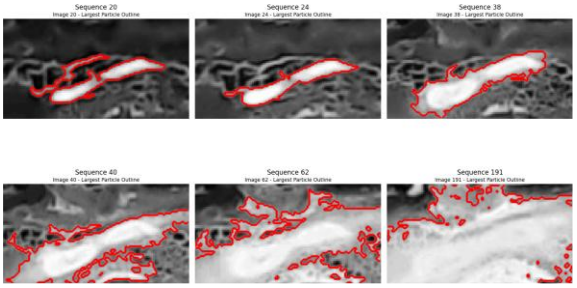
In terms of sizes, the defect areas are generally in the mid – 10^{-4} μm^2 range. For instance, Defect #1 has an area of$2.41 \times 10^4\ \mu m^2$ ($\pm 1.52\ \times 10^3$) μm^2, and Defect #3

reaches 4.24×10^4 µm^2 ($\pm 2.01 \times 10^3$) µm^2. Defect #5 is notably larger at 1.85×10^5 µm^2 ($\pm 8.94 \times 10^3$) µm^2, highlighting the tendency for these thicker coatings to develop significant isolated defect areas even though these appear as more linear or river-like features. Spot #1, measured at 1.18×10^5 µm^2 ($\pm 4.56 \times 10^3$) µm^2, further emphasizes this trend of larger isolated defects in thicker PVAl compared to PET substrates. These large defect areas align with the water uptake rates measured in the corresponding regions and suggest that even in thicker coatings.

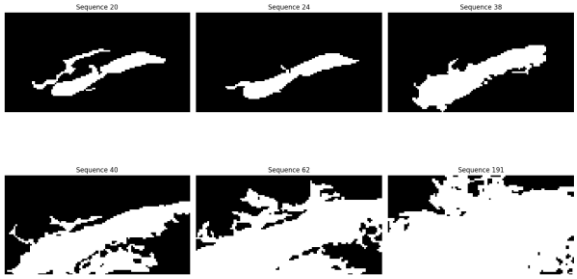
(c) 96 nm Thick PVAL (Alpine)



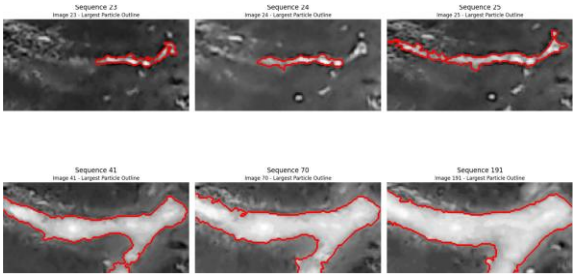
Defect #2 Outline



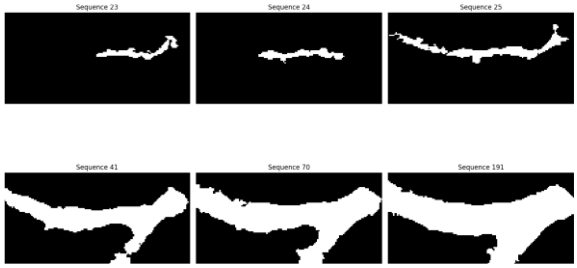
Defect #2 Isolated (Binary)



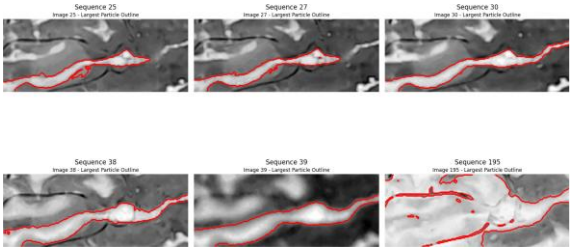
Defect #3 Outline



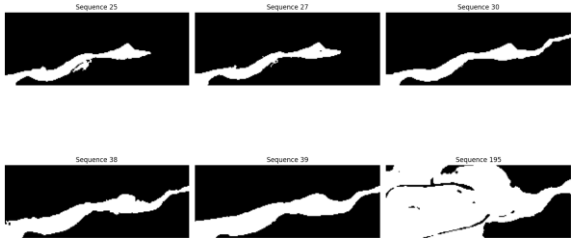
Defect #3 Isolated (Binary)



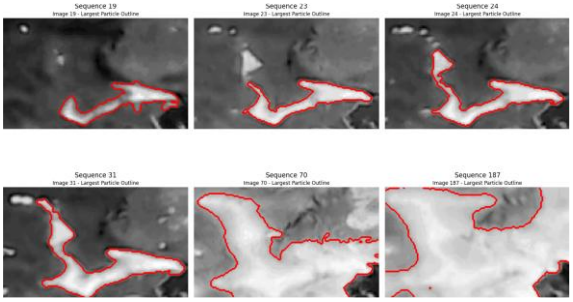
Defect #4 Outline



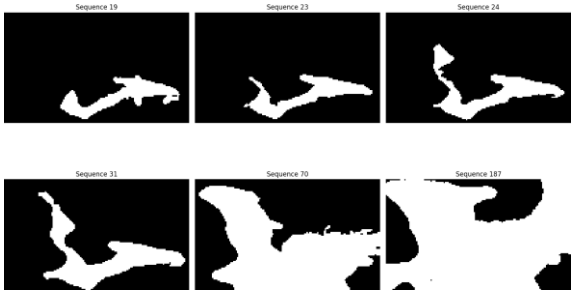
Defect #4 Isolated (Binary)

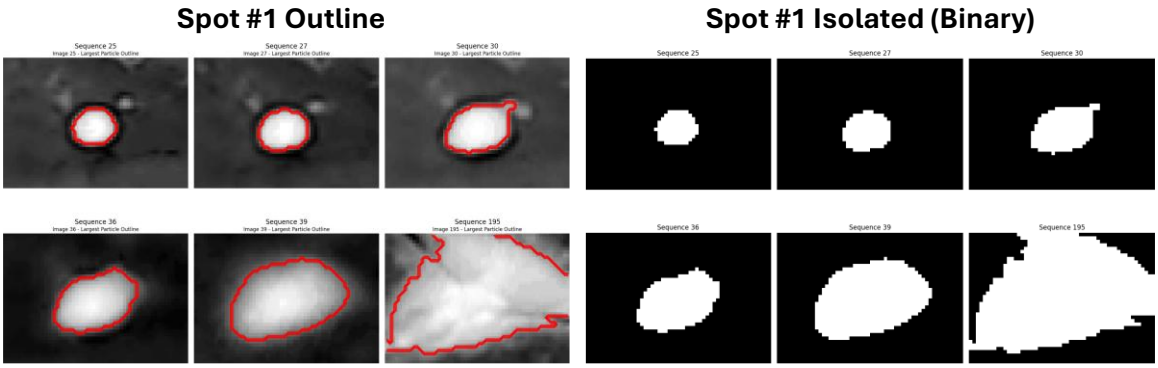


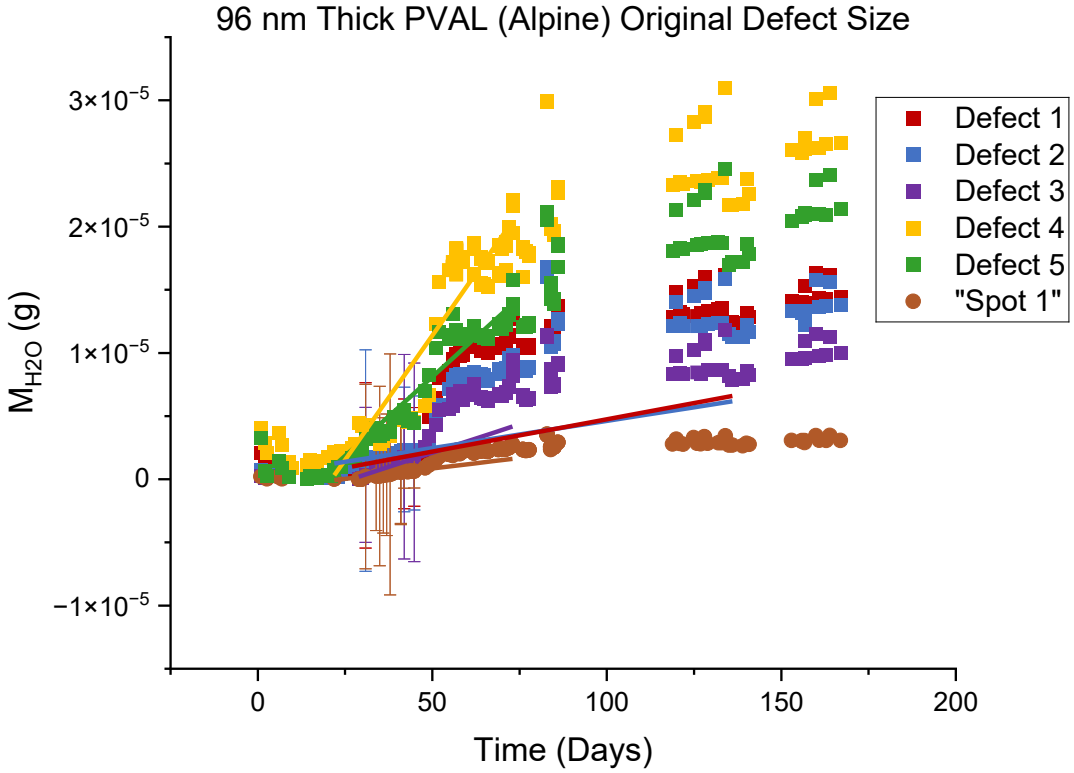
Defect #5 Outline



Defect #5 Isolated (Binary)







Defect	ROI Size (cm)	Slope (g/day)	Slope Std. Dev.	Adj. R. Squared	Defect Total Area (μm^2)	Defect Area Std. Dev.
1	1.69 by 0.72	5.13E-08	3.11E-09	0.64	2.41E+04	1.52E+03
2	1.17 by 0.63	4.32E-08	3.60E-09	0.48	2.03E+04	1.73E+03
3	1.47 by 0.72	9.01E-08	3.98E-09	0.84	4.24E+04	2.01E+03

4	0.56 by 0.39	3.94E-07	1.77E-08	0.83	1.56E+04	9.97E+02
5	2.09 by 0.82	2.50E-07	8.72E-09	0.89	1.85E+05	8.94E+03
Spot 1	1.45 by 0.86	3.31E-08	2.04E-09	0.73	1.18E+05	4.56E+03

Figure 9-46: Six regions of interest from a 96 nm AlO_x ALD-coated thick PVAl substrate highlight the evolution of defect structures across a range of sizes and shapes. Binary and outline images show wave- and rive- like defect structures, deviating from the typical circular features seen in thinner coatings or PET substrates. Defect areas range from mid-10^4 μm^2 to as large as 1.85×10^5 μm^2 for Defect #5, illustrating that thicker coatings can still exhibit significant isolated defect areas. Spot #1, measured at 1.18×10^5 μm^2 ($\pm 4.56 \times 10^3$ μm^2), further emphasizes the presence of these large, isolated defects in the thickest coated thick PVAl films. These large defect areas align with observed water uptake rates and highlight once more the complexity between AlO_x coating thickness, defect morphology and WVTR.

9.5 MOCON Aquatran Data Set for Uncoated PET

Temp. (°C)	WVTR (g/m²·day)	WVVP (KPa)	Permeability (mol/(m·s·Pa)	Relative Humidty (%)
14	2.195834	0.5593	2.52E-13	35
14	2.166635	0.5593	2.49E-13	35
14	2.781708	0.6392	2.8E-13	40
14	2.758449	0.6392	2.77E-13	40
14	2.918513	0.7191	2.61E-13	45
14	2.919326	0.7191	2.61E-13	45
14	3.263929	0.799	2.62E-13	50
14	3.203554	0.799	2.58E-13	50
14	3.732882	0.8789	2.73E-13	55
14	3.630692	0.8789	2.65E-13	55
14	4.023462	0.9588	2.7E-13	60
14	4.005838	0.9588	2.68E-13	60
14	4.542174	1.0387	2.81E-13	65
14	4.417254	1.0387	2.73E-13	65
14	5.011377	1.1186	2.88E-13	70
14	4.893035	1.1186	2.81E-13	70
14	5.413699	1.1985	2.9E-13	75
14	5.179213	1.1985	2.78E-13	75
14	5.986359	1.2784	3.01E-13	80
14	5.679705	1.2784	2.85E-13	80

14	6.275263	1.3583	2.97E-13	85
14	6.038911	1.3583	2.86E-13	85
14	6.990666	1.4382	3.12E-13	90
14	6.794582	1.4382	3.03E-13	90
14	7.106551	1.5181	3.01E-13	95
14	6.81811	1.5181	2.88E-13	95
14	7.173346	1.598	2.88E-13	100
14	6.834414	1.598	2.75E-13	100
25	4.034705	1.10985	2.33E-13	35
25	3.806938	1.10985	2.2E-13	35
25	5.108748	1.2684	2.59E-13	40
25	4.941879	1.2684	2.5E-13	40
25	5.659002	1.42695	2.55E-13	45
25	5.45106	1.42695	2.45E-13	45
25	6.478972	1.5855	2.62E-13	50
25	6.132589	1.5855	2.48E-13	50
25	7.277569	1.74405	2.68E-13	55
25	6.859857	1.74405	2.53E-13	55
25	7.665328	1.9026	2.59E-13	60
25	7.293443	1.9026	2.46E-13	60
25	8.718293	2.06115	2.72E-13	65
25	8.211894	2.06115	2.56E-13	65
25	9.644227	2.2197	2.79E-13	70
25	9.218076	2.2197	2.67E-13	70
25	10.13176	2.37825	2.74E-13	75
25	9.658257	2.37825	2.61E-13	75
25	10.96205	2.5368	2.78E-13	80
25	10.17683	2.5368	2.58E-13	80
25	11.94409	2.69535	2.85E-13	85
25	11.29536	2.69535	2.69E-13	85
25	13.01311	2.8539	2.93E-13	90
25	12.37517	2.8539	2.79E-13	90
25	13.15439	3.01245	2.8E-13	95
25	12.47714	3.01245	2.66E-13	95
25	13.60973	3.171	2.76E-13	100
25	12.91011	3.171	2.61E-13	100
38	8.961111	2.32155	2.48E-13	35
38	8.549481	2.32155	2.37E-13	35
38	11.42644	2.6532	2.77E-13	40
38	10.63582	2.6532	2.57E-13	40
38	11.15063	2.98485	2.4E-13	45

38	10.16818	2.98485	2.19E-13	45
38	12.33043	3.3165	2.39E-13	50
38	11.75168	3.3165	2.28E-13	50
38	13.90897	3.64815	2.45E-13	55
38	12.87943	3.64815	2.27E-13	55
38	15.71151	3.9798	2.54E-13	60
38	14.78114	3.9798	2.39E-13	60
38	16.90279	4.31145	2.52E-13	65
38	15.71914	4.31145	2.34E-13	65
38	18.3284	4.6431	2.54E-13	70
38	17.19777	4.6431	2.38E-13	70
38	19.91549	4.97475	2.57E-13	75
38	18.62192	4.97475	2.4E-13	75
38	22.47901	5.3064	2.72E-13	80
38	21.14092	5.3064	2.56E-13	80
38	23.69945	5.63805	2.7E-13	85
38	21.98081	5.63805	2.5E-13	85
38	25.17225	5.9697	2.71E-13	90
38	23.50883	5.9697	2.53E-13	90
38	26.51569	6.30135	2.7E-13	95
38	25.09241	6.30135	2.56E-13	95
38	27.37336	6.633	2.65E-13	100
38	25.91647	6.633	2.51E-13	100

9.6 Calcium Test Data Set for Uncoated PET

Temp. (°C)	WVTR ($g/m^2 \cdot day$)	Permeability ($mol/(m \cdot s \cdot Pa)$)	Copper (nm)	Calcium (nm)	306 Vac. Pres. (mBar)	Sat. Salt. Sol	RH (%)	Onset Time (Days)
14	0.75	74.63	20.3	492.4	1.17E-04	LiCl	65	0.60
14	0.55	55.01	20.7	404.7	1.22E-04	LiCl	65	0.40
14	0.61	61.06	20.1	515.0	1.41E-04	LiCl	65	0.30
14	1.31	131.05	20.3	482.3	1.28E-04	MgCl2	71	0.40
14	0.76	76.07	20.8	507.7	1.05E-04	MgCl2	71	0.18
14	1.44	144.27	20.0	116.0	1.06E-04	MgCl2	71	0.05
14	2.43	243.26	29.1	177.2	1.73E-04	MgCl2	71	0.04
14	2.95	294.72	29.2	315.0	1.70E-04	MgCl2	71	0.20
14	1.67	166.86	20.1	494.2	1.06E-04	NaCl	95	0.03
14	2.62	262.46	34.5	502.2	8.30E-05	NaCl	95	0.35

14	1.17	117.39	30.2	244.3	2.10E-04	NaCl	95	0.20
14	2.91	291.10	30.4	278.5	1.50E-04	NaCl	95	0.08
14	0.96	95.50	31.7	290.1	1.65E-04	NaCl	95	0.25
25	1.34	133.62	30.4	250.2	1.32E-04	LiCl	65	0.30
25	0.82	82.16	18.3	291.6	1.35E-04	LiCl	65	0.20
25	0.93	92.60	30.2	448.3	1.42E-04	LiCl	65	0.57
25	0.46	46.45	30.8	396.2	1.21E-04	LiCl	65	0.40
25	0.99	99.07	30.2	345.0	2.50E-04	LiCl	65	0.23
25	0.65	65.33	30.2	478.4	9.55E-05	LiCl	65	0.50
25	3.51	350.52	20.0	430.0	3.64E-05	MgCl2	71	0.44
25	2.12	211.58	13.0	392.8	4.00E-05	MgCl2	71	0.20
25	1.98	197.78	20.0	260.0	5.40E-05	MgCl2	71	0.08
25	5.61	560.55	20.1	141.1	1.22E-04	MgCl2	71	0.03
25	2.09	209.10	20.7	331.5	8.00E-05	MgCl2	71	0.13
25	3.20	320.21	15.2	508.0	5.37E-05	MgCl2	71	0.08
25	2.28	227.81	30.9	173.0	1.18E-04	MgCl2	71	0.05
25	2.26	226.40	29.8	328.0	1.84E-04	MgCl2	71	0.05
25	4.21	420.73	31.5	325.0	1.84E-04	MgCl2	71	0.13
25	2.60	260.40	30.1	501.5	1.46E-04	MgCl2	71	0.07
25	0.84	84.43	30.0	522.8	1.29E-04	MgCl2	71	0.08
25	3.01	300.96	20.0	442.3	7.00E-05	NaCl	95	0.05
25	2.14	213.96	20.0	224.2	3.50E-04	NaCl	95	0.05
25	1.37	136.54	18.5	183.6	1.43E-04	NaCl	95	0.03
25	1.31	130.91	18.3	229.5	5.80E-04	NaCl	95	0.06
25	4.84	483.96	30.1	508.3	2.06E-04	NaCl	95	0.04
25	4.79	479.12	30.7	355.0	1.35E-04	NaCl	95	0.04
36	1.70	169.96	30.4	315.1	1.21E-04	LiCl	65	0.14
36	2.28	228.42	30.1	601.5	1.09E-04	LiCl	65	0.30
36	2.14	214.26	29.9	480.6	1.78E-04	LiCl	65	0.10
36	1.67	166.66	30.7	440.8	1.15E-04	LiCl	65	0.15
36	2.12	212.31	20.0	402.8	1.47E-04	LiCl	65	0.08
36	1.97	196.59	20.2	491.9	1.46E-04	LiCl	65	0.09
36	0.99	99.48	20.3	490.0	1.58E-04	LiCl	65	0.09
36	1.14	113.95	20.0	421.0	1.61E-04	MgCl2	71	0.10
36	0.65	65.24	20.1	346.0	9.90E-05	MgCl2	71	0.10
36	6.65	664.94	20.2	453.9	2.01E-04	MgCl2	71	0.04
36	3.98	397.55	20.2	291.0	3.00E-04	MgCl2	71	0.09
36	6.26	626.29	20.0	400.0	1.40E-04	MgCl2	71	0.03
36	5.77	576.95	20.0	320.0	5.30E-05	MgCl2	71	0.02
36	6.40	639.97	20.6	510.3	6.50E-05	MgCl2	71	0.02
36	2.90	289.69	30.0	346.9	1.24E-04	MgCl2	71	0.07

36	8.84	884.35	30.1	309.0	1.13E-04	MgCl2	71	0.07
36	8.43	842.63	31.0	515.0	1.23E-04	MgCl2	71	0.08
36	5.87	587.15	20.3	499.6	-	NaCl	95	0.08
36	4.25	424.75	20.1	498.3	1.30E-04	NaCl	95	0.04
36	6.12	612.30	20.2	330.0	3.64E-04	NaCl	95	0.04
36	16.35	1634.90	20.7	321.7	-	NaCl	95	0.01
36	9.83	982.60	20.9	450.0	5.23E-05	NaCl	95	0.02
36	4.59	458.85	29.4	327.0	1.18E-04	NaCl	95	0.03
36	15.94	1594.35	30.2	340.0	1.13E-04	NaCl	95	0.04
36	7.35	734.54	30.6	516.2	1.27E-04	NaCl	95	0.05
51	2.78	277.51	19.5	508.8	1.30E-04	LiCl	65	0.08
51	3.68	367.53	22.0	447.2	1.27E-04	LiCl	65	0.09
51	1.80	179.57	20.9	632.8	1.16E-04	LiCl	65	0.08
51	3.64	363.65	21.2	316.0	1.13E-04	LiCl	65	0.08
51	7.08	707.53	20.5	805.2	1.25E-04	LiCl	65	0.14
51	5.18	517.87	21.0	170.0	1.32E-04	LiCl	65	0.03
51	7.82	782.23	20.4	364.9	1.29E-04	MgCl2	71	0.03
51	13.66	1366.00	20.1	526.0	1.38E-04	MgCl2	71	0.05
51	13.09	1309.10	23.0	533.3	2.32E-04	MgCl2	71	0.08
51	10.07	1007.20	20.8	354.5	1.13E-04	NaCl	95	0.04
51	11.26	1126.30	20.1	440.0	1.49E-04	NaCl	95	0.03
51	8.03	803.37	20.3	336.3	1.54E-04	NaCl	95	0.04

9.7 Python - Code for Isolated (Labelled Unique Here) and Coalescing Spots (Condensed)

```
# ------------------------------------------------------
# Python Script: Automated Image Analysis of Coated Films
# ------------------------------------------------------
import os
import time
import numpy as np
import matplotlib
import matplotlib.ticker as ticker

# Use the 'Agg' backend for non-interactive plots
matplotlib.use('Agg')
import matplotlib.pyplot as plt
import tifffile
```

```
from skimage.feature import canny
from skimage.measure import label, regionprops, find_contours
from skimage.color import rgb2gray
import pandas as pd
from natsort import natsorted
from matplotlib_scalebar.scalebar import ScaleBar
from scipy.stats import gaussian_kde
from scipy.spatial import cKDTree
from skimage.draw import line
from skimage import io
from skimage.filters import threshold_otsu

# Constants for image dimensions and pixel sizes
image_width_cm = 5.58
image_height_cm = 5.71
pixel_size_x = image_width_cm / 543  # cm/pixel
pixel_size_y = image_height_cm / 555  # cm/pixel

# Start measuring time
start_time = time.time()

# Function to convert pixel coordinates to cm
def pixel_to_cm(coords, image_shape):
    y_pixels, x_pixels = image_shape
    y_cm = (coords[:, 0] / y_pixels) * image_height_cm
    x_cm = (coords[:, 1] / x_pixels) * image_width_cm
    return np.column_stack((y_cm, x_cm))

# Function for Canny edge detection
def detect_edges_canny(img, sigma=2):
    return canny(img, sigma=sigma)

# Remove regions touching image borders to avoid artifacts
def remove_border_touching_regions(mask, label_image):
    for region in regionprops(label_image):
        minr, minc, maxr, maxc = region.bbox
        if minr <= 5 or minc <= 5 or maxr >= mask.shape[0] - 5 or maxc >=
mask.shape[1] - 5:
            label_image[label_image == region.label] = 0
    return label_image

# Count unique and coalescing spots
def count_spots(edges, calcium_layer_mask, previous_unique_spots=None,
distance_threshold=20, min_size=15, max_size=30):
    masked_edges = edges & calcium_layer_mask
```

```
    labeled_cracks = label(masked_edges)
    labeled_cracks = remove_border_touching_regions(calcium_layer_mask,
labeled_cracks)
    unique_spots, coalescing_spots = 0, 0
    coalesced_mask = np.zeros_like(edges, dtype=bool)
    unique_spots_mask = np.zeros_like(edges, dtype=bool)
    coalesced_coords, unique_coords = [], []
    current_unique_spots = set()
    filtered_out_count = 0

    for prop in regionprops(labeled_cracks):
        if not (min_size <= prop.area <= max_size):
            filtered_out_count += 1
            continue
        current_region = labeled_cracks == prop.label
        current_centroid = prop.centroid
        if previous_unique_spots:
            tree = cKDTree(list(previous_unique_spots))
            distances, _ = tree.query([current_centroid],
distance_upper_bound=distance_threshold)
            if distances[0] != np.inf and not
any(np.linalg.norm(np.array(coalesced_coords) -
np.array(current_centroid), axis=1) < distance_threshold):
                coalescing_spots += 1
                coalesced_mask |= current_region
                coalesced_coords.append(current_centroid)
                continue
        unique_spots += 1
        unique_spots_mask |= current_region
        unique_coords.append(current_centroid)
        current_unique_spots.add(current_centroid)
    print(f"Filtered out {filtered_out_count} small/large regions")
    return unique_spots, coalescing_spots, labeled_cracks, coalesced_mask,
unique_spots_mask, masked_edges, coalesced_coords, unique_coords,
current_unique_spots

# Measure region properties
def measure_crack_properties(labeled_cracks, mask):
    lengths, widths, major_axes, minor_axes, orientations, aspect_ratios =
[], [], [], [], [], []
    for prop in regionprops(labeled_cracks, intensity_image=mask):
        coords = prop.coords
        length = np.sum(np.sqrt(np.sum(np.diff(coords, axis=0) ** 2,
axis=1)))
        lengths.append(length)
```

```
        major_axes.append(prop.major_axis_length)
        minor_axes.append(prop.minor_axis_length)
        orientations.append(prop.orientation)
        aspect_ratios.append(prop.major_axis_length /
prop.minor_axis_length if prop.minor_axis_length > 0 else np.nan)
        width_measurements = [np.sum(mask[line(coords[i][0], coords[i][1],
coords[i][0] + 1, coords[i][1] + 1)]) for i in range(0, len(coords),
max(1, len(coords) // 10))]
        widths.append(np.mean(width_measurements))
    return lengths, widths, major_axes, minor_axes, orientations,
aspect_ratios

# Calculate crack density
def calculate_crack_density(edges):
    return np.sum(edges) / np.prod(edges.shape)

# Spot density (normalized to image area in cm²)
def calculate_spot_density(num_spots, image_shape):
    area_cm2 = image_height_cm * image_width_cm
    return num_spots / area_cm2

# Load images from a directory
def load_images(directory):
    files = natsorted([os.path.join(directory, f) for f in
os.listdir(directory) if f.endswith('.tif')])
    images, shapes = [], []
    for file in files:
        img = io.imread(file)
        if img.ndim == 3:
            img = rgb2gray(img)
        images.append(img)
        shapes.append(img.shape)
    return images, shapes, files

# Process images: edge detection
def process_images(images):
    return [canny(img, sigma=2) for img in images]

# Save data summary to CSV
def save_results_to_csv(output_directory, summary_data):
    os.makedirs(output_directory, exist_ok=True)
    summary_df = pd.DataFrame(summary_data, columns=[
        'Image', 'Unique Spots', 'Coalescing Spots', 'Unique Spot Density
(spots/cm^2)', 'Coalescing Spot Density (spots/cm^2)',
```

```
        'Unique Avg Length (cm)', 'Unique Std Dev Length (cm)', 'Unique
Avg Width (cm)', 'Unique Std Dev Width (cm)',
        'Unique Avg Aspect Ratio', 'Unique Std Dev Aspect Ratio', 'Unique
Avg Orientation (rad)', 'Unique Std Dev Orientation',
        'Coalescing Avg Length (cm)', 'Coalescing Std Dev Length (cm)',
'Coalescing Avg Width (cm)', 'Coalescing Std Dev Width (cm)',
        'Coalescing Avg Aspect Ratio', 'Coalescing Std Dev Aspect Ratio',
'Coalescing Avg Orientation (rad)',
        'Coalescing Std Dev Orientation', 'Density (%)', 'Std Dev Density
(%)', 'Pixel Size (Y, X)'
    ])
    summary_df.to_csv(os.path.join(output_directory,
'summary_results.csv'), index=False)
    print(f"Summary results saved to {os.path.join(output_directory,
'summary_results.csv')}")

# Create calcium layer mask based on threshold
def create_calcium_layer_mask(img):
    thresh = threshold_otsu(img)
    return img < thresh

# Main analysis pipeline
def main(directory, output_directory, selected_image_indices=None):
    images, image_shapes, files = load_images(directory)
    edges_list = process_images(images)
    summary_data, previous_unique_spots, all_unique_spots, results = [],
set(), set(), []

    for i, (edges, img, shape) in enumerate(zip(edges_list, images,
image_shapes)):
        calcium_layer_mask = create_calcium_layer_mask(img)
        unique_spots, coalescing_spots, labeled_cracks, coalesced_mask,
unique_spots_mask, edges, coalesced_coords, unique_coords,
current_unique_spots = count_spots(edges, calcium_layer_mask,
previous_unique_spots)
        previous_unique_spots.update(current_unique_spots)
        all_unique_spots.update(current_unique_spots)
        unique_lengths, unique_widths, _, _, unique_orientations,
unique_aspect_ratios = measure_crack_properties(labeled_cracks,
unique_spots_mask)
        coalescing_lengths, coalescing_widths, _, _,
coalescing_orientations, coalescing_aspect_ratios =
measure_crack_properties(labeled_cracks, coalesced_mask)
        density = calculate_crack_density(edges)
```

```
        unique_lengths_cm = np.array(unique_lengths) * image_height_cm /
img.shape[0]
        unique_widths_cm = np.array(unique_widths) * image_width_cm /
img.shape[1]
        coalescing_lengths_cm = np.array(coalescing_lengths) *
image_height_cm / img.shape[0]
        coalescing_widths_cm = np.array(coalescing_widths) *
image_width_cm / img.shape[1]
        unique_spot_density = calculate_spot_density(unique_spots, shape)
        coalescing_spot_density = calculate_spot_density(coalescing_spots,
shape)
        summary_data.append((f'Image_{i+1}', unique_spots,
coalescing_spots, unique_spot_density, coalescing_spot_density,
np.mean(unique_lengths_cm), np.std(unique_lengths_cm),
np.mean(unique_widths_cm), np.std(unique_widths_cm),
np.nanmean(unique_aspect_ratios), np.nanstd(unique_aspect_ratios),
np.mean(unique_orientations), np.std(unique_orientations),
np.mean(coalescing_lengths_cm), np.std(coalescing_lengths_cm),
np.mean(coalescing_widths_cm), np.std(coalescing_widths_cm),
np.nanmean(coalescing_aspect_ratios), np.nanstd(coalescing_aspect_ratios),
np.mean(coalescing_orientations), np.std(coalescing_orientations),
density*100, np.std(density*100), shape))
        results.append((unique_spots, coalescing_spots, coalesced_mask,
unique_spots_mask, edges, img, coalesced_coords, unique_coords, i+1))

    save_results_to_csv(output_directory, summary_data)
    print(f"Pixel size in X: {pixel_size_x} cm/pixel | Pixel size in Y:
{pixel_size_y} cm/pixel")
    for i, shape in enumerate(image_shapes):
        print(f"Image_{i+1} pixel size: {shape}")

# Execute
if __name__ == '__main__':
    directory = r"C:\Users\spet5127\Desktop\PyThon\ImageAnalysis\New"
    output_directory =
r"C:\Users\spet5127\Desktop\PyThon\ImageAnalysis\Output"
    selected_image_indices = [0, 44, 89, 93, 100, 107]
    main(directory, output_directory, selected_image_indices)
    print(f"Total run time: {time.time() - start_time:.2f} seconds")
```

9.8 Defect Analysis Largest Particle Assumption

```
import os
import time
import numpy as np
import pandas as pd
from skimage import io, measure
from skimage.color import rgb2gray
from skimage.filters import threshold_otsu
import matplotlib
matplotlib.use('Agg')  # Use the 'Agg' backend for non-interactive
plotting
import matplotlib.pyplot as plt
from natsort import natsorted
import warnings

# Suppress specific warnings (e.g., low contrast images)
warnings.filterwarnings('ignore', message='.*is a low contrast image')

# Start measuring time for code execution
start_time = time.time()

# Load and preprocess images from a directory
def load_images(directory):
    files = natsorted([os.path.join(directory, file) for file in
os.listdir(directory) if file.endswith('.tif')])
    images = []
    valid_files = []
    for file_name in files:
        img = io.imread(file_name)
        # Convert to grayscale if image is in RGB
        if img.ndim == 3:
            img = rgb2gray(img)
        if img.ndim == 2:  # Ensure the image is 2D after conversion
            images.append(img)
            valid_files.append(file_name)
    return images, valid_files

# Convert pixel coordinates to centimeters based on image dimensions
def pixel_to_cm(coords, image_shape, image_height_cm, image_width_cm):
    y_pixels, x_pixels = image_shape
    y_cm = (coords[:, 0] / y_pixels) * image_height_cm
    x_cm = (coords[:, 1] / x_pixels) * image_width_cm
    return np.column_stack((y_cm, x_cm))
```

```
# Analyze images, calculate statistics, and outline the largest particle
in each
def calculate_image_statistics_and_outline(images, image_height_cm,
image_width_cm, output_directory):
    stats = []
    outline_images = []  # Store outlines for montage creation
    outlined_images_with_contours = []  # Store images with contours for
montage
    for idx, img in enumerate(images):
        # Apply threshold to create a binary image
        thresh = threshold_otsu(img)
        binary = img > thresh

        # Label regions in the binary image
        label_image = measure.label(binary)
        regions = measure.regionprops(label_image)

        if regions:
            # Identify the largest region by area
            largest_region = max(regions, key=lambda r: r.area)

            # Calculate area in cm² and mean gray value for the largest
region
            area = largest_region.area * (image_height_cm *
image_width_cm) / (img.shape[0] * img.shape[1])
            mean_gray_value = np.mean(img[largest_region.coords[:, 0],
largest_region.coords[:, 1]])

            # Convert coordinates to cm
            coords_cm = pixel_to_cm(largest_region.coords, img.shape,
image_height_cm, image_width_cm)

            # Create an outline for the largest region
            outline = np.zeros_like(img, dtype=np.uint8)
            for coord in largest_region.coords:
                outline[coord[0], coord[1]] = 1

            # Save the outline image as a binary mask
            outline_filename = os.path.join(output_directory,
f'outline_{idx + 1}.png')
            io.imsave(outline_filename, outline.astype(np.uint8) * 255)
            outline_images.append(outline)

            # Plot and save the outlined image with contour overlay
```

```
            plt.figure(figsize=(8, 8))
            plt.imshow(img, cmap='gray')
            plt.contour(outline, colors='red', linewidths=1)
            plt.axis('off')
            outlined_img_path = os.path.join(output_directory,
f'outlined_image_{idx + 1}.png')
            plt.savefig(outlined_img_path, bbox_inches='tight',
pad_inches=0)
            plt.close()

            # Load and store the outlined image with contour for montage
            outlined_img_with_contour = io.imread(outlined_img_path)
            outlined_images_with_contours.append(outlined_img_with_contour
)

            # Record area, mean gray value, and file paths for results
            stats.append((area, mean_gray_value, outline_filename,
outlined_img_path))
        else:
            stats.append((0, 0, '', ''))
    return stats, outline_images, outlined_images_with_contours

# Save the results to a CSV file
def save_results_to_csv(output_directory, stats, files):
    os.makedirs(output_directory, exist_ok=True)
    data = {
        'Image': files,
        'Area (cm^2)': [stat[0] for stat in stats],
        'Mean Gray Value': [stat[1] for stat in stats],
        'Outline Image': [stat[2] for stat in stats],
        'Outlined Image with Contour': [stat[3] for stat in stats]
    }
    df = pd.DataFrame(data)
    output_csv_path = os.path.join(output_directory,
'image_statistics.csv')
    df.to_csv(output_csv_path, index=False)

# Create montage of images with selected indices
def create_montage(images, output_directory, montage_name, rows, cols,
selected_indices):
    selected_images = [images[i] for i in selected_indices]
    num_images = len(selected_images)
    fig, axes = plt.subplots(rows, cols, figsize=(cols * 5, rows * 5))
    axes = axes.flatten()
```

```
    for ax, img, idx in zip(axes, selected_images, selected_indices):
        ax.imshow(img, cmap='gray')
        ax.set_title(f'Sequence {idx + 1}')
        ax.axis('off')

    # Remove empty subplot axes
    for ax in axes[num_images:]:
        fig.delaxes(ax)

    montage_path = os.path.join(output_directory, montage_name)
    plt.tight_layout()
    plt.savefig(montage_path, bbox_inches='tight', pad_inches=0)
    plt.close()

# Calculate the standard deviation of mean gray values across all images
def calculate_statistics(stats):
    mean_gray_values = [stat[1] for stat in stats if stat[1] != 0]
    std_dev = np.std(mean_gray_values)
    return std_dev

# Main function to control the image analysis workflow
def main(directory, output_directory, image_height_cm, image_width_cm,
rows=3, cols=2, selected_indices=None):
    images, files = load_images(directory)
    stats, outline_images, outlined_images_with_contours =
calculate_image_statistics_and_outline(images, image_height_cm,
image_width_cm, output_directory)
    save_results_to_csv(output_directory, stats, files)

    # Set default montage selection if none provided
    if selected_indices is None:
        selected_indices = list(range(min(rows * cols,
len(outline_images))))

    create_montage(outline_images, output_directory,
'outline_montage.png', rows, cols, selected_indices)
    create_montage(outlined_images_with_contours, output_directory,
'outlined_images_with_contours_montage.png', rows, cols, selected_indices)

    # Calculate and log standard deviation of mean gray values
    std_dev = calculate_statistics(stats)
    with open(os.path.join(output_directory, 'statistics_summary.txt'),
'w') as f:
        f.write(f"Standard Deviation of Mean Gray Values:
{std_dev:.2f}\n")
```

```
# Run main processing function
if __name__ == '__main__':
    directory = r"your_image_directory_here"
    output_directory = r"your_output_directory_here"

    # Image dimensions in centimeters (edit as needed)
    image_height_cm = 5.36
    image_width_cm = 4.97
    # Define montage grid layout
    rows = 2
    cols = 3

    # Define specific images for montage (0-based index, edit as needed)
    selected_indices = [0, 1, 2, 3, 4, 5]

    main(directory, output_directory, image_height_cm, image_width_cm,
rows, cols, selected_indices)

# Print total runtime
print(f"Total run time: {time.time() - start_time:.2f} seconds")
```

10 Appendix Bibliography

[419] A. MOCON, AQUATRAN Model 2 Operator's Manual.

[420] F.I.f.P.E.a.P. IVV, Permeation measurement of films: Oxygen and water vapor permeability in comparison, 2011.

[421] S. Amberg-Schwab, M. Hoffmann, H. Bader, M. Gessler, Inorganic-organic polymers with barrier properties for water vapor, oxygen and flavors, Journal of sol-gel science and technology 13 (1998) 141–146.

[422] P. Print, Water Vapor Transmission Rate, 2024. https://www.polyprint.com/understanding-film-properties/flexographic-wvtr/.

[423] c.K. GmbH, Water vapor permeability of various plastic films. https://www.cmc.de/en/blog/know-how-5/water-vapor-permeability-of-various-plastic-films-181.

[424] E. Toolbox, Thermal Conductivity of Common Materials. https://www.engineeringtoolbox.com/thermal-conductivity-d_429.html.

[425] X. Xu, J. Chen, J. Zhou, B. Li, Thermal conductivity of polymers and their nanocomposites, Advanced Materials 30(17) (2018) 1705544.

[426] W. Lei, X. Li, Q. Chen, Z. Wang, Plasma-assisted ALD of an Al2O3 permeation barrier layer on plastic, Plasma Science and Technology 14(2) (2012) 129.

[427] H. Choi, S. Lee, H. Jung, S. Shin, G. Ham, H. Seo, H. Jeon, Moisture barrier properties of Al2O3 films deposited by remote plasma atomic layer deposition at low temperatures, Japanese Journal of Applied Physics 52(3R) (2013) 035502.

[428] T. Perevalov, O. Tereshenko, V. Gritsenko, V. Pustovarov, A. Yelisseyev, C. Park, J.H. Han, C. Lee, Oxygen deficiency defects in amorphous Al2O3, Journal of applied physics 108(1) (2010).

[429] J. Meyer, H. Schmidt, W. Kowalsky, T. Riedl, A. Kahn, The origin of low water vapor transmission rates through Al2O3/ZrO2 nanolaminate gas-diffusion barriers grown by atomic layer deposition, Applied Physics Letters 96(24) (2010).

[430] Y. Kim, N. Kim, H. Kim, S. Graham, The development of thin film barriers for encapsulating organic electronics, 2011 IEEE 61st Electronic Components and Technology Conference (ECTC), IEEE, 2011, pp. 2101–2106.

[431] E. Soleimani, N. Zamani, Surface Modification of Alumina Nanoparticles: A Dispersion Study in Organic Media, Acta Chimica Slovenica 64(3) (2017).

[432] J. Meyer, P. Görrn, F. Bertram, S. Hamwi, T. Winkler, H.H. Johannes, T. Weimann, P. Hinze, T. Riedl, W. Kowalsky, Al2O3/ZrO2 nanolaminates as ultrahigh gas-diffusion barriers—a strategy for reliable encapsulation of organic electronics, Advanced materials 21(18) (2009) 1845–1849.

[433] H. Fujiwara, Spectroscopic Ellipsometry: Principles and Applications, John Wiley & Sons2007.

[434] R.M. Azzam, N.M. Bashara, D.T. Burns, Ellipsometry and polarized light, Analytica Chimica Acta 199 (1987) 283–284.

[435] H. Scientific, What is Cauchy dispersion module? https://www.horiba.com/int/scientific/technologies/spectroscopic-ellipsometry/cauchy-dispersion-module/.

[436] A.K. Urbanek, K.E. Kosiorowska, A.M. Mirończuk, Current knowledge on polyethylene terephthalate degradation by genetically modified microorganisms, Frontiers in bioengineering and biotechnology 9 (2021) 771133.

[437] T. Srinivasa Gopal, J. Joseph, T. Govindan, Use of linear low density polythene film for frozen fish packaging, (1987).

[438] S.C. Teixeira, N.O. Gomes, T.V. de Oliveira, P. Fortes-Da-Silva, N.d.F.F. Soares, P.A. Raymundo-Pereira, Review and Perspectives of sustainable, biodegradable, eco-friendly and flexible electronic devices and (Bio) sensors, Biosensors and Bioelectronics: X 14 (2023) 100371.

[439] S. Lepak-Kuc, A. Kądziela, M. Staniszewska, D. Janczak, M. Jakubowska, E. Bednarczyk, T. Murawski, K. Piłczyńska, Z. Żołek-Tryznowska, Sustainable, cytocompatible and flexible electronics on potato starch-based films, Scientific Reports 14(1) (2024) 18838.

[440] H. Xiang, Z. Li, H. Liu, T. Chen, H. Zhou, W. Huang, Green flexible electronics based on starch, npj Flexible Electronics 6(1) (2022) 15.

[441] M. Irimia-Vladu, E.D. Głowacki, G. Voss, S. Bauer, N.S. Sariciftci, Green and biodegradable electronics, Materials Today 15(7-8) (2012) 340–346.

[442] H. Zhu, Z. Xiao, D. Liu, Y. Li, N.J. Weadock, Z. Fang, J. Huang, L. Hu, Biodegradable transparent substrates for flexible organic-light-emitting diodes, Energy & Environmental Science 6(7) (2013) 2105–2111.

[443] E. Luoma, M. Välimäki, J. Ollila, K. Heikkinen, K. Immonen, Bio-based polymeric substrates for printed hybrid electronics, Polymers 14(9) (2022) 1863.

[444] J. Kim, R. Kumar, A.J. Bandodkar, J. Wang, Advanced materials for printed wearable electrochemical devices: A review, Advanced Electronic Materials 3(1) (2017) 1600260.

[445] C.J. Reese, G.M. Musgrave, J. Wong, W. Pan, J. Uehlin, M. Zadan, O.M. Awartani, T.J. Wallin, C. Wang, Photopatternable, degradable, and performant polyimide network substrates for e-waste mitigation, RSC Applied Polymers (2024).

[446] A. Morfa, T. Rödlmeier, N. Jürgensen, S. Stolz, G. Hernandez-Sosa, Comparison of biodegradable substrates for printed organic electronic devices, Cellulose 23 (2016) 3809–3817.

[447] Y. Khan, A. Thielens, S. Muin, J. Ting, C. Baumbauer, A.C. Arias, A new frontier of printed electronics: flexible hybrid electronics, Advanced Materials 32(15) (2020) 1905279.

[448] W.O. Herrmann, H. Wolfram, Process for the preparation of polymerized vinyl alcohol and its derivatives, Google Patents, 1928.

[449] A. Polymers, Hydropol. https://www.aquapakpolymers.com/science/.

[450] E. Chiellini, A. Corti, S. D'Antone, R. Solaro, Biodegradation of poly (vinyl alcohol) based materials, Progress in Polymer science 28(6) (2003) 963–1014.

[451] R. Premraj, M. Doble, Biodegradation of polymers, Indian Journal of Biotechnology 4(2) (2005) 186–193.

[452] P. Ghosh, S. Roy, A. Banik, Usage of microbes for the degradation of paint contaminated soil and water, Microbes and Microbial Biotechnology for Green Remediation, Elsevier2022, pp. 601–617.

[453] M.R. Havstad, Biodegradable plastics, Plastic waste and recycling, Elsevier2020, pp. 97–129.

[454] C.K. GmbH, Water vapor permeability of various plastic films, 2021. https://www.cmc.de/en/blog/know-how-5/water-vapor-permeability-of-various-plastic-films-181.

[455] S. Shaikh, M. Yaqoob, P. Aggarwal, An overview of biodegradable packaging in food industry, Current Research in Food Science 4 (2021) 503–520.

[456] V. Goodship, D. Jacobs, Polyvinyl alcohol: materials, processing and applications, Smithers rapra technology2009.

[457] Y. Alvarado, C. Muro, J. Illescas, F. Riera, Chapter 5—Polymer Nanoparticles for the Release of Complex Molecules; Holban, A.-M., Grumezescu, AM, Eds, Elsevier: Amsterdam, The Netherlands, 2019.

[458] P.C. Nath, N.B. Nandi, A. Tiwari, J. Das, B. Roy, Applications of nanotechnology in food sensing and food packaging, Nanotechnology Applications for Food Safety and Quality Monitoring, Elsevier2023, pp. 321–340.

[459] B. Liu, J. Zhang, H. Guo, Research progress of polyvinyl alcohol water-resistant film materials, Membranes 12(3) (2022) 347.

[460] L.T. Sin, B.S. Tueen, Plastics and Sustainability: Practical Approaches, Elsevier2022.

[461] Y. Dong, L. Zhang, J. Shen, M. Song, H. Chen, Preparation of poly (vinyl alcohol)-sodium alginate hollow-fiber composite membranes and pervaporation dehydration characterization of aqueous alcohol mixtures, Desalination 193(1-3) (2006) 202–210.

[462] R.A. Abed, M.A. Habeeb, Preparation and study optical properties of (PVA-PVP-CrCl2) composites, Industrial Engineering Letters 3(7) (2013) 606–610.

[463] R. Singh, S. Gautam, B. Sharma, P. Jain, K.D. Chauhan, Biopolymers and their classifications, Biopolymers and their Industrial Applications, Elsevier2021, pp. 21–44.

[464] K. Katopodis, A. Kapourani, E. Vardaka, A. Karagianni, C. Chorianopoulou, K.N. Kontogiannopoulos, D.N. Bikiaris, K. Kachrimanis, P. Barmpalexis, Partially hydrolyzed polyvinyl alcohol for fusion-based pharmaceutical formulation processes: Evaluation of suitable plasticizers, International Journal of Pharmaceutics 578 (2020) 119121.

[465] B.P.F. (BPF), Polyvinyl Alcohol (PVOH).

[466] C.M. Hassan, P. Trakampan, N.A. Peppas, Water solubility characteristics of poly (vinyl alcohol) and gels prepared by freezing/thawing processes, Water soluble polymers: solutions properties and applications (2002) 31–40.

[467] A. Kumar, S.S. Han, PVA-based hydrogels for tissue engineering: A review, International journal of polymeric materials and polymeric biomaterials 66(4) (2017) 159–182.

[468] S.H. Oh, S.G. Kang, E.S. Kim, S.H. Cho, J.H. Lee, Fabrication and characterization of hydrophilic poly (lactic-co-glycolic acid)/poly (vinyl alcohol) blend cell scaffolds by melt-molding particulate-leaching method, Biomaterials 24(22) (2003) 4011–4021.

[469] Y. Liu, Y. Fu, Z. Xu, X. Xiao, P. Li, X. Wang, H. Guo, Solubilization of Fully Hydrolyzed Poly (vinyl alcohol) at Room Temperature for Fabricating Recyclable Hydrogels, ACS Macro Letters 12(11) (2023) 1543–1548.

[470] C.K. Haweel, S.H. Ammar, Preparation of polyvinyl alcohol from local raw material, Iraqi Journal of Chemical and Petroleum Engineering 9(1) (2008) 15–21.

[471] A. Enterprise, Polyvinyl Alcohol, 2024. https://ankushenterprise.com/products/chemicals/polyvinyl-alcohol/.

[472] M. Shimao, T. Tamogami, S. Kishida, S. Harayama, The gene pvaB encodes oxidized polyvinyl alcohol hydrolase of Pseudomonas sp. strain VM15C and forms an

operon with the polyvinyl alcohol dehydrogenase gene pvaA, Microbiology 146(3) (2000) 649–657.

[473] T. Suzuki, Y. Ichihara, M. Yamada, K. Tonomura, Some characteristics of Pseudomonas 0–3 which utilizes polyvinyl alcohol, Agricultural and Biological Chemistry 37(4) (1973) 747–756.

[474] B. Kim, C. Sohn, S. Lim, J.-W. Lee, W. Park, Degradation of polyvinyl alcohol by Sphingomonas sp. SA3 and its symbiote, Journal of Industrial Microbiology and Biotechnology 30(1) (2003) 70–74.

[475] P. Aisbl, S. Deconinck, Final report benefits and challenges of bio-and oxo-degradable plastics a comparative literature study, Polymers for Advanced Technologies 32(4) (2013) 1–16.

[476] F. Kawai, X. Hu, Biochemistry of microbial polyvinyl alcohol degradation, Applied microbiology and biotechnology 84(2) (2009) 227–237.

[477] E. Chiellini, A. Corti, S. D'Antone, R. Solaro, Biodegradation of PVA-based formulations, Macromolecular Symposia, Wiley Online Library, 1999, pp. 127–139.

[478] B. Bharathiraja, J. Jayamuthunagai, M. Jayakumar, M.A. Kirubakaran, P. Vivek, M. Chandran, R.P. Kumar, Biodegradation of Poly (vinyl alcohol) using Pseudomonas alcaligenes, Asian Journal of Chemistry 25(15) (2013) 8663.

[479] S. Suganthi, S. Mohanapriya, V. Raj, S. Kanaga, R. Dhandapani, S. Vignesh, J. Kalyana Sundar, Tunable physicochemical and bactericidal activity of multicarboxylic-acids-crosslinked polyvinyl alcohol membrane for food packaging applications, ChemistrySelect 3(40) (2018) 11167–11176.

[480] H.-J. Kwon, S.-M. Hong, S.-M. Park, C.W. Lee, Characterization of acid-modified polyvinyl alcohol and its application to barrier-coated paper for eco-friendly food packaging, Food Packaging and Shelf Life 43 (2024) 101271.

[481] F.-Y. Zheng, R. Li, J. Hu, J. Zhang, X. Han, X. Wang, W.-R. Xu, Y. Zhang, Chitin and waste shrimp shells liquefaction and liquefied products/polyvinyl alcohol blend membranes, Carbohydrate polymers 205 (2019) 550–558.

[482] F. Zhao, D. Yao, R. Guo, L. Deng, A. Dong, J. Zhang, Composites of polymer hydrogels and nanoparticulate systems for biomedical and pharmaceutical applications, Nanomaterials 5(4) (2015) 2054–2130.

[483] N.A. Al-Tayyar, A.M. Youssef, R.R. Al-Hindi, Antimicrobial packaging efficiency of ZnO-SiO2 nanocomposites infused into PVA/CS film for enhancing the shelf life of food products, Food Packaging and Shelf Life 25 (2020) 100523.

[484] I.L. Soares, J.P. Chimanowsky, L. Luetkmeyer, E.O.d. Silva, D.d.H.S. Souza, M.I.B. Tavares, Evaluation of the influence of modified TiO2 particles on polypropylene composites, Journal of Nanoscience and Nanotechnology 15(8) (2015) 5723–5732.

[485] K. Choo, Y.C. Ching, C.H. Chuah, S. Julai, N.-S. Liou, Preparation and characterization of polyvinyl alcohol-chitosan composite films reinforced with cellulose nanofiber, Materials 9(8) (2016) 644.

[486] V. Nayak, M.S. Jyothi, R.G. Balakrishna, M. Padaki, A.F. Ismail, Preparation and characterization of chitosan thin films on mixed-matrix membranes for complete removal of chromium, ChemistryOpen 4(3) (2015) 278–287.

[487] J. Sun, G. Sun, X. Zhao, X. Liu, H. Zhao, C. Xu, L. Yan, X. Jiang, Y. Cui, Ultrafast and efficient removal of Pb (II) from acidic aqueous solution using a novel polyvinyl alcohol superabsorbent, Chemosphere 282 (2021) 131032.

[488] S.-J. Kim, P.K. Bae, M. Choi, J.O. Keem, W. Chung, Y.-B. Shin, Fabrication and Application of Levan–PVA Hydrogel for Effective Influenza Virus Capture, ACS applied materials & interfaces 12(26) (2020) 29103–29109.

[489] X. Xu, J. Zhao, M. Wang, L. Wang, J. Yang, 3D printed polyvinyl alcohol tablets with multiple release profiles, Scientific reports 9(1) (2019) 12487.

[490] A. Cataldi, D. Rigotti, V. Nguyen, A. Pegoretti, Polyvinyl alcohol reinforced with crystalline nanocellulose for 3D printing application, Materials Today Communications 15 (2018) 236–244.

[491] M. Shabbir, S. Ahmed, J.N. Sheikh, Frontiers of textile materials: polymers, nanomaterials, enzymes, and advanced modification techniques, John Wiley & Sons2020.

[492] A. Barbato, A. Apicella, F. Malvano, P. Scarfato, L. Incarnato, High-barrier, biodegradable films with polyvinyl alcohol/polylactic acid+ wax double coatings: influence of relative humidity on transport properties and suitability for modified atmosphere packaging applications, Polymers 15(19) (2023) 4002.

[493] L.M. Pop, A. Mihaly Cozmuta, C. Nicula, L. Mihaly Cozmuta, A. Peter, Attempts to Obtain Material Based on Polyvinyl Alcohol with Barrier Properties against Water Vapor, Applied Sciences 14(10) (2024) 4310.

[494] M. Schmid, S. Sängerlaub, O. Miesbauer, V. Jost, J. Werthan, C. Stinga, D. Samain, C. Stramm, K. Noller, K. Müller, Water repellence and oxygen and water vapor barrier of PVOH-coated substrates before and after surface esterification, Polymers 6(11) (2014) 2764–2783.

[495] G. ASTM, Standard practice for determining resistance of synthetic polymeric materials to fungi, American Society for Testing and Materials, 2002.

[496] H. Klumbies, L. Müller-Meskamp, T. Mönch, S. Schubert, K. Leo, The influence of laterally inhomogeneous corrosion on electrical and optical calcium moisture barrier characterization, Review of Scientific Instruments 84(2) (2013).

[497] J. Bertrand, S. George, Atomic layer deposition on polymers for ultralow water vapor transmission rates: the Ca test, 54th Ann. Tech. Conf. Proc., 2011.

[498] A. Chamas, H. Moon, J. Zheng, Y. Qiu, T. Tabassum, J.H. Jang, M. Abu-Omar, S.L. Scott, S. Suh, Degradation rates of plastics in the environment, ACS Sustainable Chemistry & Engineering 8(9) (2020) 3494–3511.

[499] K.A. Whitehead, M. Amin, T. Deisenroth, C.M. Liauw, J. Verran, Interfacial surface properties of compression moulded hydrolysed Polyvinyl Acetate (PVAc) using different release materials, Symmetry 14(10) (2022) 2063.

[500] J. Aromaa, M. Kekkonen, M. Mousapour, A. Jokilaakso, M. Lundström, The Oxidation of Copper in Air at Temperatures up to 100 C, Corrosion and Materials Degradation 2(4) (2021) 625–640.